CONTRIBUTIONS TO THE EXPERIMENTAL INVESTIGATION AND ANALYSIS OF AEROFOIL DYNAMIC STALL

by

John Gordon Leishman B.Sc.

Dissertation submitted to the Faculty of Engineering, University of Glasgow, for the Degree of Doctor of Philosophy.

MARCH, 1984

TABLE OF CONTENTS

Page

Page

Page

ACKNOWLEDGEMENTS

The author wishes to express his sincere gratitude to Dr. Rodderick Galbraith for his supervision, assistance and advice throughout the work described in this Dissertation. Additional gratitude is expressed to Professor Bryan Richards for his guidance and support. The author also wishes to thank Mr. Geoff Byham and Mr. Tom Beddoes, of Westland Helicopters Ltd., who acted as external supervisors for the work.

The author wishes to acknowledge the financial support of the Science and Engineering Research Council (SERC) and Westland Helicopters Ltd., under SERC CASE studentship 80513408. Additional support was provided by the Royal Aircraft Establishment (RAE) under MOD agreement 2048/026XR/STR, and this is also gratefully acknowledged.

The help and advice of the following people is also gratefully acknowledged by the author:-

At Glasgow University - Mr. Lup Seto, Mr. Richard Gordon, Mrs Effie Murry-Smith, Mr. Tony Smedley, Mr. David Whitelaw, Mr. John Kinnear, Mr. Bert Carrol, Mr. Jackie Holmes, Mr. John Dunning, Mr. Nat McGee, Miss Anne KcKinnon and Mr. James Barrowman.

At the Royal Aircraft Establishments - Mr. Peter Wilby, Mr. John Riley and Mr. Dave McOwat.

At Westland Helicopters Ltd - Mr. John Perry, Mr. Chick, Mr. Brake, Mr. Stuart McDougall and Mr. Hector Figueiredo.

Finally, thanks are due to Mr. Tom Beddoes who checked the manuscript and suggested useful improvements, Mrs Pam Downton who typed the manuscript, and Miss April Caldock who aided in the preparation of the diagrams.

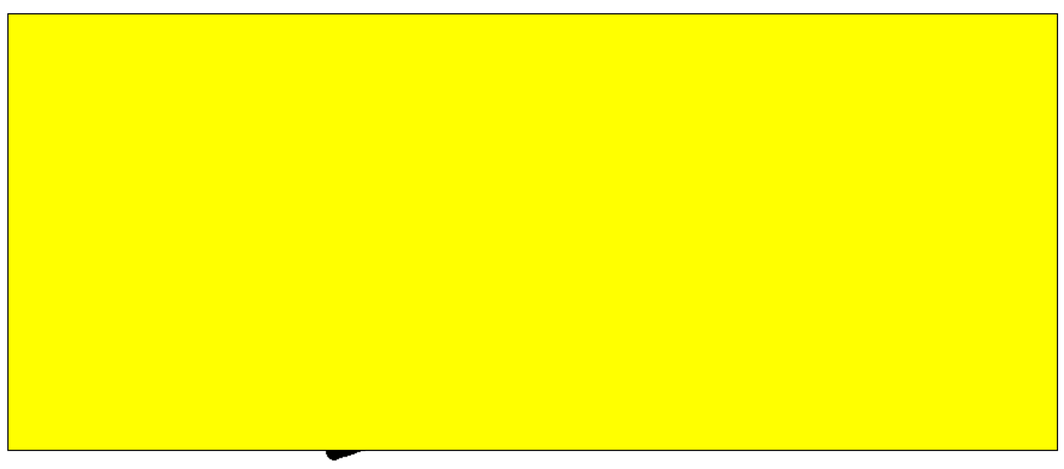

J.G. LEISHMAN

MARCH, 1984

The work described in this Dissertation was carried out at the Department of Aeronautics and Fluid Mechanics, University of Glasgow between September 1980, and October 1983, and is original in content except where indicated.

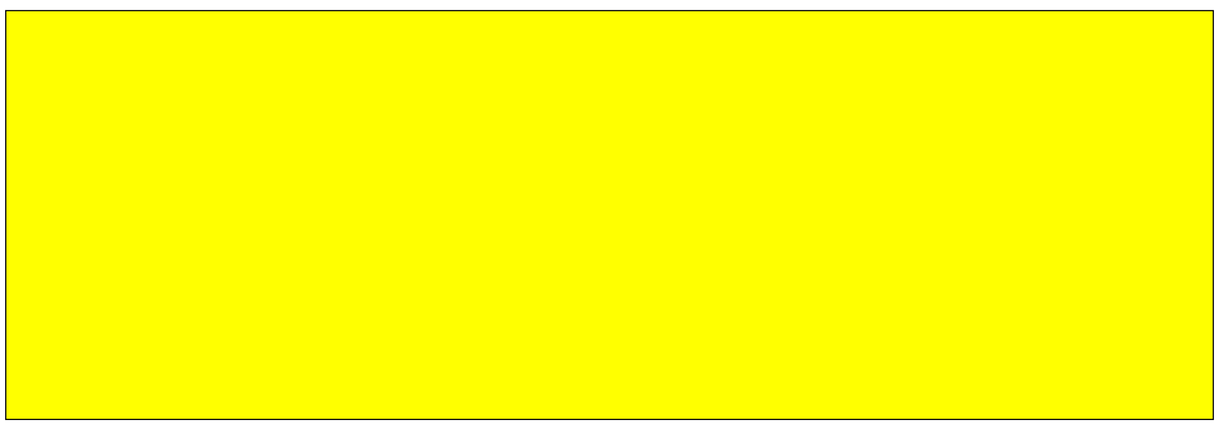

JOHN GORDON LEISHMAN

MARCH, 1984

ABSTRACT

A new facility for the investigation of dynamic stall on two-dimensional aerofoils has been developed. This facility has been used to initiate a program of research into the nature of trailing-edge flow separation effects on the dynamic stall process. An initial series of tests have been conducted to validate the results and to provide a data base for further investigations.

The facility has utilised a DEC MINC-11 micro-computer to control the tests, acquire and present the data. Details of the design of the facility, including the wind tunnel aerofoil, the aerofoil pitch drive mechanism, instrumentation and data acquisition system are described. A package of software has been developed for the microcomputer in order to perform a variety of functions relating to the successful operation of the facility.

The NACA 23012 aerofoil was selected for the initial investigations, the aerodynamic characteristics of which were examined under both static and oscillatory angle of attack conditions. The outputs from thirty miniature pressure transducers, distributed around the aerofoil chord, were acquired simultaneously along with the geometric angle of attack and free-stream dynamic pressure. A limited amount of hot-film anemometry data were also acquired for analysis.

Prior to the measurements, a series of flow visual-isation tests were conducted to assess the quality of the two-dimensional flow over the aerofoil surface, which was found to be good up to the onset of stall. Static stall was found to occur on the aerofoil by the mechanism of abrupt trailing-edge separation, with an increasing stall abruptness with increasing Reynolds number.

Generally, the qualitative features inferred during dynamic stall were similar to those documented previously by other investigators, including the formation of a vortex disturbance shed from the aerofoil leading-edge region. Although trailing-edge flow separation was found to be suppressed, even at very low pitch rates, flow reversals within the boundary layer prior to the vortex shedding were discerned. A possible interaction between the flows at the aerofoil trailing and leading-edges may have existed, although it was clear that further experiments would be required to clarify the true nature of this interaction, and relate this to the aerofoil pitch rate. Some suggestions have been put forward in order to achieve this goal based on observations in the present work.

NOMENCLATURE

C	aerofoil chord
C_L	lift coefficient
C_{L_α}	lift curve slope, /deg
$C_{L\ MAX}$	maximum lift coefficient
C_m	quarter-chord pitching moment
$C_{m\ MIN}$	minimum pitching moment
$C_{m\ LE}$	leading-edge pitching moment
C_N	normal force coefficient
Cp	pressure coefficient
D.F.	pitch damping factor, $-\oint C_m . d\alpha$
f	oscillation frequency, Hz
k	reduced frequency, $\omega C/2U$
M_∞	free-stream Mach number (also M)
Re	Reynolds number based on aerofoil chord
t	time, sec
U_∞	free-stream velocity
X	chordwise co-ordinate
Y	vertical co-ordinate
α	angle of attack, deg
$\dot{\alpha}$	pitch rate, deg/sec
α_a	oscillation amplitude, deg
α_m	mean angle of attack, deg
α_{ss}	static stall angle, corresponding to $C_{L\ MAX}$
Λ	reference angle, $\omega t \times 180/\pi$, deg
Δ	increment
ϕ	phase angle
ω	angular frequency, rad/sec
μ	viscosity

CHAPTER 1

INTRODUCTORY

1.1 Introduction

Dynamic stall occurs on a lifting aerofoil when subjected to an increase in angle of attack which takes it through the normal static stall angle at some significant rate. During this process, it is generally observed that the lift on the aerofoil increases, without any major change in the lift-curve slope, until at some angle of attack, depending on the preceding motion, a surge in the lift force and roll-off in the pitching moment occurs.

The phenomenon of dynamic stall, which is largely controlled by the viscous boundary layer on the aerofoil surface plays an important role in the successful aerodynamic design and operation of helicopter rotor blades. Under high speed forward flight conditions, the blades on the retreating side of the rotor disk encounter a reduced dynamic pressure and as a result of this, high blade performance requires high lift coefficients in this region. These large lift coefficients are generated through large angles of attack, often exceeding the maximum angle for which the boundary layer can remain attached to the aerofoil surface, and take advantage of dynamic effects on the aerofoil stall process. Until recently, it has been difficult to quantify the magnitudes of the aerodynamic loadings during dynamic stall and to define completely the significance of the aerofoil motion, the Reynolds number and free-stream Mach number.

Although much has been learned of the gross features, it is apparent that further research is required into the detailed fluid mechanics of dynamic stall.

During unsteady aerofoil motion, the fluid mechanics of the stall can be considerably different to its static counterpart. Firstly, at significant rates of pitch it has been observed that the boundary layer remains attached to the aerofoil surface to angles of attack substantially higher than could be attained under static conditions, with a corresponding increase of maximum lift. Kramer (1932) appears to have been one of the first to recognise this fact. Secondly, when stall occurs, it is often characterised by the shedding of a vortex-like disturbance from the aerofoil leading-edge region. The passage of this vortex across the aerofoil upper surface not only induces increases in lift, but also significantly increases the nose-down pitching moment, due to the redistribution of chordwise pressure. A conceptual understanding of this vortex shedding phenomenon was first given by Ham (1968). After the vortex disturbance passes the aerofoil trailing-edge, a sudden loss of lift occurs, accompanied by a peak in the pitching moment. Subsequently, the flow progresses to a state of full separation over the aerofoil upper surface, and when the angle of attack falls below the static stall angle, the flow will reattach from the leading-edge. The dynamic stall process is illustrated schematically in Fig. 1.1 for a NACA 0012 aerofoil under an oscillatory change of angle of attack.

Experimental investigations by numerous researchers, have shown that the details of dynamic stall depend on a large number of parameters (Table 1.1). Furthermore, a number of

phenomena have been noted that may share roles of importance in determining the onset of stall. The characteristic leading-edge vortex shedding phenomena has been well documented in the literature (see for example - Ham et al, 1968; Scruggs, 1971; Johnson et al, 1972; Carr et al, 1977.) Various degrees of vortex shedding intensity may occur, depending primarily on the aerofoil motion and the extent to which stall is penetrated. Under "strong" dynamic stall conditions, that is when the fluid mechanics are dominated by the vortex shedding phenomena, the qualitative results have been shown to be relatively independent of the parameters listed, for example in Table 1.1. However, under "light" stall conditions, the greatest variability in the fluid mechanics are evident, with the aerofoil geometry and static separation characteristics being important factors for consideration. A discussion of the features of "light" and "strong" dynamic stall are given by McCroskey et al, (1980). Also, it appears that "light" dynamic stall is an area into which further research should be directed.

Theoretically, the fluid mechanics of dynamic stall are governed by the Navier-Stokes equations. Because of the enormous amount of computing time involved in their solution and the present inability to successfully model turbulence, this approach has not been widely contemplated. However, analysis by the Navier-Stokes equations for laminar flow on oscillating aerofoils has led to some interesting results (see Mehta, 1977).

Experimentally, a number of approaches have been made to examine the features of dynamic stall under widely varying conditions. Much of this research has been carried out

using two-dimensional wind tunnel tests on oscillating aerofoils by the helicopter (and related) industries, where stall is often a limiting factor of the rotor design and accurate predictions are consequently of great importance. As a product of this research, a number of semi-empirically based dynamic stall predictive models have been developed, which have been used with variable amounts of success to determine the dynamic airloadings on helicopter rotors.

Although much has been learned of dynamic stall, it is clear that its understanding is still far from complete. Theoretical methods for analysis are still in their infancy, primarily because of present computational limitations. Until such time when a more complete theoretical analysis is possible, more research is required into the detailed experimental aspects of dynamic stall.

The present work is concerned with the development of a facility to investigate aspects of dynamic stall on two-dimensional aerofoils in the environment of a wind tunnel, and in particular, to provide preliminary information into the effects of trailing-edge separation on the onset of the dynamic stall process.

1.2 Background to the problem considered.

1.2.1 Helicopter rotor environment

The helicopter, by design, operates within its own turbulent wake. Thus, there are numerous unsteady aerodynamic phenomena to which the rotor blades may be subjected to within the course of a single rotor revolution. Unsteadiness exists, to some degree, throughout the rotor flight envelope, however, the severity of the dynamic airloads

associated with the unsteady aerodynamics depends upon the actual flight conditions, i.e. forward flight, manoeuvers, etc. Some of the most obvious unsteady aerodynamic phenomena that contribute to the rotor airloadings are illustrated in Fig (1.2).

In order to maintain lateral trim and propulsive force in forward flight, the rotor blades are subjected to a (once per rev.) periodic change in angle of attack. Stall may then occur on the retreating side of the rotor disk where the angle of attack is greatest. A typical angle of attack distribution for a contemporary helicopter rotor in forward flight at a moderately high speed is illustrated in Fig 1.3. Up to the onset of stall, the loadings on the rotor can be represented by quasi-static aerodynamics. When stall occurs however, the rotor blade dynamics and elastic properties become important in determining the local blade angles of attack, and the subsequent aerodynamic loadings and aero-elastic response can lead to the onset of stall flutter. This phenomenon often limits the rotor flight envelope and consequently, the understanding of dynamic stall and the prediction of its onset, is important from a rotor design point of view. Excellent reviews on the occurrence of dynamic stall within the helicopter rotor environment are given by Jones (1972) and Byham et al (1977).

1.2.2 Static aerofoil stall

Stall is most easily described in terms of a normal force (or lift) relationship with the aerofoil angle of attack. At low angles of attack, no significant amounts of boundary layer separation are present on the aerofoil surface, and

the normal force varies linearly with angle of attack (as predicted by inviscid flow theory). At higher angles of attack however, the normal force versus angle of attack relationship becomes non-linear; the decrease in the slope of the curve being due to thickening of the boundary layer (and perhaps some trailing-edge separation). Further increases of the angle of attack lead to larger deviations from the linear relationship, and eventually a condition corresponding to a maximum in the normal force is reached, after which a further increase of angle of attack leads to a decrease of the normal force. The viscous flow about the aerofoil under these conditions is characterised by large separated regions on the aerofoil upper surface and in the wake - and the aerofoil is said to be stalled. In addition to the normal force variation during stall, the pitching moment variation about the quarter-chord axis shows large changes from the near zero value characteristic of unstalled flow, indicating a significant change in the centre of pressure.

There are a number of mechanisms that can be involved during the static stall of an aerofoil in subsonic flow. A general stall classification has been postulated by McCullough et al (1951), in which there are three categories:

(1) thin-aerofoil stall,

(2) leading-edge stall,

(3) trailing-edge stall.

As the name suggests, thin-aerofoil stall is usually observed on thin or sharp leading-edged aerofoils, and is categorised by the formation of a "long bubble", in which the reattachment point moves rearward with increasing angle of attack. Stall occurs when the reattachment point reaches the trailing-edge.

Leading-edge stall is usually related to the formation of a laminar separation bubble just downstream of the leading-edge suction peak. With increasing angle of attack, the leading-edge adverse pressure gradient becomes too great for the boundary layer to support, and the resulting separation leads to an abrupt loss of lift. Observations indicate that there may be two subsets of the leading-edge stall class. One is known as "bubble bursting", which is due to the sudden failure of the turbulent boundary layer to reattach to the aerofoil surface. The other is due to "reseparation", which is an abrupt separation of the turbulent boundary layer downstream of the laminar separation bubble. Gault (1956), and more recently Van den Berg (1980), have shown that in the majority of practical aerofoil applications, reseparation may be the more likely mechanism of leading-edge stall. A correlation curve has been obtained by Evans et al (1959), in which a relationship was formed between the suction peak velocity and an idealised adverse velocity gradient on aerofoils which exhibited stall by the reseparation mechanism. As will be described later, use can be made of this correlation to predict the angle of attack for stall, but only for this class of aerofoil.

Trailing-edge stall generally occurs on moderately thick aerofoils ($\geq$10% X/C). With increasing angle of attack, the turbulent boundary layer at the aerofoil trailing-edge eventually reaches a condition when it can no longer sustain the adverse pressure gradient and separates from the surface. Again, trailing-edge stall can be divided into two subsets: gradual, or abrupt. With a gradual trailing-edge stall, a well rounded peak in the lift-curve slope is generally evident.

With an abrupt trailing-edge stall however, there is little change in the lift-curve slope prior to stall, and it is often difficult to distinguish from a leading-edge stall in the absence of any further information.

Examples of the characteristics of the three basic types of static stall described above are illustrated schematically in Fig. 1.4. It should be noted however, that an aerofoil may exhibit a stall characteristic which is a hybrid of the basic stall types. Also, Reynolds number effects are often significant in relation to the aerofoil stalling characteristics (see for example; McCullough, 1955 and Gault, 1957).

1.2.3 Laminar separation bubbles and turbulent separation.

From the foregoing, and as a preface to the discussion of dynamic stall, it is clear that two important flow phenomena require further detailed consideration; the formation of a laminar separation bubble, and turbulent separation.

For many aerofoils, the transition from laminar to turbulent boundary layer flow is carried out via a separation bubble (Fig 1.5). The bubble begins at the point of laminar separation, and the flow above the separation zone becomes turbulent. Under moderately adverse pressure gradients, the turbulent boundary layer will reattach to the aerofoil surface and close the separation bubble. The length of this bubble is typically 1-2% of chord, and generally makes a small, but significant alleviation to the leading-edge adverse pressure gradient (Fig 1.6). Under certain aerofoil pressure loadings, the leading-edge adverse pressure gradient becomes too great for turbulent reattachment downstream of the bubble to occur, and the bubble is said to have "burst". This subsequently

leads to an abrupt separation over the remainder of the aerofoil upper surface, with a corresponding loss of lift. Studies on laminar separation bubbles have been carried out by many investigators, including Gault (1955), Owen et al (1955), Woodward (1967), Dobbing (1972) and Erlich (1973).

Apart from the previously described reseparation mechanism, turbulent separation first occurs near the trailing-edge of an aerofoil and moves forward with increasing angle of attack. Separation refers to the detachment of the flow from the aerofoil surface, and in steady two-dimensional incompressible flow its onset corresponds to the vanishing of the average surface shear stress; that is where

$$\tau_w = \mu \frac{\partial u}{\partial y}\bigg|_{y=0} = 0$$

The separating boundary layer subsequently exists as a free shear layer which forms the boundary of the aerofoil wake (see Figs 1.7 and 1.11). This classical definition of separation, however, has been shown to be strictly true only for laminar flows, and that turbulent separation is not a single event but rather occurs over a zone which encloses a transition from attached to separated flow. This is detailed by Sandborn et al (1961), and extended by Kline et al (1981).

1.2.4 Dynamic stall.

The performance of an aerofoil during dynamic stall plays an important role in determining the overall performance of a helicopter. The lift from the aerofoil (and hence the thrust from the rotor) is highly dependent on the aerofoil dynamic stall characteristics and their variation within the unsteady periodic environment of the rotor flowfield. Furthermore, undesirable effects such as stall flutter give rise to aircraft

vibration and undue stress levels which can reduce the fatigue life of the rotor - hence the requirement for an adequate understanding of the dynamic stall phenomenon.

One of the major reasons that dynamic stall is more difficult to analyse than static stall is its dependence on a much wider range of parameters. Furthermore, a number of boundary layer phenomena may share roles of importance in determining the stall onset and the subsequent development of separated flow. Attempts have been made both experimentally and theoretically to analyse the mechanisms involved and to assess their relative importance.

It has been recognised for some time, that the boundary layer remains attached to the aerofoil surface to higher angles of attack under unsteady conditions, than could be obtained under static conditions. Carta (1971) postulated that the departure of the aerofoil pressure distribution at a given angle of attack from its steady flow counterpart may be of importance in delaying the onset of separation, due to the alleviation of chordwise pressure gradients. McCroskey (1973) showed that this postulation was essentially valid, although it was clear that other mechanisms were involved in the stall delay. Singleton et al (1973) and Nash et al (1973) have examined the development of an unsteady boundary layer in a prescribed external pressure distribution. Their work has shown that, time-dependence results in delays of the pressure development and in the onset of flow reversal within the boundary layer. They have suggested that these mechanisms could also be of significance during the conditions which exist on an aerofoil in pitching motion.

The classical Prandtl boundary layer equations which are simplifications to the full Navier-Stokes equations, give considerable insight into the analysis of the flow development on an unsteady aerofoil. (The Prandtl boundary layer momentum equation is defined in Fig 1.9). Several authors have utilised these boundary layer equations, incorporating a turbulence model modified to include unsteady terms, to investigate some of the problems associated with the delay in the onset of dynamic stall. For example, Fig 1.8 illustrates a situation of an aerofoil at a relatively large angle of attack undergoing pitching motion. At the leading-edge, large external pressure gradients exist, and the unsteady derivative in the boundary layer equation, dU/dt, is relatively unimportant compared with the spatial gradient U.dU/dX. Because of this, the leading-edge laminar boundary layer development would be expected to differ only slightly from its static counterpart, and this speculation has been borne out by calculation and experiment (see McCroskey et al, 1975). However, at the aerofoil trailing-edge, the unsteady boundary layer derivatives and the external velocity gradients are of comparable magnitude, and the aerofoil motion would generally have a considerable influence on the onset of flow reversal and separation (Fig. 1.10).

Both the effects of pressure gradient modifications and the development of the unsteady boundary layer have been analytically examined by Scruggs et al (1974) who have shown that the onset of flow reversal is delayed on a pitching aerofoil. It should be pointed out that flow reversal and separation are distinct boundary layer phenomena in unsteady

flows and the point where the average surface shear stress, τ_w, is zero, has no special significance. This has been demonstrated by Telionis (1977) and Williams (1977). Also, Sears et al, (1975) have indicated that for unsteady flows, separation always occurs downstream of the flow reversal point. Experimentally, this phenomenon has been shown to exist on a pitching aerofoil by McCroskey et al, (1976), where suppression of trailing-edge separation and observations of regions of flow reversal prior to separation were evident. This situation is illustrated, for example, in Fig (1.11) for a pitching aerofoil with minor trailing-edge separation, and is detailed in Fig (1.12).

Numerous experiments have shown the presence of a vortex-like disturbance, which is shed from the vicinity of the aerofoil leading-edge during dynamic stall. The consequences of this vortex in relation to the airloadings have been indicated previously. The actual process of the vortex initiation, however, has been the subject of a certain amount of controversy. Four boundary layer phenomena have been identified as possible mechanisms for the initiation of vortex shedding:

(1) The "bursting" of a laminar separation bubble.

(2) Reseparation downstream of a laminar separation bubble.

(3) Propogation of flow reversals within the turbulent boundary layer, towards the aerofoil leading-edge.

(4) Leading-edge shock wave - boundary layer interaction (for Mach numbers $\gtrsim 0.3$).

Initiation of leading-edge vortex shedding may involve one or more of these mechanisms, and will depend on the aerofoil geometry, etc. (as listed in Table 1.1). Further details of

vortex initiation mechanisms are given by Young (1981).-

As mentioned previously, deep dynamic stall is characterised by a well defined vortex shed from the leading-edge region, which subsequently dominates the aerofoil flow-field. It has been shown by McCroskey et al (1980), that under these conditions qualitative results for different aerofoils are very similar, except when the flow becomes supersonic at the leading-edge region at higher Mach numbers ($\gtrsim$0.3). Light dynamic stall on the other hand, that is when only small amounts of separation are allowed to develop on the aerofoil before the angle of attack is reduced, is known to be especially sensitive to all the parameters listed in Table 1.1. The quantitative behaviour is closely related to the static boundary layer separation characteristics, for example, leading-edge versus trailing-edge separation and changes in this behaviour with variations in the aerofoil motion, Reynolds and Mach numbers. It appears however, that irrespective of an aerofoil's static stalling characteristics, under dynamic conditions, the trend is towards leading-edge separation, although it is clear that this is an area where further research is required.

1.2.4 Predictive methods

Several approaches have been taken in the past to predict and analyse dynamic stall, both theoretical and empirical. Theoretical progress remains rather slow on this difficult problem, although a number of semi-empirical methods have been developed and continue to be improved. All the techniques that exist invoke assumptions and restrictions and are often tailored to model features of a specific stall regime. Brief

descriptions of current approaches are reviewed by McCroskey (1978) and Beddoes (1979).

The most fundamental formulation of the equations of motion for a viscous, compressible fluid are the Navier-Stokes equations. The present inability to solve for the turbulent boundary layer and the computing effort required, has so far limited their solution to low Reynolds numbers ($<10^4$), which are much lower than is realistic for most practical applications. The specific problem of dynamic stall under harmonic angle of attack variations has been examined by Mehta (1977), which probably represents the present state-of-the-art for this approach. Correlations with flow visualisations performed by Werlé (1976) for identical flow conditions have met with considerable success. The dynamic stall development was also found to be qualitatively similar to that which has been observed at higher Reynolds numbers. This has also been verified by low Reynolds number flow visualisations carried out by McAlister et al, (1977).

Current computational limitations and difficulties in defining the flow-field have, however, restricted most dynamic stall analyses to boundary layer and viscous-inviscid interaction approaches. The relevance of the Prandtl boundary layer equations in the understanding of dynamic stall onset, has been indicated previously. Calculations have so far indicated possible mechanisms (eg Scruggs et al, 1974), but it is clear that a coupled viscous-inviscid interaction procedure is required to overcome limitations of this approach.

Viscous-inviscid analyses have been made by Crimi et al, (1972), Crimi (1974) and Rao et al, (1978), each with variable amounts of success when applied to unsteady aerofoil problems.

Crimi et al based their analysis on a laminar separation bubble bursting criterion, but which has not gained widespread acceptance because of certain shortcomings in the analysis. This method has however, been examined in more detail by Shamroth et al, (1974), but modelling of trailing-edge separation was not included in the analysis. Rao et al, (1978) have modelled the effects of trailing-edge separation, but simplifications and assumptions in their analysis have led only to limited success. Recently, the justification of a laminar separation bubble bursting analysis for vortex initiation under dynamic conditions has been called into question by some investigators. By the application of a bounday layer trip designed to eliminate the leading-edge bubble, McCroskey et al, (1980) have shown that for aerofoils tested, the qualitative dynamic stall behaviour was similar to that of the untripped aerofoil. This observation suggests that bubble bursting may not be as an important mechanism as was previously thought, and that reseparation or the rapid forward movement of a thin region of reversed flow from the trailing-edge may be the more likely mechanism for vortex initiation. This is not to say that bubble bursting does not exist as a stall trigger mechanism, only that vortex shedding can exist without the presence of a laminar separation bubble. Clearly, interactions between flow reversals and the separation bubble may exist, and further research is required to confirm this speculation.

A number of semi-empirical predictive models for dynamic stall have been formulated, mainly on the basis of experimental data from oscillating two-dimensional aerofoil wind tunnel tests. Contributions in this field have been made by Johnson

(1969), Arcidiacono et al (1970), Bielewa (1975), Ericcson et al (1976), Beddoes (1978) and Tran et al (1980). These models attempt to correlate force and moment data as functions of the relevant parameters. Common to all the models is the fact that unsteady effects increase with increasing pitch rate, that is, rate of change of angle of attack. Also, it is clear that dynamic stall events develop over a finite time period. Hence, the non-dimensional parameters $\dot{\alpha}C/U_\infty$ and $U_\infty \Delta t/C$ appear in some form in all the empirical models. Current models are reviewed by Beddoes (1979), who also detailed one model of particular interest. This model is based on the concept of time delays, in recognition of the fact that dynamic stall events occupy finite time periods. As mentioned previously, there is a strong trend towards leading-edge type separation under unsteady conditions, irrespective of the aerofoil static characteristics, etc. This suggests that the use of a leading-edge flow criterion may be appropriate to indicate the onset of separation. The correlation of Evans et al, (1959) can be used to predict the angle of attack for stall onset for aerofoils which exhibit static stall by the reseparation mechanism (see for example Kao, 1974). This has been extended to the unsteady case by Beddoes (1978) who has incorporated it within the time-delay model, giving confident predictions of separation onset within a global model of dynamic stall. Beddoes has found however, that the behaviour of aerofoils which exhibited trailing-edge separation statically, were found to be more difficult to predict, especially at low pitch rates where the impact of trailing-edge separation is more significant.

1.2.6. Experimental facilities

McCroskey (1971) has shown that three-dimensional effects associated with the helicopter rotor geometry do not significantly contribute to the dynamic stall process. Further, Hicks et al (1971) have analytically shown that three-dimensional effects associated with the steady turbulent boundary layer on the rotor do not significantly delay the onset of stall. These observations lend encouragement to the investigation of dynamic stall on two-dimensional aerofoils. Experimental work has mainly proceeded along lines intended to simulate actual flight conditions for a helicopter rotor, and in the majority of cases, large data bases have been generated for use in semi-empirical dynamic stall predictive models. A number of experimental facilities have been developed, mainly within the USA (NASA, Boeing-Vertol), the UK (ARA) and France (ONERA). In particular, the NASA-Ames facility (see Carr et al, 1977 and McAlister et al, 1978) has been extensively used to examine the fundamental aspects of dynamic stall and probably represents the source of the bulk of published information on this complex phenomenon. In general, the features of each facility are very similar, with the use of a two-dimensional aerofoil undergoing pitching motion in a wind tunnel. Chordwise pressure information is usually recorded from miniature pressure transducers which are logged either in an analogue or digital format. Previously, only the ARA facility (see Landon, 1977) has utilised real-time analogue-to-digital conversions, the others using analogue records with off-line digitisation. An important disadvantage with the latter method is that data analysis is generally performed some time after the data was actually

recorded, and this procedure often makes a subsequent re-run of the test difficult or impossible if corrupted data is found. Also, with analogue recording, the analysis procedure is a much larger and more complex task, and in general, the advantages of on-line digitisation far outweigh analogue recording techniques in this respect.

One of the objectives of the present work was to design and develop an experimental facility for the investigation of dynamic stall, using a microcomputer to control the experiments, perform real-time analogue-to-digital data acquisition, with the corresponding analysis and presentation of results.

1.3 Purpose of the present work

The main objectives of the present work have been indicated or implied in the previous Sections. The objectives may be stated more precisely as follows:-

(1) to select an aerofoil profile, typical of current helicopter rotor profiles, which exhibits stall by the mechanism of trailing-edge separation at low Mach numbers.

(2) to suggest modifications to the selected aerofoil, that may enable the enhancement of trailing-edge separation, but without significantly altering the leading-edge pressure distribution.

(3) to design and develop both mechanical and electronic hardware to investigate the aerofoil's steady and unsteady aerodynamic characteristics within the environment of a low-speed wind tunnel, and to interface transducer outputs to a microcomputer for acquisition.

(4) to develop software for the microcomputer in order to acquire, process and present the data relating to the aerofoil aerodynamic characteristics.

(5) to investigate the steady and unsteady aerodynamic characteristics of the selected aerofoil profile for a wide range of test conditions in order to validate the test facility, and also to provide a data base for subsequent investigations.

(6) To make a preliminary investigation into the effects of trailing-edge flow separation on the dynamic stall process for the selected aerofoil, and to assess the direction in which future research in this area should be directed.

1.4 Outline of the Dissertation

The main body of the Dissertation is divided into eight Chapters headed by the Introductory.

Chapter 2 presents the reasoning behind the choice of aerofoil section for the present work. The latter part of this Chapter deals with an investigation into geometry modification of the basic aerofoil designed to enhance separation at the aerofoil trailing-edge.

The details of the experimental apparatus are described in Chapter 3. This Chapter is divided into two main sections. The first part describes the mechanical aspects of the hardware, with the second part dealing with the data acquisition system and the interface of transducers to the microcomputer.

Chapter 4 presents details of the software which was written to control the experiment, acquire the data and

present the results.

In Chapter 5, a summary is made of conditions under which the aerodynamic tests were carried out.

The results and discussion of the tests described in Chapter 5 are presented in Chapters 6 and 7; Chapter 6 dealing with the static tests, and Chapter 7 with the oscillatory tests.

Finally, Chapter 8 summarises the work of the previous Chapters, and highlights the main conclusions of the Dissertation. Also, a few suggestions are made to improve the experimental test facility and consideration is given to further research into trailing-edge flow separation effects on aerofoil dynamic stall.

CHAPTER 2

SELECTION OF AEROFOIL PROFILE

2.1 Introduction

As discussed in Chapter 1, aerofoil stalling characteristics are generally divided into three basic categories: thin-aerofoil stall, leading-edge stall or trailing-edge stall. Further, the leading-edge stall category can be subdivided into either laminar separation bubble "bursting" or reseparation, and trailing-edge stall, can be subdivided into either progressive or abrupt. Various combinations of all the preceding stall types are also known to exist.

For helicopter rotor applications, most aerofoils in general usage tend to lie within the leading-edge or abrupt stall category. However, the more recent use of cambered and unconventional aerofoil profiles have expanded the variability of stall characteristics, mainly towards trailing-edge stall types.

Under unsteady motion, trailing-edge separation has been noted to have certain effects on the dynamic stall onset. (See McCroskey et al, 1977, 1980 and Beddoes, 1979). Beddoes has speculated - that irrespective of an aerofoil's static stall characteristics, under unsteady motion gross flow separation is still dominated by flow conditions at the aerofoil leading-edge, although trailing-edge separation still has some degree of influence, especially at low pitch rates. The exact nature of the influence of trailing-edge separation on the stall onset is at present unclear, although

it is known that a certain amount of flow reversal takes place within the boundary layer at the aerofoil trailing-edge, prior to the onset of separation.

Two further objectives in the present work were defined on the basis of the preceding discussion. Firstly, to select a suitable aerofoil profile with a leading-edge suction distribution similar to those currently used in rotor applications, but which exhibited limited trailing-edge separation at low Mach numbers. Secondly, to suggest modifications to the basic aerofoil in order to enhance the degree of trailing-edge separation.

2.2 Basic profile

The aerofoil chosen for the current investigation was the NACA 23012 (Fig 2.1). This choice was made after consultations with Westland Helicopters Limited and was based on two main considerations:

(1) From reported lift and pitching moment data by Loftin et al, (1949) and Althaus et al, (1980) the NACA 23012 exhibits a rounding-off of the lift-curve slope close to maximum lift, which at low Reynolds numbers is characteristic of trailing-edge separation. With increasing Reynolds number however, the onset of stall becomes more abrupt, which is more characteristic of a leading-edge stall type. Thus, if tested under unsteady conditions, this aerofoil offered possible scope for the investigation of the dynamic effects of trailing-edge separation.

(2) The NACA 23012 is typical of current and projected helicopter main rotor profiles, and accumulation of unsteady pressure data at the lower Reynolds/Mach number regime, more appropriate to the inboard sections of the retreating blade,

may assist in dynamic stall prediction modelling.

Although originally reported by Jacobs et al, (1935) the NACA 23012 aerofoil and derivatives have received attention from the helicopter industries during the 1960's and 1970's.

Prior to this, helicopter rotor structural and dynamic problems were of primary consideration, and the symmetric NACA 0012 profile gave a good compromise for rotor requirements in terms of maximum lift, minimum pitching moments and drag divergence characteristics. Use of leading-edge camber, such as on the NACA 23012, leads to a significant aerodynamic improvement over the symmetric profile (Fig 2.2). An optimisation of leading-edge camber and nose radius has been carried out on the NACA 23012 aerofoil by Davenport et al (1966), resulting in the Boeing-Vertol VR profiles, which gave a further improvement in the aerodynamic characteristics for rotor applications. A similar investigation has also been carried out by Gregory et al, (1968). More recently, Wilby (1980) has reviewed the developments on a new series of aerofoils especially for use as helicopter rotor blade sections.

The NACA 23012 profile is derived from the NACA 230 camberline and the NACA 0012 thickness distribution, by plotting the thickness distribution normal to the camberline, as described by Abbott et al, (1945). The camberline and thickness distribution are defined by a number of theoretical aerodynamic and geometric considerations, which give the NACA 23012 profile a design lift coefficient of 0.3, a maximum camber at 15% chord, and a thickness ratio of 12%. The camberline and thickness distribution are both described by

algebraic expressions, making the co-ordinate generation procedure trivial when automatic digital processing is employed.

2.3 Modified profile

The secondary objective of this part of the work, was to suggest modifications to the basic NACA 23012 aerofoil profile, which may enable the enhancement of boundary layer separation at the aerofoil trailing-edge, but without significantly altering the leading-edge pressure distribution. It was suggested by Westland Helicopters' personnel, that this could possibly be accomplished by:-

(1) the application of blemishes, wedges or some other protuberance on the aerofoil upper surface trailing-edge to fix the position of separation, or

(2) the use of geometry modifications at the trailing-edge, thereby modifying the adverse pressure gradient, to which the boundary layer ultimately responds.

Effects on the NACA 0012 aerofoil by trailing-edge protuberances has been reported by Jacobs (1932), who concluded that the protuberance fixed the separation at a point on the aerofoil surface over a small range of angle of attack. Unpublished work by McCroskey and his co-workers at NASA-Ames (Private communication, 1981), made use of wedges to enhance trailing-edge separation, again with a similar conclusion. For unsteady aerofoil motion, the use of protuberance was considered unsatisfactory for the present work, particularly when any surface protuberance may prevent or disturb the movement of a time-dependent flow reversal within the boundary layer, and possibly obscure the true nature of the final stall process.

The use of aerofoil geometry modifications was considered a more satisfactory, although more complicated approach to the problem. Modifications to the leading-edge of the NACA 0012 aerofoil have been experimentally tested by McAlister et al, (1977). This approach gives a large degree of control over the leading-edge pressure gradient, which subsequently governs the initial development of the boundary layer, quite often changing the stall characteristic. However, in the present work, the requirement was that the leading-edge geometry remained fixed whilst modifying the trailing-edge, thereby closely maintaining the leading-edge pressure distribution, but possibly rendering the boundary layer more susceptible to separation at the trailing-edge.

Various trailing-edge geometry modifications were considered, and their effects on the pressure distribution and predicted separation points were assessed analytically. Initially, the superposition method (see Abbott et al, 1945) was used to conduct the examination, but was quickly superseded in favour of a numerical potential-flow analysis. This vortex-panel aerofoil flow analysis is discussed by Leishman and Galbraith (1981). Also, a potential flow-boundary layer interaction analysis discussed by Smetana et al (1975), was used to give estimations of the boundary layer development and separation point on selected modified geometries.

The modifications to the NACA 23012 aerofoil profile examined, were as follows:

(1) Replacement of the linear camberline (aft of 20.25% chord) by a parabolic camberline, starting at various chordwise locations.

(2) As (1), but using a cubic camberline.

(3) As (1), but using a NACA a = X camberline.

(4) Thickness variations aft of maximum thickness.

The modifications for camber, were made by matching local values of gradient and ordinates, and plotting the thickness distribution normal to this modified camberline. Similar matchings were made, in cases of thickness modifications, on the upper and lower aerofoil profiles.

A data base for the NACA 23012 was generated for the comparisons, using fifty aerofoil co-ordinates. Potential flow pressure data was presented graphically, and was used directly to compare with the "modified" pressure distributions. Additionally, the potential velocity gradient, U.dU/dX, was compared to give an indication of the possible likelihood of the boundary layer to exhibit separation. This comparison was performed on an intuitive basis.

Preliminary results from arbitrary geometry modifications showed that, as the majority of the pressure recovery took place within the first 20% chord, it was difficult to make gross changes to the pressure distribution, whether at the leading or trailing-edge, by moderate trailing-edge geometry modifications alone. Systematic variations of the four types of modification were carried out, with the modification initiating at various chordwise locations. Generally, camberline modifications were found more effective in changing the pressure and velocity gradient distributions, and subsequently the investigations into thickness modifications were discontinued.

Depending on the chordwise position of the modification initiation, a small disturbance was often found in the chordwise pressure distribution near this location. Analysis showed

that the boundary layer thickened in the region immediately downstream of this pressure disturbance. Also, the predicted separation point often stabilised in this region with increasing angle of attack. Parabolic camberline modifications were found to have comparatively large effects on the pressure and velocity gradients over large parts of the chord. Cubic camberline modifications, unless large, made little change, except in the region of 90% to 100% chord. Also, the modification initiation position was determined to be of secondary importance between 20.25% and 40% chord, and to reduce the number of test cases, this point was subsequently fixed at 35% chord. NACA a = X camberline modifications were successful in producing almost linear trailing-edge adverse pressure gradients, but generally were either too localised (a = 0.9), or little different from the basic distribution (a = 0.4), in each case giving little change to the predicted separation point onset with increasing angle of attack. Some examples of the various geometry changes and their effects are illustrated in Figs 2.3 to 2.7.

2.4 Conclusions and implications of aerofoil modifications

Based on the results from the analytic investigation into trailing-edge geometry modifications on the NACA 23012 aerofoil, a number of conclusions were made. It should be noted, that these conclusions are based on "engineering" predictions of the likelihood of trailing-edge separation enhancement.

(1) Parabolic or NACA a = X camberline modifications appeared to offer the greatest flexibility for varying the aft portion of the aerofoil pressure distribution, without significantly altering the leading-edge distribution.

Further, the variability in the angle of attack for-predicted separation onset was largest using these modifications.

(2) The effect of varying the "start of modification" point was found minimal between 20.25% and 40% chord, and was subsequently fixed at 35%. This was also found to be a good compromise in terms of the structural design of the wind tunnel model.

(3) In order to assess the true validity of an aerofoil profile designed for enhanced trailing-edge separation by the previously discussed method, it was recommended that a prospective design be experimentally tested (under static conditions) and the results compared with the theoretical analysis and experimental data from the basic NACA 23012 profile.

CHAPTER 3

DESCRIPTION OF THE EXPERIMENTAL APPARATUS

3.1 Introduction

Chapter 2 has dealt with the reasoning behind the choice of aerofoil section used for the proposed investigation. In the present Chapter, a detailed description of the experimental apparatus is presented. The structural design of the aerofoil wind tunnel model is described, followed by details of the model support structure and the pitch-drive mechanism. A multi-channel signal processing system was developed, in order to interface signals from the measurement sensors to a micro-computer for digitisation. A unique feature of the experiments, was in the use of a commercially available microcomputer for data acquisition, analysis and presentation, and details of role of this microcomputer is described.

The experiments were performed in the University of Glasgow's 1.61 x 2.13 metre, low-speed wind tunnel. The test aerofoil spanned the 1.61m vertical dimension of the wind tunnel, with angle of attack variations about the quarter-chord axis enabled by means of a hydraulic actuator and crank mechanism. The aerofoil was constructed of a laminated mahogany and Tufnol profile mounted on a steel spar. A centre-span instrument section contained pressure transducers and hot-film anemometry gauges, that were used to investigate the steady and unsteady aerodynamic characteristics of the aerofoil section.

Primary data were obtained from thirty miniature pressure

transducers, which were distributed around the aerofoil chord at mid-span. Instantaneous values from these transducers, along with the aerofoil angle of attack and the free-stream dynamic pressure in the wind tunnel working section were recorded. A specially developed multi-channel analogue signal conditioning system was used to interface the outputs from the transducers to a microcomputer analogue-to-digital (A/D) converter. This system consisted of suitably band-limited amplifiers, with a sample-and-hold capability to eliminate time-skew between the multiplexed channels.

The microcomputer used was a DEC MINC-11 with an LSI-11/23 16-bit processor, 256K bytes of RAM and a 1.0M byte dual floppy disk system. An A/D converter with a 32-channel multiplexer, a 4-channel D/A converter, a programmable real-time clock and an IEEE interface enabled communications with the hardware. Data acquisition, reduction, analysis and presentation were carried out using this microcomputer.

The design, manufacture and assembly of the experimental apparatus was carried out at the University of Glasgow during the period October 1980 to December 1982, apart from the wind tunnel aerofoil, which was manufactured at Westland Helicopters Limited, Yeovil, between October 1981 and April 1982.

3.2 Mechanical components

3.2.1 Introductory comments

In this section, the design and assembly of the mechanical components relating to the experimental set-up are considered. A brief description of the wind tunnel in which the experiments were conducted is presented, along with a few

results from the calibration procedure. Details of the design of the aerofoil model are given, with a description of the supporting structure, which transferred loadings from the aerofoil to the wind tunnel framework. The aerofoil angle of attack was varied by a hydraulic actuator and crank arrangement, and the design of this assembly is also described.

3.2.2 Wind tunnel

The experiments were conducted in the University of Glasgow's low-speed "Handley-Page" wind tunnel. (See Hounsfield, 1940). This wind tunnel is an atmospheric-pressure closed-return type, with a 1.61 x 2.13m (5'3"x7') octagonal working section (Figs 3.1 and 3.2). For short periods of time, the wind tunnel may be operated to give a maximum air velocity of 61m/S which corresponds to a Mach number of approximately 0.18, and Reynolds number of 4.6 x 10^6 per-metre chord. For continuous running however, velocities up to 40m/S may be obtained.

Prior to the experiments, the wind tunnel working section and surroundings were refurbished. A re-calibration of the wind tunnel flow was carried out, which is documented by Gordon et al (1982). A few results from this re-calibration are shown in Figs 3.3 and 3.4.

3.2.3 Wind tunnel model design

The geometrical size of the aerofoil wind tunnel model was determined from both physical and aerodynamic considerations. It was practically more feasable to mount the aerofoil vertically in the wind tunnel, and this therefore determined the span (1.61 metres). The aerofoil chord was determined by maximising the chord with respect to standard blockage and

streamline curvature correction factors (see Pope, 1954), which were constrained below specified values. On this basis a chord of 0.55 metres was found to be optimum in terms of maximising the Reynolds number, but without unnecessarily compromising the tests due to interference effects.

The model structure was designed to withstand maximum predicted loadings under both static and dynamic conditions, with an adequate margin for safety. Additionally, as the forcing torque was to be applied at one end, sufficient torsional stiffness was provided to minimise any spanwise twisting during dynamic tests, the design condition being for an oscillation amplitude of 10^{o} at a frequency of 10Hz.

At the preliminary design stage, a number of model constructional configurations and structural materials were considered, including steel, aluminium, wood and fibre-composites. Material cost and constructional simplicity (hence manufacturing time), were the two primary considerations which governed the final design. After consultation with Westland Helicopters Limited, it was decided that the design configuration which would allow prompt construction, would involve the use of laminated mahogany and Tufnol ø aerofoil profile mounted on a steel spar.

As discussed previously in Chapter 2, a design feature incorporated was that the aerofoil leading-edge geometry forward of 35% chord remained fixed, whilst the aerodynamic effects of different trailing-edge geometries were to be examined. In order to facilitate this, a joint was provided at the 33% chord position. Additionally, a Tufnol centre

---

ø Tufnol is a man-made fibreous material which resembles certain types of wood, but has increased strength, durability and stability.

section was designed to allow ease of transducer installation and replacement. This instrumentation section was constructed as depicted in Figs 3.7 and 3.9.

In order to minimise stress concentrations at wood joints and spar attachment points, it was necessary to provide a large bearing surface between the profile shape and the spar. Accompanied by the requirement to provide sufficient bending and torsional stiffness, this led to the spar cross-sectional geometry shown in Fig 3.8b. The upper and lower leading-edge profiles were bolted to the spar, followed by the trailing-edge profile (Figs 3.7 and 3.8a). The Tufnol instrument section was then installed, with the necessary transducer wiring passing along spanwise channels and exiting through holes in the spar end-flanges.

When determining the spar cross-sectional dimensions, a number of basic assumptions were made:

(1) All loads were carried by the spar alone.

(2) Applicability of the Engineer's Theory of Bending.

(3) The cross-section was 100% effective.

(4) Bending and shear loads applied to the spar by the actuator were neglected.

(5) A uniform spanwise aerodynamic loading.

Also, for design purposes, the spar was assumed to extend beyond the wind tunnel working-section, and to have uniform properties. Support at each end was via self-aligning bearings which allowed in-plane rotation but no displacement. The bending moment and shear equations were calculated with reference to the sketches in Fig 3.10. Design loading conditions (dynamic) of $C_N Max = 2.2$ at a wind velocity of 61m/S, with a factor of safety of 1.5 were imposed.

A maximum mid-span deflection of 2.5mm (0.1") was also specified. On the basis of the foregoing, an initial spar geometry based on bending stiffness and shear calculations only was determined.

As the model was to be oscillated with the forcing torque applied at one end, consideration was given to the spanwise torsional twist at the extreme operating conditions, in order that no significant spanwise pressure gradients were to be generated during the aerodynamic tests. Calculations for this part of the work were performed by Westland Helicopters Limited with the recommendation - that the torsional stiffness of the initial design be increased by a factor of three. The final geometry therefore had sufficient bending and torsional stiffness for the operational loading conditions likely to be encountered, with an adequate margin for safety.

The final design of the spar consisted of two parts; a main symmetrical part with a bolt on upper flange (see Fig 3.8b). This configuration was favoured as adaptability was ensured when dealing with other aerofoil profiles using the same spar. Bolt-on circular flanges were provided at the ends of the spar, which recessed into the wind tunnel walls providing an effective air-tight seal, and also facilitated mounting to the support structure and pitch-drive mechanism. Slots were provided in the flanges to enable instrumentation wiring to pass to the data acquisition equipment.

After manufacture and assembly, the model was installed in the wind tunnel to check and adjust for fit. By progressive shaping, 1.5mm (1/16") slots were made between the model and the wind tunnel walls, which were subsequently sealed using

felt glued to the edges of the model. This felt was soaked with a silicon based lubricant to reduce friction and permit an air-tight seal at the aerofoil/wind tunnel junctions.

The aerofoil surface was varnished and rubbed-down in a chordwise direction using 600 grade wet-and-dry abrasive to give a standard finish. Final polishing was performed using a proprietary wax polish.

After installation, the aerofoil model and support structure natural frequency in the bending mode was determined to be approximately 30Hz. Because of certain system limitations, the torsional mode natural frequency was not determined exactly, but was estimated to be in excess of 50Hz. In both cases, the displacements were highly damped. Also, a check was made on the spanwise twist at various oscillation frequencies and amplitudes, using accelerometers mounted on the aerofoil trailing-edge. The twist was found to be negligible at the system operating limits (an oscillation amplitude of 14^{o} at a frequency of 5Hz).

3.2.4 Model support structure

The dynamic and aerodynamic loadings from the aerofoil, were reacted to the wind tunnel framework by two transversly mounted beams illustrated in Fig 3.6. These support beams were fabricated from 77mm (3") square steel box section of 6mm (1/4") thickness, onto which mounting flanges and bearing housings were welded. The beams were accurately aligned, dowelled and bolted to the tunnel framework. The model was supported via a self-aligning bearing on each support beam, with thrust being taken by a single bearing on the top support. Details of the support structure are shown in Fig 3.11.

3.2.5 Pitch drive mechanism

Angle of attack variations of the aerofoil about the quarter-chord axis, were imparted by means of a hydraulic actuator and crank mechanism, which is depicted in Figs 3.12 and 3.13. The crank was rigidly connected to the tubular part of the spar by a welded sleeve and keyway. Provision for adjustment of the aerofoil working range of angle of attack was made by a threaded pushrod, which was normally adjusted for the angle of attack range: $-5^{o} \leq \alpha \leq 30^{o}$. The pivot pin was accurately machined and lapped into a phosphor-bronze bush to achieve a close tolerance fit with negligible backlash.

The actuator used was a UNIDYNE 907/1 type with a normal dynamic thrust of 6.1 KN (1380 lbf), operated at a supply pressure of 20 MN/m^2 (3000 PSI). A MOOG 76 Series 450 Servo Valve was used with a UNIDYNE Servo Controller System. Feedback was normally available via a linear displacement transducer situated in the base of the actuator, however, for the present work, this was disconnected in favour of an angular displacement transducer, as described in Section 3.3.5. A schematic diagram of the actuator control system is shown in Fig 3.14.

The actuator was mounted horizontally below the wind tunnel working-section by means of a sturdy supporting framework. Also, because of the geometrical arrangement of the drive mechanism, the actuator was allowed to pivot at the supported end on a hinge.

Extensive tests were carried out on the pitch drive mechanism prior to commissioning of the facility, including the determination of feedback gain for optimum response,

and structural integrity tests under fault conditions. Input signals to the actuator controller were provided for the static tests, by one of the MINC D/A converters, and by a FARNELL DSG2 synthesised signal generator for oscillatory tests. The amplitude and frequency output from the signal generator were set under software control via the MINC IEEE bus, and enabled precise oscillation frequencies to be achieved ($< \pm$ 0.001 Hz). The amplitude of the oscillatory input signal to the Servo Controller - to give a specific amplitude in angle of attack - was found to be dependent on the mean position of the actuator, and hence the amplitude and mean angle could not be set as precisely as frequency without resorting to complex calibration procedures. The normal sequence of events used, was to set the oscillation mean angle before increasing the amplitude in small increments under software control until the approximate amplitude was achieved. Fine adjustments could then be made via the Controller gain and offset potentiometers, with reference to the angle of attack protractor on the wind tunnel floor. In most cases, the mean angle and amplitude could be set to $< \pm 0.20^{o}$ by this method. The motion obtained during oscillatory tests was almost purely sinusoidal, and a Fourier analysis of the motion is shown in Table 3.1 for various amplitudes, mean angles and frequencies.

3.3 Electronic components

3.3.1 Introductory comments

In this section, details of the interface of the measurement sensors with the MINC microcomputer are presented. Measurements from thirty miniature pressure transducers were

acquired, along with measurements of the aerofoil angle of attack and free-stream dynamic pressure. The transducer output signals were amplified, where appropriate, and interfaced to the microcomputer multiplexed A/D via sample-and-hold circuits. The digitised data were subsequently recorded on 0.5M byte capacity floppy disks for analysis. A schematic representation of the data acquisition system is shown in Fig 3.15.

3.3.2 Pressure transducers

The chordwise surface static pressure distribution at the aerofoil mid-span was measured using thirty miniature silicon strain-gauge pressure transducers. Each transducer was of sealed gauge construction, with one side of the pressure sensitive diaphram sealed at a reference pressure during manufacture.

The locations of the pressure transducers on the aerofoil, are shown in Fig 3.16. Due to their small size, 2.0mm (0.080") diameter, ENTRAN EPI-080 transducers were used for the aerofoil leading-edge region, where the pressure orifices were in close proximity, and also for a few locations on the upper surface trailing-edge. Each of this type of transducer was positioned approximately 2.0mm below a 1.0mm diameter pressure orifice, in a close tolerance machined slot. For the remainder of the aerofoil, KULITE LSQ-56 and LSQ-57 series transducers were utilised The larger LSQ-57 type transducers were used at locations where the available locating material thickness was large, except on the lower surface, where each one was connected to the aerofoil surface via a short length of 0.8mm bore

diameter PVC tubing. The flat type LSQ-56 transducers were used at the trailing-edge and two locations above the thickest part of the spar. Each transducer was located in machined slots using RTV[ø], which served to provide mounting rigidity and to facilitate an airtight seal. Also, the RTV was applied as sparingly as possible to allow for future removal. Examples of the method of location for each type of transducer are shown in Fig 3.17. After installation, each transducer was subjected to a pressure test of + 6.9 KN/m^2 (10 PSI) to check for leakage and serviceability.

As the KULITE transducers had been used previously in another experiment, they were checked and re-calibrated by the Royal Aircraft Establishment, Farnborough. The ENTRAN transducers were provided with calibrations by the manufacturer. Additionally, re-calibrations were carried out in-situ, using a somewhat tedious procedure, however, these calibrations were found to agree to within $\pm$1.5% of the quoted values.

The pressure transducers were powered in parallel by a FARNELL "S" SERIES temperature stabilised D.C. voltage source, via separate 100Ω series resistors situated on the signal conditioner circuit boards. Because of the different transducer impedances (250Ω to 1100Ω), the actual excitation voltages for each transducer ranged from 5 to 6 Volts, and the calibrations were linearly scaled from the quoted values where appropriate after accurate measurements were made of the individual excitation voltages.

The transducer wiring passed along slots in the model interior and exited through holes in the spar end-flanges

---

ø Room Temperature Vulcaniser

before terminating at an AMPHETOL ASTRO/348 multi-pin connector plug. Between the transducers and the plug, both the input and output signal pair wires were twisted together to maximise common-mode rejection by the signal conditioner. Between the plug and the signal conditioners, the output signal pairs were twisted and shielded. The transducer power supplies however, were individually shielded, but untwisted as this was unnecessary.

It was estimated that the pressure transducer signals were normally reproduced to within 30 N/m^2 (0.004 PSI) over the range of Reynolds numbers and temperatures. The transducer offset drift was normally controlled to within $\pm$ 15 N/m^2 (0.002 PSI). Temperature sensing was not employed within the model, because it was not clear how effective this would have been in indicating the temperature changes at individual transducers. Instead, the air temperature was monitored in the wind tunnel settling chamber, and not allowed to vary more then 2^{o}C during the course of a sequence of runs.

The dynamic pressure in the wind tunnel working section, was normally determined using the standard pressure drop technique, discussed by Pope (1954). For the present work, however, a Pitôt-static probe was mounted on the tunnel sidewall approximately one chord length upstream of the aerofoil leading-edge. This probe was connected to a FURNESS MDC FC 002 micromanometer which had an accuracy of $\pm$ 0.49 N/m^2 (7 x 10^{-5} PSI) under steady conditions, from a digital presentation of the dynamic pressure (in mm H_2O) on the instrument. Also, an analogue output from the micromanometer was interfaced to the MINC microcomputer multiplexer (channel number 0) via a low drift operational amplifier circuit.

Prior to the experiments, a calibration of the output from this amplifier circuit (as read by the A/D), was performed against the dynamic pressure (as read on the micromanometer digital display). A cubic least squares fit was performed on the data, as shown in Fig 3.18, and the coefficients used in all data reduction sequences. The net accuracy of the dynamic pressure measurements were estimated to be $\pm$ 0.2mm H_2O (2.0 N/m^2, 2.85 x 10^{-4} PSI).

The output from the micromanometer was sampled via A/D multiplexer channel number 0 (as described above), at 100Hz over a one second period immediately prior to any test. The averaged value was recorded in the Run Information Block at the beginning of the run data file, and was used for reference purposes, such as the calculation of Reynolds number etc. Additionally, the instantaneous output was recorded in each multiplexer sweep during the data acquisition procedure (see Section 4.4).

Due to blockage effects, the dynamic pressure reduced with increasing angle of attack, as shown for example in Fig 3.19. It was impractical to maintain a constant dynamic pressure with the present wind tunnel control system, therefore, the dynamic pressure was set with the aerofoil angle of attack at approximately 0^o for static tests, and the mean angle for oscillatory tests. Generally, the dynamic pressure reduction/variation during the course of a run, was less than 7% of the initial/mean reading, except for high amplitude oscillations into and out of stall at low frequencies, and for angles of attack greater than 22^o during static tests. For oscillatory tests, the dynamic pressure varied almost harmonically with the angle of attack. The

amplitude of the variation however, reduced with increasing aerofoil oscillation frequency (Figs 3.20 to 3.22), and under the most severe conditions examined (low frequency, high amplitude, near the static stall angle) the dynamic pressure variation phase angle was found to lag behind the angle of attack by a few degrees. This introduced an error of less than 1% in the measurements of the normal force and pitching moment coefficients.

3.3.3 Signal conditioners

Amplification of the low voltage pressure transducer outputs were performed using individual signal conditioning circuit-boards of an RAE design. (See Welsh et al, 1980). The basic circuit-board design was modified slightly to allow a smaller (32-way) multi-pin connector plug to be used, and for additional signals to be input for setting-up purposes. On a recommendation from the designers, the transducer temperature sensitivity compensation circuitry was eliminated from the present conditioners due to setting-up and stability problems. Also, due to the present inability to calibrate and test for transducer temperature offset drift under controlled conditions, the offset compensation circuitry was switched-out. Therefore, all recorded data relied on the internal offset temperature compensation of the pressure transducer, and in practice this was found to be satisfactory, but not entirely effective. Additionally, the National Semiconductors UA741CP operational amplifiers, were replaced by Motorola 741NCP type on the present design. A circuit diagram of the signal conditioner is shown in Fig 3.23.

Thirty signal conditioners were manufactured, tested and set-up, prior to installation in the conditioning rack, where each one was individually matched to a pressure transducer. The gain of each conditioner could be infinitely varied from 10 to 2000, with offset adjustment approximately $\pm$ 10 Volts. The gains and offsets were specifically adjusted to each transducer depending on the pressure levels encountered, in order to utilise the full range of the A/D converter.

Frequency response tests were performed on randomly selected conditioners after construction, which were found to have a flat response up to a -3dB cut-off at approximately 3500Hz, with a 20dB/decade roll-off thereafter. As separate anti-aliasing filters were not employed in the present data acquisition system, a further modification was undertaken to limit the -3dB cut-off frequency of the conditioner to approximately 300Hz. This value was chosen as a compromise between passing the required signal bandwidth and minimising aliasing errors in the converted data values. A typical set of results from these frequency response tests are shown in Fig 3.24.

The conditioner gains were determined by inputing a range of appropriate signals from a DC voltage calibrator and determining the input/output ratio. Gain variation with time was found to be small or negligible. Finally, to account for the increase in gain when the transducer was in-circuit, the measured gains were corrected as shown in Fig 3.25.

3.3.4 Sample-and-hold device

As in any multiplexed analogue-to-digital conversion system, time-skew errors between channels can be important

if input slew rates are high, and the multiplexer switching/ settling times and A/D conversions are relatively slow. With the present system, a single A/D conversion was performed in approximately 30 μS, and, with a multiplexer settling time of 9 μS, and a software delay for channel selection and entry into memory of 5 μS, a single A/D conversion was available in about 44 μS. Thus, a time-skew error of approximately 32 x 44 μS = 1.41mS would exist between the first and last converted channels, and was clearly significant if the inputs were highly time-dependent, as was generally true for the present work.

To overcome time-skew errors, a thirty-one channel analogue sample-and-hold device was designed to interface between the signal conditioners and the multiplexer, hence providing simultaneous sampling on all 32-channels; the first sampled channel used the sample-and-hold on the A/D converter, with this conversion taking place during the sampling period of the other 31-channels. Sampling initiation was enabled by the 5 Volt negative-going TTL clock pulse from the MINC microcomputer real-time clock, which was suitably buffered to activate the circuitry.

The device consisted of four removable modules in a standard 19" rack. Three modules contained ten channels each, with a fourth module containing a single channel and the necessary power supply for the whole unit. A circuit diagram for a single channel is shown in Fig 3.26. Prior to the experiments, extensive tests were made to check for correct operation of all channels. No significant problems were apparent, although the uncertainty of the held voltage increased at sampling frequencies below about 10Hz as

depicted in Fig 3.27. Consequently a sampling frequency lower limit of 20Hz was imposed during the experiments.

A detailed account of the design and construction of the sample-and-hold device is reported by Galbraith, Barrowman and Leishman (1982).

3.3.5 Angular displacement transducer

An angular displacement transducer was constructed based on a 10KΩ precision linear wire-wound potentiometer. The potentiometer was mounted in an aluminium housing on sliding rails with anti-backlash springs, and geared to the model rotational-axis in the ratio 5:1, as shown in Figs 3.6, 3.13 and 3.28. A supply voltage to the potentiometer was provided from channels 0 and 1 on the MINC digital-to-analogue converters.

The output voltage from the potentiometer was interfaced to the junction circuit shown in Fig 3.29, which served to condition the signal for three purposes:

(1) Determination of the aerofoil instantaneous angle of attack. (via multiplexer channel-31).

(2) Data acquisition initiation. (via Schmitt trigger No. 2 on the MINC real-time clock).

(3) A feedback voltage to the hydraulic actuator controller.

The transducer angle of attack voltage was calibrated from measurements of the aerofoil trailing-edge position relative to the wind tunnel centre-line. A precision angular scaling was drawn on a BENSON 1302 pen plotter, and accurately positioned on the wind tunnel floor for this purpose. A semi-automatic data acquisition computer program was written and implemented on the MINC microcomputer to enable simultaneous

plotting of data points as they were obtained, followed by subsequent analysis. (See Section 4.3). Examination of Fig 3.30, which shows a typical set of results, will show that the calibration is slightly non-linear, presumably due to a slight eccentricity in the transducer gearing. A cubic least squares data fit was found satisfactory in representing the calibration, and the coefficients were used in all data reduction sequences. The maximum absolute error in the determination of the angle of attack was estimated to be $\pm$ 0.1° over the working range, and periodic re-calibration showed negligible variation of the calibration coefficients.

3.3.6 Microcomputer system

A DEC MINC-11ø microcomputer was used for data acquisition, data manipulation, monitoring and controlling external hardware. The integrated hardware/software system of the MINC provided powerful computational resources combined with flexible input/output capability for both analogue and digital laboratory equipment. The basic architecture of the MINC allowed for standard laboratory interface modules, such as A/D, D/A etc., to plug directly into up to eight quad-slots in the chassis and thereby communicate with the CPU and/or other modules. Because of this flexibility, the microcomputer could be quickly configured to requirements of a particular experimental system.

During the development phase of the present work, the MINC was configured with an LSI-11/03 16-bit processor and 64K bytes of RAM (Random Access Memory). The experiments were performed however, using a fully upgraded system to a LSI-11/23 16-bit processor with FPF-11 floating point hardware, a

---

ø Digital Equipment Corporation Modular INstrument Computer.

memory management unit (MMU) for 18-bit memory addressing, and a full compliment of 256K RAM. Mass storage was via an RX02 1.0M byte dual floppy disk system, of which approximately 0.5M bytes were available for user software and data. A VT105 terminal was used for direct input/output communication with the MINC, with a VT100 terminal being used for graphics. ø The VT100 was equipped with VT640 retro-graphics, with hard-copy available via a RIVA PRINTGRAPHICS and ANADEX dot-matrix printer system. A schematic of the MINC microcomputer system is shown in Fig 3.31.

To interface with external equipment, a number of laboratory modules were utilised:

(1) Analogue-to-digital converter (MNCAD)-The MNCAD A/D converter was a successive approximation type with auto-zeroing, that translated the instantaneous value of a voltage applied to the input into a 12-bit binary value. Conversion time was approximately 30 μS, although, multiplexer settling-time, channel selection and transfer of the data to memory increased this to 44 μS. The unit also contained a 16-channel multiplexer (16 single-ended channels, or 4 single-ended and 6 differential channels).

(2) Multiplexer (MNCAM)-In addition to the internal multiplexer on the MNCAD module, a MNCAM 16-channel multiplexer was utilised to increase the total number of channels to 32. Multiplexer channel selection, A/D start, and data transfer was achieved under software control, with all necessary associated timing protocol being performed by the CPU. (Details of the A/D conversion sequence are described in Chapter 4).

ø Graphics enhancement hardware.

(3) Real-Time Clock (MNCKW) - The MNCKW real-time clock was used as a time-base generator, communicating with the A/D via user software. The desired overflow rate was determined from the experimental requirements at run-time, in most cases this being 128-times the model oscillation frequency. For oscillatory tests, one of the MNCKW Schmitt triggers was used for data sampling initiation and clock start, by setting the trigger voltage to correspond to an angle of attack output from the displacement transducer.

(4) Digital-to-Analogue converter (MNCAA) - The MNCAA module housed four independent 12-bit D/A converters, which could be addressed via software. Each DAC was provided with a mode/range switch that permitted selection of uni-polar or bi-polar operation, with a variety of output ranges. Two channels of the MNCAA were used to power the angular displacement transducer, with a further channel used to set the aerofoil angle of attack (via the actuator controller) during static runs. The remaining channel was a spare for future system expansion.

(5) IEEE Instrument bus interface (IBV11-A) - An IBV11-A IEEE interface was installed in the processor compartment on the MINC chassis. The IEEE interface allowed communications to or from the MINC to any instrument on the bus which conformed to the IEEE (1975) standard. DEC software was used to support the IEEE interface.

3.3.7 Hot-film anemometry

A DISA constant temperature anemometry system was used with DISA SSR47 glue-on film probes to examine the aerofoil upper surface boundary layer shear stress characteristics.

These probes were placed opposite corresponding pressure transducers, at six chordwise locations within ± 15mm of the centre span.

Four 56C01 CTA units and 56C16 CTA bridges with 56N20 signal conditioners were originally available, however, a fault in one CTA unit necessitated its return to the manufacturer, and was not available during the course of the experiments. Further, damage to one probe and another with unusually high leads resistance restricted the present work to the use of three probes at 7.5%, 62% and 90% chord. The outputs from the CTA units were interfaced to an SE-Labs SE2100 multi-channel Ultra-Violet recorder via potentiometer type attenuators, which permitted sensitivity adjustment.

No calibration or linearisation was performed on the CTA signals, as the objective of the present work was only to document the qualitative behaviour of the boundary layer shear stress characteristics. The frequency content of the hot-film signals however, were band-limited to 500 Hz.
A schematic diagram of the hot-film anemometry system is shown in Fig 3.32.

3.3.8 Sources of noise and interference

As with any analogue data transmission and acquisition system, noise and interference can be a significant problem. This generally manifests itself as a noise signal superimposed on the signal which is actually required to be measured. Noise and interference usually takes the form of two types, electromagnetic and electrostatic, with electromagnetic being the most common, especially in the form of radio frequency noise (RF) and stray AC magnetic fields. Often, it is impractical,

if not impossible, to eliminate noise pick-up from the system, although much can be done to reduce its effects and recover the required signal by some simple techniques.

For the present work, extreme care was taken to minimise the effects of noise and interference on the measured signals. From each pressure transducer, the output signal wires were twisted together in order to maximise common mode rejection by the signal conditioner. Also, each set of signal pairs were individually shielded, which is particularly effective for reducing electrostatic interference. At entry to the signal conditioners, some noise and RF interference was found superimposed on the signals. However, much of this was removed within the conditioner, as it was band-limited to 300 Hz. At the exit from the signal conditioners, the signals were found to be remarkably noise free.

All signal wires within the data acquisition equipment were individually shielded. Similarly, the signal wires were individually shielded from the data acquisition equipment to the MINC microcomputer multiplexer. All signal shields were connected to analogue ground at one end of the cable length in order to eliminate noise generation due to ground-loops.

Finally, a single-point dedicated ground was provided, to which the data acquisition equipment analogue-ground was connected. Also, all external apparatus were referenced to this ground potential.

3.4 Conclusions

A new facility for the investigation of the steady and unsteady aerodynamic characteristics of two-dimensional aerofoils at low Mach numbers has been described. A unique

feature of the facility was in the use of a commercially available microcomputer for real-time data acquisition and analysis. Also, a customised multi-channel analogue signal processing system has been developed to interface low-output transducer signals to the microcomputer for digitisation.

Although a considerable number of problems were encountered with both the hardware and the data acquisition equipment, all these problems were solved prior to the successful commissioning of the facility during June 1983. Validation of the functionality of the dynamic stall test facility is shown by the results for the NACA 23012 aerofoil profile, in Chapters 6 and 7.

CHAPTER 4

DESCRIPTION OF THE SOFTWARE

4.1 Introduction

As with any computer based data acquisition and processing system, extensive software development is normally necessary, and the present system was no exception. Software for data acquisition, reduction and presentation was required to be comprehensive, well documented and primarily, should be "user friendly" with a minimum of user interaction with external experimental hardware. It was the objective of this part of the work, to develop a range of software for use with the dynamic stall facility discussed in Chapter 3. This software was designed for specific implementation on the MINC-11 microcomputer, and enabled a user to perform a range of tasks associated with the successful operation of equipment, and in the processing of data.

4.2 Preliminary review

The operating system used on the MINC microcomputer was DEC RT-11 Version 4.0. All of the software was written for the present work using FORTRAN IV and MACRO-11 assembly language. In general, FORTRAN programs were used for the control, data reduction and presentation sequences, although a number of MACRO assembly programs were called as subroutines for data acquisition and general laboratory module programming. Although software for laboratory module programming was supplied by the computer manufacturer, the generality and flexibility of the software however, limited the data handling speed considerably. In particular, to realise the full

capability of the analogue-to-digital converter (A/D), the decision was made to write specific routines in MACRO assembly code to optimise the particular task, resulting in considerably greater maximum A/D sampling speeds. A comparison of A/D sampling speeds using DEC and the customised routines are shown in Table 4.1, which enables the overall system performance with various hardware configurations to be assessed. Further, the LSI 11/03 processor used initially, was upgraded to an LSI 11/23 with a memory management unit (MMU) and FPF-11 floating point hardware (as described in Section 3.3.6), resulting in a general increase of computing performance by a factor of approximately 1.5.

The maximum memory capacity of the MINC microcomputer was 256K bytes, although only 64K were directly addressable by the processor. Memory above the 64K byte boundary was addressed via the MMU, but could not be accessed directly via the MACRO A/D data acquisition routines for data storage, limiting, therefore, the actual memory space for the operating system, real-time data and program to 64K. This was true for both the Single Job (SJ) and Foreground/ Background (F/B) Monitors, although the higher memory could be addressed by using VIRTUAL type data declarators. The memory may be addressed directly however, when using the Extended Memory Monitor (XM), although real-time data acquisition via the laboratory modules and/or IEEE interface was not possible, thereby making the XM Monitor suitable only for data processing and analysis.

In practice, the F/B or SJ Monitor was used for the present work, and after loading the necessary control program,

approximately 16K bytes were left for actual data storage. This corresponded to some 8K A/D samples, and the memory space was used as a first-in-first-out (FIFO) buffer, writing data to disk when full. In practice, the size of the FIFO buffer determined the number of continuous cycles of aerofoil motion that could be recorded.

Two methods were examined to try and alleviate the memory restriction. One was double data buffering, in which data transfers to disk took place during dormant periods between data samplings. The overall data acquisition rate however, was limited primarily by the slowest peripheral device, which in this case was the RX02 floppy disk system. (The RX02 floppy disk system consisted of dual disk drives. The system volume (DY0:) contained the necessary operating system software and other frequently used software. The user volume (DY1:) was used for programs and data storage.) With double buffering, it was found that the maximum A/D sampling rate was reduced to approximately half the maximum rate over direct memory access, and although it could be used successfully, say, to examine successive cycles of the aerofoil motion, the maximum sampling resolution[ø] was sacrificed at comparatively low aerofoil oscillation frequences. Also, with double buffering, another problem arose, in that when creating space on the disk for the data, more than twice the amount of data space was required to exist as contiguous free data blocks on the disk file. No method was found to circumvent this anomaly with the disk system, and must presumably have been an in-built feature of the disk handler.

ø The sampling resolution was defined as the number of data sweeps per cycle of aerofoil motion.

Thus, the benefits of A/D double buffering could only be realised with low sampling rates, or alternatively, with a hard disk system (ie > 20M bytes).

The second way examined to try and improve the memory utilisation, was by the use of memory above the 64K boundary as a virtual array "fast disk". In other words, instead of writing data from the FIFO buffer directly to disk, data was first transferred to the upper memory "virtual" array. This latter transfer was considerably faster, although nothing was gained in the sense that at least once cycle of aerofoil motion was still "lost" during the data transfer, and data transfer to disk must take place when the virtual array space was full via lower memory. Further, contiguous free disk space during the write sequence became a problem with the (possibly) larger amount of data to be transferred.

All the disk read/write software was written using FORTRAN callable subroutines contained in the System Library (SYSLIB). Conventional FORTRAN formatted sequential access files (via READ and WRITE statements) were not utilised due to the slow read/write speeds and inefficient use of disk space. Instead, unformatted binary direct access files (via the SYSLIB subroutines) were used extensively throughout the written software giving a read/write speed increase of about one order of magnitude, and a twofold reduction in disk storage space over the formatted sequential access files.

Details of the software were divided into three basic categories:-

(1) Pre-run tasks.

(2) Run-time tasks.

(3) Post-run tasks.

Within each category, a general description of the function of the routines are described. Particular emphasis has been placed on the description of the run-time software, as this involved a large proportion of the total time devoted to the software development.

Most of the MINC graphic presentation software was developed for "quick look" examination of data from individual runs, with comparisons between runs carried out manually. Additionally, some data were transferred to a mainframe computer when it was necessary to have high resolution pen-plots for formal presentation purposes.

4.3 Pre-run software

4.3.1 Calibration routines

Calibrations were required for the following transducers:-

(1) Pressure (chordwise).

(2) Angular displacement (angle of attack).

(3) Dynamic pressure (Pitôt-static probe).

(1) All of the pressure transducers were provided with calibrations carried out by the manufacturers. Additionally, the KULITE transducers were re-calibrated at RAE Farnborough. Further calibrations were performed in-situ. Data input and presentation for all these calibration tests were performed using the routine TRNCAL which allowed simultaneous plotting of the data points followed by a linear least-squares line fit, from which the calibration was obtained.

(2) Semi-automatic calibration of the angular displacement transducer was performed using the routine ANGCAL. The voltage output from the transducer was interfaced to the MINC via multiplexer channel-31, and was calibrated against

the aerofoil angle of attack, which was read off from scaling provided on the wind tunnel floor. Automatic incrementing of the aerofoil angle of attack was enabled via a D/A converter. Simultaneous plotting, followed by an optional least squares linear or cubic curve fit was performed on the data. An example of the calibration is shown in Fig 3.30.

(3) Calibration of the Pitôt-static probe and micromanometer output was performed in a similar way to (2), using the routine PSCAL, with the voltage input on multiplexer channel-0 (from micromanometer) calibrated against the wind tunnel dynamic pressure (as read by the LED display on the micromanometer). The calibration curve is shown in Fig 3.18 and was corrected for the tunnel centre-line dynamic pressure before being used in the data reduction sequences.

4.3.2 Set-up routines

The set-up software comprised of a group of separate routines which allowed the user to update channel calibration, gain and offset files for use by the data acquisition software.

Updates on the channel calibration and gain files were performed using the routines CALSET and GNSET respectively, entering the data via the VT105 terminal. The data were recorded in files on the MINC system volume (DY0:) and were subsequently accessed by the data acquisition software at run-time.

Immediately prior to a run, the offsets on each channel were recorded using the routine OFFSET. Each channel was sampled simultaneously at a frequency of 100 Hz over a five second period, and the averaged values were recorded on the system volume.

The channel calibrations, gains and offsets were also recorded as part of a single data block at the beginning of each run data file (see Section 4.4.1 and Table 4.2), for use during the data reduction sequence.

4.3.3 Monitor routines

Information on the status of the A/D multiplexer channels were performed using the routines ADSTA1 and ADSTA2.

The routine ADSTA1 allowed a record of the multiplexer channel status, such as whether it was single ended, quasi-differential etc., along with it's input, to be made on the terminal and/or printer. This routine was useful when setting up the A/D and multiplexer for the first time prior to a series of runs.

A constantly updated tabulated set of A/D values from up to 32 channels could be performed using the routine ADSTA2, the values being presented on the VT105 terminal as raw octal A/D values and the corresponding voltages. The routine was essentially a multi-channel DVM[ø], and was used extensively when setting the channel offsets to the required values prior to a run. It also gave an immediate indication of faulty transducers or signal conditioners, by off-scale or erratic readings.

The wind tunnel status, such as velocity, Mach number and dynamic pressure, along with the aerofoil Reynolds number and angle of attack were displayed on the VT105 terminal using the routine TUNSET. The mean values of these parameters, in both metric and imperial units, were automatically updated on

---

ø Digital Volt-Meter.

the terminal approximately once per second. The basic purpose behind this routine, was to allow the quick setting of the wind tunnel to any desired Mach or Reynolds number, prior to a sequence of runs.

4.4 Run-time software

4.4.1 Run control routines

Two main programs were written in FORTRAN to control the sequence of events for:-

(1) Static runs (STREX2)

(2) Oscillatory runs (SIREX2)

The setting-up sequence for each type of run was largely similar although the actual data acquisition process and data handling was completely different. In each case, however, data was recorded via an unformatted binary direct access file on disk, with the first 256 word block on the file containing values for a variety of run definition constants, such as the run number, sample rate, temperature, barometric pressure, gains, calibrations offsets etc., as shown in Table 4.2. The run number, air temperature and barometric pressure were manual inputs. Gains, calibrations and offsets were read from previously generated files on the system volume (DY0:), as described in Section 4.3.2. The data after the initial run information block, contained the raw A/D conversions as sequential samples from channel 0 to 31 (see Table 4.3). During the data reduction sequence, the run information data block was used to generate the required channel values in non-dimensionalised or engineering units from the raw A/D values.

In the case of static runs, the aerofoil angle of attack was set via the D/A converter and actuator Controller. The

angle of attack during oscillatory tests was controlled-by a synthesised signal generator. The necessary parameters such as oscillation frequency and amplitude were set by user input to the data acquisition program SIREX2, which in turn set the aerofoil motion from the signal generator via the IEEE bus. When the actual data acquisition was ready to proceed, entry was made into the relevant sub-routine, ADSCOV or ADBUFF. On-line data averaging and integrated load presentation was performed only during the static runs.

The data acquisition processes for the two types of tests, are described further in Section 4.4.2. Flow charts for the sequence of steps involved in a static and oscillatory run, are shown in Fig 4.1 and Fig 4.2 respectively.

4.4.2 High speed A/D conversion routines

The main requirement of the A/D data acquisition process was to enable sampling of 32 multiplexed channels to be carried out and the data transferred to disk in the minimum time period. The maximum sampling rate required, was determined by the maximum aerofoil model oscillation frequency and the sampling resolution (the number of 32-channel sweeps per cycle). For adequate resolution, a value of 128 data sweeps per cycle were considered optimum to define the aero-dynamic characteristics of the unsteady aerofoil motion. Also, a maximum oscillation frequency of approximately 5 Hz was required to achieve the necessary reduced frequencies at the Reynolds numbers of interest. This in turn led to a required maximum A/D sampling rate of approximately 5 x 128 = 640 Hz over 32-channels.

With software suppled by the computer manufacturer, the desired sampling frequencies could not be achieved (Table 4.1). Although this software (DEC REAL-11/MNC) was inherently flexible, most of the subroutines were not designed for high speed execution. The decision was made therefore, to write specific A/D conversion routines to optimise the sampling sequence for the current data acquisition requirements, and thereby increase the maximum sampling rate. This was done using MACRO-11 assembly language, following the necessary protocol required by the A/D hardware (see DEC Microcomputer Interfaces Handbook, 1980).

Multiplexer channel selection and A/D sampling initiation were accomplished under software control by assertion of data bits in the A/D control/status register (CSR). The A/D control logic would set another bit in the CSR when the conversion was complete and the converted data was available in the A/D data buffer register (DBR), where it remained until the processor was notified, under software control, for the data transfer to memory. Thus, a sequence of A/D conversions could be performed and the data transferred to memory by appropriate use of the CSR and DBR.

An additional feature of the DBR was designed to allow programmed setting of the D/A comparitor vernier, to offset differences in the A/D values due to differences in the analogue ground potential. The value used in the present work was found using a DC voltage calibrator referenced to the analogue ground. The actual value however, was unimportant when relative measurements were to be carried out, as in the present work, so long as all external apparatus

were referenced to the same analogue ground potential.-

It was theoretically possible to start the conversion on a subsequent channel before storing the previous conversion in memory, with a small increase in overall conversion speed. This procedure was examined, although, it was found unsuccessful in the majority of cases, especially during a large number of successive A/D conversions, the conversion sequence being halted at an arbitrary channel (as indicated by the channel selector LED on the multiplexer). It was assumed that a priority processor interrupt sequence was interferring with the A/D control logic under certain conditions, although this could not be verified. By disabling the computer 50 Hz line-clock however, the regularity at which the halt occurred during the conversion sequence was reduced, although not eliminated. As a by-product of disabling the line-clock, a further increase in the maximum A/D conversion rate was found, as indicated in Table 4.1.

Alternatives for performing the 32-channel A/D conversion sequence were considered. By examining the software execution time for each sequence, it was immediately apparent that a lengthy code explicit bit setting operations (i.e. MOV commands) had significant speed advantages over implicit bit setting operations (i.e. ADD, DEC, INC, TST commands). Thus, the lengthy but somewhat faster explicit bit setting code sequence was utilised.

The data sampling sweep of the 32-channels was controlled using the programmable real-time clock module, set to over-flow at the selected sampling rate. The procedure was to set-up the clock and A/D CSR's and DBR's after entry into the

data acquisition subroutine from the controlling FORTRAN routine. The subroutine was then made to wait at a particular portion until predefined start conditions had been fulfilled. In the case of oscillatory tests (using the ADBUFF subroutine), the start condition was the firing of Schmitt trigger number-two (ST2), by one of the angular displacement transducer outputs (see Section 3.3.5). The firing of ST2 simultaneously caused the clock to start counting at the preset rate, and initiated the start of the first data sweep. For any cycle, the start condition for a multiple clock driven sweep was the firing of ST2, thus ensuring phase locked sampling. In the case of static tests (using ADSCOV[ø] subroutine), the clock was started after entry to the subroutine, and the first sweep was initiated on the first clock overflow. In both cases, further sweeps through the 32 channels occurred on each clock overflow, until the total number of sweeps for that run had been completed, or the FIFO buffer was filled with data being written to disk when appropriate. Use was not made of the processor interrupt facility during the data acquisition processes (except in the case of double buffering) as no useful work was to be performed during idle time periods.

The results for the designed data acquisition sub-routines were very encouraging. While the specification of the A/D conversions predicted a maximum sampling rate of approximately 300 Hz per channel over 32-channels for the DEC software, this was increased to approximately 600 Hz using the presently described software. The maximum

---

ø The ADSCOV routine was basically the same as the ADBUFF routine apart from the definition of the A/D initiation conditions.

throughput rate was determined by looking for clock errors. The last step of a 32-channel sweep was to check for a clock overflow, prior to initialising for another sweep. If a premature clock overflow was found, the run was aborted.

For the oscillatory tests, up to two successive cycles of aerofoil motion could be recorded before data transfer to disk was necessary. Disk writes were done using a FORTRAN subprogram called from the MACRO data acquisition routine (see Section 4.4.2). In the case of static tests, one-hundred sweeps at a constant angle of attack were gathered using the ADSCOV subroutine, before averaging and storage in a temporary array buffer. Disk writes then took place after data from eight angles of attack had been gathered, which corresponded to one 256 word block on disk. A flowchart for the ADBUFF routine is shown in Fig 4.3.

4.4.2 Utility routines

During the course of the software development, a number of utility programs were developed, for use with the A/D, D/A, real-time clock and IEEE bus. Most of this software has been written in MACRO assembly language to facilitate high speed operation. The bulk of these routines are described in a supplementary report by Leishman (1983), and have been generalised to provide an optional high-speed enhancement of the DEC REAL-11/MNC software, particularly for A/D conversion sequences. These routines were not specific to the present work, and could be used successfully in other applications.

As mentioned in Section 4.2, conventional FORTRAN read/write operations were not used due to inefficient disk

storage and slow access speeds. Instead, routines contained within the RT-11 system library (SYSLIB) were used for all read/write operations. In the case of oscillatory tests, a FORTRAN subroutine to control the disk write sequence, was called from the ADBUFF data acquisition subroutine. It was easier to perform the write sequence in FORTRAN, as it saved subroutine carry-over, and monitoring of a large number of parameters within the MACRO routine.

Two FORTRAN subroutines were written to translate the required numerical values of amplitude and frequency to character strings suitable for the DSG2 signal generator interpretation logic. These character strings were subsequently sent via the IEEE bus.

4.5 Post-run software

4.5.1 Data reduction

Reduction of the raw A/D values to channel voltages or non-dimensionalised quantities was accomplished using the FORTRAN routine DSDR83. The DSDR83 routine was completely general, in the sense it could reduce both static and dynamic data so long as it conformed to the standard raw data format described previously in Section 4.4.1. Averaging of successively recorded cycles was an optional feature which could be implemented by the user.

At program entry, the run number was requested as input. Following this, the program looked for the required data file on the disk. If found, the Run Information Block (RIB) was read, and on the basis of this data, the user was prompted as to the format of the data reduction sequence. If the data

file was not found, the data reduction was terminated.

In the first instance, the RIB was updated to include values for the test parameters, such as Reynolds number, reduced frequency, flow velocity etc. These parameters were calculated on the basis of run-time temperature and barometric pressure using standard expressions for density, viscosity and sonic velocity. The parameters were then directly available for use by the plotting and/or analysis routines. Also, additional parameters were included in the RIB to identify the user responses in the data reduction sequence (i.e. to whether the data has been averaged). The updated RIB was then recorded as the first block in the processed data file.

In order to standardise the data reduction sequence, raw A/D data was read and processed block-by-block. Each raw data block consisted of 256 words (i.e. 512 bytes, 256 A/D values or 8 A/D sweeps), which were first converted to floating-point values, i.e. voltages. Raw data in the range 0_8 to 7777_8 were converted to the range $\pm$ 5.12 Volts. If the user had not opted for further processing, this data was written to disk, and processing on the next block continued.

Further processing normally involved conversion to standard non-dimensional pressure coefficients. This was done by applying offset, gain, calibration and correction factors to the data. The pressure coefficients were then determined by dividing the chordwise pressure data by the instantaneous dynamic pressure (the first data value in any sweep).

If cycle averaging was to be performed on the data, the block numbers of corresponding data within subsequent cycles were calculated at this stage. As the data from each cycle were essentially phase-locked, interpolation between data points was unnecessary. Data from subsequent cycles were directly added to an accumulator and finally averaged, prior to writing the data to disk. Similar processing on the next raw data block was then continued.

An additional feature of the data reduction routine, was that "half" data blocks could be handled. "Half" data blocks were likely to be recorded when sampling higher aerofoil oscillation frequencies. (In these cases, the run-time software suggested an alternative sampling rate and resolution, should the maximum A/D sampling frequency limit be exceeded). "Half" blocks or "overlapping" cycles on one block were then possible, and the DSDR83 data reduction routine was designed to re-organise the data should this occur.

The processed data buffer was twice the size (in words) as a raw data block. In otherwords, the processed data values were recorded as real numbers, which required 2 words (4 bytes). Thus, as mentioned in Section 4.2, certain difficulties may be encountered with disk storage space limitations. In fact, a run of ten cycles of 128 data sweeps per cycle (i.e. 40K words) was found to be the limit in terms of handling and processing convenience. A complete set of unaveraged processed data from such a run would occupy some 80K (unformatted) words on the disk. In any case, ten cycles were considered near optimum to bring out the main features of the aerodynamics(as the

results of Chapter 7 show).

A flowchart for the data reduction program DSDR83 is shown in Fig 4.4.

4.5.2 Data analysis

Time factors primarily dictated the amount of computer analysis which could be performed on the recorded data within the context of the present work. Although extensive scientific subroutines for Fourier analysis and signal processing were available, the current ability for only a limited data set to be stored on disk at any given time made it impractical to consider extensive data analysis in the time period available.

Consequently, the analysis of data recorded from the investigation of the NACA 23012 aerofoil unsteady aerodynamic characteristics has concentrated mainly on parametric comparisons of integrated pressure forces and moments, relevant chordwise pressures and time history responses. From the large bulk of recorded data, however, global comparisons of this nature will be shown in Chapter 7, to highlight features of the aerodynamics which may warrant further investigation and analysis at a later date.

Two FORTRAN subroutines were written, and used extensively in the present work:-

(1) Normal force and pitching moment evaluation from the chordwise pressure distribution, designated CNCM.

(2) Chordwise net aerodynamic damping evaluation, designated CMDALP.

(1) CNCM routine: The trapezium method was used for chordwise integration of the aerofoil pressure distribution, in order

to evaluate the normal force, C_N, and quarter-chord pitching moment, C_m. Linear extrapolations to the aerofoil trailing-edge, from the pressures at locations 1 and 30 were performed. Trapezoidal integration of chordwise pressure distributions to give total loadings is an accepted technique, and is comparatively accurate so long as a relatively close spacing of pressure points are available. Additionally, the transformation integration procedure described by Davis et al (1980), was implemented as an option within the CNCM subroutine. This transformation procedure has the effect of ameliorating the leading-edge suction peak and more evenly spacing out the chordwise pressure points, and is useful when the data points are comparatively sparse. For the present work, no major differences in the results from the two techniques were apparent, and all the presented normal force and pitching moment data have been evaluated using the trapezium method for consistency.

(2) CMDALP routine: The net chordwise aerodynamic damping, $-\oint C_m.d\alpha$, was evaluated by trapezoidal integration. This damping represents the net work performed by the airstream on the aerofoil, and is positive for an anticlockwise circuit of C_m against α.

4.5.3 Data presentation

A suite of programs were written to graphically present the data recorded from the current tests. Most of this software was written in FORTRAN, and utilised a customised plotting package which was implemented for use on the MINC microcomputer. Additionally, software was written to allow

data comparisons to be made for sets of selected runs on a GEC 4070 main-frame computer using the GINO series of plotting packages.

The MINC plotting routines were written primarily to facilitate "quick look" presentations of the data. Due to time and disk space limitations, minimal software was written to allow direct comparisons and correlations between a number of selected data sets, most of this being done on the GEC 4070 computer after a lengthy data transfer process. With the present RX02 floppy disk system up to five (5) raw data files may reside on the user disk at any one time. Approximately twenty-five (25) averaged processed files may be accommodated on a user disk, but to enable this, many time consuming disk copying operations were necessary. Nevertheless, by careful strategy, it was theoretically possible to create software to enable comparisons to be made between run data sets, although this may only be done on a relatively small scale. The problems discussed above, are common when trying to handle a large data base with small mass storage devices, and some suggestions are put forward in Chapter 8 as to the most profitable line of approach for solution.

Returning to the current plotting software, the following routines have been written:-

(1) Chordwise Cp distributions. (Cp versus X/C)

(2) Cp time histories. (Cp versus t)

(3) C_N and C_m versus α

(4) C_N versus C_m

(5) Isomeric chordwise pressure plots. (Cp = f (X/C,t))

(6) Cp contour plots. (Iso-Cp contours w.r.t. X/C and t)

Each routine could operate on averaged or unaveraged data, as generated by the DSDR83 data reduction routine. Additionally, two versions of each routine were available; one for quick on-line examinations, another for presentation purposes, with suitable headings and run information data, as shown for example, in Fig 6.9. Further, separate routines were provided for static and dynamic data presentations, each with suitable axes scaling. All these plotting routines have been allocated names DSPLNN, where NN is the plot code number. The routines are documented in supplementary work by Leishman (1983), but, they will be also briefly discussed here as a preface to the results of Chapters 6 and 7.

(1) Cp~X/C: Standard chordwise non-dimensional pressure coefficients were produced using the DSDR83 data reduction routine, and were read block-by-block, that is in blocks of 4 sets of α, by the plotting routines. Because of the high cycle resolution, it was usually only necessary to plot data for every fourth α. Symbols were provided at each data point, and straight line segments drawn between each. Upper and lower pressure distributions could be produced, although to preserve clarity, it was usually only necessary to plot the upper surface.

(2) Cp ~ t: This was a convenient way of plotting all the data from an averaged file or the first cycle from unaveraged data. Again, the data was read block-by-block, from which the individual transducer pressure time histories were constructed. To preserve clarity, each channel time history construction was offset on the y-axis by an amount ΔCp which was determined by adding a value of two times N,

where N was the pressure transducer chordwise location-number, to the actual Cp values. The usefulness of this presentation can be appreciated, for example, in Figs 7.72 to 7.158.

(3) C_N and $C_m \sim \alpha$: Presentation of integrated normal force and pitching moments against angle of attack was one of the most useful plots for a parametric analysis. Again, averaged or unaveraged data could be dealt with. After the completion of a run, or batch of runs, examination of the C_N, $C_m \sim \alpha$ plots enabled the user to assess the validity of the data very quickly, and to decide whether repetition of the run was necessary.

(4) $C_N \sim C_m$: The usefulness of this type of plot has been commented on by McCroskey et al (1978), as it eliminates the angle of attack, α, from the presentation. In practice however, the type of plot obtained, from say an oscillation near the static stall angle, highlights the "non-repeat-ability" of the flow during the separated part of the cycle, and often detracts from the general trend of the data. Thus, it was more useful to work with averaged data when using this type of plot.

(5) $Cp = f(X/C,t)$: Isometric chordwise pressure plots versus time, were produced on the MINC microcomputer and also on a GEC 4070 computer. This was a convenient way of presenting all the chordwise pressure data (see Figs 7.71 to 7.159), and allowed interpretation of global features in the aerodynamics. C_N and $C_m \sim \alpha$ plots were also produced at the same time for comparison.

(6) Cp contour plots: This type of presentation was performed on a GEC 4070 computer using the GINOSURF plotting

package. The plots consisted of contours of equal values of Cp plotted against non-dimensional chord and time. An example is shown in Fig 6.17 for a static run. Due to time limitations however, little use was made of this method of presentation. Further, interpretation of the data was often complex, and consequently this type of presentation has not been included in the oscillatory data of Chapter 7.

4.6 Conclusions

A package of software has been successfully developed and implemented on the MINC microcomputer for use with the previously described dynamic stall facility. This software permitted a wide range of functions, related to the operation of the facility, to be performed by a user with a minimum of programming knowledge. Included within the software were routines for data preparation, hardware monitoring, data acquisition, data reduction, data analysis and data presentation.

Perhaps the most significant contribution to the package has been in the development of the data acquisition routines. Primarily, the high speed A/D conversion routines, which have been written in MACRO assembly code and have been optimised in order to perform specific sequences of A/D conversions. Also, a degree of input/output automation has been built-in to the run-time software, primarily to minimise user interaction with external experimental hardware, and to increase the run repeatability for a given set of parameters.

Finally, some of the software for MINC laboratory module programming which was developed in the present work, has been

recompiled, and is described by Leishman (1983). This software has been generalised for use in different applications, and provides an optional high speed enhancement of DEC REAL 11/MNC software.

CHAPTER 5

SUMMARY OF TEST CONDITIONS

5.1 Introduction

In Chapter 3, a description of the experimental apparatus has been presented. In Chapter 4, details were given of the software used on the MINC microcomputer, in order to control the experiment and process the data. In the present Chapter, a summary is given of the test conditions under which the aerodynamic investigations were carried out. Also presented, are details of the test procedures, and the role of the previously described software as an integral part of these procedures.

It is well known, that differences in aerodynamic characteristics of the same aerofoil section are apparent, when tested in different wind tunnels (e.g. Fig 5.1). This is mainly due to the effects of solid and wake blockage, interference, three-dimensionality and free-stream turbulence, and these effects are discussed in detail by Pope (1954). Prior to quantitative measurements being made in the present facility, oil-flow visualisation was carried out to examine the quality of the two-dimensional flow over the aerofoil upper surface, and to assess possible effects on chordwise pressure measurements.

For static tests, quantitative measurements were carried out at Reynolds numbers between 0.8 and 2.0 million, and for discrete angles of attack between -4^{o} and 28^{o}. Oscillatory measurements were carried out at Reynolds numbers of 1.0 and 1.5 million, over the range of mean angles, oscillation

amplitudes and frequencies which are summarised in Table 5.1.

In all the tests, the flow was allowed to develop under transition free conditions. Also, the Mach number varied in proportion to the Reynolds number via the relationship: $M_\infty \simeq 1.14 \times 10^{-7}$ Re.

5.2 Flow visualisation

Flow visualisation tests were carried out on the NACA 23012 aerofoil, prior to the installation of pressure transducer and hot-film instrumentation, with all the pressure orifices sealed. No quantitative measurements were made at this stage, as the objective was to study the steady flow around the aerofoil, and to note the onset of any unusual separation phenomena which may affect mid-span pressure measurements.

The flow visualisation was effected by using a mixture of odina oil and saturn-yellow "dayglo" powder. The oil mixture was first uniformly smeared as a thin film over the upper surface of the aerofoil, followed by setting the angle of attack, and raising the wind speed from zero to the test value. Development of the flow pattern was allowed to proceed until either, no further development was likely, or in regions of oil accumulations, gravitational effects began to distort the result. The flow pattern was illuminated by ultra-violet light, causing the "dayglo" pigment to flouresce in the visible range. Black and white photographs were taken using ILFORD XP1 film, with a yellow filter to give good contrast.

The tests were carried out for a range of angles of attack, at Reynolds numbers of 1.45 and 1.85 million. These

Reynolds numbers were chosen as a compromise between either obtaining steady flow patterns in a reasonable time period, or obliterating them altogether in regions of high surface shear or oil accumulations. A summary of the results obtained from the flow visualisation tests are presented in Section 6.2.

5.3 Static tests

Static tests were carried out at Reynolds numbers of 0.8, 1.0, 1.2, 1.4, 1.5, 1.6, 1.8 and 2.0 million. Data in the form of chordwise pressure, free-stream dynamic pressure, and the aerofoil angle of attack were recorded using a standardised test procedure. Additionally, limited amounts of boundary layer information were obtained from hot-film anemometry, at Reynolds numbers of 1.0, 1.5 and 2.0 million.

The test sequence was developed by considering data from a number of preliminary runs. An interactive program was written for use on the MINC microcomputer which enabled automatic angle of attack incrementation, on-line data averaging and processing, and presentation of integrated loads during the run. A run consisted of data collected at 128 discrete angles of attack between approximately -4^{o} and 28^{o}. (64 on the upstroke and 64 on the downstroke). After the angle of attack had been re-adjusted, the flow was allowed to stabilise for approximately half a second, before data sampling was initiated. (This time delay, was determined after examining the effects of a delay ranging from zero to 5 seconds).

Because of the moderate demands on the MINC's

computational resources during static tests, the opportunity was taken to condense recorded data by performing averaging during the run, rather than after the run was complete. Thus, at each angle of attack, 100 sample sweeps were taken over a one second period, followed by immediate averaging prior to writing to a temporary array buffer and subsequently to disk. Also, in order to give an indication of the validity of the data, integrated pressure loads were calculated and displayed simultaneously on the VT100 graphics terminal during the run. Data from the range of static tests are presented in Chapter 6.

5.4 Oscillatory tests

The parameters that were varied under oscillatory angle of attack conditions were Reynolds number, mean angle, amplitude and frequency of the oscillation. The effect of Reynolds number was studied at 1.0 and 1.5 million. Principal ranges of mean angle, amplitude and reduced frequency were $6^{\circ} \leq \alpha_m \leq 20^{\circ}$, $2^{\circ} \leq \alpha_a \leq 10^{\circ}$ and $0.01 \leq k \leq 0.2$ respectively; the discrete values being given in Table 5.1.

As in the case of static tests, data were recorded in the form of instantaneous chordwise pressures, free-stream dynamic pressure and the aerofoil angle of attack, using a standardised test procedure. A control and data acquisition program was written on the MINC microcomputer for this purpose. For these tests, the majority of the micro-computer's resources were devoted to data acquisition and recording, the data processing being performed at the end of a sequence of runs. Ten cycles of oscillatory motion

were generally recorded, downloading the data to disk after every second cycle. Usually, 128 data sweeps per cycle were sampled at evenly spaced time intervals, however, at higher frequencies, slightly fewer data sweeps were sampled in order to keep within the maximum A/D sampling limit. Data sampling initiation was determined via the level on a Schmitt trigger, which was normally set to fire at, or close to, the mean angle of attack, α_m. Thus, phase locked sampling was ensured for all recorded cycles. Limited amounts of boundary layer information were obtained for a restricted range of oscillatory conditions, at a Reynolds number of 1.5 million. A summary of these conditions are also presented in Table 5.1.

A comprehensive discussion of the main results from the oscillatory tests are presented in Chapter 7.

5.5 Measurement accuracy and sources of error

References to the accuracy of individual instruments and transducers have been cited throughout the preceding Chapter, however, a brief summary of the measurement accuracies will be made here.

The pressure signals were estimated to be reproduced to within $\pm$ 30 N/m^2 ($\pm$ 0.004 PSI) for Reynolds numbers greater than one million. The corresponding non-dimensional pressure coefficients were estimated to be within $\pm$ 0.05. Errors in the values of normal force and pitching moment coefficients were estimated to be less than 0.025 and 0.005 respectively.

The angle of attack was measured relative to the wind tunnel centre-line, and the error in this measurement was

estimated to be less than 0.1^{o}. No corrections were performed to the angle of attack measurements to account for flow angularity and streamline curvature in the wind tunnel working section. These effects however, were estimated to contribute less than a 0.2^{o} error to the absolute measurement of the angle of attack.

During oscillatory tests, the mean angle attack, α_m, was set manually prior to the start of the oscillation. Data acquisition initiation was enabled via a Schmitt trigger on the real time clock, to start at, or close to, α_m. Due to unresolved difficulties with the actuator controller, the specified mean angle of attack was occasionally violated during the oscillation, depending on the selected amplitude and frequency, although, only in a few cases did this exceed $\pm$ 0.2^{o}. The errors in the oscillation amplitude and frequency were estimated to be less than $\pm$ 0.1^{o} and 0.001 Hz respectively.

Despite efforts to monitor instrumentation performance during, and between test runs, various problems sometimes arose which only became apparent during the post-run data reduction and analysis. In the majority of cases, these problems were rectified, and the run, or runs, repeated as necessary. In some instances however, the problems were of a more subtle nature, requiring detailed investigation, although, it was generally possible to correct the problems without significantly compromising the accuracy of the results. For example, a faulty or erratic pressure transducer response could be replaced by interpolating between neighbouring values. In one specific case, 50 runs were recorded at Reynolds number of 1.45×10^{6} and a

reduced frequency of 0.01, in which the dynamic pressure value was found to be in error, possibly due to crosstalk on that channel because of an incorrectly routed signal cable. By correcting the readings for the (almost) constant crosstalk level, the data was considered to be essentially valid, although in a few cases, the data values may lie outwith the normal error bands quoted.

Pressure transducer offset drift proved to be one of the more difficult sources of error to control. End-to-end checks of channel zero offsets were made under a variety of conditions, such as air temperature rise, run duration, etc. In general, the drift was found to be significantly reduced at air temperatures above 25°C, and consequently, all tests were carried out at, or above, this temperature, although not exceeding 35°C. Transducer sensitivity variation with temperature, was estimated to be within acceptable limits for this temperature range, based on an analysis of the repeatability of static test data at various mean temperatures.

5.6 Static and oscillatory run procedures

In this section typical procedures used to perform a static or oscillatory run are described, with usage of computer software indicated where appropriate. As mentioned previously in Section 4.4, after initiating the appropriate control/data acquisition program, the user was provided with prompts when changes to the hardware status were required. As the control/data acquisition software has been described previously, no further reference to these control sequences will be made here. Operational

experience suggested that long term pressure transducer and signal conditioner stability was obtained by allowing a "warm-up" period of at least seven days. In the following procedures, this "warm-up" period was assumed to have been completed.

A typical static or oscillatory run procedure was as follows:

(1) The wind tunnel was first started, and run until the air temperature has reached at least 25°C but not more than 30°C. This was to bring the pressure transducers into a temperature range where the offset drift compensation was more effective.

(2) The MINC microcomputer and the actuator hydraulic pump were also started at this stage. (Approximately 15 minutes were required for the A/D converter, and 30 minutes for the hydraulic fluid, to reach operating temperature if started from cold).

(3) After the wind tunnel air temperature had reached approximately 30°C, the tunnel was shut-down, and the transducers were allowed to "soak" for approximately 15 minutes to permit thermal stability.

(4) Meanwhile, the monitor routine ADSTA2 could be used to check the transducer/amplifier status and to allow the user to adjust offsets where necessary. Also, checks could be made at this stage for currency of channel calibrations and offsets, updating if necessary via the CALSET and GNSET routines.

(5) After stage (4) had been completed, the tunnel could be started again, and run at the required test velocity. This was normally done for 5 minutes or until the air

temperature rose by one ^{o}C, whichever occurred sooner.
(6) Meanwhile, the run time data acquisition disk (static or dynamic) may be loaded, checking that enough space for the data existed on disk as contiguous free data blocks.
(7) Also, the hydraulic actuator controls must be checked at this stage and the appropriate values for feedback gain set on the ten-turn potentiometer. If conducting an oscillatory test, the Schmitt trigger voltage level was set to fire at the required angle of attack. This was usually the mean angle of the oscillatory cycle, αm.
(8) On completion of stage (5), the tunnel was shut-down, and the channel datum values were logged using the routine OFFSET, when the air flow had ceased.
(9) Immediately after stage (8), the appropriate run-time data acquisition routine (STREX2 or SIREX2) was initiated, and the procedures continued as per the flowcharts in Fig 4.1 and 4.2. Both these run-time routines contained the necessary prompts to conduct the test, and return to the status of stage (8). A maximum of five runs, or until the tunnel air temperature rose by $2^{o}C$, could be completed during one tunnel run, before it was necessary to re-log the channel datum values.

5.7 Conclusions

Aerodynamic tests have been detailed in order to investigate the steady and unsteady characteristics of the NACA 23012 aerofoil section. Although the data from such an investigation was useful as an end product within itself, the bulk of these data however, constituted a validation of the present data acquisition system. Also,

as the basic NACA 23012 aerofoil profile was designated to serve as a reference standard for future tests on derived aerofoils, it was necessary to record data for a wide range of oscillatory conditions. This permitted a parametric analysis into the effects of the motion on the aerofoil aerodynamics, and allowed an assessment of the conditions under which particular aerodynamic phenomena were most pronounced.

CHAPTER 6

RESULTS AND DISCUSSION (1) - STATIC TESTS

6.1 Introduction

Chapter 5 has dealt with a summary of the test conditions under which both the steady and unsteady aerodynamic characteristics of the NACA 23012 aerofoil were investigated. In the present Chapter, a detailed discussion of the results observed and measured from the static investigation are presented, and preface the unsteady aerofoil data of the next Chapter.

Prior to the recording of chordwise pressure data, an assessment was made as to the quality of the two-dimensional flow over the aerofoil surface using an oil film technique, and the results of this investigation are also briefly described in this Chapter.

6.2 Flow visualisation

6.2.1 Introductory comments

The influence of any three-dimensional flow developments during tests to obtain two-dimensional (2-D) aerofoil characteristics is particularly important. In the presence of induced downwash and cross-flow conditions, the chordwise pressure measuring station may not be in a region of 2-D flow and may lead to misinterpretation of the data. Moss et al (1971) have reported of strong three-dimensional flow near maximum lift, with a subsequent influence on force and pitching moment measurements, both under static and oscillatory conditions. Observations of premature flow

separation in the corners between an aerofoil and the wind tunnel walls, and the development of spanwise separation fronts, have been discussed by Gregory et al (1971), who investigated problems associated with measurements of 2-D aerofoil characteristics in wind tunnels. Application of boundary layer control on the wind tunnel side-wall, was found to make little difference to the onset of three-dimensional flow patterns, which appeared to be an inherent characteristic of the stalling process. Carr et al (1977) found similar three-dimensional separation phenomena, but the degree of three-dimensional flow development was found to be reduced during unsteady tests, and by the application of end-plates close to the aerofoil/wind tunnel wall junction. It has also been noted by Gregory et al that spanwise flow variations appear to be affected by the aerofoil profile and aspect ratio. Similarly, wind tunnel configurations and test conditions appear also to influence the onset of three-dimensional flows (Fig 5.1).

On the basis of the above observations, it was important to have a knowledge of the extent and form of the three-dimensionality for a suitable range of angles of attack, before assessing any measured static pressure distributions. Therefore, it was decided to use an oil film technique, in order to investigate the aerofoil spanwise flow pattern in the present test arrangement. This technique has been detailed previously in Section 5.2. Tests were carried out at Reynolds numbers of 1.45 and 1.85 million for a range of discrete angles of attack. Similar flow patterns were obtained for both Reynolds numbers, but for simplicity, the

discussion of the results in the next section are restricted to the lower Reynolds number.

6.2.2 Discussion

It should be appreciated, that in these tests the model was mounted vertically in the wind tunnel, so that in regions of weak surface shear and oil accumulations, gravitational effects gave a downward bias to the oil flow. Also, as the wind speed was raised from zero to the test value after setting the angle of attack, the flow pattern does not necessarily represent the situation which might be obtained when the stall is approached at constant Reynolds number, by an increase in angle of attack.

Figure 6.1 shows the flow developments obtained on the NACA 23012 aerofoil at various angles of attack at a Reynolds number of 1.45×10^6. Up to an angle of attack of 12°, the flow was essentially two-dimensional with little or no separation at the aerofoil/wind tunnel wall junction, although minor trailing-edge separation was apparent. Transition from a laminar to turbulent boundary layer was clearly shown via a laminar separation bubble, which grew smaller in width, and moved closer to the leading-edge with increasing angle of attack. At 14°, the trailing-edge separation had increased, although in a non-uniform manner, across the span. The laminar separation bubble was still clearly in evidence, but with a slight irregular appearance, possibly due to local variations of surface roughness or profile shape. Also, accumulations of oil in the bubble region distorted the appearance somewhat.

The occasional turbulent streaks, which cut through the laminar separation bubble, are caused by minor blemishes at the aerofoil leading-edge, which induce transition.

Trailing-edge separation increased rapidly with any further increase in angle of attack. At 14.2°, flow reversals covered almost 50% of chord, and first indications of vortices at the outer span regions appeared. Although the flow pattern was still largely symmetrical at this stage, the separation front was distinctly non-uniform and unsteady.

At 15.0°, flow separation occurred at about 10% chord in the vicinity of one local spanwise position. (On examination of the aerofoil leading-edge after the test, a small amount of roughness was found where this early flow separation took place). Also, the two vortices began to form quite clearly, although, the upper vortex was notably of greater strength at this stage. The laminar separation bubble was still present at the aerofoil leading-edge, although the aerofoil could be classified as being stalled.

Asymmetry of the vortex positions occurred at an angle of attack of 16°, with the lower one considerably further inboard. Whether or not the vertical mount had any effect on this asymmetry could not be verified, although gravitational effects did distort the flow pattern slightly.

With any further increase in angle of attack, the vortex symmetry improved, but at 20°, their intensity had diminished, with flow reversals covering almost 80% of the aerofoil surface. The laminar separation bubble was still evident, but, the spanwise irregularity had increased,

with the bubble being more pronounced at the outer span. This was almost certainly due to reduced angles of attack in these regions caused by significant downwash from the two vortices.

At an angle of attack of 25^{o}, the flow separated very close to the aerofoil leading-edge, with weak flow reversals covering the majority of the surface. It was also observed that the laminar separation bubble had finally disappeared.

It was interesting to note that the separation bubble moved closer to the leading-edge, and diminished in width with increasing angle of attack, but remained obstinately present up to, and beyond the stall. Also of interest was the fact that, no significant corner flow separation existed at the lower angles of attack, prior to the onset of three-dimensional flow. This latter observation was contrary to what was expected, as indicated by the results of Gregory et al (1971). Further, the presence of a "horseshoe" vortex wrapped round the aerofoil close to the tunnel floor and ceiling was observed throughout the tests, and this may have played some part in keeping the flow attached at the aerofoil/tunnel wall junctions. This "horseshoe" or "scarf" vortex is a characteristic feature of the flow when an obstacle such as an aerofoil protrudes from a wall, but is of relatively small scale and was unlikely to have any significant effect on the flow external to the aerofoil/wind tunnel junction. These "horseshoe" vortices can be seen in the photographs of Fig 6.1.

Interpretations of the turbulent separation point variation at mid-span as a function of increasing angle of

attack are shown in Fig 6.18. A comparison has also been made in Fig 6.21 with reattachment point data inferred from the hot-film and pressure results at a Reynolds number of 1.5×10^6. It was noted that a closer correlation existed for the downstroke of the static test, indicating that as a result of the technique used, the visualisation test procedure may be more representative of the flow reattachment process after stall.

Further observations of the three-dimensional stall developments on the NACA 23012, and on the NACA 0012 aerofoil in a different wind tunnel, are discussed by Seto, Leishman and Galbraith (1983).

6.2.3 Conclusions

Based on oil-flow visualisations carried out on the NACA 23012 aerofoil at a Reynolds number of 1.45×10^6, the following conclusions were made:-

(1) The aerofoil exhibited turbulent trailing-edge separation and had a trailing-edge stalling characteristic.

(2) The laminar separation bubble played no direct part in the stalling process, and was present after the flow had separated over more than 80% of the aerofoil surface.

(3) Two-dimensional flow conditions were found to exist until the trailing-edge separation began to move towards the leading-edge, whereupon, three-dimensionality increased and two distinct votices were formed at outer span positions. The intensity of these two vortices were relatively insignificant below angles of attack of 14.2° (i.e. the "stalling" angle).

(4) The turbulent separation front was found to be irregular and unsteady as the stall was approached.

(5) There was no indication of separation at the aerofoil/tunnel junction prior to the establishment of three-dimensional flow.

(6) Generally, it was unlikely that the three-dimensional flow developments on the aerofoil during static tests, would be of significance prior to the attainment of maximum lift. The mid-span pressure measurements could thus be interpreted with some degree of confidence.

6.3 Static data

6.3.1 Introductory comments

The quantitative measurements performed with the aerofoil at a steady angle of attack provided a reference for the oscillatory results, discussed in the next section, and formed a basis for comparison with data from other wind tunnels.

The static data were recorded using a standardised test procedure, and consisted of data sets at 128 discrete angles of attack over the range -4^{o} to 28^{o}, at Reynolds numbers between 0.8 and 2.0 million.

Because of the small transducer outputs at the lowest Reynolds number, the transducer temperature offset drift was often significant in relation to the values actually measured. The data for the downstroke part of the test at this Reynolds number must therefore be interpreted with some degree of caution (see for example, the pitching moment versus angle of attack curve in Fig 6.11). It appeared that the pitching moment evaluation was more

sensitive to the transducer offset drift than the normal force evaluation. This was primarily because of the chordwise region in which "high drift" transducers were located.

It should be noted, that in all the tests the Mach number varied in proportion to the Reynolds number via the relation $M_\infty \simeq 1.14 \times 10^{-7}$ Re. Also, because of blockage effects, the flow velocity (and hence Reynolds number) reduced during the tests with increasing angle of attack (Fig 3.19), although the instantaneous value of dynamic pressure was used when calculating the pressure coefficients. Wind tunnel wall corrections were not applied to the presented data.

A limited amount of hot-film data were recorded in an anologue format from three chordwise positions, along with the corresponding pressure transducer outputs. These data formed the basis for comparisons with the oscillatory tests, in relation to flow reversal and separation phenomena.

6.3.2 Lift and pitching moment characteristics

The normal force coefficient, lift coefficient, leading-edge and quarter-chord pitching moments as functions of angles of attack, are shown in Figs 6.2, 6.3 and 6.4. The lift parameters which are usually considered to be of most importance are the maximum lift coefficient, the lift-curve slope, and the angle of attack for zero lift. Pitching moment parameters of similar importance are the moment coefficient at zero lift, and at $dC_m/d\alpha = 0$ prior to stall. From the data obtained, the values of these parameters have been plotted as functions of Reynolds number

in Figs 6.5 to 6.8.

(1) Maximum lift coefficient: The maximum lift was the parameter most strongly affected by variations in Reynolds number. Over the range for which the aerofoil was tested, the maximum lift coefficient, C_L MAX, increased monotonically with increasing Reynolds number (Figs 6.2, 6.4 and 6.5). Also, the angle of attack for which stall occurred (α_{ss}) was found to vary only slightly with Reynolds number. In most cases it was not possible to obtain an exact value for the stalling angle, and to a lesser extent C_L MAX, because of the abrupt nature of the stall characteristic. At lower Reynolds numbers, however, α_{ss} tended toward 14.3° and at the higher Reynolds numbers, closer to 14.7°.

(2) Lift curve slope: By definition (Abbott et al, 1945), the slope of the lift-curve is obtained from the tangent to the curve at the design lift coefficient. In general, most aerofoils tend to exhibit a near linear variation of C_L with angle of attack at lower lift, so that the lift-curve slopes can be obtained easily in accordance with this definition. For some of the NACA sections, however, slight non-linearities are found in the lift-curves close to the design lift coefficient (see Abbott et al, 1945). The present aerofoil was no exception, and the non-linear behaviour was apparent around the design lift coefficient of 0.3 (see Fig 6.2). Similar results have been obtained by Althaus et al (1980) for the NACA 23012 aerofoil (Fig 6.23). Because of this non-linear behaviour, two methods were used to obtain the lift-curve slope. One was obtained using a linear least squares data fit between C_L = 0.0 and

C_L = 1.0. The other was obtained in a similar fashion between C_L = 0.0 and the design lift coefficient, C_L = 0.3 (see Loftin et al, 1949). Both sets of data are presented in Fig 6.6, and in general, the trend was for the lift-curve slope to increase with increasing Reynolds number, although the scatter in the data was considerably greater using the latter method.

(3) Angle for zero lift: From the recorded data, the angle of attack at which zero lift was obtained was found to vary only slightly within the range of Reynolds numbers examined. For this range the zero lift angle was determined to be approximately $-0.7^{o} \pm 0.03^{o}$.

(4) Pitching moments: Values of the quarter-chord pitching moments at zero lift and $dCm/d\alpha$ = 0, showed only a small variation with Reynolds number. As shown in Fig 6.7, these pitching moments tended to become more negative at higher Reynolds numbers. The well rounded trend in the pitching moment characteristic near maximum lift at low Reynolds number, indicated that trailing-edge flow separation was present. The flattening of this curve with increasing Reynolds number indicated the suppression of the trailing-edge separation.

(5) Behaviour near maximum lift: A considerable difference was found in the shape of the lift curve close to C_L MAX with a gradual transition from a well rounded peak at lower Reynolds numbers, characteristic of trailing-edge stall, to a very abrupt stall at Reynolds numbers greater than 1.8 x 10^6, more characteristic of a leading-edge type stall. Again observation of the character of the lift variation indicated that trailing-edge separation was suppressed with

increasing Reynolds number. This transitional nature of the stall "abruptness" on the NACA 23012 was also recorded by Loftin et al (1949). Also, the NACA 23012 aerofoil was classified to be an exception to the correlation of stalling characteristics with Reynolds number and aerofoil geometry as postulated by Gault (1957). According to this correlation, the NACA 23012 aerofoil should exhibit a trailing-edge stall characteristic at higher Reynolds numbers, but, because of the abruptness of stall, was classified as a leading-edge stall type. Gault pointed out, however, the correlation may be valid for this aerofoil, if the abrupt nature of the stall was due to a rapid movement of the trailing-edge separation point towards the leading-edge. In the next few sections, details of the chordwise pressure distributions and surface flow shear stress measurements are presented, which infer that the NACA 23012 aerofoil does in fact exhibit a trailing-edge stall characteristic at the Reynolds numbers tested, although often of an abrupt nature. As noted by McCroskey et al (1980), this abrupt trailing-edge stall type is often mistaken for a leading-edge type of stall, in the presence of lift and pitching moment data only.

As the angle of attack was increased past the stall, the lift diminished, but stabilised soon after between C_L = 0.8 and 0.9. At approximately 21^{o}, a second abrupt reduction in the lift and pitching moment coefficients were observed. This was subsequently found to coexist with complete flow separation on the aerofoil chord.

On the downstroke part of the test, the loci of the

lift and pitching moment coefficients followed a different path between about 21^{o} and 19^{o}, which corresponded to a delay in the return to attached flow conditions at the leading-edge. Similarly, during further flow re-attachment near the static stall angle, slightly lower values of lift were obtained (Figs 6.11 and 6.16) accompanied by a slightly more rounded peak in the $C_L \sim \alpha$ curve. This was obtained for all the Reynolds numbers tested and was clear evidence that the stall process was dependent on the directional change of angle of attack.

6.3.3 Chordwise pressure distributions and time history characteristics

Typical chordwise pressure distributions up to the onset of stall at Reynolds numbers of 1.0, 1.5 and 2.0 million are shown in Figs 6.9, 6.12 and 6.14 respectively. Additionally, three-dimensional representations of the chordwise distributions at Reynolds numbers of 1.0 and 2.0 million are shown in Figs 6.11 and 6.16.

At each Reynolds number, a smooth pressure distribution was generally obtained up to an angle of attack of approximately 14^{o}. There were, however, exceptions to this smooth trend at locations within the first 10% to 20% chord, which manifested itself as a discontinuous rate of pressure change with increasing angle of attack. This was especially noticeable at the location at 7.5% chord, at a Reynolds number of 1.0 million. Examination of the hot-film records showed the presence of laminar to turbulent boundary layer transition in this region, and the perturbation in the smooth pressure curve was subsequently attributed to the presence of a laminar separation bubble. This discontinuous

rate of pressure change was also apparent at a Reynolds number of 2.0 million, however in this particular case, the discontinuity was present up to the onset of stall. At first, a certain amount of suspicion was directed to incorrectly logged datum values for this location, however, repetition of the test for a number of occasions showed this not to be the case, and consequently the measured values were considered to be valid. Again, this was attributed to the presence of a laminar separation bubble, and was clear evidence that its location varied with Reynolds number.

At a Reynolds number of 1.0 million, the pressure signals showed a distinct divergence at the trailing-edge region at an angle of attack of 14.32^{o}, which was indicative of separation. The amount of trailing-edge separation increased rapidly with any further increase of angle of attack. Similarly, at Reynolds numbers of 1.5 and 2.0 million, trailing-edge separation was indicated prior to stall, although in these cases, its onset occurred at an angle of attack of approximately 14.5^{o}, and progressed more rapidly toward the leading-edge. The differences in the rate of forward movement of trailing-edge separation were manifested by the increasing abruptness of stall with increasing Reynolds number, discussed previously. This was also indicated in the time-history presentations in Figs 6.10, 6.13 and 6.15.

The separation point stabilised at approximately 15% chord after the stall, with attached flow over the aerofoil leading-edge. Leading-edge suction was obtained up to an angle of attack of approximately 22^{o}, whereupon the remaining

suction suddenly collapsed, with the subsequent constant pressure region indicating separation over the entire upper surface (c.f. flow visualisation tests). This phenomenon was also discerned from the time-history and isometric chordwise pressure plots.

An alternative presentation of the chordwise pressure distributions are shown in Fig 6.17. This Figure took the form of iso-pressure values as a function of time (or reference angle), and served to illustrate the sequences of flow separation and reattachment over the aerofoil chord.

6.3.4 Hot-film anemometry records

Boundary layer information was obtained from hot-film gauges, the outputs from which were recorded at discrete angles of attack for Reynolds numbers of 1.0, 1.5 and 2.0 million, using the apparatus described in Section 3.3.7. These data were recorded in the form of oscillograph traces. Each trace was a record of the voltage output from three hot films at $x/c = 0.90$, 0.62 and 0.075. A representative oscillograph trace at a Reynolds number of 1.5 million is shown in Fig 6.22. The vertical scale on the trace represented the tangential boundary layer shear stress (uncalibrated), with the horizontal axis being time. It should be pointed out, however, that time had no special significance for the static tests, and that transducer responses were only valid during periods when the aerofoil was stationary. The angle of attack and corresponding pressure responses at each hot-film location were also recorded (again uncalibrated), with the angle of attack traces taking the form of a series of "steps".

Examination of the hot-film traces with varying angle of attack, revealed distinct changes in the character of the signals that appeared symtomatic of either laminar, turbulent, reversed, or separated flows. Subjective decisions were often required to isolate events of the boundary layer behaviour, and for a turbulent boundary layer, random fluctuations complicated the interpretations further.

The results showed that the individual hot-film gauge signal trends at each Reynolds number were qualitatively similar, although corresponding events were reached at slightly different angles of attack. At low angles of attack (say $\approx 5^{o}$) the magnitude and fluctuation amplitude of the hot-film signals indicated that the flow was laminar at 7.5% chord, but turbulent at the locations at 62% and 90% chord. As the angle of attack was increased to approximately 10^{o}, the hot-film gauge at 7.5% chord showed a progressive drop in output, followed by a very abrupt increase at about 11^{o}, indicating transition from laminar to turbulent boundary layer flow. Prior to the transition however, a change in the character of the hot-film and pressure transducer signals indicated the possible presence of a laminar separation bubble, although, this could not be verified directly. On the basis of the flow visualisation results, it is likely that a laminar separation bubble existed at the aerofoil leading-edge, although the presence of the film gauge and pressure orifices may have altered the bubble location somewhat. A further increase of the angle of attack resulted in an increase in the hot-film signal fluctuation amplitude at 7.5% chord,

which coincided with the onset of turbulent separation at the aerofoil trailing-edge.

Estimations of the turbulent separation point were inferred from a combination of both pressure and hot-film records. A distinct divergence in the pressure signal was apparent as the separation point passed across the transducer. Similarly, the hot-film record showed a drop in output and an increase in fluctuation amplitude at separation. Attached flow was maintained up to an angle of attack of about 14^{o}, after which the separation point moved quickly toward the aerofoil leading-edge across the hot-films at 90% and 62% chord, during half a degree increment in angle of attack. Separation was not indicated at the 7.5% chord position until the angle of attack reached approximately 22^{o}. The estimations of flow separation point are plotted against angle of attack in Fig 6.20. Due to the limited number of film gauges, however, it was difficult to estimate the locus of the separation point, although general trend curves are shown. By including separation data inferred from the digitally recorded pressure signals, the trend curves were significantly improved. With increasing Reynolds number, the onset of separation at 90% chord was delayed very slightly, although the rate at which separation progressed towards the leading-edge increased. Also, attached flow was sustained at the leading-edge region to higher angles of attack at the higher Reynolds numbers after the onset of trailing-edge separation and subsequent stall.

The lift coefficient variation near stall is presented in Fig 6.24 in relation to the separation point, which was estimated from the chordwise pressure distribution. At a

Reynolds number of 1.0 million, a pronounced non-linear behaviour of the lift-curve was obtained prior to stall. Separation at 97% chord was not detected from the pressure responses until well after this non-linear behaviour had begun, and was attributed mainly to thickening of the boundary layer, and not separation. Trailing-edge separation however, was indicated prior to the attainment of maximum lift. At the higher Reynolds numbers, the lift-curve slope prior to stall showed much less degradation, and generally coincided with the onset of trailing-edge separation.

Fig 6.22 shows that the general boundary layer development was reversed during the flow re-attachment process, with corresponding events reached at slightly lower angles of attack. For example, flow re-attachment was not established at the hot film gauge at 7.5% chord until 2^{o} below that at which separation was obtained during the upstroke of the test. Similarly, flow re-attachment at the film positions at 62% and 90% chord was obtained at angles of attack approximately half a degree below that of separation. Consequences of this delay in the flow re-attachment can also be observed in relation to the lift and moment coefficients in Figs 6.11 and 6.16, with a slight hysteresis apparent.

An interesting comparison was drawn between the flow re-attachment data and inferred separation points from the flow visualisation tests (Fig 6.21). The correlation between the two sets of data was much closer than that for the separation data, indicating that the technique used during the visualisation tests, may be more indicative of

the return to attached flow after stall. This possibility has also been pointed out by Gregory et al (1971).

6.3.5 Comparison with data from other sources

Lift and pitching moment data for the NACA 23012 aerofoil were compared with data presented by Loftin et al (1949), and Althaus et al (1980), at Reynolds numbers of 1.0, 1.5 and 2.0 million. The qualitative behaviour of the lift data from all three sources was found to correlate well. In all cases, increasing values of C_L MAX with increasing Reynolds number was apparent, however, at Reynolds number of 2.0 million, the present C_L MAX was considerably less than that from the other two sources (see Fig 6.5). This was attributed mainly to wind tunnel interference effects, and differences were to be expected. In all cases, the stalling angle was approximately equal for all three Reynolds numbers; this being about 14.5^{o}. The qualitative behaviour of the Althaus pitching moment data however, differred significantly from both the present and the Loftin data, but this may be due to the fact that only a few data points have been presented by Althaus (Fig 6.23).

6.3.6 Kirchoff modelling

The mathematical theory of separating potential flows - usually termed Kirchoff or Helmholz flows - are reviewed by Thwates (1960), and Woods (1961). Perhaps, more appropriately, this theory can be said to be a modification to the potential flow due to a specified trailing-edge

stagnation point location, or an effective Kutta condition.

Recently Beddoes (1981), has shown that the Kirchoff flow theory may be used with aerofoil experimental or inferred flow separation point data, to give successful reconstructions of lift, moment and drag behaviour. For the case of a flat plate at an angle of attack α, the lift coefficient, C_L, can be approximated in terms of the chordwise location of the separation point, f, viz:

$$C_L = \pi\alpha\left(1+\sqrt{f}\right)^2/2$$

and for a general aerofoil, this expression can be replaced by:

$$C_L = C_{L\alpha}\alpha\left(1+\sqrt{f}\right)^2/4$$

where $C_{L\alpha}$ is the lift curve slope determined from test data in the low angle of attack range, and α is now measured relative to the zero lift angle.

To conclude the static test results discussed in this section, the Kirchoff flow model has been applied as an inverse procedure in order to calculate the position of chordwise separation from the measured lift data, viz:-

$$f = \left\{2\left(C_L/C_{L\alpha}.\alpha\right)^{0.5} - 1\right\}^2$$

Calculations of the separation point at Reynolds numbers of 1.0, 1.5 and 2.0 million are presented in Fig 6.24. The lift curve slope was determined on the basis of a linear least squares data fit between C_L = 0.0 and C_L = 1.0. Also, because of numerical difficulties when evaluating the above expression, at low values of α, this part of the curve has been extrapolated.

Generally, a good correlation existed between indicated

separation points from hot-film and pressure data, and the calculated separation point using the Kirchoff model, especially after the onset of stall. However, the Kirchoff flow model consistently over-predicted separation onset from the measured lift data. As mentioned previously, rounding-off of the lift-curve slope was often initiated before the detection of trailing-edge separation, and this was considered to be mainly due to boundary layer displacement effects.

It was perhaps somewhat surprising, that the Kirchoff flow model reproduced the approximate separation point location as a function of angle of attack, to such a degree of accuracy. Hence, for the particular test condition examined, the Kirchoff flow model could be considered a valid model for the approximate representation of trailing-edge flow separation on the aerofoil lift behaviour.

6.3.7 Conclusions

Based on static data recorded for the NACA 23012 aerofoil at Reynolds numbers between 0.8 and 2.0 million, the following main conclusions were made:

(1) The aerofoil exhibited stall by the mechanism of trailing-edge separation for all Reynolds numbers within the range tested.

(2) The onset of trailing-edge separation was delayed to higher angles of attack with increasing Reynolds number.

(3) The rate of forward movement of the separation point increased with increasing Reynolds number.

(4) The maximum lift increased with increasing Reynolds number, accompanied by an increase of the stall abruptness. (Manifestations of (3) and (4).).

(5) The possible presence of a laminar separation bubble was indicated at the aerofoil leading-edge from both pressure and hot-film responses.

(6) After stall, the flow re-attachment occurred at slightly lower angles of attack than for the corresponding separation.

(7) The flow re-attachment process after stall (i.e. downstroke of the static test) was more representative of the technique used for the flow visualisation tests.

(8) The hot-film anemometry results often required subjective interpretation, although main boundary layer events such as transition and separation were recognised. These interpretations formed the basis for tests performed under unsteady conditions.

CHAPTER 7

RESULTS AND DISCUSSION (2) - OSCILLATORY TESTS

7.1 Introduction

In Chapter 6, a detailed discussion of the results obtained from the static investigation of the NACA 23012 aerofoil aerodynamic characteristics were presented. In the present Chapter, the results recorded from the oscillatory tests are examined, and important features of the data are discussed.

The oscillatory aerofoil data were recorded using a standardised testing procedure, and consisted of a maximum of 128 instantaneous pressure distributions, with the corresponding aerofoil angle of attack and free-stream dynamic pressure, over each cycle. To permit a comparative analysis, ten cycles of oscillatory motion were recorded and subsequently ensemble averaged to reduce the effects of randomness in the flow, prior to the analysis of the pressure loadings. The majority of the data from the parametric summary have been presented in the form of normal force and quarter-chord pitching moment versus angle of attack curves, and although not all the plots are referenced in the text, a proportion has been included for completeness.

A limited amount of hot-film data were recorded in an analogue format, and were used to help identify the main boundary layer phenomena during the unsteady aerofoil motion. Interpretation of the hot-film data required a certain amount of subjective judgement, although in the majority of the tests, careful examination revealed the

main boundary layer characteristics.

All the digital data from the oscillatory tests were recorded on DEC standard RX02 floppy disks, and are retained at the Department of Aeronautics and Fluid Mechanics, University of Glasgow. The total amount of raw data consisted of some 40M bytes, with a standard file length of 80K bytes.

7.2 Parametric analysis

7.2.1 Introductory comments

Oscillatory pressure data were recorded for five-hundred test cases, which consisted of systematic variations of the mean angle of attack, α_m, the oscillation amplitude, α_a, the reduced frequency, k, and the Reynolds/Mach number (as indicated by Table 5.1).

A wide range of test cases were recorded in order to facilitate a detailed parametric analysis, especially since the basic NACA 23012 aerofoil profile was designated to serve as a reference standard, for future tests on derived aerofoils using the present test facility. A summary of the results obtained from these parametric tests are described in the following Sections.

7.2.2 Effect of Reynolds/Mach number variation

Of the various parameters that were examined, the effect of Reynolds/Mach number variation was found to be the least significant. Tests were carried out at Reynolds numbers of 1.0 and 1.5 million, which corresponded to Mach numbers of approximately 0.08 and 0.12. Although the Mach number could not be varied independently of the Reynolds number, minor effects were discernable between corresponding

sets of parameters at the two Reynolds/Mach numbers examined. Because of the low Mach number, these effects were considered attributable mainly to the variation of Reynolds number. From existing experimental data, Mach number appeared to become a more dominating parameter only when the flow around the aerofoil approached supercritical (see for example McCroskey et al, 1980).

For the oscillatory test cases examined in detail in the present work, the Reynolds number increase generally manifested itself by slightly greater values of $C_{N\ MAX}$ and $-C_{m\ MIN}$, as in the case of the static tests. This was attributed mainly to a delay in the onset of flow separation at the higher Reynolds number, with correspondingly larger leading-edge suction peaks being achieved. Further, observations indicated that for cases where a dynamic stall vortex was present, the strength of this vortex appeared slightly greater at the higher Reynolds number. A slight delay in the return to attached flow during the downstroke of the oscillatory cycle was also observed.

Apart from these minor effects, the qualitative behaviour of the chordwise pressure distributions and integrated loadings were largely similar at each of the two Reynolds numbers examined. Subsequently, the discussion of results from the remainder of the parametric analysis has been restricted to that from the higher Reynolds number of 1.5 million.

7.2.3 Effect of mean angle of attack variation

The effects of changing the mean angle of attack, whilst maintaining a constant oscillatory amplitude and reduced frequency, are generalised in Figs 7.1 to 7.20 in the form

of plots of normal force, C_N, and pitching moment, C_m, against angle of attack, α, and are compared with static data which is indicated by the dotted curve.

At the lowest reduced frequency examined (k = 0.01), the C_N and C_m behaviour was essentially quasi-static, in the sense that departures from the static behaviour were minimal throughout the cycle. This was certainly true at the lower and higher mean angles of attack, but where the oscillation centred near the static stall angle ($\alpha_{ss} \approx 14^\circ$), a certain amount of hysteresis was apparent (Fig 7.2). An increase of the oscillation amplitude had the effect of increasing this hysteresis (Fig 7.4), but dynamic effects such as the overshoot of C_N, were small except again for oscillations centred near α_{ss}. Some evidence of weak leading-edge vortex shedding was also indicated under these conditions.

Dynamic effects became more significant at a reduced frequency of 0.05 and amplitude of 4°, (Figs 7.5 and 7.6), although the C_N and C_m behaviour was still largely quasi-static at mean angles below and above that of the static stall angle. Again, by increasing the amplitude of the oscillation to 10°, dynamic effects became further pronounced, with significant C_N overshoots and large nose-down pitching moments generated due to large changes of the centre of pressure caused by the vortex shedding phenomenon (Figs 7.7 and 7.8). Also, at this reduced frequency for mean angles greater than 12°, secondary peaks in the C_N and C_m characteristics were apparent prior to the attainment of α_{MAX}. This was considered to be due to a secondary vortex, although its strength was considerably

less than the primary dynamic stall vortex. This phenomenon is shown for the chordwise pressure distributions depicted, for example, in Fig 7.131.

For reduced frequencies greater than 0.05, the C_N and C_m behaviour for mean angles less than the static stall angle were found to be qualitatively similar for matching parameters, with the characteristic elliptical C_N and C_m curves indicating separation free flow. With increasing reduced frequency, the mean angle was required to be raised in order to induce separation during part of the cycle. For an oscillation amplitude of 4^o, this qualitatively similar behaviour was continued throughout the range of mean angles, with similar hysteresis loops generated at correspondingly greater mean angles of attack. For an oscillation amplitude of 10^o, greater variability between C_N and C_m hysteresis loops were apparent, although again, by increasing the mean angle of attack, a qualitatively similar behaviour could be obtained at the higher frequencies. For example, the hysteresis loops obtained for $\alpha = 14 + 10 \sin \omega t$ at $k = 0.10$, were changed significantly by increasing the reduced frequency to 0.15 or 0.20, however, a similar behaviour could be re-established by increasing the mean angle of attack to 16^o or 18^o (see Figs 7.12 to 7.20). Secondary vortex shedding was very pronounced for mean angles of attack greater than 16^o, and appeared to occur predominently at lower reduced frequencies (< 0.15).

7.2.4 Effect of amplitude variation

The effect of oscillation amplitude was examined for a range of constant mean angles and reduced frequencies. C_N and $C_m \sim \alpha$ curves for increasing amplitude are shown in

Figs 7.21 to 7.50, the static behaviour being shown by the dotted curve.

Often, the trends observed in conjunction with amplitude variations were qualitatively similar to those observed for frequency changes (see Section 7.2.5), at least to the extent that the onset of separation and the occurrence of dynamic stall was a function of the rate of change of angle of attack, $\dot{\alpha}$, this being proportional to the oscillation amplitude, αa.

At low reduced frequencies, i.e. k = 0.01, the C_N and C_m behaviour was largely quasi-static and relatively independent of amplitude, but with a certain amount of hysteresis apparent when the angle of attack passed through the normal static stall angle (Fig 7.24).

At the higher reduced frequencies, dynamic effects of amplitude variation were significant, with the onset of separation being delayed as the amplitude was increased, until evidence of a dynamic stall vortex appeared (e.g. Fig 7.34). For oscillations centred near the static stall angle, the effects of amplitude increase were very significant, (see for example Figs 7.30, 7.36 and 7.42), with large C_N and C_m hysteresis loops. Again, evidence of secondary vortex shedding was apparent also for most of the test cases where a strong primary vortex occurred. (See Section 7.6). The important differences between moment stall and lift stall are emphasised here. Moment stall, that is when a significant divergence of the $C_m \sim \alpha$ characteristic occurs, is due to the leading-edge vortex formation and chordwise passage. Lift stall on the other hand, occurs when the dynamic stall vortex passes the aerofoil

trailing-edge, and this leads to a very abrupt loss of lift. Whereas, under static conditions, lift stall and moment stall occur coincidently, under dynamic moment stall will precede lift stall.

7.2.5 Effect of reduced frequency variation

Of the parameters investigated, the most significant was found to be the reduced frequency of the aerofoil oscillation. C_N and C_m versus α curves are shown for constant mean angles and amplitudes, and for increasing reduced frequencies in Figs 7.51 to 7.70, the static behaviour being represented by the dotted curve.

At low mean angles, where the instantaneous angle of attack did not exceed the static stall angle, the characteristic potential flow type elliptical curves were obtained for both C_N and C_m versus α (see for example, Figs 7.51 and 7.53). These curves appeared as sinusoids when viewed as a function of ωt (e.g. Fig 7.159). With increasing reduced frequency, the elliptical hysteresis loops widened, and the C_N curve in particular began to rotate clockwise about the static curve, with a rotational centre near that of the mean angle of the oscillation. This is a characteristic which is predicted by unsteady inviscid flow theory.

When the oscillation amplitude was such that separation occurred for part of the cycle (Fig 7.54), the separation could generally be suppressed by increasing the reduced frequency, giving a return to the elliptical hysteresis loops. This trend was generally true for the full range of mean angles below the static stall angle. For the higher

mean angles, separation could not generally be suppressed significantly by increasing the reduced frequency. This was clearly indicated in the chordwise pressure distributions depicted in Figs 7.119 to 7.157.

During cases where a dynamic stall vortex was inferred, the vortex formation was delayed with increasing reduced frequency. As a consequence of this, $C_{N\ MAX}$ and $C_{m\ MIN}$ tended to occur at higher angles of attack. At low reduced frequencies (k = 0.05) vortex inception and chordwise passage occurred prior to the maximum angle of attack, α_{MAX} (see Figs 7.64 and 7.66). At a reduced frequency of 0.05, secondary vortex shedding was indicated for the higher amplitude cases, this also occurring prior to α_{MAX}. As the reduced frequency was increased however, the secondary vortex passage occurred at a later portion of the cycle (Fig 7.166), and was of diminished intensity. Analysis also showed that the primary dynamic stall vortex traversed the aerofoil chord at approximately 40% of the free-stream velocity, and the secondary vortex at approximately 70% of the free-stream velocity.

At the higher reduced frequencies ($\geq$0.15), vortex inception and chordwise passage occurred close to α_{MAX}, and at the highest reduced frequency (0.2), the aerofoil angle of attack had started to decrease prior to the vortex having fully traversed the chord, as shown in Figs 7.62 and 7.138. Also, during the dynamic stall vortex formation and chordwise passage, the normal force and pitching moment behaved non-linearly with respect to angle of attack.

7.2.6 Pitch damping characteristics

For pitching moment versus angle of attack curves, the

area enclosed by the locus and sense of transcription have an important physical significance. The net work done by the aerofoil on the surrounding airstream, is proportional to the integral $-\oint C_m . d\alpha$. This integral is equivalent to the net area enclosed by the $C_m \sim \alpha$ curve and is positive for an anticlockwise circuit. If the integral is negative, this represents a net extraction of energy from the airstream by the aerofoil, and indicates an unstable situation. For example, this condition could lead to an aeroelastic phenomenon called stall flutter on a helicopter rotor blade.

Fig 7.175 shows the effect of reduced frequency on aerofoil damping for the full range of mean angles and oscillation amplitudes. In each case, the damping was obtained by trapezoidal numerical integration of the $C_m \sim \alpha$ data, and the figure is presented to summarise the aerofoil damping characteristics over the full parametric range. At low mean angles, i.e. $\alpha_m \leq 10^o$, approximately neutral or positive damping was generally indicated throughout the range of amplitudes and reduced frequencies. As the mean angle of oscillation was increased further however, there was a strong trend towards negative damping with increasing reduced frequency. At the highest frequency of 0.2, the damping was always strongly negative when the angle of attack exceeded the static stall angle. It was interesting to note however, that there appeared to be a single reduced frequency ($k = 0.1$) for which the damping was approximately neutral over the full range of mean angles and amplitudes, and indicated the transition from positive to negative damping. This can be explained in terms of the relative phasing of the aerofoil motion, the onset of separated flow

and the delay in the return to attached flow.

By correlating the damping against the mean angle of attack (Fig 7.176) and the maximum angle of attack (Fig 7.177), the variability between data at different mean angles and amplitudes at a given reduced frequency was diminished. This was perhaps more clearly shown in Fig 7.177, and indicates that the maximum angle of attack is an important parameter when correlating oscillatory aerofoil data.

7.2.7 Maximum normal force and pitching moment characteristics

The maximum normal force data provided an indication of the useful lifting effort from the aerofoil, but could only be related in terms of the minimum pitching moment, as this was perhaps the more important parameter if considered for application to an elastic rotor blade.

Fig 7.178 indicates the effect of reduced frequency on the maximum normal force and minimum pitching moment for a range of mean angles and oscillation amplitudes. For these data, there generally appeared to be an increasing trend in $C_{N\ MAX}$ and $-C_{m\ MIN}$ with increasing amplitude. As the frequency was increased however, the peak loads were observed to reach a turning point and decrease, for oscillations about mean angles below 16^{o}. At the higher mean angles, these values appeared to reach a plateau, although the downward trend may have appeared if the reduced frequency had exceeded 0.2. Generally however, increasing the reduced frequency tended to diminish the magnitude of the maximum loadings for reduced frequencies greater than 0.1.

Correlations of $C_{N\ MAX}$ and $C_{m\ MIN}$ plotted against the mean angle, α_m, (Fig 7.179) and the maximum angle of attack, α_{MAX}, (Fig 7.180) were performed, as in the case of the aerofoil damping. Again, the variability between different sets of parameters were found to be considerably reduced, especially for correlations against α_{MAX}. As for the damping, this suggested that the maximum angle of attack was an important parameter for consideration when correlating oscillatory aerofoil data. A similar point has been made by Wilby (1980).

Finally, the maximum normal force, $C_{N\ MAX}$ and the minimum pitching moment, $C_{m\ MIN}$ were correlated against the corresponding angle of attack. This was performed for the entire data set, as shown in Fig 7.181. It was interesting to note that both $C_{N\ MAX}$ and $C_{m\ MIN}$ tended to relate linearly to the angle of attack, both in the attached and separated flow regemes. This also implied a linear relationship for the location of the centre of pressure at $C_{N\ MAX}$ (or $C_{m\ MIN}$) as a function of angle of attack.

7.2.8 Pitching moment versus normal force crossplot

An alternative presentation of the unsteady aerofoil characteristics was in the form of a crossplot of the normal force, C_N, versus the pitching moment, C_m. This method of presentation has the advantage that it eliminates the dependence on the angle of attack, α. Carr et al (1977), have commented on this presentation and have attempted to generalise the unsteady force and moment characteristics, however, with variable success. A certain amount of data

from the present work has been generalised in the form of C_N versus C_m crossplots in Figs 7.169 to 7.174, to highlight certain behavioural aspects. Again, the static behaviour is shown by the dotted curve.

Fig 7.169 shows the effects of increasing the reduced frequency at mean angles of attack of 6^o and 8^o with an amplitude of 4^o. At a reduced frequency of 0.01, the C_N C_m characteristic largely followed the static behaviour, as might be expected. As the reduced frequency was increased further, however, the $C_N \backsim C_m$ curves opened out into ellipses. Comparing with the C_N and $C_m \backsim \alpha$ data of Fig 7.51 will show that the widening elliptical curve trend was particularly predominant in C_m, thus reflecting the C_m characteristic at this low mean angle of attack.

As the oscillation amplitude was increased to 10^o, and the maximum angle of attack exceeded the normal static stall angle, the deviations from the static characteristic at low frequency indicated that separation was present for part of the cycle (c.f. Fig 7.52). By increasing the reduced frequency, however, the return to the elliptical curves indicated that the separation was suppressed. Again, as the mean angle of attack was increased, it was necessary to raise the reduced frequency in order to suppress the separation.

At mean angles of attack near the static stall angle, the hysteresis in the C_N characteristic became large as compared with low mean angles, where there was little C_N hysteresis. Thus, the $C_N \backsim C_m$ crossplot did not predominantly reflect the $C_m \backsim \alpha$ characteristic, and was consequently more difficult to interpret. For a mean angles

of attack of 15° and 16°, and an amplitude of 4° (Fig 7.171), qualitatively similar $C_N \backsim C_m$ characteristics were obtained with increasing frequency. As the oscillation amplitude was increased to 10° however, small secondary loops appeared within the main curve (Fig 7.172). Referring to Fig 7.64, these secondary loops could be explained quite simply in terms of the formation of a secondary vortex. After the occurrence of $C_{N\ MAX}$, which implied that the primary dynamic stall vortex had almost fully traversed the aerofoil chord, both the lift and pitching moment dropped abruptly, indicating that the vortex had passed the aerofoil trailing-edge. Shortly after, a secondary peak in both C_N and C_m often appeared (e.g. $\alpha = 15 + 10 \sin \omega t$; $k = 0.05$) which was characteristic of the secondary vortex shedding. This gave rise to a reverse trend in the sense of transcription of the $C_N \backsim C_m$ curve, and with the corresponding decrease in pitching moment, a loop was formed within the main curve prior to the return to the (almost) quasi-static behaviour.

Increasing the mean angle of attack to 18° and 20° (Figs 7.173 and 7.174), again, neglecting the occurrence of secondary loops, the qualitative $C_N \backsim C_m$ behaviour was similar, the primary loops increasing in size as the reduced frequency was increased. Also, however, it was noted that the development of the secondary loops occurred at lower values of C_N with increasing frequency. This could be explained in terms of the phase of the secondary vortex passage velocity ($\approx 70\%\ V_\infty$) and the aerofoil motion (i.e. $\dot{\alpha}$).

7.2.9 Conclusions from the parametric investigation

From the parametric investigation into the effects of Reynolds number, mean angle of attack, oscillation amplitude and reduced frequency, the following main conclusions were made:

(1) The dependence of Reynolds number between 1.0 and 1.5 million was small or negligible.

(2) There was a strong dependence on the mean angle of attack, with large amounts of hysteresis in the normal force and pitching moment characteristics for mean angles near that of the static stall angle.

(3) For low mean angles of attack and amplitudes for which the static stall angle was not exceeded, eliptical normal force and pitching moment curves characterised separation free flow.

(4) For conditions under which the static stall angle was exceeded by a small margin, and slight separation was indicated, the separation could generally be entirely suppressed by increasing the reduced frequency of the oscillation.

(5) For higher mean angles of attack separation could not be entirely suppressed by increasing the reduced frequency, although could generally be reduced, especially during the upstroke of the aerofoil motion.

(6) The most significant of the parameters that were investigated, was found to be the reduced frequency of the aerofoil oscillation.

(7) The effects of amplitude variation on the aerodynamic characteristics were large, this again being particularly pronounced at mean angles of attack near that of the static stall angle.

(8) The occurrence of a dynamic stall vortex was found for oscillations which centred near the static stall angle.

(9) The strength of the dynamic stall vortex was highly dependent on the frequency and amplitude of the oscillation, and to limited extent on the mean angle of attack.

(10) The occurrence of secondary vortex shedding was found for most cases where a strong primary vortex was formed, and was predominantly apparent for reduced frequencies between 0.05 and 0.15.

(11) The inception of leading-edge vortex shedding was delayed with increasing reduced frequency.

(12) The leading-edge vortex was found to occur at approximately the same chordwise location for the cases examined, this being approximately 20% chord.

(13) The primary dynamic stall vortex was found to traverse the aerofoil chord at a rate approximately 40% of the free-stream velocity. The secondary dynamic stall vortex was found to traverse the chord considerably faster at approximately 70% of the free-stream velocity.

(14) During the leading-edge vortex formation and chordwise passage significant non-linear behaviour of the normal force and pitching moment versus angle of attack was apparent.

(15) Positive or neutral aerofoil damping generally occurred for reduced frequencies less than 0.10. With further increases of reduced frequency however, there was a strong trend towards negative aerodynamic damping for all combinations of mean angles and amplitudes.

7.3 Hot-film anemometry records

7.3.1 Introductory comments

Unsteady boundary layer information was obtained for the oscillatory aerofoil tests in a similar manner to the static tests reported in Section 6.3.4. As discussed previously, the hot-film anemometry data required subjective decisions in order to isolate the observations that were made of the flow behaviour. Further, as single element hot-film gauges were used, forward and reversed flow could not be directly distinguished because the outputs from the gauges could never become negative. Instead, a minimum point was formed as the boundary layer flow changed direction. Also, in a turbulent boundary layer, the random fluctuations complicated the interpretation of the various flow phenomena.

As in the case of static tests, data were recorded in the form of oscillograph traces. The outputs recorded from the film gauges and corresponding pressure transducers were uncalibrated and provided only a qualitative representation of the boundary layer shear stress behaviour. In each case the outputs were recorded as a function of time. Results were obtained at a constant Reynolds number of 1.5 million for mean angles of attack of 6^{o}, 15^{o} and 20^{o}, and for reduced frequencies of 0.01, 0.05, 0.10, 0.15 and 0.20. For each test case, the amplitude of the oscillation was 10^{o}, with several cycles of output being recorded for analysis.

7.3.2 Analysis and discussion

At a mean angle of attack of 6^{o}, the behaviour of the boundary layer appeared to be essentially quasi-static at

the lowest reduced frequency of 0.01, with indications of flow reversal and separation occurring at the same chordwise position at approximately the same instant in time (Fig 7.182). As found for the static tests, flow reversal (and separation) progressed from the trailing-edge towards the leading-edge, accompanied by an abrupt drop in the value of the leading-edge suction. The symmetry of the transducer outputs with respect to the maximum angle of attack indicated that the flow reattachment process occurred essentially in reverse to flow separation at this low reduced frequency, although at slightly lower angles of attack.

As the reduced frequency was increased to 0.05 however (Fig 7.183), the first effects of unsteady aerofoil motion on the boundary layer development became apparent, with flow reversals taking place at 90% and 62% chord prior to separation. (Separation was generally indicated more clearly by pressure transducer signal divergence, rather than the hot-film gauge response). Also, for this reduced frequency, the leading-edge pressure at 7.5% chord showed only a gradual drop of output prior to flow re-attachment. With any further increase of reduced frequency, attached flow persisted for the entire oscillatory cycle (Fig 7.184). The small mean outputs from the film gauges at 62% and 90% chord however, indicated that the flow came close to reversal at $k = 0.10$. This tendency however, was eliminated at $k = 0.15$ and 0.20 (Fig 7.194). The effect of reduced frequency on the point of laminar to turbulent transition at 7.5% chord showed almost a linear behaviour, as shown in Fig 7.195.

By increasing the mean angle of attack to 15^{o}, a dramatic change in the character of the transducer signals was observed, especially for reduced frequencies greater than 0.01. At the lowest frequency, the boundary layer behaviour was largely quasi-static, with flow reversal and separation progressing towards the leading-edge (Fig 7.185). The symmetry of the traces about α_{MAX} also reflected the quasi-static behaviour. For a reduced frequency of 0.05, unsteady effects in the boundary layer became noticeable, with flow reversal preceding separation. As the reduced frequency was increased to 0.1, however, further unsteady effects were indicated (Fig 7.187). Again, flow reversal was observed to pass over the gauge at 90% chord, followed by the gauge at 62% chord. Almost simultaneously as the flow reversed at 62% chord, a distinct divergence of both the pressure and hot-film signals at 7.5% chord was observed, followed by distinct perturbations in all the transducer outputs. By comparing the chordwise pressure plots of Fig 7.133, it was inferred that these perturbations were the imprint made by the passage of a dynamic stall vortex, with successive peaks in pressure at successive chordwise locations as a function of time. Minimal changes in the pressure signals at 62% and 92% chord were observed prior to the formation of this vortex. The large increase in the surface shear stress as the vortex passed the hot-film gauges indicated that the vortex passage induced a reverse flow region of considerable strength. After the vortex passage, the nature of the pressure signals indicated separated flow. In fact, the vortex passage induced flow separation, which proceeded from the leading-edge to the trailing-edge.

Increasing the reduced frequency further produced qualitatively similar transducer responses, although the onset of flow reversal and subsequent progression towards the leading-edge occurred at higher angles of attack. This is shown in Fig 7.192 where the flow reversal point is plotted against angle of attack for various reduced frequencies. Leading-edge transition trended asymtotically to $\alpha = 12.5^{\circ}$ as shown in Fig 7.195.

At a mean angle of 20°, no significant features in the transducer outputs were observed as compared with $\alpha_m = 15^{\circ}$, other than an increase in the fluctuation amplitude of the hot-film signals (Figs 7.190 and 7.191). Again, flow reversal was observed to pass from the trailing-edge towards the leading-edge (Fig 7.193) prior to the occurrence of a dynamic stall vortex. Quite noticeable however, was the imprint of a possible secondary vortex (c.f. Fig 7.70), and this phenomenon is discussed further in Section 7.6.

7.3.3 Conclusions from hot-film analysis

To summarise the results of this section, a number of conclusions were made on the basis of the hot-film analysis:

(1) Flow reversal was found to occur approximately coincidentally with separation only at low reduced frequencies ($k = 0.01$).

(2) For reduced frequencies greater than 0.01, flow reversal preceded the onset of separation.

(3) For low mean angles of attack, flow reversal and separation could be completely suppressed by increasing the reduced frequency.

(4) At higher mean angles of attack, an increase of reduced frequency still had the effect of reducing separation

for a given oscillatory amplitude, but not eliminating it.

(5) The onset of flow reversal was delayed to higher angles of attack with increasing reduced frequency.

(6) The rate of forward movement of flow reversal was reduced with increasing frequency, and also to some extent with amplitude.

(7) In cases where a dynamic stall vortex occurred, flow reversal passed the gauge at 62% chord prior to vortex initiation.

(8) The passage of the primary dynamic stall vortex induced flow separation on the aerofoil upper surface, which occurred from the leading-edge to the trailing-edge.

7.4 Analysis of unsteady flow regimes on the NACA 23012 aerofoil

7.4.1 Below stall

When the oscillation was confined to angles of attack below the normal static stall angle, the boundary layer on the aerofoil upper surface remained attached throughout the cycle. This produced the characteristic potential-flow-type elliptical traces of $C_N \sim \alpha$ and $C_m \sim \alpha$, as shown for example for $\alpha = 8 + 4 \sin \omega t$ in Fig 7.53. The trace in each case, was formed in an anti-clockwise sense. With increasing reduced frequency, these elliptical shapes widened, and rotated about an axis approximately equal to the mean angle of attack. When viewed as a function of ωt, both C_N and C_m appeared as sinusoids (see for example, Fig 7.161).

The primary effects of oscillations in this low angle of attack regime can be predicted using unsteady potential flow theory (see Bisplinghoff et al, 1955). However,

secondary effects due to boundary layer displacement - thickness make accurate quantitative prediction of the aerofoil behaviour considerably more difficult.

7.4.2 Stall onset

The stall onset condition represented the limiting case for the maximum lift that could be obtained without significant penalty in the pitching moment. For practical purposes, the no-stall and stall onset regimes were similar, since the boundary layers remain thin throughout the oscillatory cycle. A typical case is shown in Fig 7.54 for $\alpha = 8 + 10 \sin \omega t$, where at a reduced frequency of 0.15, the shapes of the $C_N \sim \alpha$ and $C_m \sim \alpha$ curves indicated that only slight separation existed during the cycle. The "distorted" elliptical $C_N \sim \alpha$ curve appeared characteristic of the stall onset condition throughout the parametric range studied.

With increasing reduced frequency, the degree of flow separation during the cycle was suppressed, with a return to the smooth elliptical $C_N \sim \alpha$ and $C_m \sim \alpha$ curves, characteristic of the no-stall regime. Trailing-edge separation was apparent only at the lowest reduced frequency of 0.01, but made only minor effects on the final stall behaviour. This is discussed further in Section 7.5.

Finally, the stall onset condition is amenable to theoretical analysis by boundary layer and viscid/inviscid interaction approaches, and the results permit good quantitative predictions of the aerofoil behaviour.

7.4.3 Light Stall

When the maximum angle of attack during the oscillatory cycle exceeded the normal static stall angle, the unsteady

behaviour was characterised by significant phase-lags and hysteresis in the separation and reattachment of the flow. Evidence of leading-edge vortex shedding was often indicated under light stall conditions, but from the magnitude of the perturbation in the chordwise pressure distribution, the vortex generally appeared well diffused. A typical example of light stall is shown for $\alpha = 10 + 10 \sin \omega t$ at a reduced frequency of 0.16, in Figs 7.56 and 7.97.

The $C_N \sim \alpha$ and $C_m \sim \alpha$ curves under light stall conditions appeared to follow a characteristic "figure-of-eight" shape, which was especially pronounced in the case of the pitching moment, C_m. The introduction of this secondary loop in the $C_m \sim \alpha$ curve gave rise to neutral or negative damping. By increasing the reduced frequency of the oscillation however, separation could often be suppressed, giving a return to positive damping, but this was generally true only for the lower mean angles of attack (i.e. $\leq 10^o$).

7.4.4 Strong stall

The stall behaviour in this regime was strongly dominated by the vortex shedding phenomenon, which has been discussed previously. The passage of this vortex from the leading-edge region across the aerofoil surface produced aerodynamic loadings which were considerably different to the corresponding static values. Large amounts of hysteresis in the normal force and pitching moment were generally evident over a large part of the cycle, especially during the return to attached flow. A degree of randomness between successive cycles indicated that the stall process itself was partially non-repeatable, especially in terms of the development and strength of the dynamic stall vortex.

A typical case of strong dynamic stall is illustrated in Figs 7.64 and 7.133, for $\alpha = 15 + 10 \sin \omega t$ at a reduced frequency of 0.1, where a large overshoot in the normal force and pitching moment was apparent. From existing experimental data however, it appears that this "non-linear" overshoot is primarily a low Mach number phenomenon. Also, secondary vortex shedding was often indicated during cases of strong dynamic stall, and both these effects are discussed further in Section 7.6.

The initiation of the leading-edge vortex appeared to take place at approximately the same chordwise position for cases of strong dynamic stall, with the first disturbances in the smooth pressure distributions appearing at approximately 15% chord. From the hot-film data recorded, flow reversal at <u>least</u> up to 62% chord was found to precede the vortex development. The velocity at which the primary stall vortex traversed the aerofoil upper surface was determined to be approximately 40% of the free-stream velocity, and was found to be relatively independent of the reduced frequency, amplitude etc. When present, the secondary vortex was found to traverse the chord considerably faster, at about 70% of the free-stream velocity.

7.5 Comments on trailing-edge separation during unsteady aerofoil motion

One of the objectives of the present work was to examine the relative importance of trailing-edge flow separation on the dynamic stall characteristics of the NACA 23012 aerofoil, and on the basis of initial observations, to assess the direction for which further research in this area should be directed.

Trailing-edge separation appears to be involved to some degree in most examples of aerofoil stall. Even with minor trailing-edge separation, the associated reduction of upper surface suction introduces a non-linear behaviour in the lift and pitching moment (see Fig 1.3). For steady conditions, the point at which $\tau w = 0$ is generally approximately coincident with the turbulent separation point. Under unsteady conditions however, this relationship changes, with flow reversal in the boundary layer preceding separation. The definition of the conditions under which separation actually takes place is a somewhat subjective, however, it is generally accepted that the flow detaches from the aerofoil surface to form a wake which encloses a reversed flow region. Immediately prior to this point, it has been observed that the boundary layer quickly thickens, with a lowering of the surface shear stress. After separation, there is a distinct change in the magnitude of the static pressure in the wake region, and the pressure distribution in the wake is usually characterised by a constant pressure region extending to the aerofoil trailing-edge.

From measurements performed in the present work, boundary layer reversal and separation characteristics under static conditions were compared with those under dynamic conditions. Under dynamic conditions, separation was more clearly indicated by a divergence in the pressure transducer output signal as the flow separation point passed over the transducer location. The increased fluctuation amplitude of the hot-film signal after the passage of a point of flow reversal made the interpretation of separation from the hot-film

response alone, very difficult.

As mentioned previously, the aerofoil used in these tests (NACA 23012) exhibited an abrupt trailing-edge stall characteristic under static conditions. Under oscillatory conditions, even at the lowest reduced frequency tested (0.01), it was found that the trailing-edge separation was almost entirely suppressed. However, when it did occur, the rate of forward movement was even more abrupt than in the static case. A typical example of this can be observed in Fig 7.77 for $\alpha = 6 + 10 \sin\omega t$ at k = 0.01, and also in Fig 7.101 for $\alpha = 13 + 4 \sin\omega t$ at k = 0.01, although in the latter case, a small perturbation characteristic of vortex shedding appeared near the leading-edge. Hot-film measurements were recorded for the case $\alpha = 6 + 10 \sin\omega t$, and at the lowest reduced frequency of 0.01, flow reversal was found to be almost coincident with a divergence in the pressure signals. With increasing reduced frequency, both flow reversal and separation were suppressed, and at k = 0.15, were completely eliminated.

7.6 Comments on the formation of the dynamic stall vortex

The formation of the characteristic dynamic stall vortex is a most difficult phenomenon to explain. In the past, the mechanisms involved in the vortex formation have been the subject of certain amount of speculation by many investigators. (See Young (1981) for a review of these mechanisms). It was not the intention to speculate further on vortex formation mechanisms from the work described here, as no unique mechanisms were observed that have not been documented previously by other investigators.

Only in a few instances were hot-film data recorded when the presence of a strong dynamic stall vortex was indicated. However, for all the cases examined, boundary layer flow reversal, at least as far as 62% chord, was found to precede the vortex shedding. This was accompanied by a significant reduction of the lift-curve slope, which suggested that the boundary layer reversal may have been coupled with an increase of the boundary layer thickness. Also, the vortex development may be expected to occur, at least initially, within a thin region close to the aerofoil surface, and this would introduce a non-linear lift-curve behaviour. In order to examine the boundary layer mechanisms further, would require highly detailed measurements over a large portion of the aerofoil chord.

Secondary vortex formation was evident for certain cases in the present work, and appeared to occur in most instances where a strong primary vortex was formed. This was predominantly at the higher mean angles of attack. It was interesting to note however, that the imprint of a secondary vortex was indicated after the primary vortex passed the aerofoil trailing-edge. It may have been that the formation of this secondary vortex was induced by the primary vortex upwash flow-field, after its passage downstream of the aerofoil trailing-edge. In fact, it may be that the interpretation of a secondary vortex was incorrect, and that the pressure disturbance on the aerofoil chord may be purely due to the upwash flow-field from the strong primary vortex. Further experiments would be required to substantiate this speculation. Also, three-dimensional flow phenomena in the wind tunnel possibly complicated the aerofoil loadings in

the presence of a strong primary dynamic stall vortex.

7.7 Comments on unsteady flow reattachment

The return to attached flow, when the angle of attack fell below the normal static stall angle during an oscillatory cycle, was found to be distinctly different to that observed for the separation onset. In general, this manifested itself as a delay in the flow reattachment point, which appeared to proceed at a rate approximately half the free-stream velocity. The rate appeared to be slightly greater as the reduced frequency of the oscillation was increased, and this can be seen in Figs 7.139 to 7.157 for $\alpha = 18 + 4 \sin \omega t$ and $\alpha = 18 + 10 \sin \omega t$. Flow reattachment at the leading-edge region (i.e. the first 10-15% chord) appeared to re-establish itself fairly readily when the angle of attack decreased below 20° (if and when this angle was actually exceeded). The return to attached flow over the remainder of the aerofoil however, began at angle of attack near the static stall angle, α_{ss}, with the angle of attack for flow reattachment decreasing with increasing reduced frequency.

7.8 Repeatability of oscillatory data

For oscillations below stall, the repeatability of the normal force and pitching moment data were excellent (Fig 7.196). For oscillations in which the static stall angle was exceeded however, and varying amounts of flow separation existed, significant randomness in the normal force and pitching moment data was obtained. First observations indicated that this was particularly pronounced close to $C_{N\ MAX}$ and during the reattachment portion of the

oscillatory cycle (Fig 7.197). Overall, however, the repeatability was generally good for portions of the cycle with attached flow.

In order to facilitate parametric comparisons, it was useful to remove the majority of the randomness by averaging the pressure data over a number of cycles. Hardware limitations primarily dictated the total number of cycles which could be recorded for any given set of parameters, and for the present work, the total number of cycles was limited to ten. (See Section 4.5.1 for further description). Averaging over this number of cycles was found to eliminate a large portion of the randomness in the data.

It was clear however, that by increasing the averaging process to include twenty or more cycles, the randomness in the data could be reduced further, although not drastically (say, $\Delta C_N = 0.05$). To show the effect of averaging, a single test case was examined ($\alpha = 15 + 10 \sin \omega t$; $k = 0.15$) in which thirty cycles of data were recorded, and compared with data averaged over an increasing number of cycles. These data are shown in Figs 7.198 to 7.200, in the form of arithmetic differences between corresponding data points during the oscillatory cycle. From these data, it was clear that the qualitative features of the normal force and pitching moment were preserved by averaging over five or more cycles, although the actual arithmetic differences shown in Figs 7.199 and 7.200 tend to exaggerate this fact at certain parts of the cycle. It was very noticeable however, that the largest differences occurred at $C_{N\ MAX}$ and for parts of the cycle where

significant flow separation existed. This was attributed mainly to the inherent randomness of the stall process itself, and to unavoidable irregularities in the free-stream flow.

Hence, it may be concluded that the technique used in the present parametric comparisons, by which ten cycles of data were ensemble averaged, gave highly representative aerofoil loadings and were unlikely to be significantly improved by the recording of more cycles.

7.9 Comparison with experimental data from other sources

To conclude the results of the present Chapter, it was a useful exercise to compare and contrast the current unsteady data for the NACA 23012 aerofoil with available existing data for a similar aerofoil, primarily as an additional validation of the data acquisition and processing procedure. To the author's knowledge, the NACA 23012 aerofoil has not been previously tested under unsteady conditions, although aerofoils of similar profile have been tested by Liiva et al (1968), and McCroskey et al (1980), amongst others. Generally, most of these tests have been performed at higher Mach numbers (≥ 0.25) than the present tests (≤ 0.12).

In particular, Liiva et al (1968) have examined the aerodynamic characteristics of the NACA 23010 - 1.58 aerofoil (modified 23010) for a range of unsteady conditions. The NACA 23010 - 1.58 aerofoil has a thickness to chord ratio of 10% as opposed to 12% for the NACA 23012, however, the overall aerodynamic characteristics should be largely similar. Although the NACA 23010 - 1.58 was tested at a much higher Mach number (0.4), it was instructive to compare

the characteristics of the two aerofoils for approximately matching unsteady parameters. It should be noted, however, that the Liiva data for the NACA 23010 - 1.58 has been harmonically analysed, and the presented C_N and $C_m \sim \alpha$ characteristics have been reconstituted from the first few harmonics.

The comparisons between the two data sets are shown in Figs 7.201 to 7.209 in the form of C_N and C_m versus angle of attack, the data for the NACA 23010 -1.58 being shown on the left of the Figure. Also, it is rather unfortunate that the scaling for the two sets of plots are different, but this should not detract significantly from the comparisons.

Figs 7.201 to 7.205 compare the behaviour of the two aerofoils as the mean angle of attack was increased at a reduced frequency of approximately 0.05. At the lowest mean angle ($\approx 8^{\circ}$), the behaviour of both aerofoils indicated separation free flow, as shown by the characteristic eliptical C_N and C_m loops (Fig 7.201). As the mean angle was increased to approximately 10°, however, the departures from the eliptical loops indicated that separation was present for part of the cycle (Fig 7.202). At a mean angle of 12°, (Fig 7.203) the aerodynamic behaviour of the two aerofoils were still remarkably similar, although in this case, the C_N and C_m overshoots for the NACA 23012 aerofoil were quite pronounced, as compared with the NACA 23010 - 1.58. As mentioned previously, this C_N and C_m overshoot appears to be primarily a low Mach number phenomenon, and this was also borne out in Fig 7.204 for a mean angle of attack of 15°.

It was interesting to note that the shapes of the C_m loops were also qualitatively similar, apart from the C_m overshoot for the NACA 23012. At a mean angle of approximately 18^o (Fig 7.205), the C_N and C_m behaviour was still qualitatively similar, apart again, from the C_N overshoot. Also, in this case, the NACA 23012 data showed evidence of secondary vortex shedding (smaller secondary peaks in C_N and C_m at an angle of attack of approximately 22^o). Again, this secondary vortex shedding appears to be only a low Mach number phenomenon, and was not indicated for the NACA 23010 - 1.58 data.

Figs 7.206 to 7.209 compare the characteristics as the reduced frequency was increased at a constant mean angle of attack of 12^o, and an amplitude of $5^o/6^o$. Again, the C_N and C_m behaviour of the two aerofoils were qualitatively similar, apart from the previously mentioned C_N and C_m overshoots. As the frequency was increased, the curves tended to collapse to the eliptical curves characteristic of separation free flow.

In conclusion, it may be said that - although the Mach numbers were significantly different for the two data sets, the qualitative normal force and pitching moment behaviour for approximately matching parameters were largely similar, and this was not necessarily to be expected.

A comparison was also drawn with the present data, and with oscillating aerofoil data obtained from the NASA Ames 2.0 x 3.0 m wind tunnel. A selection of aerofoils have been tested in this facility by McCroskey et al (1980). In fact, both the qualitative and quantative features of oscillatory aerofoil data from the Ames wind tunnel showed

remarkable similarities to the present data, particularly for certain aerofoils. Also, the secondary vortex shedding phenomenon, which has been discussed previously, was often present in the data from the Ames facility.

Fig 7.210 compares the net aerodynamic loadings for the AMES-01, VR-7 and NLR-1 aerofoils which were acquired in the Ames wind tunnel, with the present data for the NACA 23012 aerofoil. The Ames data were recorded at a Mach number of 0.25, compared with the present data, which were recorded at a Mach number of 0.12. The characteristics of the VR-7 aerofoil were found to be very similar to the NACA 23012 at reduced frequencies of 0.10 and 0.05 respectively. Also, both the AMES-01 and the NLR-1 showed a largely similar behaviour. In all cases, the secondary vortex shedding phenomenon was apparent near the maximum angle of attack.

7.10 Summary of conclusions

A comprehensive range of oscillatory tests have been conducted on the NACA 23012 aerofoil, and the results have been analysed. Both chordwise pressure, and limited boundary layer data were recorded for the analysis. The main conclusions derived from the analysis have been stated in the preceding Sections,and this final Section serves to briefly summarise these main conclusions.

Generally, the unsteady aerodynamic characteristics of the NACA 23012 aerofoil were qualitatively similar to features which have been documented previously by other investigators. This included the formation of a dynamic stall vortex, and indications of flow reversal within the boundary layer, prior to the vortex formation.

The effect of Reynolds number was found to be small for the range examined. Both the effects of mean angle of attack and oscillation amplitude were large, especially when the angle of attack range included the normal static stall angle. The most dominant parameter was found to be the reduced frequency of the pitching oscillation, the resultant aerodynamic loadings being also highly dependant on the mean angle of attack and the oscillation amplitude. Generally, the effect of increasing the reduced frequency of the oscillation was to reduce the amount of flow separation which may have existed during the cycle at lower frequencies.

Boundary layer shear stress measurements were recorded only for a limited range of conditions, although from these data, it was apparent that the important boundary layer events could be isolated. Flow separation was indicated by both a pressure signal divergence, and an increase of the shear stress fluctuation amplitude. By increasing the reduced frequency of the pitching oscillation, flow reversal within the boundary layer was found to precede separation. During cases where a dynamic stall vortex was indicated, trailing-edge flow reversals were found to proceed towards the aerofoil leading-edge prior to the vortex formation. Unfortunately, no measurements were performed of the boundary layer thickness under flow reversal conditions.

There were a few characteristics that appeared to be well pronounced in the present set of tests, and may be presumably a function of both the aerofoil, and of the low Reynolds/Mach number regime in which the tests were conducted. These characteristics included:-

(a) the significant non-linear behaviour in the lift-curve slope during the formation and development of the dynamic stall vortex.

(b) the significant overshoots in the normal force and pitching moment characteristics as the dynamic stall vortex neared the aerofoil trailing-edge.

(c) secondary vortex shedding, which appeared to occur predominantly in cases where a strong primary vortex was indicated.

The reduction of the lift-curve slope during the formation of the leading-edge vortex was presumably due to boundary layer thickness effects. This may have occurred during the trailing-edge flow reversal process, or near the vortex formation itself. Minor trailing-edge separation may also have occurred. Indeed a combination of these effects may have caused the lift-curve slope reduction.

During the passage of the vortex across the aerofoil chord, the lift-curve slope increased, peaking just prior to $C_{N\ MAX}$. It was noted however, that in nearly all cases, $C_{N\ MAX}$ occurred approximately on a line which was a linear extrapolation of the static lift curve (see Fig 7.181). From a consideration of other experimental data at higher Mach and Reynolds numbers (e.g. McCroskey, 1980; Wood, 1979; Liiva, 1968), this often occurred, although the non-linear lift-curve slope behaviour prior to $C_{N\ MAX}$ was not always apparent. As might be expected however, certain boundary layer thickness effects may increase as the Reynolds/Mach number was reduced.

Secondary vortex shedding was a phenomenon which was very pronounced in the present set of tests during cases of strong primary vortex shedding. Again, however, this may have been a type of wind tunnel interference characteristic, in the presence of a strong primary vortex. This secondary vortex phenomenon also appeared prominent in the NASA Ames 2 x 3 m wind tunnel (see McCroskey et al 1980).

Trailing-edge flow separation was found to occur on the NACA 23012 aerofoil during static tests, although the progression of separation towards the aerofoil leading-edge was often of an abrupt nature. During the oscillatory tests, trailing-edge separation was almost entirely suppressed, even at the lowest reduced frequency examined (0.01). Flow reversals within the boundary layer however, were often present in the absence of separation, and this phenomenon may be related to the aerofoil static separation characteristics. This perhaps verifies a possible mechanism for the initiation of the leading-edge vortex formation, although it was clear that significantly more measurements of the unsteady boundary layer characteristics would be required for conclusive evidence to be provided.

CHAPTER 8

SUMMARY OF MAIN CONCLUSIONS AND SUGGESTIONS FOR FUTURE RESEARCH

In this final Chapter, a summary is made of the main conclusions of the present work, and some suggestions and recommendations are made for future research.

The objectives of the present work were outlined in Chapter 1, and on the whole, these objectives have been largely fulfilled. These objectives were:

(1) to select an aerofoil profile, typical of current helicopter rotor profiles, which exhibits stall by the mechanism of trailing-edge separation at low Mach numbers.

(2) to suggest modifications to the selected aerofoil, that may enable the enhancement of trailing-edge separation, but without significantly altering the leading-edge pressure distribution.

(3) to design and develop both mechanical and electronic hardware, to investigate the aerofoil's steady and unsteady aerodynamic characteristics within the environment of a low-speed wind tunnel, and to interface transducer outputs to a microcomputer for acquisition.

(4) to develop software for the microcomputer in order to acquire, process and present the data relating to the aerofoil aerodynamic characteristics.

(5) to investigate the steady and unsteady aerodynamic characteristics of the selected profile for a wide range of test conditions, in order to validate the

test facility, and also to provide a data base for subsequent investigations.

(6) to make a preliminary investigation into the effects of trailing-edge flow separation on the dynamic stall process, and to assess the direction in which future research in this area should be directed.

In Chapter 2, the aerofoil profile chosen for the investigation was the NACA 23012. This aerofoil profile is typical of current aerofoils used for helicopter main rotors, and exhibits a trailing-edge stall characteristic at low Reynolds numbers. To enhance the degree of trailing-edge flow separation, consideration was given to the use of protuberances, although the use of trailing-edge profile modifications was considered more appropriate. A series of analytical experiments were carried out on the NACA 23012 aerofoil with modified trailing-edge camberlines. This was done by examining the effects on the potential flow pressure distributions and the predicted turbulent separation points. Although certain trailing-edge camber-line modifications were found to have significant effects, it was recommended that a prospective aerofoil modification be experimentally tested, under static conditions, to verify the validity of this approach.

In Chapter 3, details of the experimental apparatus used to investigate the aerodynamic characteristics of the aerofoil were presented. This comprised of a facility for the investigation of dynamic stall on two-dimensional aero-foils in a low-speed wind tunnel. Both the mechanical design, and the electronics of the transducer signal conditioning equipment were described. The signals from

the measurement transducers were interfaced, via the signal conditioning equipment, to a microcomputer for real-time analogue-to-digital conversion. This microcomputer was a DEC MINC-11, and the microcomputer was used to perform a wide variety of tasks associated with the control of the experiments and the processing of data. Although the facility was subsequently proved to fulfill the primary design objectives, there was scope for improvement in some areas, and a few suggestions are made below:-

(1) The current design of the aerofoil model, although satisfactory, is far from ideal, primarily in the effort required for installation in the wind tunnel (the mass being approximately 60kg). Work is currently underway at the University of Glasgow, however, on a wind tunnel aerofoil of fibre-composite construction, which should be approximately one-third of the mass of the existing design. It is expected that the fibre-composite model will replace the existing design in due course.

(2) Pressure transducer installation and removal is presently a rather difficult and tedious operation. With some careful design work, it should be possible to improve the locating technique and increase the turn-around time between tests on different wind tunnel models, when using the same pressure transducers.

(3) At present, the pressure transducer temperature induced offset drift compensation circuitry on the signal conditioners has not been utilised due to the inability to monitor the offset drift under controlled conditions. Hence, reliance had been placed on the internal compensation circuitry of the pressure transducer, but this was found not to be

entirely effective. By constructing an environmental chamber, in which both temperature and pressure could be independently varied, it should be possible to set-up the offset compensation circuitry on the conditioning board, and thereby reduce the effects of one of the sources of error most difficult to control.

(4) As mentioned in Section 3.2.5, the amplitude of the input oscillatory signal to the Servo-Actuator Controller, to give a specific amplitude of the aerofoil angle of attack, was found to be dependent on the mean angle of attack. Hence, it was often difficult to set precisely, both the mean angle and amplitude of the aerofoil oscillation. Solution of this problem would eliminate further minor sources of error, and reduce the total time period to perform a specified test condition. This could be accomplished in two ways. Firstly, by the use of a "look-up" table of correction factors which were a function of the mean angle and amplitude levels. Secondly, by an automatically calculated correction factor, determined on the basis of the desired and actual angle of attack range, using the angular displacement as a feedback via the A/D.

Incorporation of the above mentioned items, should result in a significant improvement of the experimental facility, in terms of reducing sources of error and minimising operator workload.

In Chapter 4, a description of the software developed for the present work was given. This software was written on the MINC microcomputer, and enabled a wide range of functions, relating to the operation of the experiments,

to be performed. The software included routines for hardware monitoring, data acquisition, data analysis and data presentation. Perhaps the biggest contribution to this software was by the analogue-to-digital converter routines. These routines were written in MACRO assembly code, and were designed to optimise the A/D conversion sequence and maximise the data throughput rate to memory.

Although the developed software was by no means, fully comprehensive, the initial software requirements were achieved. There existshowever, scope for future software development, specifically in the areas of data analysis and presentation. Limitations on the degree of software development, however, are imposed by the lack of available memory and mass storage on the MINC microcomputer system. Currently, only 64k of memory were directly available to store the operating system, user program and data, although a further 192k of memory were indirectly available. This limitation was imposed by the architecture of the MINC processor, and the ability to utilise analogue and digital input/output hardware only with certain operating systems. It is possible, however, that by the use of the latest update of the RT-11 operating system - Version 5, that a number of specific data acquisition and processing problems associated with the present configuration may be alleviated.

With the current RX02 dual floppy disk system, only 0.5M bytes were available for user program and data. Generally, this corresponded to a maximum of five raw data sets (of ten cycles). Data processing and analysis required at least one disk copying operation, and with a large data set to handle, disk and file housekeeping can become highly

labour intensive. In order to alleviate mass storage - restrictions, it would be necessary to replace the existing floppy disk system, with a hard disk system of at least 20M byte capacity. Alternatively, networking to a mainframe computer with ample mass storage devices, should be acceptable.

Chapter 5 has dealt with a summary of the test conditions under which the aerodynamic investigations were conducted. These tests were defined in order to encompass a wide range of conditions, and permit a parametric analysis of the aerofoil's aerodynamic characteristics. Both static and oscillatory tests were defined, and standard procedures to conduct the tests were developed on the basis of preliminary investigations.

The analysis of the results from the static tests were discussed in Chapter 6. Initially, a series of oil-flow visualisation tests were conducted in order to examine the onset of any unusual three-dimensional separation phenomena on the aerofoil upper surface, and to assess the possible effects on chordwise pressure measurements. The development of three-dimensional flow was found to be relatively minor, at angles of attack up to the aerofoil stall, whereupon two vortices developed at the aerofoil outer-span regions. It was subsequently concluded, that the measured chordwise pressures could be interpreted with a high degree of confidence prior to stall.

Chordwise pressure measurements were recorded at discrete angles of attack from -4^{o} to 28^{o}, at Reynolds numbers between 0.3 and 2.0 million. It was found that the aerofoil exhibited a trailing-edge stall characteristic

over this Reynolds number range, with an increase in the maximum lift and degree of stall abruptness, with increasing Reynolds number.

In Chapter 7, analysis of the results from the oscillatory tests were considered. These tests were conducted for a range of mean angles of attack, oscillation amplitudes and frequencies, at Reynolds numbers of 1.0 and 1.5 million. It was found that the effect of Reynolds number on the unsteady airloads was very minor over the small range examined. Both the effects of mean angle of attack and oscillation amplitude were found to have large effects on the airloadings, especially when the angle of attack range included the static stall angle. The most dominant parameter, however, was found to be the reduced frequency of the pitching oscillation. This was found to have large effects on the aerofoil airloadings, but generally, the effect of increasing the reduced frequency of the oscillation was to reduce the amount of flow separation which may have been present during the cycle at lower frequencies.

Generally, the unsteady aerodynamic characteristics of the NACA 23012 aerofoil were qualitatively similar to characteristics previously observed by other investigators on other aerofoils. This included the formation of a vortex disturbance which was shed from the aerofoil leading-edge region during dynamic stall, and the observation of trailing-edge boundary layer flow reversals prior to the vortex formation. There were however, a few characteristics that appeared quite pronounced in the present set of tests. These included, the significant

non-linear lift-curve slope behaviour during the formation and chordwise passage of the dynamic stall vortex, the significant overshoots of normal force and pitching moment, and the occurrence of secondary vortex shedding.

Boundary layer shear stress data were recorded at three chordwise locations, for a limited range of conditions, although from these data, a considerable amount of boundary layer behaviour could be inferred. Events such as laminar to turbulent transition, flow reversal and separation, were interpreted on the basis of the shear stress and corresponding pressure responses. For the unsteady tests, flow reversal was found to precede flow separation at the aerofoil trailing-edge. Also, the onset of flow reversal was delayed, and the rate of chordwise movement towards the leading-edge increased, with increasing reduced frequency. In cases where a dynamic stall vortex was indicated, trailing-edge flow reversals were found to precede the vortex shedding phenomenon.

The final objective of the present work was to comment on the formation of trailing-edge flow separation during the unsteady aerofoil tests, and try to assess the direction in which future research on this phenomenon should be directed.

From the present work, it was shown that flow reversals with the boundary layer were present on the pitching aerofoil in the absence of trailing-edge separation. Also, for the cases examined, boundary layer flow reversal was found to precede vortex shedding from the aerofoil leading-edge region. On the basis of these observations, it was

likely that interactions between the trailing-edge flow reversals and leading-edge separation existed, although further experiments with more detailed measurements, would be required to clarify the nature of this interaction. This could possibly be accomplished by using a greater number of hot-film anemometry gauges over the aerofoil upper surface. Also, it would be useful to have corresponding measurements of the boundary layer thickness, perhaps by using hot-wires displaced from the aerofoil surface. The nature of the trailing-edge/leading-edge flow interaction must be established as a function of the aerofoil pitch rate, that is, rate of change of angle of attack. Specifically, as a ramp motion (i.e. constant pitch rate), as this would eliminate time-history effects of the aerofoil motion on the aerodynamic flowfield.

Of course, discrete chordwise measurements is only one technique as a means of investigating the aerofoil flowfield. The final objective is to clarify the nature of the trailing-edge/leading-edge flow interaction, and not necessarily to quantify the behaviour. This could be established, perhaps, by using some kind of flow visualisation technique, although the shortcomings and difficulties of this approach are recognised.

Assuming therefore, that a suitable range of experiments can be devised to clarify the nature of the flow interaction, how then can the degree of interaction be controlled or changed? In Chapter 2, it was suggested that aerofoil trailing-edge camberline modifications may enable the degree of trailing-edge separation (or flow reversal) to be enhanced. This then, was one possible

methodology. The application of a "trip" or roughness, at the aerofoil leading-edge, designed to modify the nature of the boundary layer, was another possible course of action. Also, in Chapter 6 it was noted, for the particular aerofoil tested, that the degree of trailing-edge flow separation was sensitive to variations of Reynolds number. Thus, a series of carefully selected experiments, designed to exploit this Reynolds number dependence may prove worthwhile.

-oOo-

REFERENCES

1. Abbott, I.H., von Doenhoff, A.E.; Stivers, L.S.: Summary of Airfoil Data, NACA Report No. 824, 1945.

2. Althaus, D., Wortmann, F.X.: Stuttgarter Profilkatalog 1 - Experimental Results from the Laminar Wind Tunnel of the Institut fur Aero - und Gaschynamik der Universitut Stuttgart. Eriedr, Vieweg & Sohn, 1980.

3. Arcidiacono, P.J., Carta, F.O., Casellini, L.M., Elman, H.L.: Investigation of Helicopter Control Loads Induced by Stall Flutter. USAAVLABS TR, 70-2, 1970.

4. Beddoes, T.S.: Onset of Leading Edge Separation Effects Under Dynamic Conditions and Low Mach Number. Pre-print 78-63, 34th Annual Forum of AHS, 1978.

5. Beddoes, T.S.: Prediction Methods for Unsteady Separated Flows. Paper 15, AGARD Report 679, 1979.

6. Beddoes, T.S.: An analytic model for Trailing Edge Stall. Westland Research Paper R.P. 637, 1981.

7. Bielewa, R.L.: Synthesised Unsteady Airfoil Data with Applications to Stall Flutter Calculations. AHS Annual Forum, Reprint 935, 1975.

8. Bisplinghoff, R.L., Ashley, H.; Halfman, R.L.: Aeroelasticity, 1st ed., Addison - Wesley, 1955.

9. Byham, G.M., Beddoes, T.S.: The Importance of Unsteady Aerodynamics in Rotor Calculations. AGARD-CP-227, 1977.

10. Carr, L.W., McAlister, K.W., McCroskey, W.J.: Analysis of the Development Airfoil Experiments. NASA TN-D 8382, 1977. (Also AIAA J. Vol. 14, No.1, Jan. 1976).

11. Carta, F.O.: Effect of Unsteady Pressure Gradient Reduction of Dynamic Stall Delay. Engineering Note, J. of Aircraft, 1971.

12. Crimi, P., Reeves, B.L.: A Method for Analysing Dynamic Stall of Helicopter Rotor Blades, NASA CR-2009, 1972. (Also AIAA paper 72-37, 1972).

13. Crimi, P.: Investigation of Nonlinear Inviscid and Viscous Effects in the Analysis of Dynamic Stall. NASA CR-2335, 1974.

14. Davenport, F.J., Front, J.V.: Airfoil Sections for Rotor Blades - a Reconsideration. 22nd Annual National Forum, AHS, 1966.

15. Davis, S.S., Malcolm, G.N.: Experimental Aerodynamics of Conventional and Supercrtical Airfoils. NASA TM-81221, 1980.

16. DEC Staff: Microcomputer Interfaces Handbook. Digital Equipment Corporation (DEC), 1980.

17. Dobbing, A.E., Ingen, von J.L., Kooi, J.W.: Some Research on Two-dimensional Laminar Separation Bubbles. AGARD CP 102, 1972.

18. Ericcson, L.E., Reding, J.P.: Quasi-Steady and Transient Dynamic Stall Characteristics. AGARD CP-204, paper No. 24, 1976.

19. Erilich, E.: Methodes de Visualisation du Bubble de Decollement de Bord d'attaque et Analyse Resultats. (Methods for Visualising the Leading Edge Separation Bubble and Analysis of the Results). ONERA TP1295, 1973.

20. Evans, W.T., Mo:., K.W.: Analysis of Computed Flow Parameters for a Set of Sudden Stalls in Low Speed Two-dimensional Flow. NASA TN D-85, 1945.

21. Galbraith, R.A. McD., Barrowman, J., Leishman, J.G.: Description of the Sample and Hold Circuits for the Glasgow University Dynamic Stall Facility. GU AERO report No. 8208, 1982.

22. Gault, D.E.: An Experimental Investigation of Regions of Separated Laminar Flow. NACA TN 3505,1955.

23. Gault, D.E.: A correlation of Low Speed Airfoil Section Stalling with Reynolds number and Airfoil Geometry. NACA TN-3963, 1956.

24. Gordon, R.D., Galbraith, R.A. McD., Murray-Smith, E., Leishman, J.G.: A Collection of Data from the Glasgow University "Handley-Page" Wind Tunnel Calibration. Unpublished, 1980.

25. Gregory, N., Wilby, P.G.: NPL 9615 and NACA 0012 - A Comparison of Aerodynamic Data. ARC CP No. 1261, 1968

26. Gregory, N., Quincey, V.G., O'Reilly, C.L., Hall, P.J.: Progress Report on Observations of Three-dimensional Flow Patterns Obtained during Stall Development on Aerofoils, and on the Problem of Measuring Two-dimensional Characteristics. A.R.C. CP 1146, 1970.

27. Ham, N.D.: Aerodynamic Loading on a Helicopter Blade During Pitching Motion in the Presence of Stall. Sc.D. Thesis, MIT, 1968.

28. Ham, N.D.: Aerodynamic Loading on a Two-dimensional Airfoil During Dynamic Stall. AIAA. J. Vol 6 No. 10, 1968.

29. Hicks, J.G., Nash, J.F.: The Calculation of Three-dimensional Turbulent Boundary Layers on Helicopter Rotors. NASA CR-1845, 1971.

30. Hounsfield, F.R.S.: The Handley-Page Low-Speed Wind Tunnel, Aircraft Engineering, July, 1940.

31. Jocobs, E.N.: Airfoil Characteristics as affected by protuberances. NACA Report 446, 1932.

32. Jocobs, E.N., Clay, W.C.: Characteristics of the NACA 23012 Airfoil from Tests in the Full-Scale and Variable Density Tunnel. NACA Report 530, 1935.

33. Johnson, W.: The Effect of Dynamic Stall on the Response and Airloading of Helicopter Rotor Blades. J. AHS Vol 14(2), 1969.

34. Johnson, W., Ham , N.P.: On the Mechanism of Dynamic Stall. J. AHS Vol 17, 1972.

35. Jones, J.P.: Unsteady Aerodynamics of Helicopter Rotors. AGARD-R-595, 1972.

36. Kao, H.C.: Some Aspects of Airfoil Stall in Low Speed Flow. J of Aircraft, Vol 11, No. 3, 1974.

37. Kline, S.J., Bardina, J., Strawn, R.: Correlation and Computation of Detachment and Reattachment of Turbulent Boundary Layers on Two-dimensional Faired Surfaces. AIAA Paper 81-1220, 1981.

38. Kramer, M.: Increase in the Maximum Lift of an Aerofoil due to a Sudden Increase in its Effective Angle of Attack Resulting from a Gust. NACA Technical Memorandum 678, 1932.

39. Landon, R.H.: A Description of the ARA 2-D Pitch and Heave Rig and some Results from the NACA 0012 Wing. ARA Memo 199, 1977.

40. Leishman, J.G., Galbraith, R.A. McD.: An Algorithm for the Calculation of the Potential Flow about an Arbitary Aerofoil. GU AERO Report No. 8102, 1981.

41. Leishman, J.G.: A Software Enhancement Package for MINC Laboratory Programming. GU AERO Notes, May 1983.

42. Liiva, J., Davenport, F.J., Grey, L., Walton, I.C.: Two-dimensional Tests of Airfoils Oscillating Near Stall. Vol 1 USAAVLABS Technical Report 68-13A, 1968.

43. Loftin, L.K., Hamilton, A.S.: Aerodynamic Characteristics of 15 NACA Aerofoil Sections at 7 Reynolds Numbers from 0.7×10^6 to 9.0×10^6. NACA TN 1945, 1949.

44. Mehta, U.B.: Dynamic Stall of an Oscillating Aerofoil. AGARD CP-227, 1972.

45. Moss, G.F., Murdin, P.M.: Two-dimensional Low-Speed Tunnel Tests on the NACA 0012 Section, including Measurements made during Pitching Oscillations at the Stall. ARC CP 1145, 1968.

46. McAlister, K.W., Carr, L.W.: Water Tunnel Experiments on an Oscillating Airfoil at Re = 21000. NASA TM-78446, 1977.

47. McAlister, K.W., Carr, L.W., McCroskey, W.J.: Dynamic Stall Experiments on the NACA 0012 Airfoil. NASA TP 1100, 1978.

48. McCroskey, W.J.: Measurements of Boundary Layer Transition, Separation and Streamline Direction on Rotating Blades. NASA TN D-6321, 1971.

49. McCroskey, W.J.: Inviscid Flowfield of an Unsteady Airfoil. AIAA J. Vol 11, No. 8, 1973.

50. McCroskey, W.J., Philippe, J.J.: Unsteady Viscous Flows on Oscillating Airfoils. AIAA J. Vol 13, 1975.

51. McCroskey, W.J.: Recent Developments in Dynamic Stall. Symposium on Unsteady Aerodynamics. Kinney R.B. ed, Tuscon, Arizona, 1975.

52. McCroskey, W.J., McAlister, K.W., Carr, L.W.: Dynamic Stall Experiments on Oscillating Airfoils. AIAA J., Vol 14, No. 1, 1976.

53. McCroskey, W.J.: Some Current Research in Unsteady Fluid Dynamics. J. Fluids Eng. 99, 1977.

54. McCroskey, W.J.: Prediction of Unsteady Separated Flows on Oscillating Airfoils. AGARD LS-94, 1978.

55. McCroskey, W.J., McAlister, K.W., Carr, L.W., Pucci, S.L., Lambert, O., Indergrand, R.F.: Dynamic Stall on Advanced Airfoil Sections. AHS Pre-print 80-01, 1980 (also J. AHS Vol 26, No. 3, 1981).

56. McCullough, G.B., Gault, D.E.: Examples of Three Representative Types of Airfoil Section Stall at Low Speed, NACA TN 2502, 1951.

57. McCullough, G.B.: The Effect of Reynolds Number on the Stalling Characteristics and Pressure Distribution of Four Moderately Thin Airfoil Sections. NACA TN-3524, 1955.

58. Nash, J.F., Carr, L.W., Singleton, R.E.: Unsteady Turbulent Boundary Layers in Two Dimensional Incompressible Flow. AIAA Paper No. 73-650, 1973.

59, Owen, P.R., Klanfer, L.: On the Laminar Boundary Layer Separation from the Leading Edge of a Thin Aerofoil. ARC CP-220, 1955.

60. Pope, A., Harper, J.J.: Low Speed Wind Tunnel Testing. John Wiley & Sons, 1966.

61. Rao, B.M., Maskew, B.: Theoretical Prediction of Dynamic Stall on Oscillating Airfoils. ASH Annual Forum Pre-print 78-62, 1978.

62. Sandborn, V.A., Kline, S.J.: Flow Models in Boundary Layer Stall Inception. Trans. ASME. J. Basic Eng. Vol 83, 1961.

63. Scruggs, R.M.: An Investigation of near Wake in Airfoil Dynamic Stall. G.I.T.A.E.R. Report No. 71-1, 1971.

64. Scruggs, R.M., Nash, J.F., Singleton, R.E.: Analysis of Flow-Reversal Delay for a Pitching Foil. AIAA Paper 78-183, 1974.

65. Scruggs, R.M., Nash, J.F., Singleton, R.E.: Analysis of Dynamic Stall using Unsteady Boundary Layer Theory. NASA CR-2462, 1974.

66. Sears, W.R., Telionis, D.P.: Boundary Layer Separation in Unsteady Flow. SIAM J. Appl. Math. Vol 28 No. 1. 1975.

67. Shamroth, S.J., Keskorsky, J.P.: A Weak Interaction Study of the Viscous Flow about Oscillating Aerofoils. NASA CR132425, 1974.

68. Singleton, R.E., Nash, J.F., Carr, L.W., Patel, V.C.: Unsteady Turbulent Boundary Layer Analysis. NASA TM X-62, 242, 1973.

69. Smetana, : Light Aircraft Lift, Drag and Pitching Moment Prediction NASA CR- , 1976.

70. Telionis, D.P.: Unsteady Boundary Layers, Separated and Attached. AGARD CP-227, Paper No. 16, 1977.

71. Thwaites, B. (ed.): Incompressible Aerodynamics. Oxford Clarendon Press, 1960.

72. Tran, C.T., Petot, D.: Semi-Empirical Model for the Dynamic Stall of Airfoils in View of the Application to the Calculation of Responses of a Helicopter Blade in Forward Flight. Paper 48, 6th European Rotorcraft and Powered Lift Forum, 1980.

73. Van den Berg, B.: Role of Laminar Separation Bubbles in Airfoil Leading-edge Stalls. AIAA J. Vol 19, No. .5, 1981, (also AIAA paper 81-4104, 1981).

74. Welsh, B.L., Pyne, C.R.: A Method to Improve the Temperature Stability of Semi-conductor Strain Gauge Transducers. J. Phys. E: Sci. Instrum. Vol 13, 1980 (also RAE Technical Report 77155, 1977).

75. Werlé, H.: Visualisation Hydrodynamic de L'ecoulement Autaur d'une Palo Oscillante, ONERA Technical Report No. 56/1369AN, 1976.

76. Wilby, P.G.: The Aerodynamic Characteristics of some New RAE Blade Sections and their Potential Influence on Rotor Performance. 5th European Rotorcraft and Powered Lift Aircraft Forum, 1979. (also Vertica Vol 14, Pergamon Press, 1980).

77. Williams, J.G. III: Incompressible Boundary Layer Separation. Annual Review of Fluid Mechanics, Vol 9, 1977.

78. Wood, M.E.: Results of Oscillatory Pitch and Ramp Tests on the NACA 0012 Blade Section. ARA Memo 220, 1979.

79. Woods, L.C.: The Theory of Subsonic Plane Flow. Cambridge University Press, 1961.

80. Woodward, D.S.: An Investigation of the Parameters Controlling the Behaviour of a Laminar Separation Bubble. RAE TM/A 1003, 1967.

81. Young, W.H. Jr.: Fluid Mechanics Mechanisms in the Stall Processes for Helicopters. NASA TM 81956, 1981.

82. Seto, L.Y., Leishman, J.G. and Galbraith, R.A.McD.: An Investigation of three-dimensional stall developments on NACA 0012 aerofoils. GU AERO Report No. 8300, Jan. 1983.

83. Reichert, G., Wagner, S.N.: Some Aspects of the Design of Rotor-Airfoil Shapes. AGARD CP-111, Paper 14, 1972.

BIBLIOGRAPHY

1. Beddoes, T.S.: A Qualitative Discussion of Dynamic Stall. Paper 3, AGARD Report 679, 1980.

2. Beddoes, T.S.: Unsteady Flows Associated with Helicopter Rotors. Paper 7, AGARD Report 679, 1980.

3. Beddoes, T.S.: Representation of Airfoil Behaviour. Paper 2, AGARD CP. 337, 1983.

4. Carlson, R.G., Blackwell, R.H., Commerford, G.L., Morick, P.H.: Dynamic Stall Modelling and Correlation with Experimental Data on Airfoils and Rotors. AHS/NASA Ames Specialist Meeting on Rotorcraft Dynamics, 1974.

5. Carta, F.O.: Unsteady Normal Force on an Airfoil in a Periodically Stalled Inlet Flow. J. Aircraft Vol 4 No. 5, 1967.

6. Carta, F.O., Commerford, G.L., Carlson, R.G.: Determination of Airfoil and Rotor Blade Dynamic Stall Response. J. AHS Vol 18, 1973.

7. Carta, F.O.: Analysis of Oscillatory Pressure Data Including Dynamic Stall Effects. NASA CR-2394, 1974.

8. Dadone, L.U.: Two-dimensional Wind Tunnel Test of an Oscillating Rotor Airfoil. NASA CR 2914, 1977.

9. Dadone, L.U.: Rotor Airfoil Optimisation: An Understanding of the Physical Limits. ASH Pre-print 78-4, 34th Annual Forum of AHS, 1978.

10. Favier, D., Maresca, C., Rebont, J.: Dynamic Stall due to Fluctuations of Velocity and Incidence. AIAA Journal Vol 20, No.7, 1982.

11. Galbraith, R.A. McD., Leishman, J.G.: A Microcomputer Based Test Facility for the Investigation of Dynamic Stall. Paper E3, International Conf. on the Use of the Micro in Fluid Eng., 1983.

12. Garelick, M.S.: Non-steady Airloads on Dynamically Stalling Two-dimensional Wings. M.S. Thesis, MIT, 1967.

13. Ham, N.D., Garelick, M.S.: Dynamic Stall Considerations in Helicopter Rotors. J. AHS, Vol 13, No. 2, 1968.

14. Ham, N.D.: Some Recent MIT Research on Dynamic Stall. J. of Aircraft, Vol 9, No. 5, 1972.

15. Harris, F.D., Pruyn, R.R.: Blade Stall - Half Fact, Half Fiction. J. AHS Vol 13, No. 2, 1968.

16. Johnson, W.: Comparison of Three Methods for Calculation of Helicopter Rotor Blade Loading and Stresses due to Stall. NASA TN D-7833.

17. Lambourne, N.C.: Experimental Techniques in Unsteady Aerodynamics. AGARD R-679, 1980.

18. Leishman, J.G., Hanna, J., Galbraith, R.A. McD.: Modelling of Trailing-Edge Separation on Arbitrary Two-dimensional Aerofoils in Incompressible Flow using an Inviscid Flow Algorithm. GU AERO Report No. 8202, 1982.

19. Liiva, J.: Unsteady Aerodynamic and Stall Effects On Helicopter Rotor Blade Airfoil Sections. J. of Aircraft Vol 6, No. 1, 1969.

20. Martin, J.M., Empey, R.W., McCroskey, W.J., Caradona, F.X.: An Experimental Analysis of Dynamic Stall on an Oscillating Airfoil. J.AHS Vol 19, No. 1, 1974.

21. McCroskey, W.J.: Dynamic Stall of Airfoils and Helicopter Rotors. AGARD-R-595,1972.

22. McCroskey, W.J., Fisher, R.K.: Detailed Aerodynamic Measurements on a Model Rotor in the Black Stall Regime. J. AHS Vol 17, No. 1, 1972.

23. McCroskey, W.J., Carr, L.W., McAlister, K.W.: Dynamic Stall Experiments on Oscillating Airfoils. AIAA Paper 75-125, 1975.

24. McCroskey, W.J., Pucci, S.L.: Viscous-Inviscid Interaction on Oscillating Airfoils. AIAA Paper 81-0051, 1981.

25. McCroskey, W.J.: Unsteady Airfoils. Annual Review of Fluid Mechanics, 1982.

26. McCroskey, W.J., McAlister, K.W., Carr, L.W., Pucci, S.L.: An Experimental Study of Dynamic Stall on Advanced Airfoil Sections, NASA TM 84245, 1982.

27. Nash, J.F.: Further Studies of Unsteady Boundary Layers with Flow Reversal. NASA-CR-2767, 1976.

28. Nash, J.F., Scruggs, R.M.: Unsteady Boundary Layers with Reversal and Separation AGARD CP-227, 1977.

29. Parker, A.G., Bicknell, J.: Some Measurements of Dynamic Stall. J. of Aircraft Vol 11, No. 7, 1974.

30. Pearcey, H.H., Wilby, P.G., Reiley, M.J., Brotherhood, P.: The Derivation and Verification of a New Rotor Profile on the Basis of Flow Phenomena. Paper 16, AGARD CP-111, 1972.

31. Philippe, J.J.: Dynamic Stall; An Example of Strong Interaction between Viscous and Inviscid Flows. Paper 21, AGARD CP 227, 1977.

32. Prouty, R.W.: State-of-the-Art Survey of Two-dimensional Airfoil Data. J. AHS, Vol 20, No.10, 1975.

33. St. Hilaire, A.L., Cart , F.O., Jepson, W.D.: The Influence of Sweep on the Aerodynamic Loading of an Oscillating NACA 0012 Airfoil. Paper 79-4 AHS 35th National Forum, 1979.

34. Velkoff, H.R., Ghai, R.L.: Hot Wire Measurements of Stall and Separation on Helicopter Rotor Blades. Vertica Vol 3, 1979.

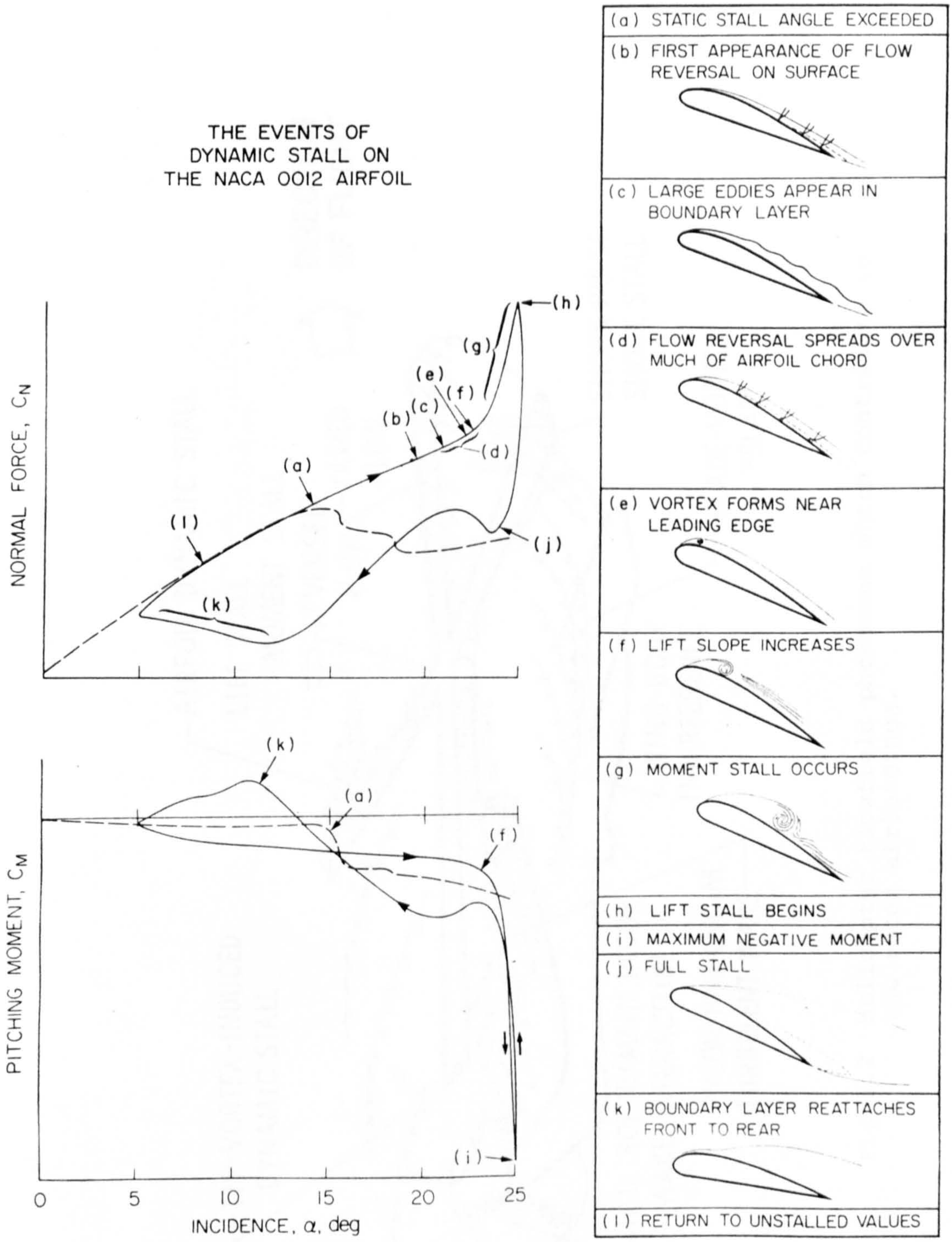

Figure 1.1 The events of dynamic stall on the NACA 0012 aerofoil (from Carr et al, 1977)

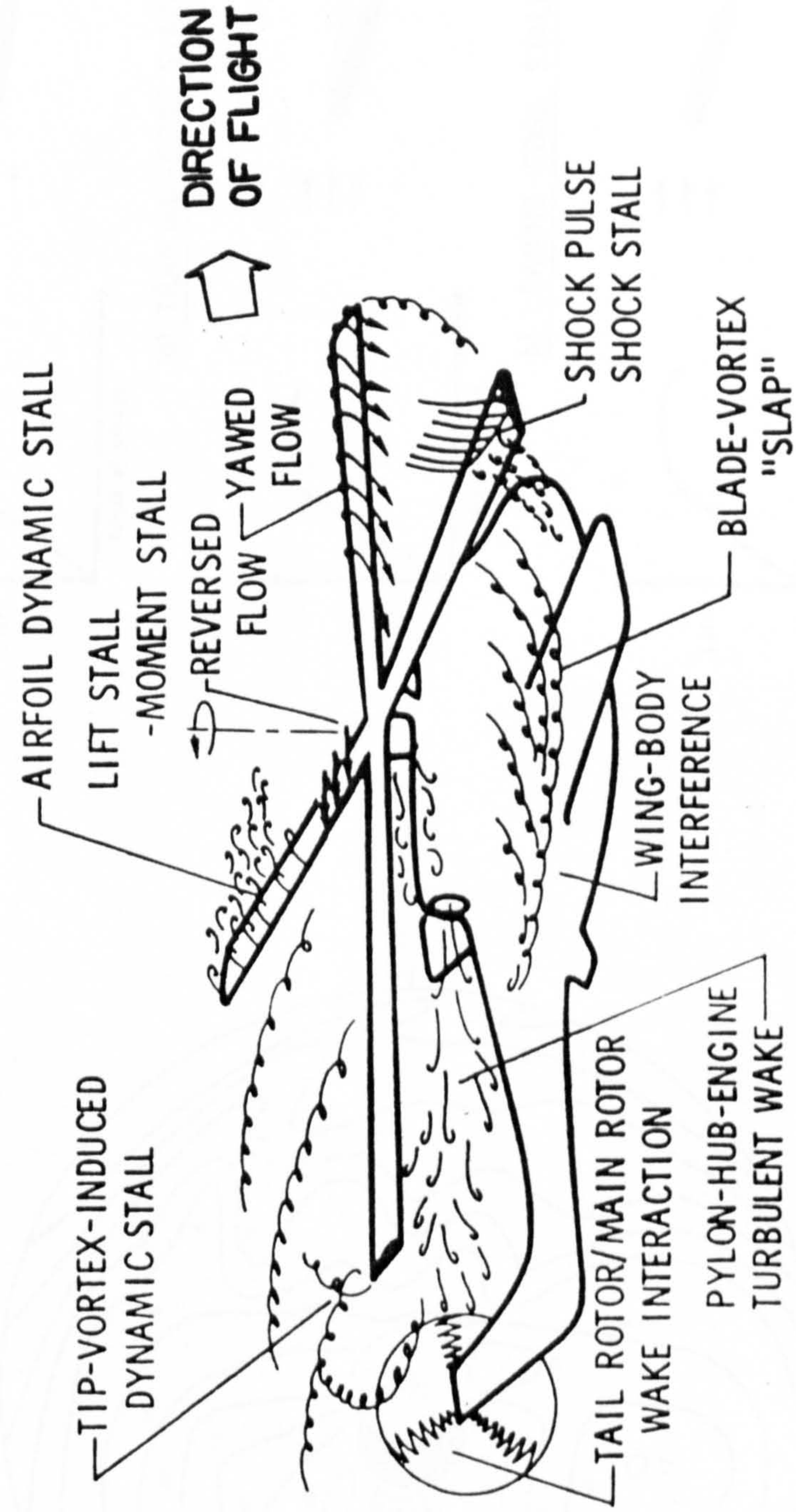

Fig 1.2 Helicopter flowfield phenomena which contribute to the rotor airloadings.

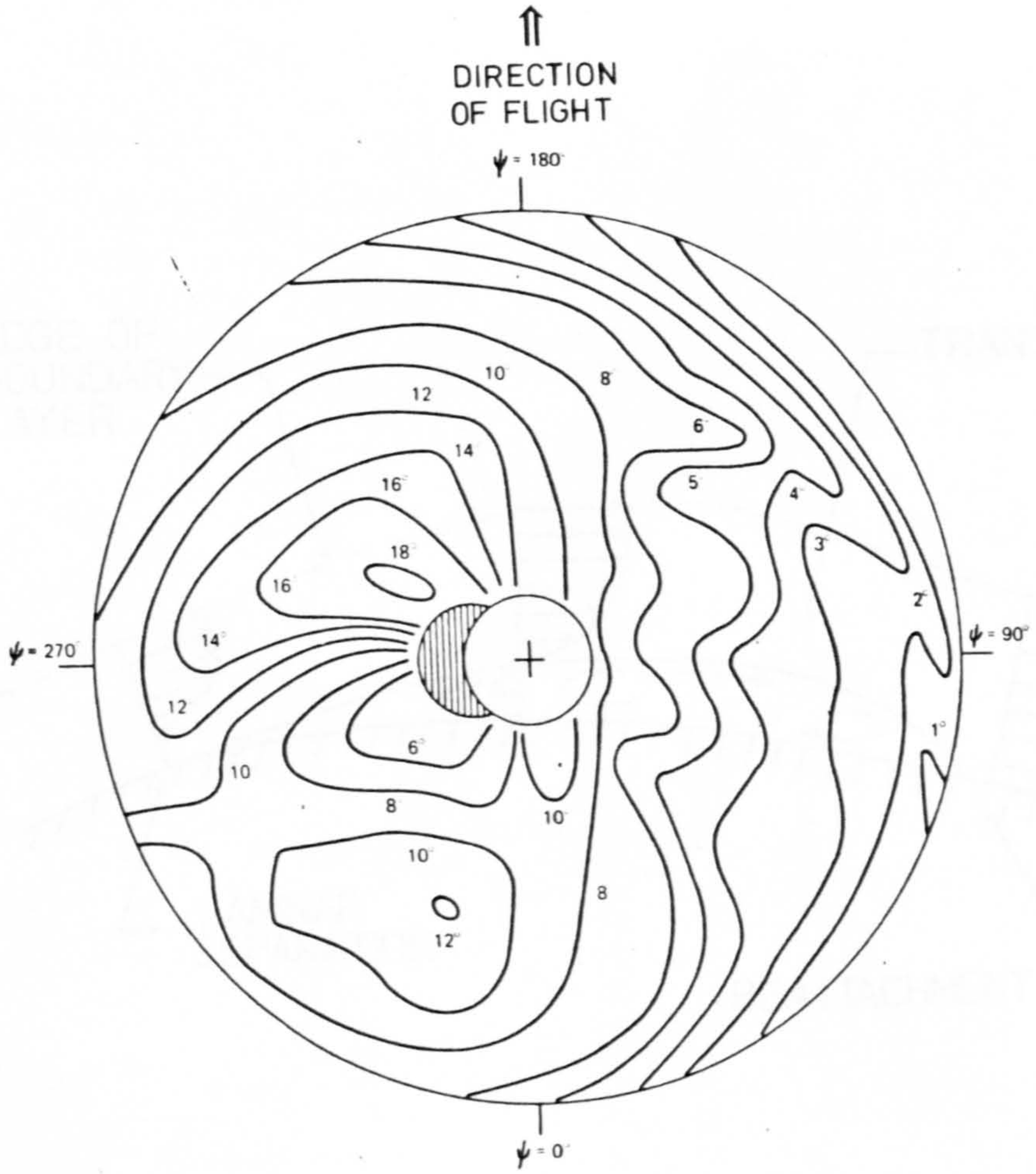

Figure 1.3 Typical rotor angle-of-attack distribution in forward flight

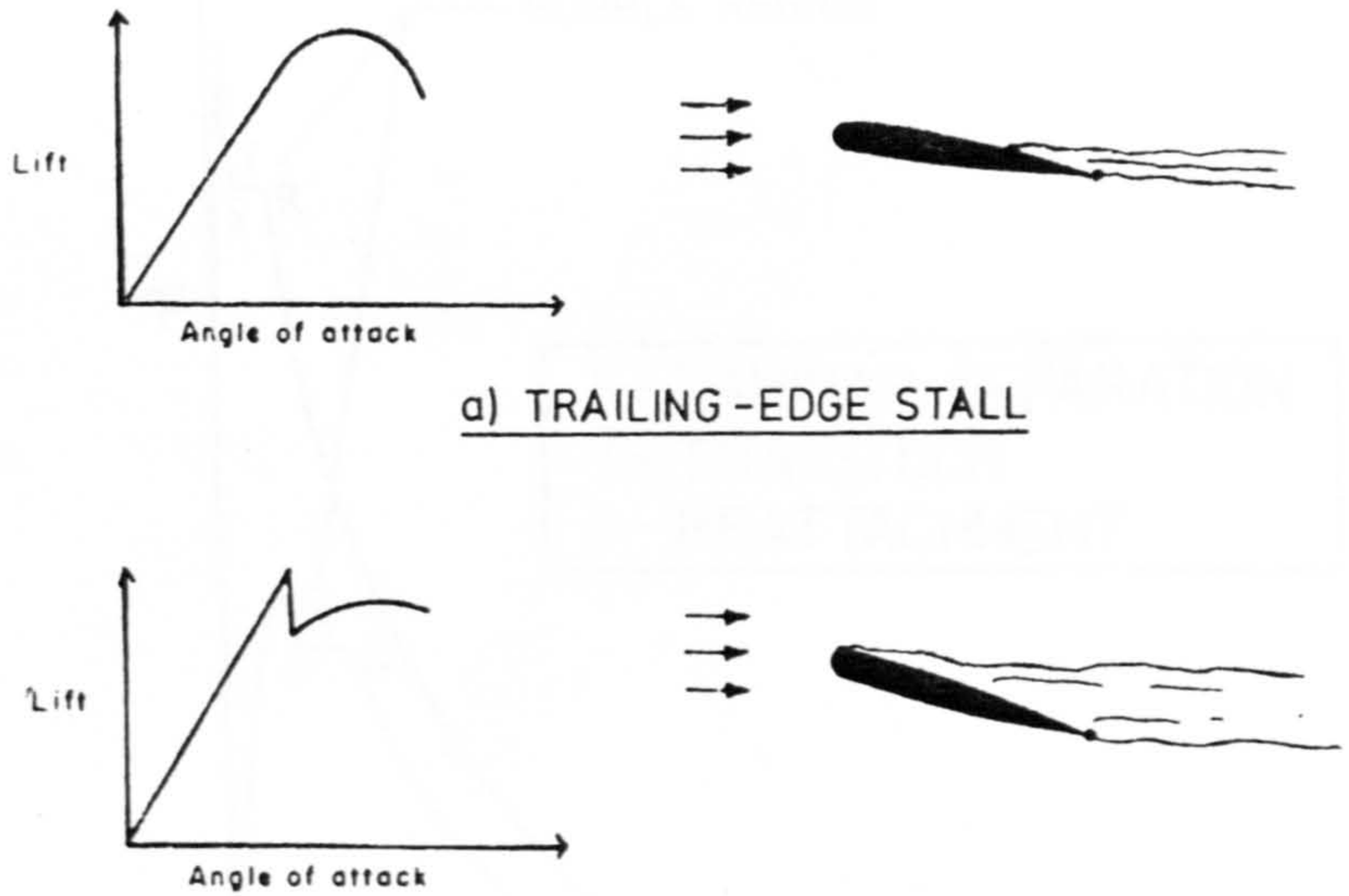

a) TRAILING-EDGE STALL

b) LEADING-EDGE STALL

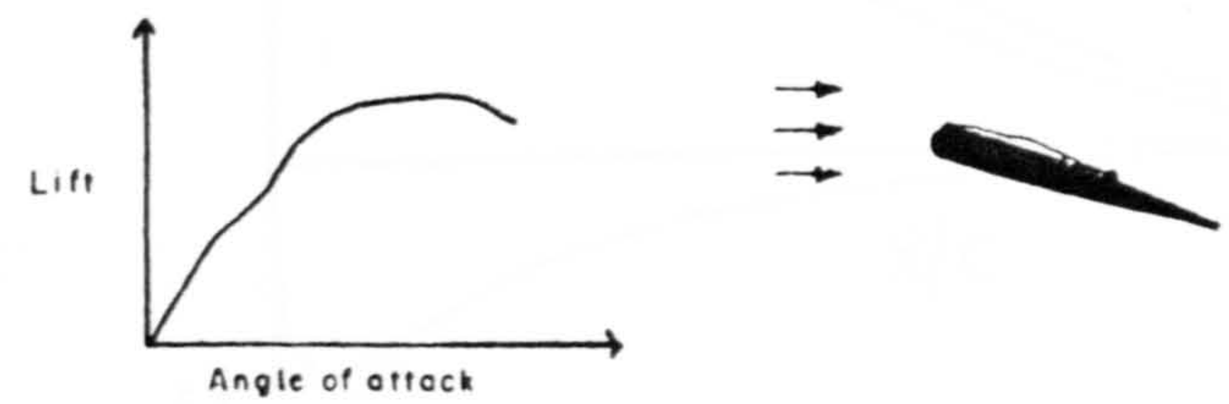

c) THIN AEROFOIL STALL

Figure 1.4 The three types of basic aerofoil stall

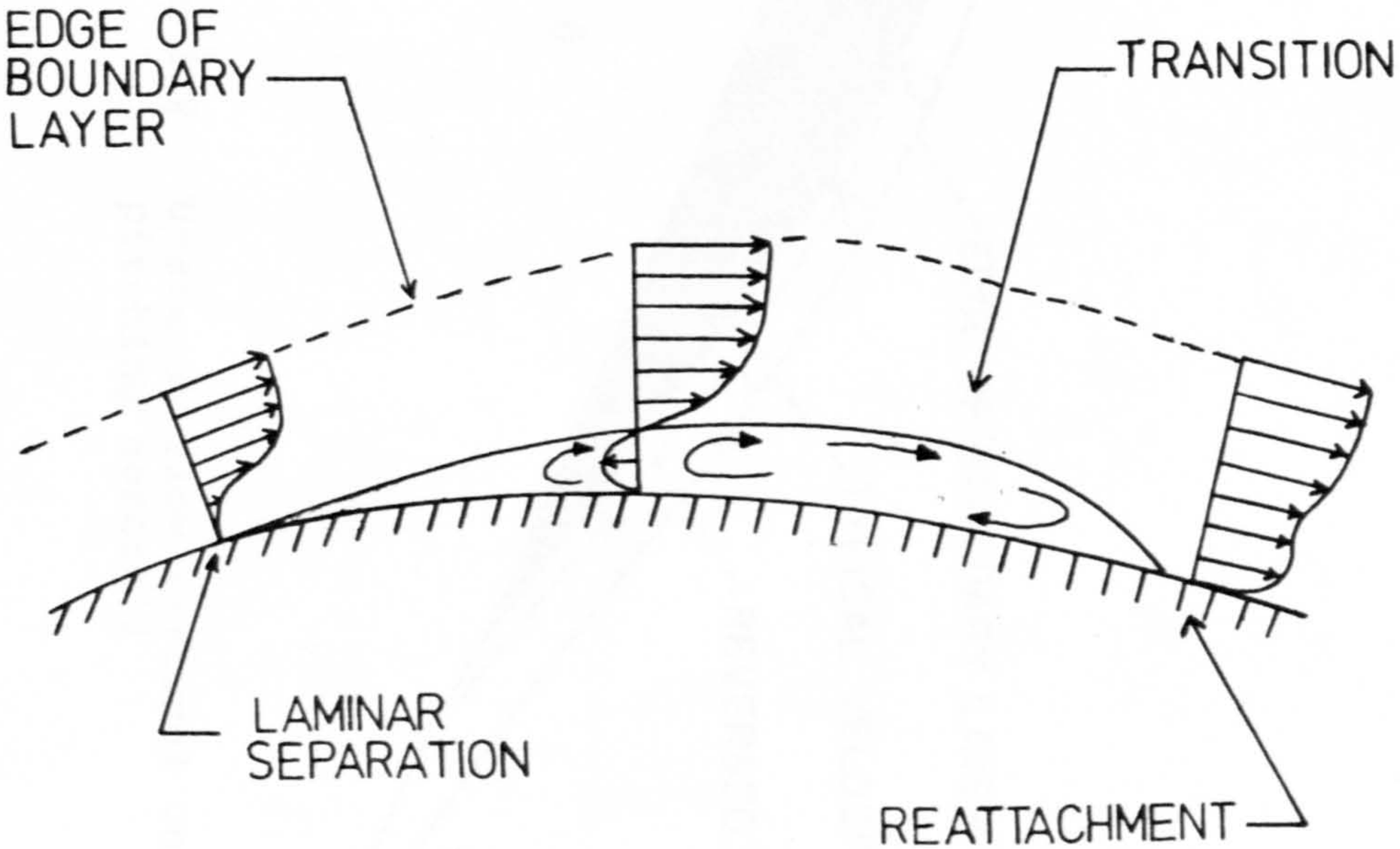

Figure 1.5 Structure of a laminar separation bubble

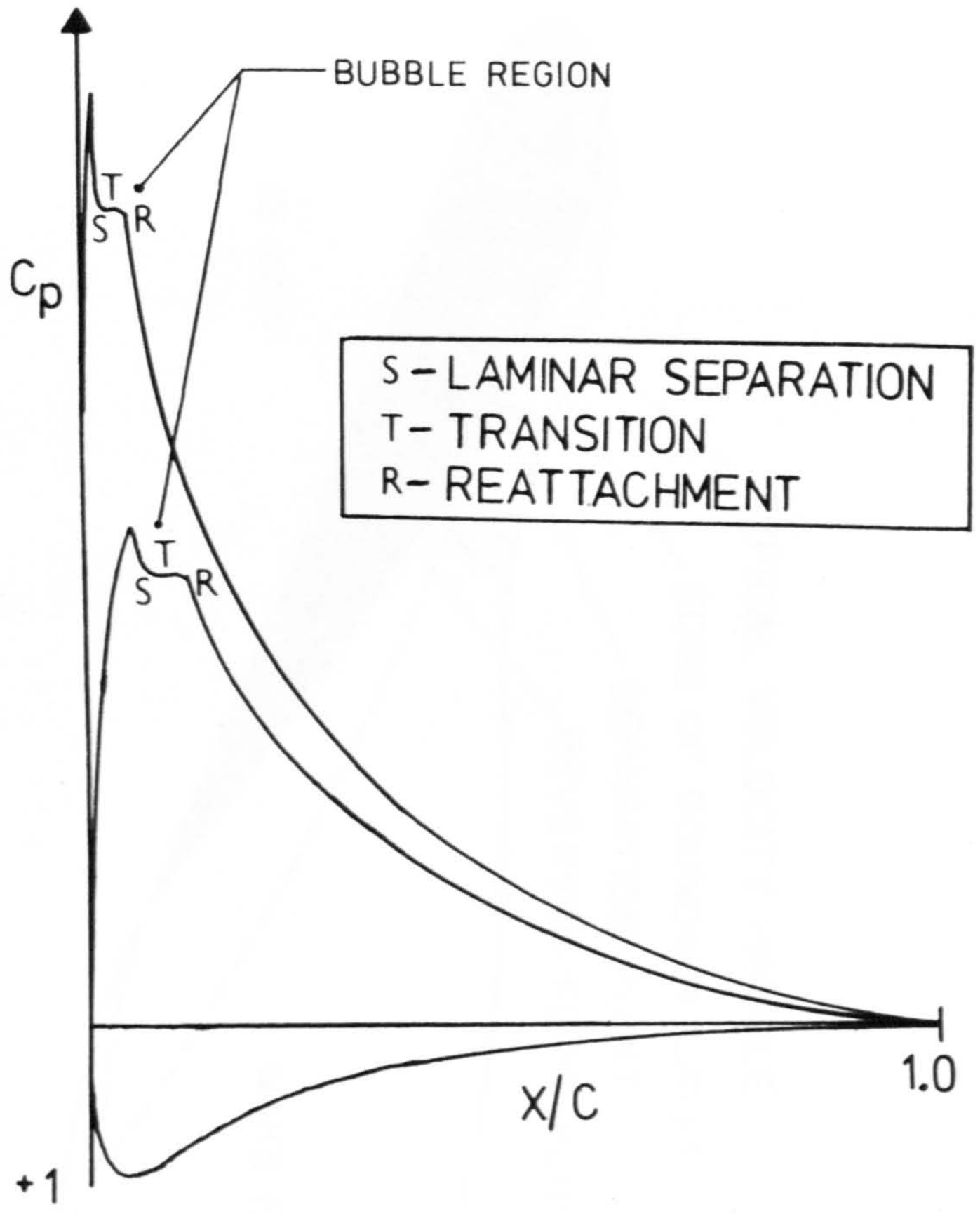

Figure 1.6 The effect of a laminar separation bubble on a typical aerofoil pressure distribution.

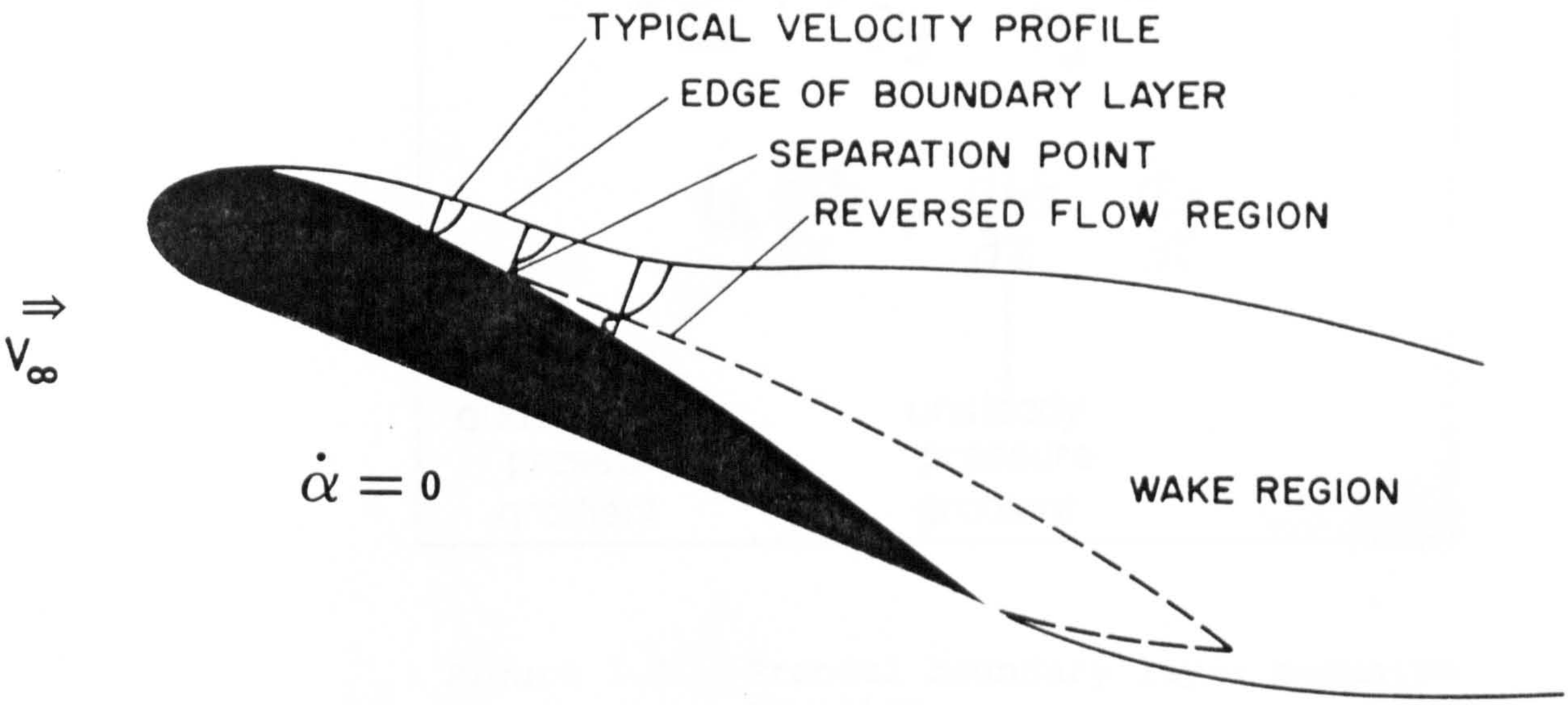

Figure 1.7 Steady separation on an aerofoil

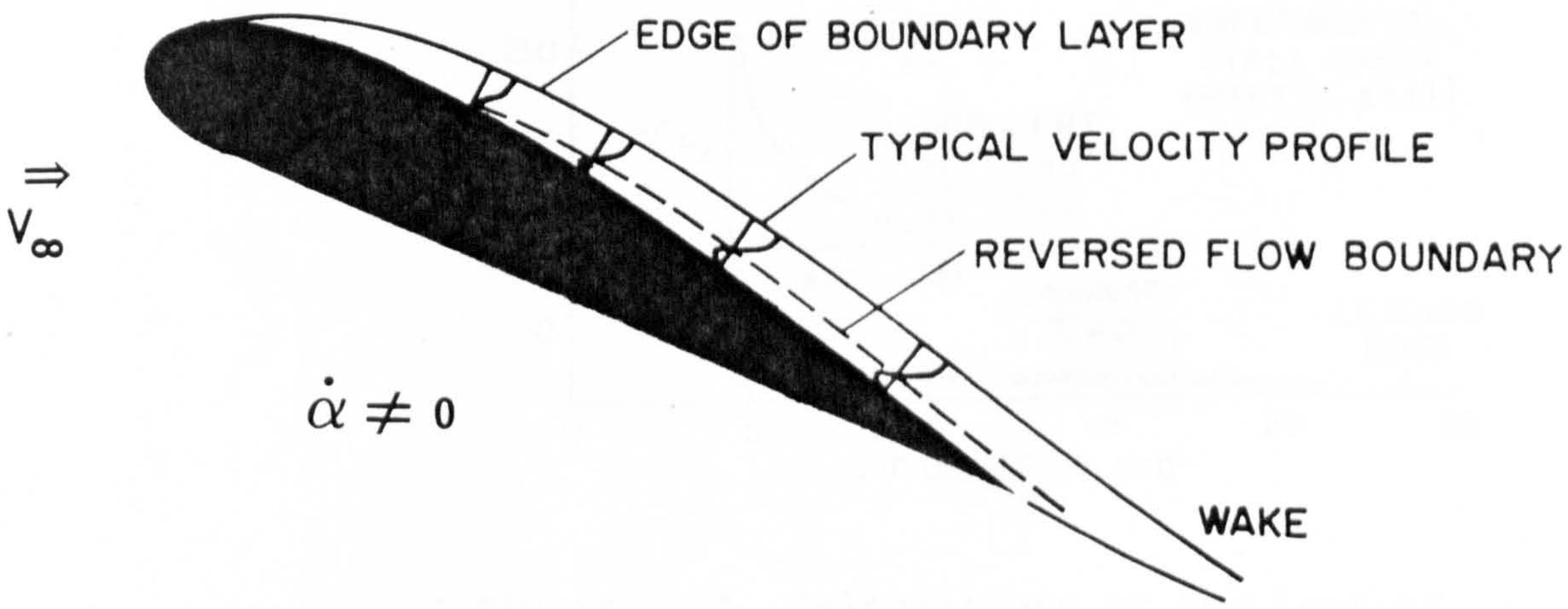

Figure 1.8 Unsteady flow reversal on a pitching aerofoil

$$u\frac{\partial u}{\partial x} + v\frac{\partial u}{\partial y} - \frac{\partial \tau}{\partial y} =$$

$$U_e\frac{\partial U_e}{\partial x} + \frac{\partial U_e}{\partial t} - \frac{\partial u}{\partial t}$$

quasi-steady pressure gradient

unsteady pressure gradient

Figure 1.9 Prandtl boundary layer momentum equation.

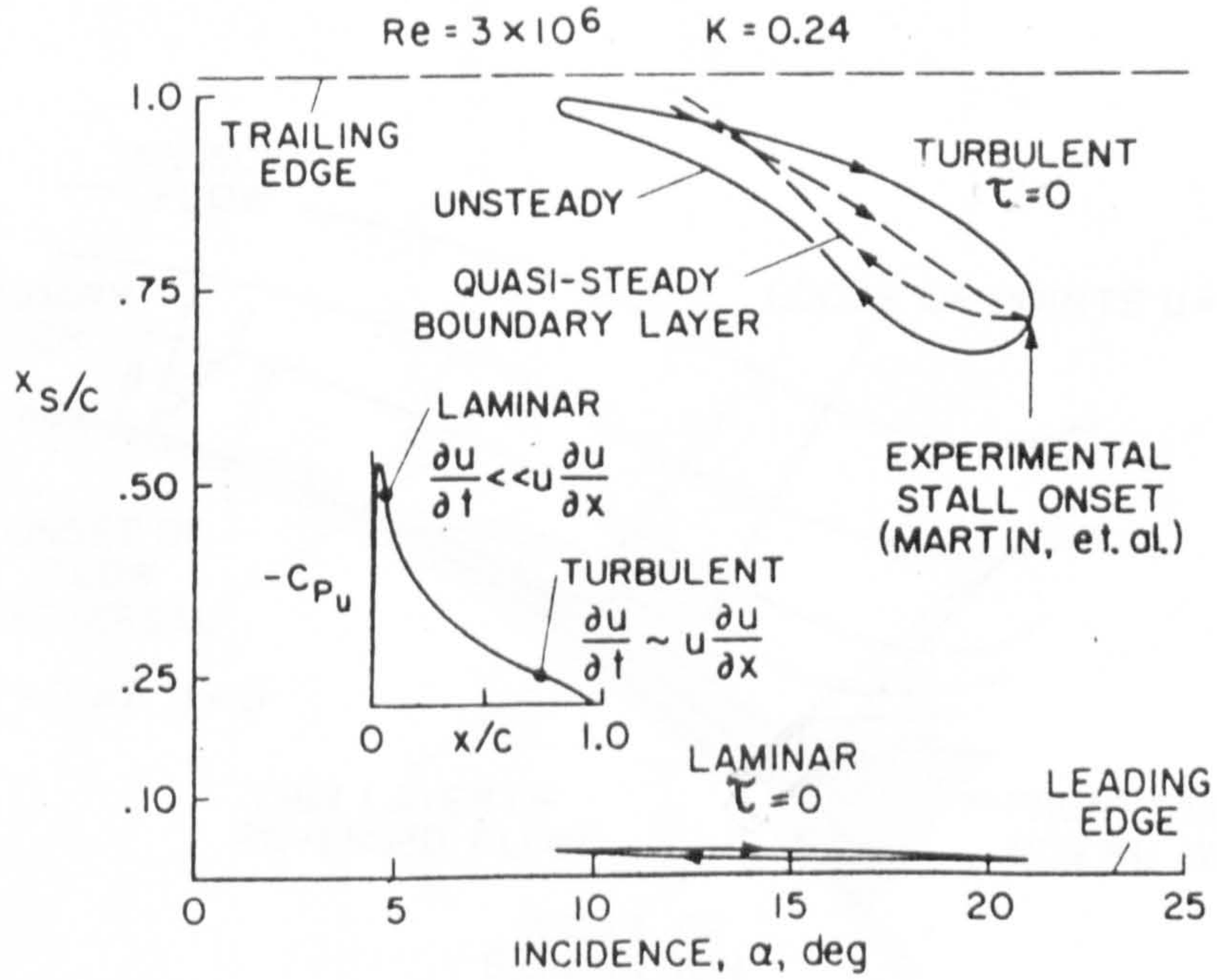

Figure 1.10 Calculations of the loci of laminar and turbulent flow reversal on an oscillating NACA 0012 aerofoil (from McCroskey, 1975)

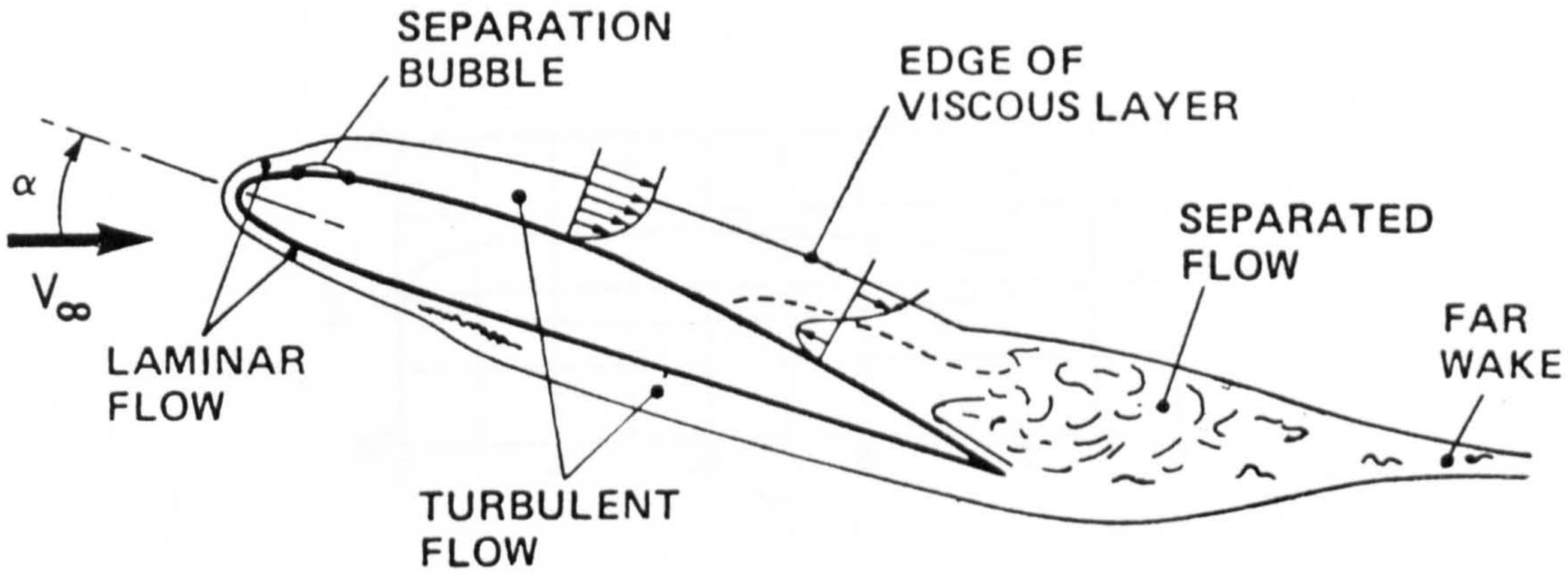

Fig 1.11 Flowfield structure on a pitching aerofoil with minor trailing-edge separation.

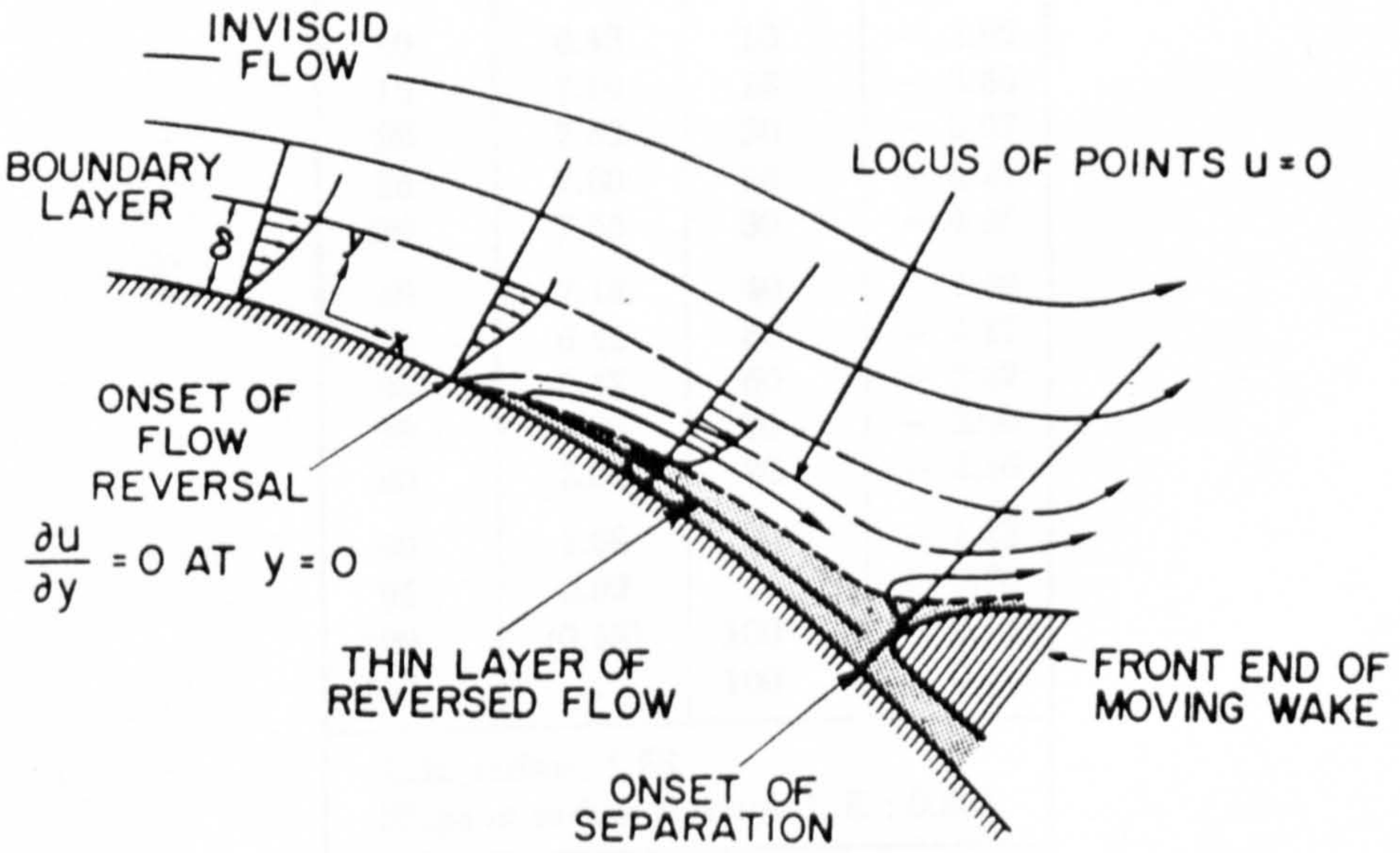

Fig 1.12 Detail of the flowfield structure near separation on a pitching aerofoil. (FROM SEARS AND TELIONIS, 1975)

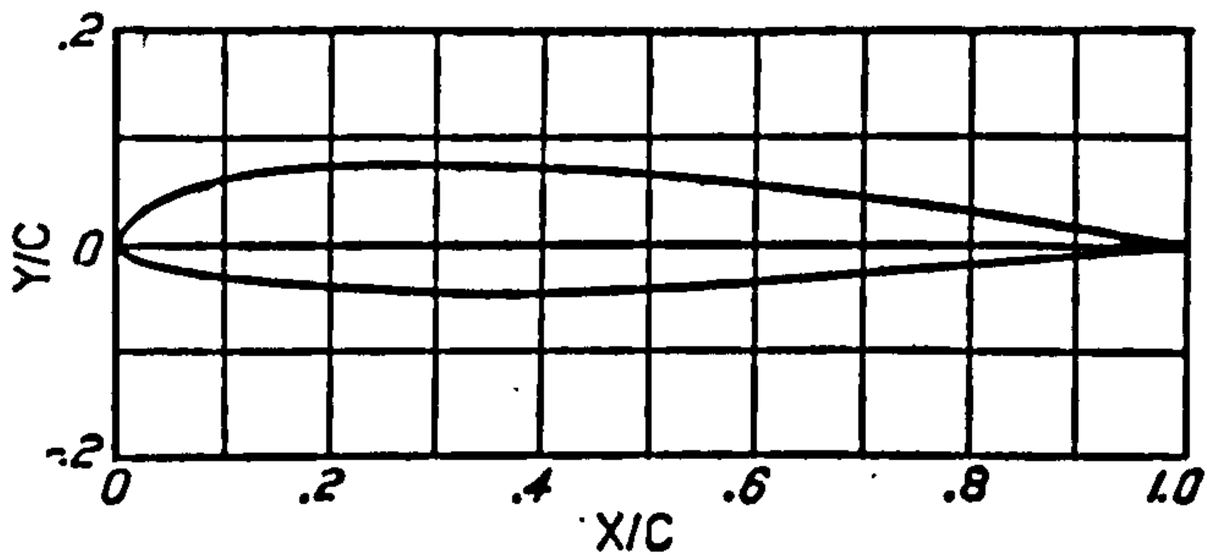

NACA 23012

(Stations and ordinates given in per cent of airfoil chord)

Upper surface		Lower surface	
Station	Ordinate	Station	Ordinate
0	.....	0	0
1.25	2.67	1.25	— 1.23
2.5	3.61	2.5	— 1.71
5.0	4.91	5.0	— 2.26
7.5	5.80	7.5	— 2.61
10	6.43	10	— 2.92
15	7.19	15	— 3.50
20	7.50	20	— 3.97
25	7.60	25	— 4.28
30	7.55	30	— 4.46
40	7.14	40	— 4.48
50	6.41	50	— 4.17
60	5.47	60	— 3.67
70	4.36	70	— 3.00
80	3.08	80	— 2.16
90	1.68	90	— 1.23
95	0.92	95	— 0.70
100	(0.13)	100	(— 0.13)
100	.....	100	0

L.E. radius: 1.58
Slope of radius through L.E.: 0.305

Figure 2.1 NACA 23012 aerofoil profile and co-ordinates

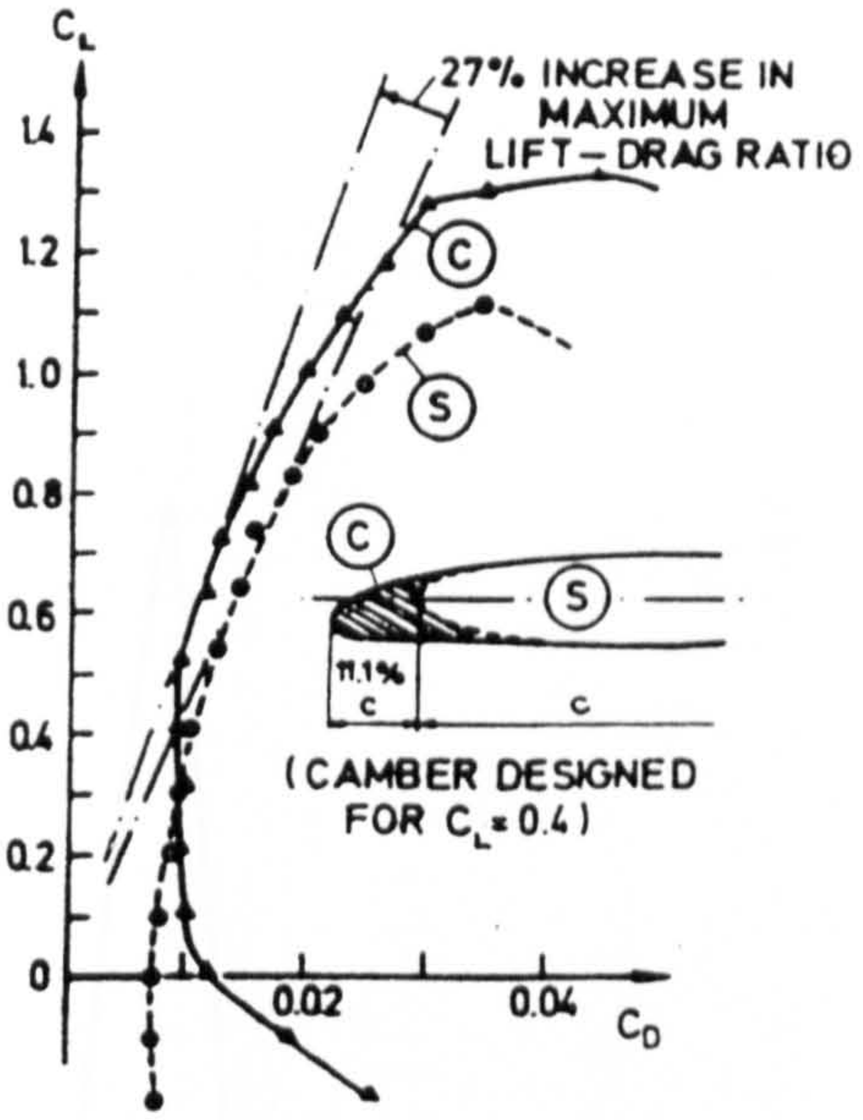

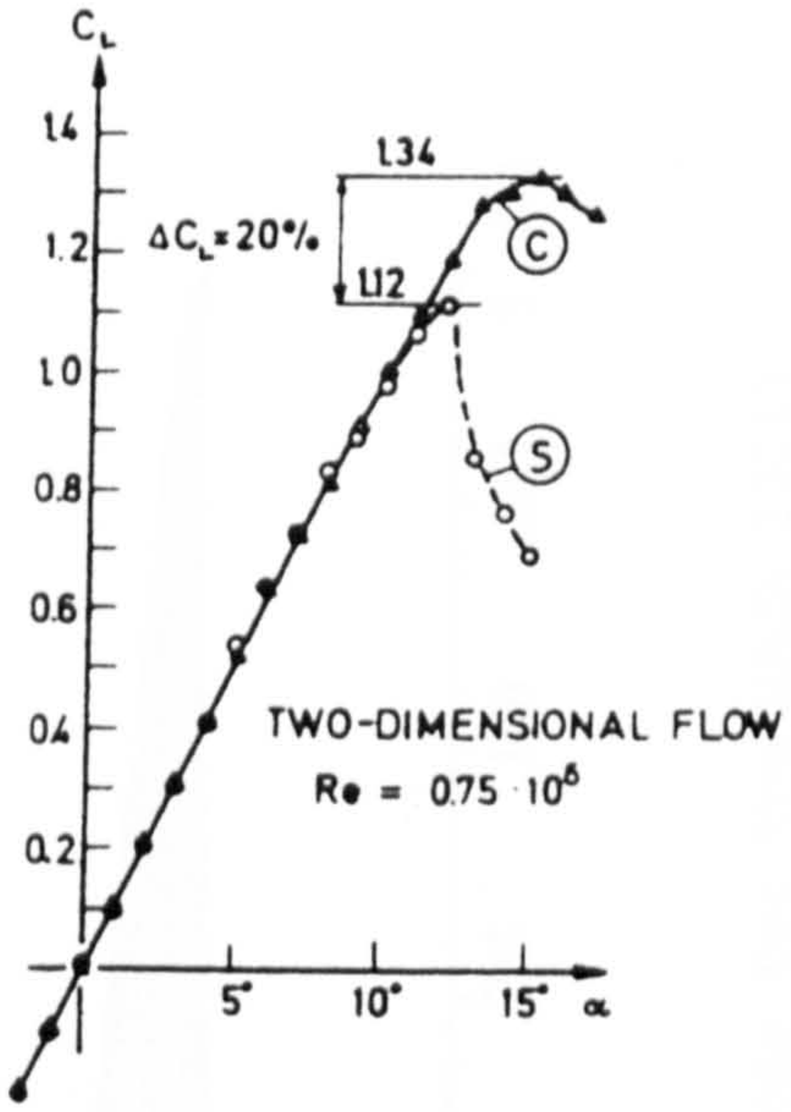

(S) SYMMETRIC AEROFOIL

(C) CAMBERED AEROFOIL

Figure 2.2 Effect of leading-edge camber on the characteristics of an aerofoil

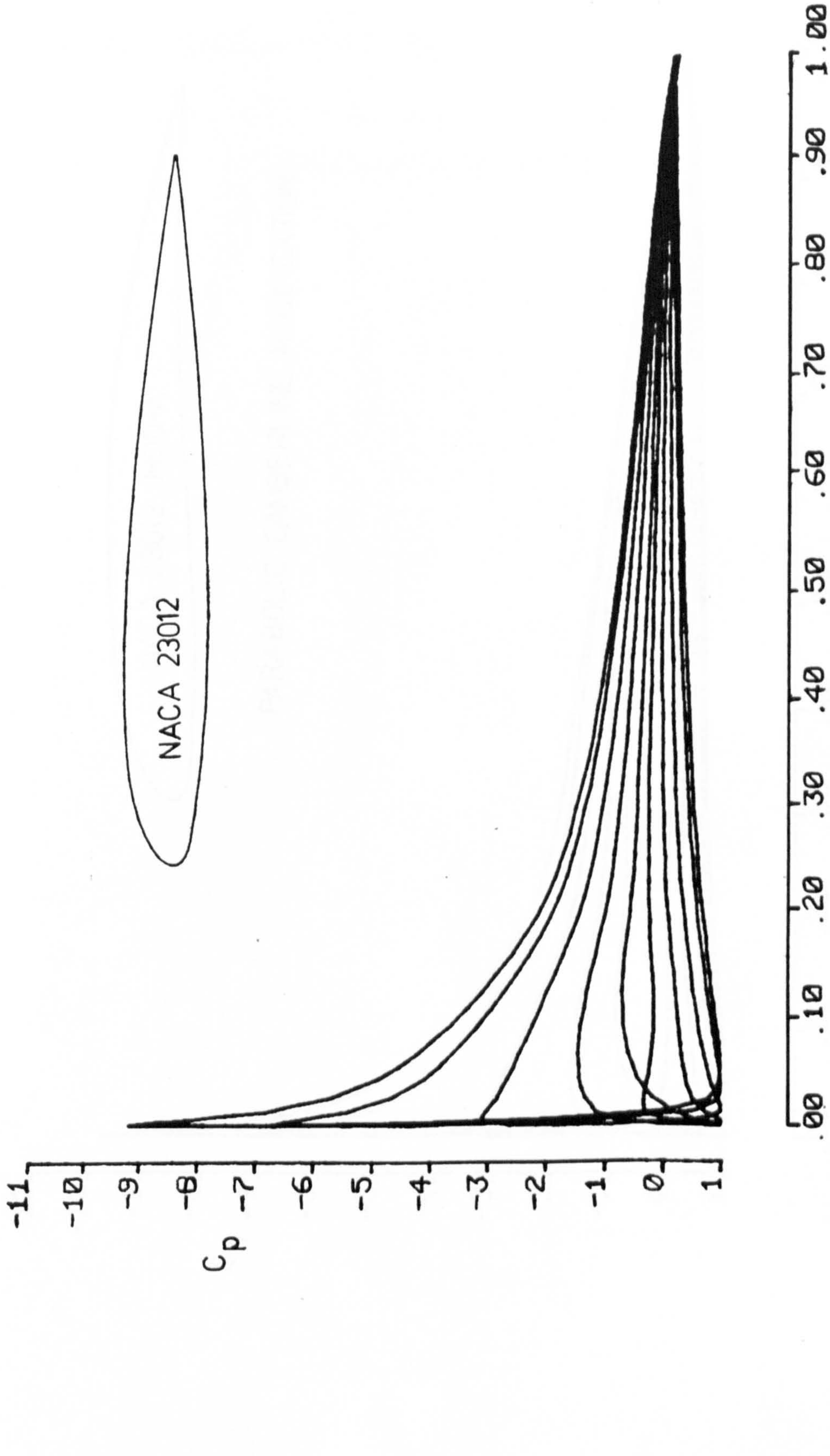

Figure 2.3 Chordwise pressure distributions for the NACA 23012 aerofoil at $\alpha = 0^o$, 4^o, 8^o, 12^o and 14^o

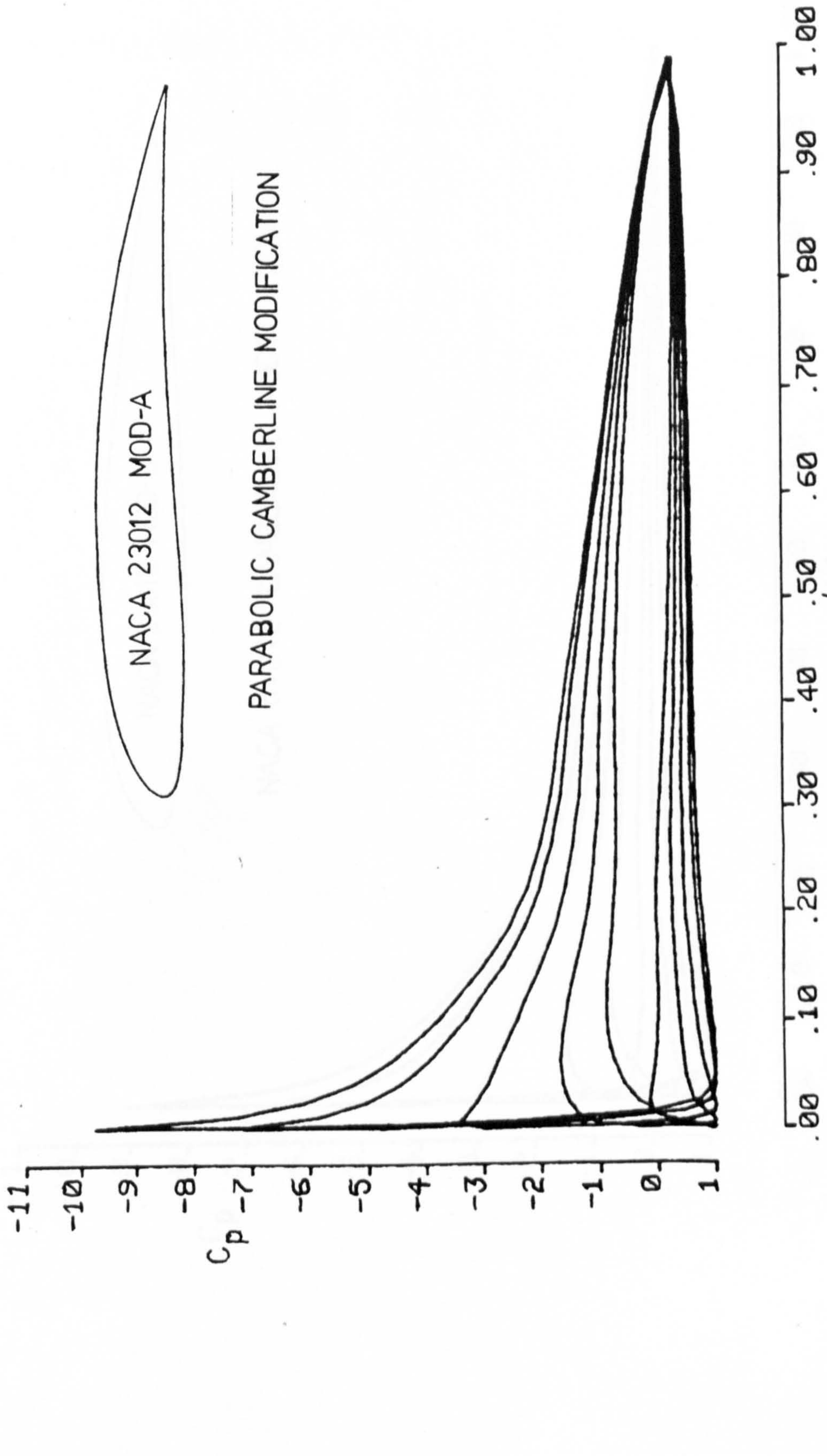

Figure 2.4 Chordwise pressure distributions for the NACA 2312 (MOD–A) aerofoil at $\alpha = 0^o$, 4^o, 8^o, 12^o and 14^o

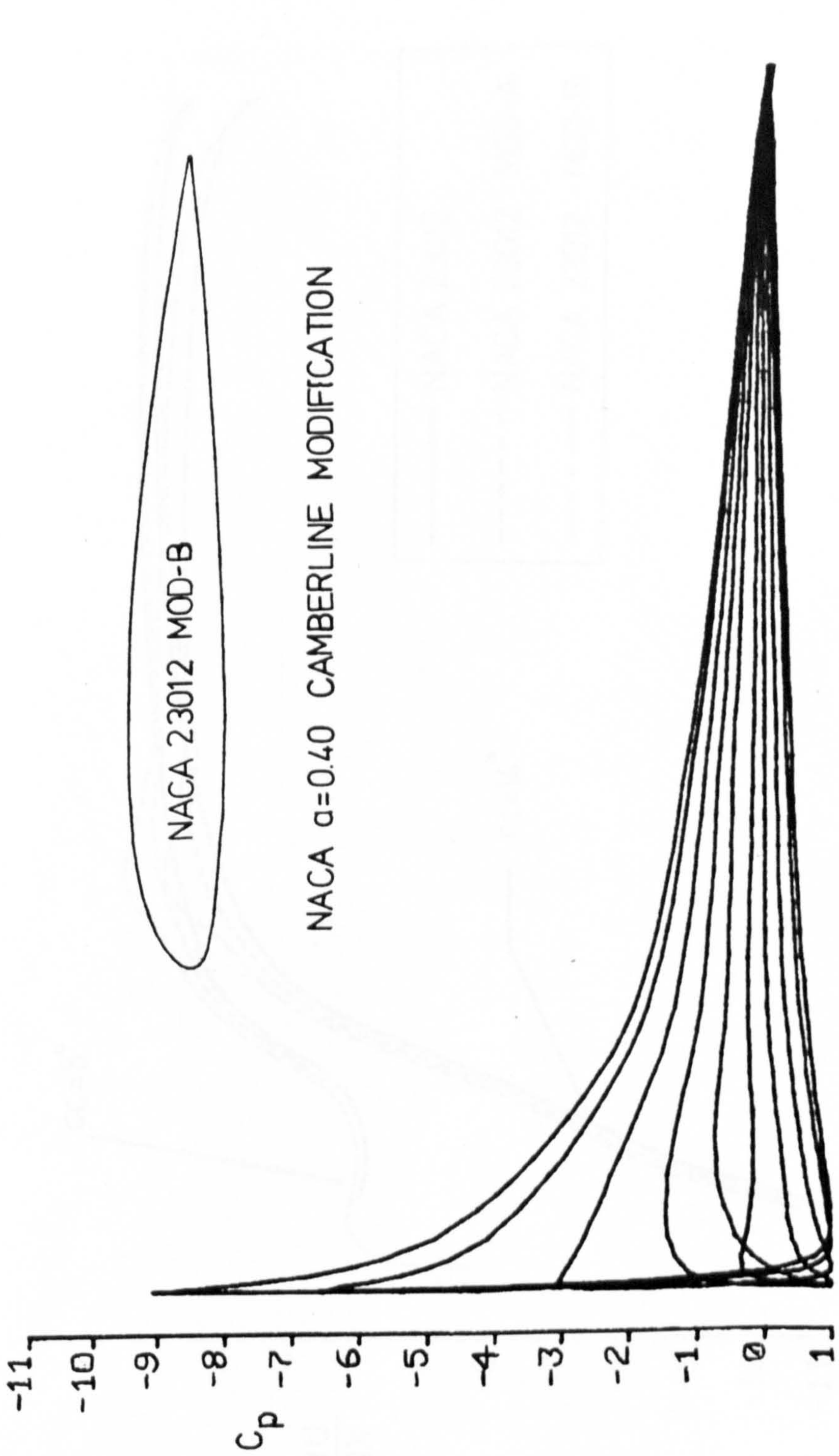

Figure 2.5 Chordwise pressure distributions for the NACA 23012 (MOD-B) aerofoil at $\alpha = 0^{o}$, 4^{o}, 8^{o}, 12^{o} and 14^{o}

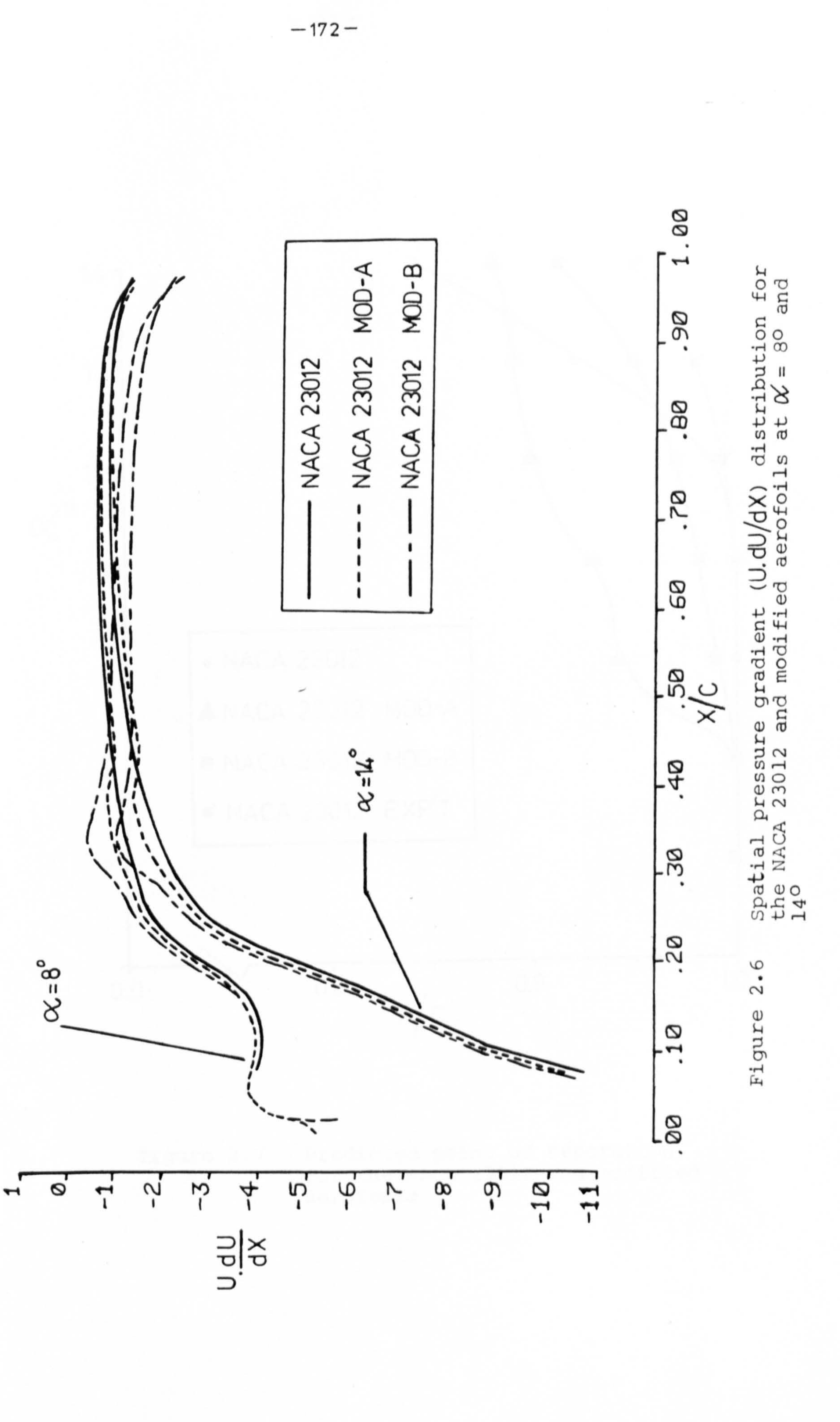

Figure 2.6 Spatial pressure gradient (U.dU/dX) distribution for the NACA 23012 and modified aerofoils at α = 8° and 14°

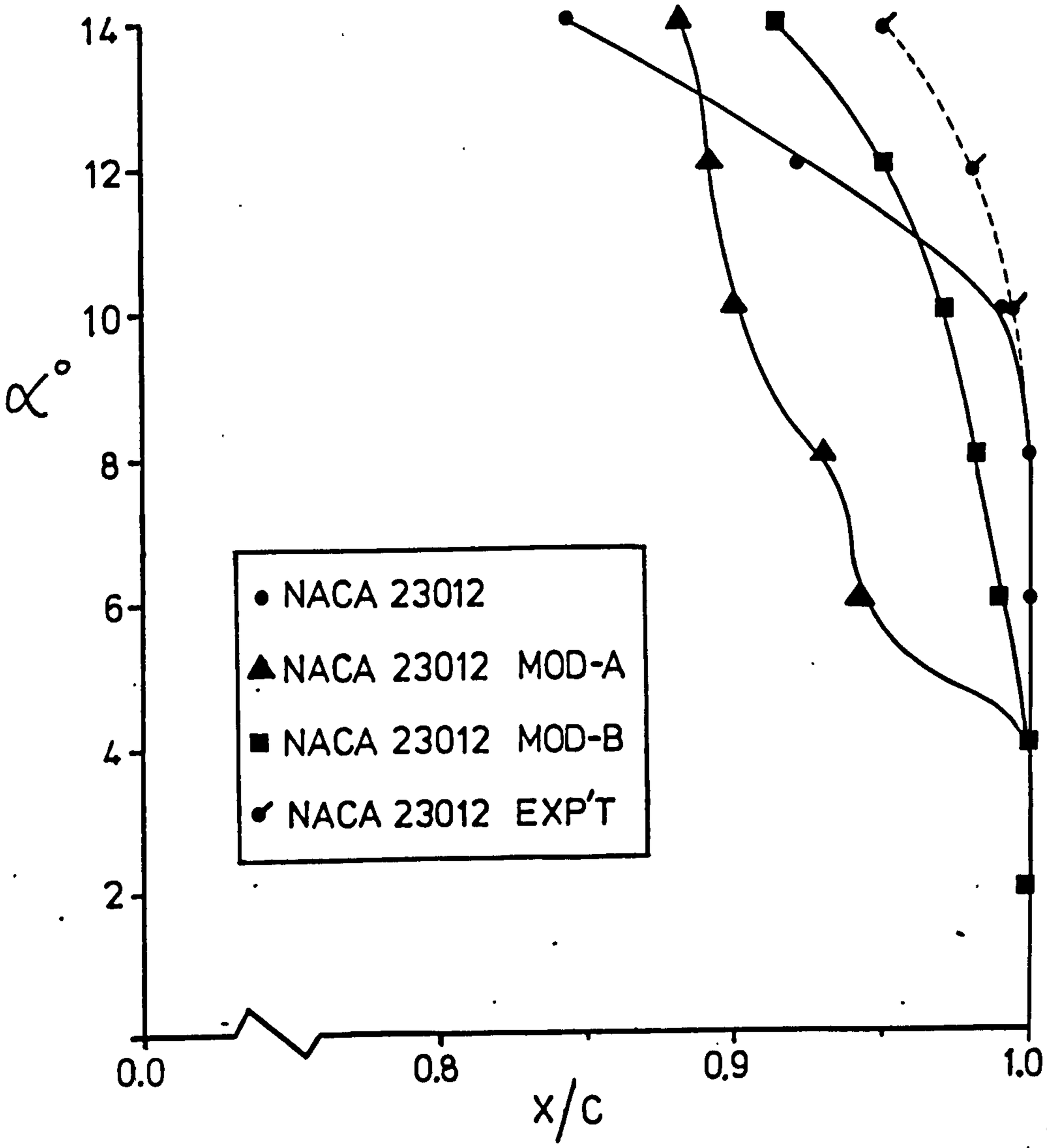

Figure 2.7 Predicted point of separation for the NACA 23012 and modified aerofoils

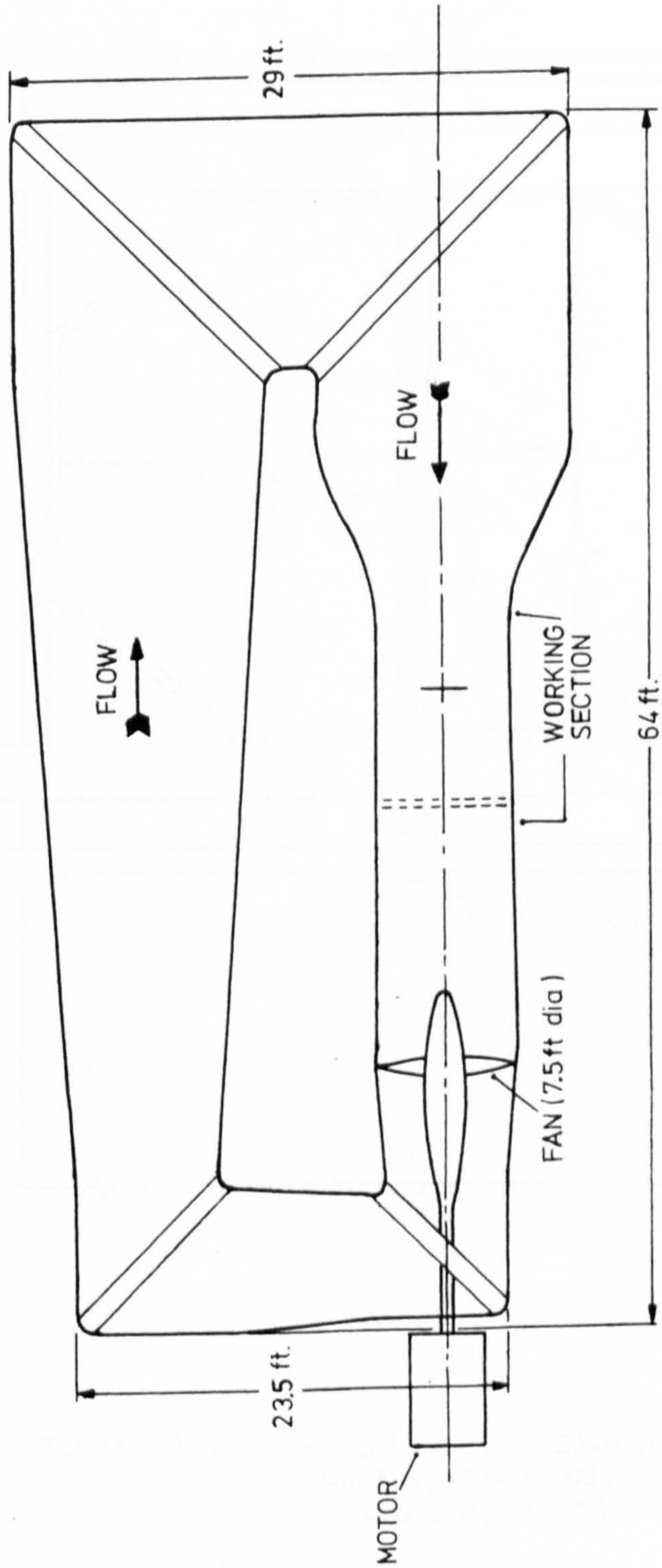

Figure 3.1 Plan view of the Glasgow University "Handley Page" 7ft x 5ft 3in wind tunnel.

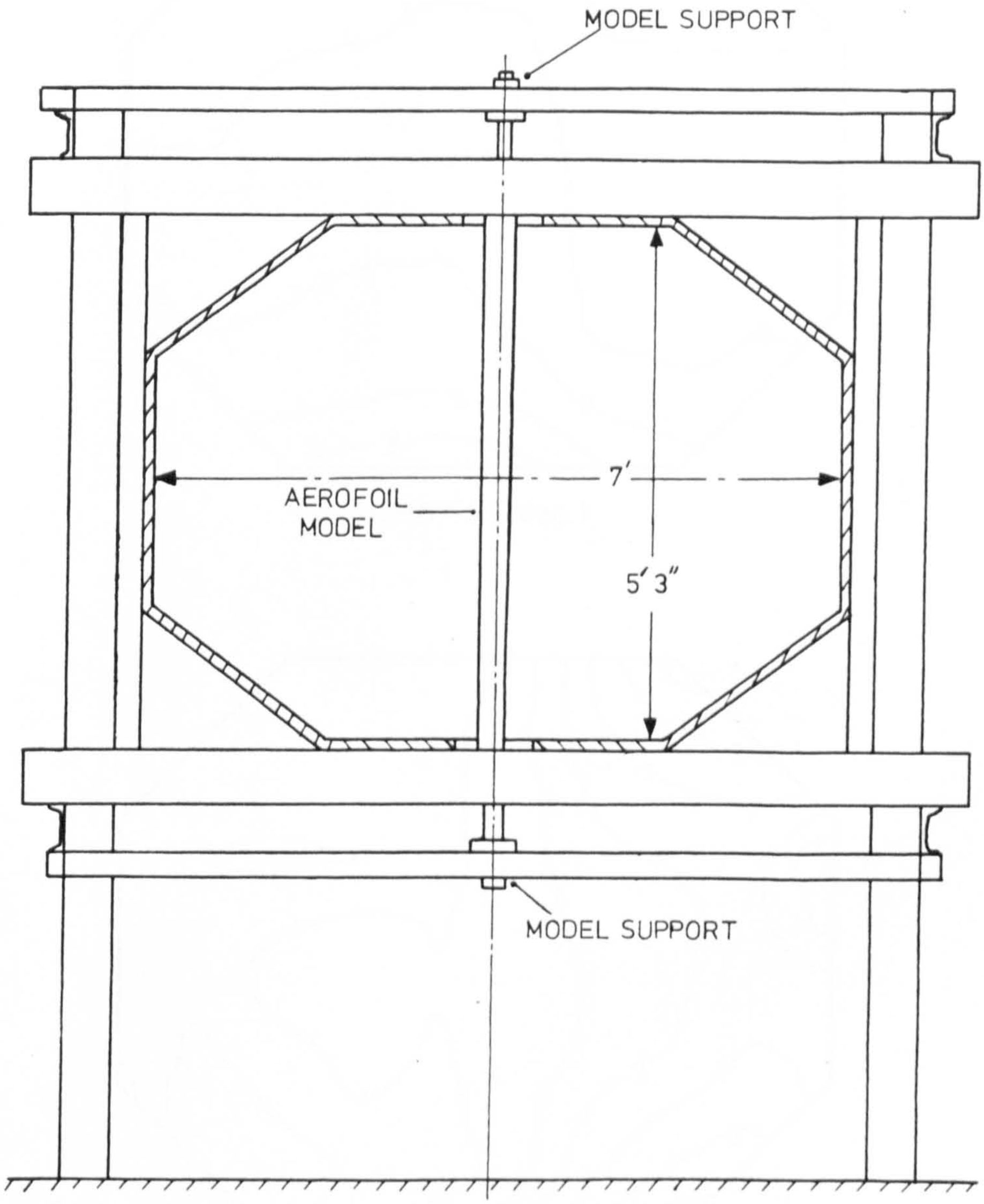

Figure 3.2 Detail of the Glasgow University "Handley Page" wind tunnel working section.

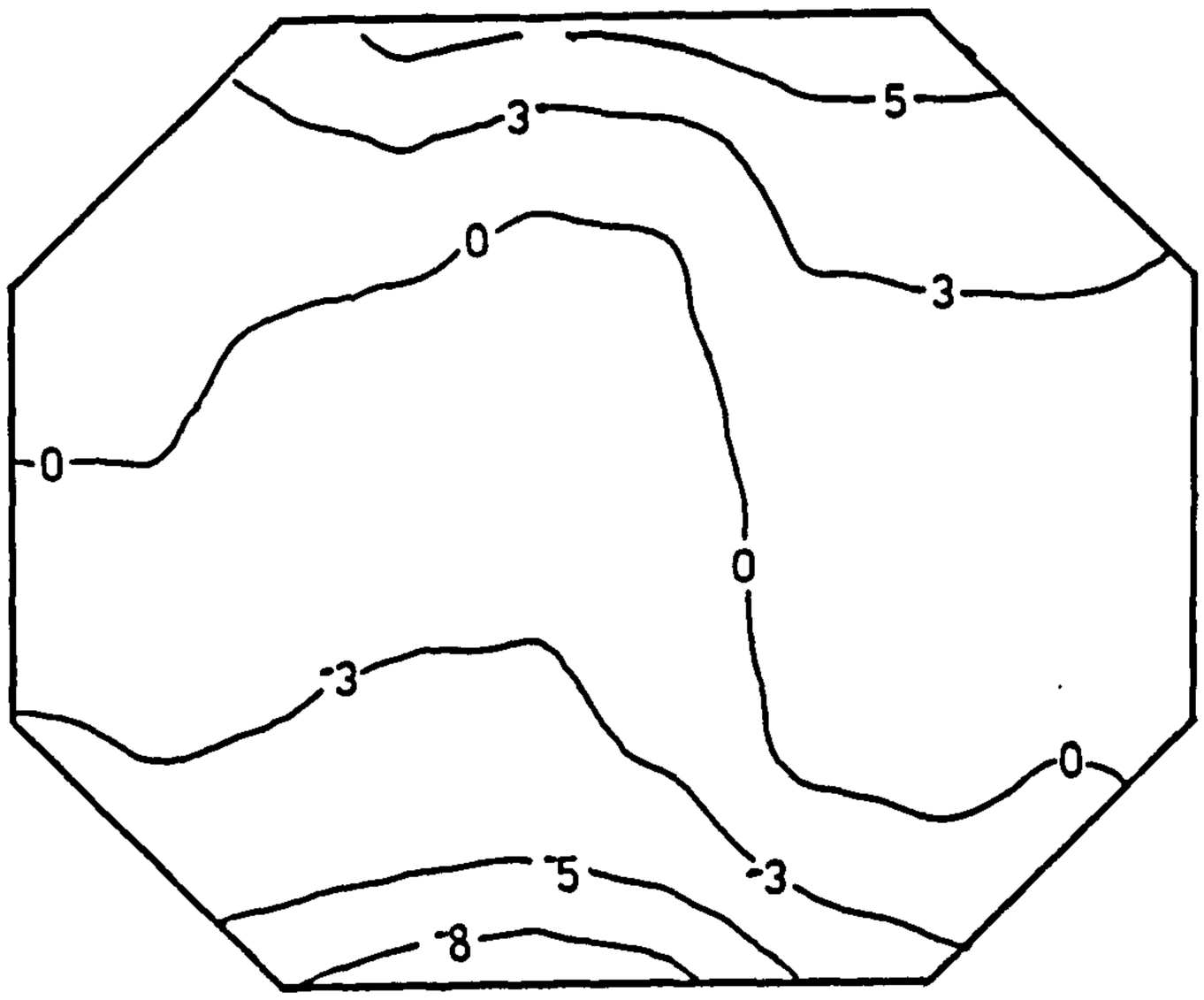

DOWNWASH (deg.)

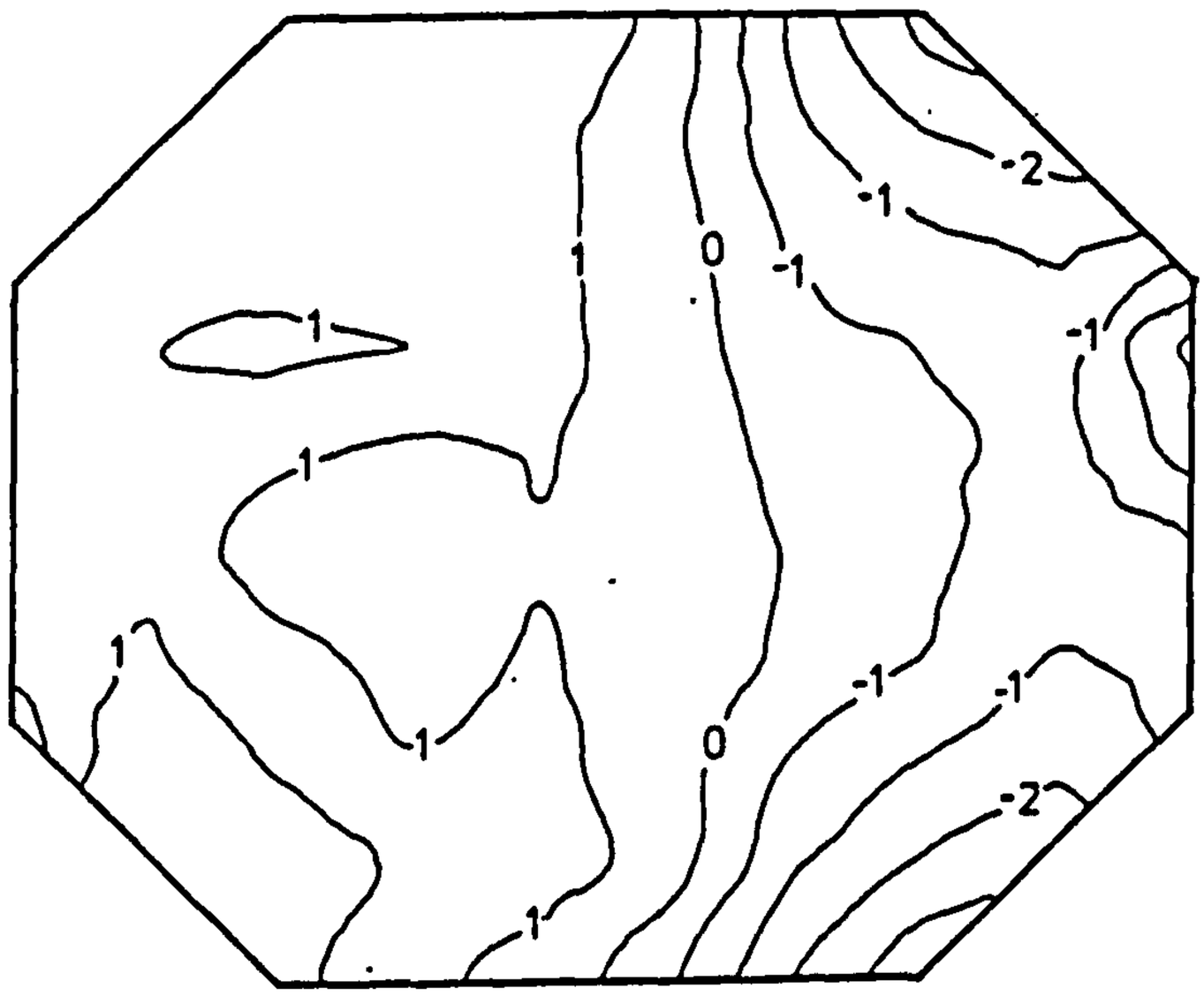

YAW (deg.)

Figure 3.3 Wind tunnel calibration - flow angularity contour plots.

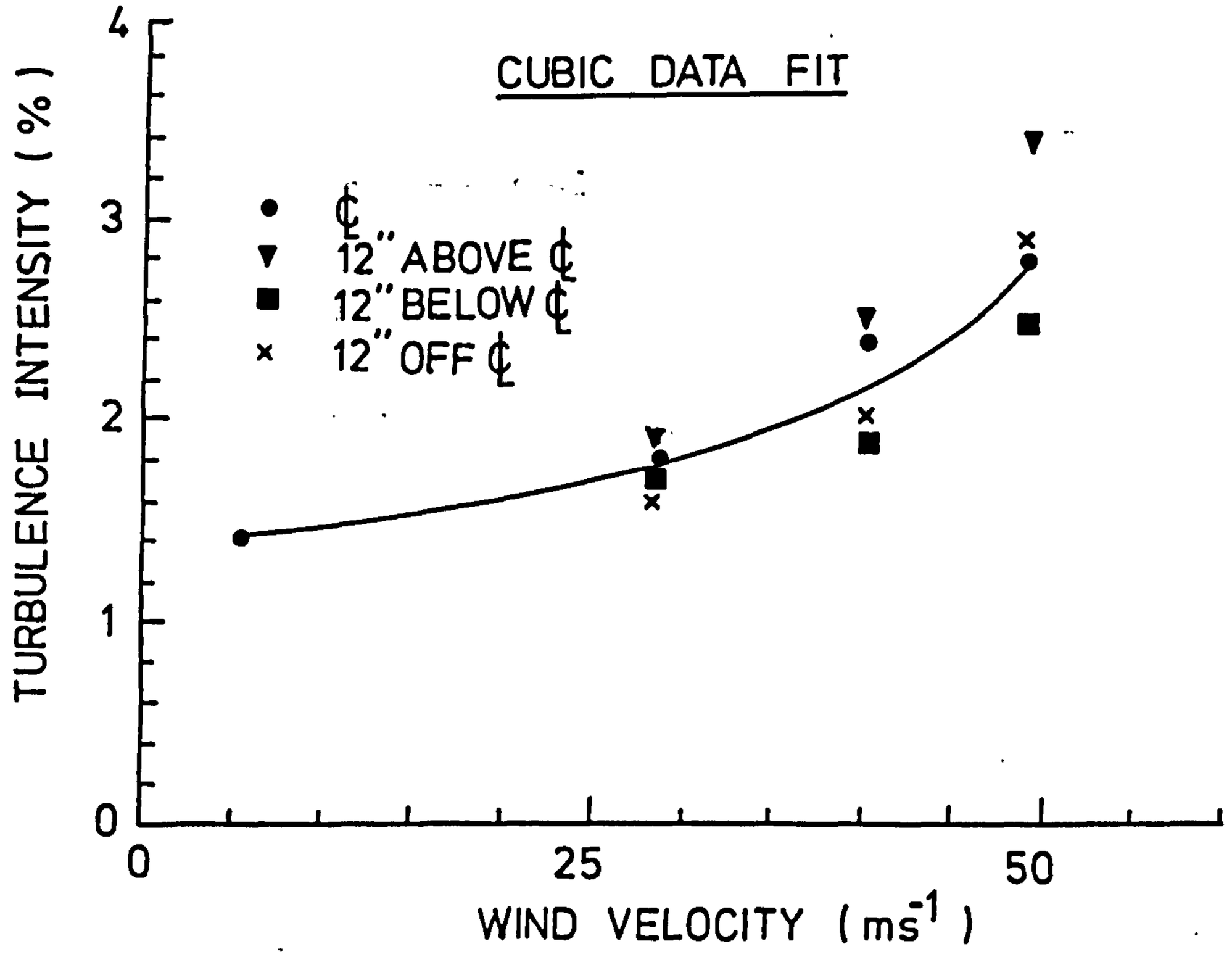

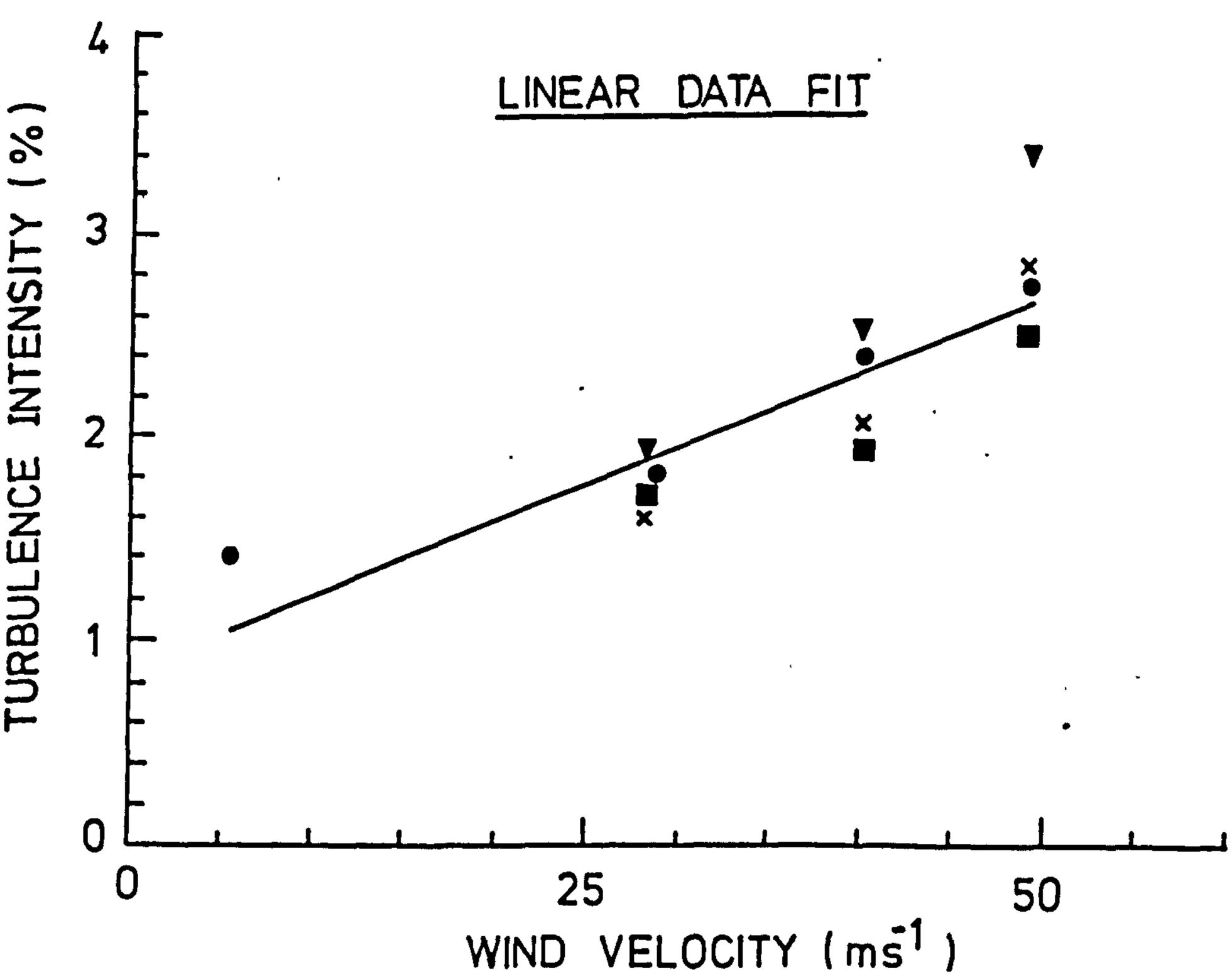

Figure 3.4 Wind tunnel calibration - turbulence measurements.

Figure 3.5 View of the aerofoil model in the wind tunnel.

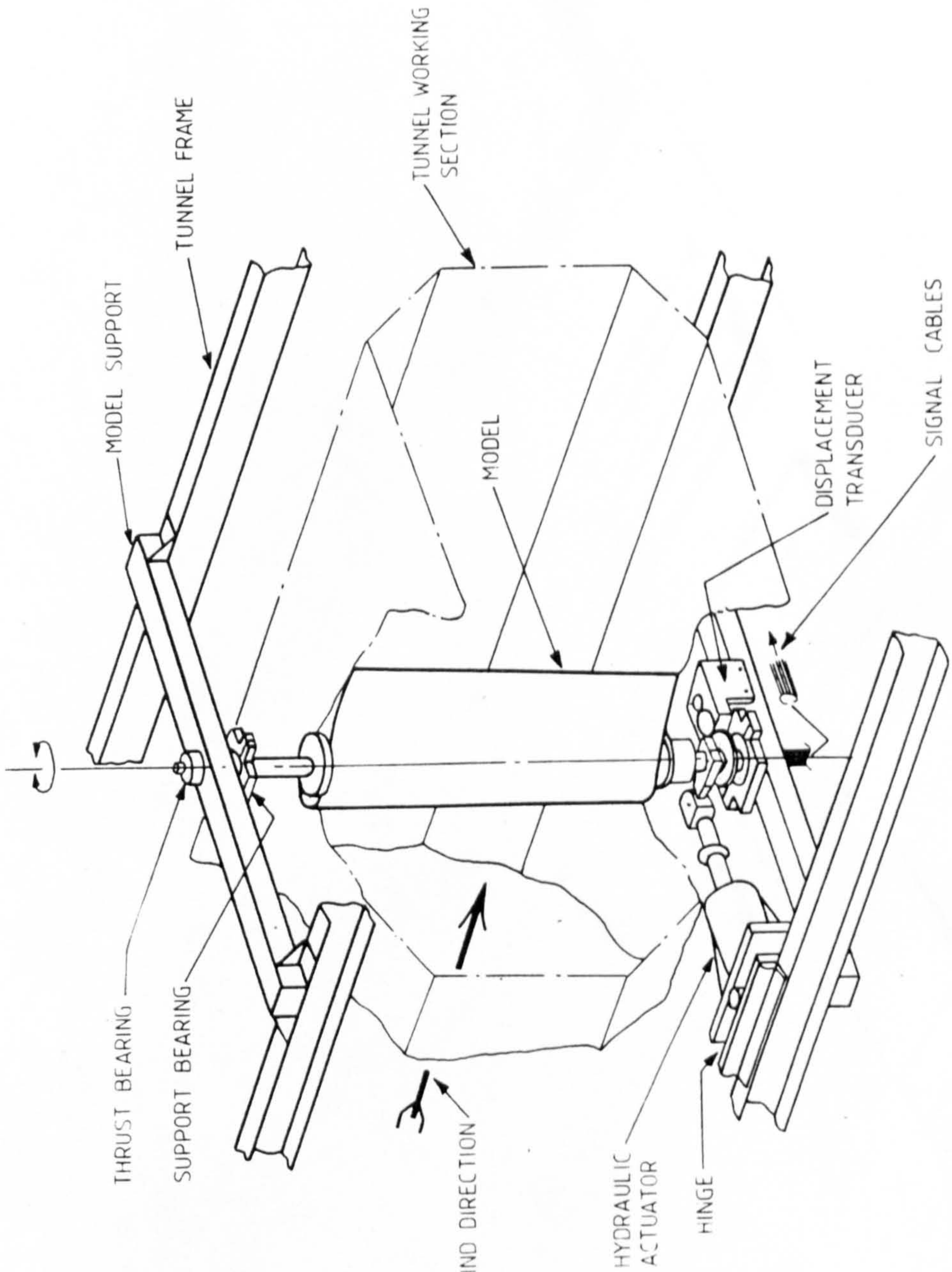

Figure 3.6 General arrangement of the aerofoil, the support structure and the pitch-drive mechanism.

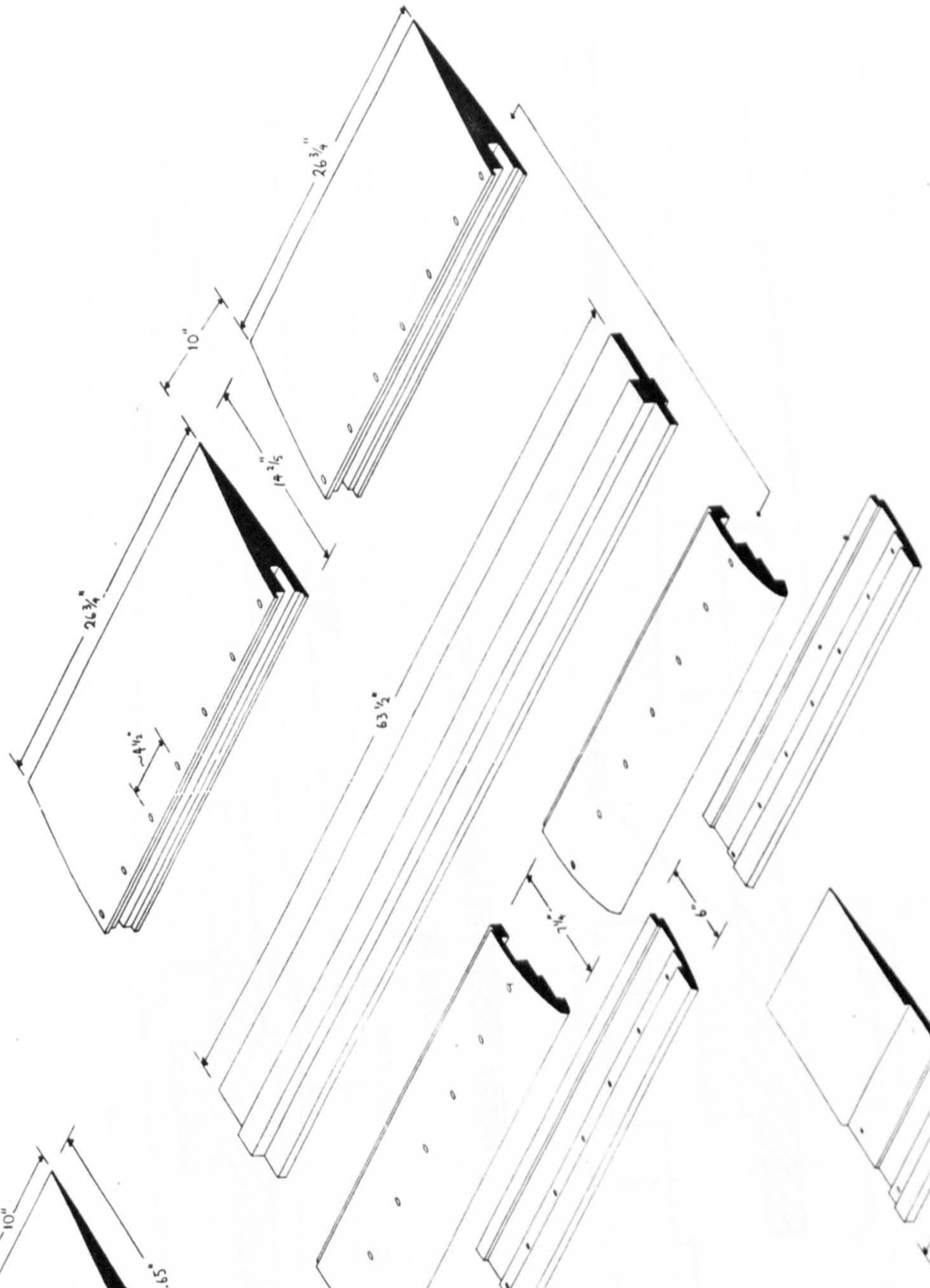

Fig 3.7 Wind tunnel aerofoil model structure assembly.

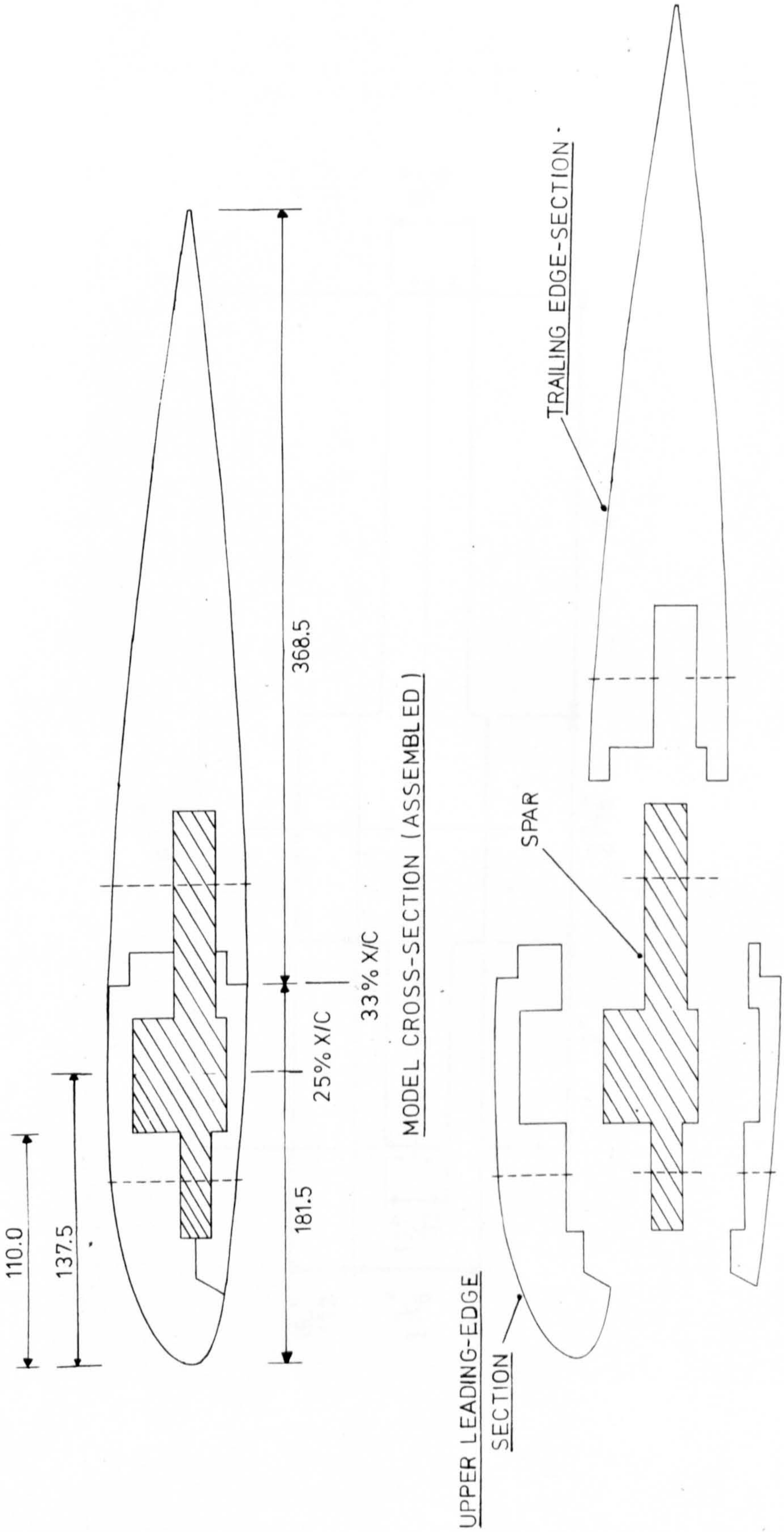

Fig 3.8a. Detail of the aerofoil model cross-sectional assembly.

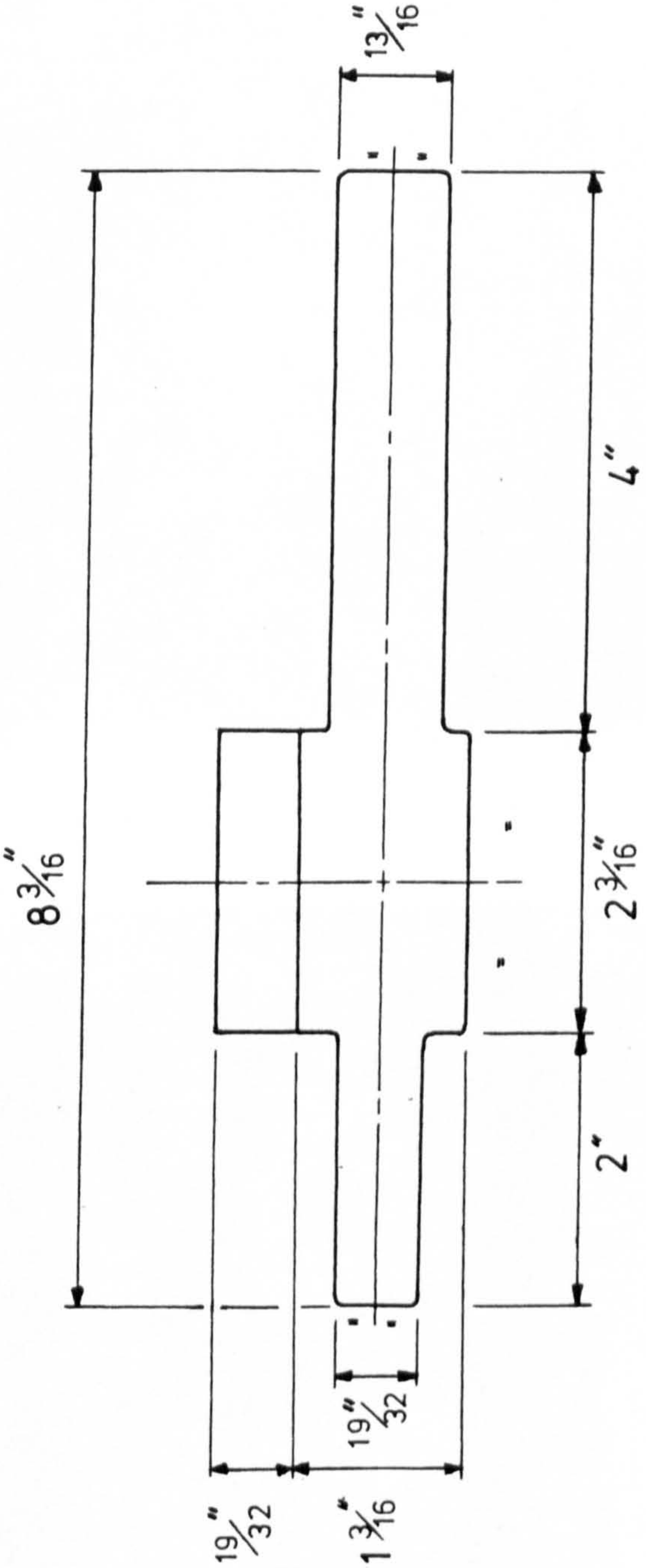

Fig 3.8b. Detail of the aerofoil model spar.

Figure 3.9 Detail of centre instrument section.

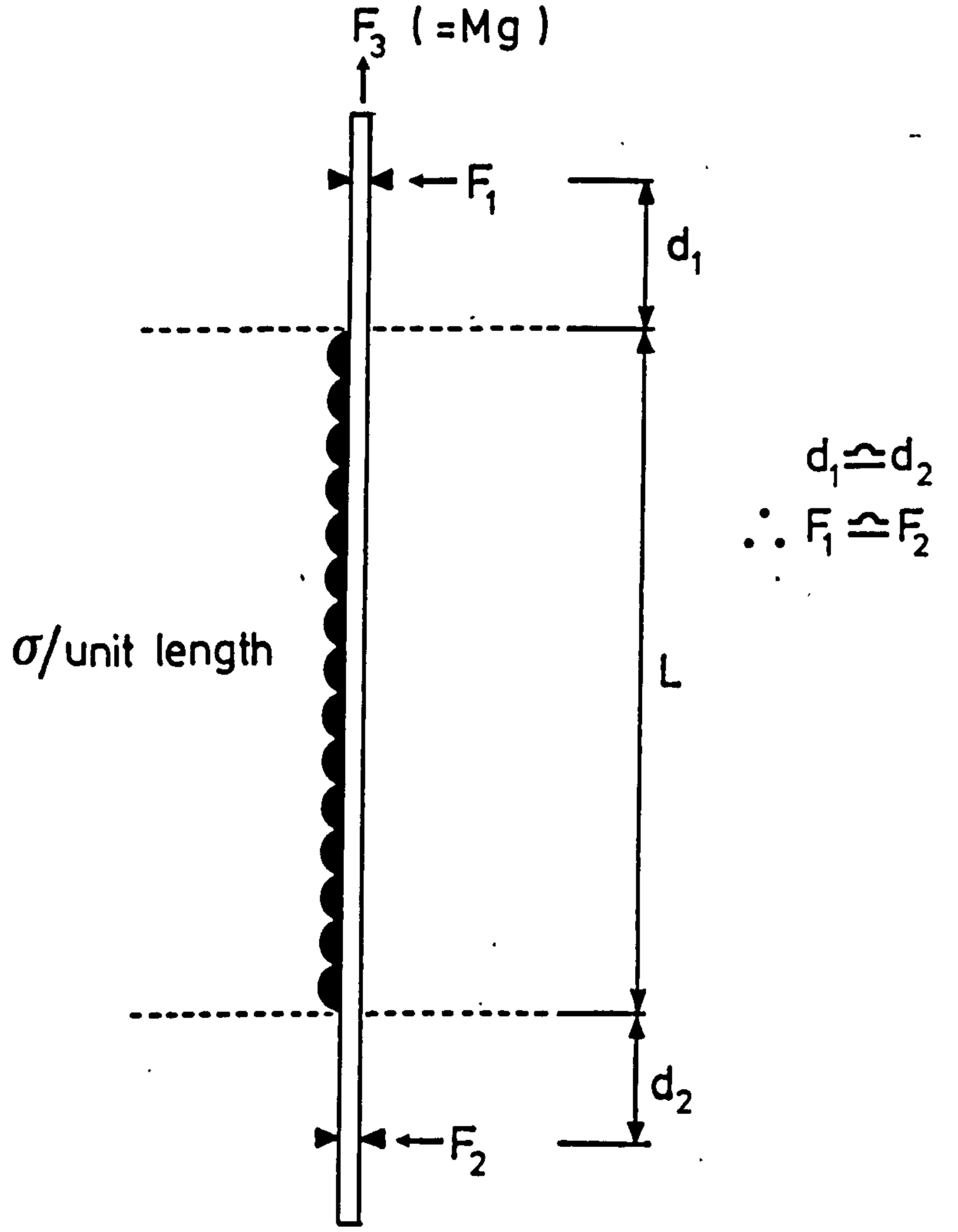

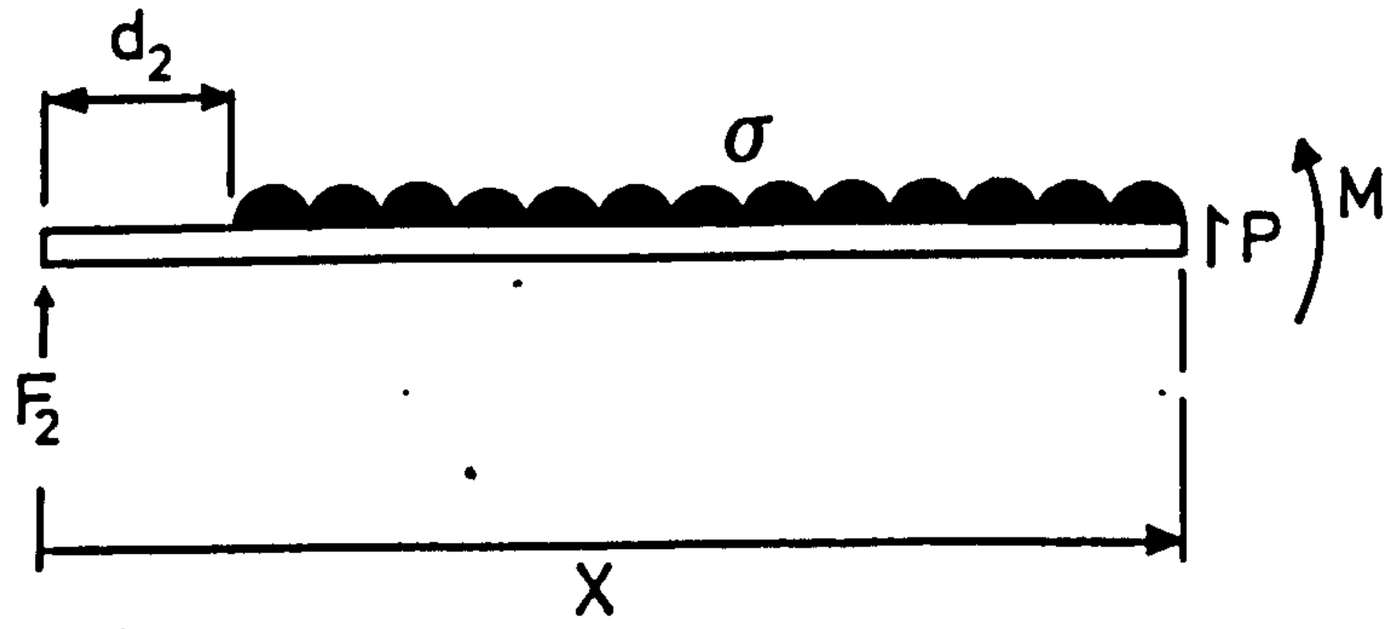

From $X=0$ to $X=d_2$; $M = F_2.X$

$P = -F_2$

From $X=d_2$ to $X=d_2+L$; $M = F_2 - \sigma.(X-d_2)^2/2$

$P = \sigma.(X-d_2) - F_2$

Fig 3.10 Idealised loadings on the wind tunnel model for structural design purposes.

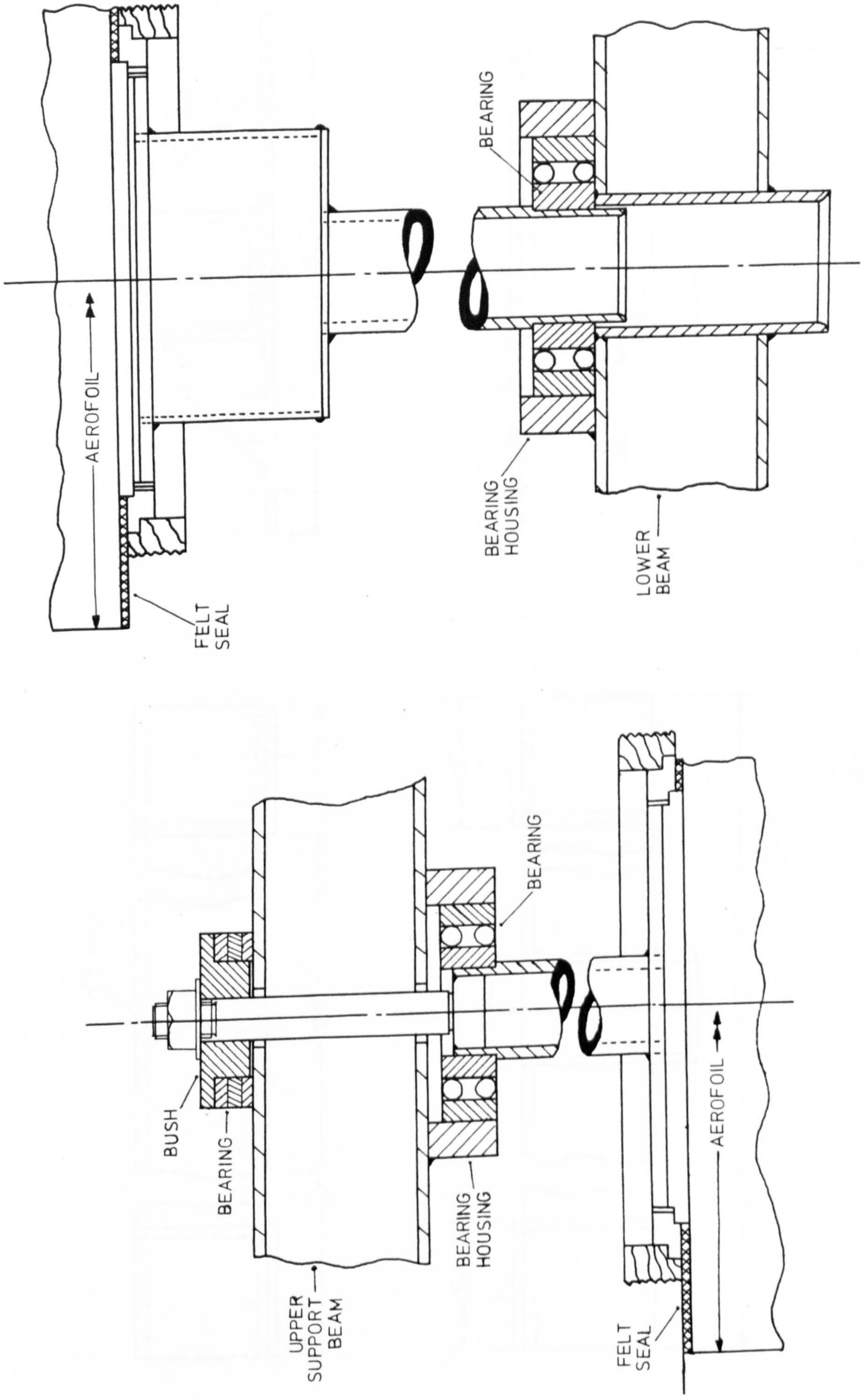

Fig 3.11 Detail of the wind tunnel model supporting structure.

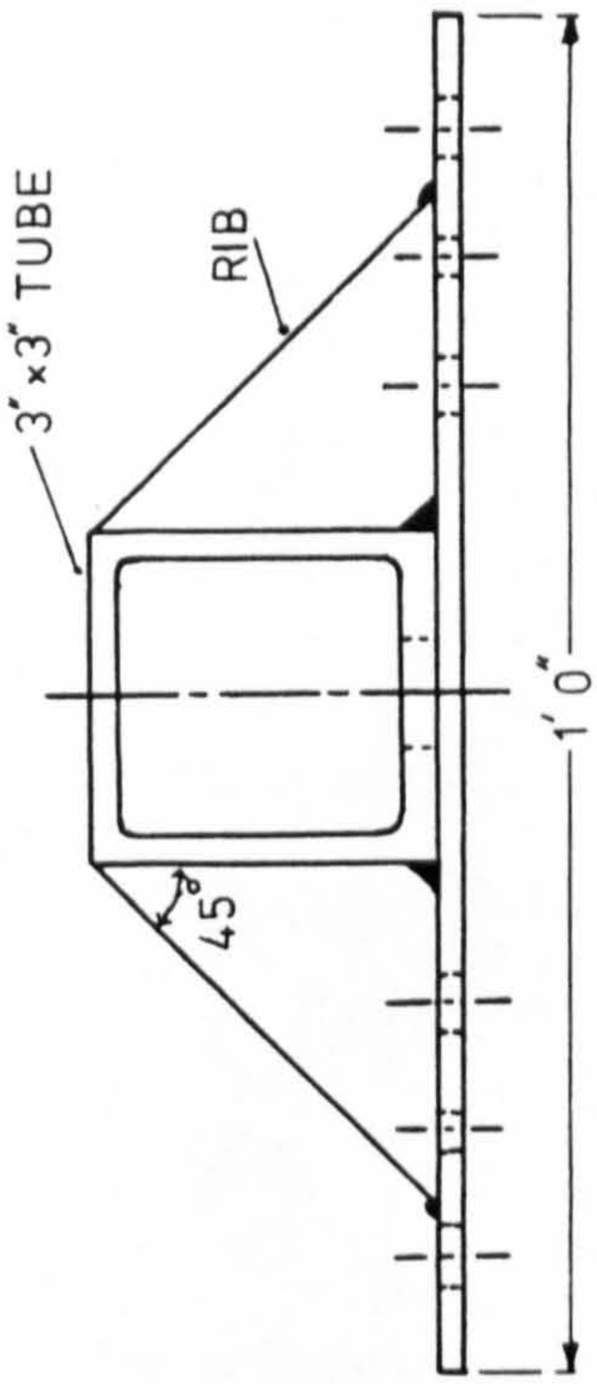

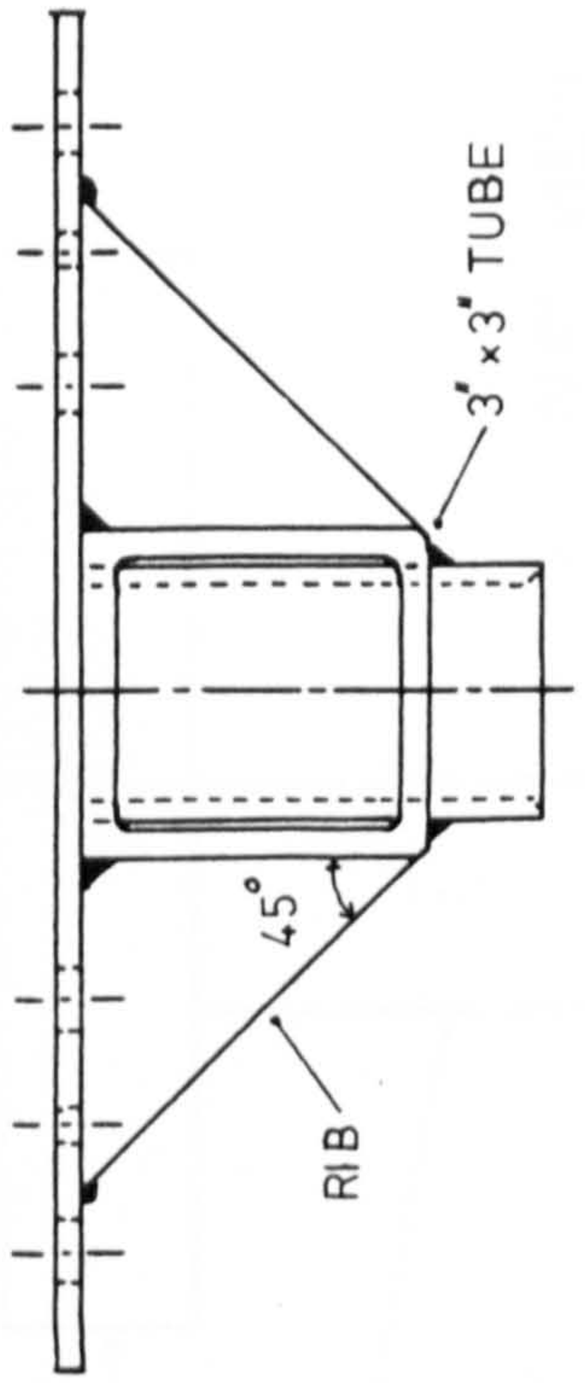

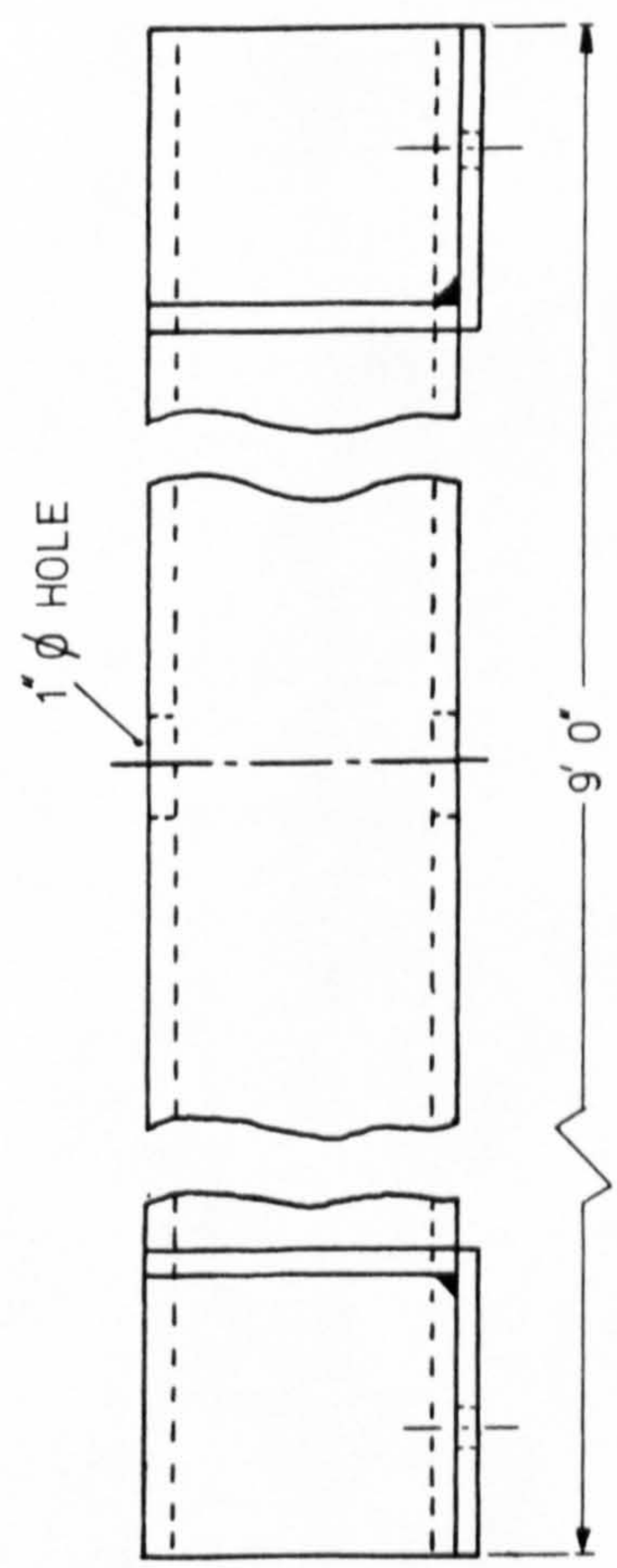

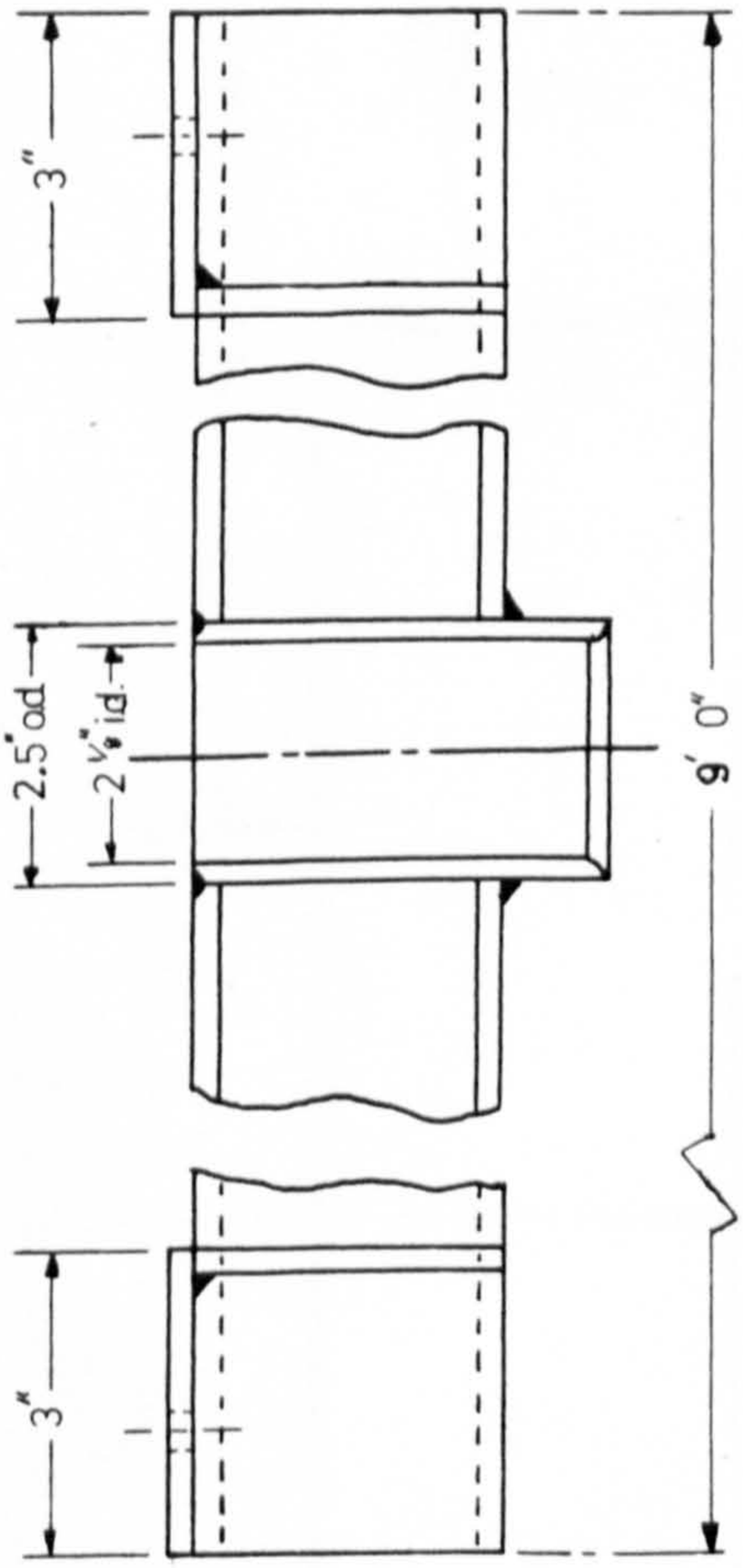

- continued.

Fig 3.11

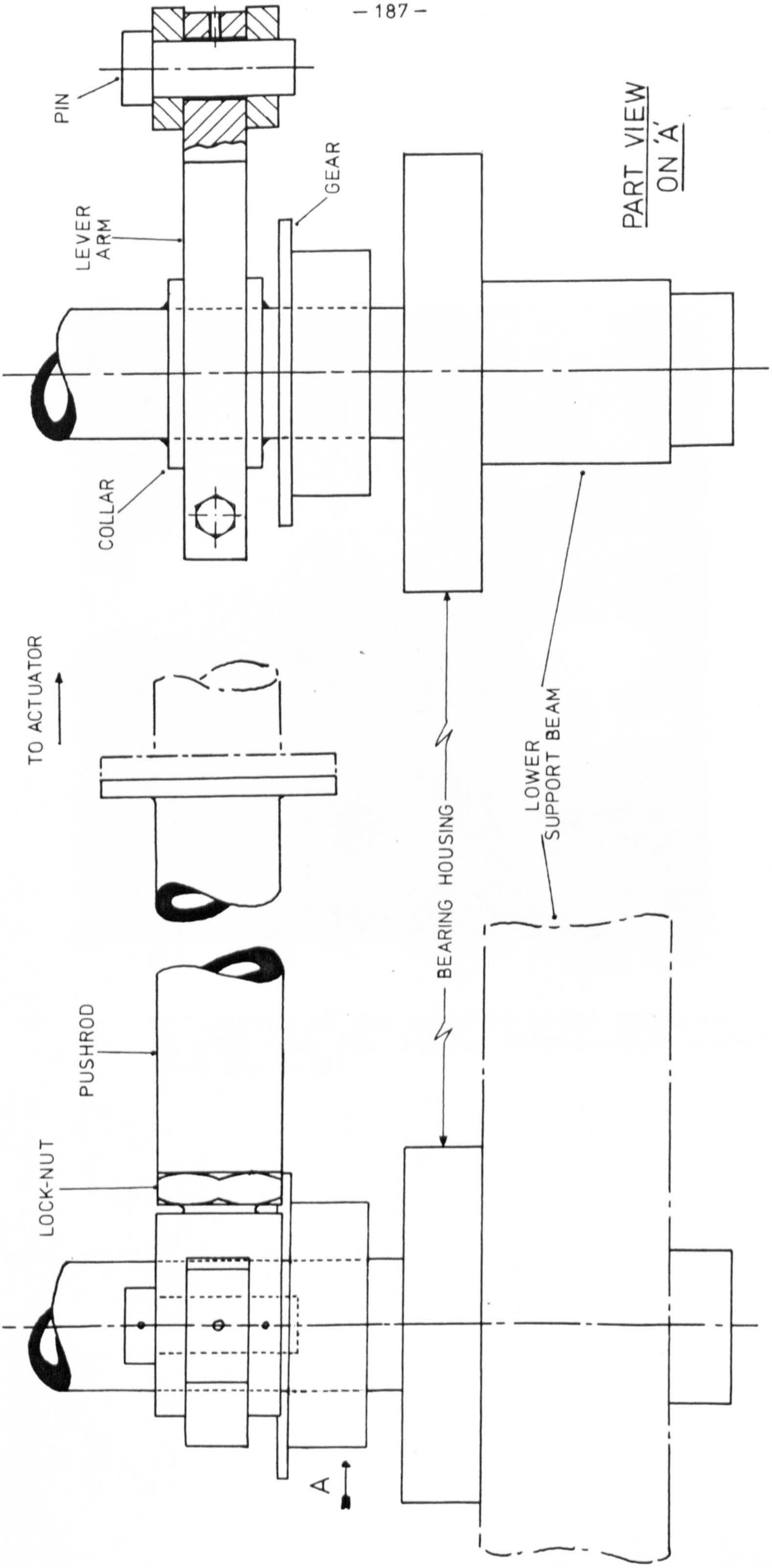

Fig 3.12 Detail of aerofoil pitch drive mechanism.

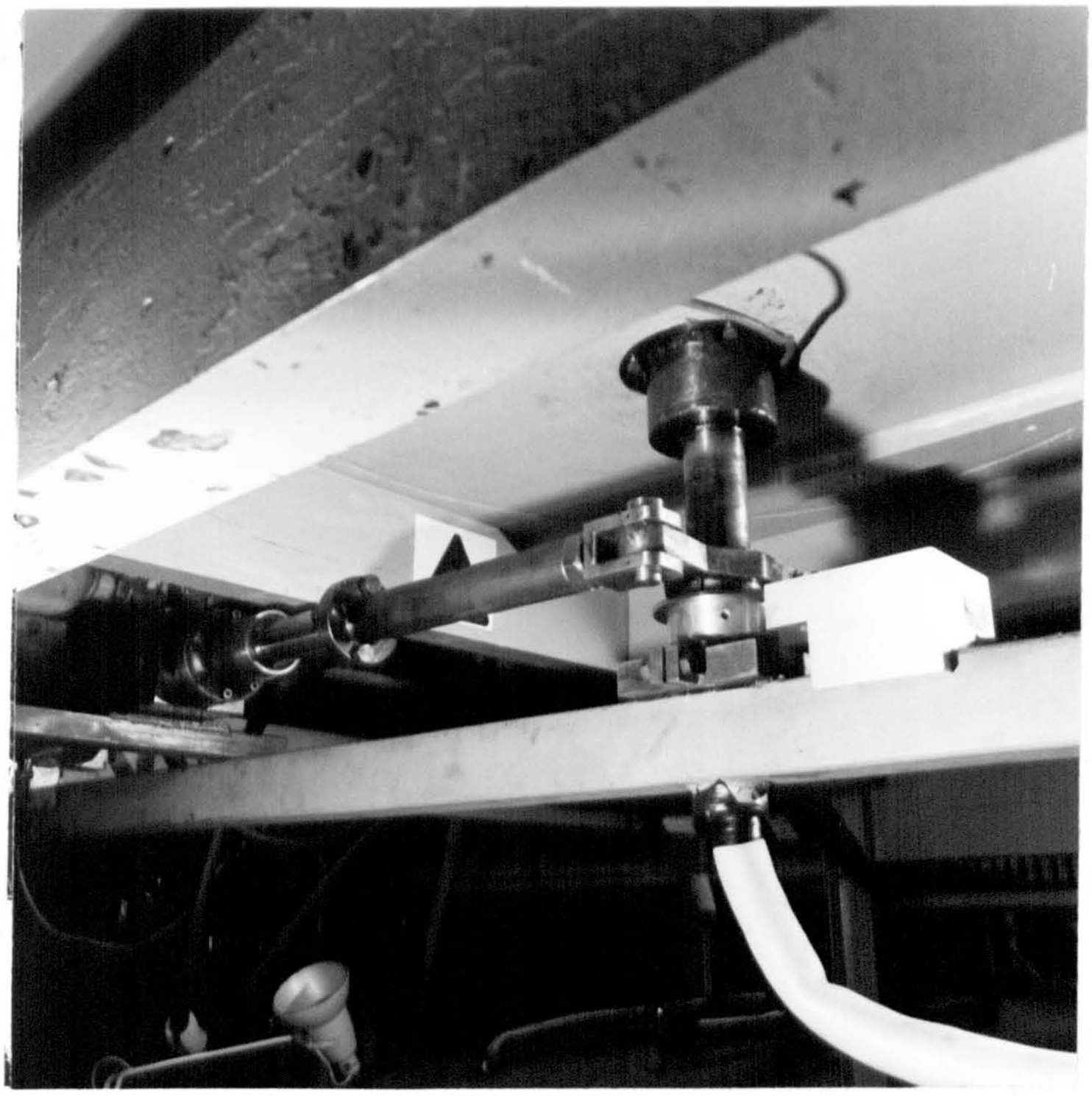

Fig 3.13 Photograph of the aerofoil pitch drive mechanism, showing also the angular displacement transducer. (See Fig 3.28)

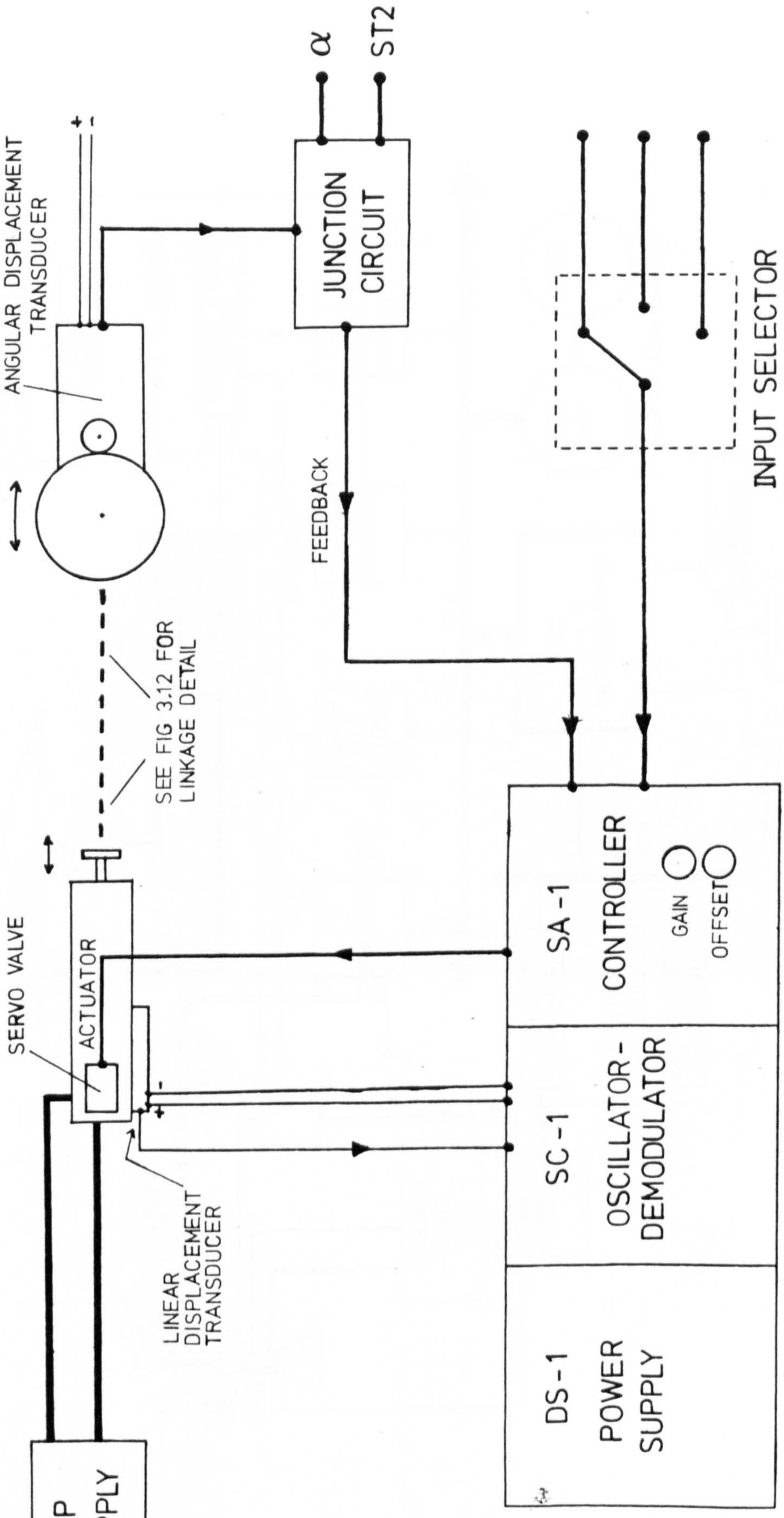

Fig 3.14 Schematic of the Servo Actuator Control System.

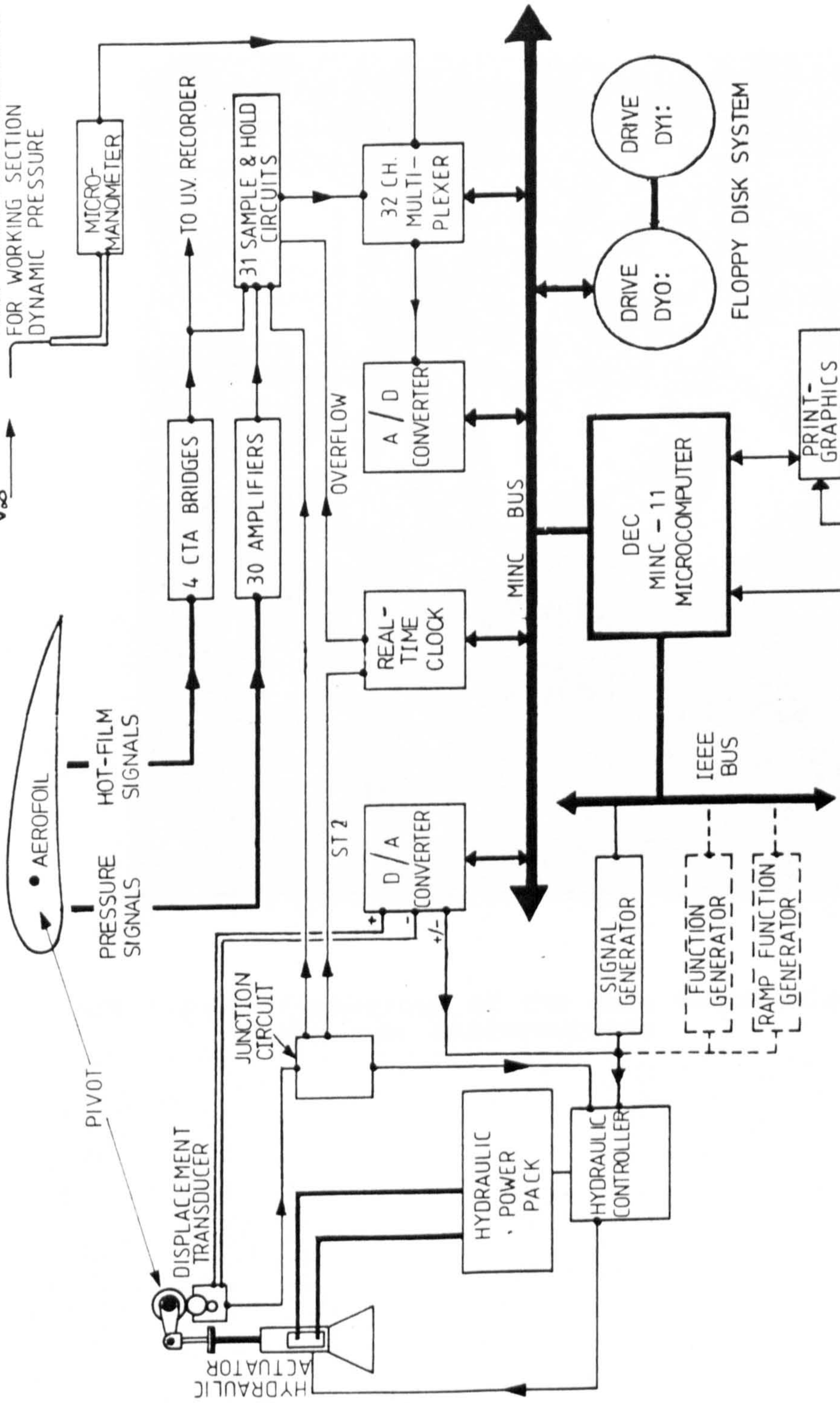

Fig 3.15a. Schematic of the Data Acquisition and Control System.

Fig 3.15b. Photograph of the data acquisition equipment and the MINC microcomputer.

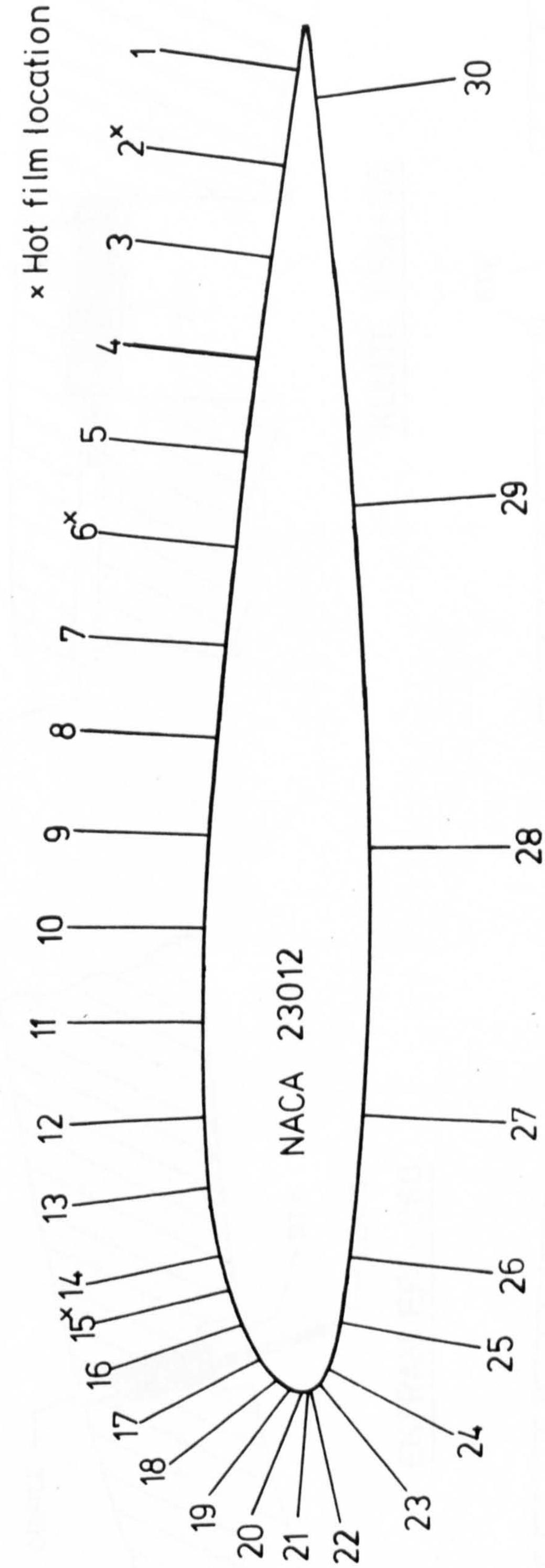

X/C (1)=0.97	(9)=0.41	(17)=0.025 (24)=0.02
X/C (2)=0.90	(10)=0.34	(18)=0.01 (25)=0.05
X/C (3)=0.83	(11)=0.27	(19)=0.005 (26)=0.10
X/C (4)=0.76	(12)=0.20	(20)=0.0005 (27)=0.20
X/C (5)=0.69	(13)=0.15	(21)=0.000 (28)=0.40
X/C (6)=0.62	(14)=0.10	(22)=0.000 (29)=0.65
X/C (7)=0.55	(15)=0.075	(23)=0.01 (30)=0.95
X/C (8)=0.48	(16)=0.05	

Figure 3.16 Location of pressure transducers and hot film gauges.

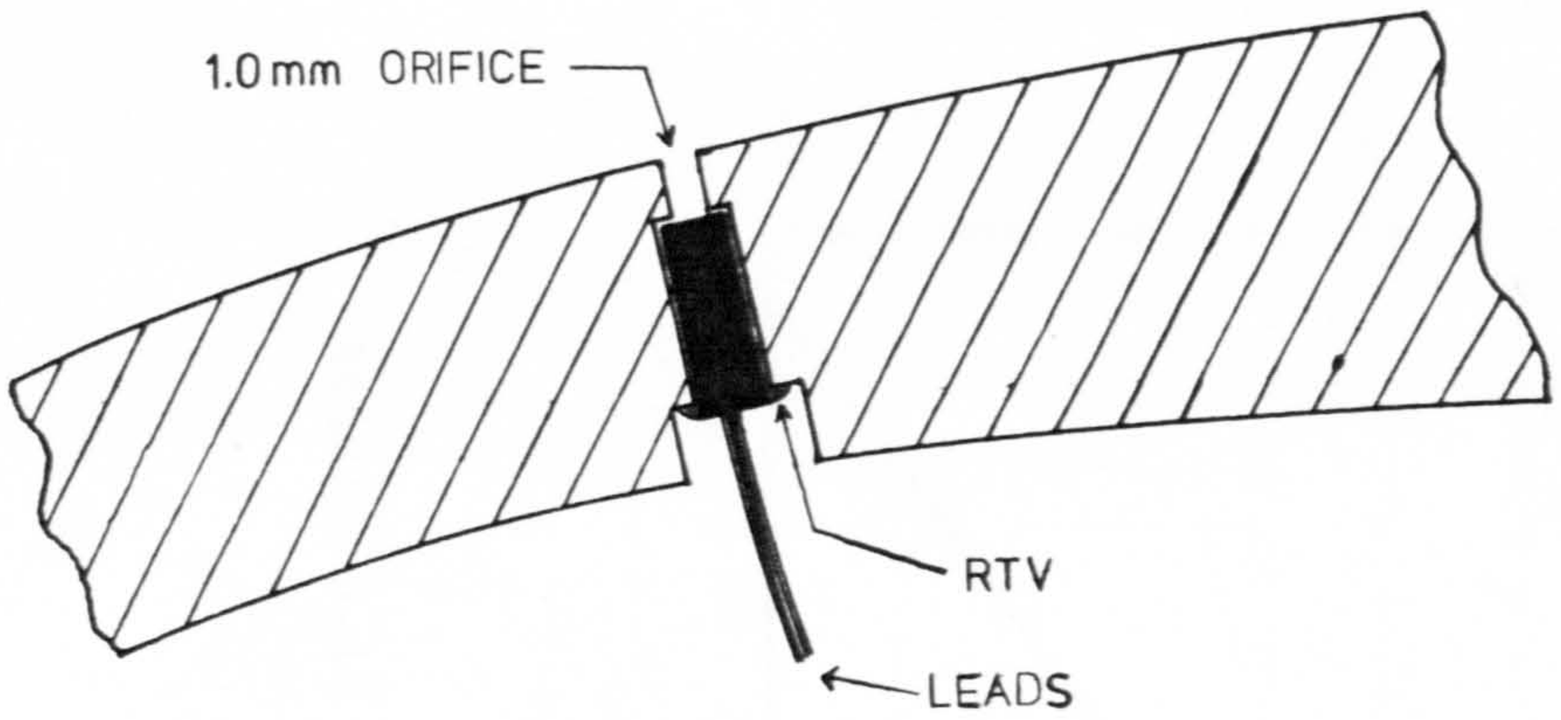

ENTRAN EPI-080

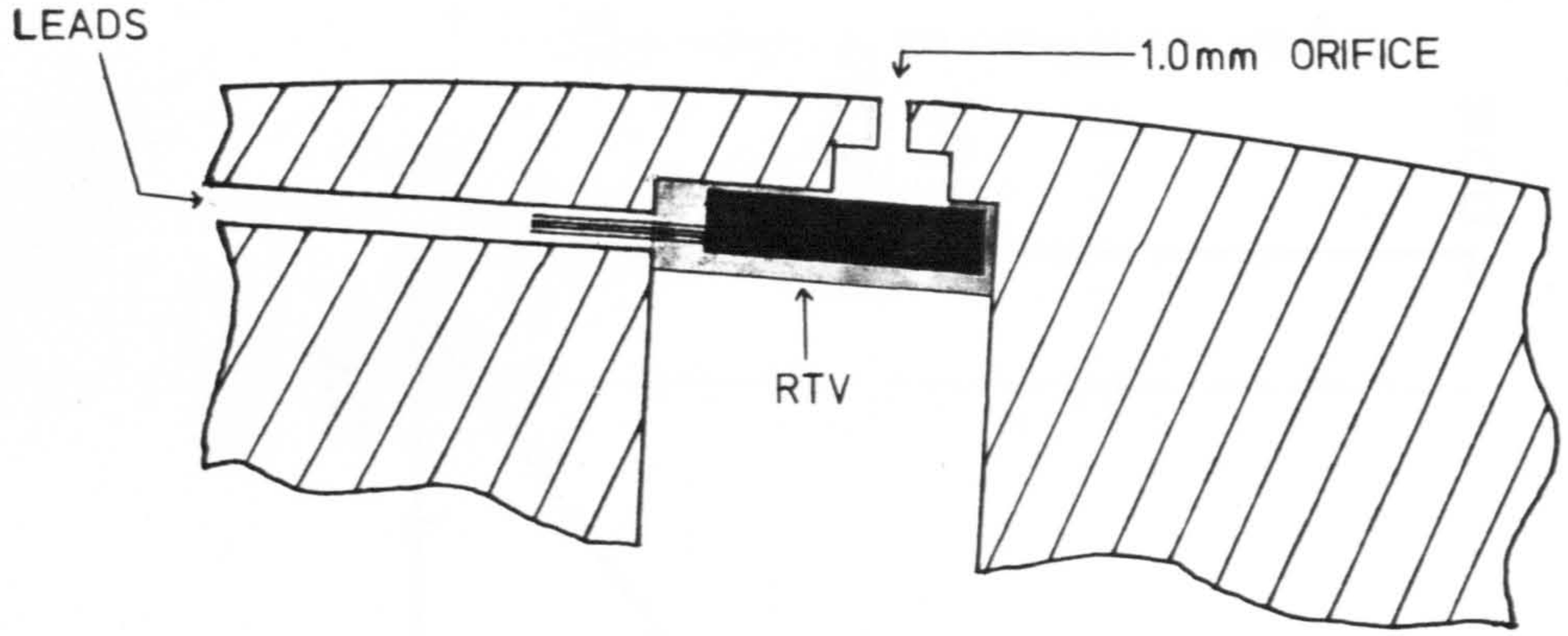

KULITE LSQ-56

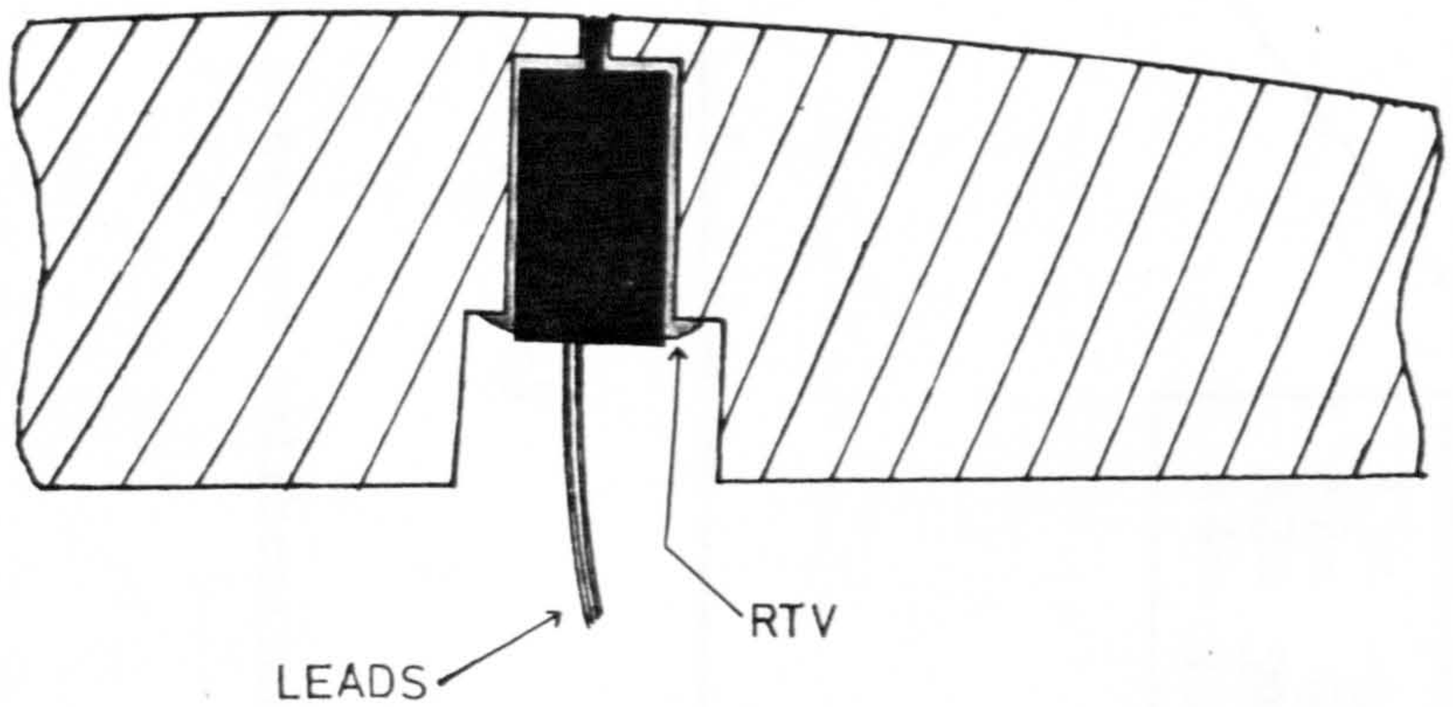

KULITE LSQ-57 (upper surface)

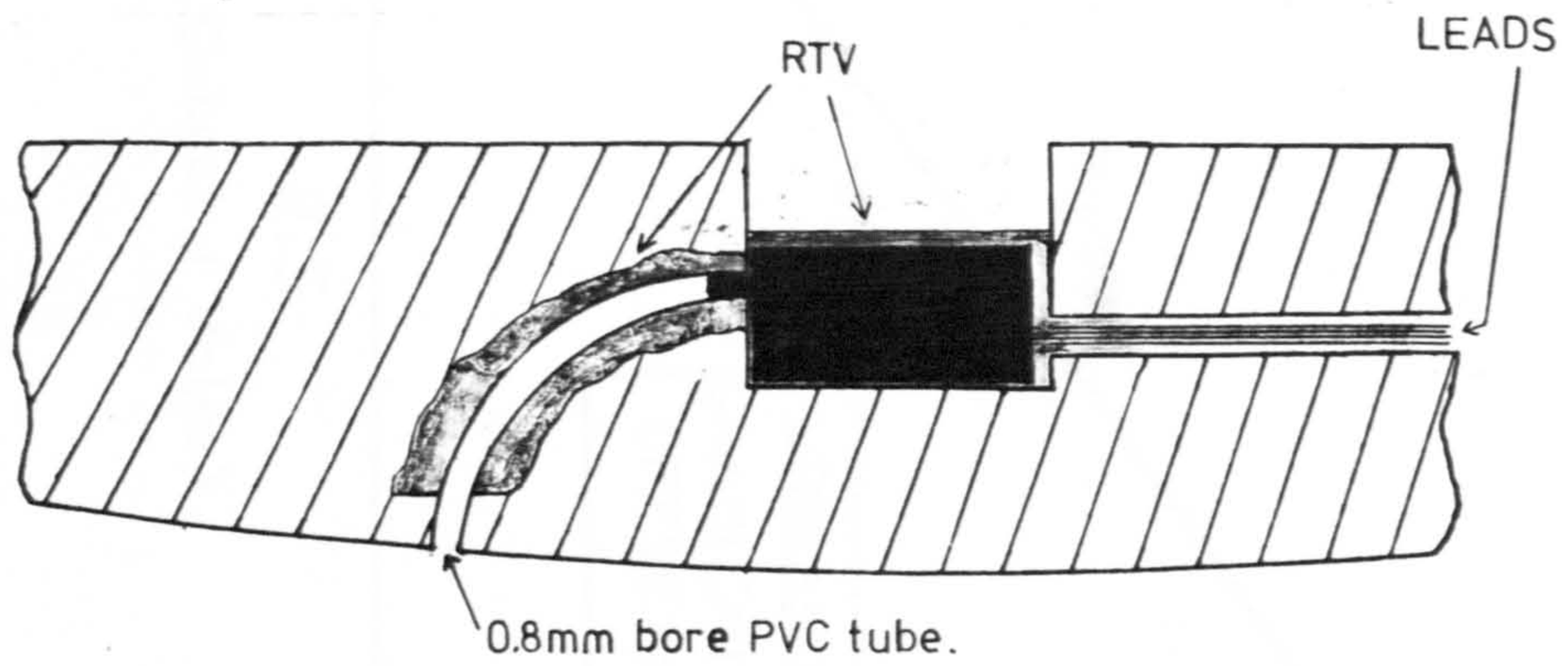

KULITE LSQ-57 (lower surface)

Fig 3.17 Examples of the methods of pressure transducer installation in the aerofoil model.

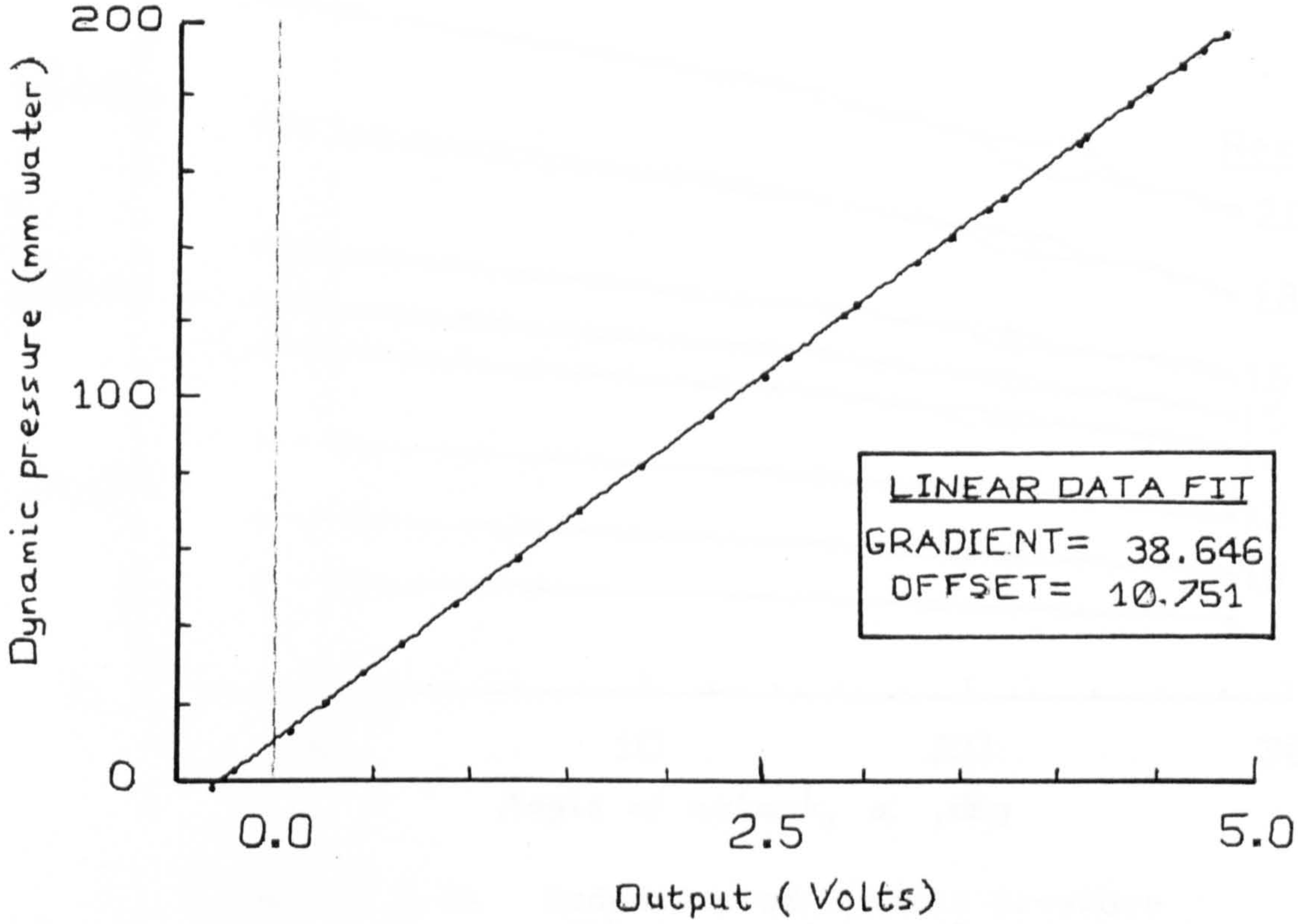

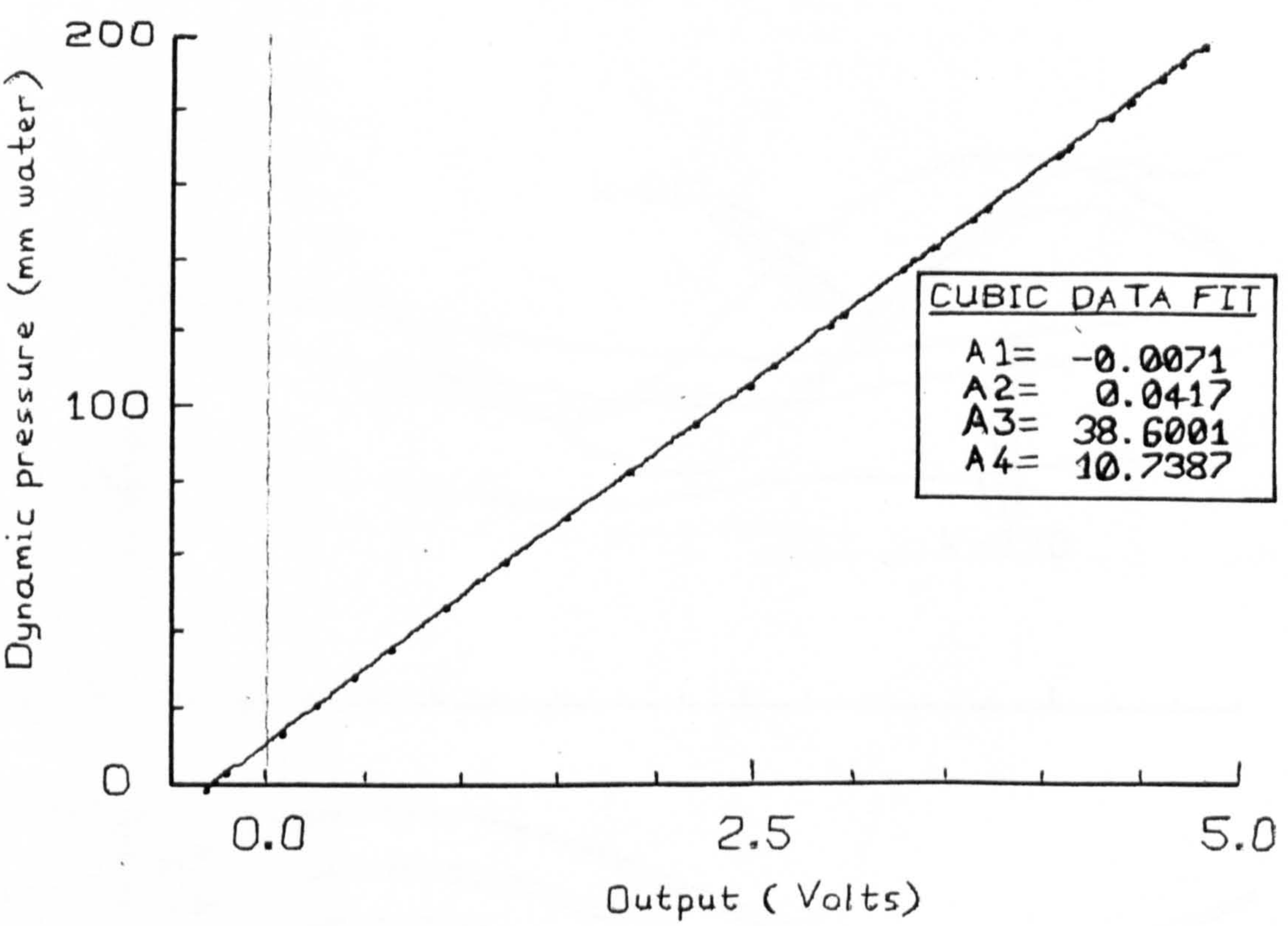

Figure 3.18 Dynamic pressure calibration.

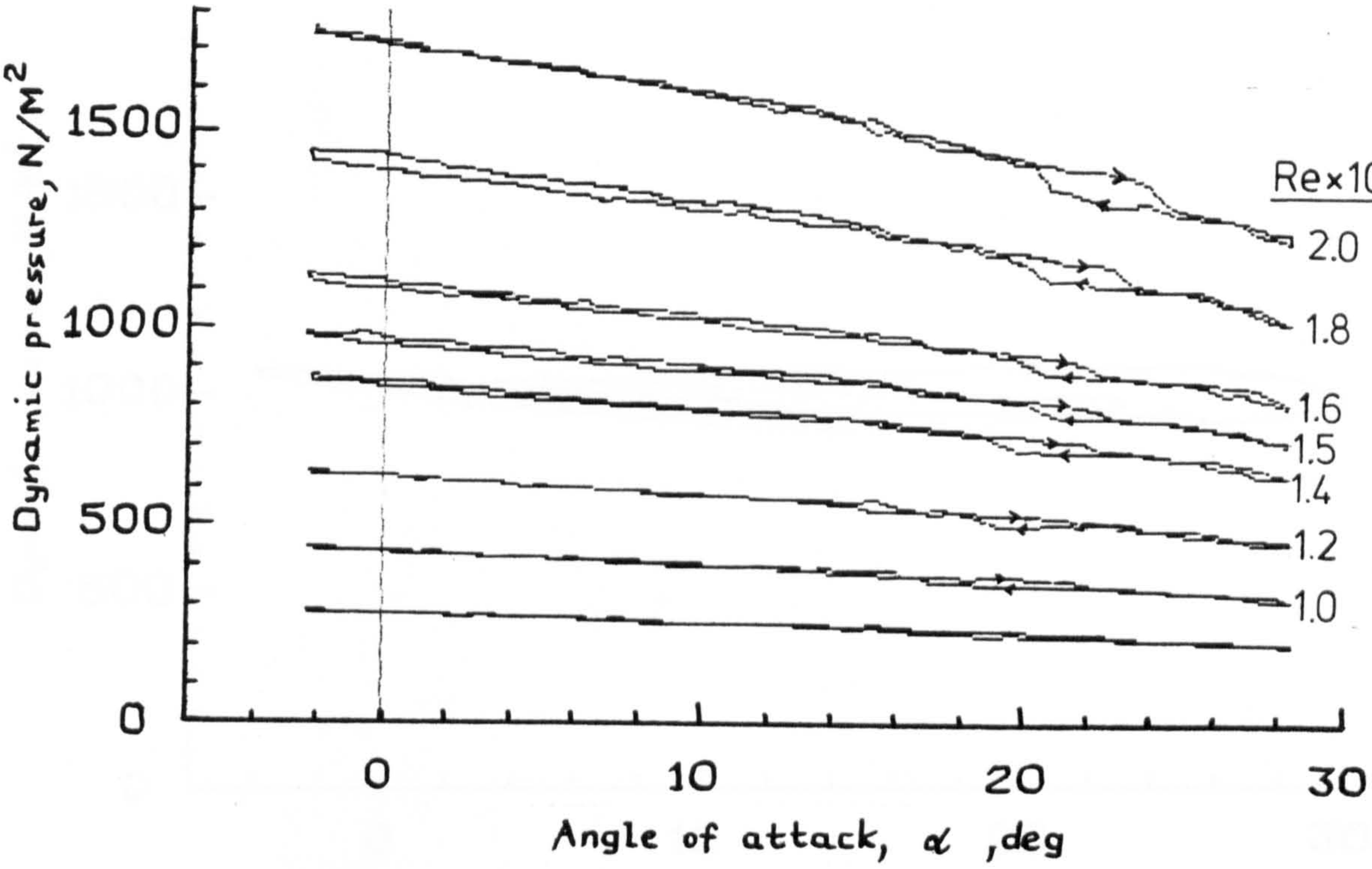

Figure 3.19 Reduction of dynamic pressure with increasing angle of attack.

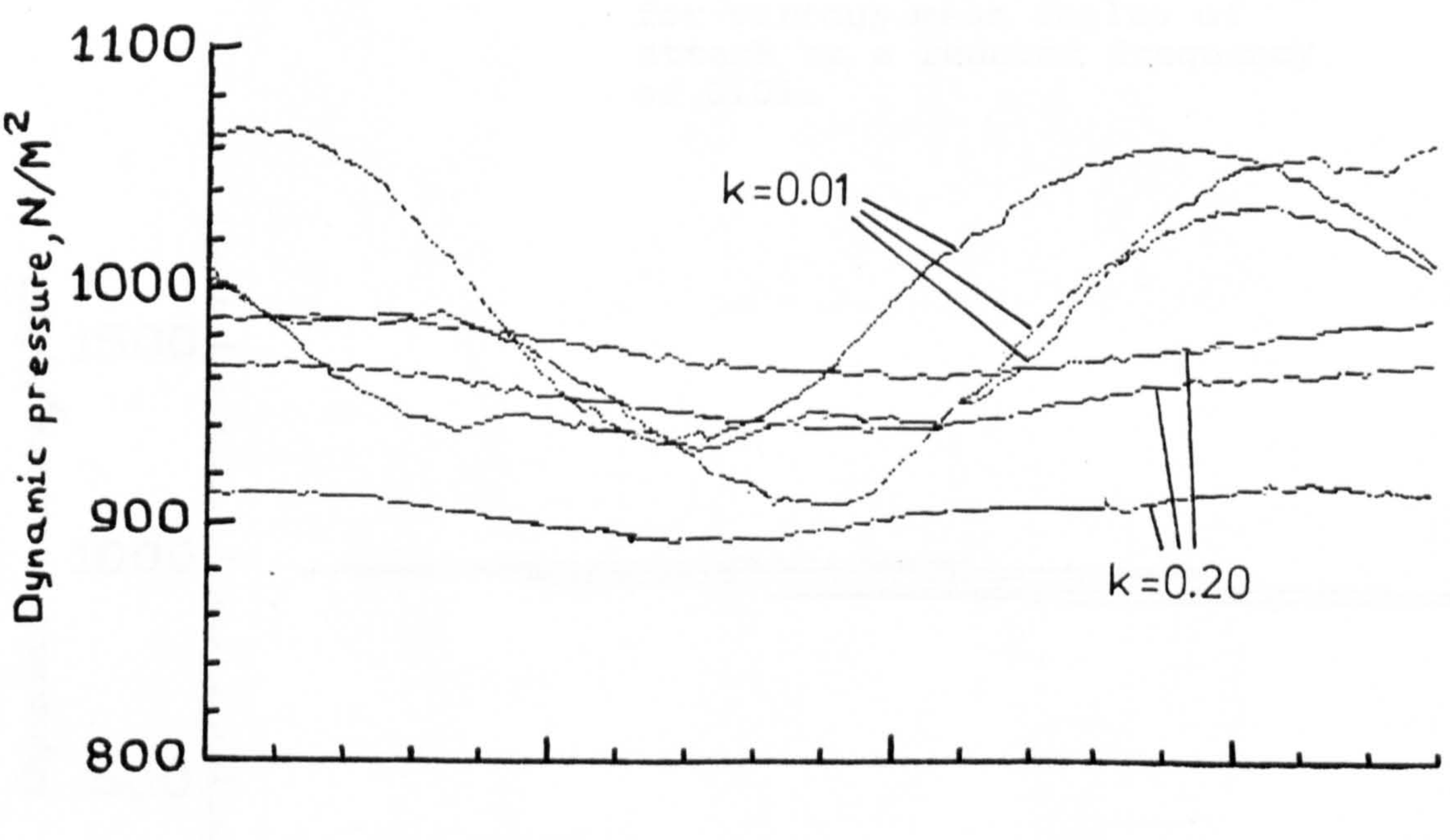

Figure 3.20 Variation of dynamic pressure during oscillatory tests.

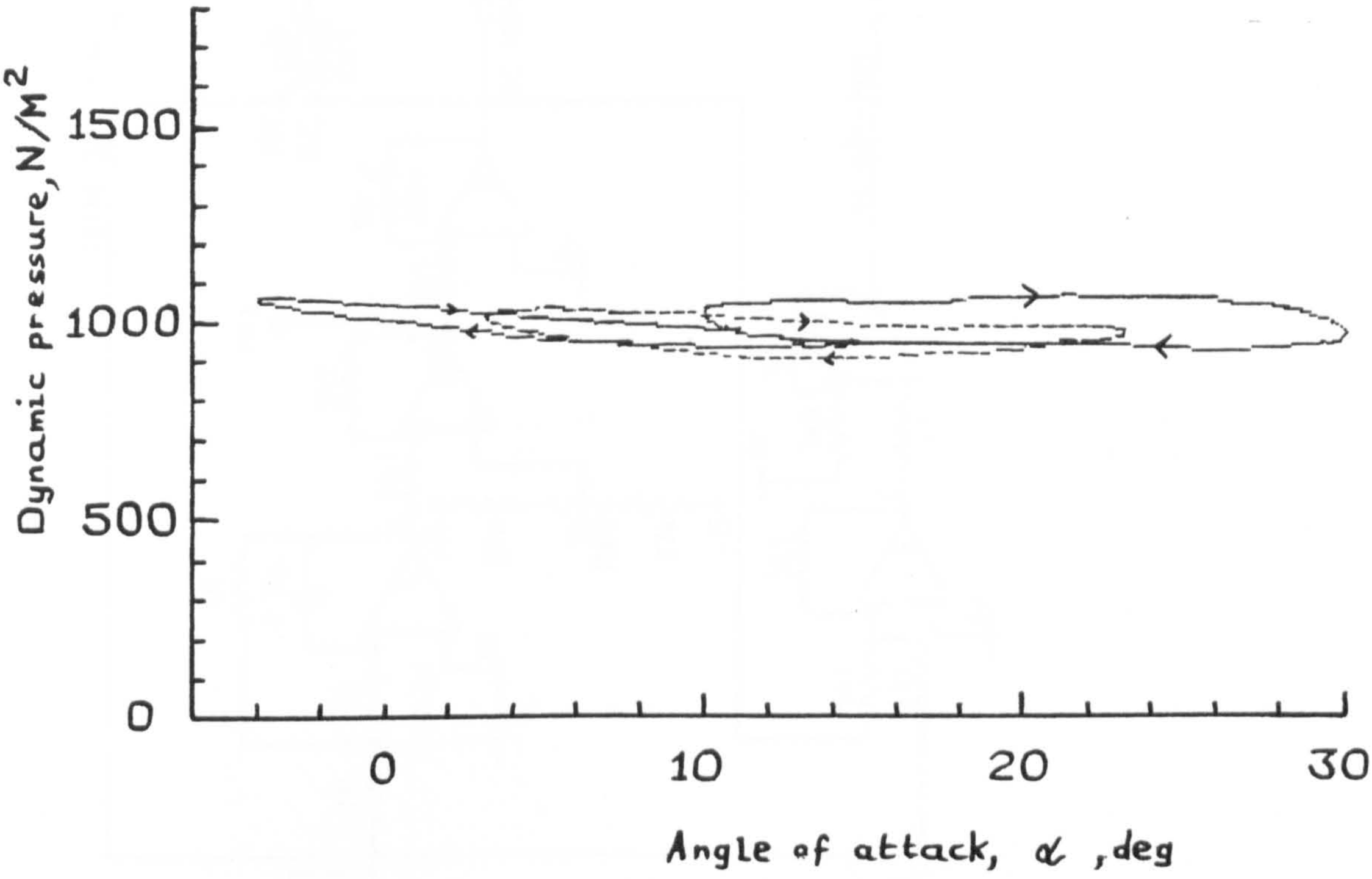

Figure 3.21 Variation of dynamic pressure for various mean angles of attack at a reduced frequency of 0.01.

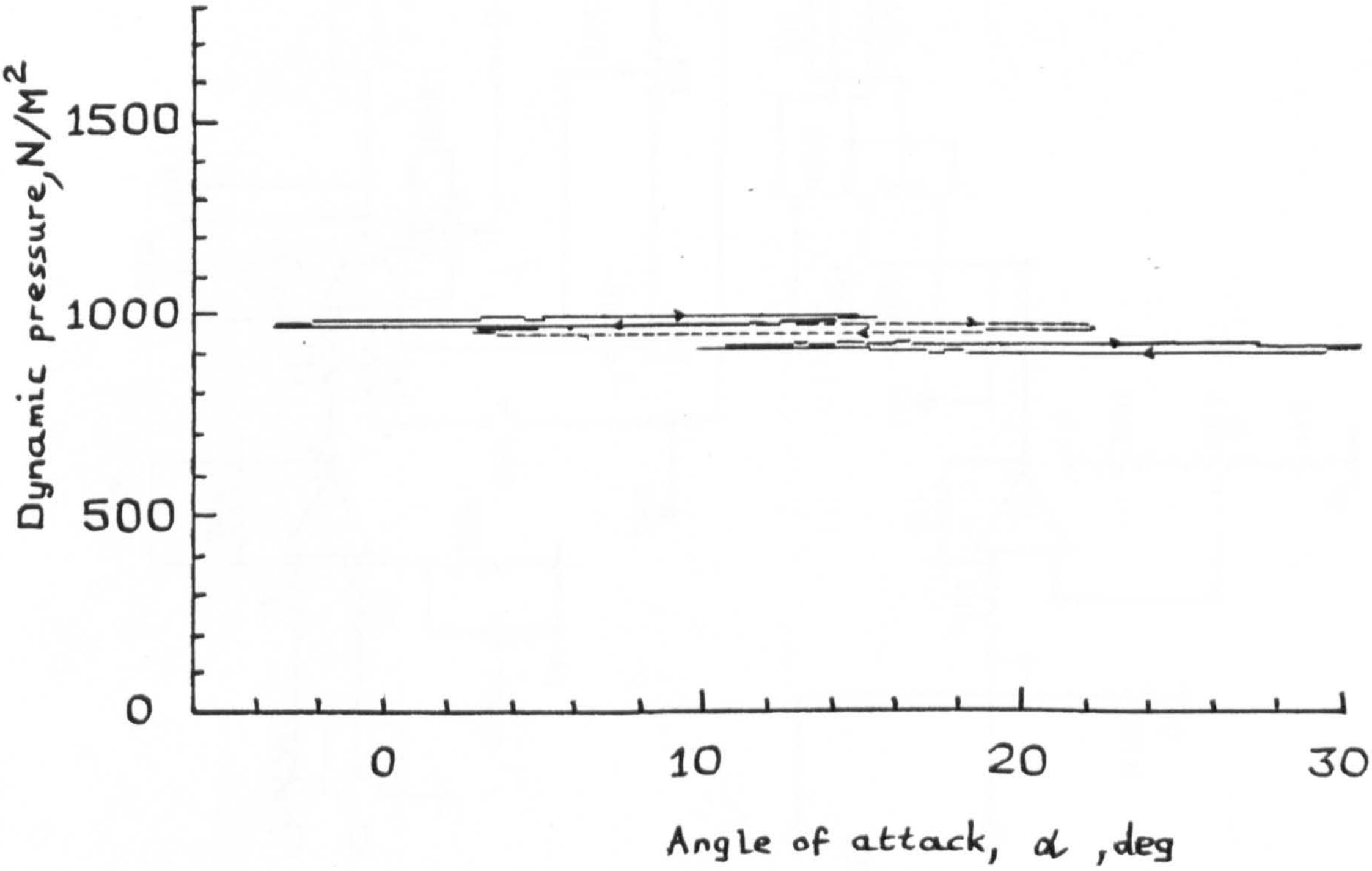

Figure 3.22 Variation of dynamic pressure for various mean angles of attack at a reduced frequency of 0.20.

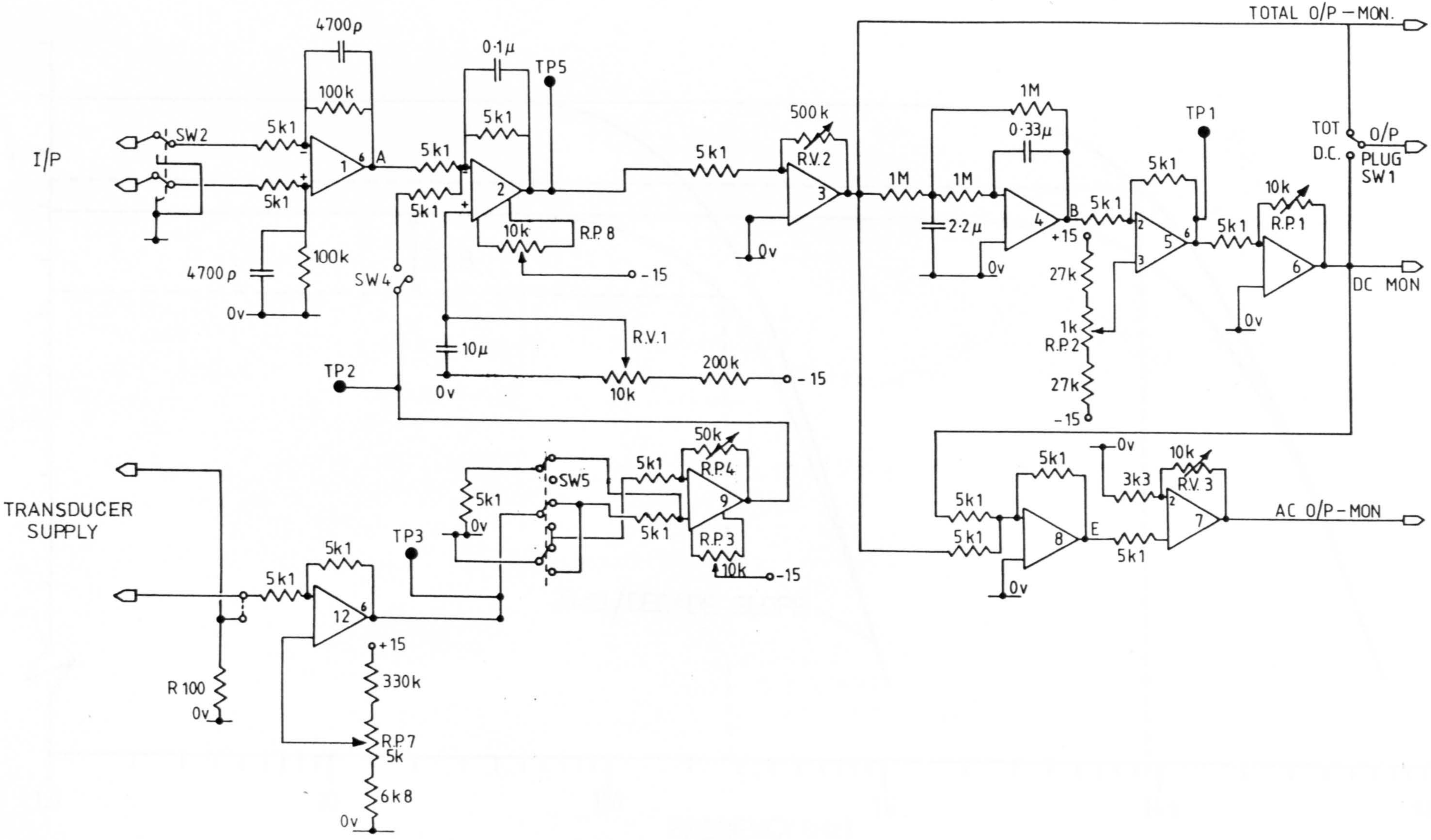

Figure 3.23 Circuit diagram for pressure transducer signal conditioner.

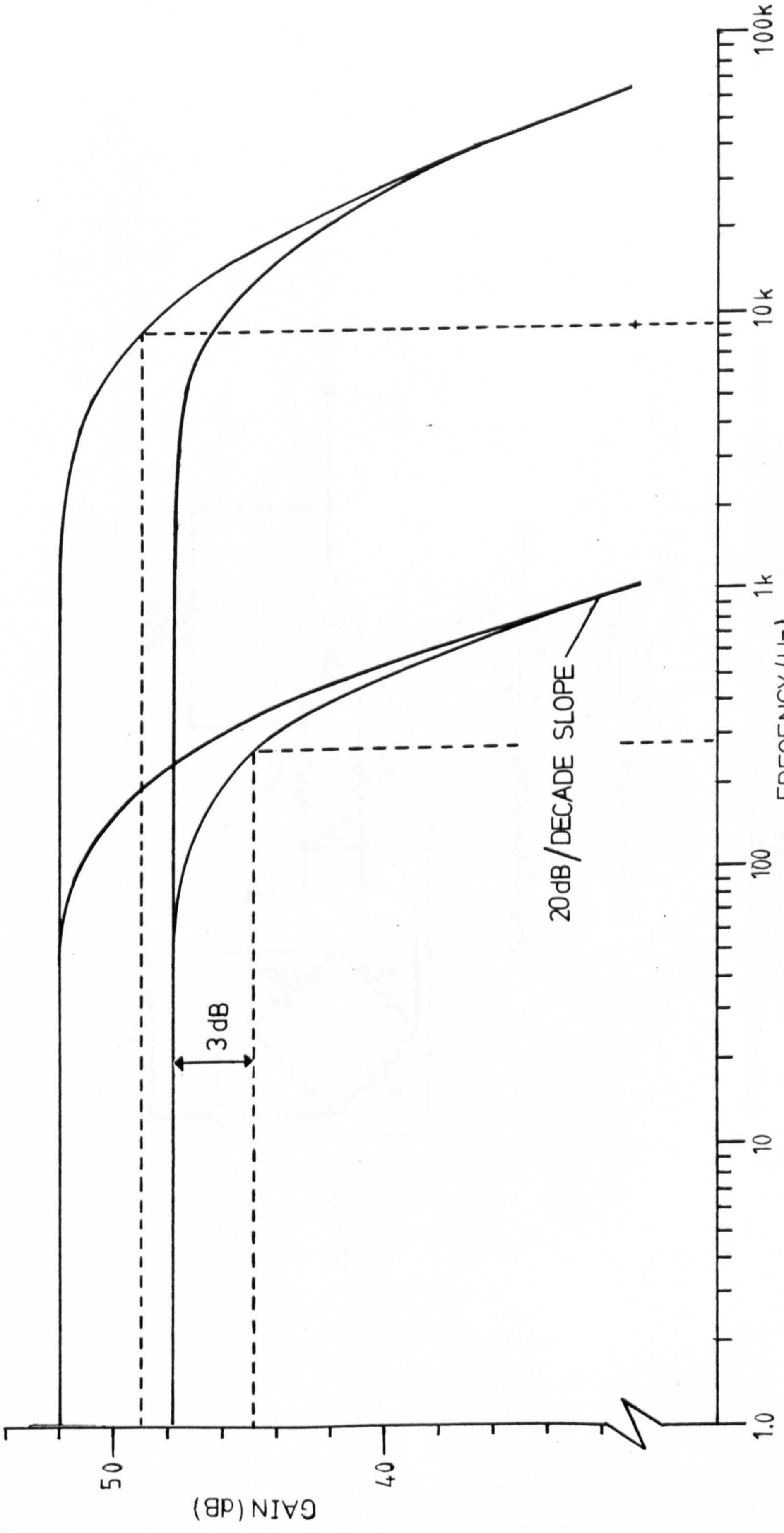

Figure 3.24 Signal conditioner frequency response.

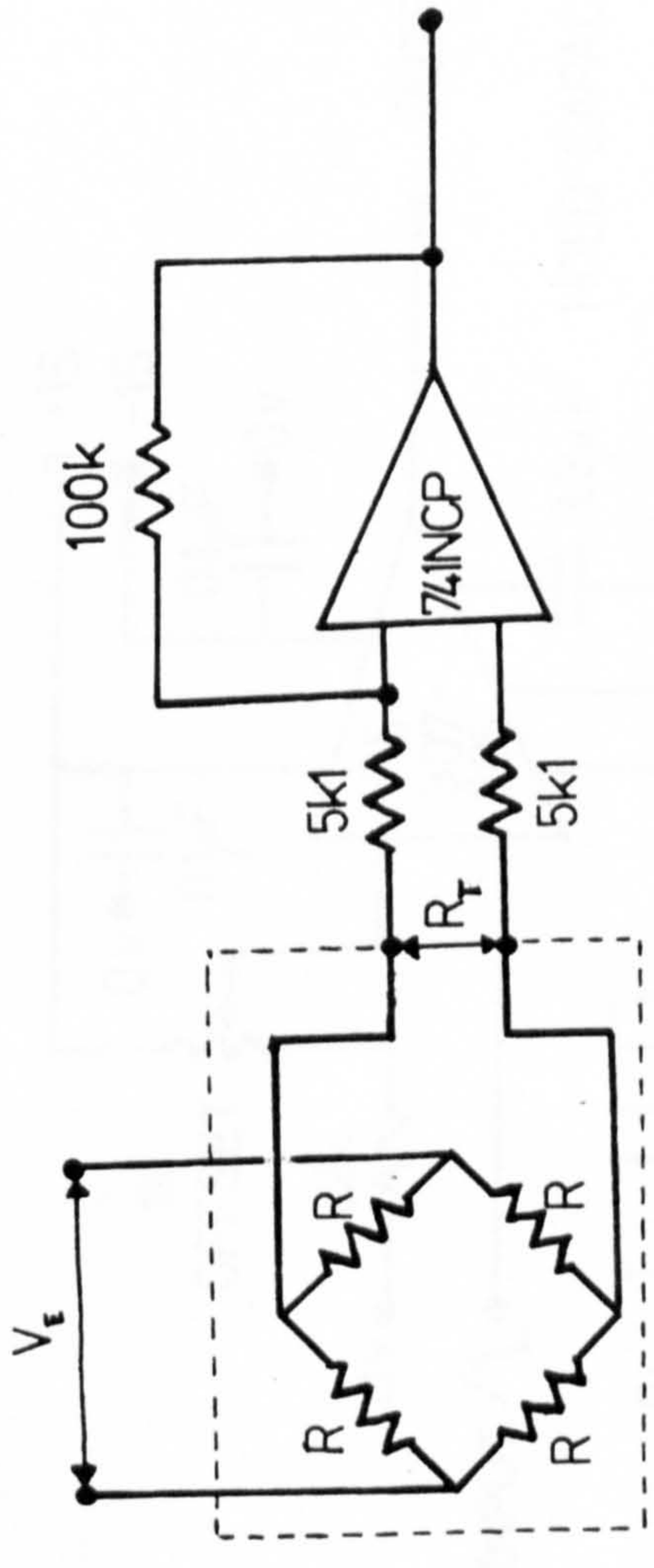

$$\text{GAIN(open-circuit)} = -\frac{100\times10^3}{10.2\times10^3} = 9.8$$

$$\text{GAIN(in-circuit)} = -\frac{100\times10^3}{10.2\times10^3 + R_T}$$

$R_T \ll R$

Figure 3.25 Correction of signal conditioner gain when pressure transducer is "in-circuit".

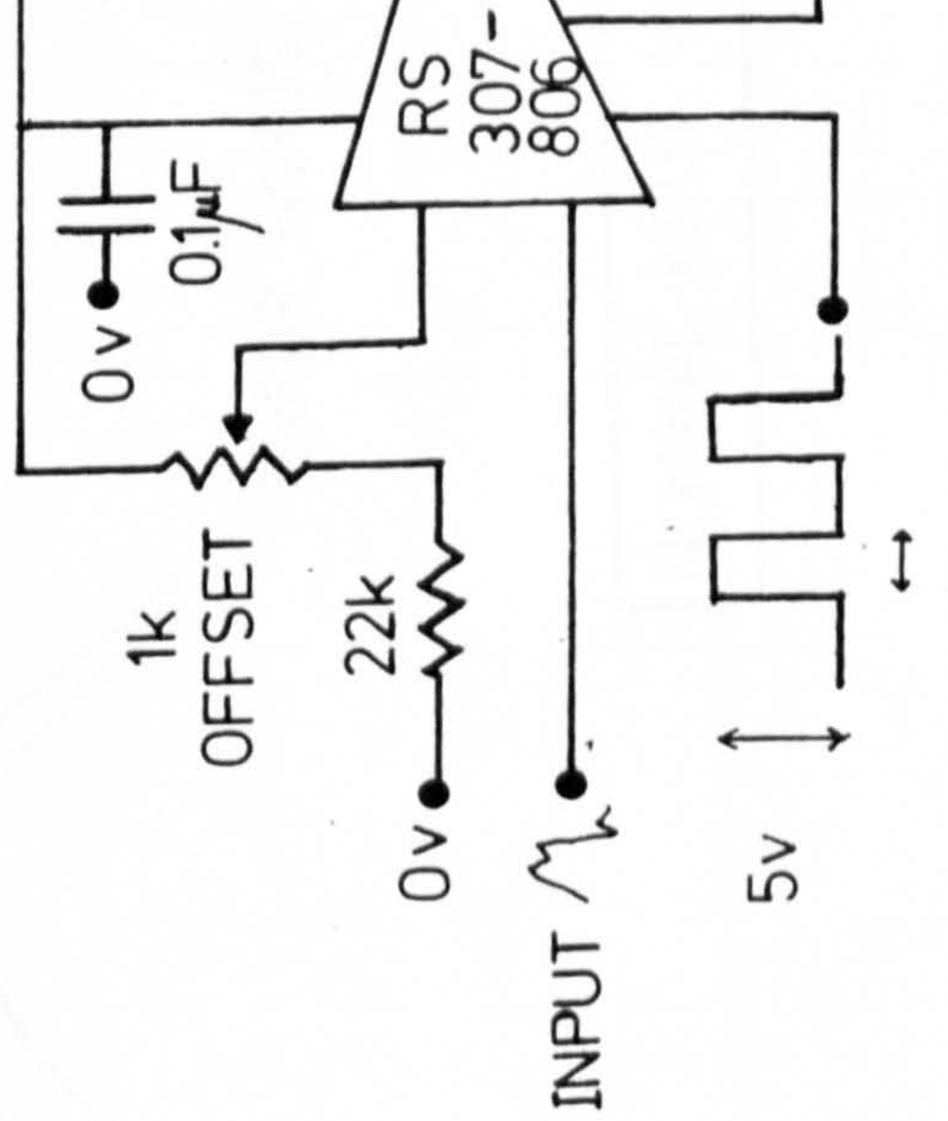

Figure 3.26 Circuit diagram of sample-and-hold.

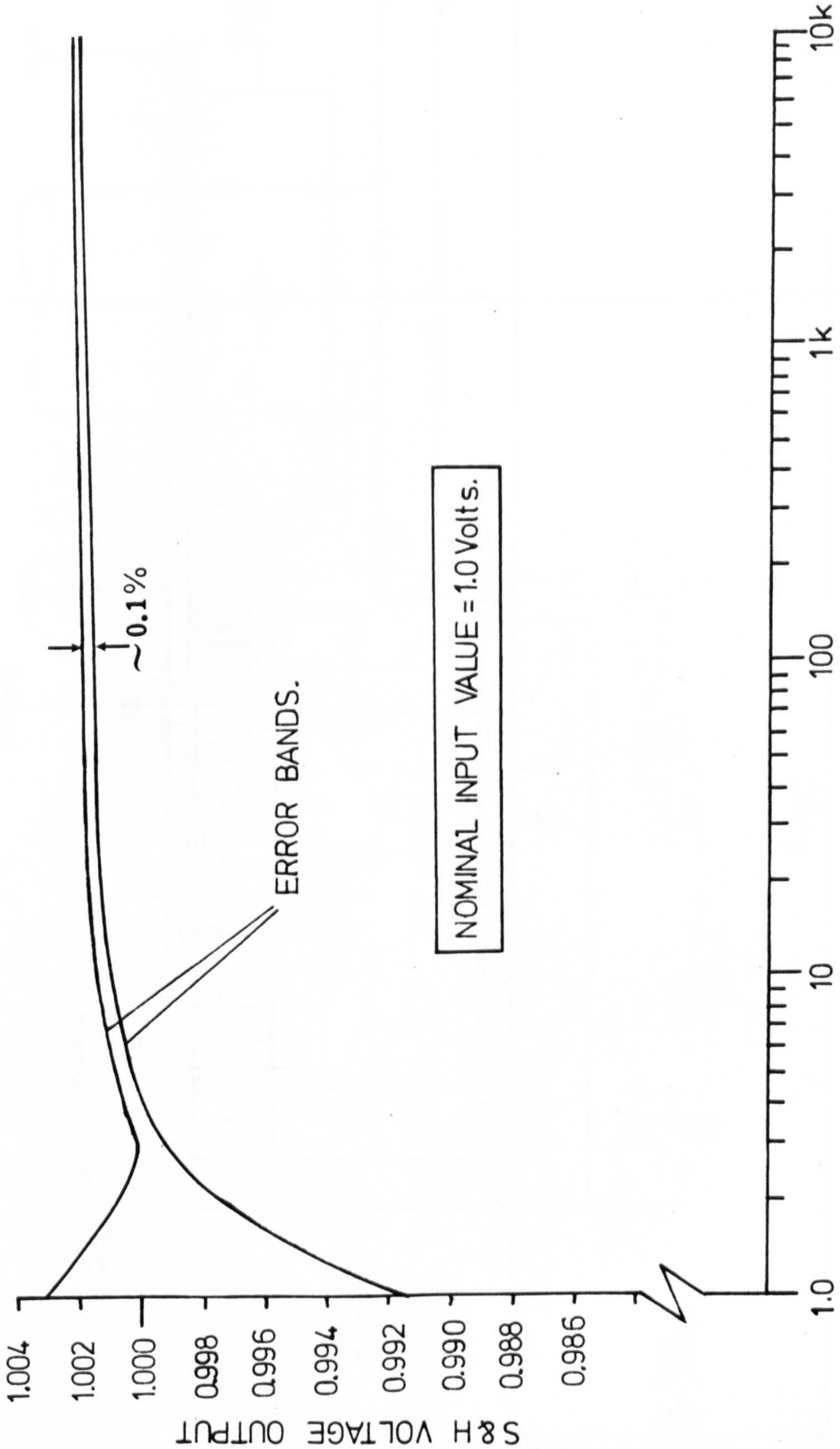

Figure 3.27 Frequency response of sample-and-hold.

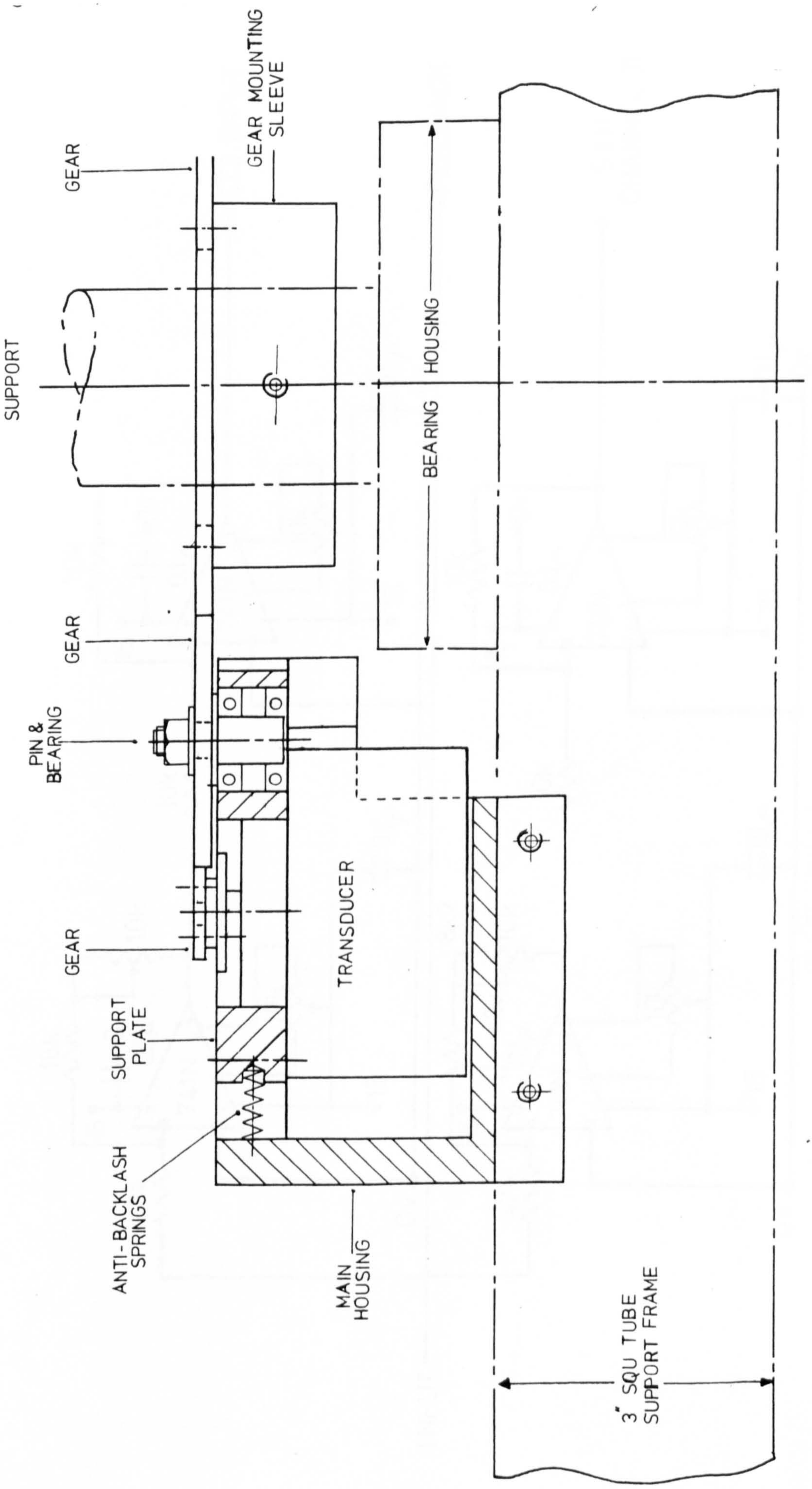

Fig 3.28 Cross-section of the angular displacement assembly. (See also Fig 3.12).

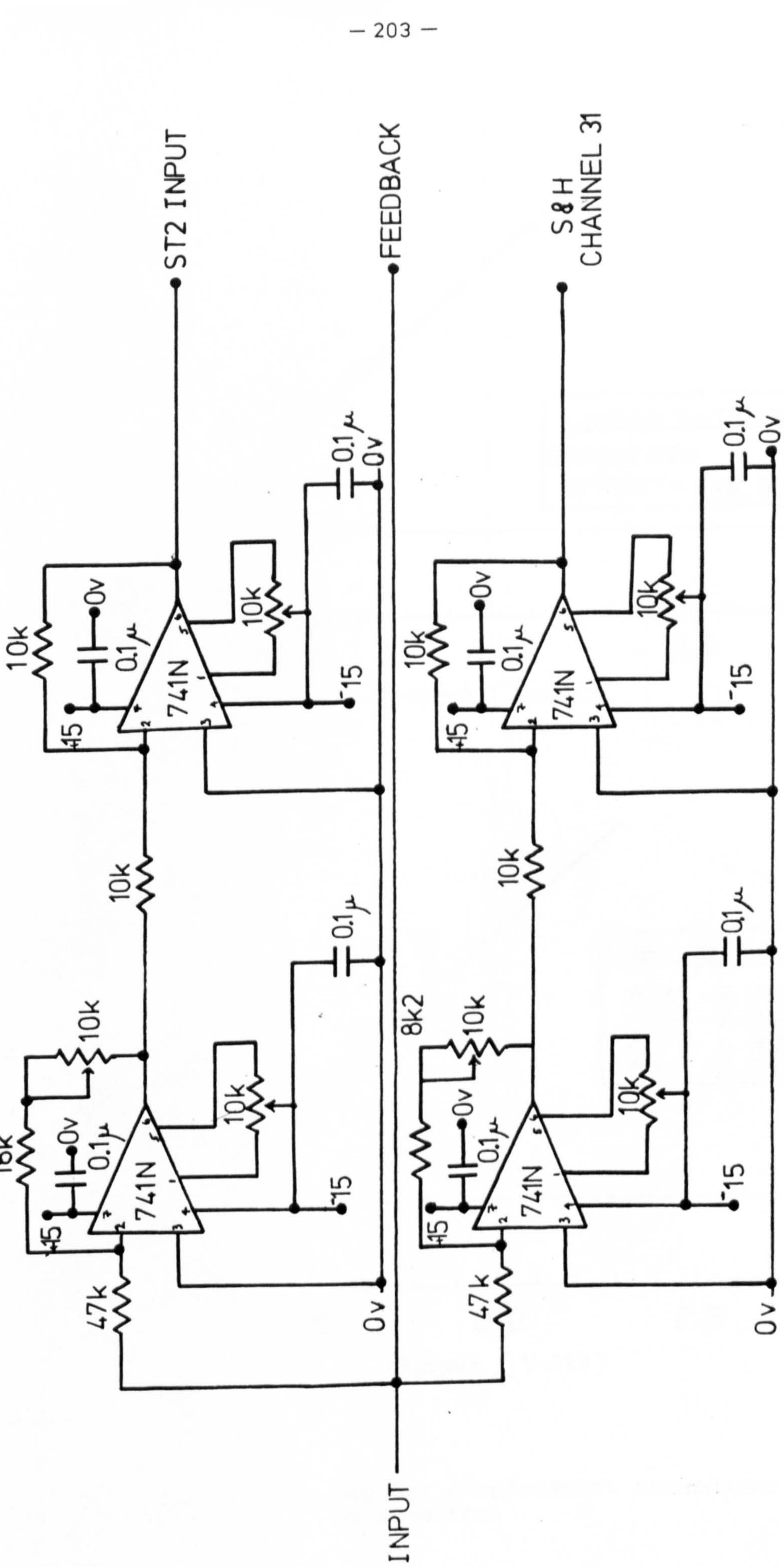

Figure 3.29 Angular displacement transducer junction circuit.

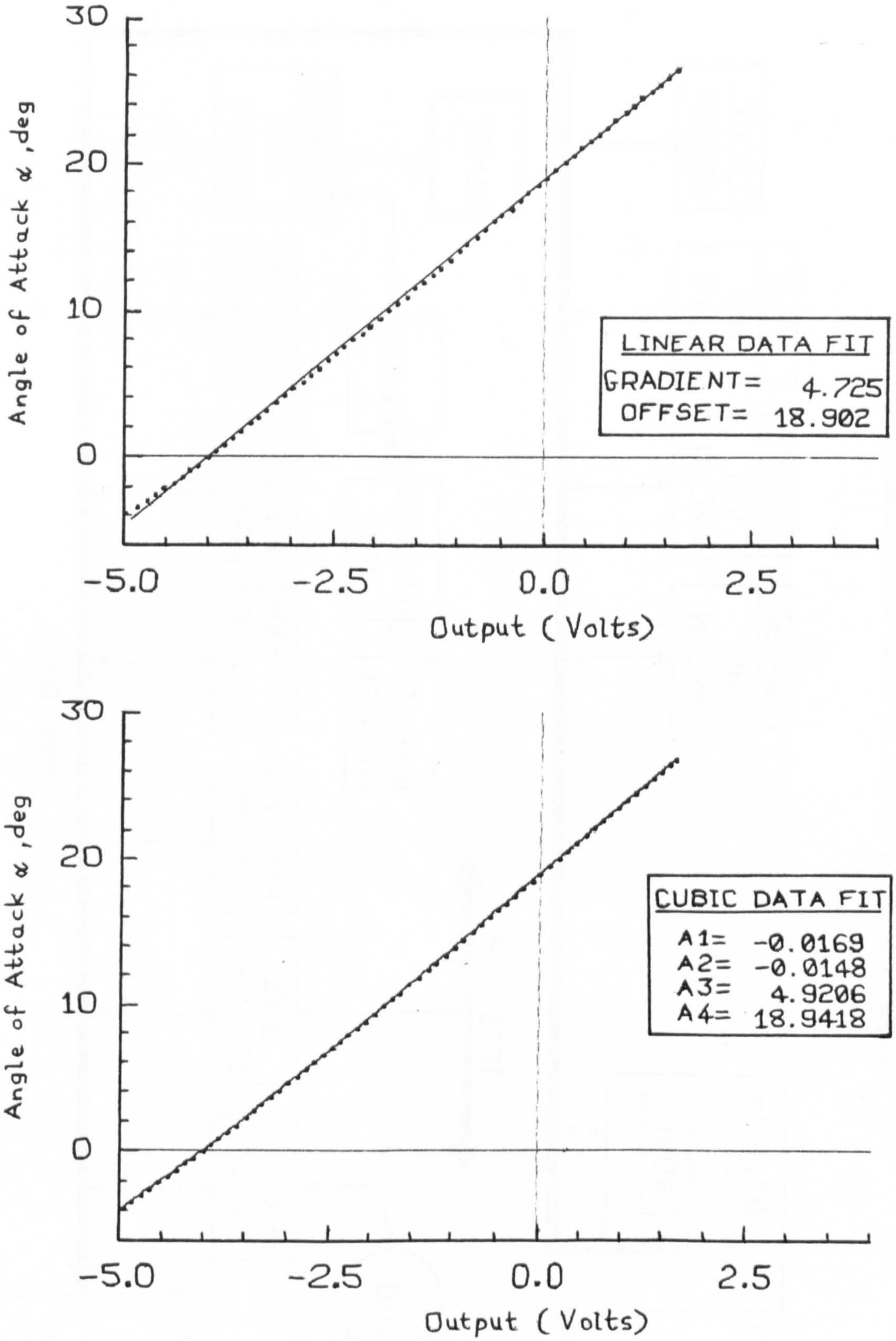

Figure 3.30 Angular displacement transducer calibration.

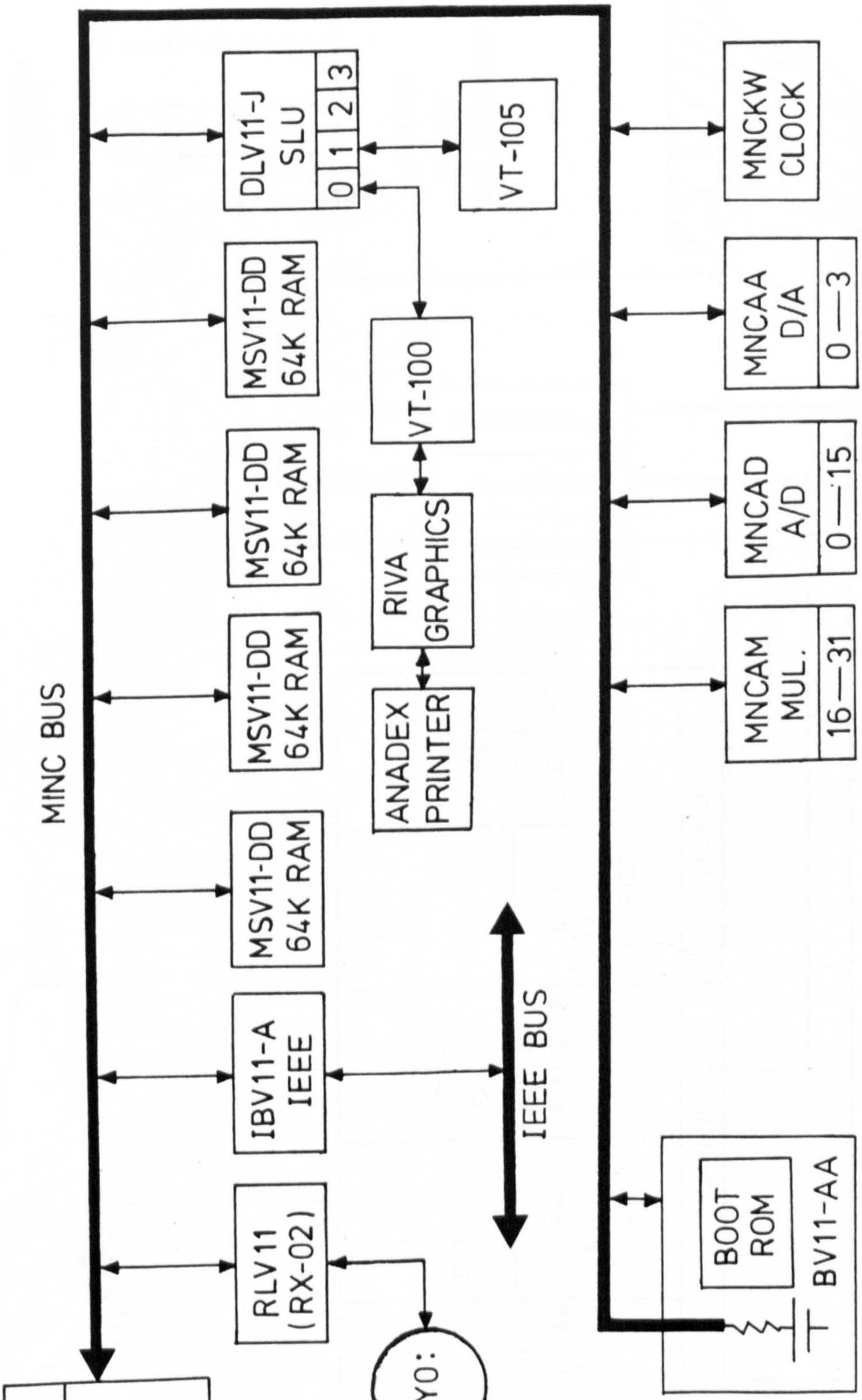

Figure 3.31 Schematic of MINC microcomputer system.

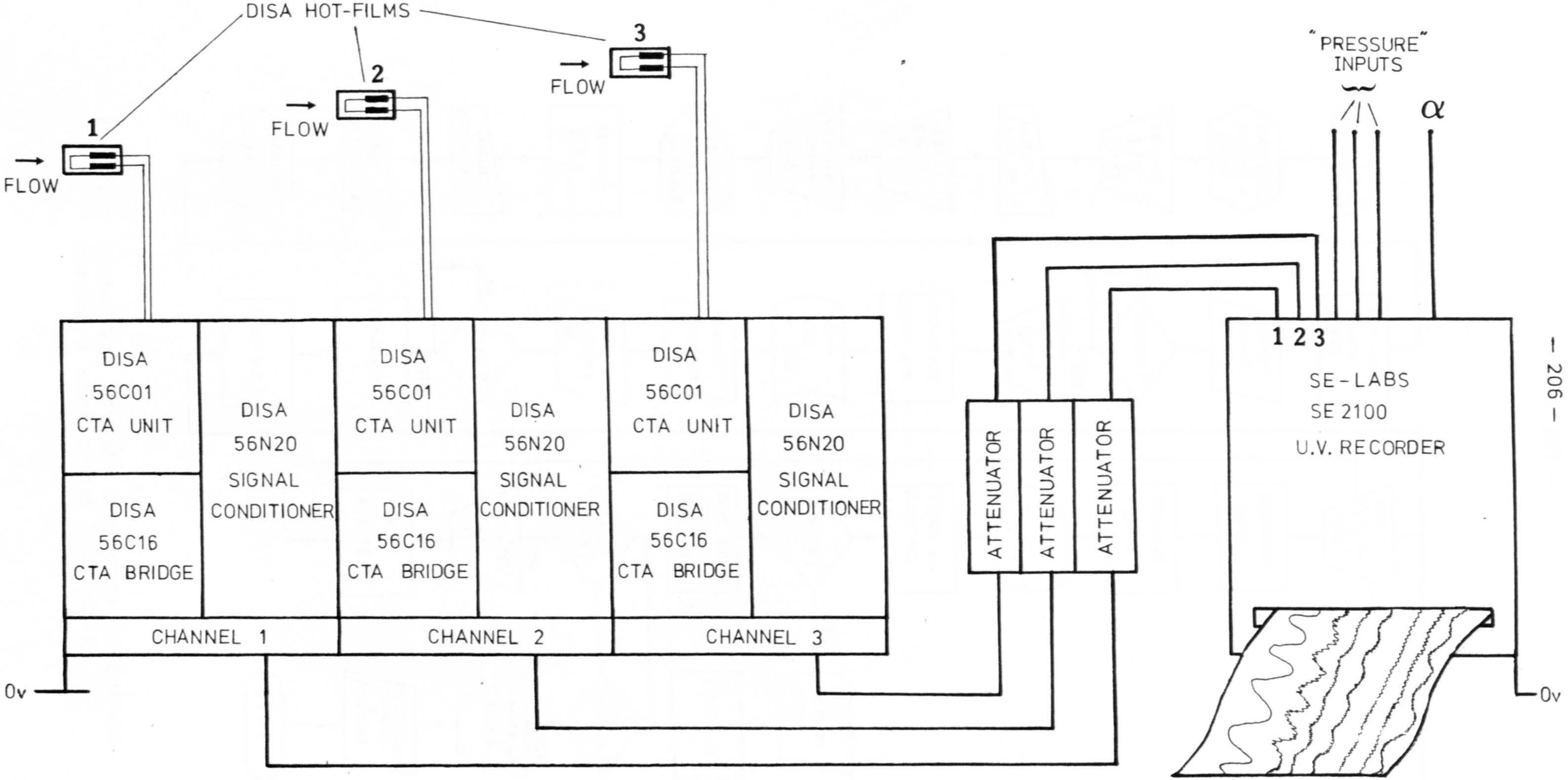

Fig 3.32 Schematic of the hot-film anemometry system.

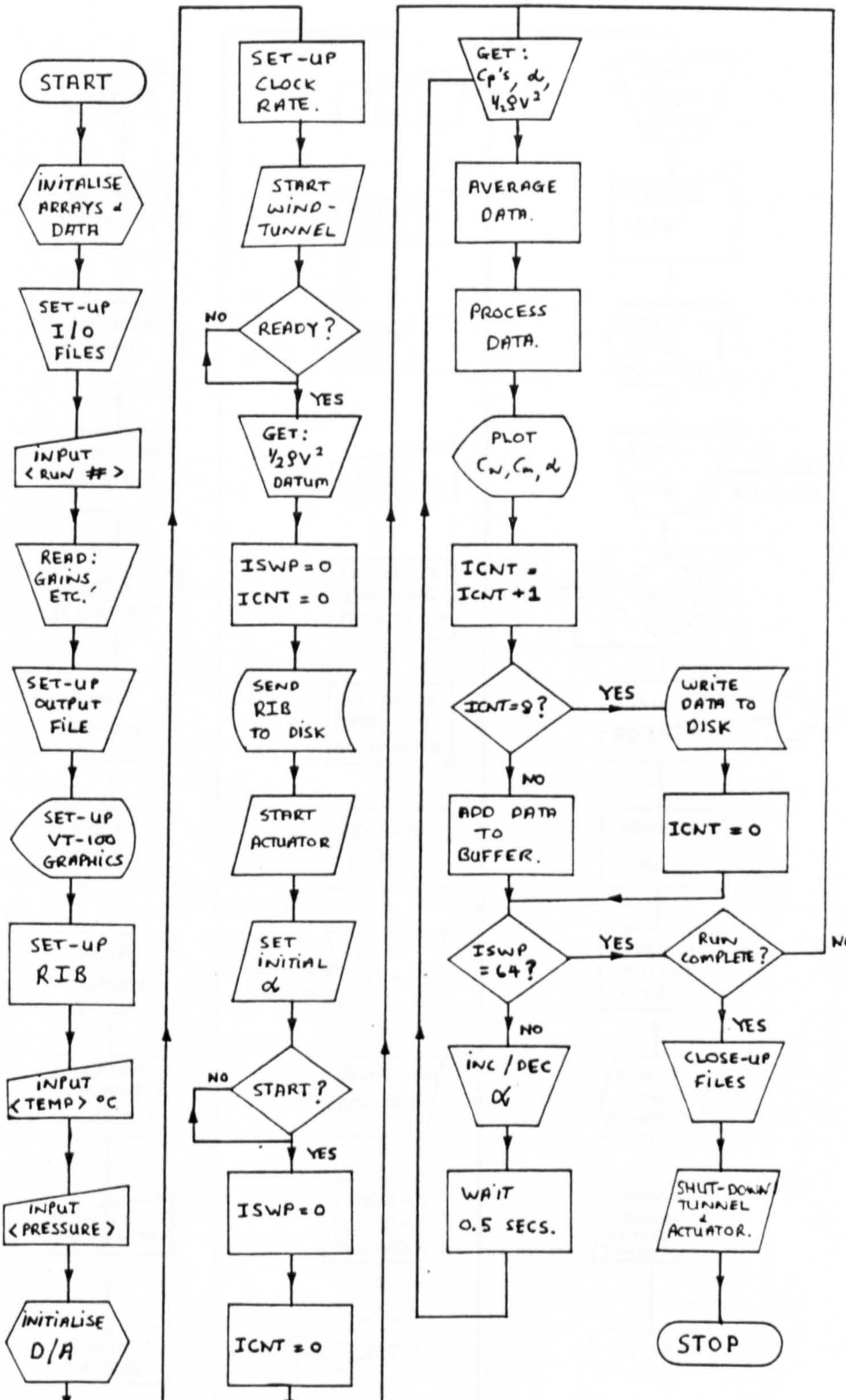

Fig 4.1 Flowchart for the sequence of events during a static run (STREX2).

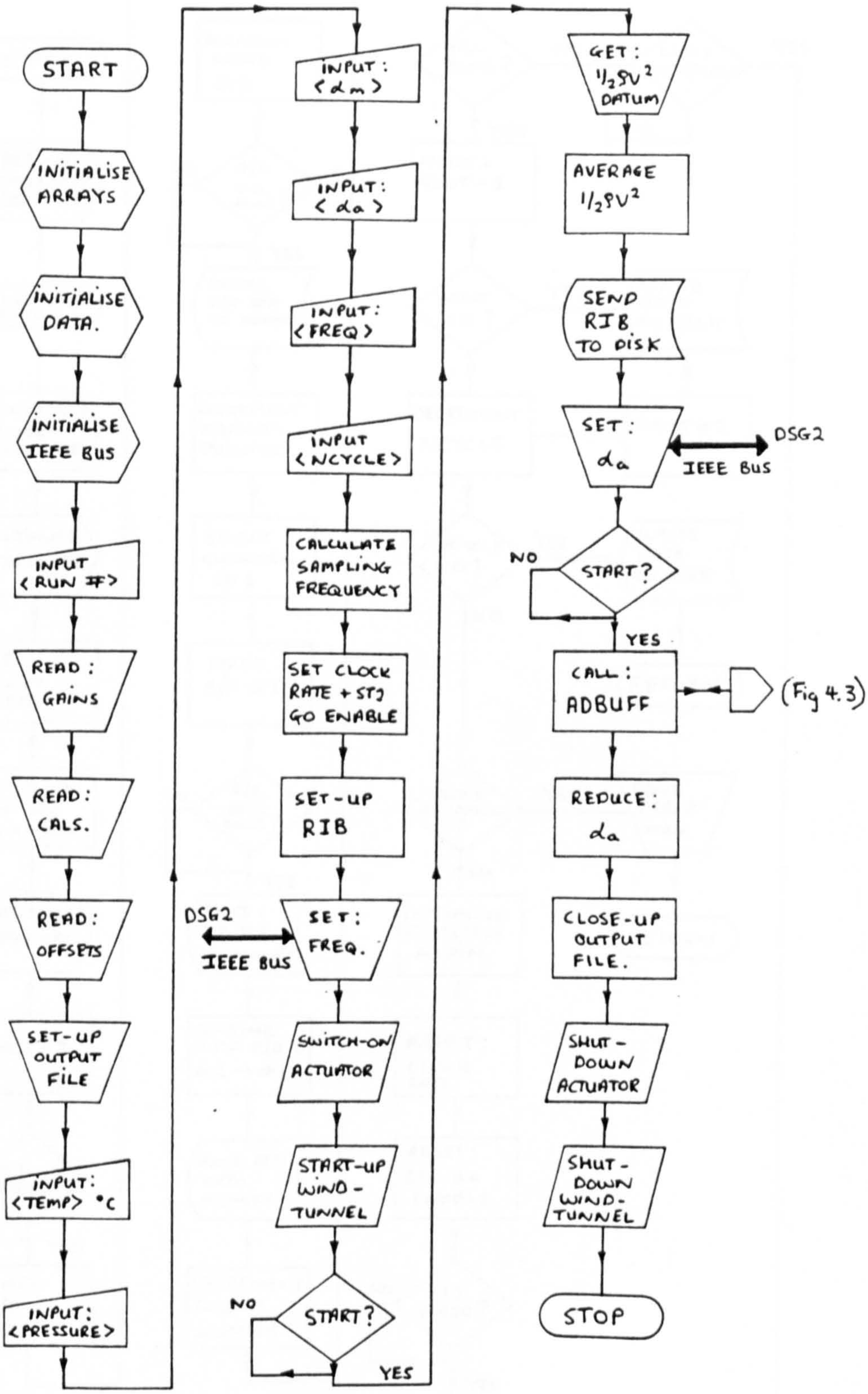

Fig 4.2 Flowchart for the sequence of events during an oscillatory run (SIREX2).

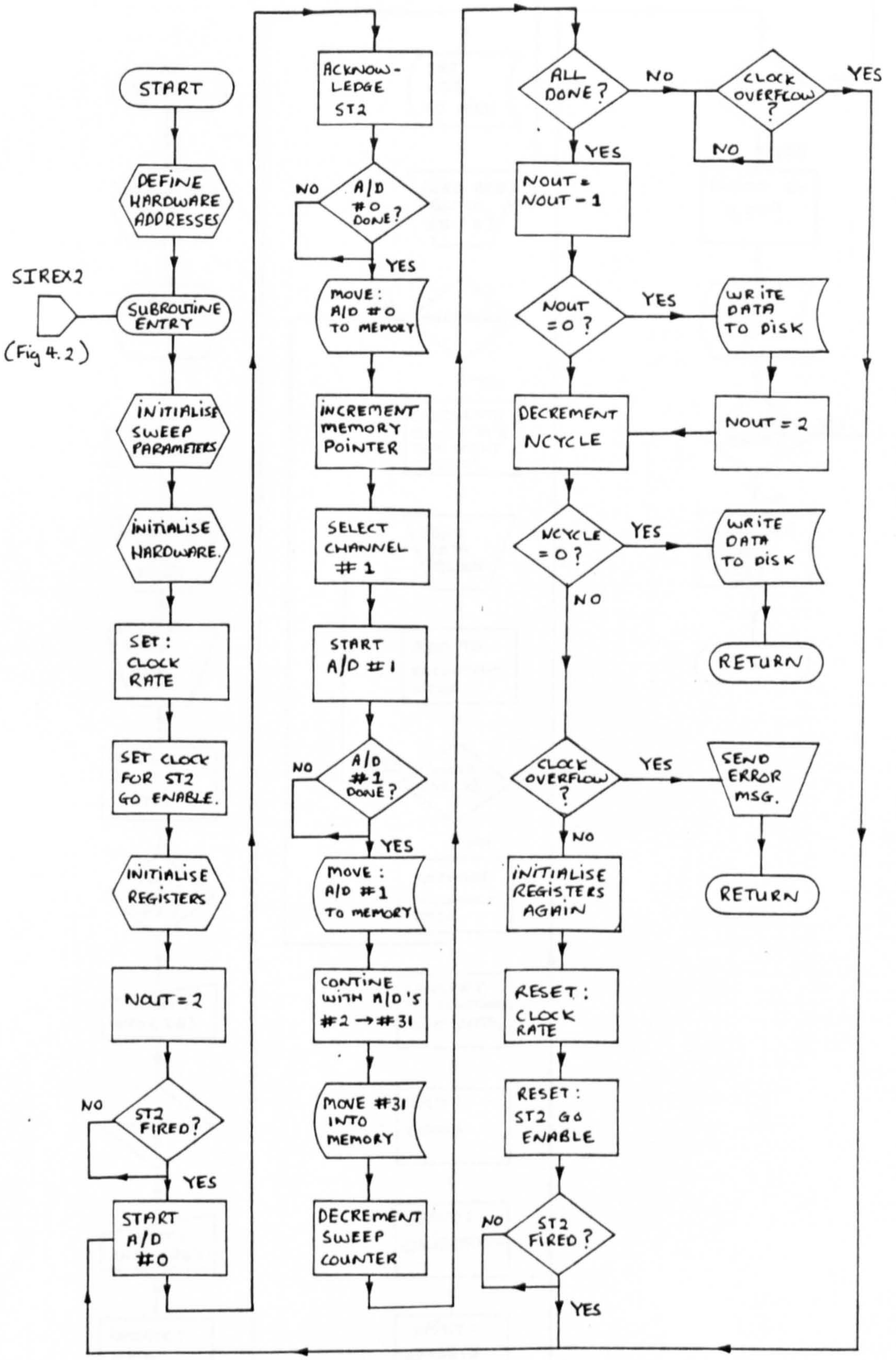

Fig 4.3 Flowchart for the high-speed A/D conversion routine, ADBUFF.

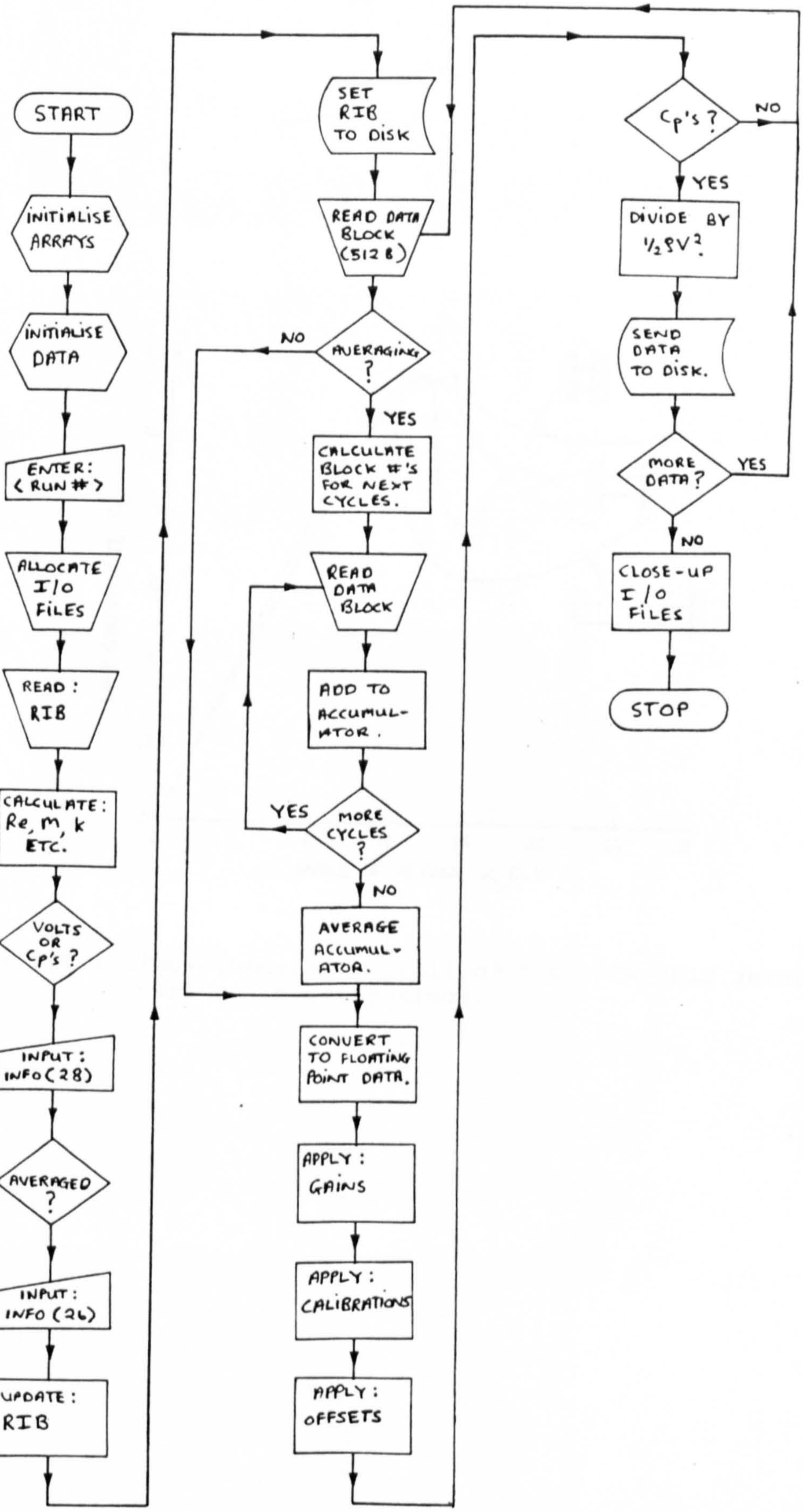

Fig 4.4 Flowchart for the data reduction routine, DSDR83.

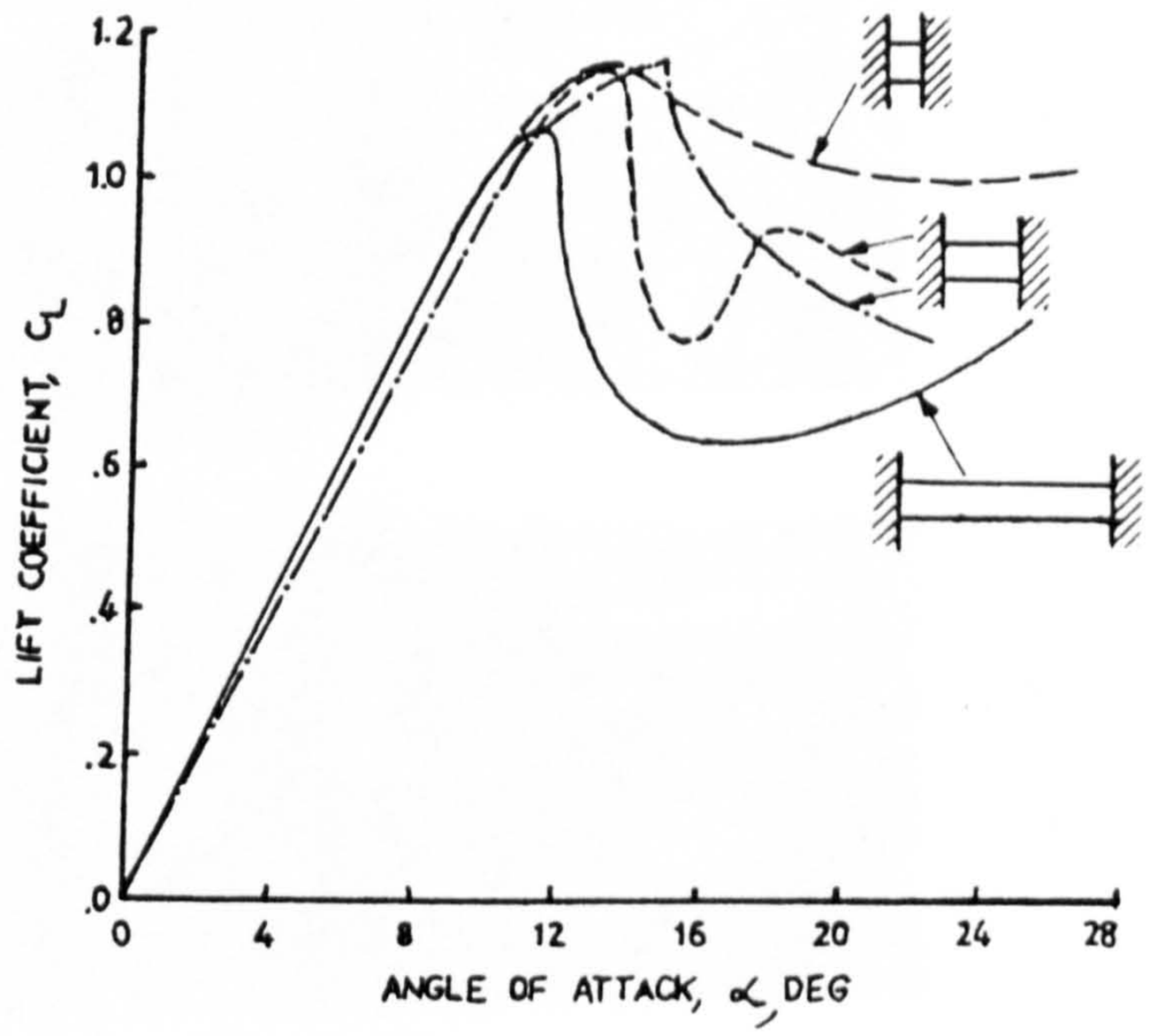

Fig 5.1 Two-dimensional stall of the NACA 0012 aerofoil by various investigations.

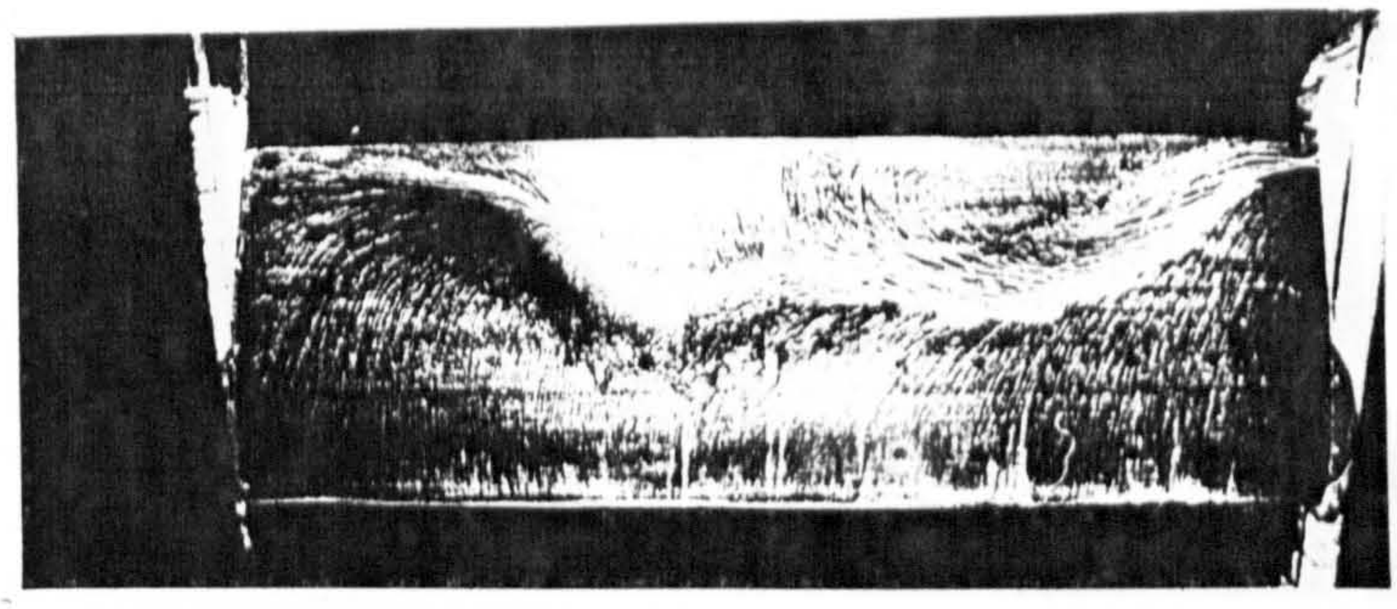

α=14.2°

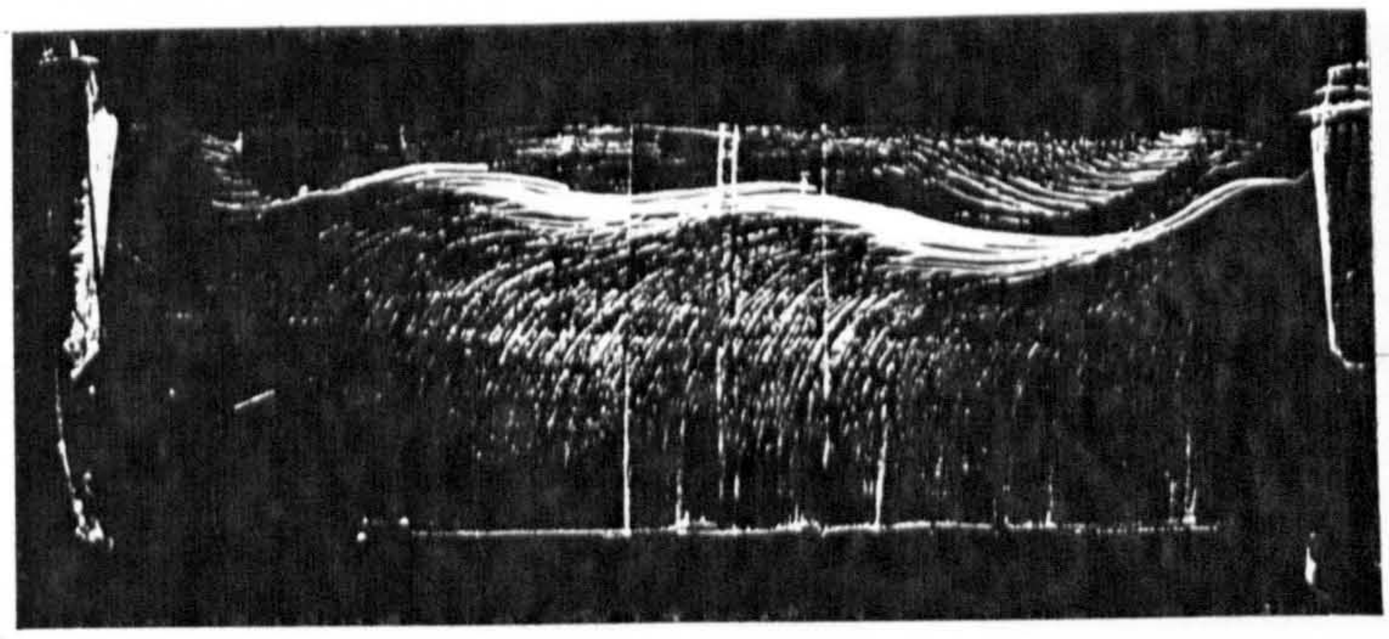

α=14.0°

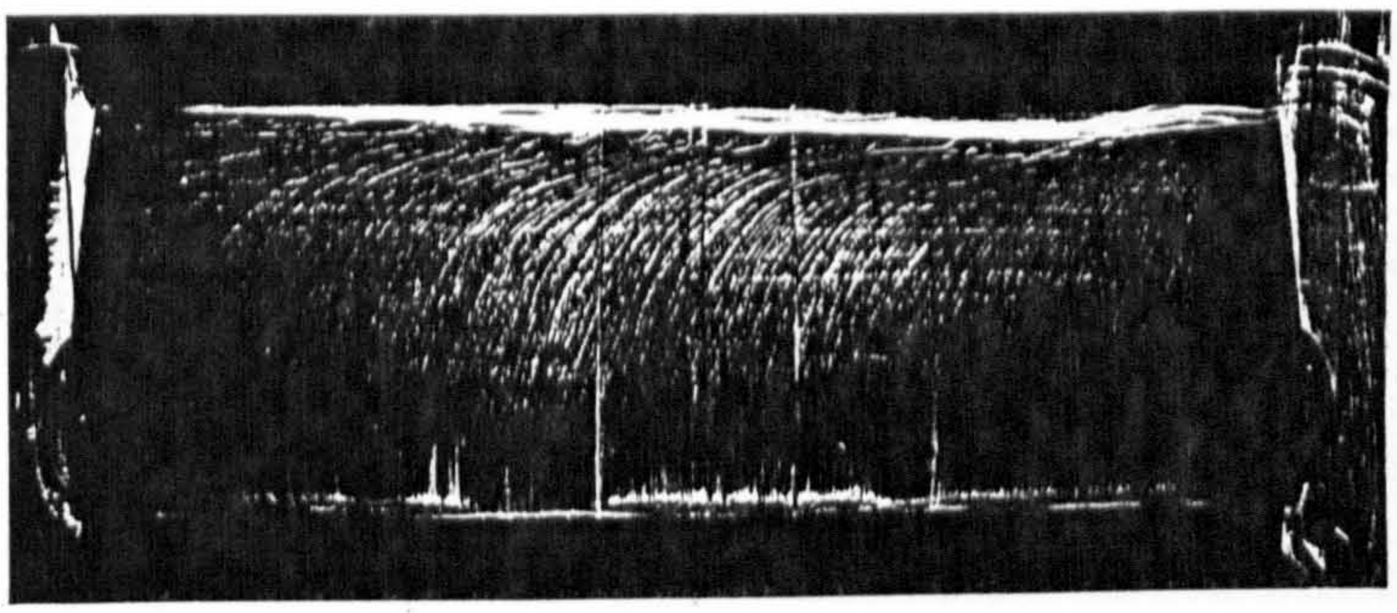

α=12.0°

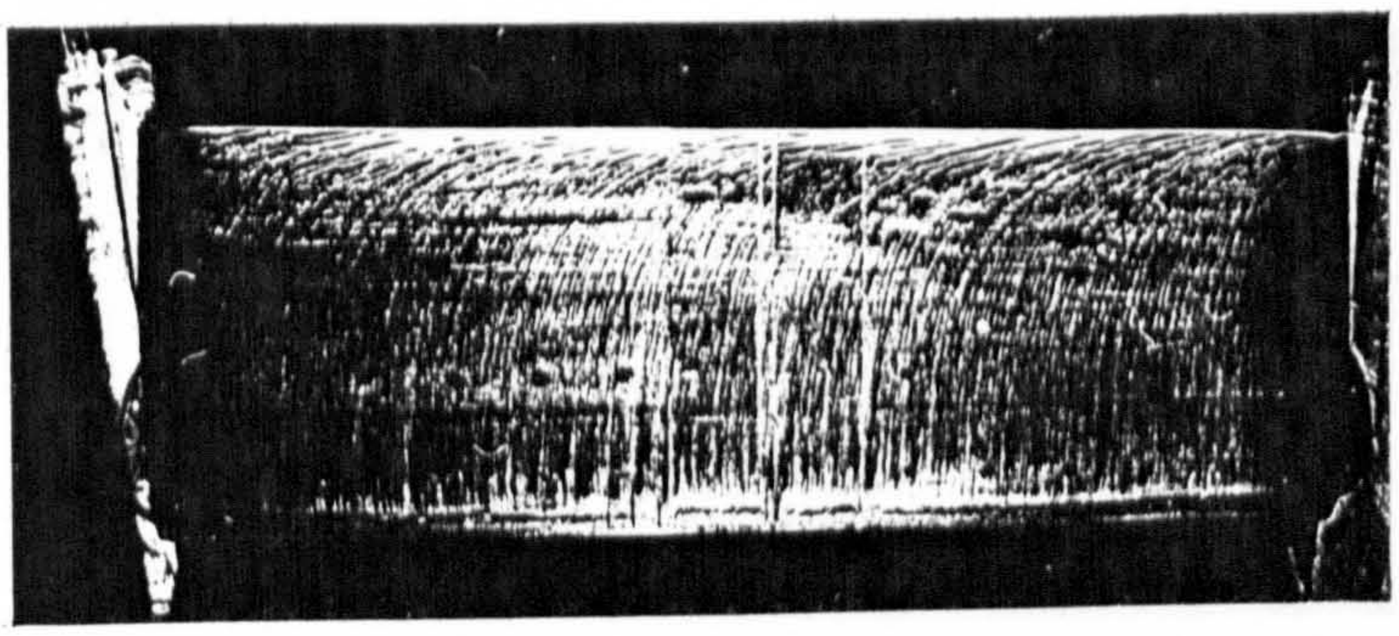

α=10.0°

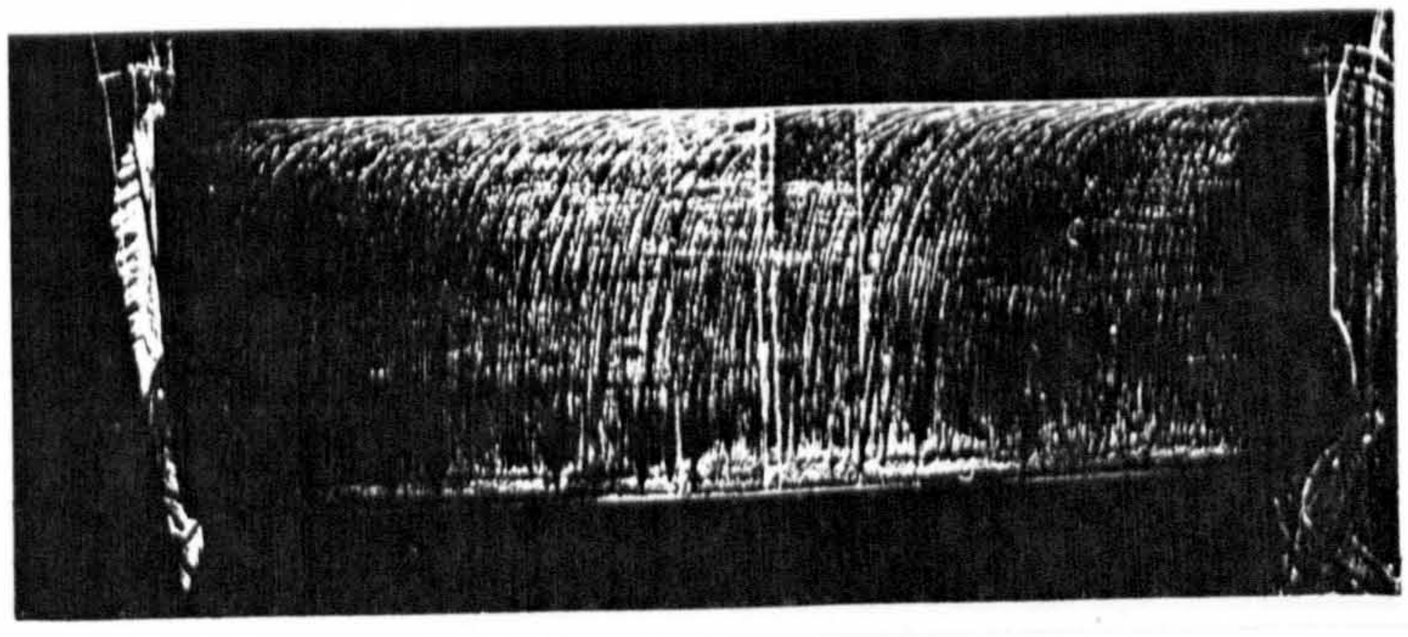

α= 8.0°

Figure 6.1 Upper surface oil-flow photographs for various angles of attack at Re = 1.45 x 10^6.

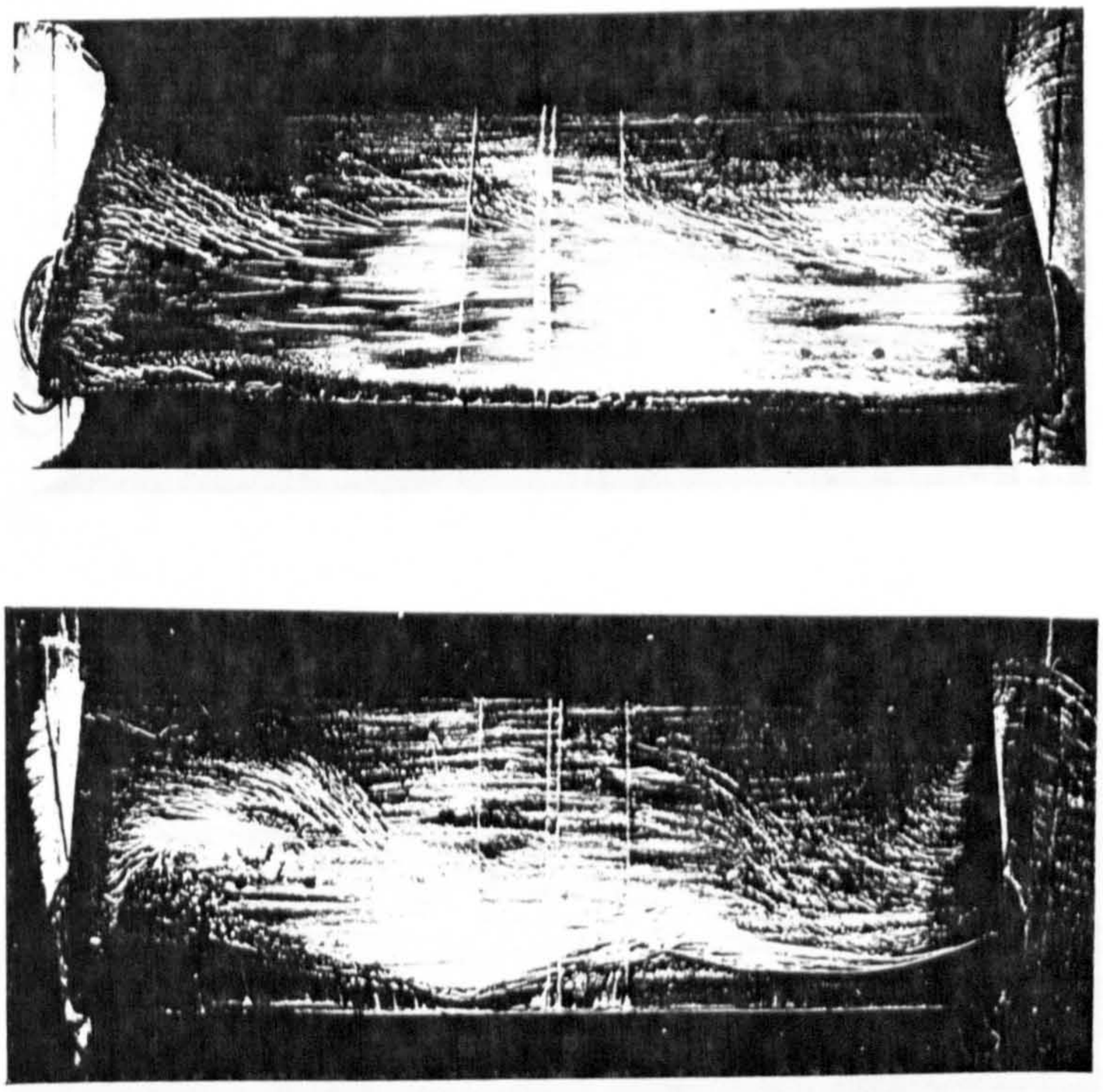

$\alpha = 25.0^\circ$

$\alpha = 20.0^\circ$

$\alpha = 16.0^\circ$

$\alpha = 15.0^\circ$

- Concluded.

Figure 6.1

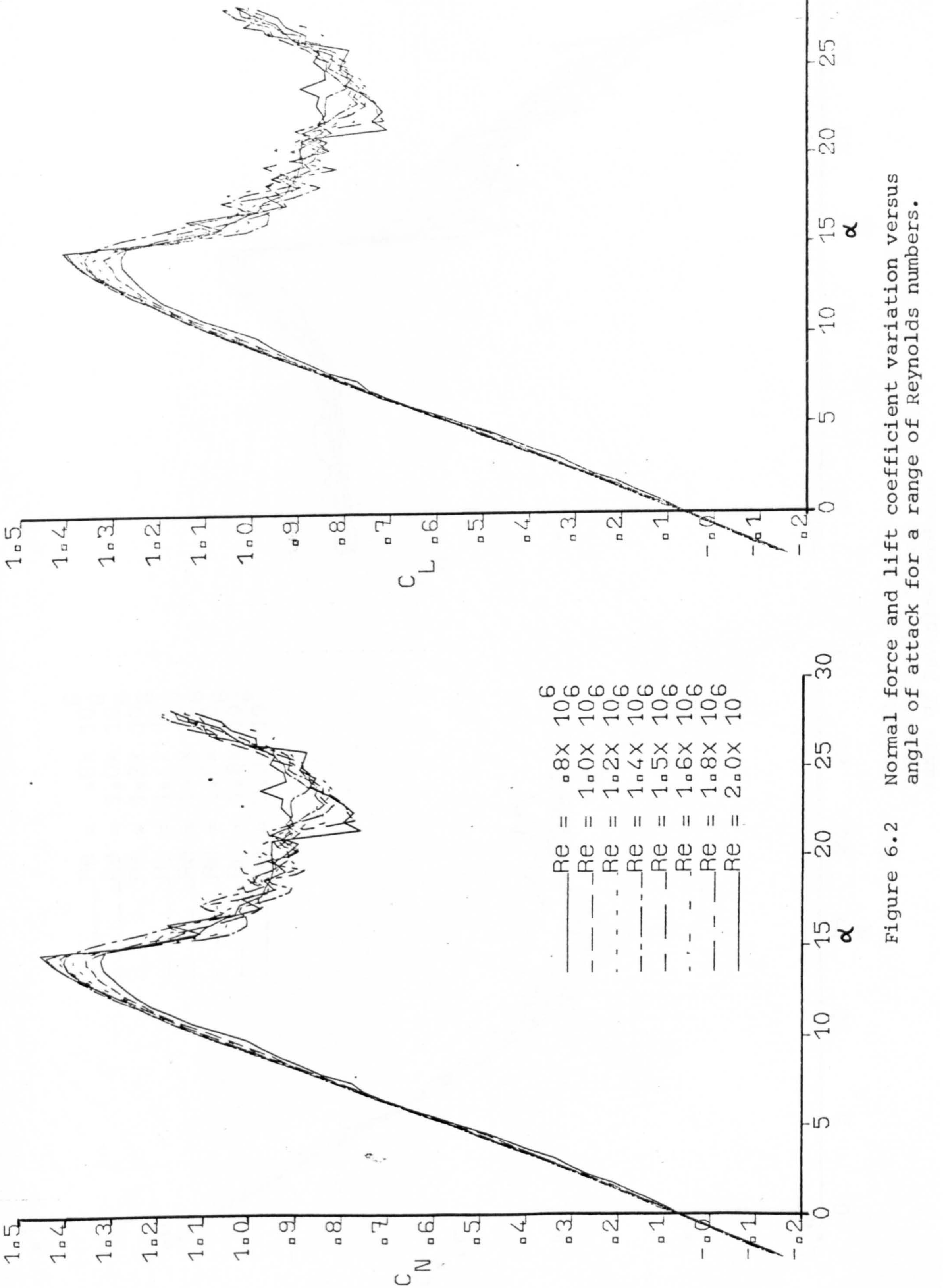

Figure 6.2 Normal force and lift coefficient variation versus angle of attack for a range of Reynolds numbers.

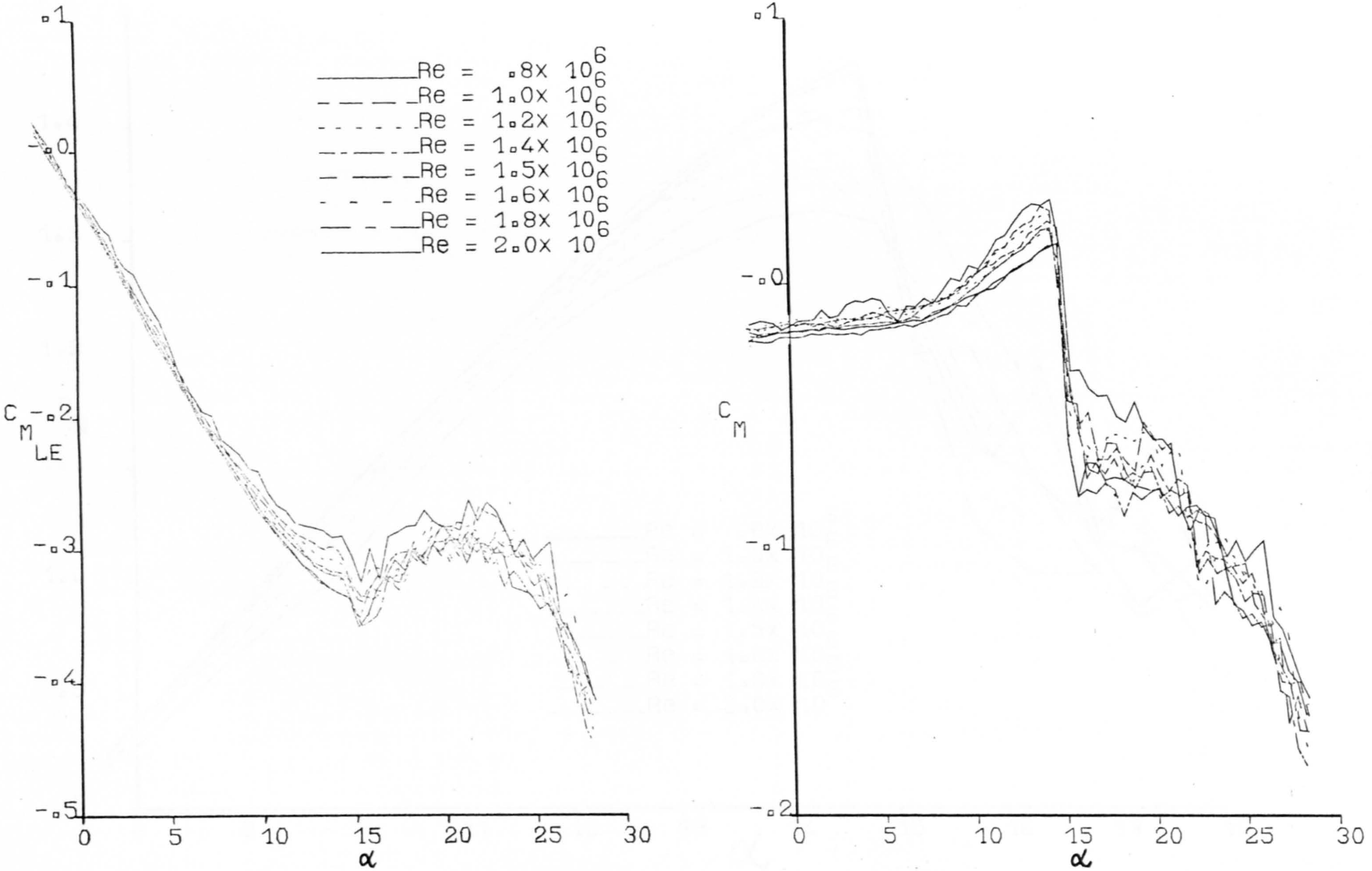

Figure 6.3 Leading-edge and quarter-chord pitching moment characteristics versus angle of attack for a range of Reynolds numbers.

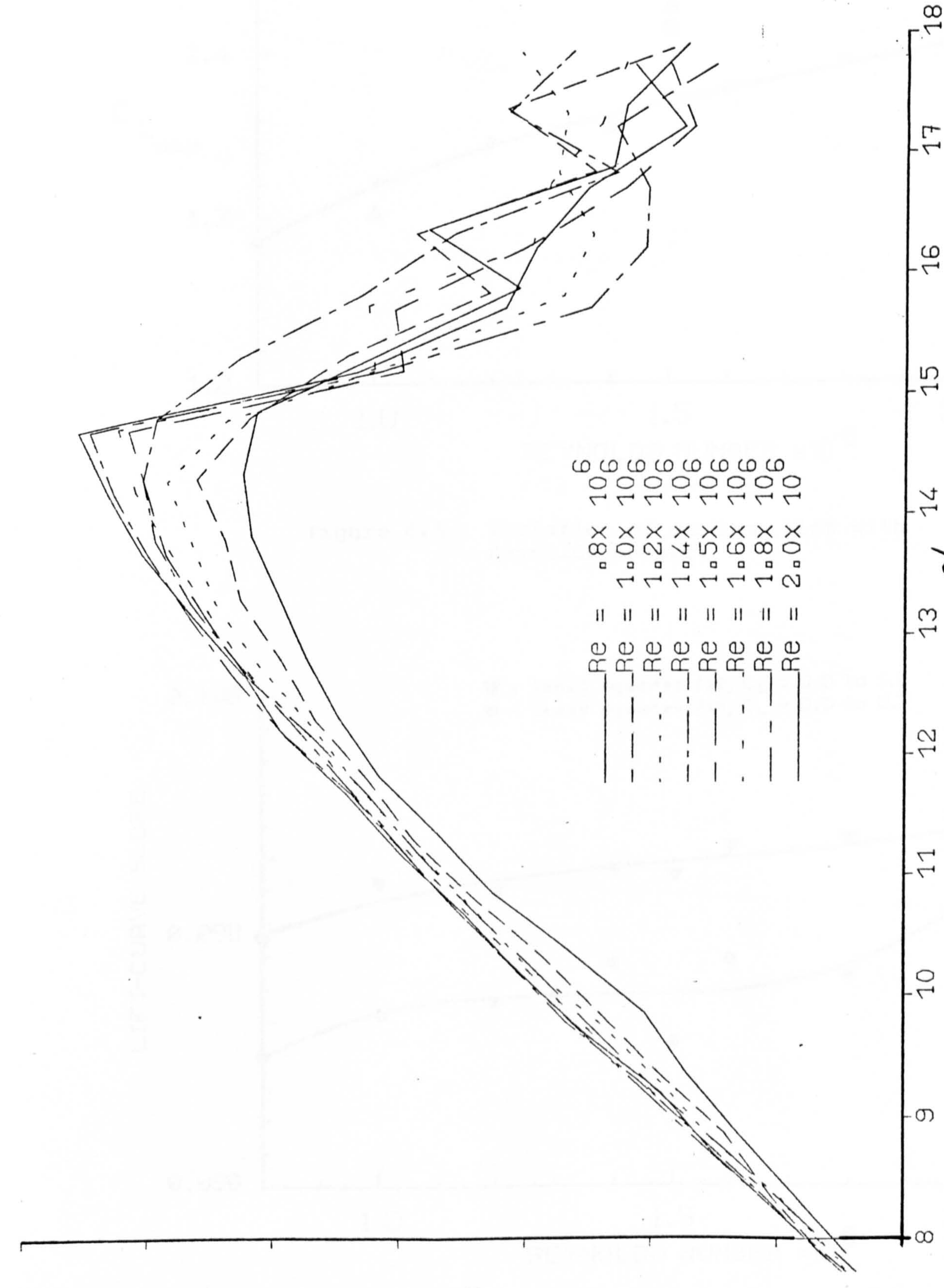

Figure 6.4 Detail of maximum normal force variation versus angle of attack for various Reynolds numbers.

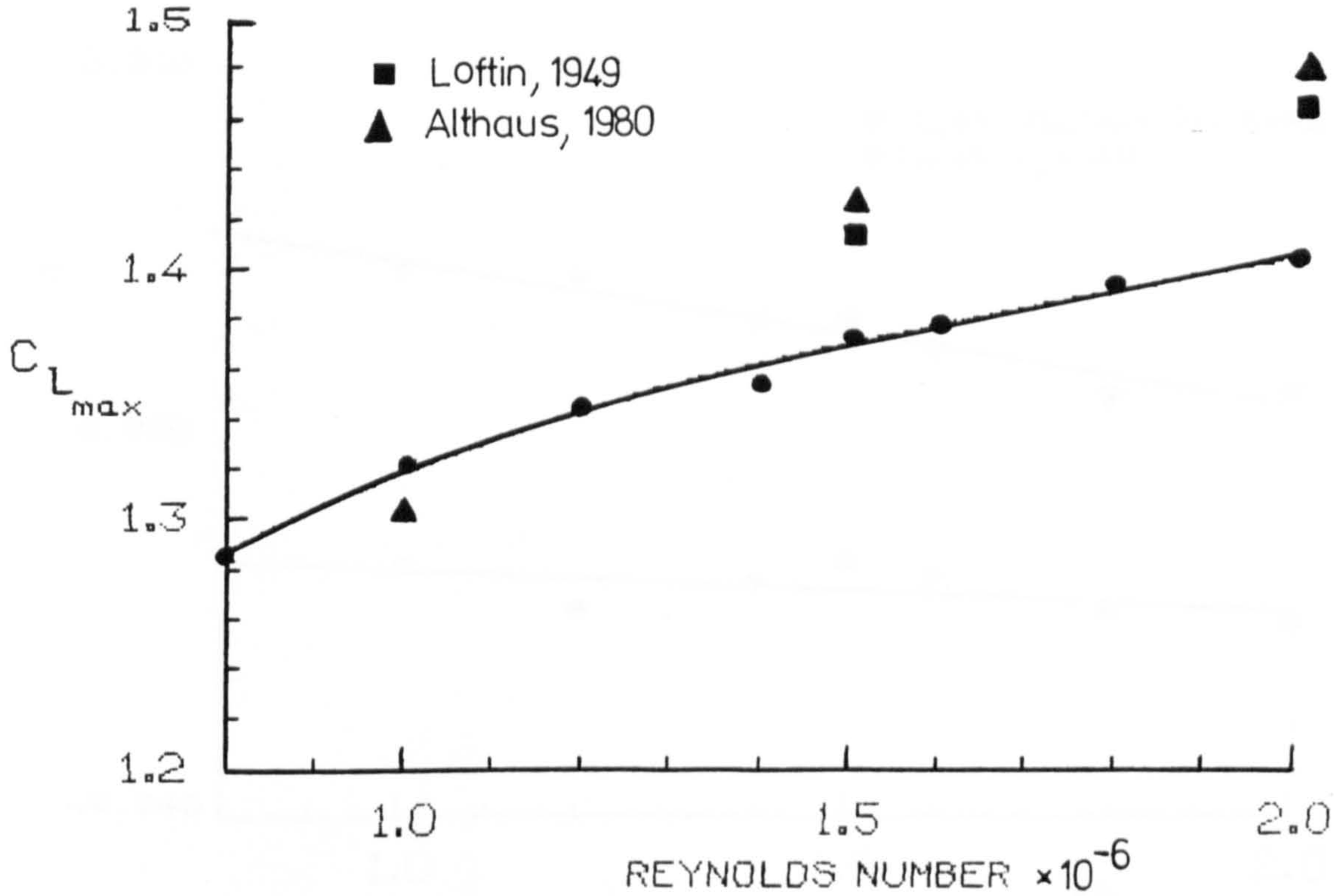

Figure 6.5 Variation of maximum lift with Reynolds number.

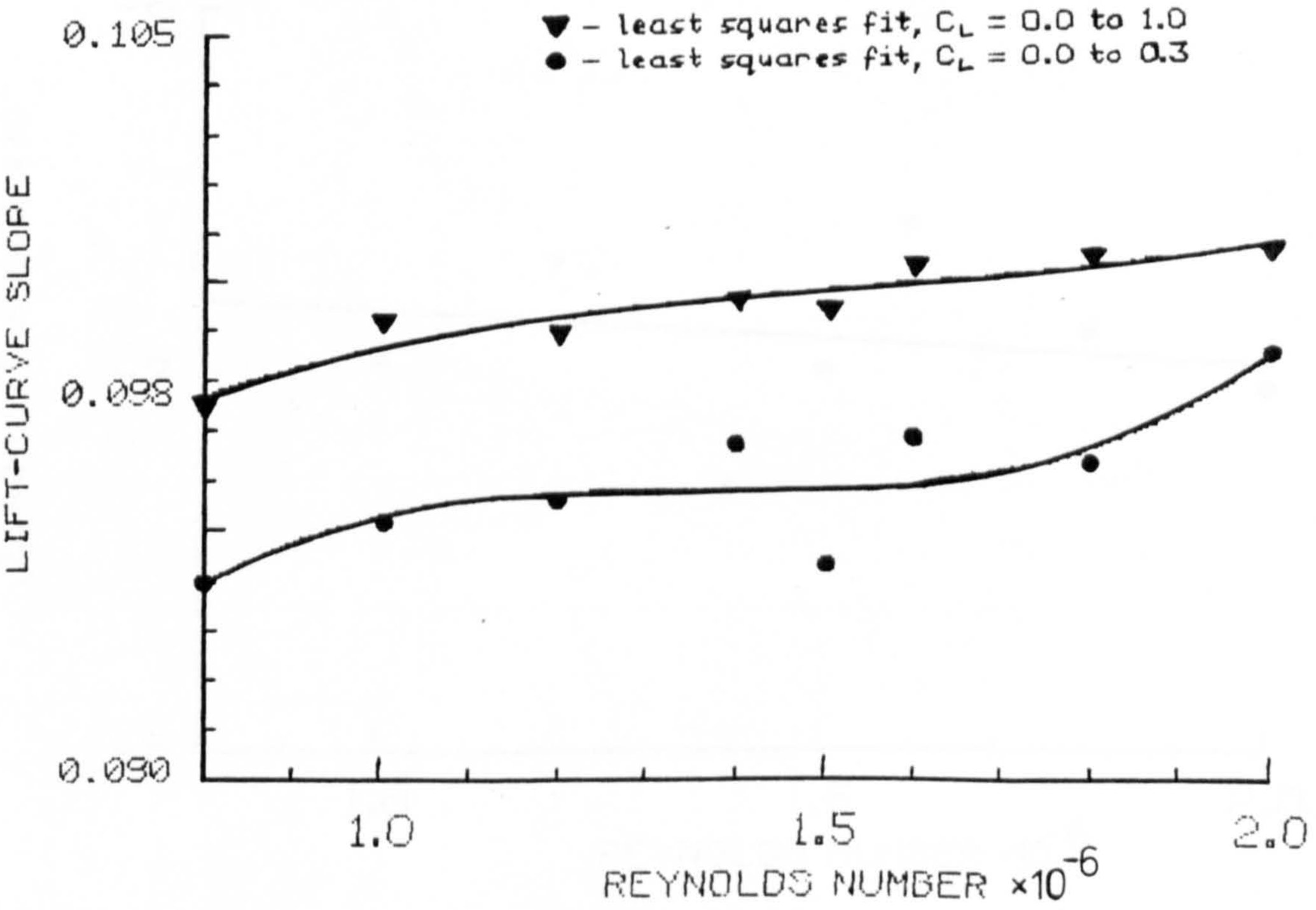

Figure 6.6 Variation of lift-curve slope with Reynolds number.

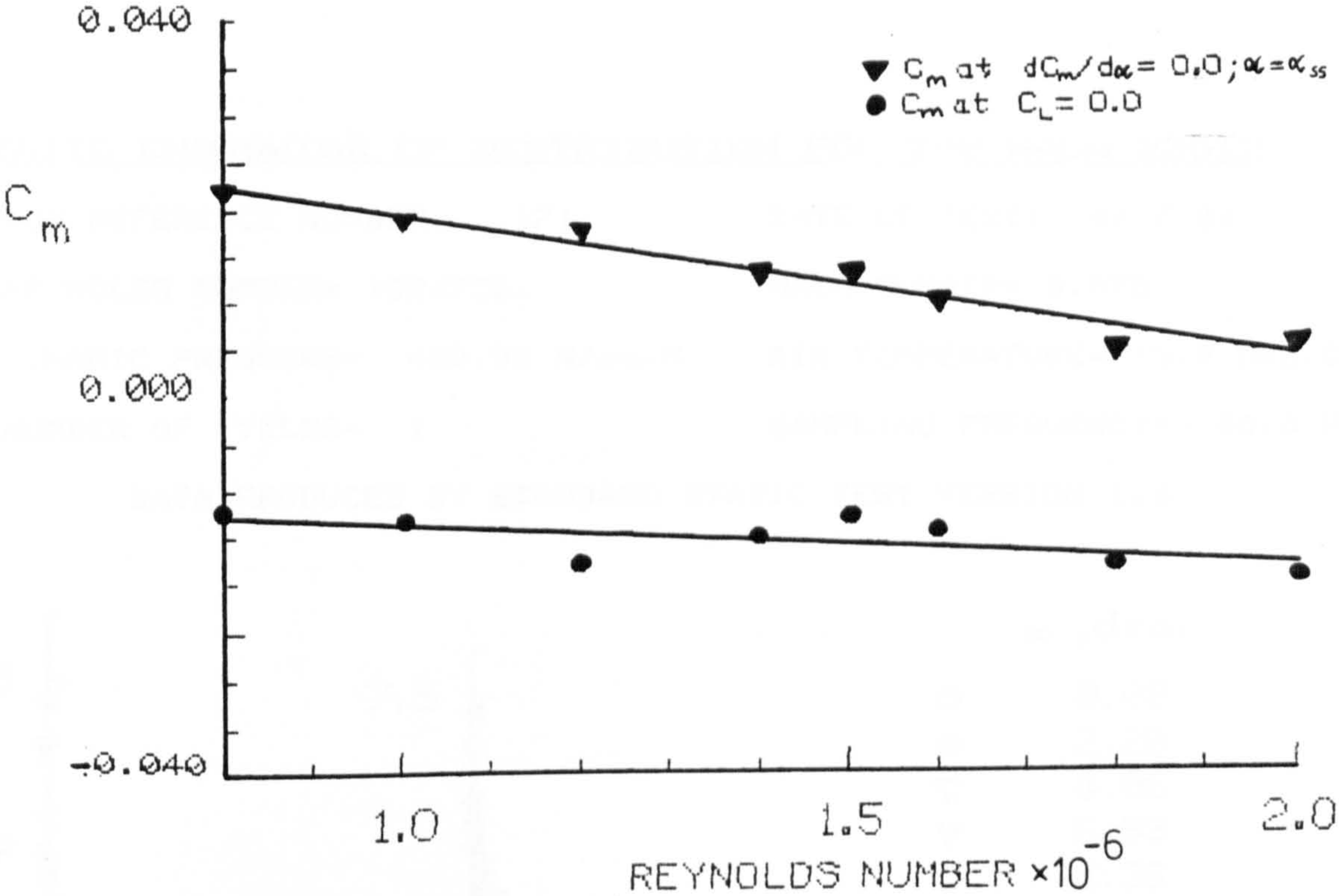

Figure 6.7 Pitching moment variation with Reynolds number.

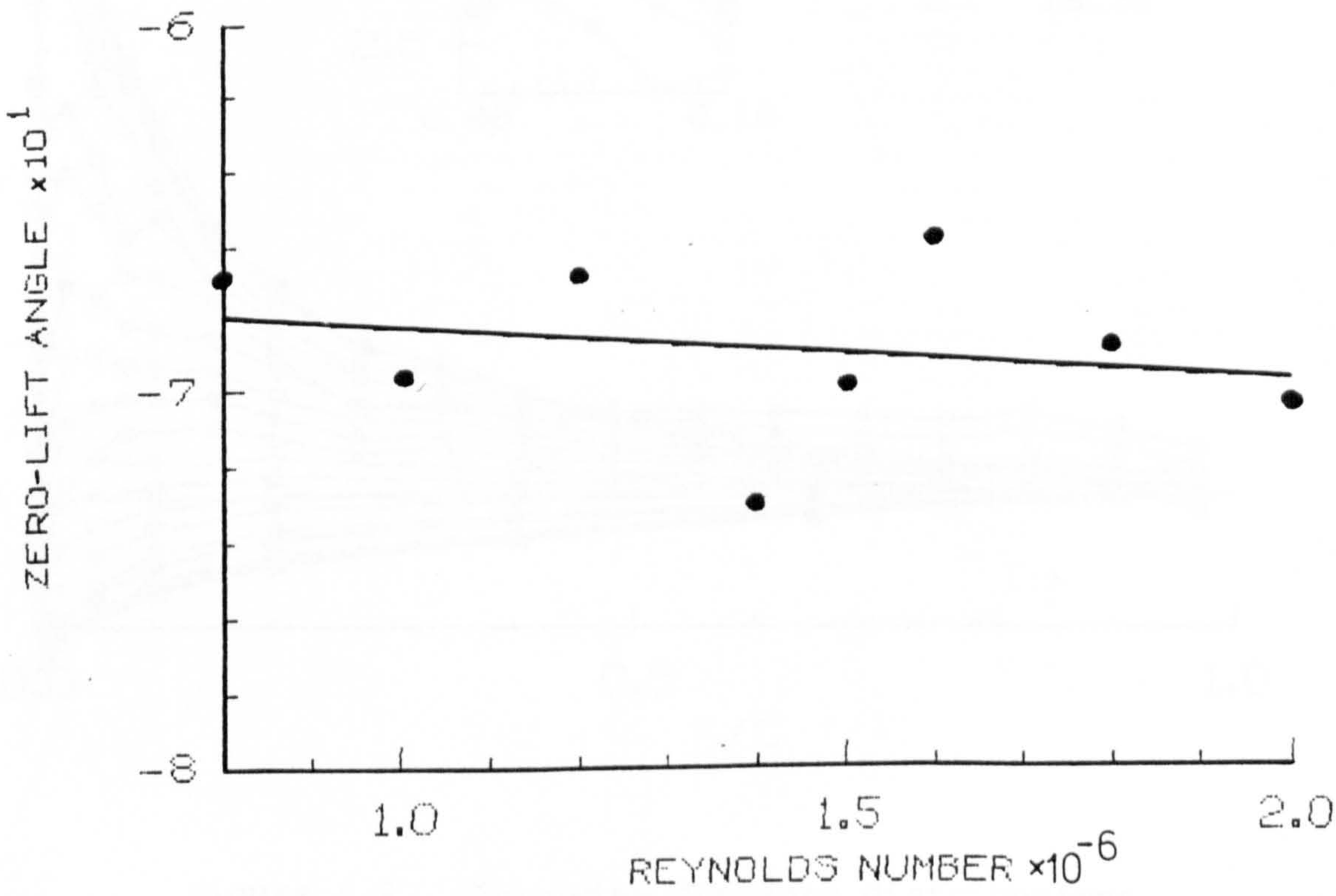

Figure 6.8 Zero-lift angle variation with Reynolds number.

STATIC CHORDWISE CP DISTRIBUTION FOR THE NACA 23012

RUN REFERENCE NUMBER: 171 DATE OF TEST: 4/ 7/83

REYNOLDS NUMBER= 1024756. MACH NUMBER= 0.075

DYNAMIC PRESSURE= 439.96 N/sq.M AIR TEMPERATURE= 25.0 Deg.C

NUMBER OF CYCLES= 1 SAMPLING FREQUENCY= 100.0 Hz.

DATA PRODUCED BY STANDARD STATIC TEST VERSION 1.3

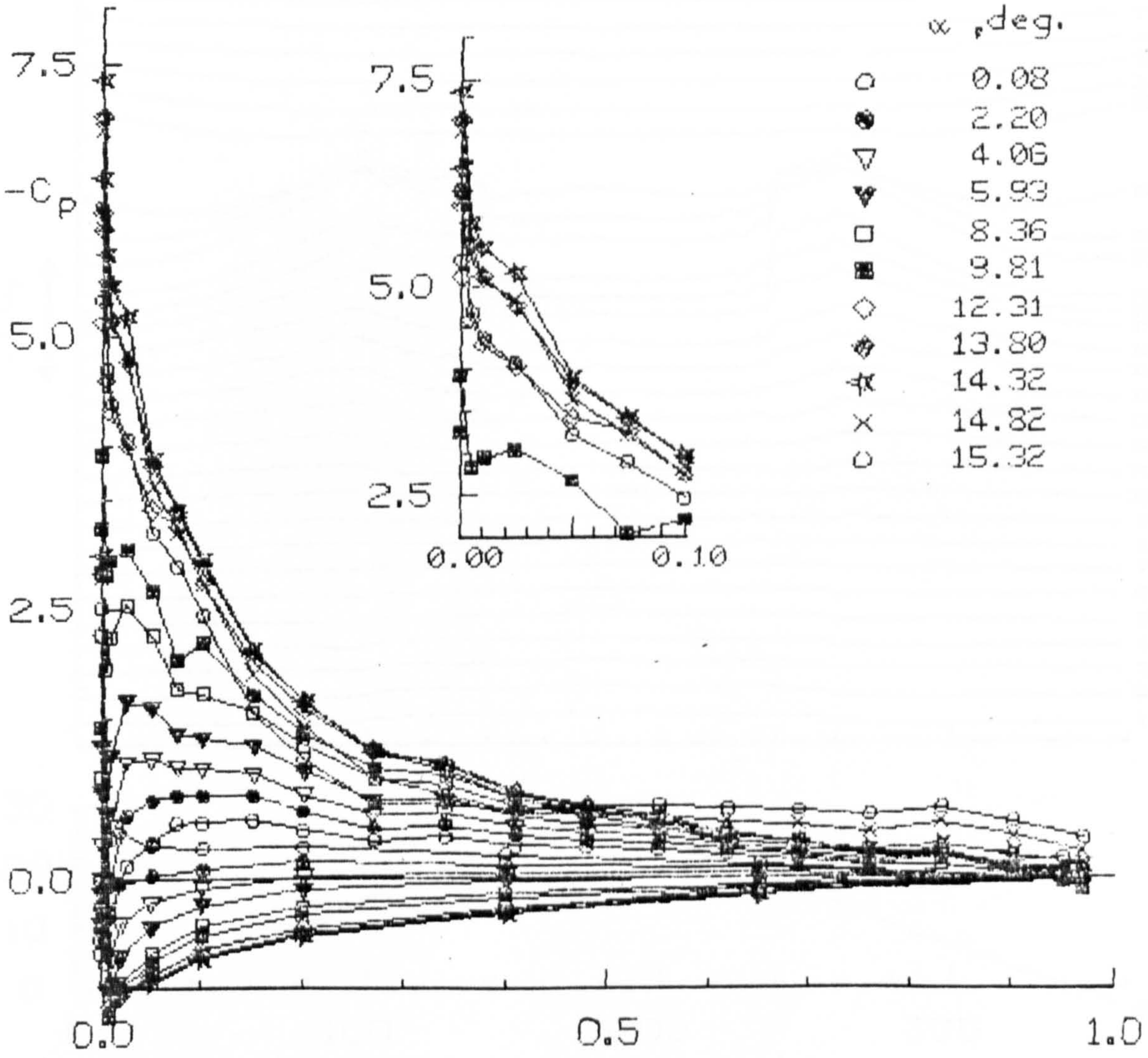

Figure 6.9 Chordwise pressure distributions for various angles of attack at Re = 1.0 x 10^6.

STATIC CP TIME HISTORIES FOR THE NACA 23012

RUN REFERENCE NUMBER: 171 DATE OF TEST: 4/ 7/83

REYNOLDS NUMBER= 1024756. MACH NUMBER= 0.075

DYNAMIC PRESSURE= 439.96 N/sq.M AIR TEMPERATURE= 25.0 Deg.C

NUMBER OF CYCLES= 1 SAMPLING FREQUENCY= 100.0 Hz.

DATA PRODUCED BY STANDARD STATIC TEST VERSION 1.3

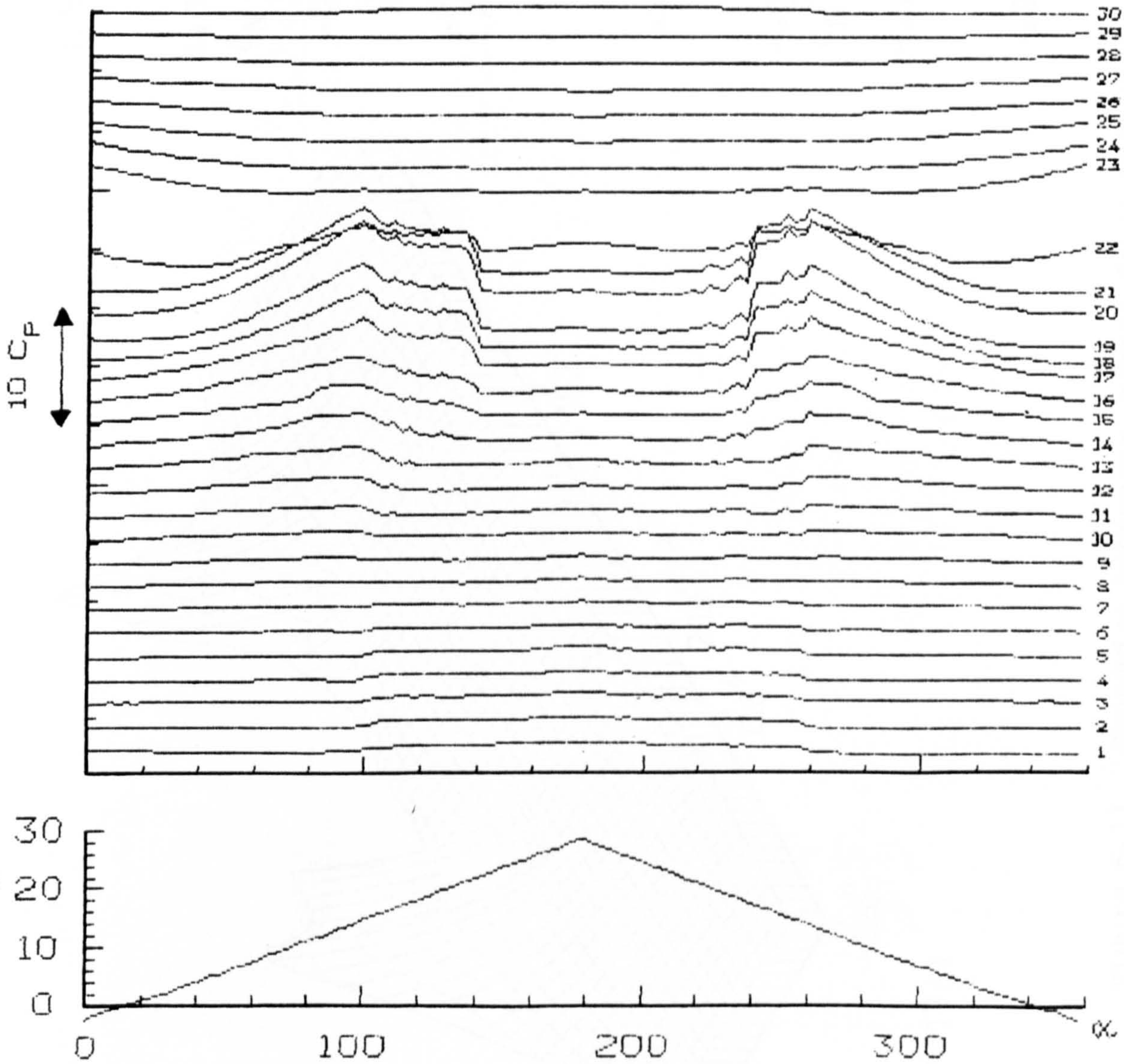

Figure 6.10 Pressure coefficient "time" histories at Re = 1.0×10^6.

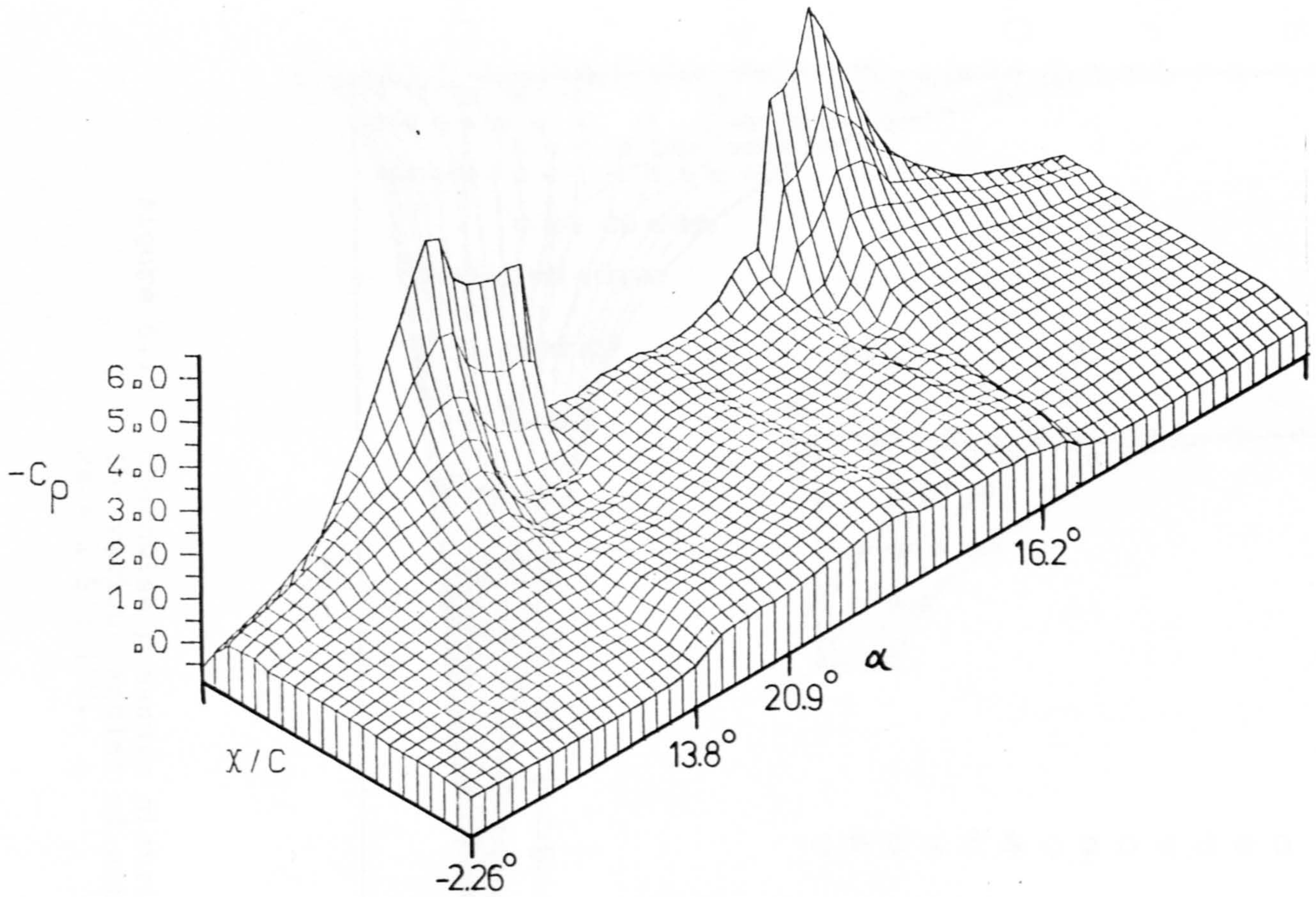

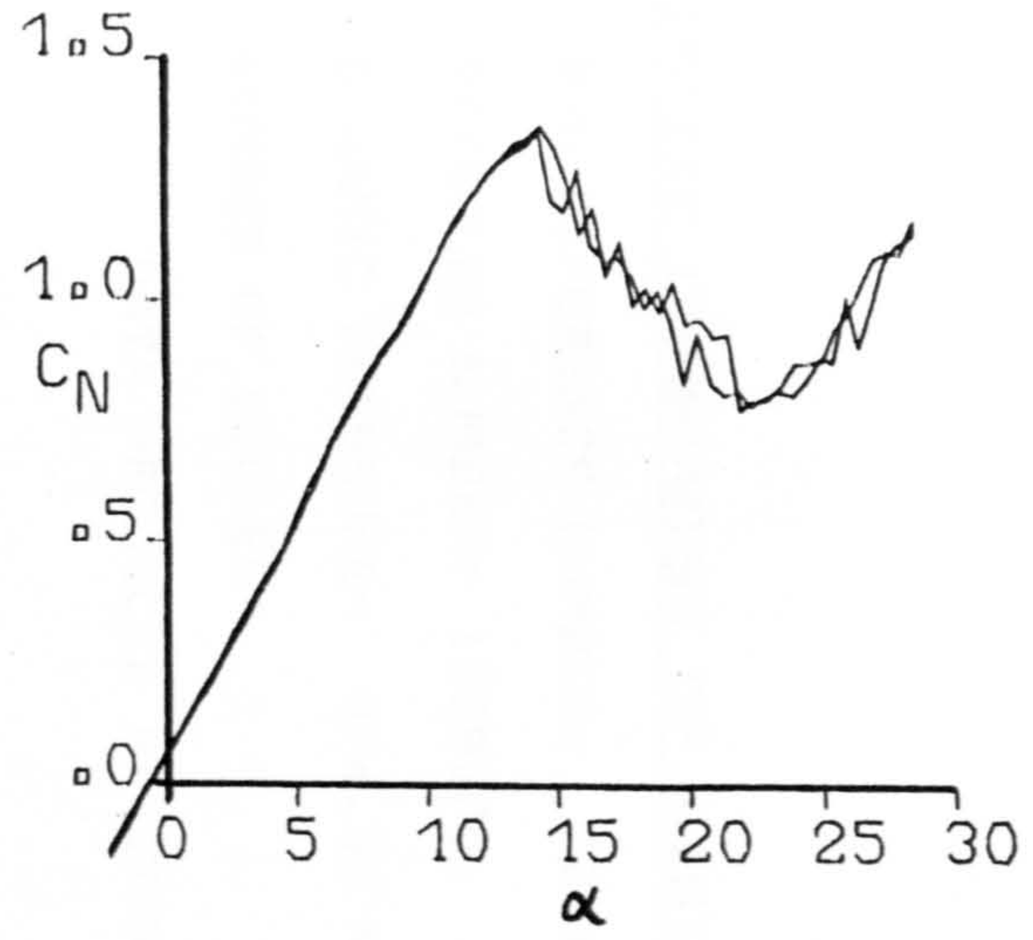

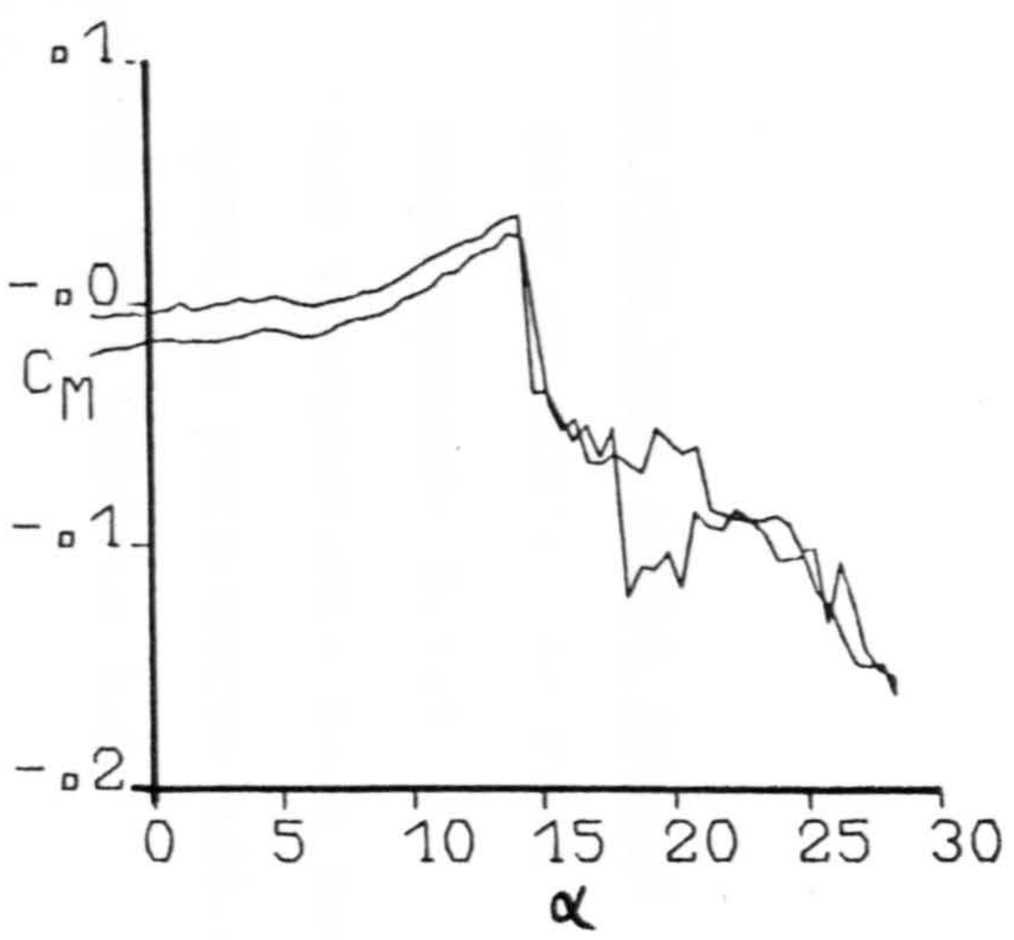

Figure 6.11 Chordwise pressures, normal force and pitching moment variation during a static run at Re = 1.0×10^6.

STATIC CHORDWISE CP DISTRIBUTION FOR THE NACA 23012

RUN REFERENCE NUMBER: 201 DATE OF TEST: 4/ 7/83

REYNOLDS NUMBER= 1529270. MACH NUMBER= 0.112

DYNAMIC PRESSURE= 974.33 N/sq.M AIR TEMPERATURE= 24.0 Deg.C

NUMBER OF CYCLES= 1 SAMPLING FREQUENCY= 100.0 Hz.

DATA PRODUCED BY STANDARD STATIC TEST VERSION 1.3

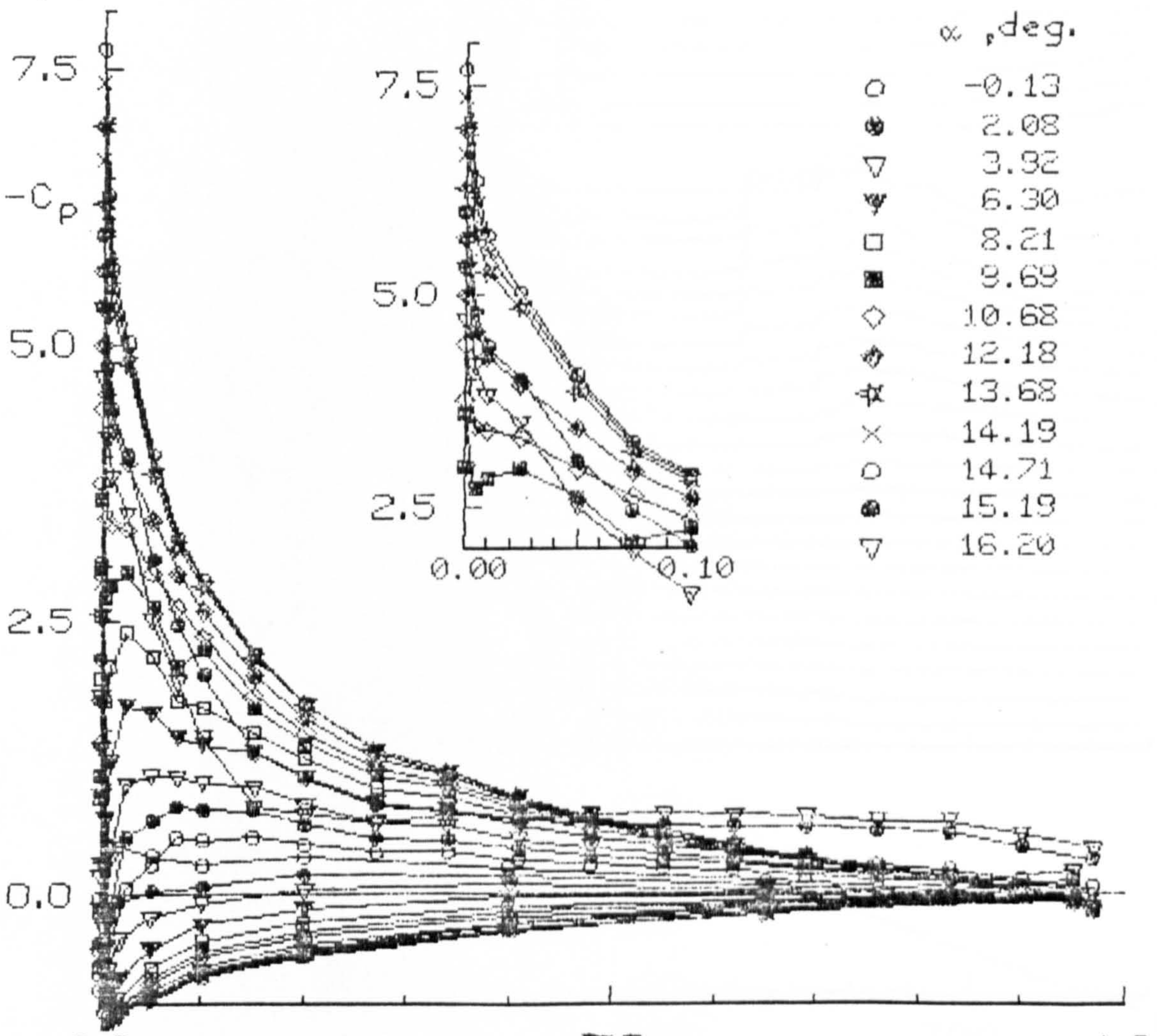

Figure 6.12 Chordwise pressure distributions for various angles of attack at Re = 1.5 x 10^6.

STATIC CP TIME HISTORIES FOR THE NACA 23012

RUN REFERENCE NUMBER: 201 DATE OF TEST: 4/ 7/83

REYNOLDS NUMBER= 1529270. MACH NUMBER= 0.112

DYNAMIC PRESSURE= 974.33 N/sq.M AIR TEMPERATURE= 24.0 Deg.C

NUMBER OF CYCLES= 1 SAMPLING FREQUENCY= 100.0 Hz.

DATA PRODUCED BY STANDARD STATIC TEST VERSION 1.3

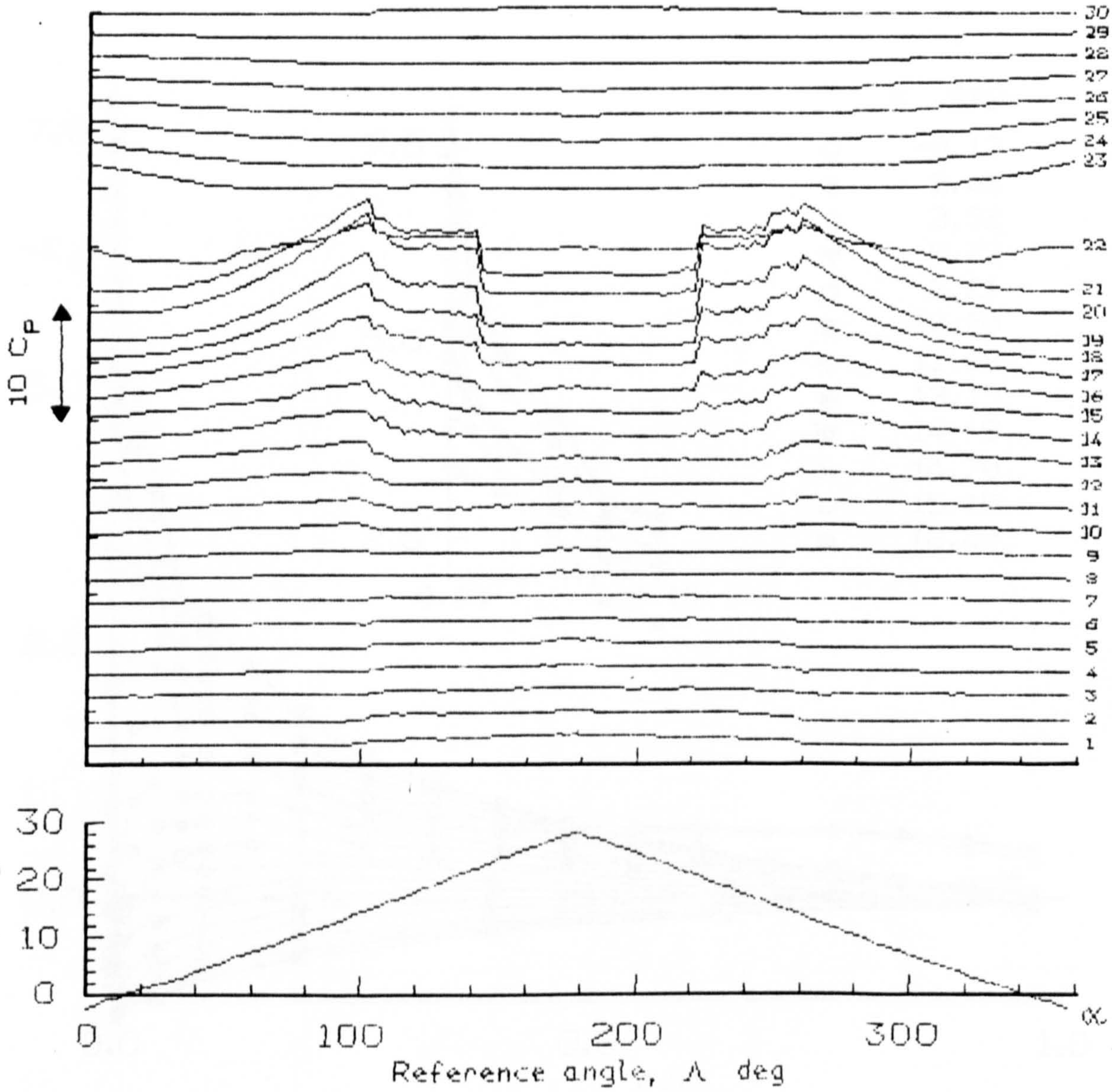

Figure 6.13 Pressure coefficient "time" histories at Re = 1.5 x 10^6.

STATIC CHORDWISE CP DISTRIBUTION FOR THE NACA 23012

RUN REFERENCE NUMBER: 231 DATE OF TEST: 4/ 7/83

REYNOLDS NUMBER= 2014476. MACH NUMBER= 0.149

DYNAMIC PRESSURE= 1738.46 N/sq.M AIR TEMPERATURE= 29.0 Deg.C

NUMBER OF CYCLES= 1 SAMPLING FREQUENCY= 100.0 Hz.

DATA PRODUCED BY STANDARD STATIC TEST VERSION 1.3

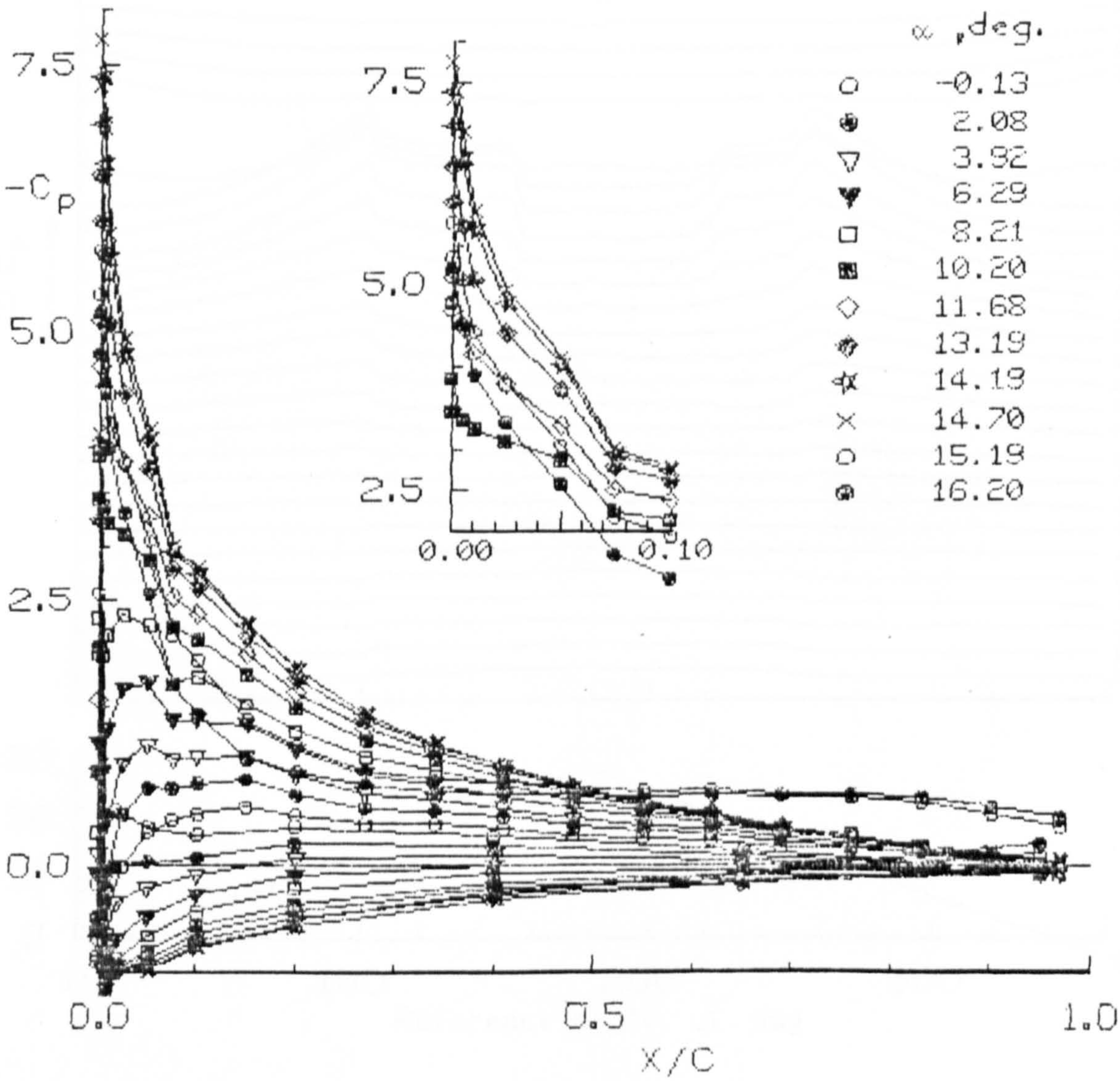

Figure 6.14 Chordwise pressure distributions for various angles of attack at Re = 2.0 x 10^6.

STATIC CP TIME HISTORIES FOR THE NACA 23012

RUN REFERENCE NUMBER: 231 DATE OF TEST: 4/ 7/83

REYNOLDS NUMBER= 2014476. MACH NUMBER= 0.149

DYNAMIC PRESSURE= 1738.46 N/sq.M AIR TEMPERATURE= 29.0 Deg.C

NUMBER OF CYCLES= 1 SAMPLING FREQUENCY= 100.0 Hz.

DATA PRODUCED BY STANDARD STATIC TEST VERSION 1.3

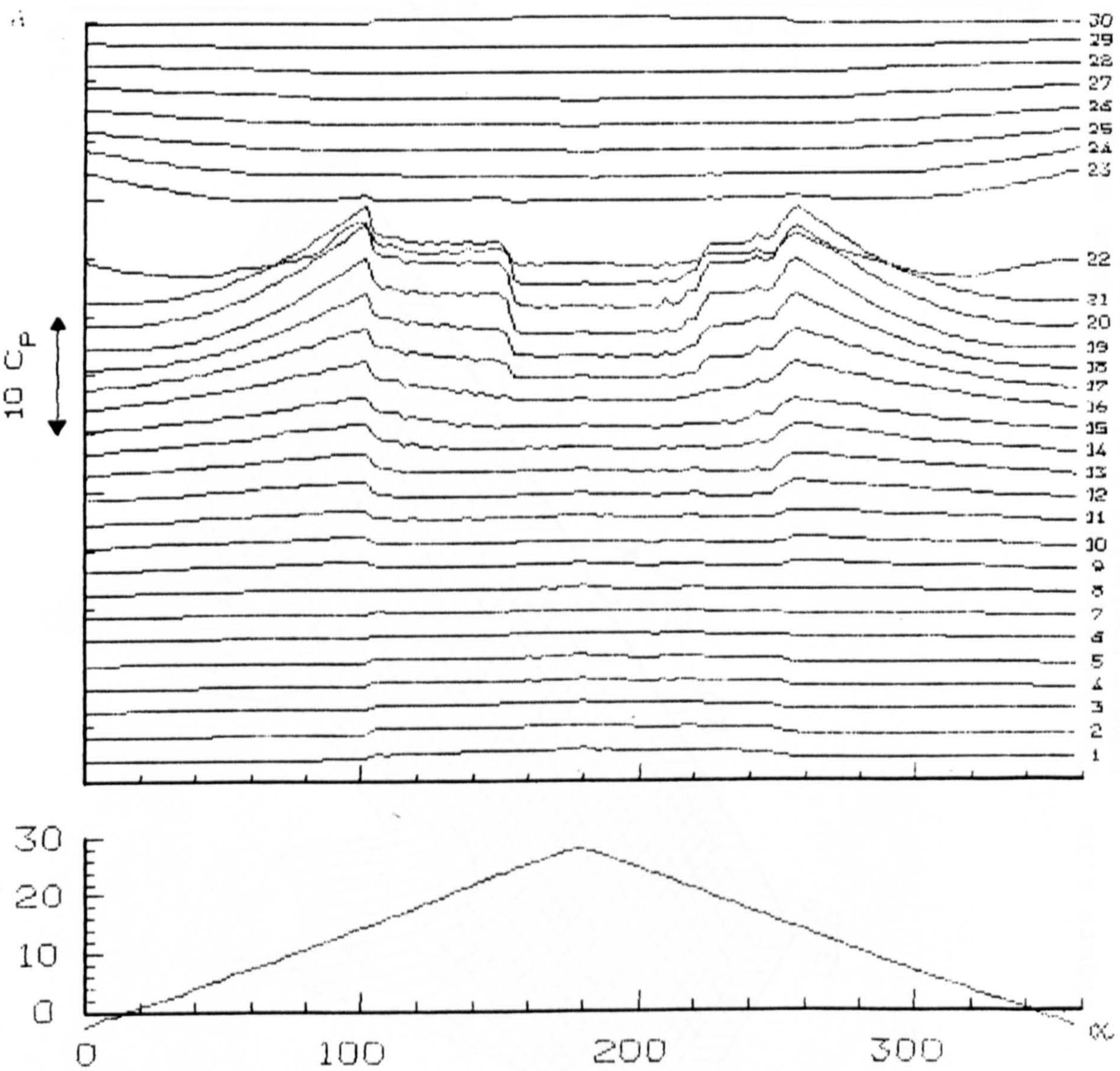

Figure 6.15 Pressure coefficient "time" histories at Re = 2.0 x 10^6.

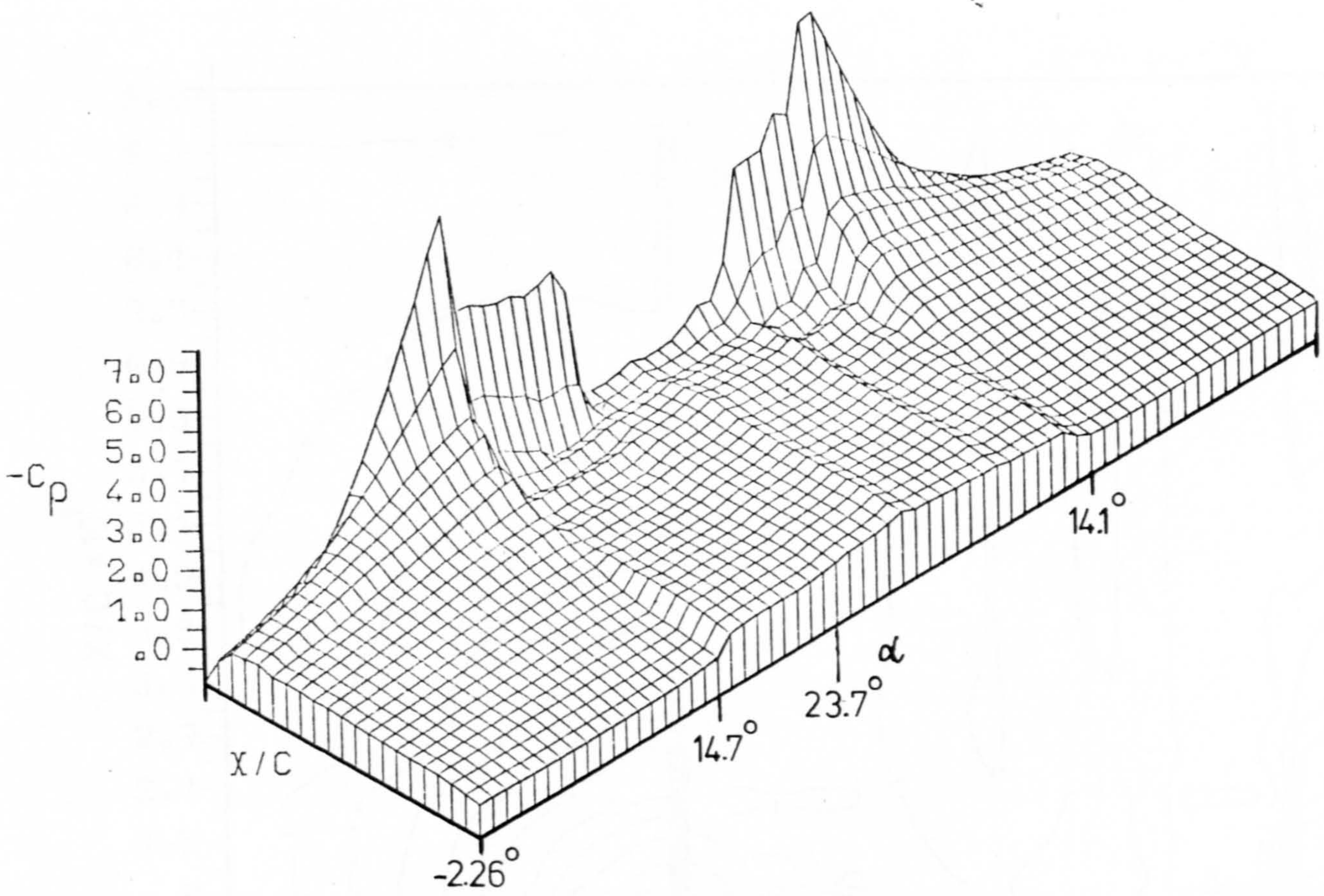

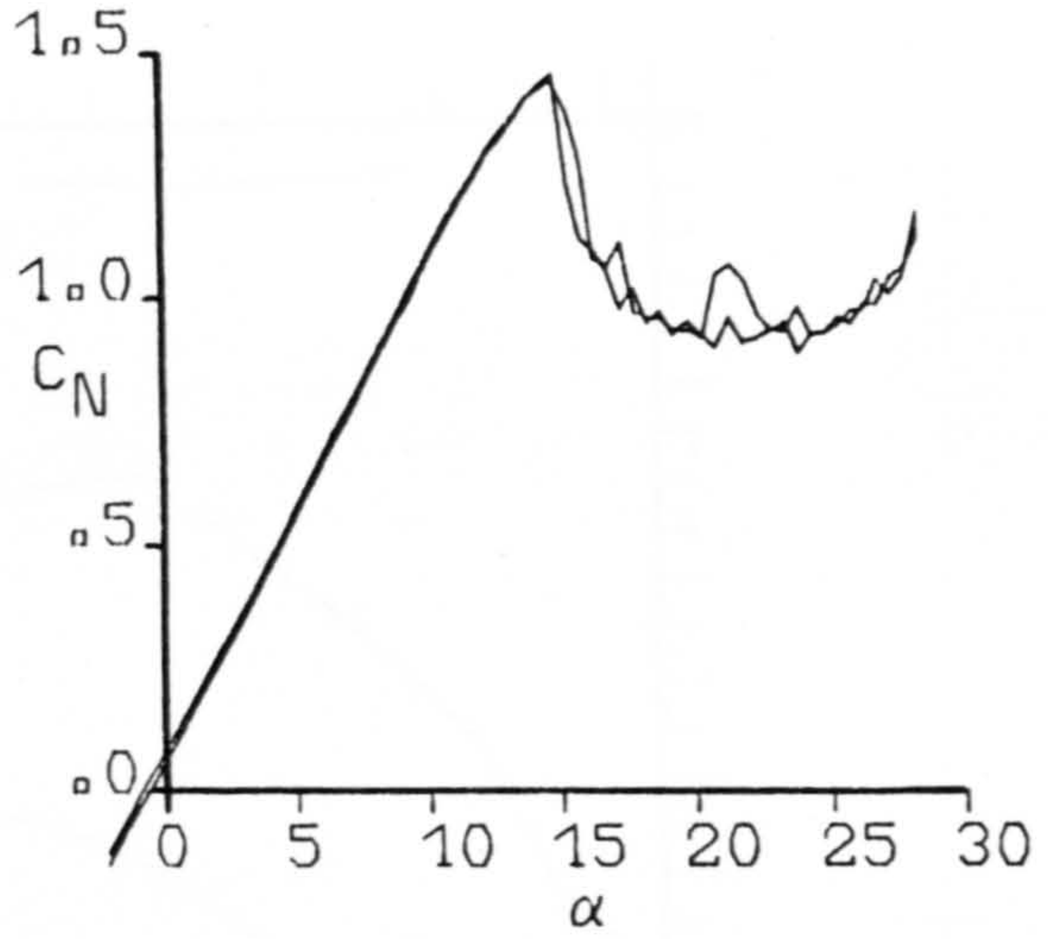

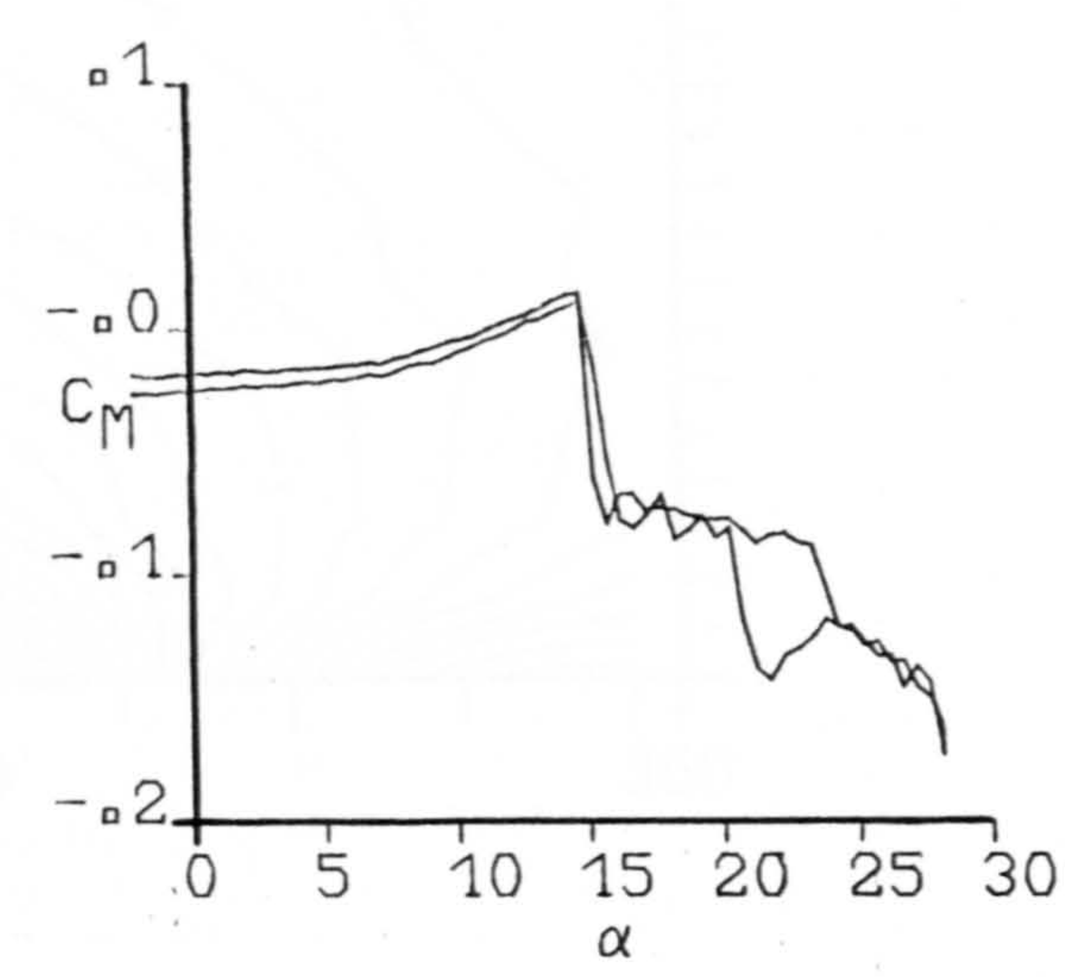

Figure 6.16 Chordwise pressures, normal force and pitching moment variation during a static run at Re = 2.0×10^6.

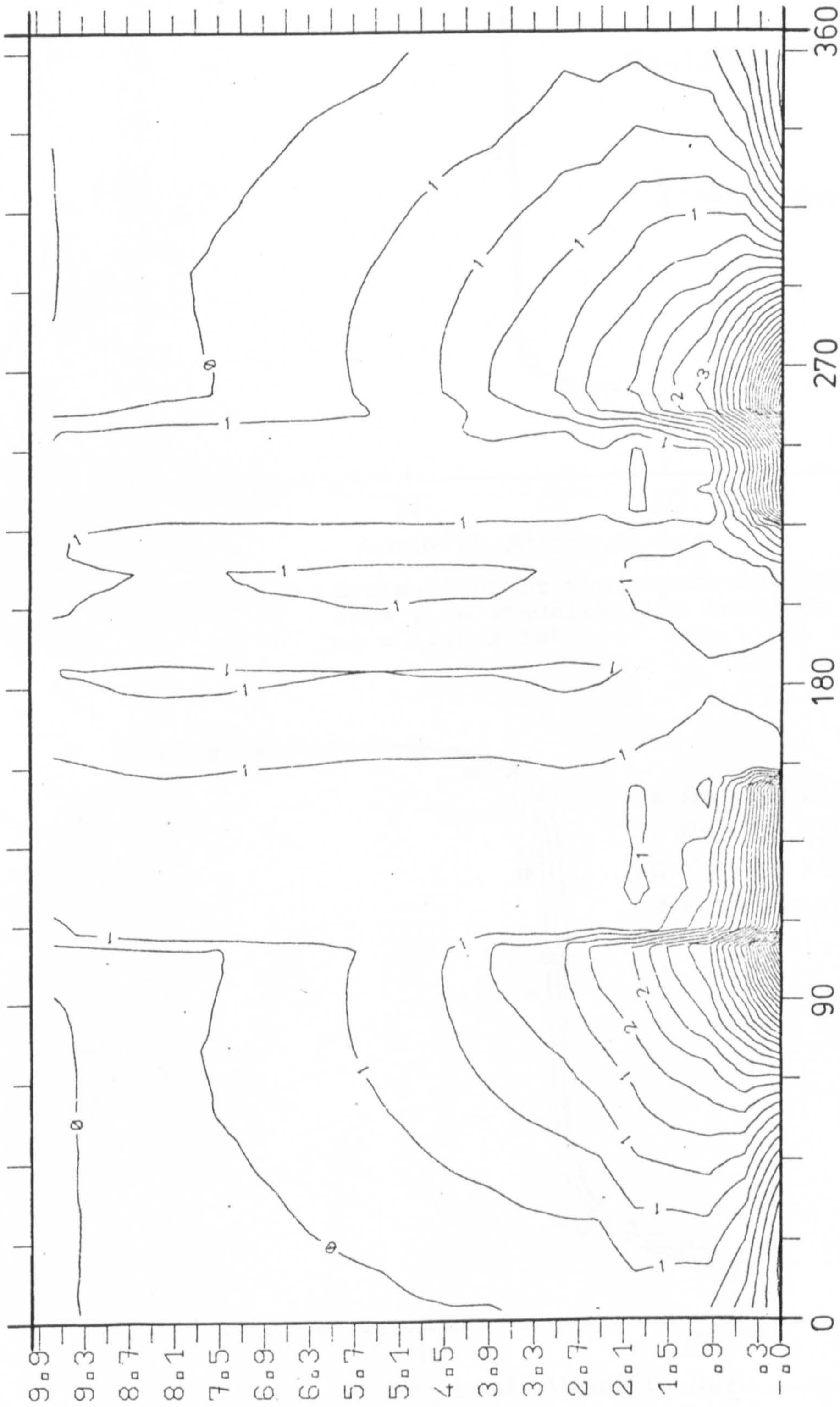

Figure 6.17 Contours of equal pressure on the aerofoil upper surface during a static test at Re = 1.5 x 10⁶

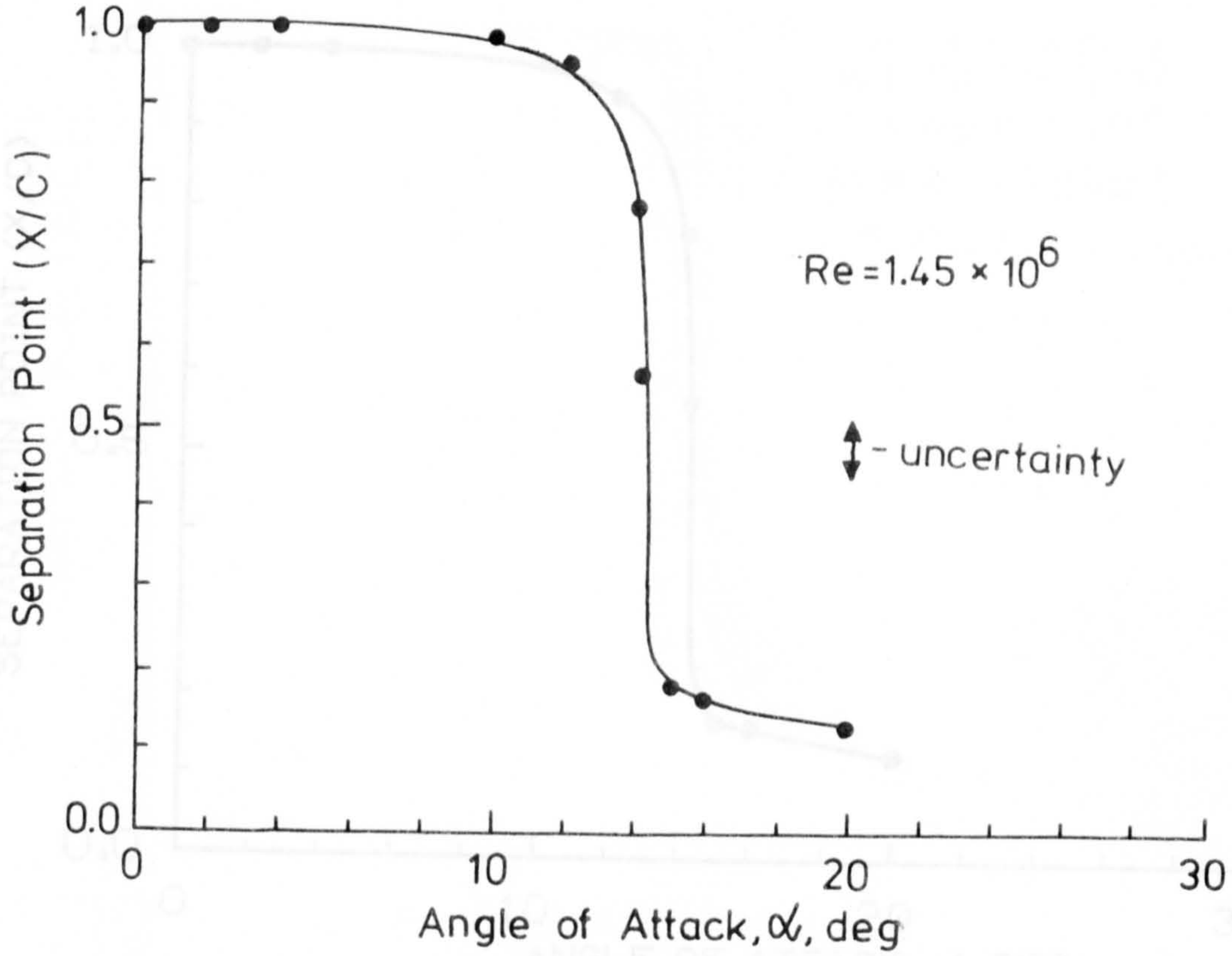

Fig 6.18 Estimations of the separation point from flow visualisation tests at Re = 1.45 x 10^6

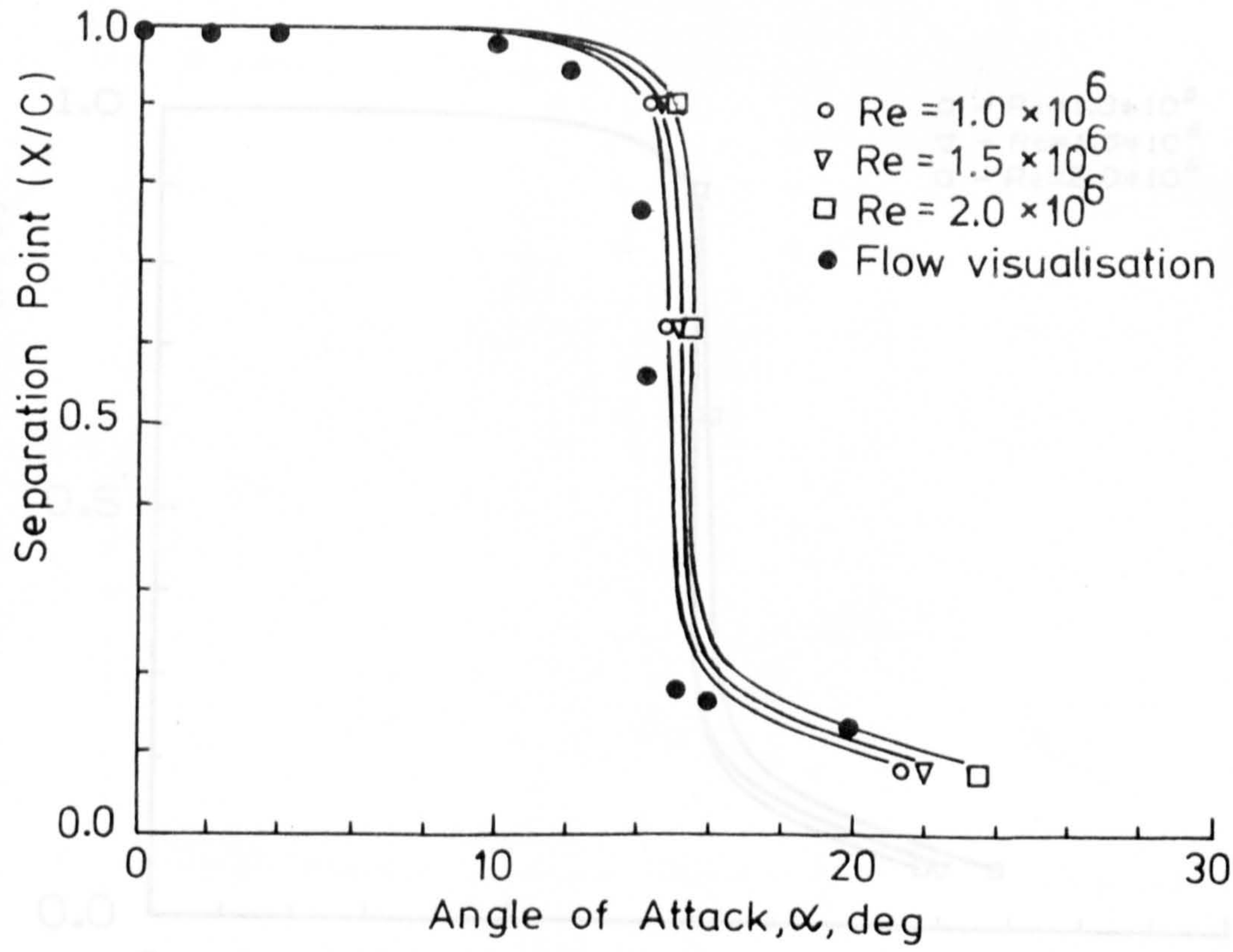

Fig 6.19 Locus of separation point estimations from hot-film interpretations at various Reynolds numbers.

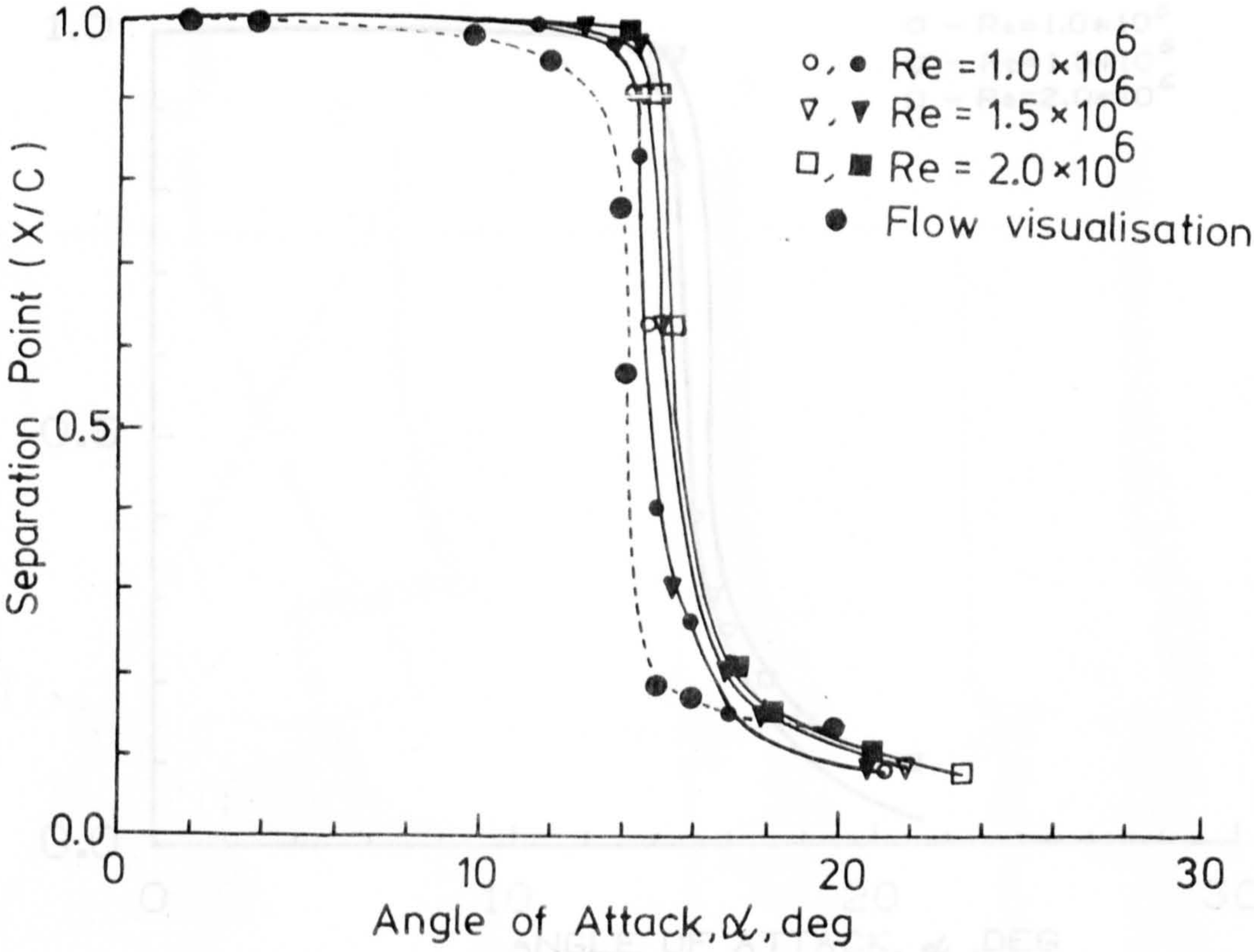

Fig 6.20 Locus of separation point estimations from both hot-film and pressure responses at various Reynolds numbers.

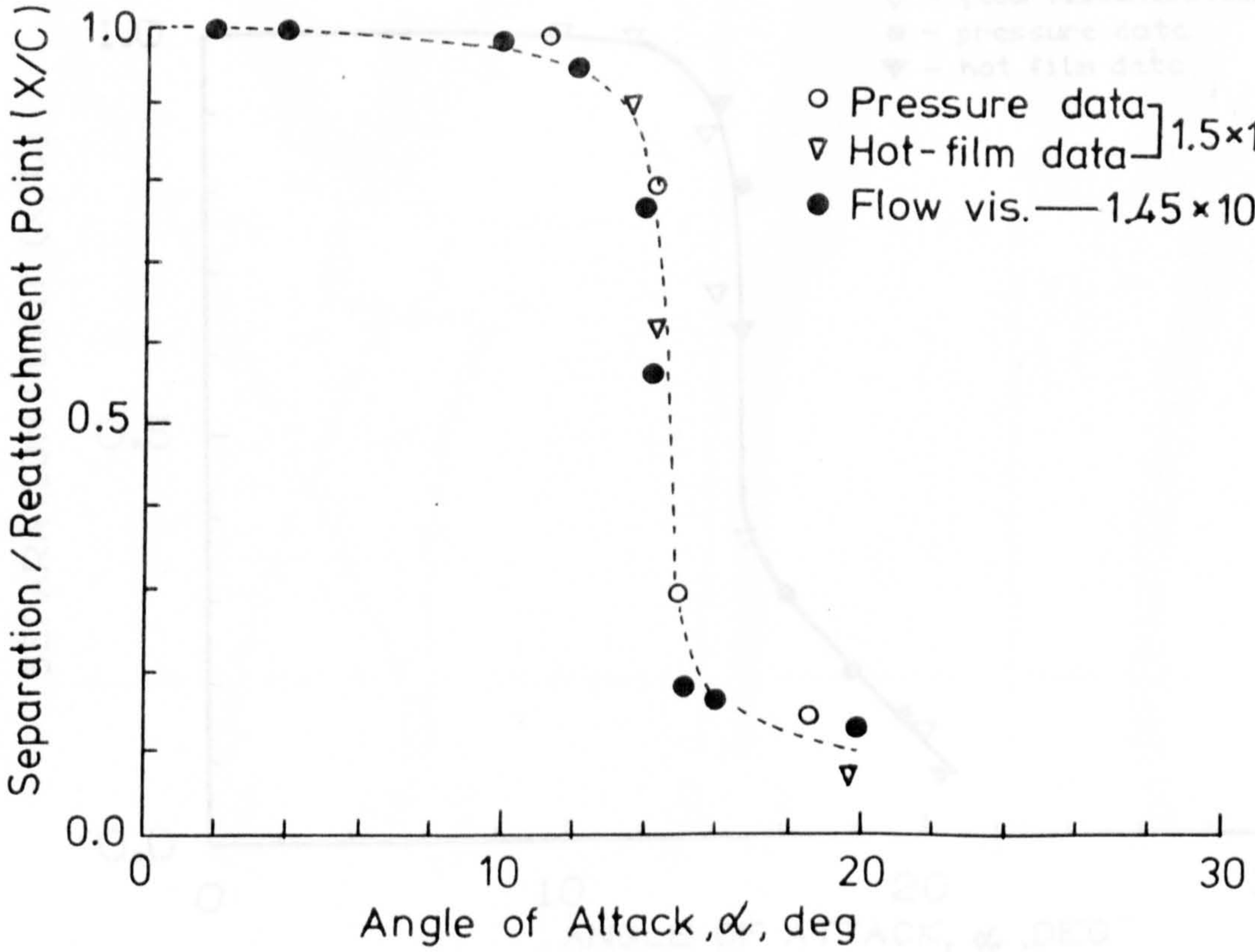

Fig 6.21 Comparison of flow reattachment point estimations at Re = 1.5 x 10^6 with flow visualisation separation point estimations at Re = 1.45 x 10^6.

Figure 6.22 Typical hot-film record for a static run at Re = 1.5 x 10^6.

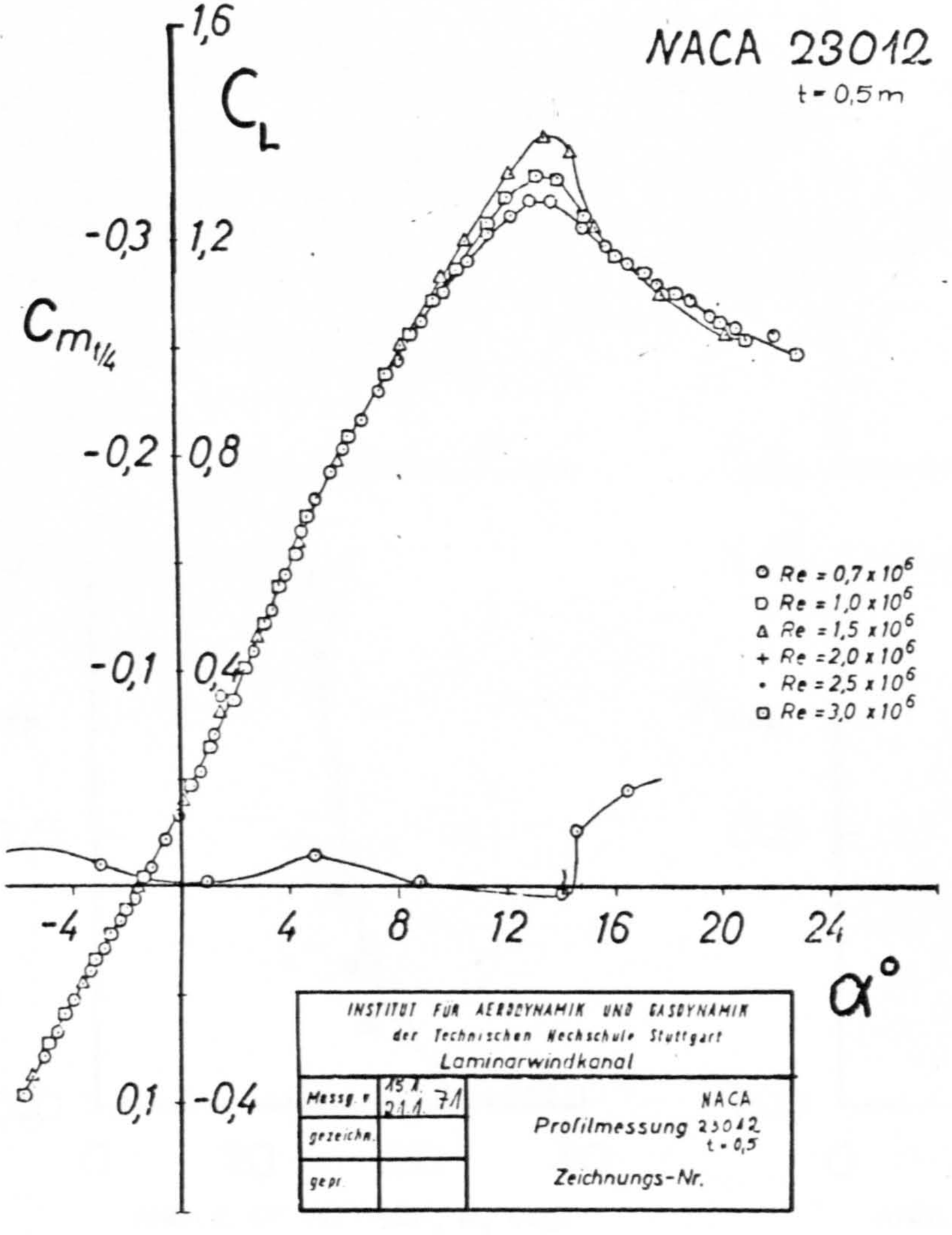

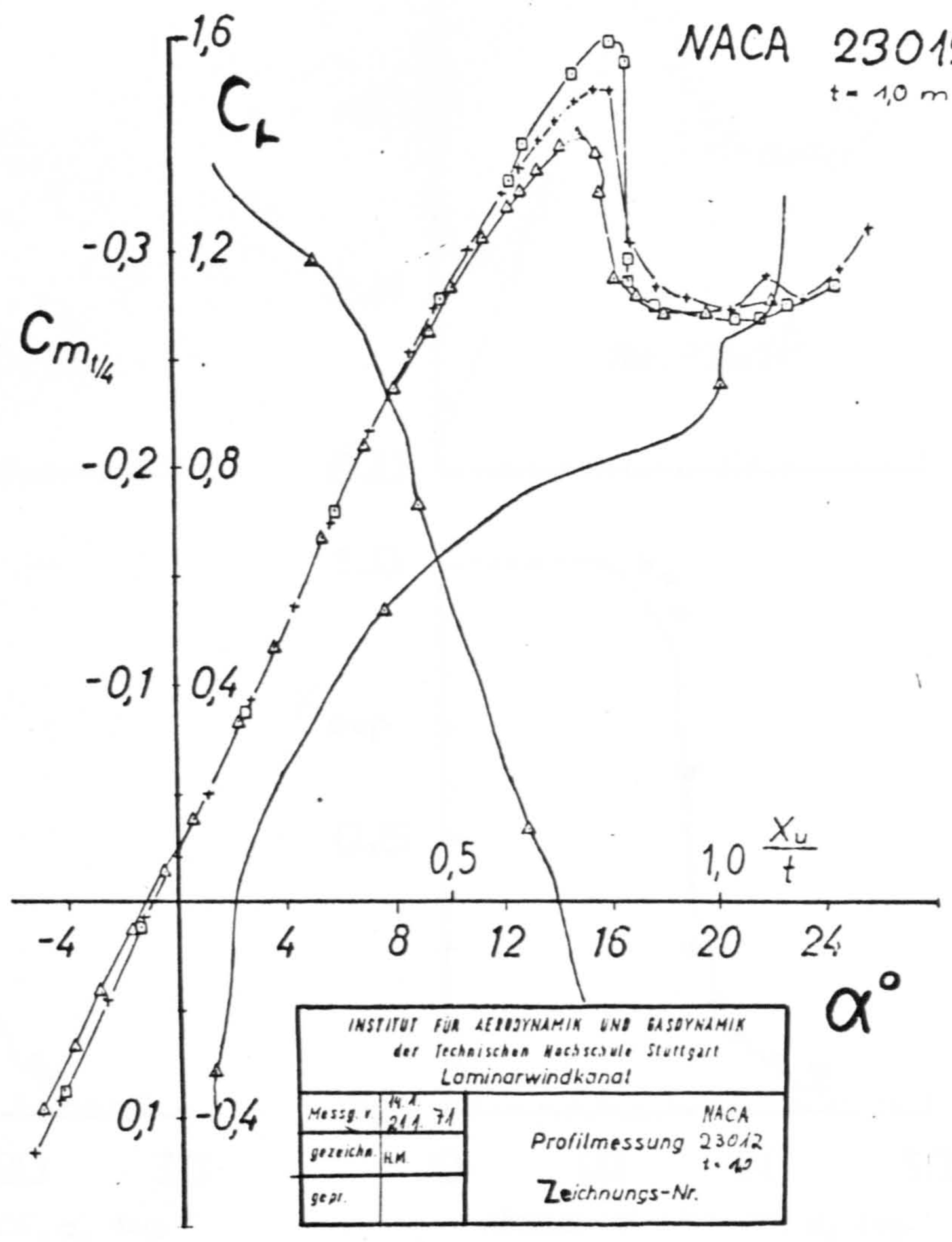

Figure 6.23 Lift and pitching moment data for the NACA 23012 aerofoil (from Althaus, 1980).

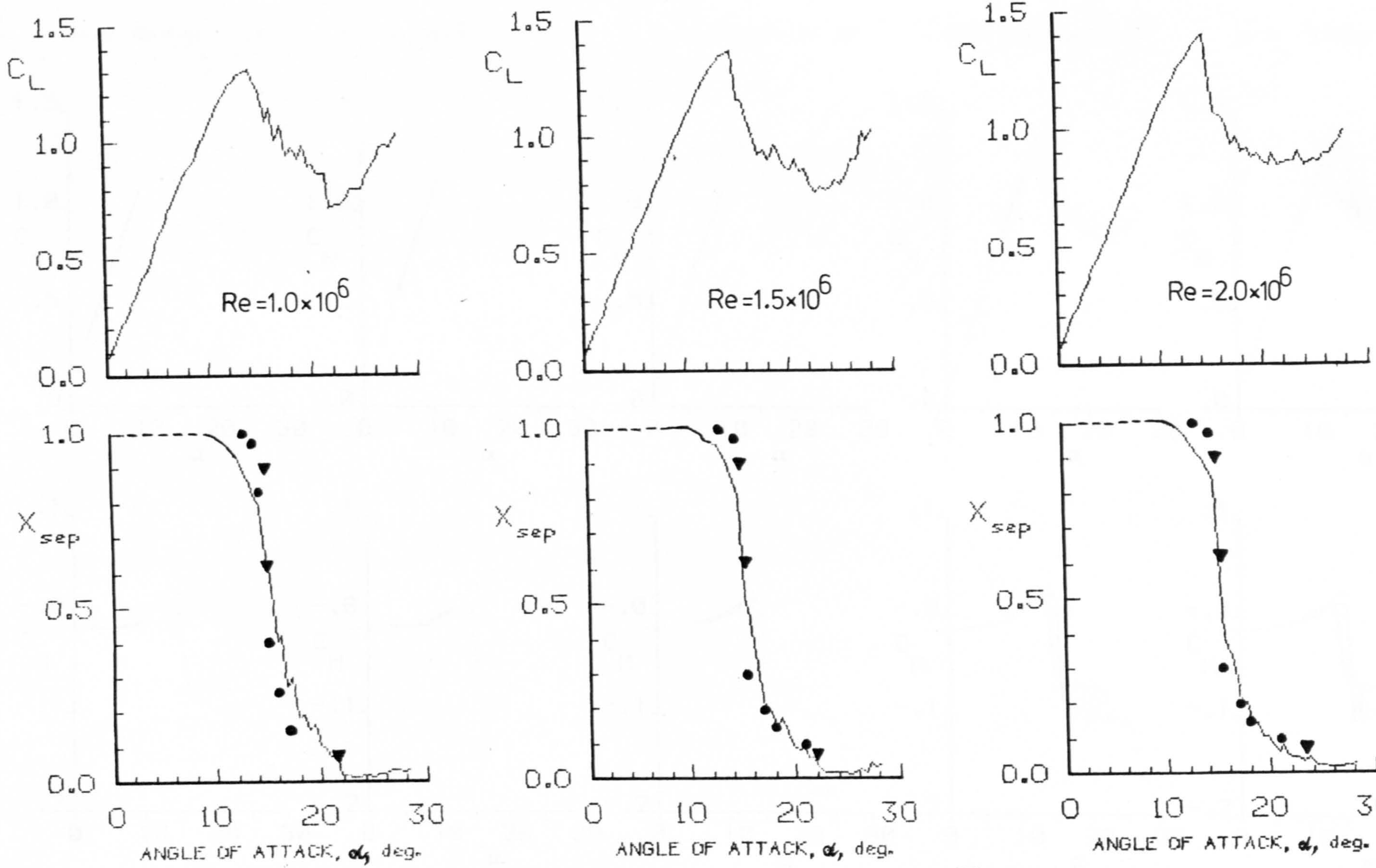

Figure 6.24 Calculations of separation point from Kirchoff theory and compared with pressure and hot-film separation estimations at various Reynolds numbers.

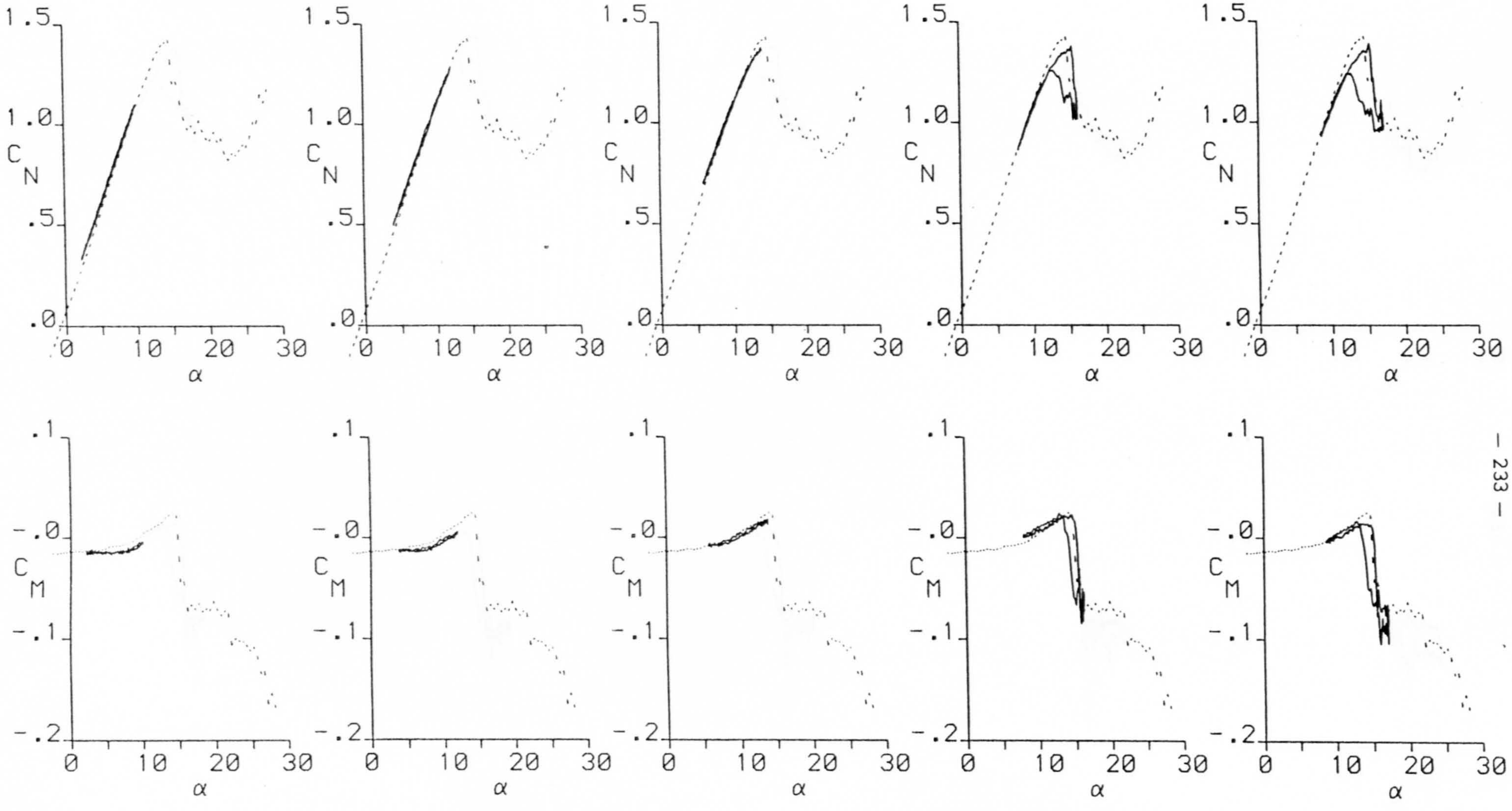

FIG.(7.1) EFFECT OF MEAN ANGLE VARIATION AT $\alpha_a = 4^\circ$ AND K= .01

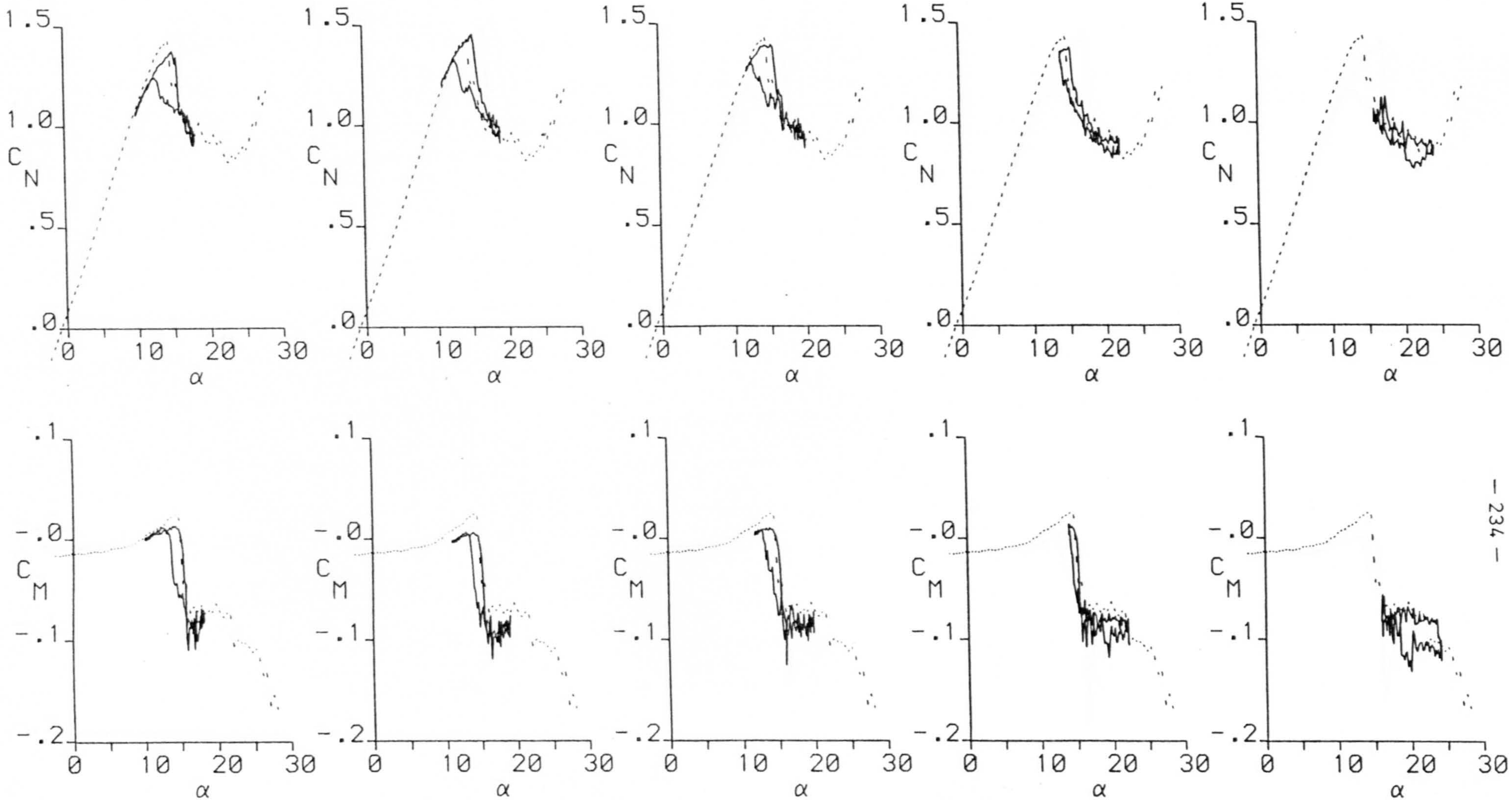

FIG.(7.2) EFFECT OF MEAN ANGLE VARIATION AT $\alpha_a = 4^\circ$ AND K= .01

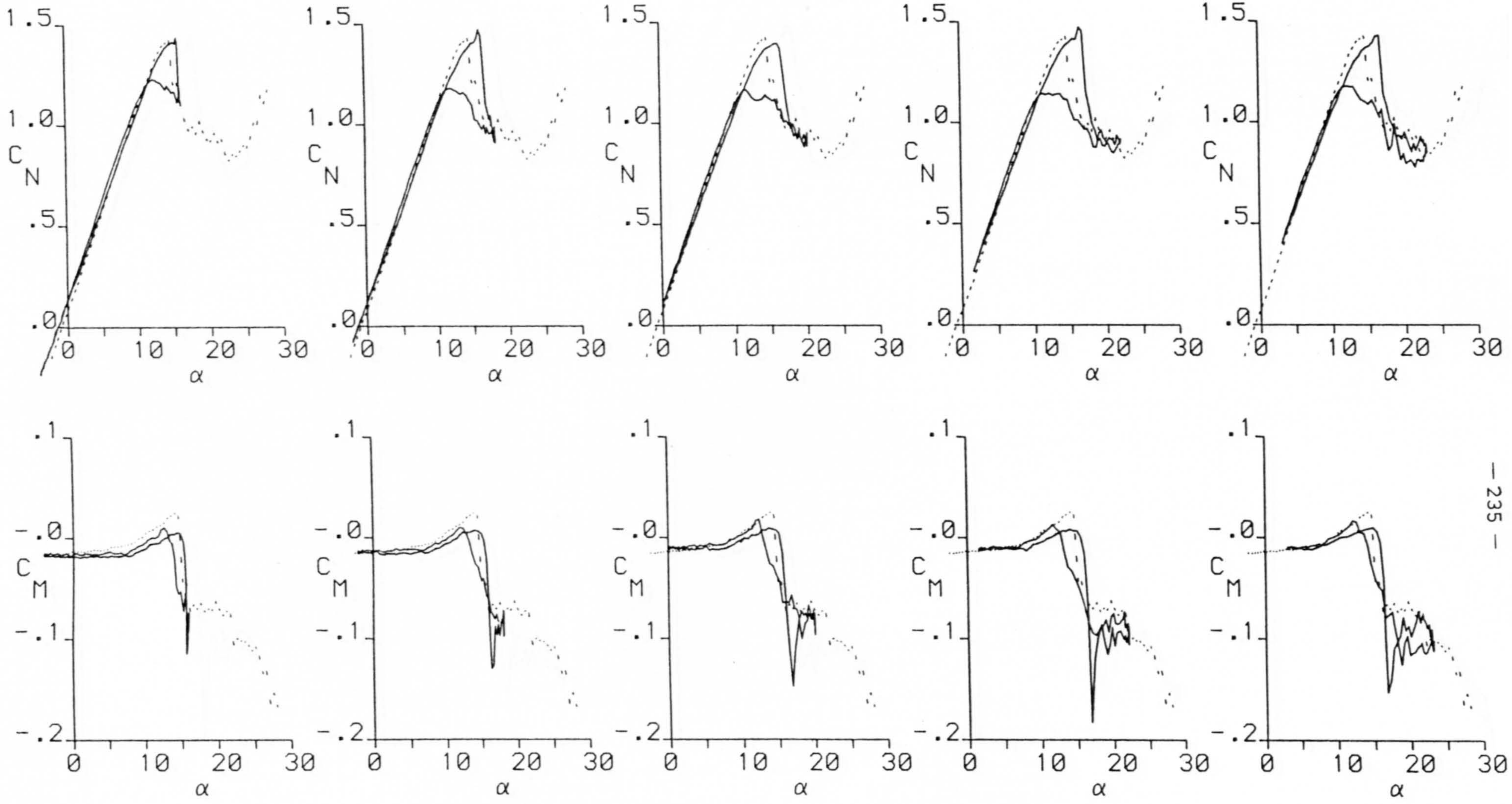

FIG.(7.3) EFFECT OF MEAN ANGLE VARIATION AT $\alpha_a = 10^{\circ}$ AND K= .01

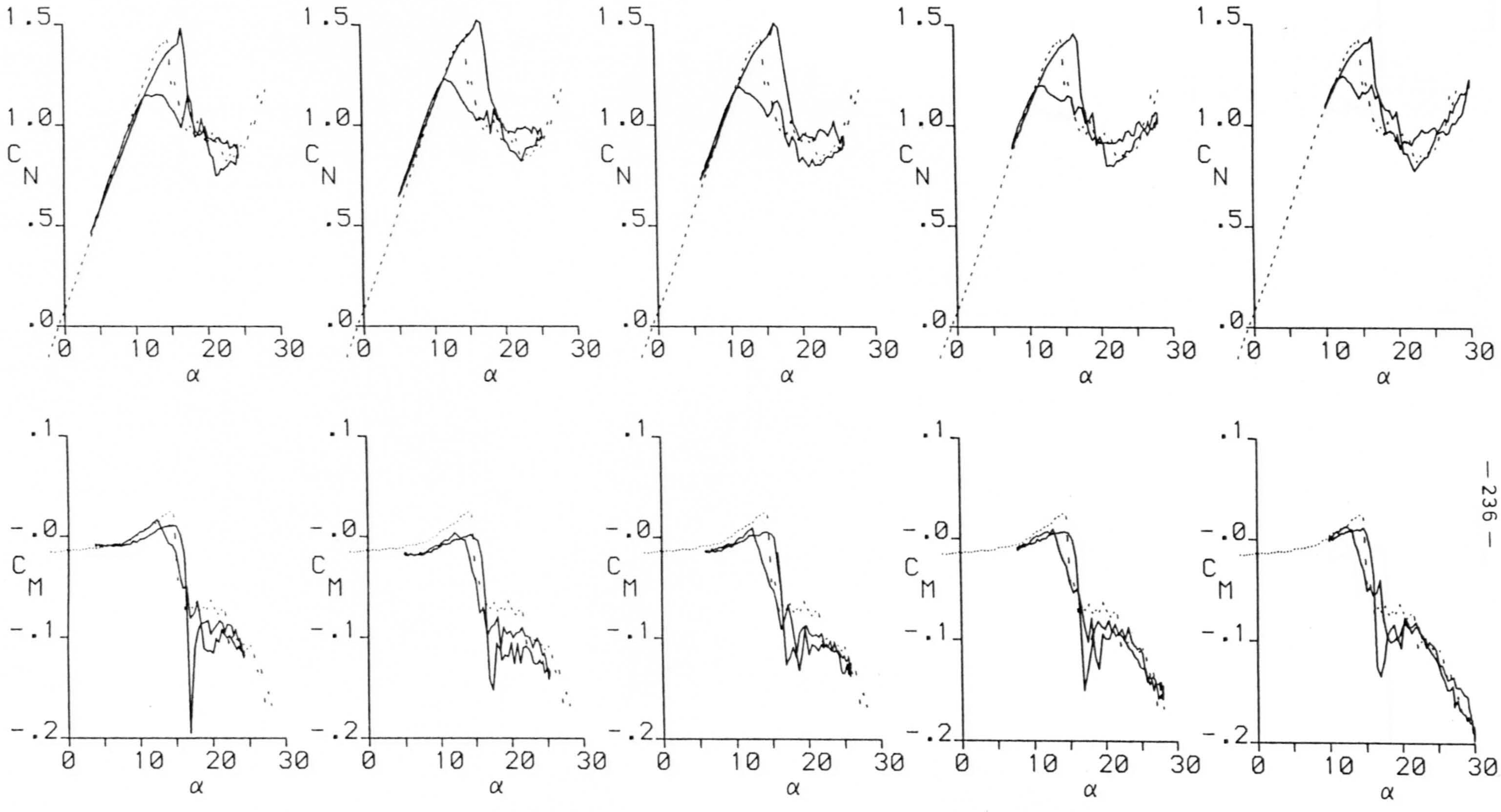

FIG.(7.4) EFFECT OF MEAN ANGLE VARIATION AT $\alpha_a = 10^\circ$ AND K= .01

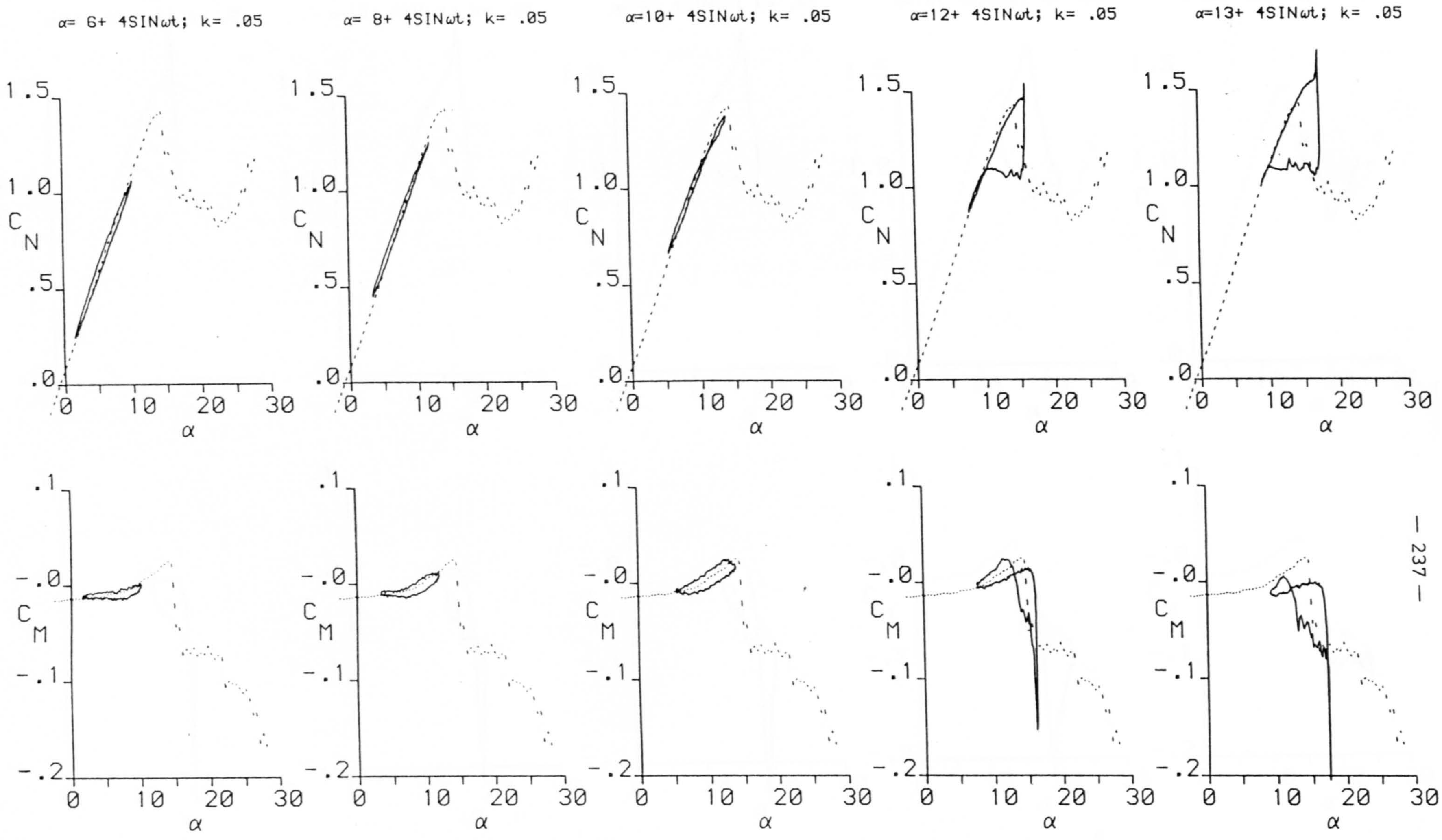

FIG.(7.5) EFFECT OF MEAN ANGLE OF ATTACK VARIATION AT $\alpha_a = 4^\circ$ AND K= .05

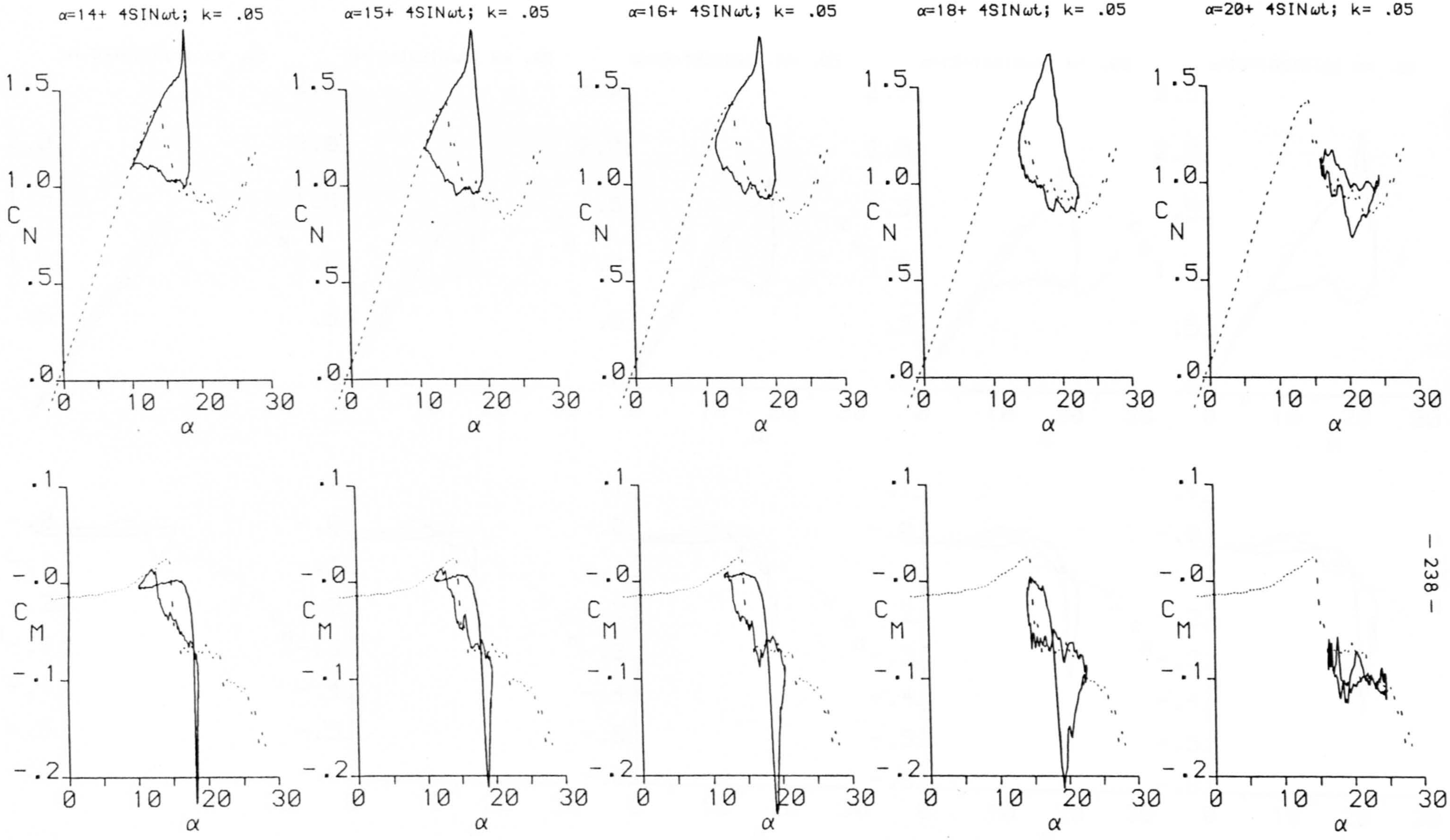

FIG.(7.6) EFFECT OF MEAN ANGLE OF ATTACK VARIATION AT $\alpha_a = 4^\circ$ AND K= .05

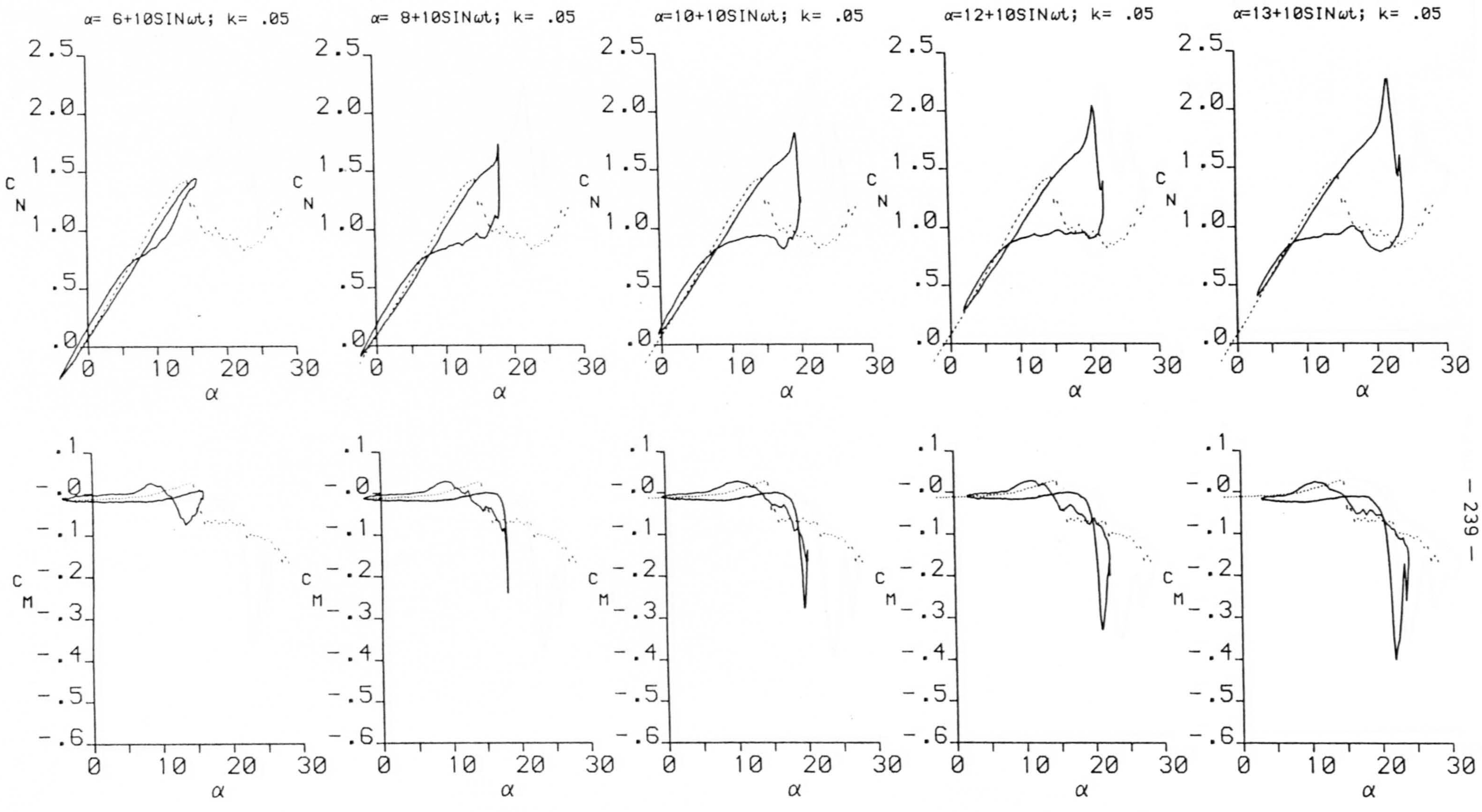

FIG.(**7.7**) EFFECT OF MEAN ANGLE OF ATTACK VARIATION AT $\alpha_a = 10^\circ$ AND K= .05

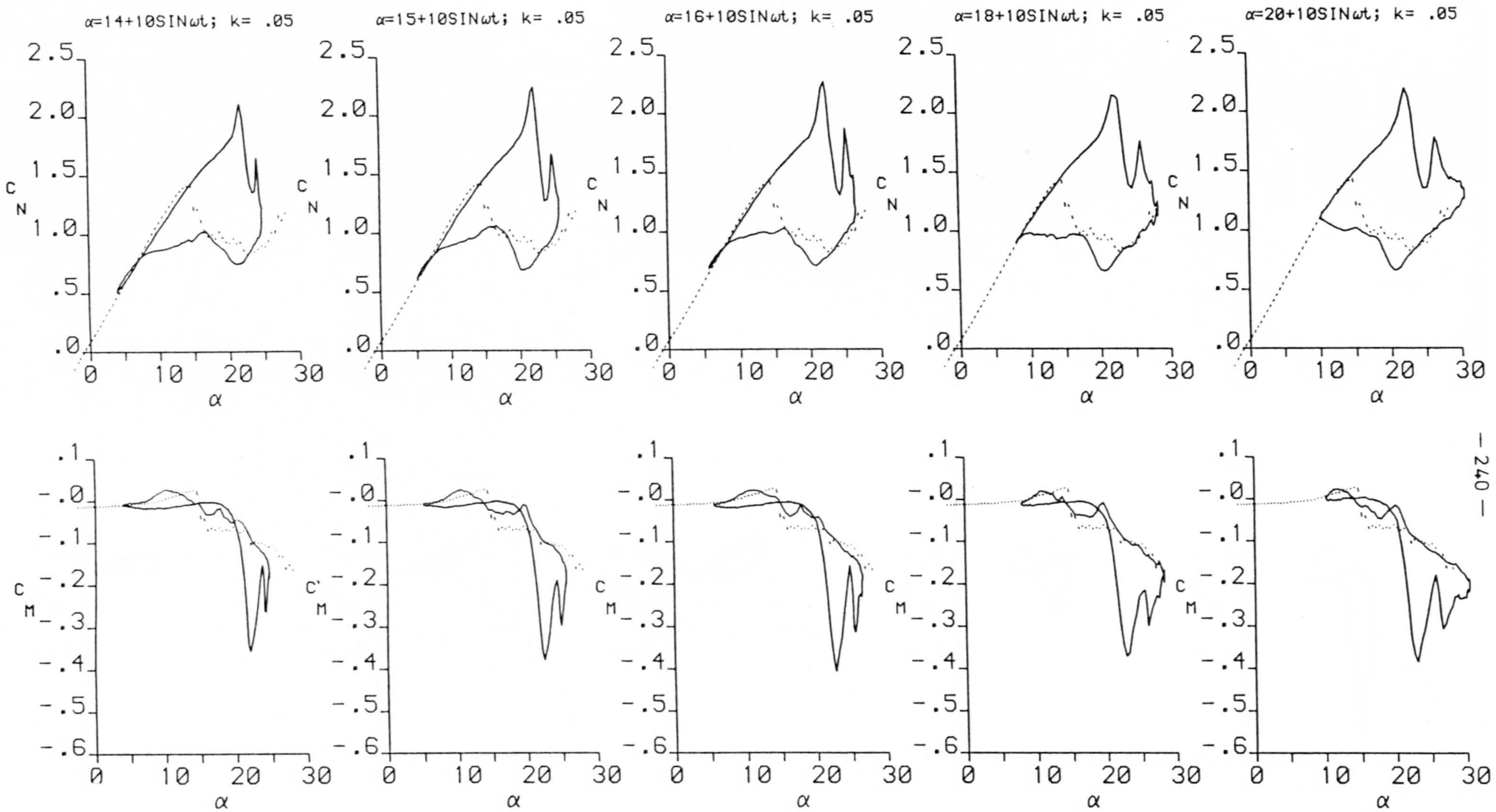

FIG.(7.8) EFFECT OF MEAN ANGLE OF ATTACK VARIATION AT $\alpha_a = 10^{\circ}$ AND K= .05

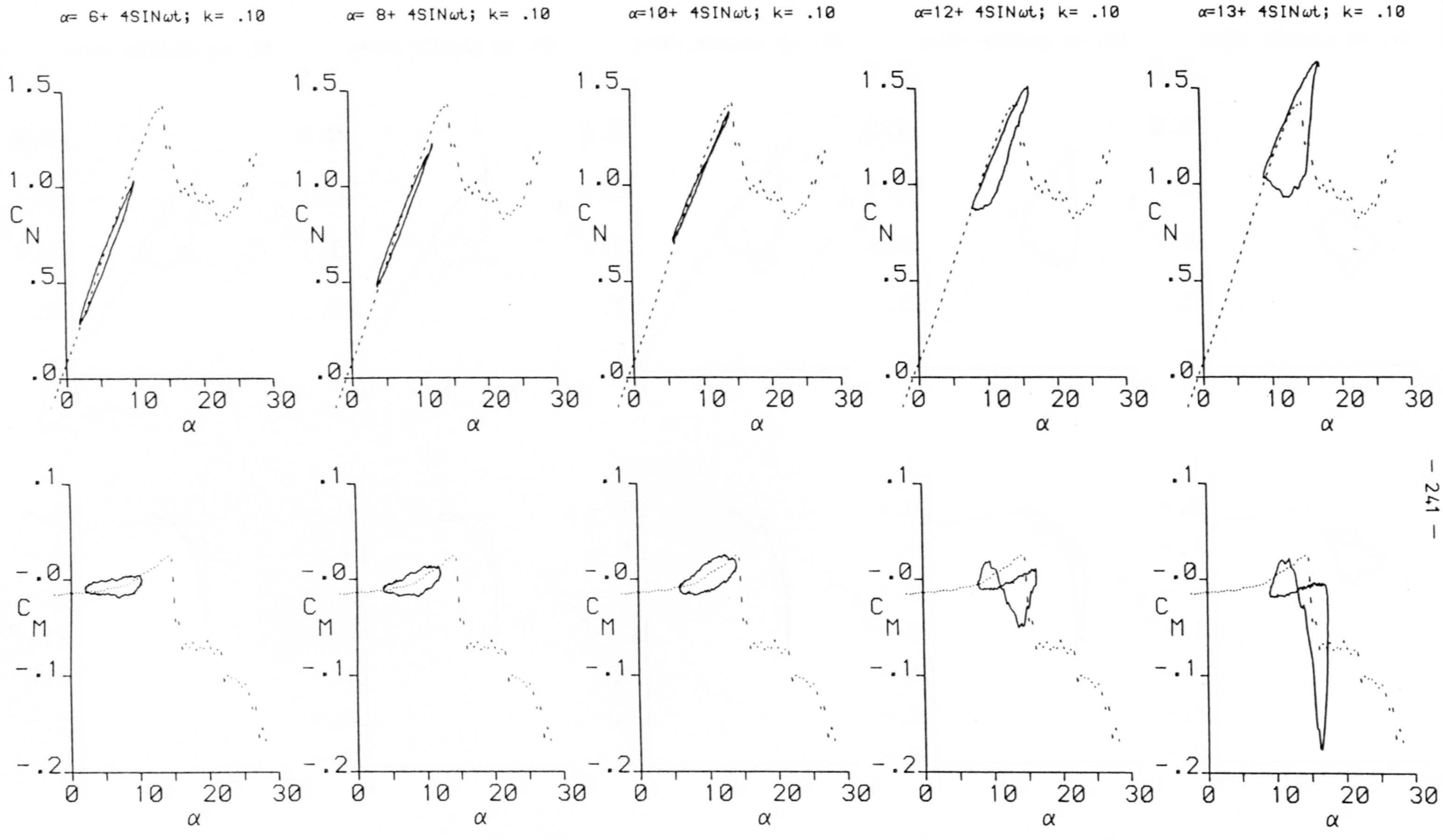

FIG.(7.9) EFFECT OF MEAN ANGLE OF ATTACK VARIATION AT $\alpha_a = 4^\circ$ AND K= .10

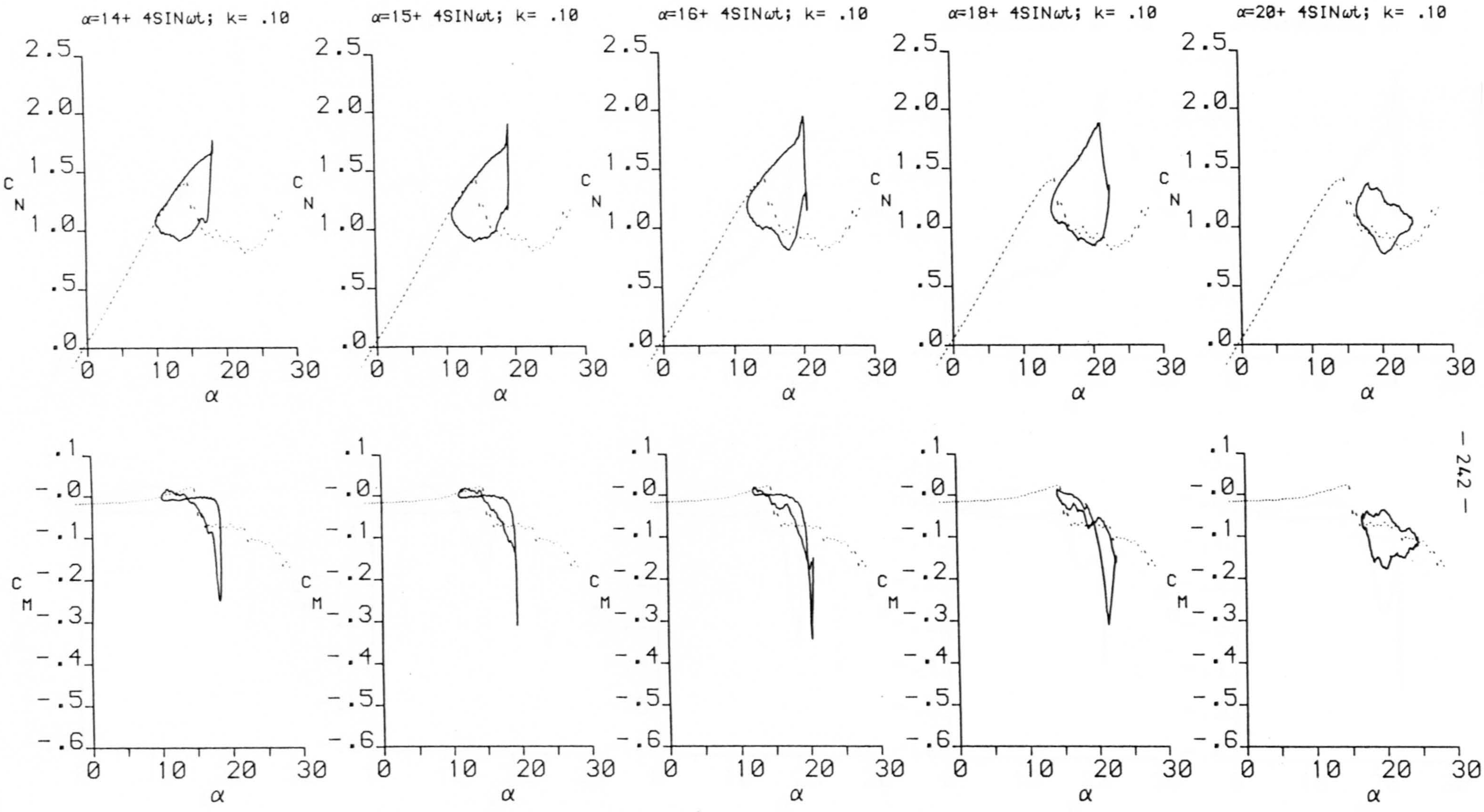

FIG.(7.10) EFFECT OF MEAN ANGLE OF ATTACK VARIATION AT $\alpha_a = 4^\circ$ AND K= .10

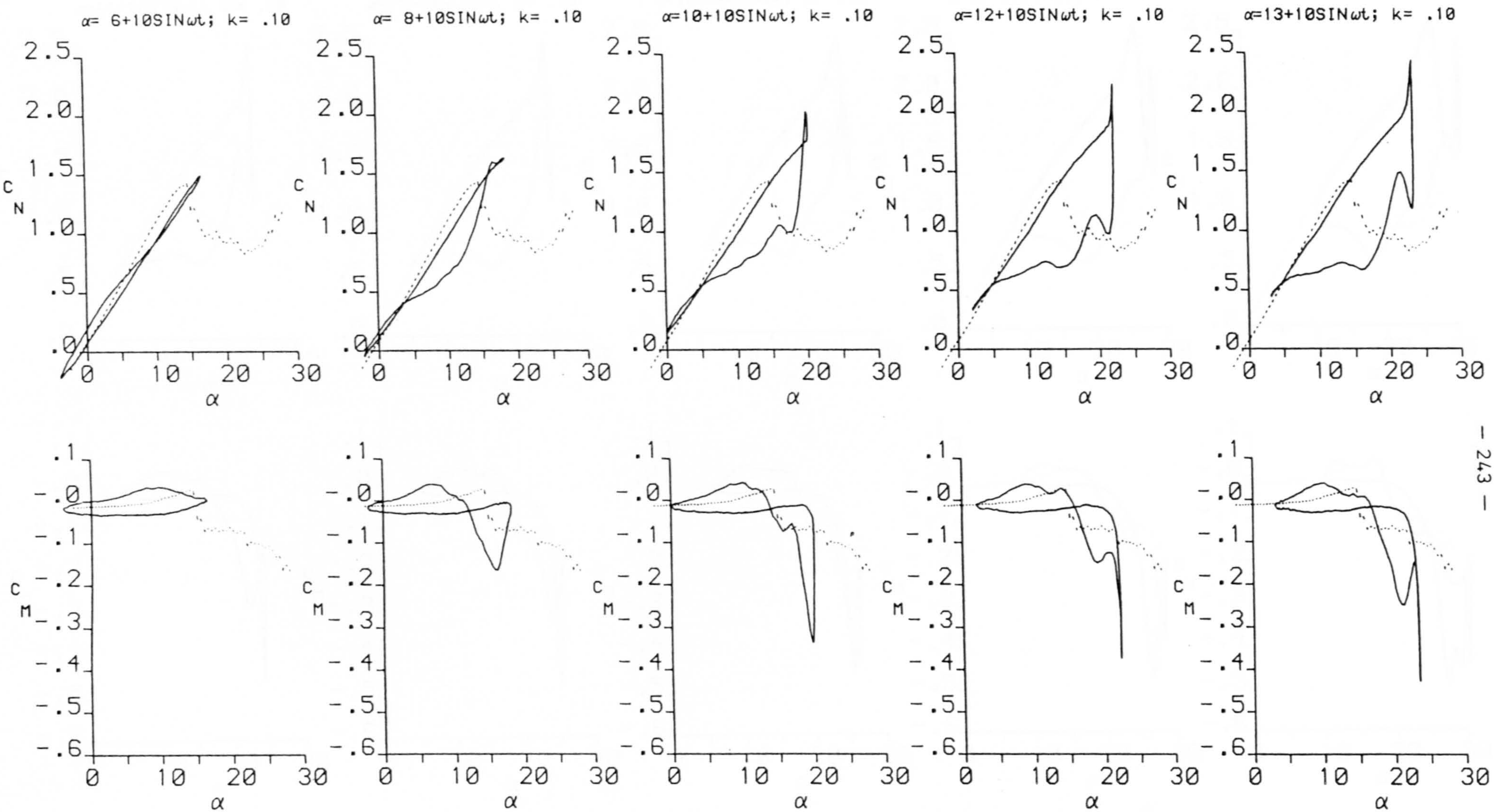

FIG.(7.11) EFFECT OF MEAN ANGLE OF ATTACK VARIATION AT $\alpha_a = 10^{\circ}$ AND K= .10

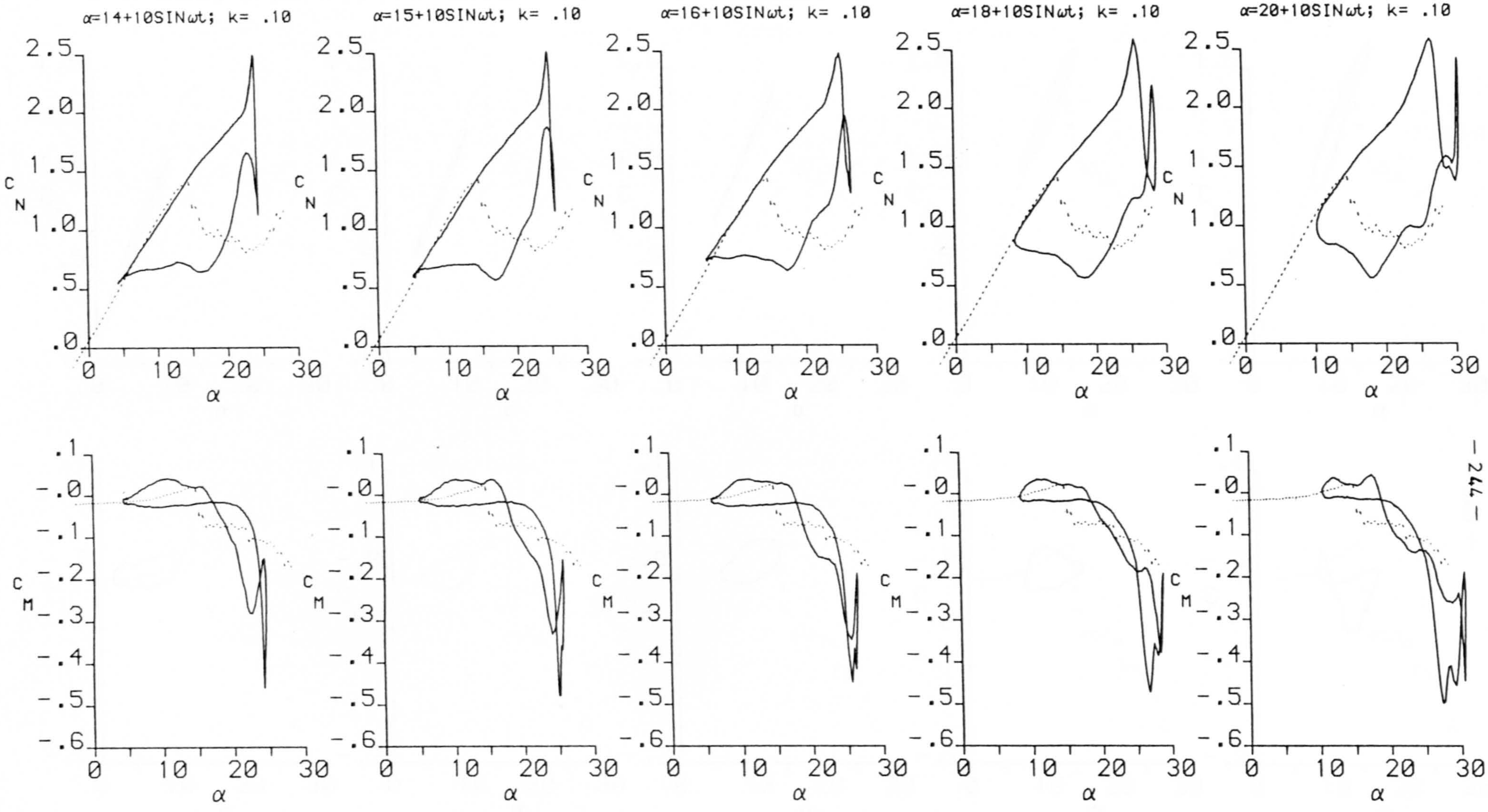

FIG.(7.12) EFFECT OF MEAN ANGLE OF ATTACK VARIATION AT α_a =10° AND K= .10

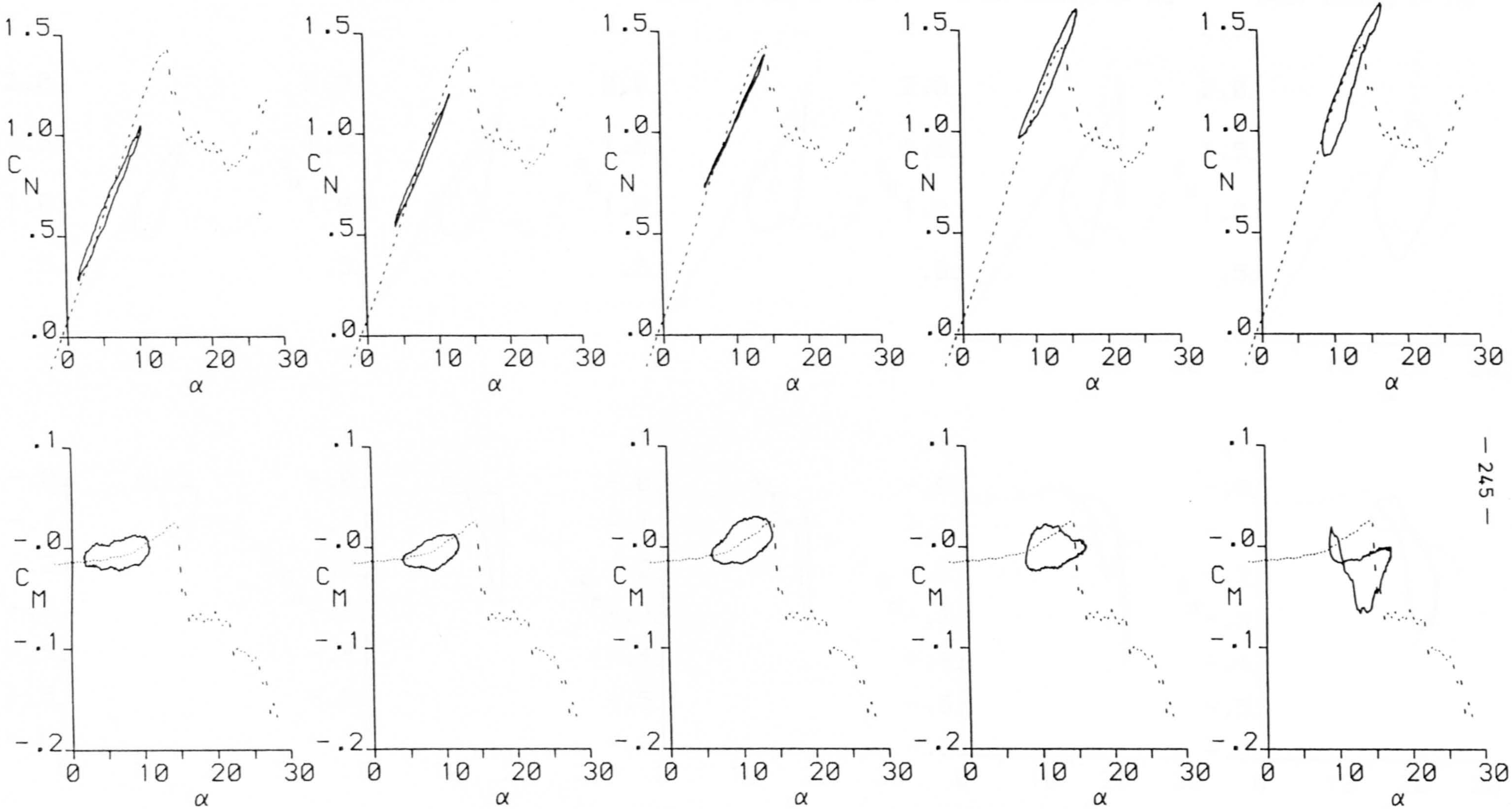

FIG.(7.13) EFFECT OF MEAN ANGLE OF ATTACK VARIATION AT $\alpha_a = 4^\circ$ AND K= .15

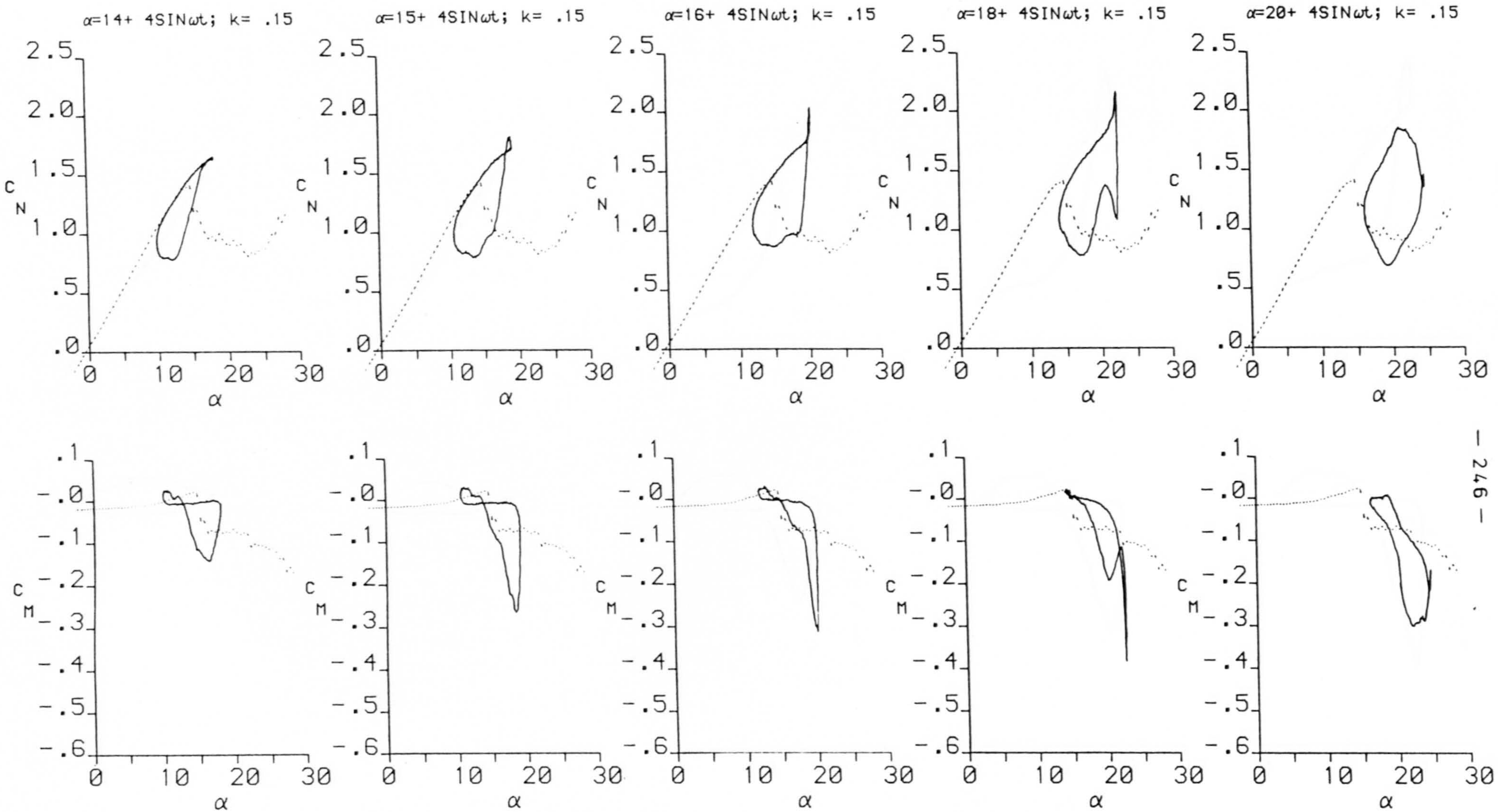

FIG.(7.14) EFFECT OF MEAN ANGLE OF ATTACK VARIATION AT $\alpha_a = 4^\circ$ AND K= .15

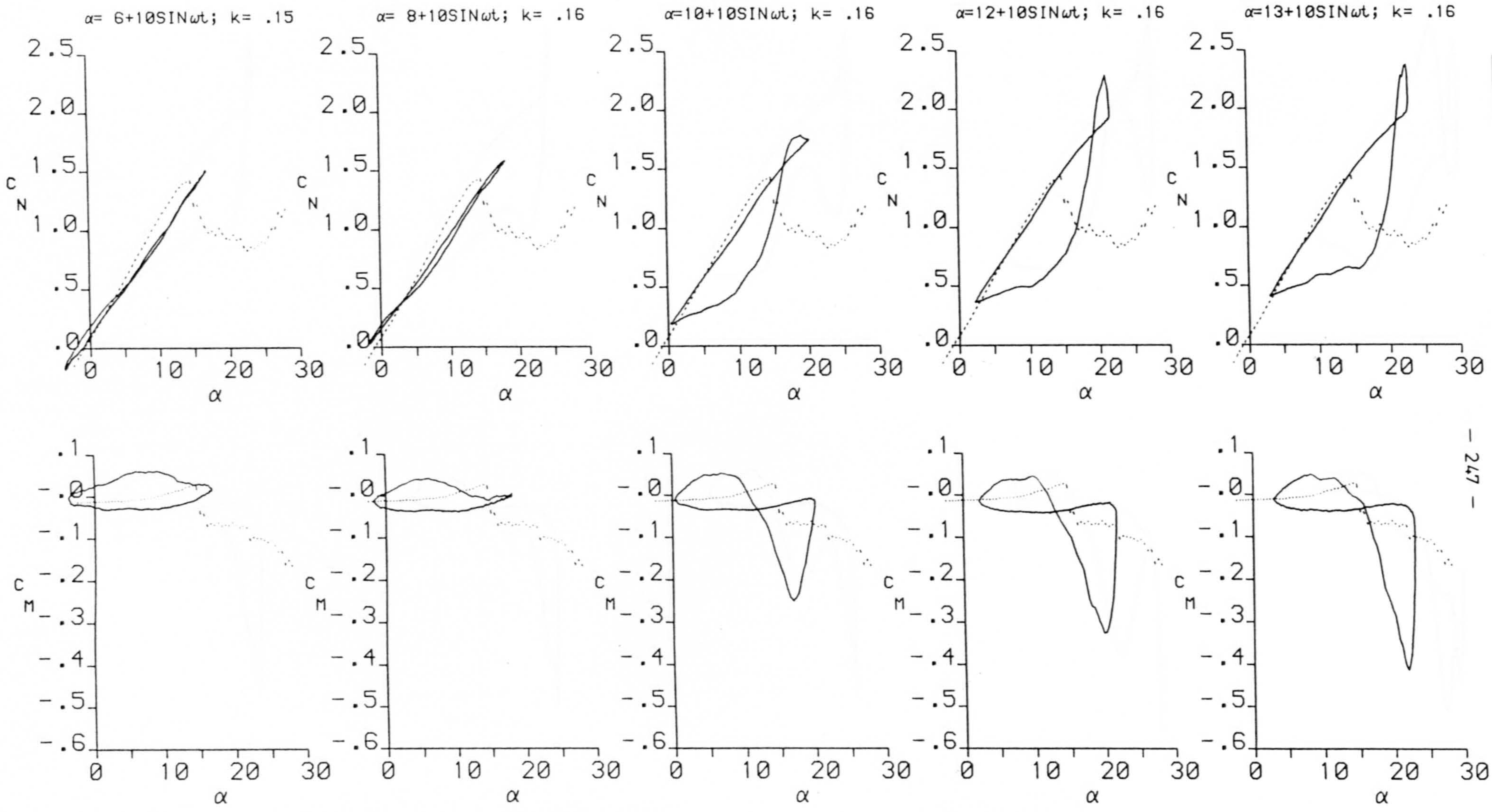

FIG.(7.15) EFFECT OF MEAN ANGLE OF ATTACK VARIATION AT α_a =10° AND K= .15

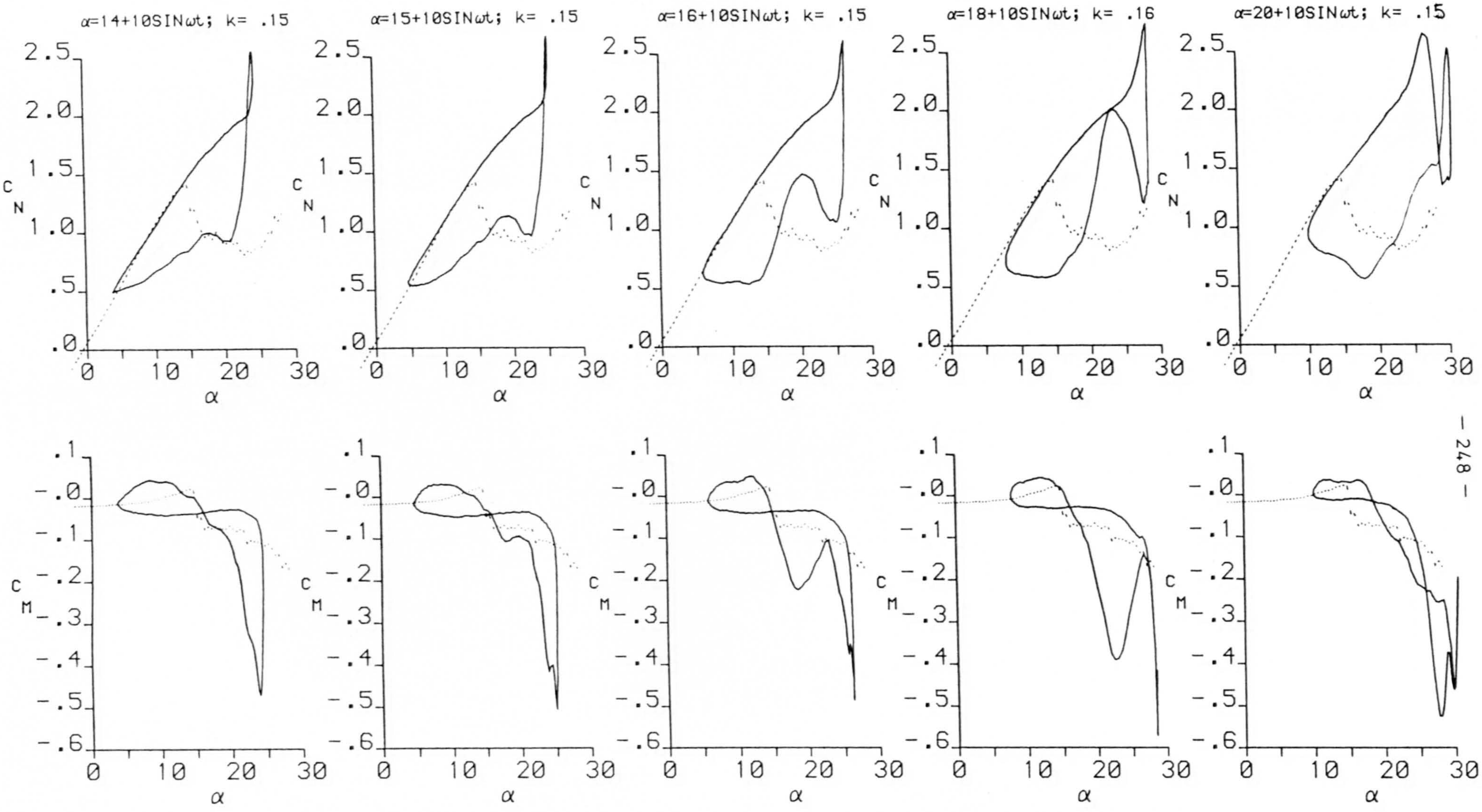

FIG.(7.16) EFFECT OF MEAN ANGLE OF ATTACK VARIATION AT $\alpha_a = 10^\circ$ AND K= .15

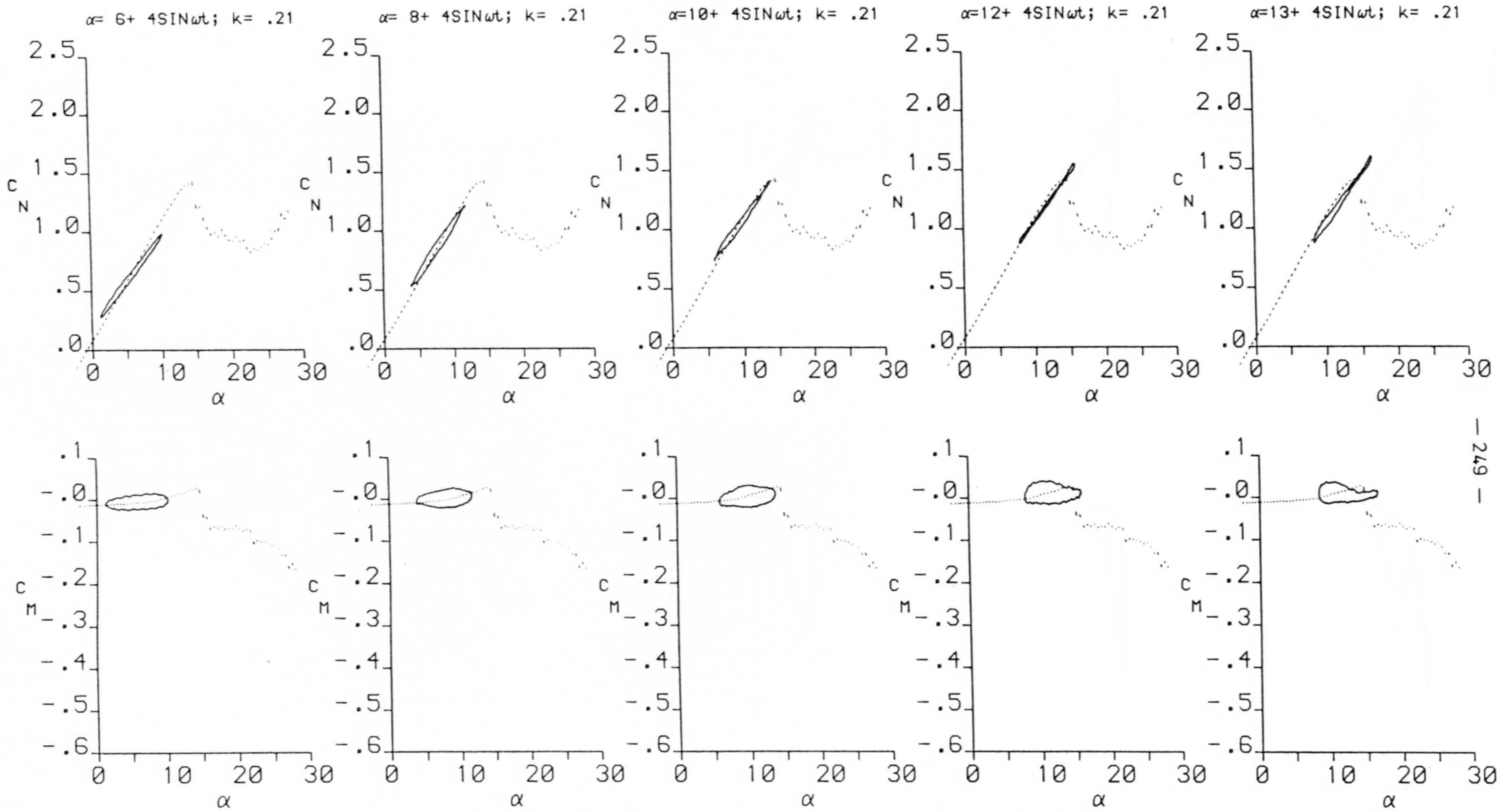

FIG.(7.17) EFFECT OF MEAN ANGLE OF ATTACK VARIATION AT $\alpha_a = 4^\circ$ AND K= .21

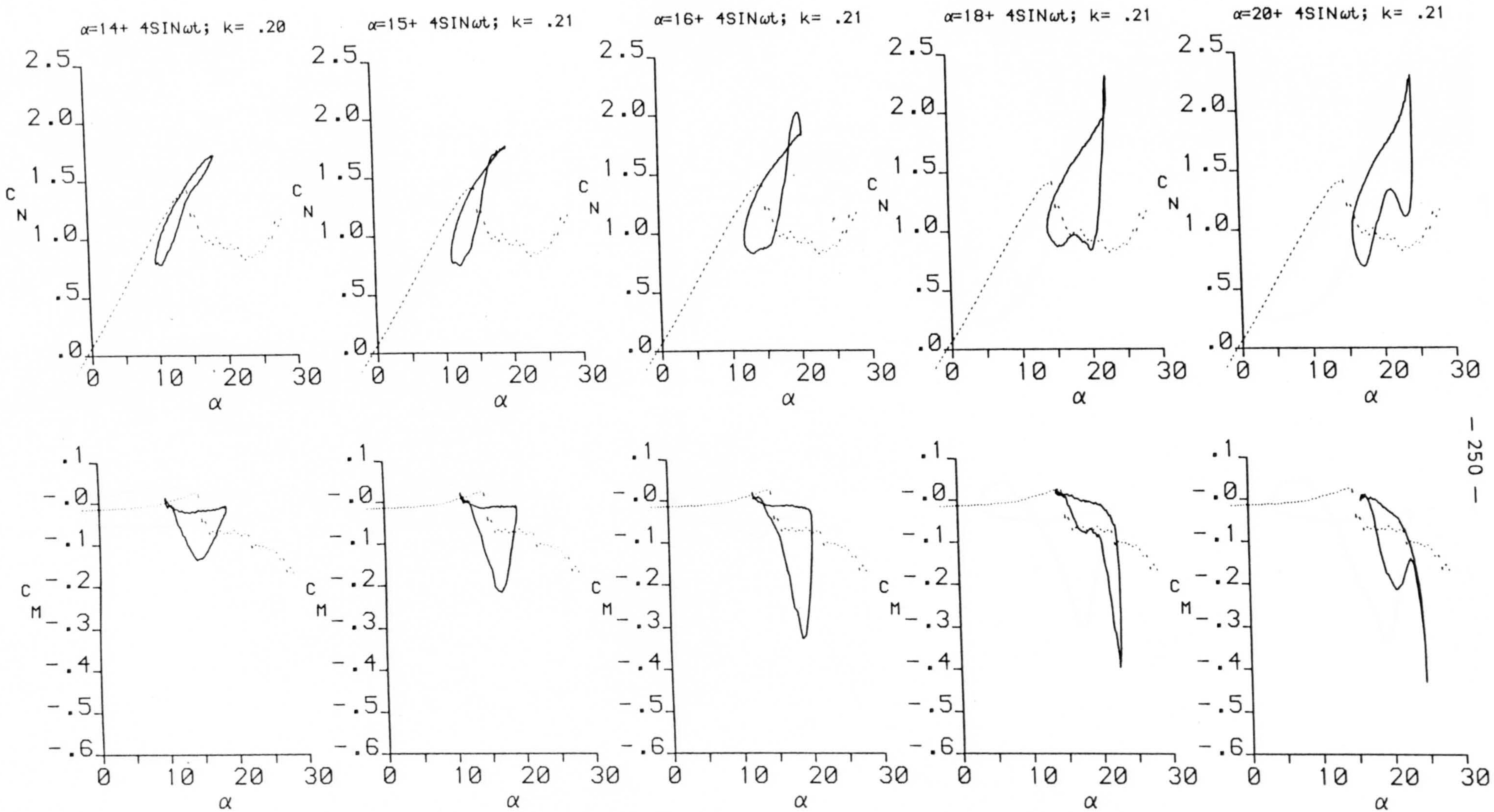

FIG.(7.18) EFFECT OF MEAN ANGLE OF ATTACK VARIATION AT $\alpha_a = 4^\circ$ AND K= .20

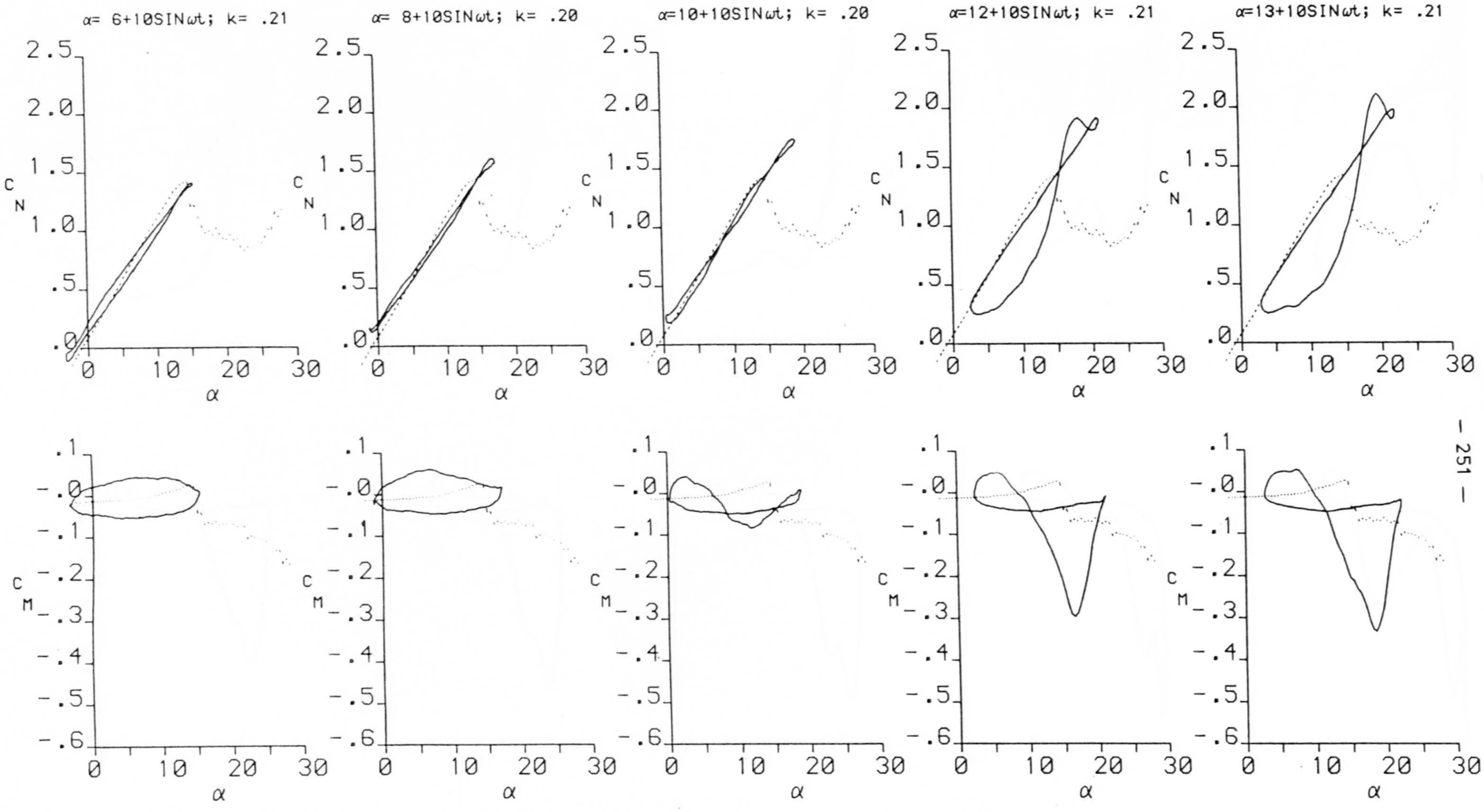

FIG.(7.19) EFFECT OF MEAN ANGLE OF ATTACK VARIATION AT $\alpha_a = 10^\circ$ AND K= .21

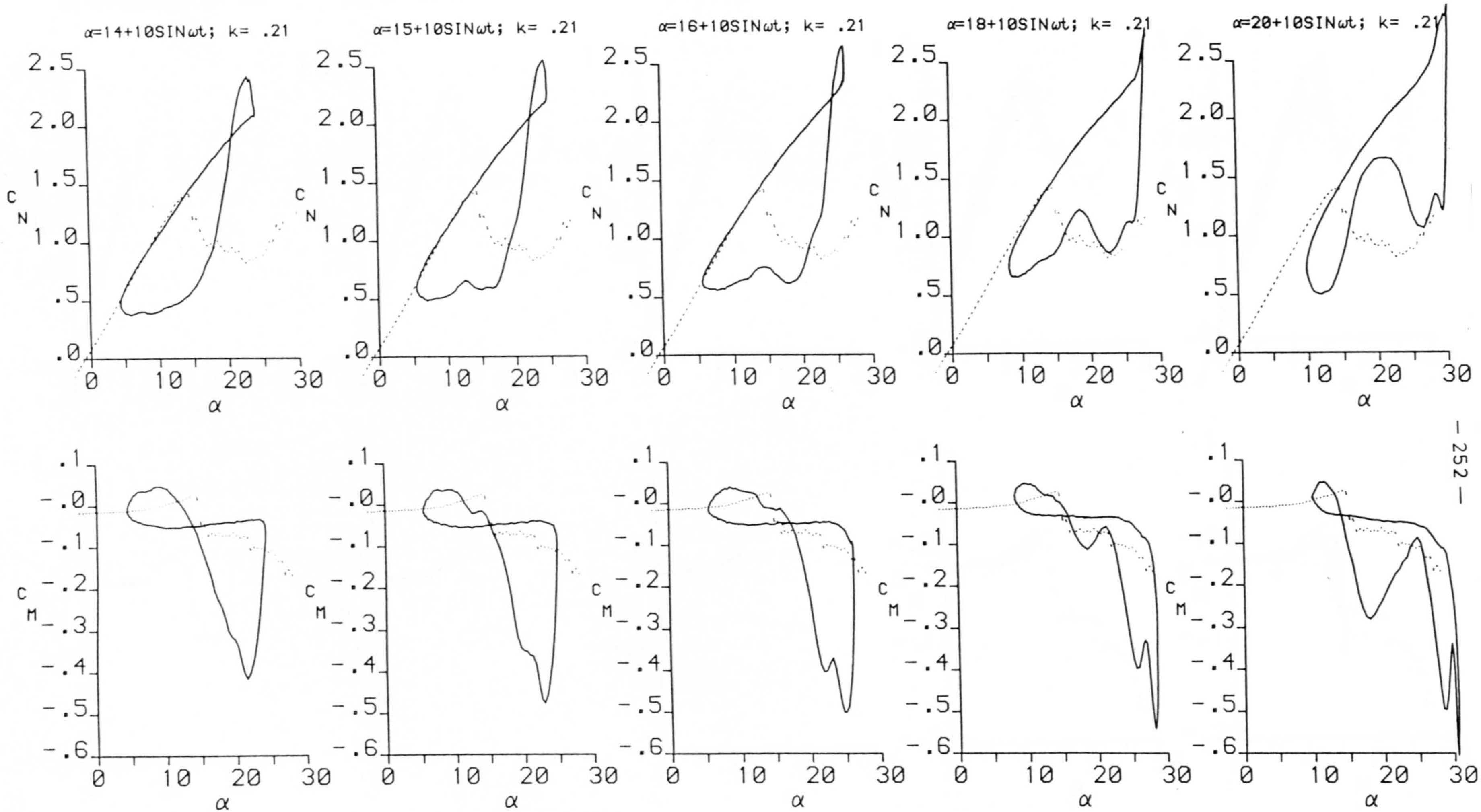

FIG.(7.20) EFFECT OF MEAN ANGLE OF ATTACK VARIATION AT $\alpha_a = 10^\circ$ AND K= .21

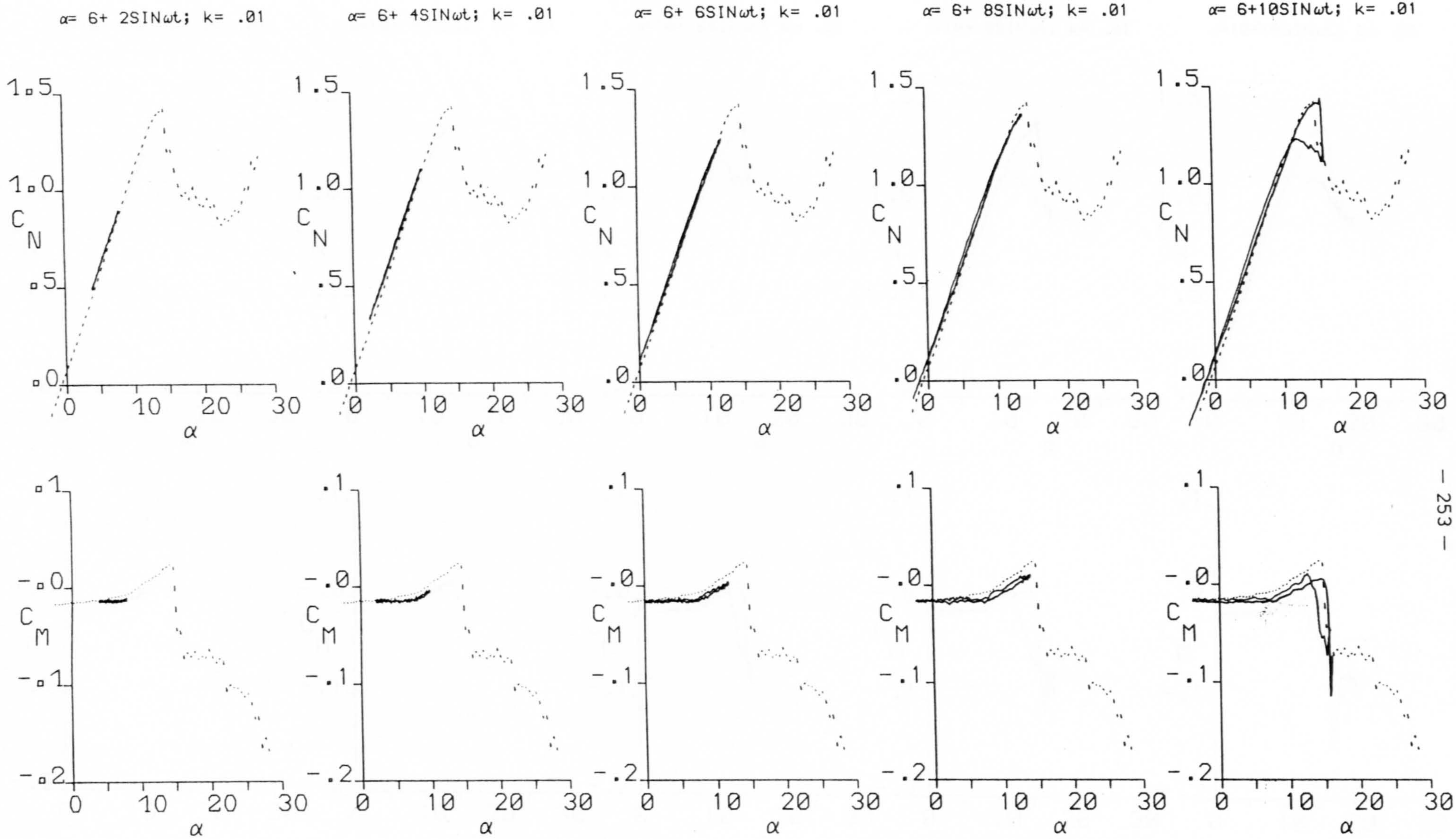

FIG. (7.21) EFFECT OF AMPLITUDE VARIATION AT $\alpha_M = 6^\circ$ AND K= .01

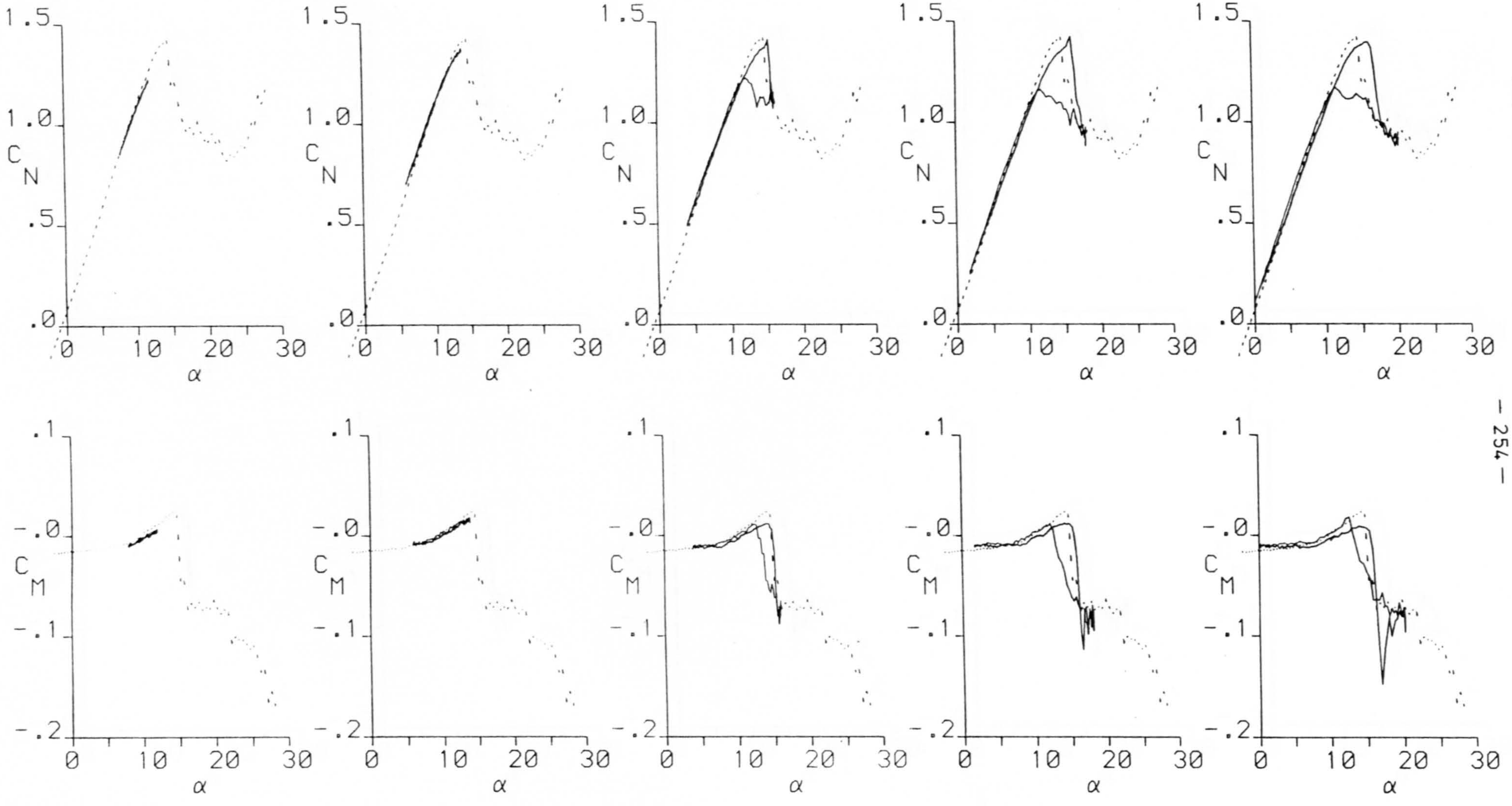

FIG.(7.22) EFFECT OF AMPLITUDE VARIATION AT $\alpha_M = 10^\circ$ AND K= .01

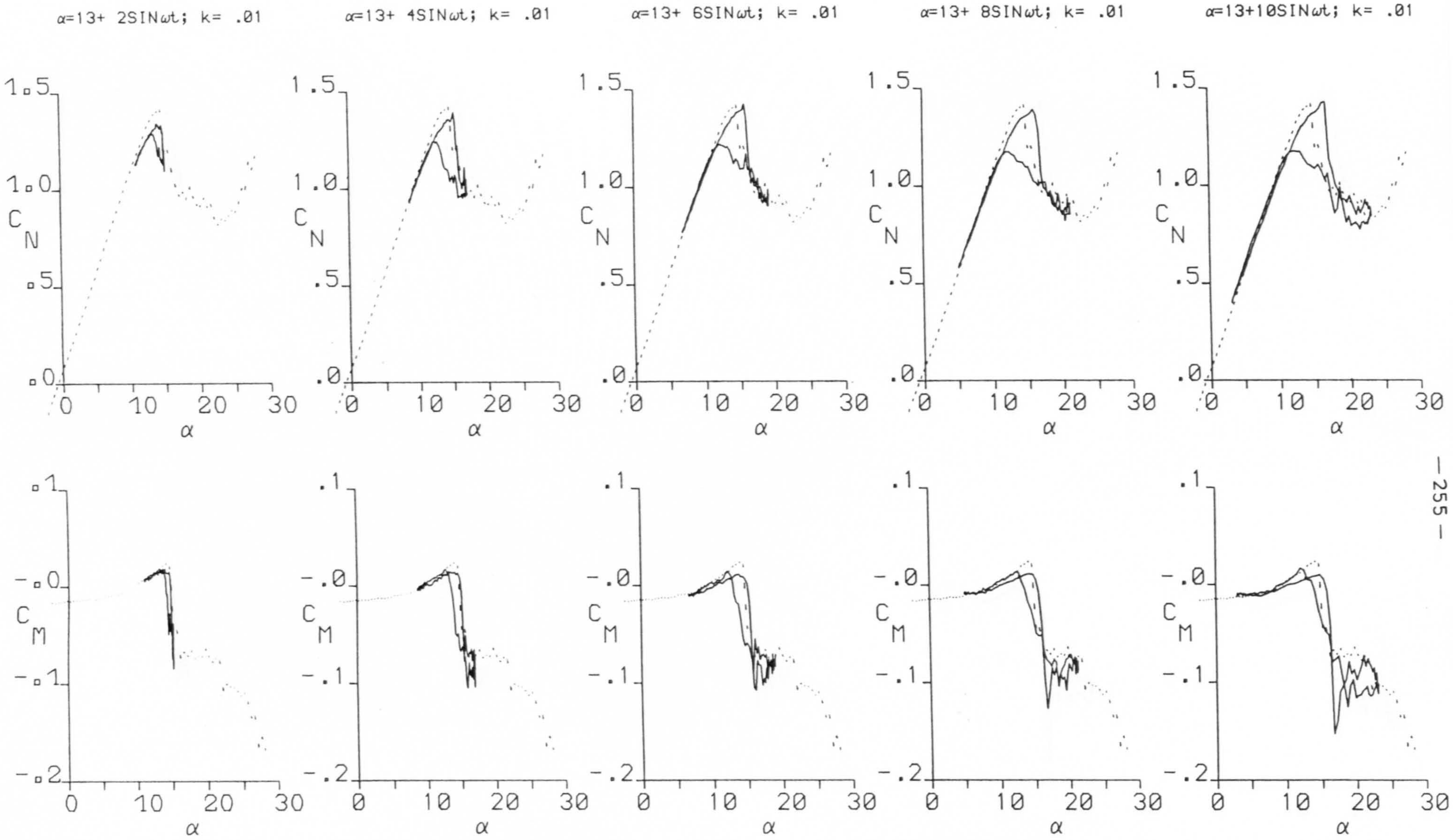

FIG. (7.23) EFFECT OF AMPLITUDE VARIATION AT $\alpha_M = 13^\circ$ AND K= .01

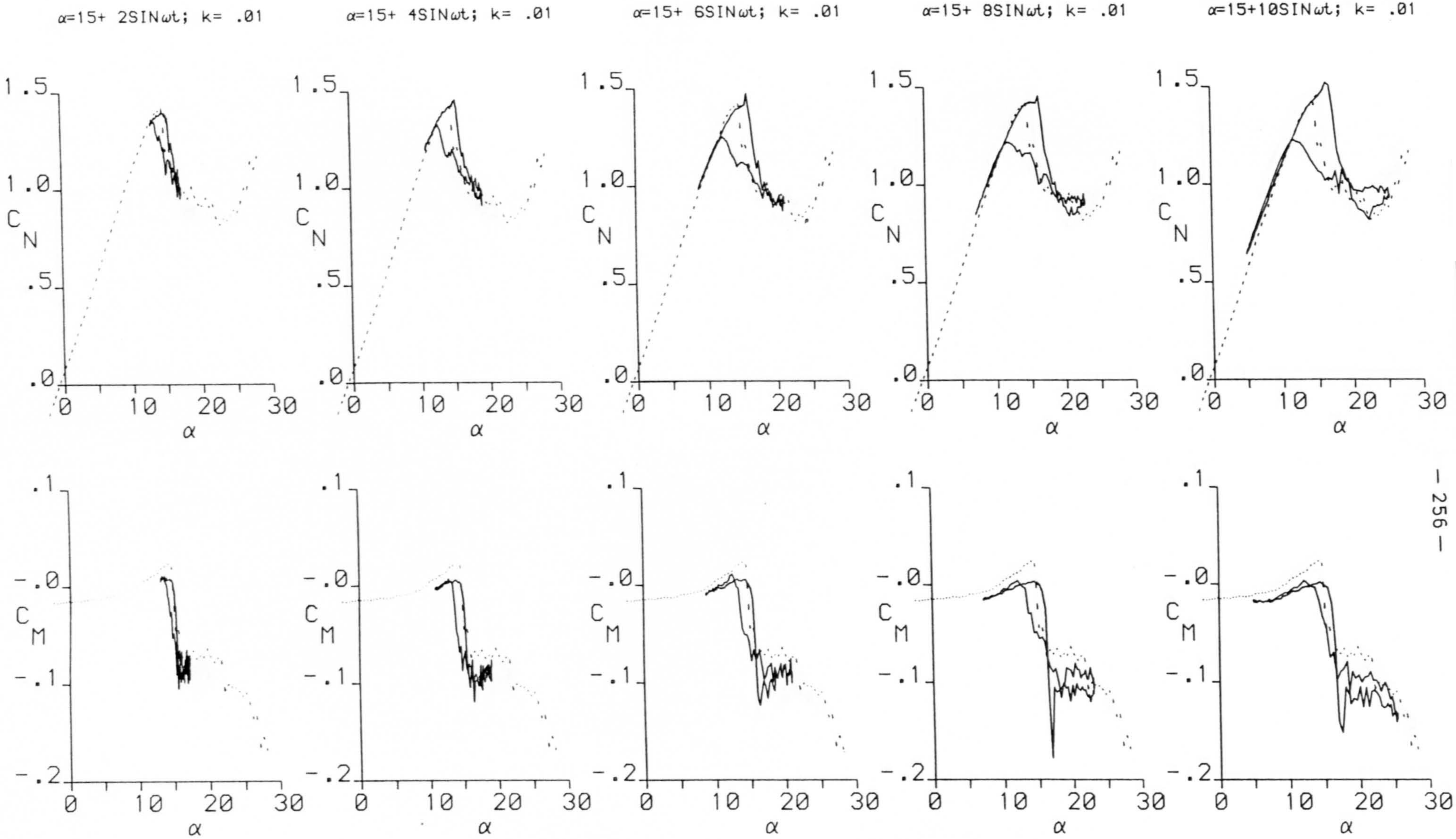

FIG.(7.24) EFFECT OF AMPLITUDE VARIATION AT $\alpha_M = 15^\circ$ AND K= .01

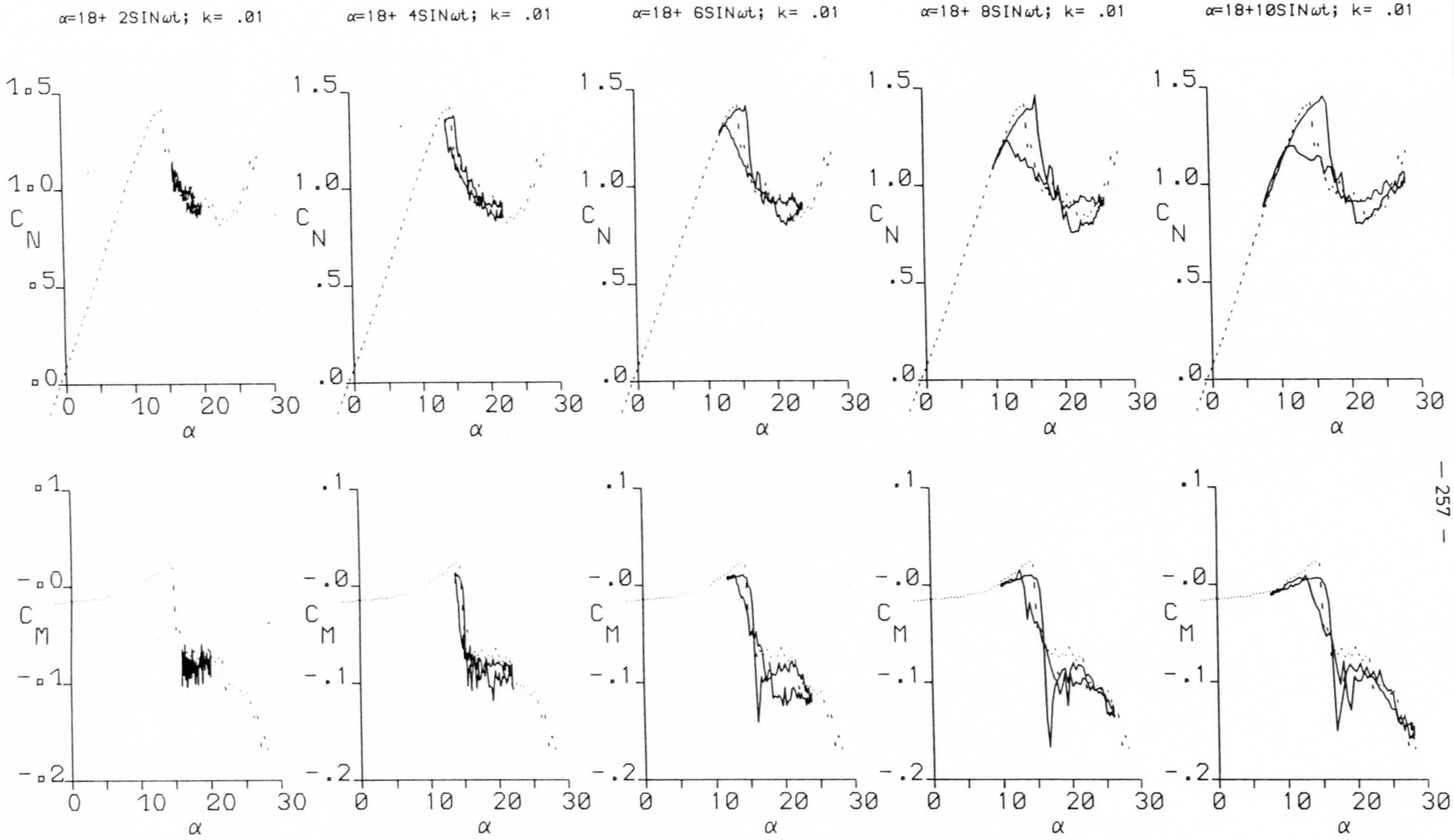

FIG. (7.25) EFFECT OF AMPLITUDE VARIATION AT $\alpha_M = 18^\circ$ AND K= .01

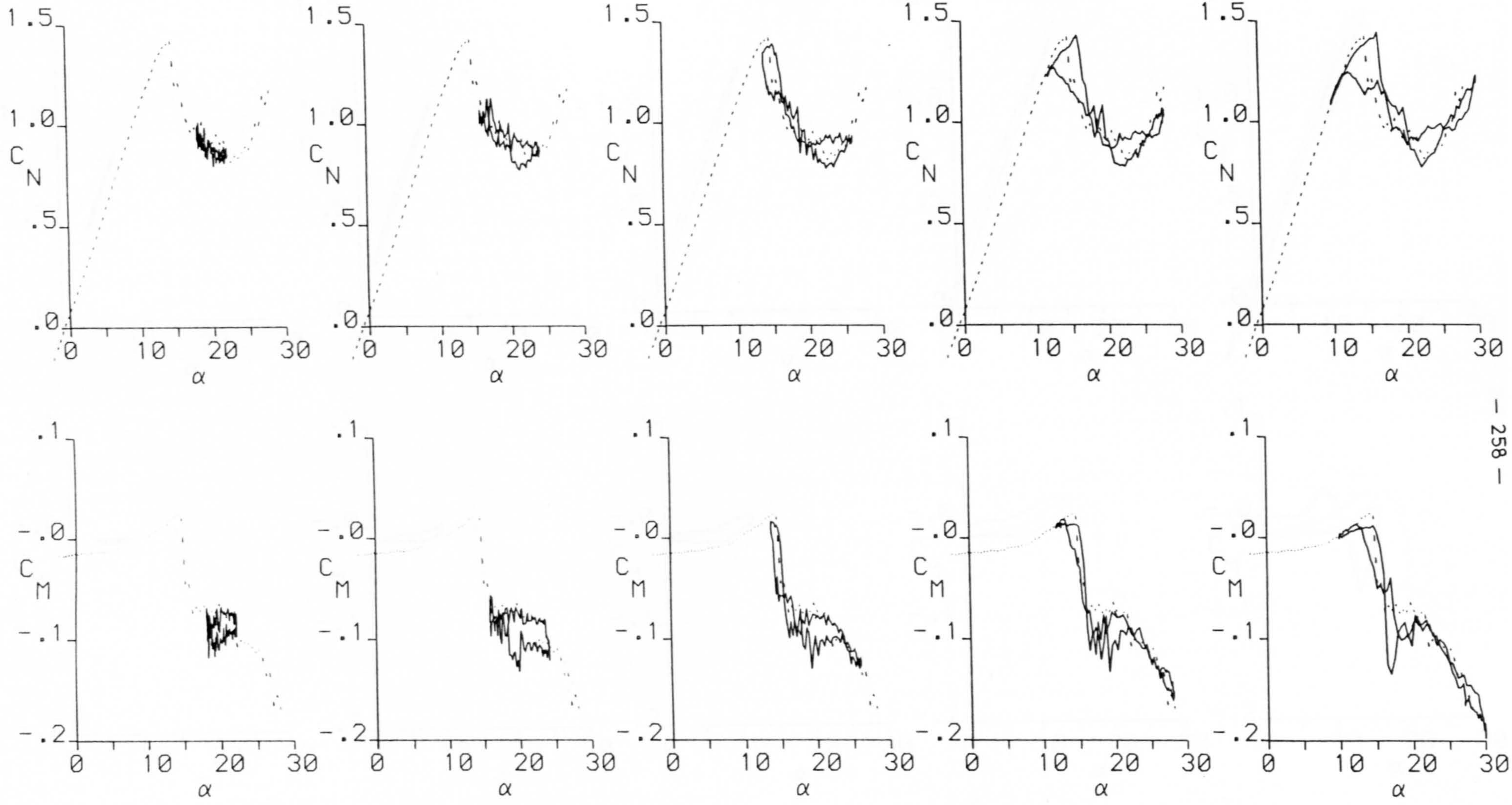

FIG.(7.26) EFFECT OF AMPLITUDE VARIATION AT $\alpha_M = 20^\circ$ AND K= .01

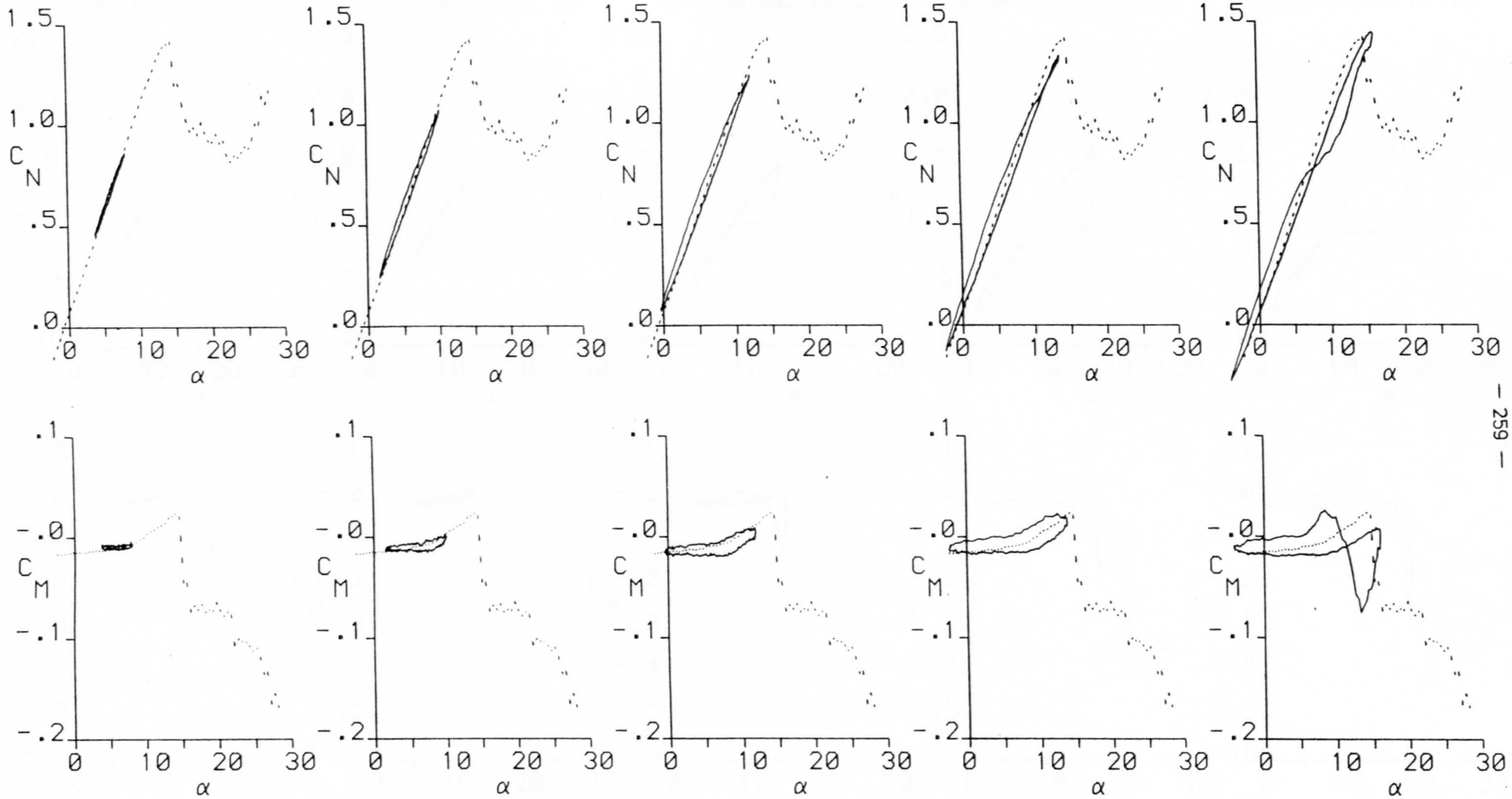

FIG.(7.27) EFFECT OF AMPLITUDE VARIATION AT $\alpha_M = 6^\circ$ AND K= .05

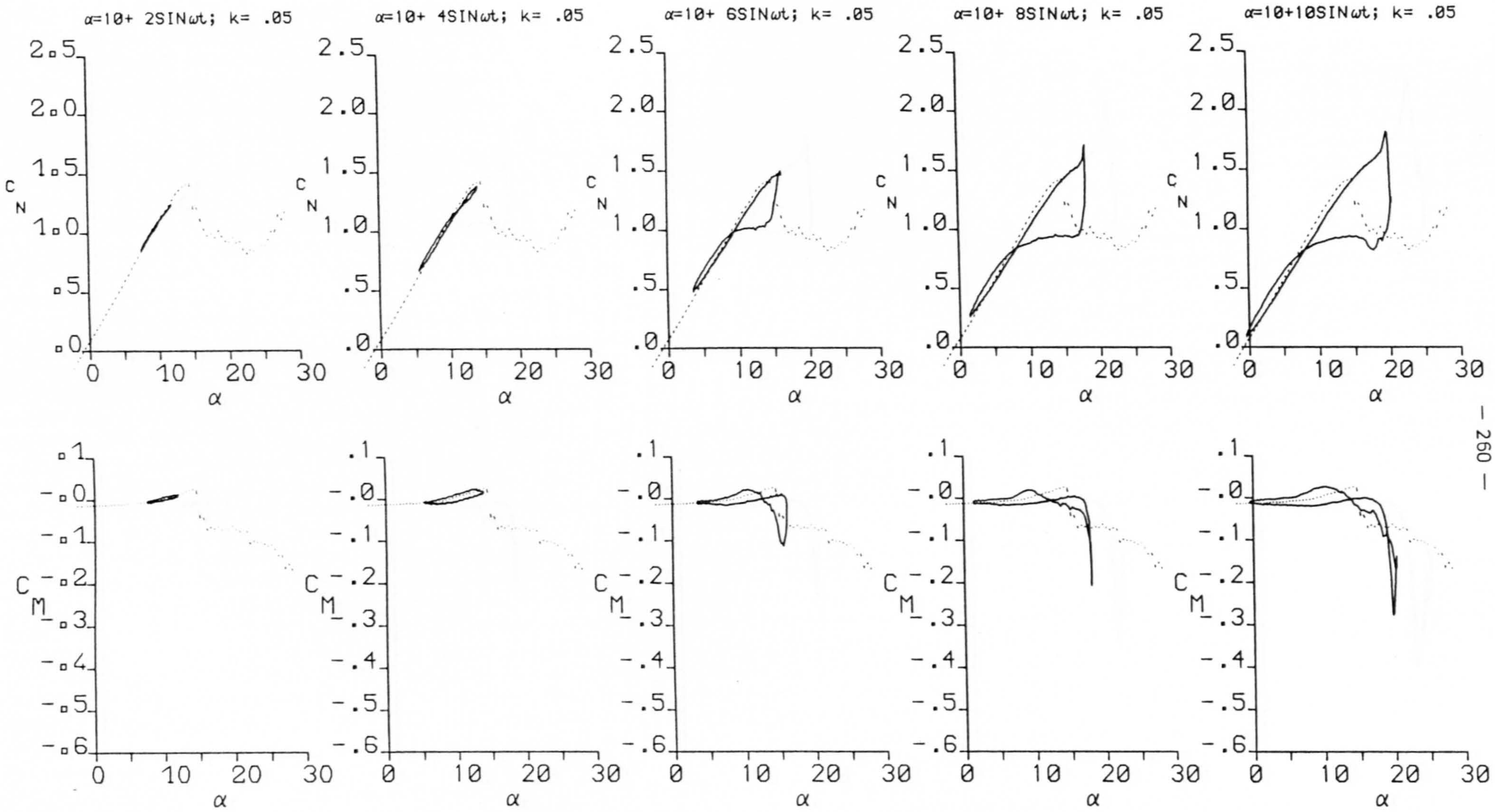

FIG. (7.28) EFFECT OF AMPLITUDE VARIATION AT $\alpha_M = 10^\circ$ AND K= .05

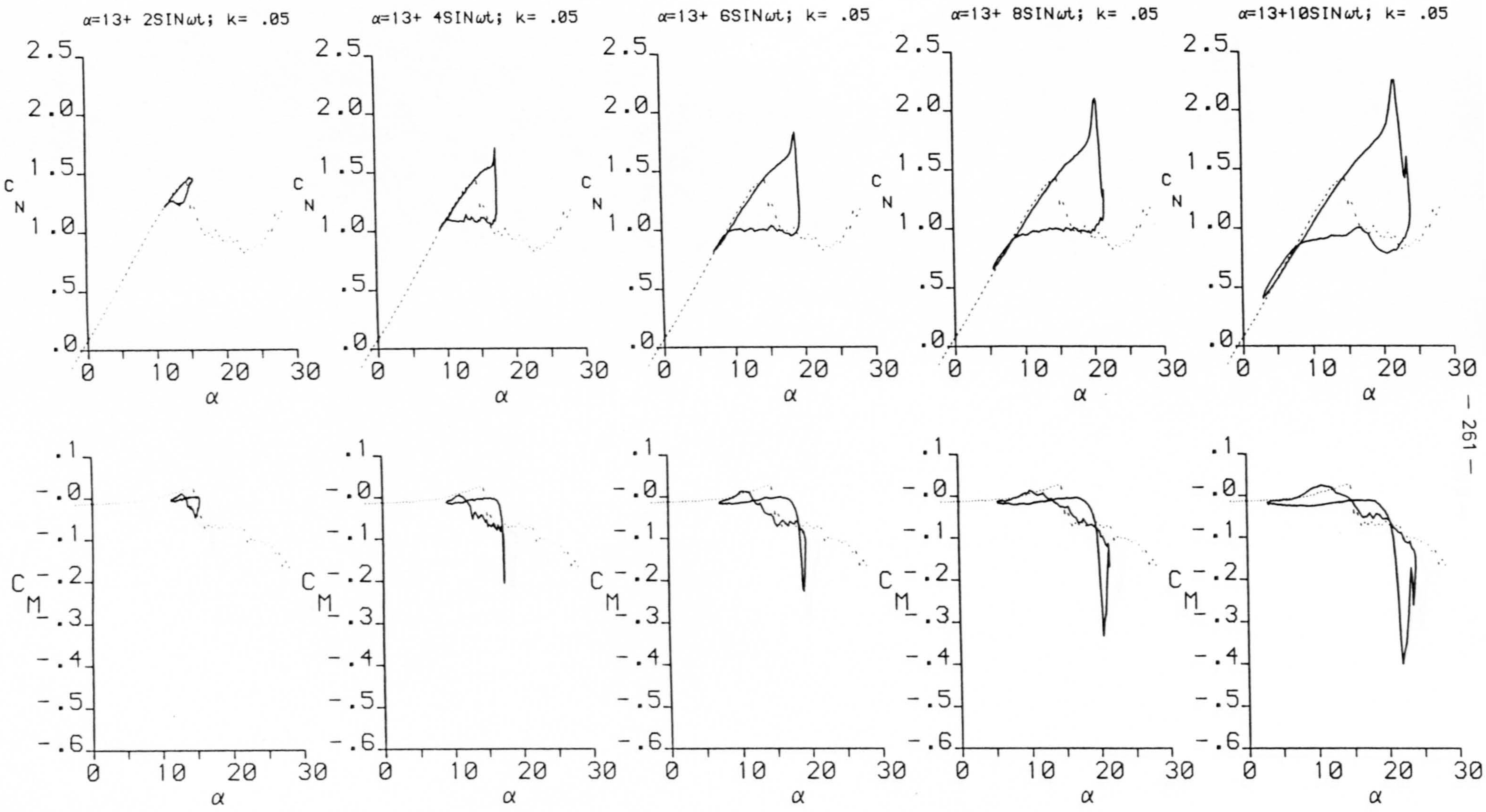

FIG.(7.29) EFFECT OF AMPLITUDE VARIATION AT $\alpha_M = 13^\circ$ AND K= .05

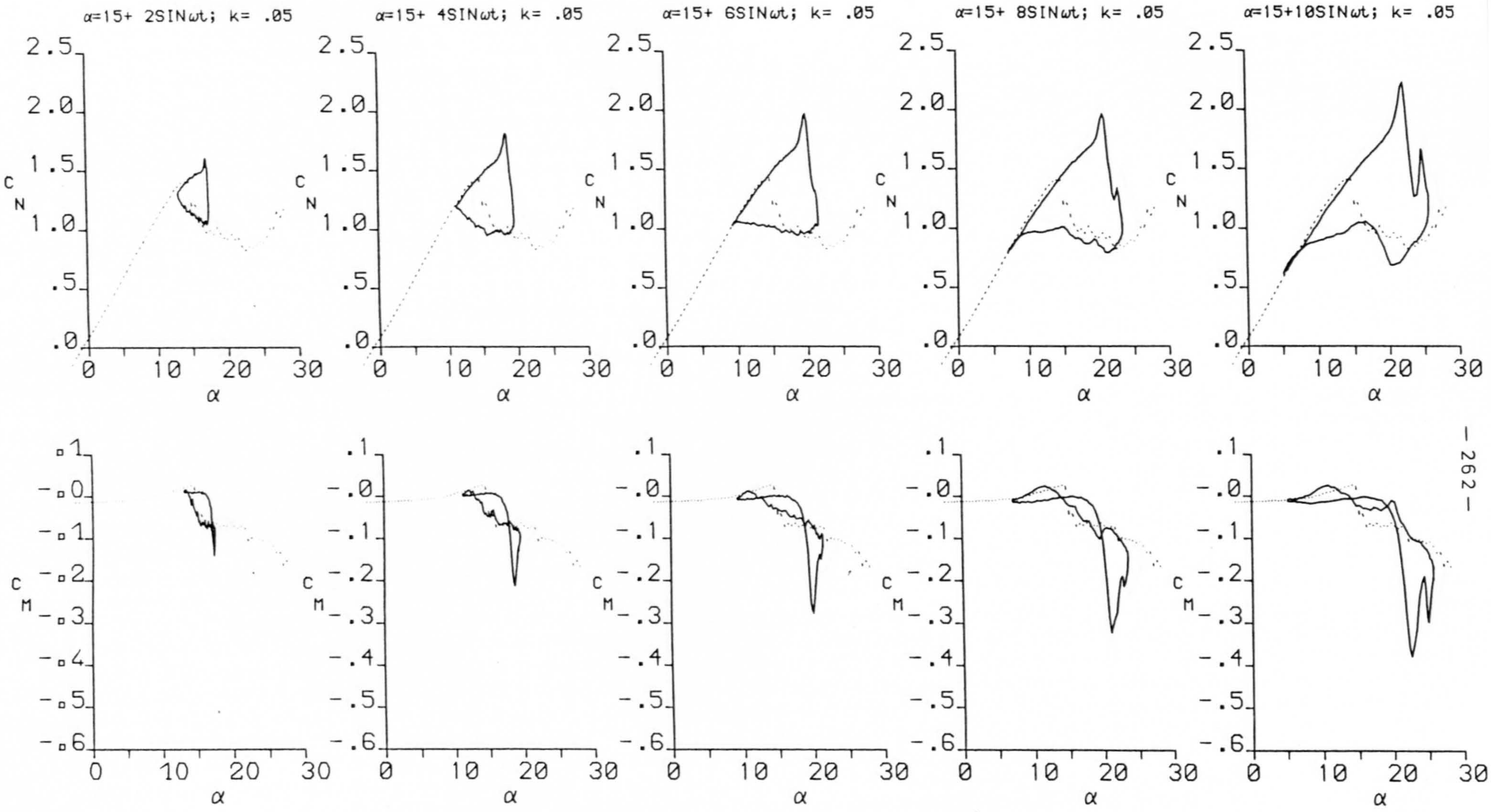

FIG. (7.30) EFFECT OF AMPLITUDE VARIATION AT $\alpha_M = 15^\circ$ AND K= .05

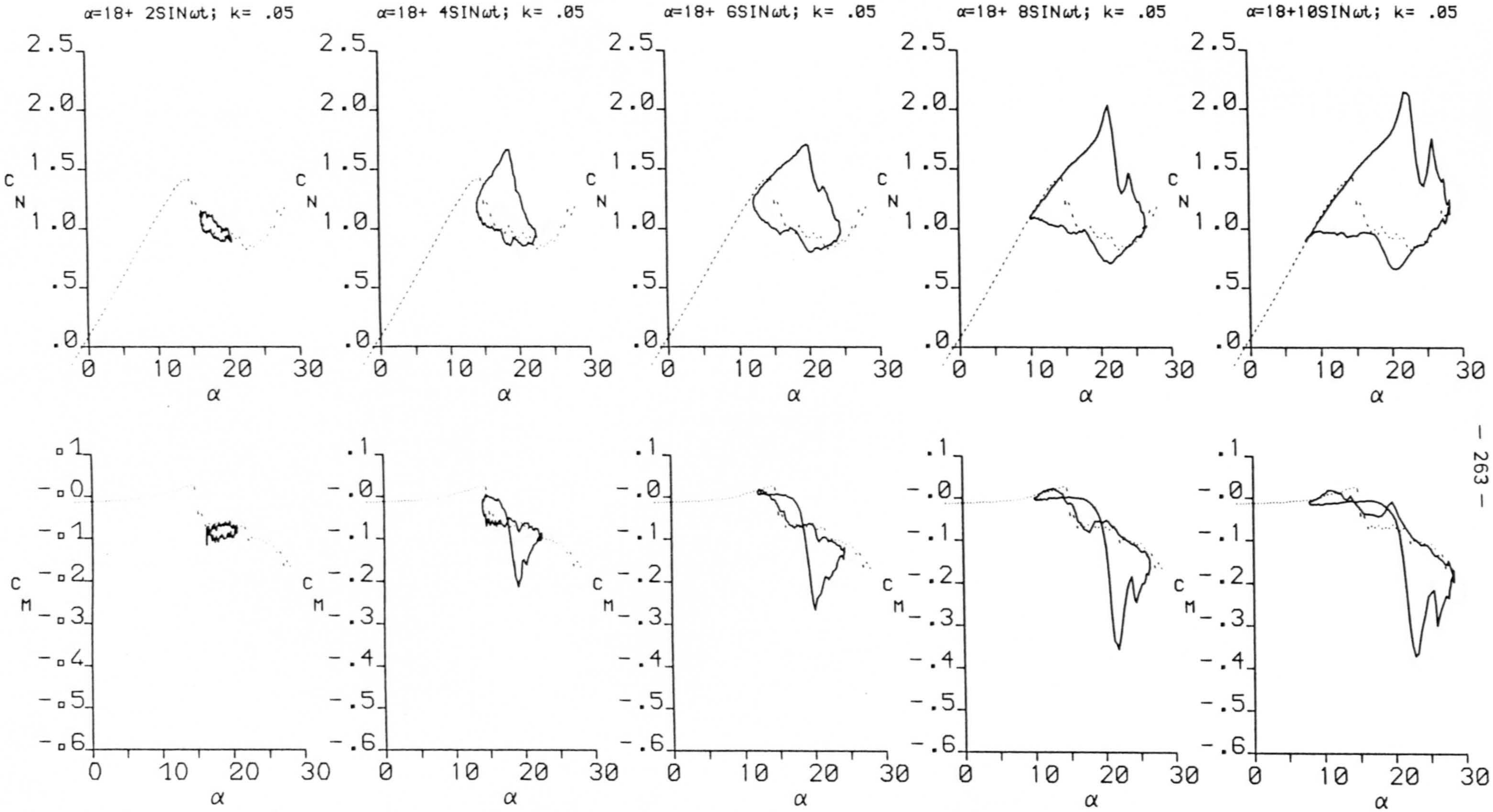

FIG. (7.31) EFFECT OF AMPLITUDE VARIATION AT $\alpha_M = 18^\circ$ AND K= .05

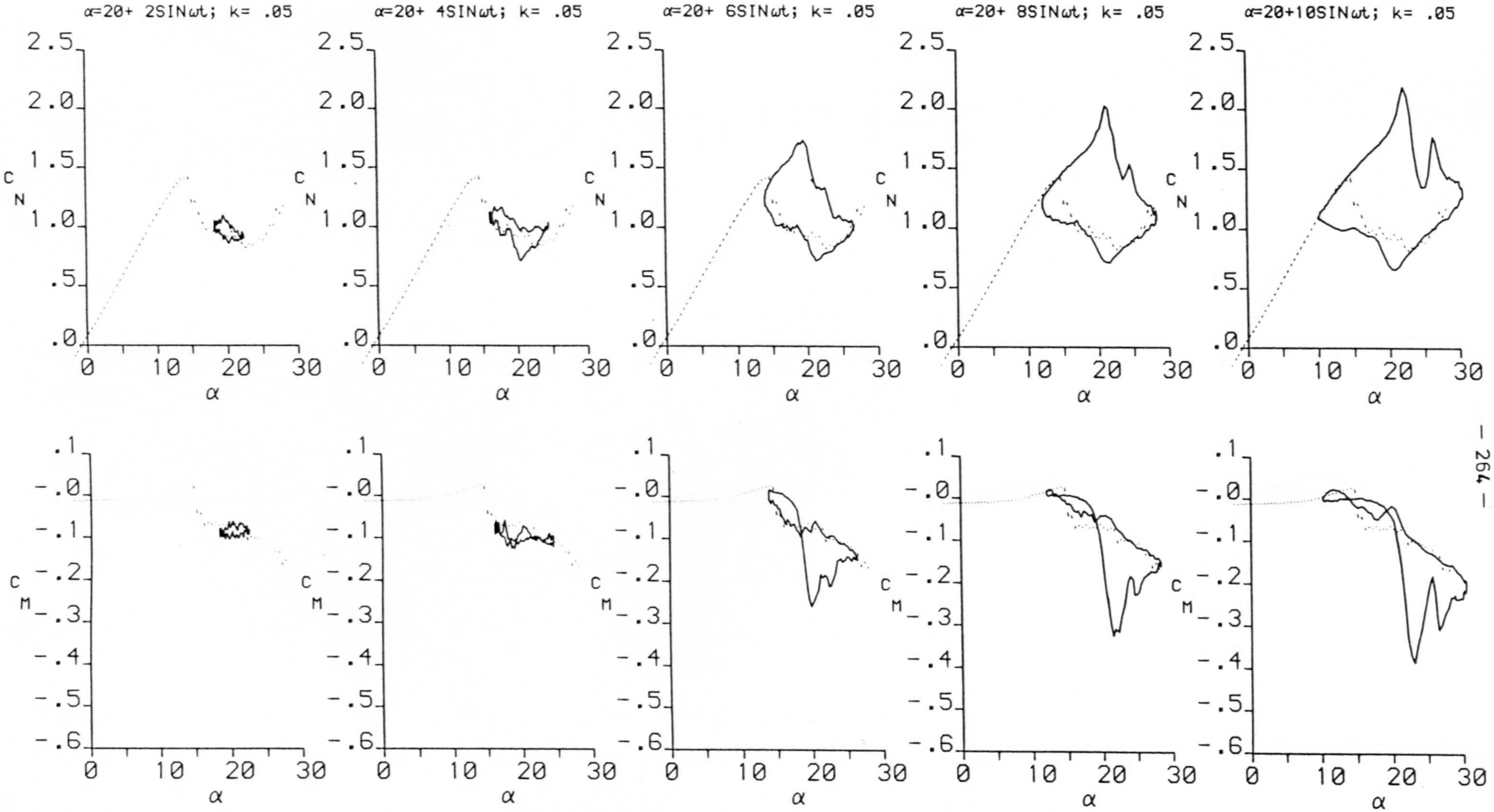

FIG.(7.32) EFFECT OF AMPLITUDE VARIATION AT $\alpha_M = 20^\circ$ AND K= .05

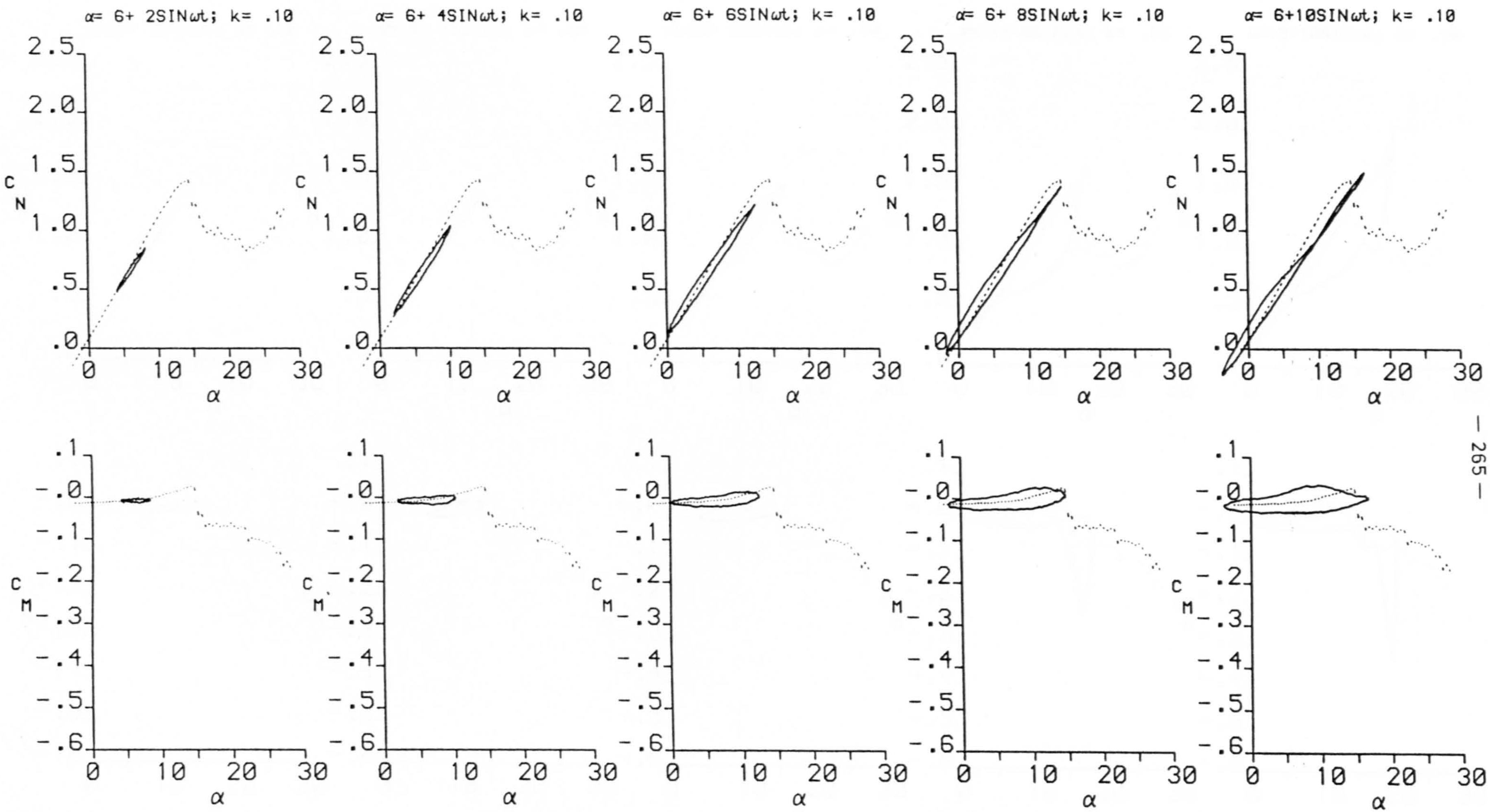

FIG.(7.33) EFFECT OF AMPLITUDE VARIATION AT $\alpha_M = 6^\circ$ AND K= .10

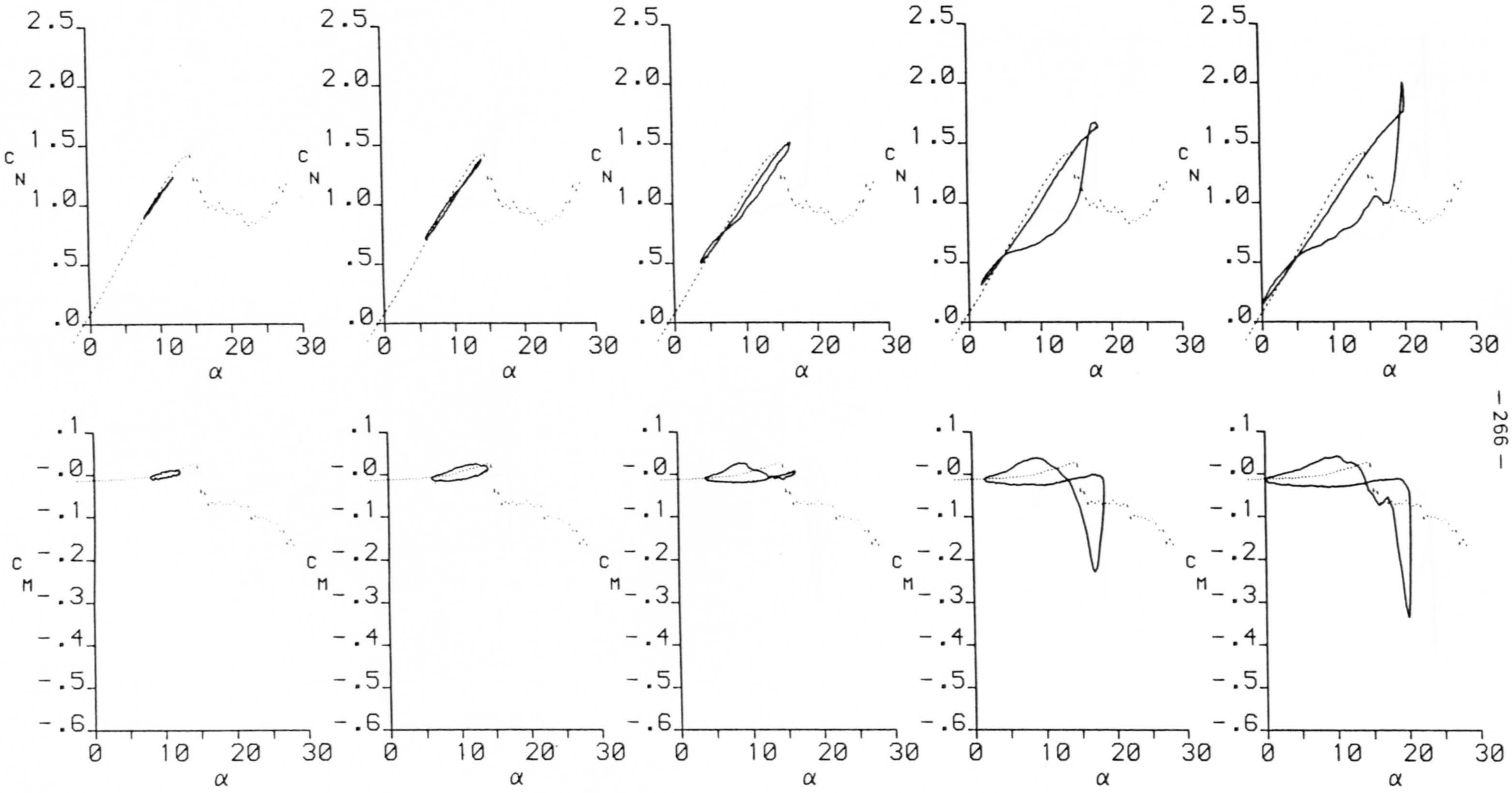

FIG.(7.34) EFFECT OF AMPLITUDE VARIATION AT $\alpha_M = 10^\circ$ AND K= .10

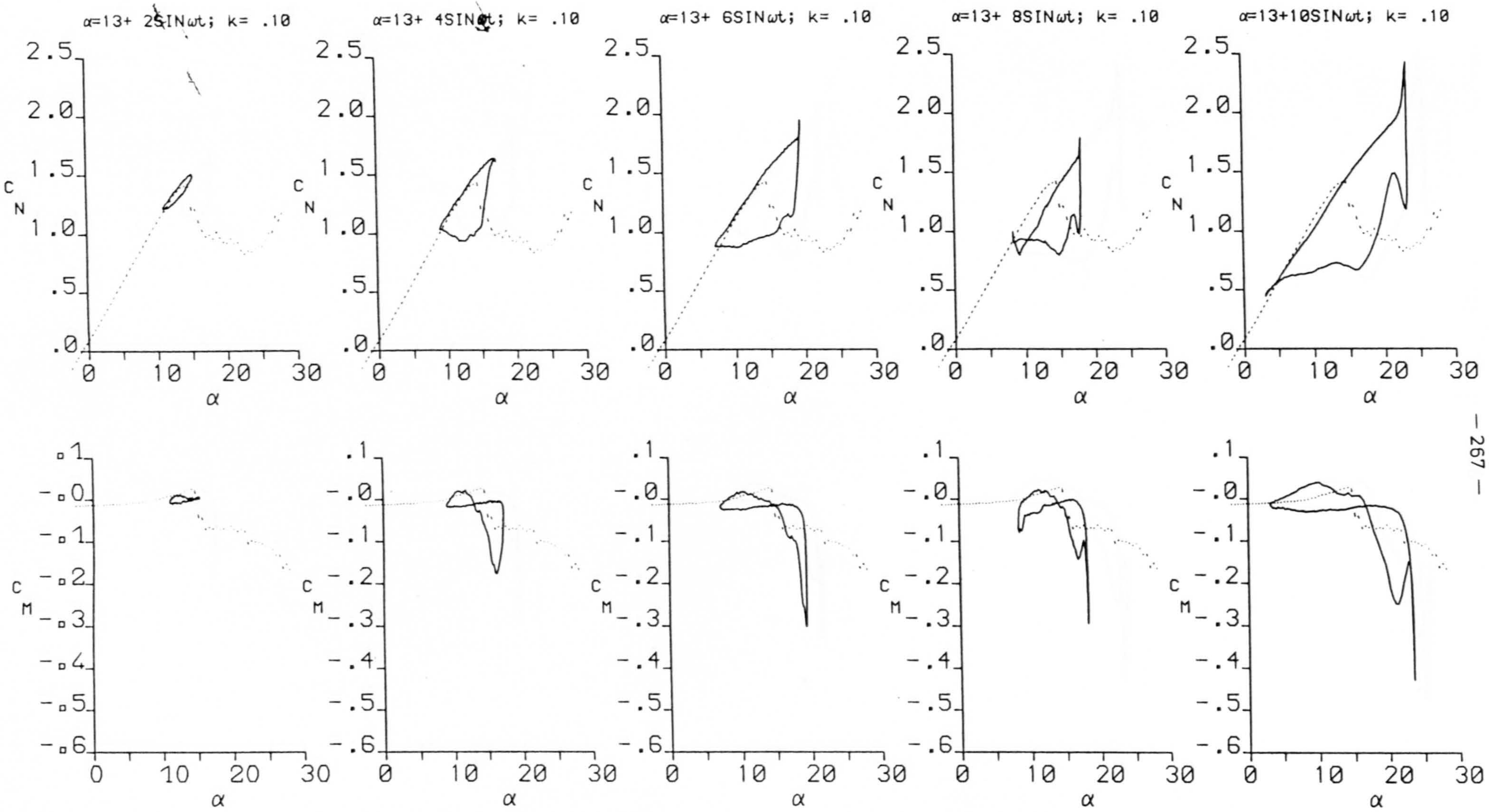

FIG. (7.35) EFFECT OF AMPLITUDE VARIATION AT $\alpha_M = 13^\circ$ AND K= .10

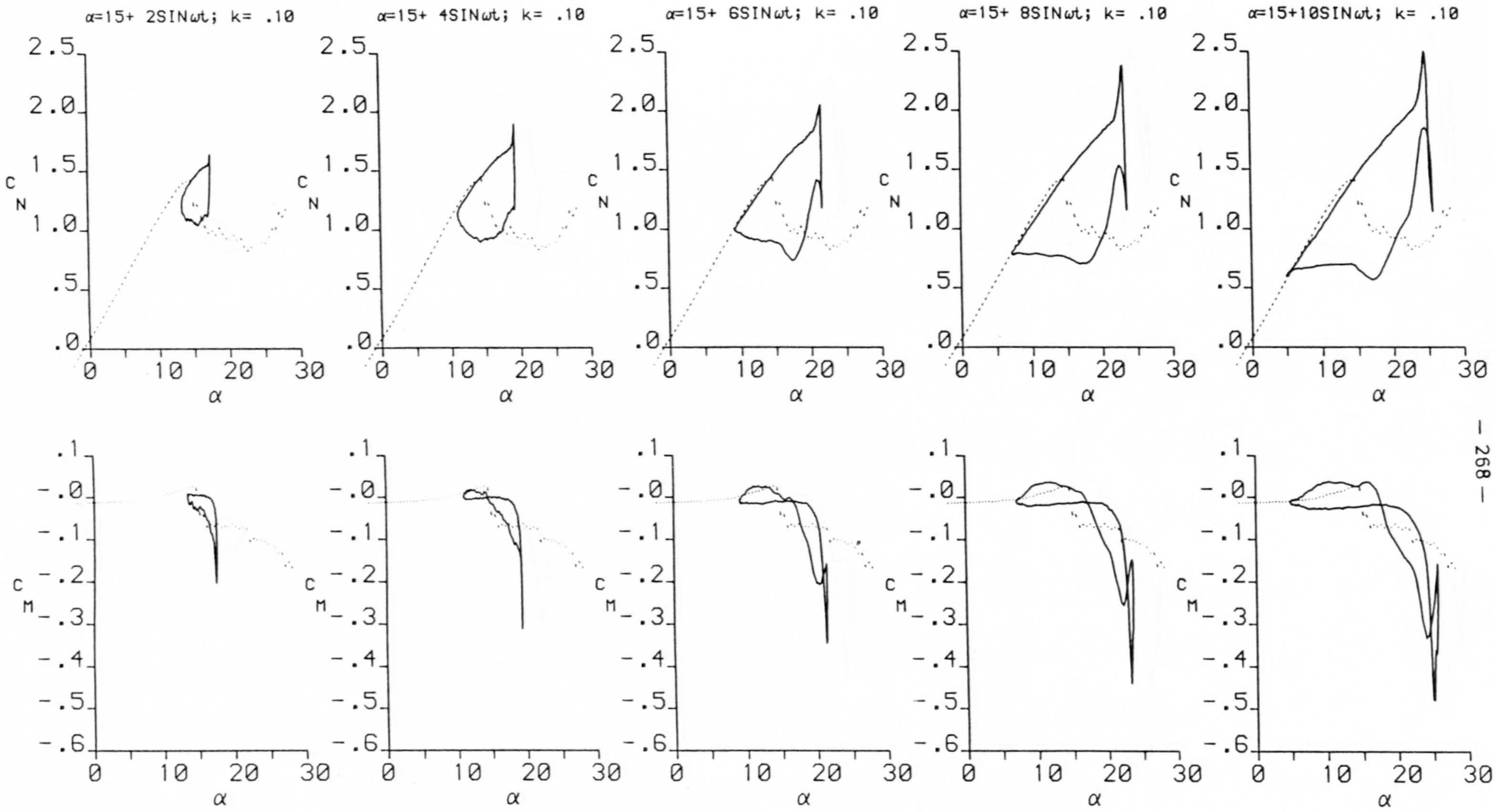

FIG.(7.36) EFFECT OF AMPLITUDE VARIATION AT $\alpha_M = 15^\circ$ AND K= .10

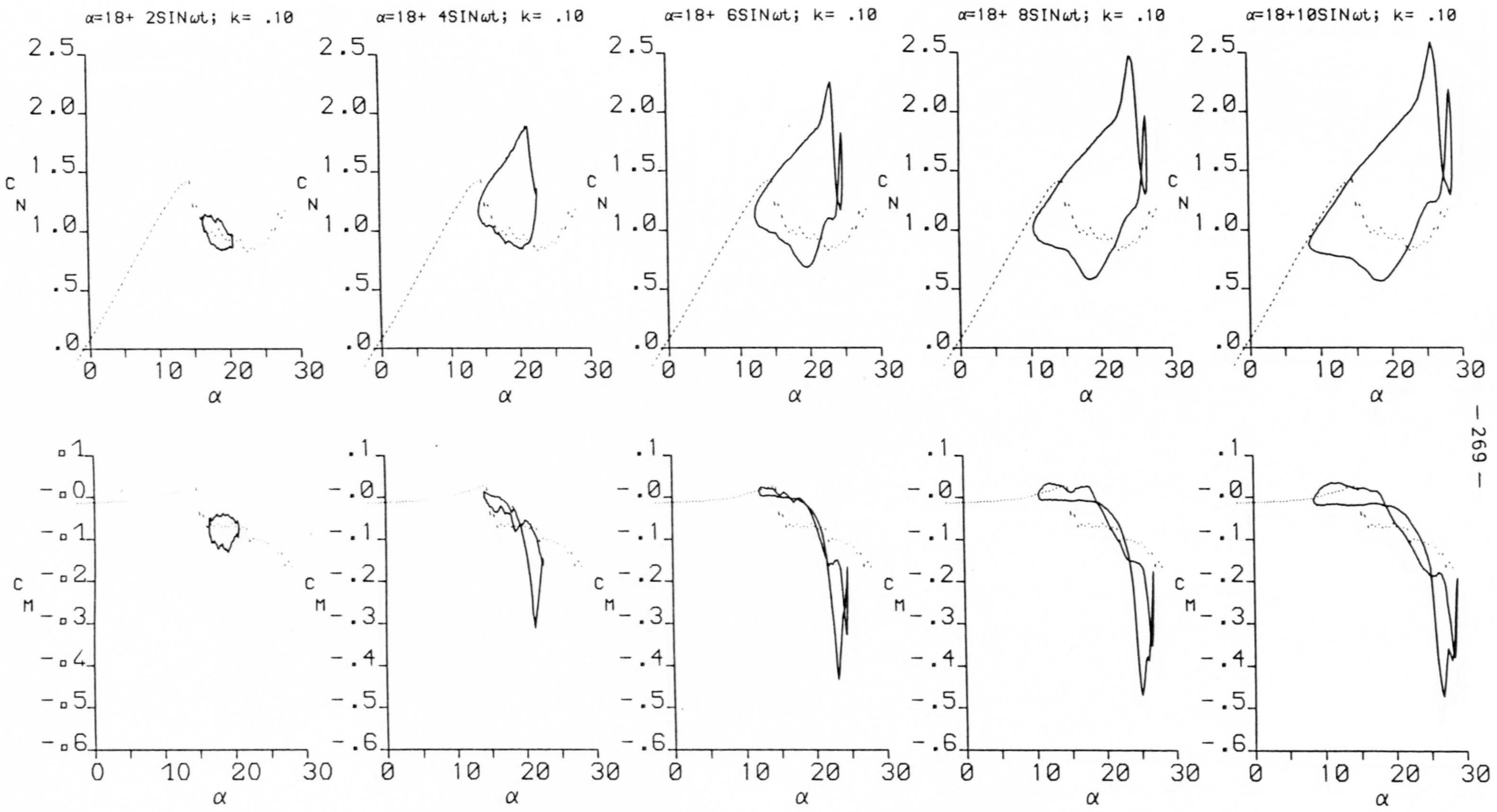

FIG. (7.37) EFFECT OF AMPLITUDE VARIATION AT $\alpha_M = 18^\circ$ AND K= .10

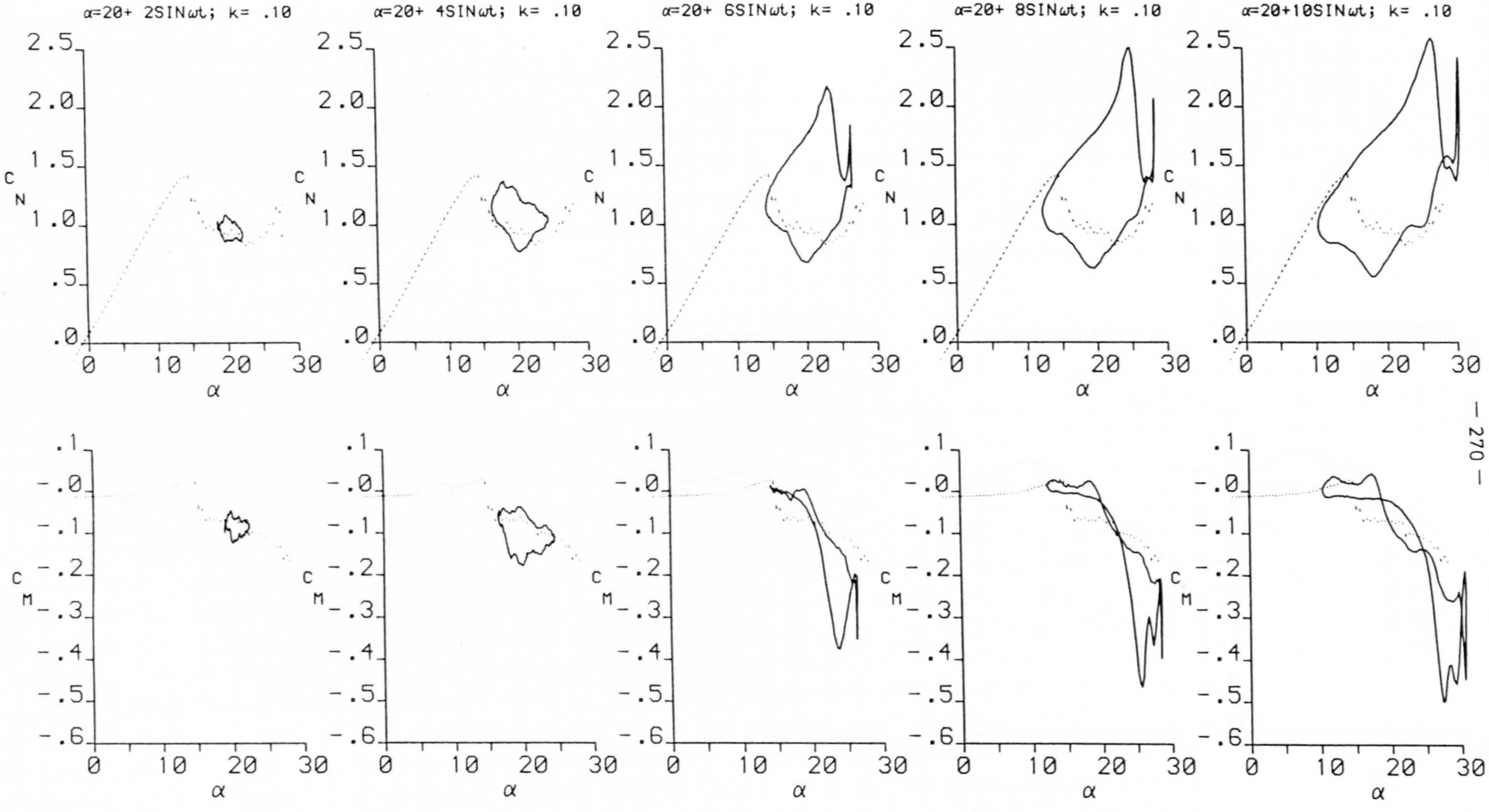

FIG.(7.38) EFFECT OF AMPLITUDE VARIATION AT $\alpha_M = 20^\circ$ AND K= .10

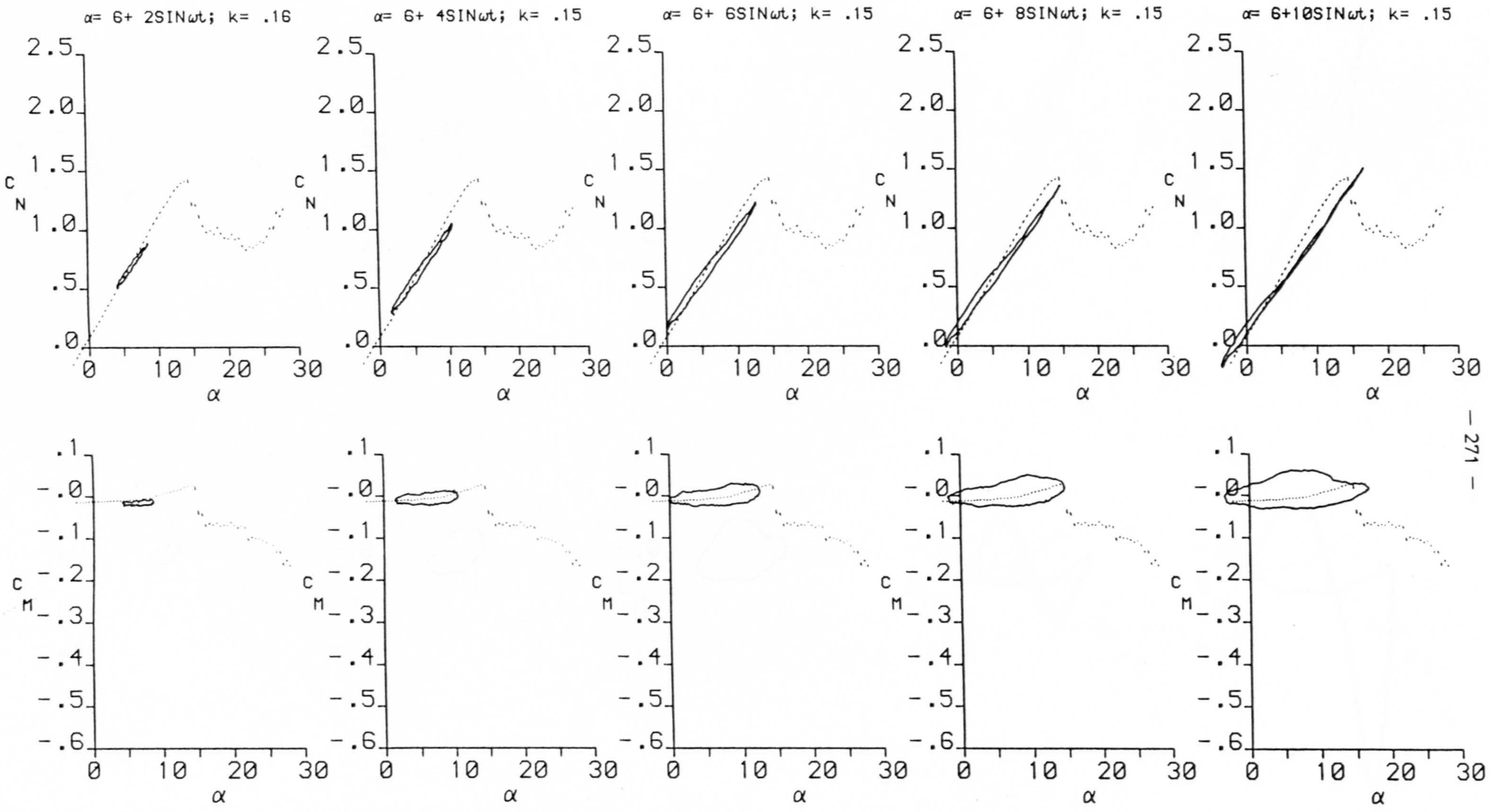

FIG.(7.39) EFFECT OF AMPLITUDE VARIATION AT $\alpha_M = 6^\circ$ AND K= .16

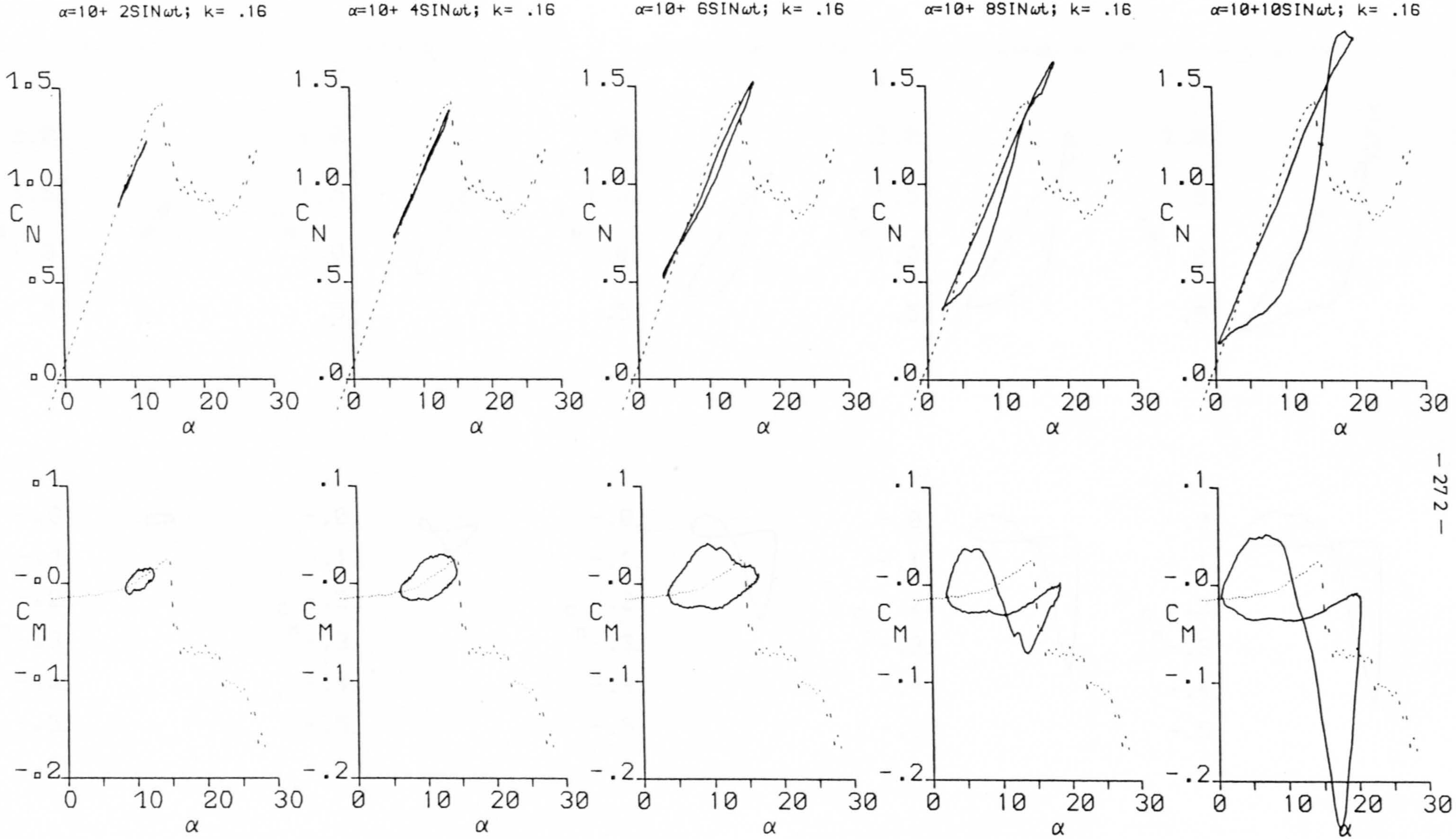

FIG. (7.40) EFFECT OF AMPLITUDE VARIATION AT $\alpha_M = 10^\circ$ AND K= .16

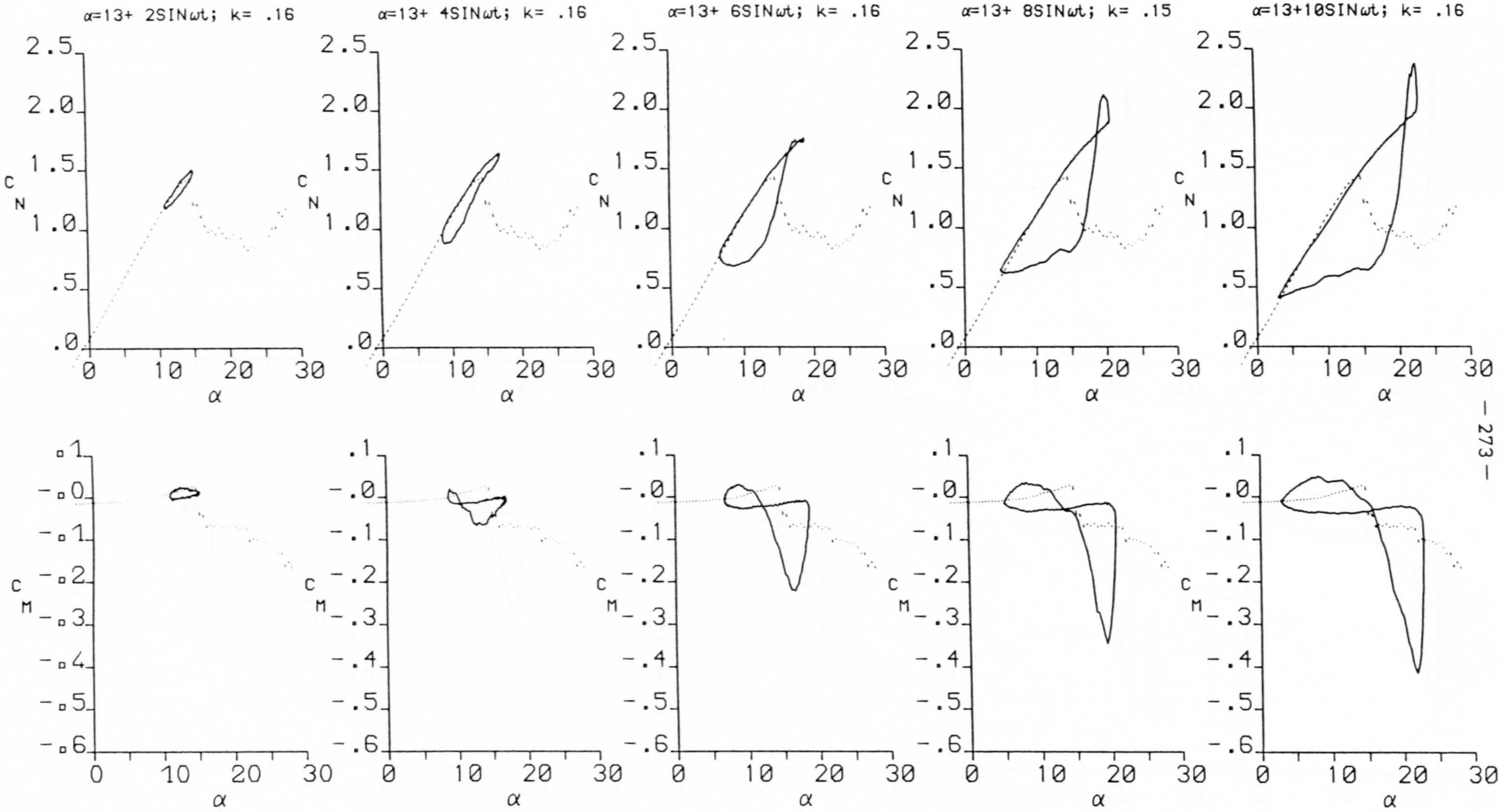

FIG.(7.41) EFFECT OF AMPLITUDE VARIATION AT $\alpha_M = 13^\circ$ AND K= .16

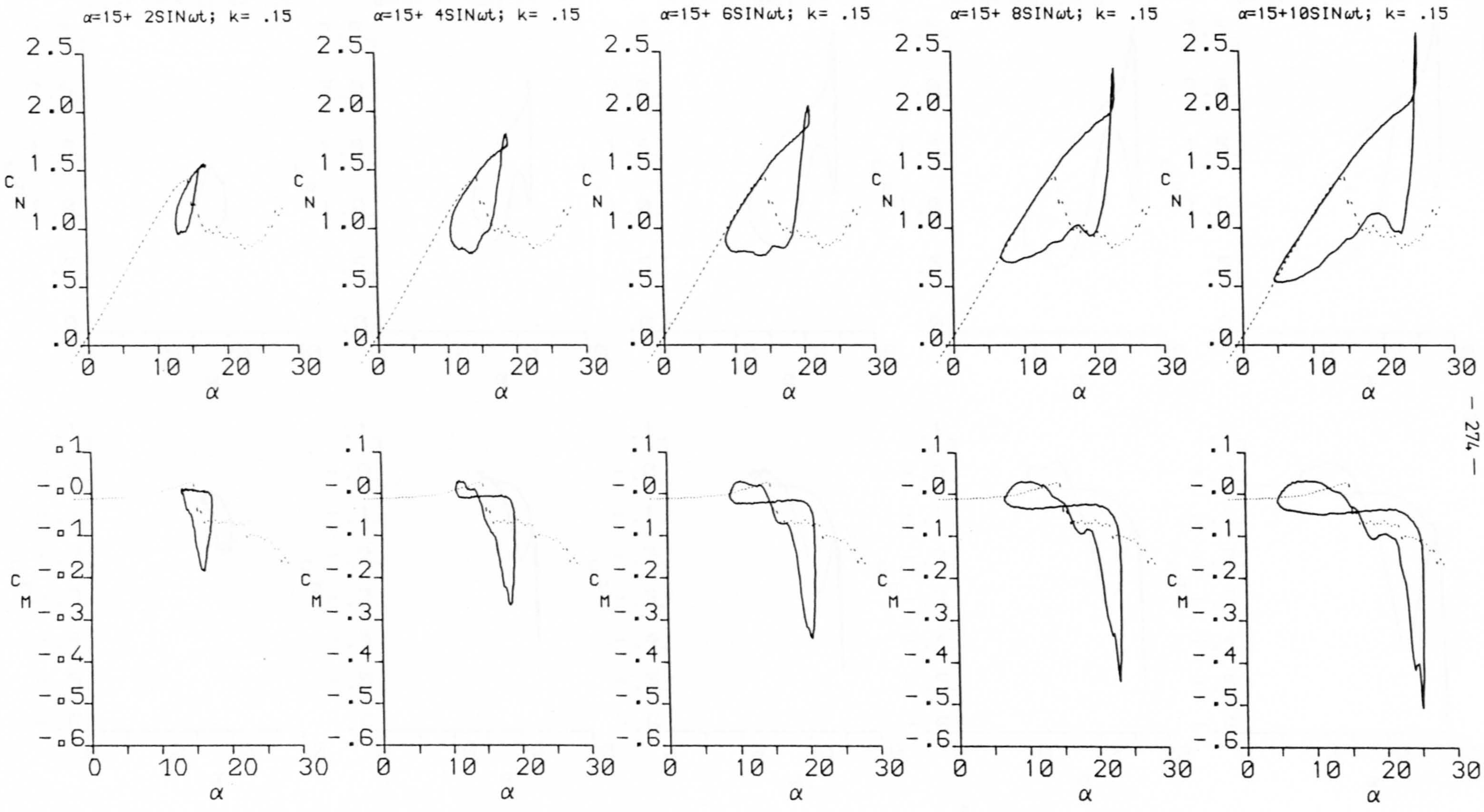

FIG. (7.42) EFFECT OF AMPLITUDE VARIATION AT $\alpha_M = 15^\circ$ AND K= .15

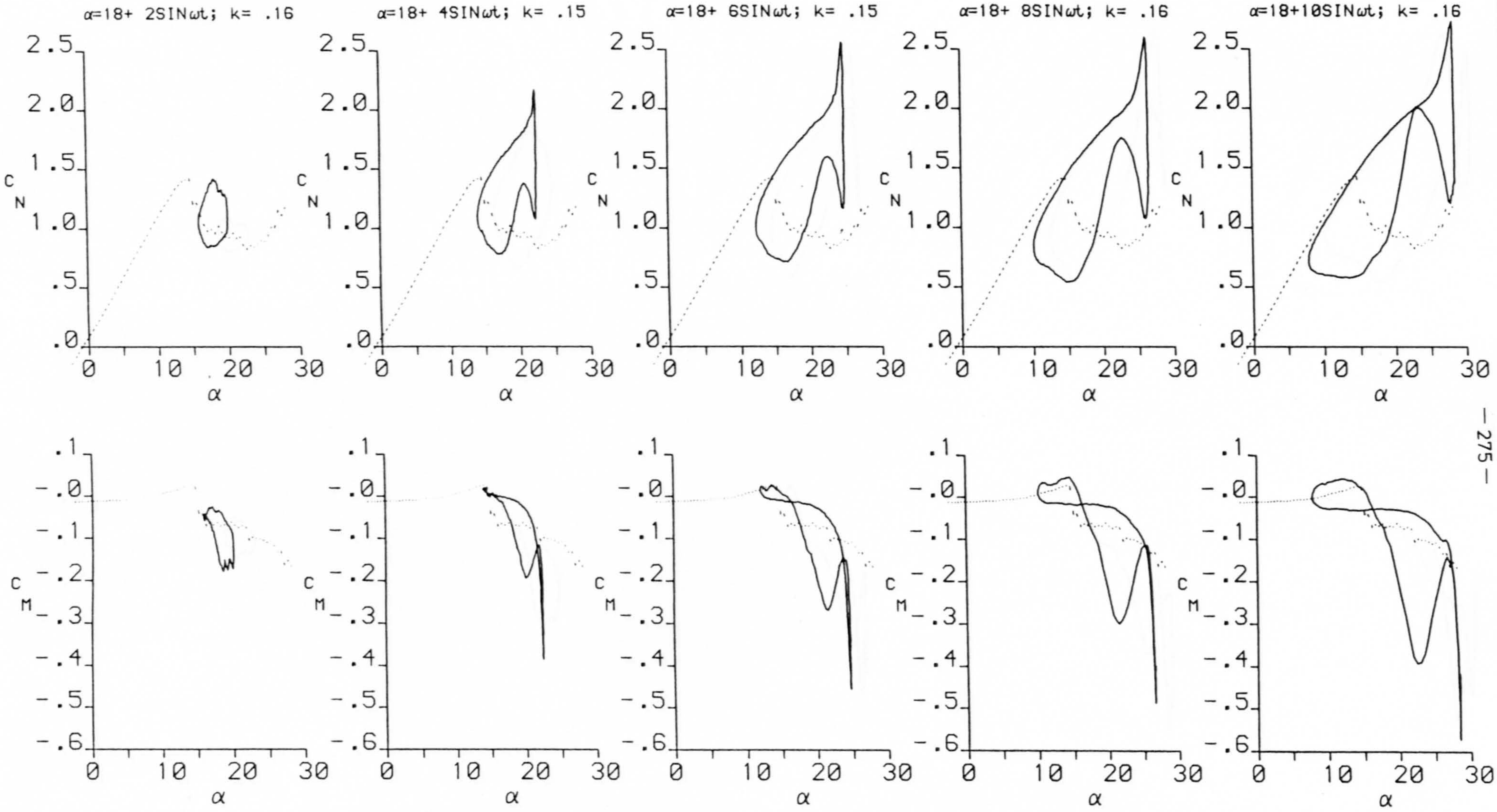

FIG.(7.43) EFFECT OF AMPLITUDE VARIATION AT $\alpha_M = 18^\circ$ AND K= .16

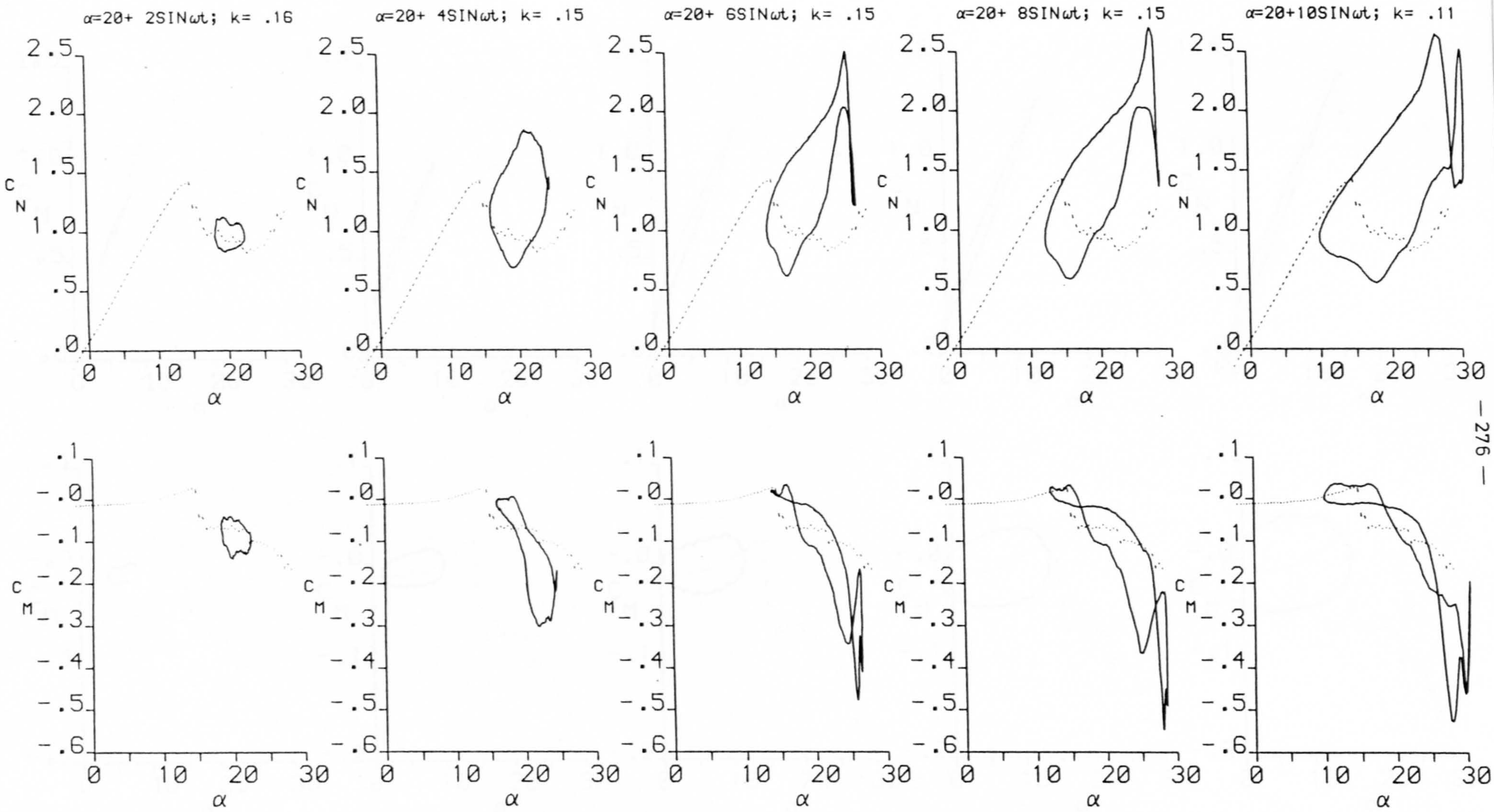

FIG.(7.44) EFFECT OF AMPLITUDE VARIATION AT $\alpha_M = 20^\circ$ AND K= .16

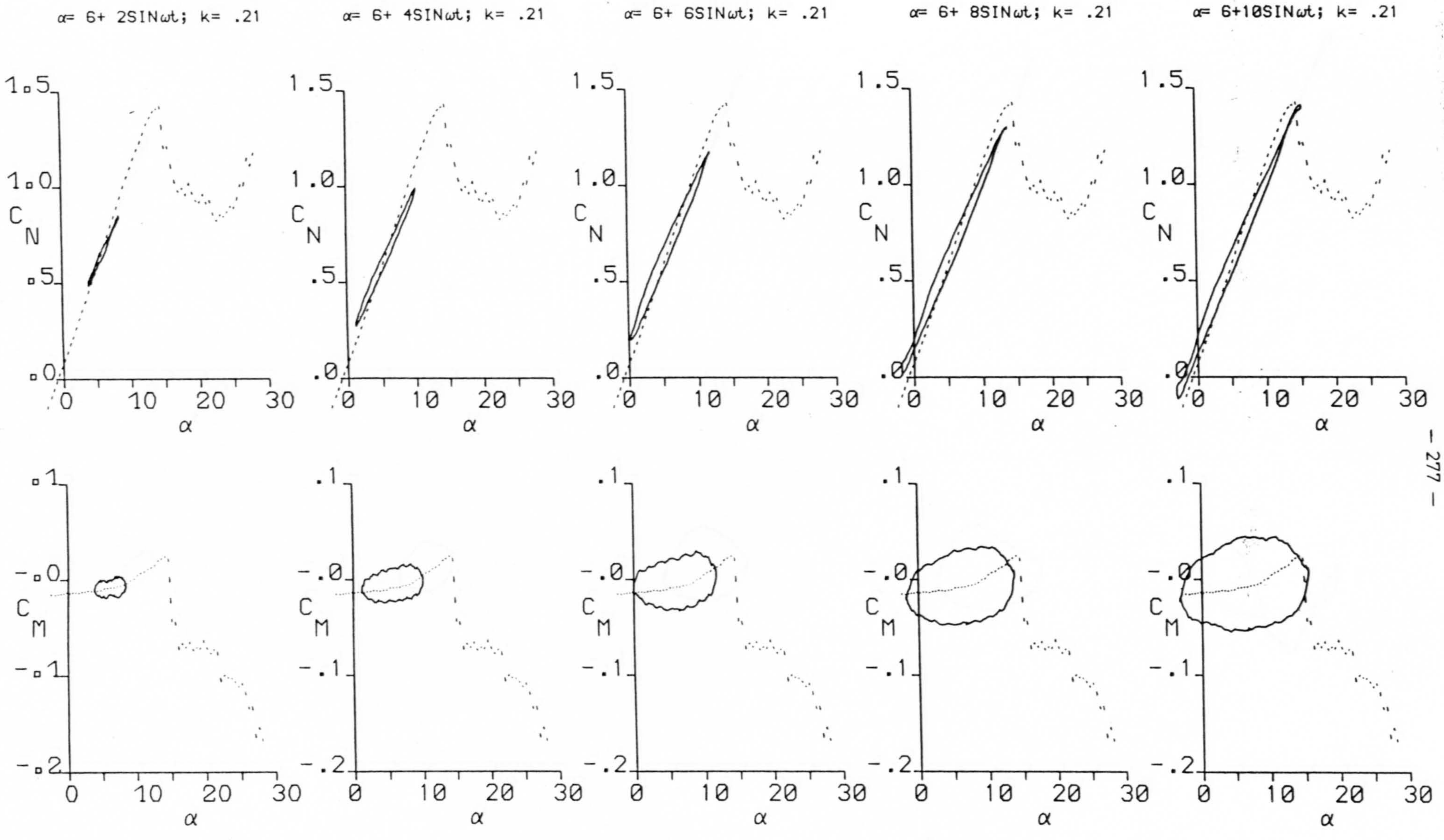

FIG. (7.45) EFFECT OF AMPLITUDE VARIATION AT $\alpha_M = 6^\circ$ AND K= .21

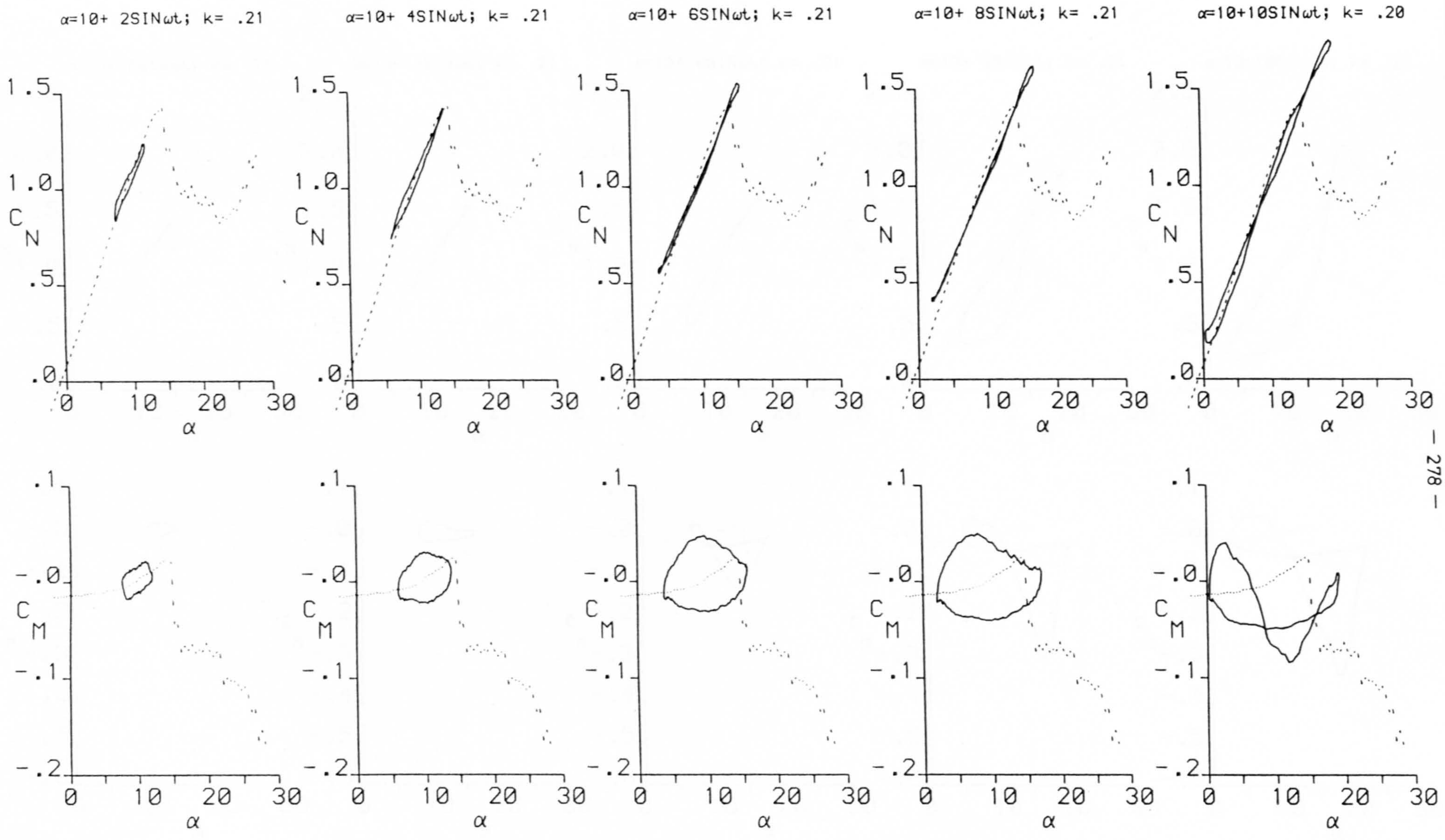

FIG.(7.46) EFFECT OF AMPLITUDE VARIATION AT $\alpha_M = 10^\circ$ AND K= .21

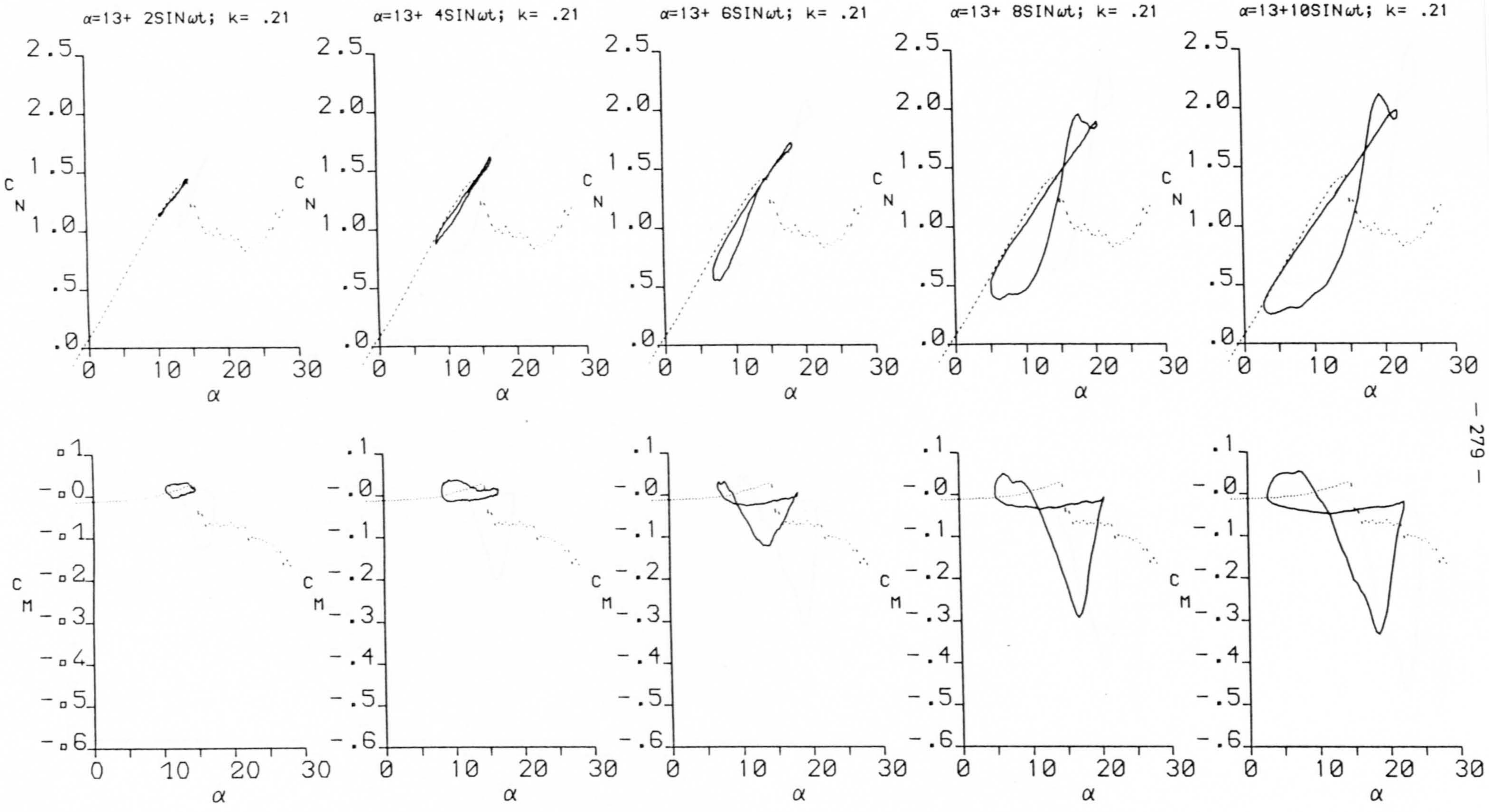

FIG. (7.47) EFFECT OF AMPLITUDE VARIATION AT $\alpha_M = 13^\circ$ AND K= .21

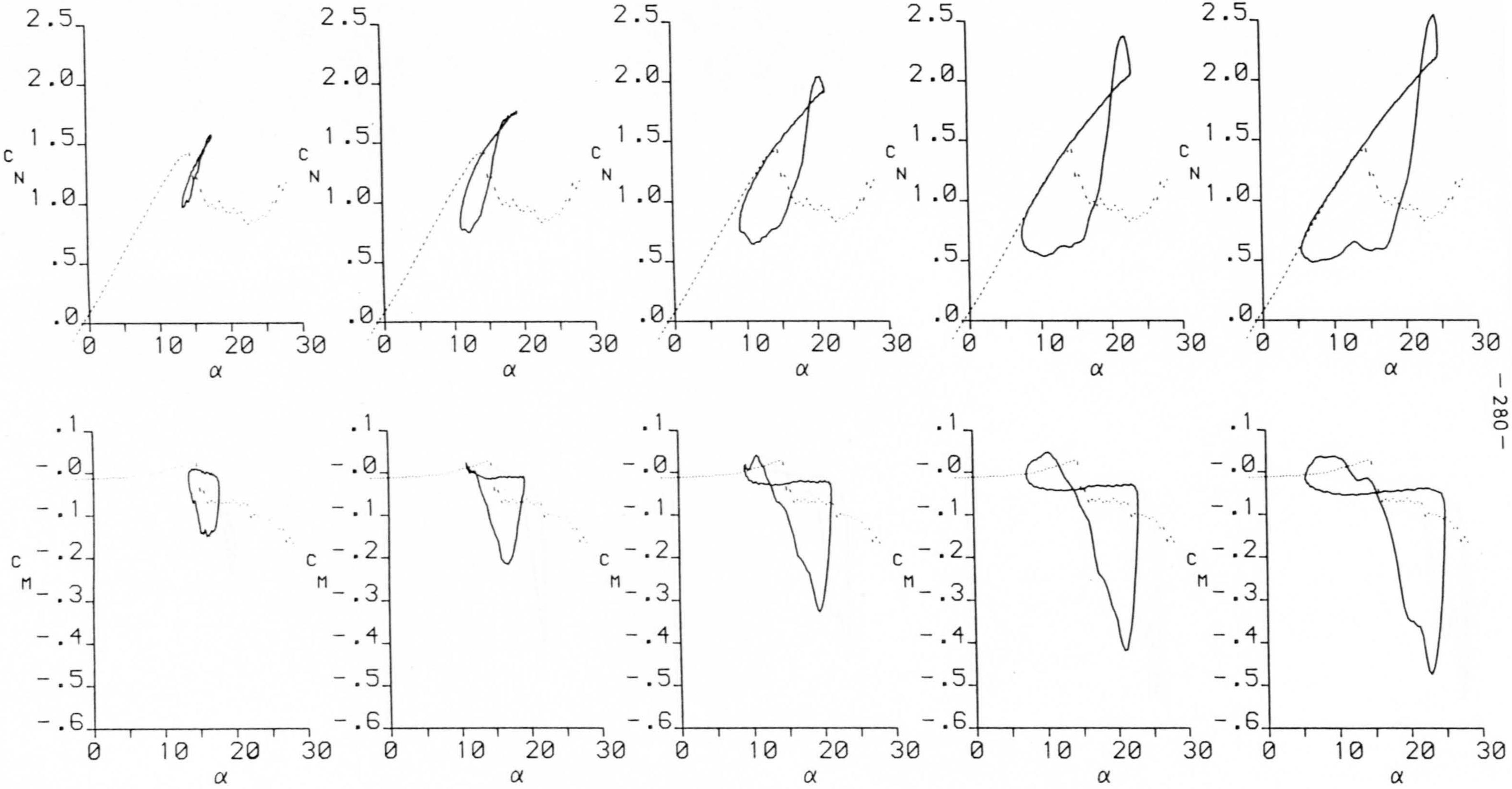

FIG.(7.48) EFFECT OF AMPLITUDE VARIATION AT $\alpha_M = 15^\circ$ AND K= .21

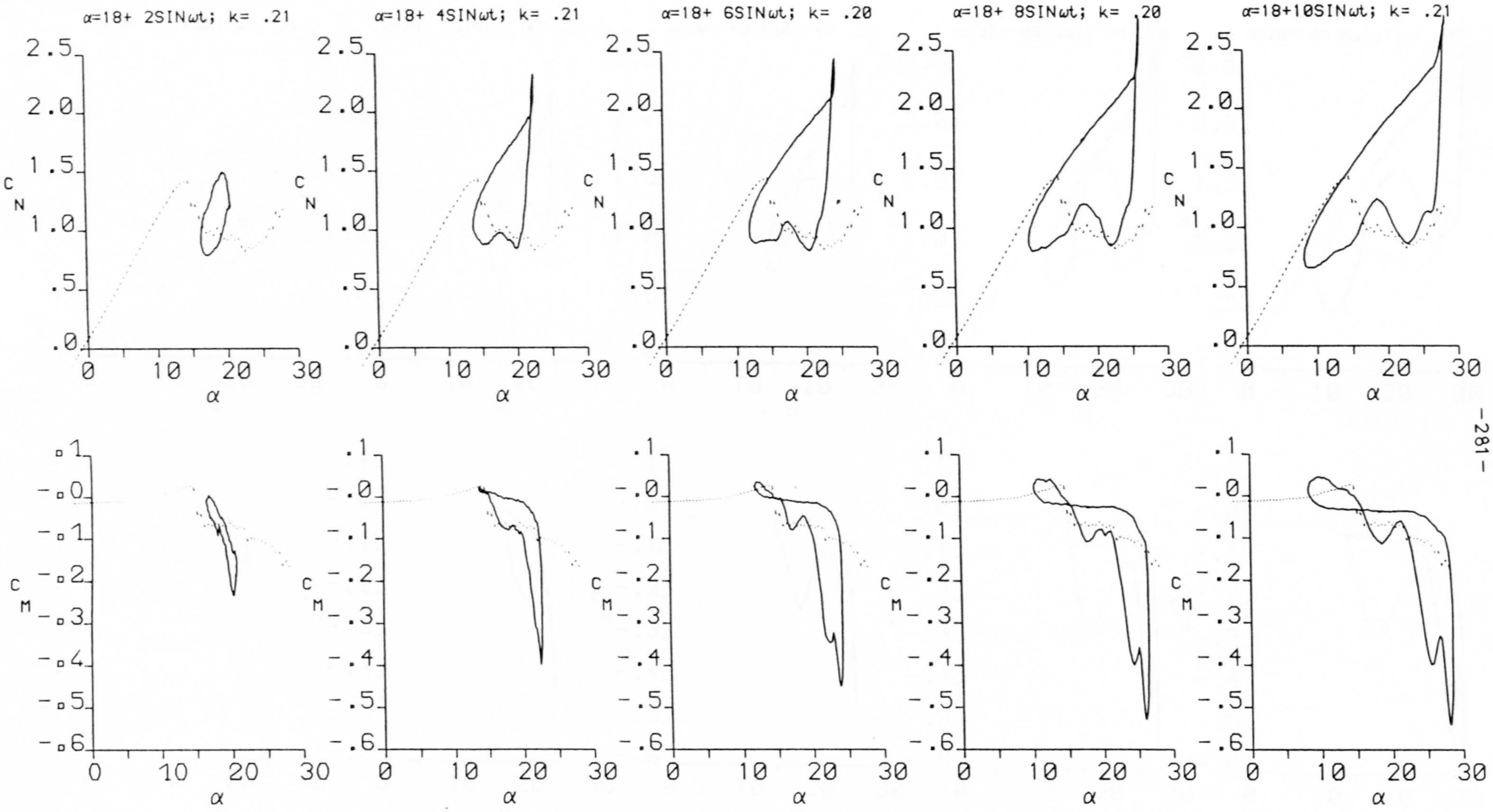

FIG. (7.49) EFFECT OF AMPLITUDE VARIATION AT $\alpha_M = 18^\circ$ AND K= .21

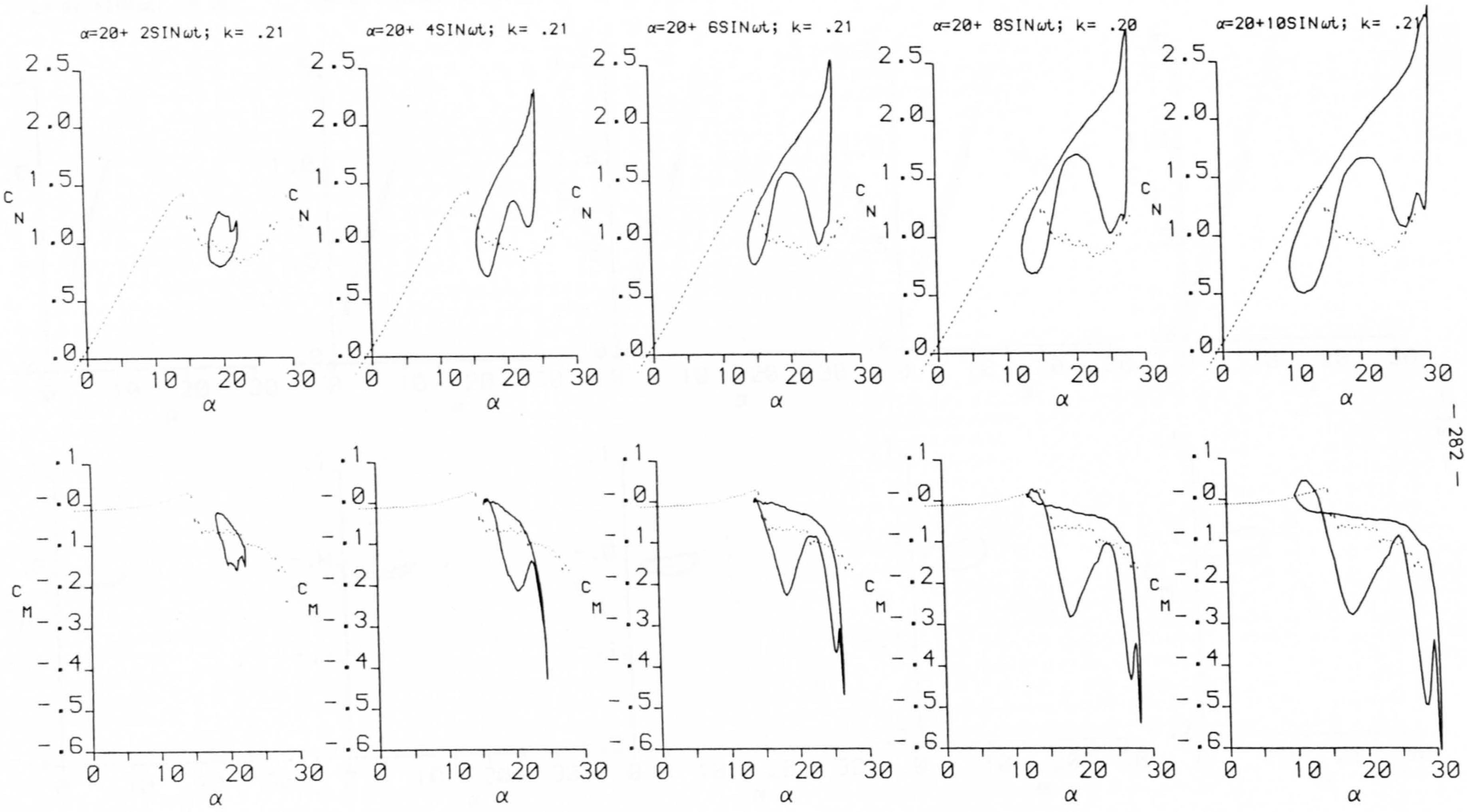

FIG.(7.50) EFFECT OF AMPLITUDE VARIATION AT $\alpha_M = 20^\circ$ AND K= .21

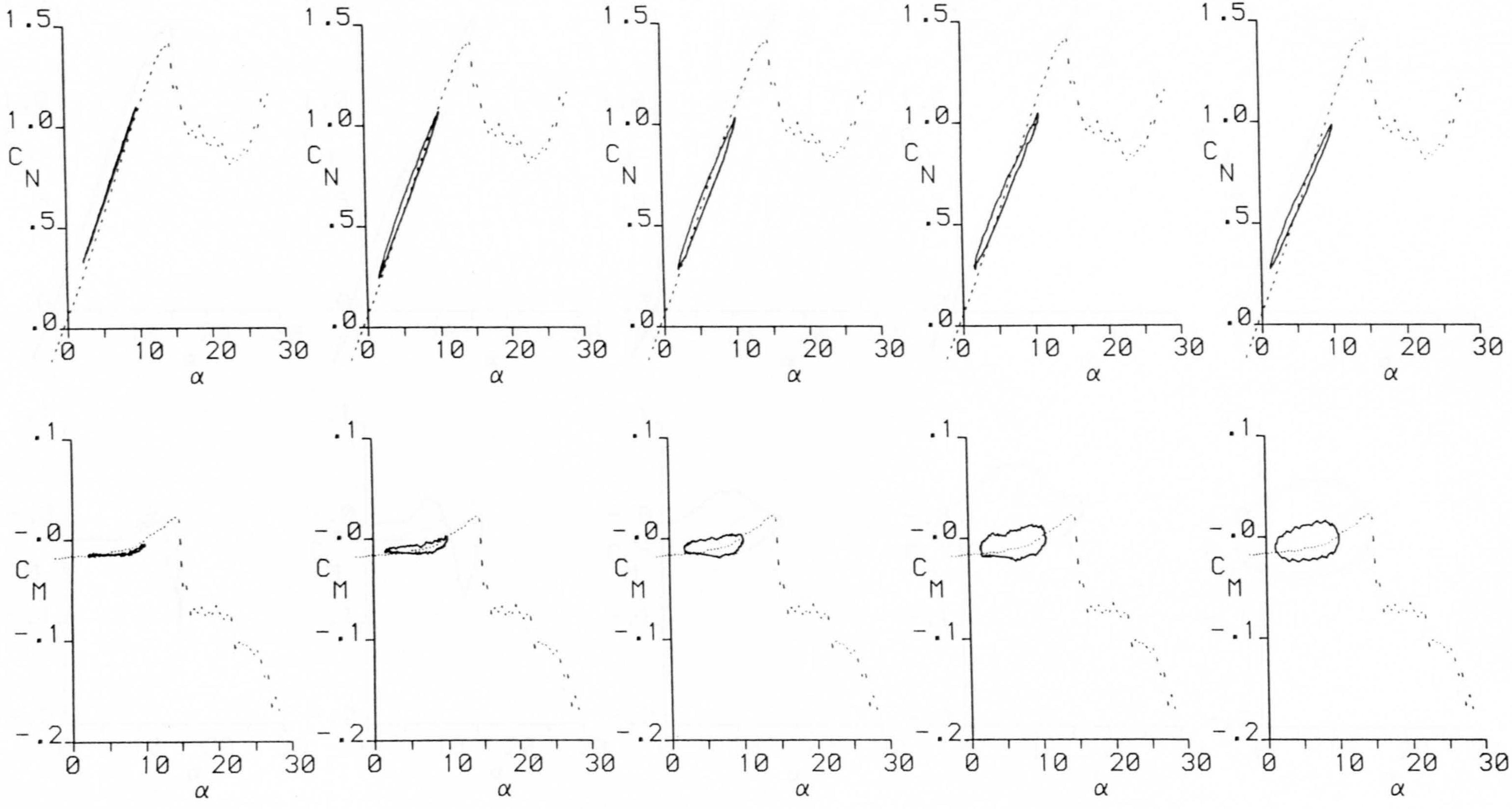

FIG.(7.51) EFFECT OF REDUCED FREQUENCY VARIATION AT α_m = 6 AND α_a = 4

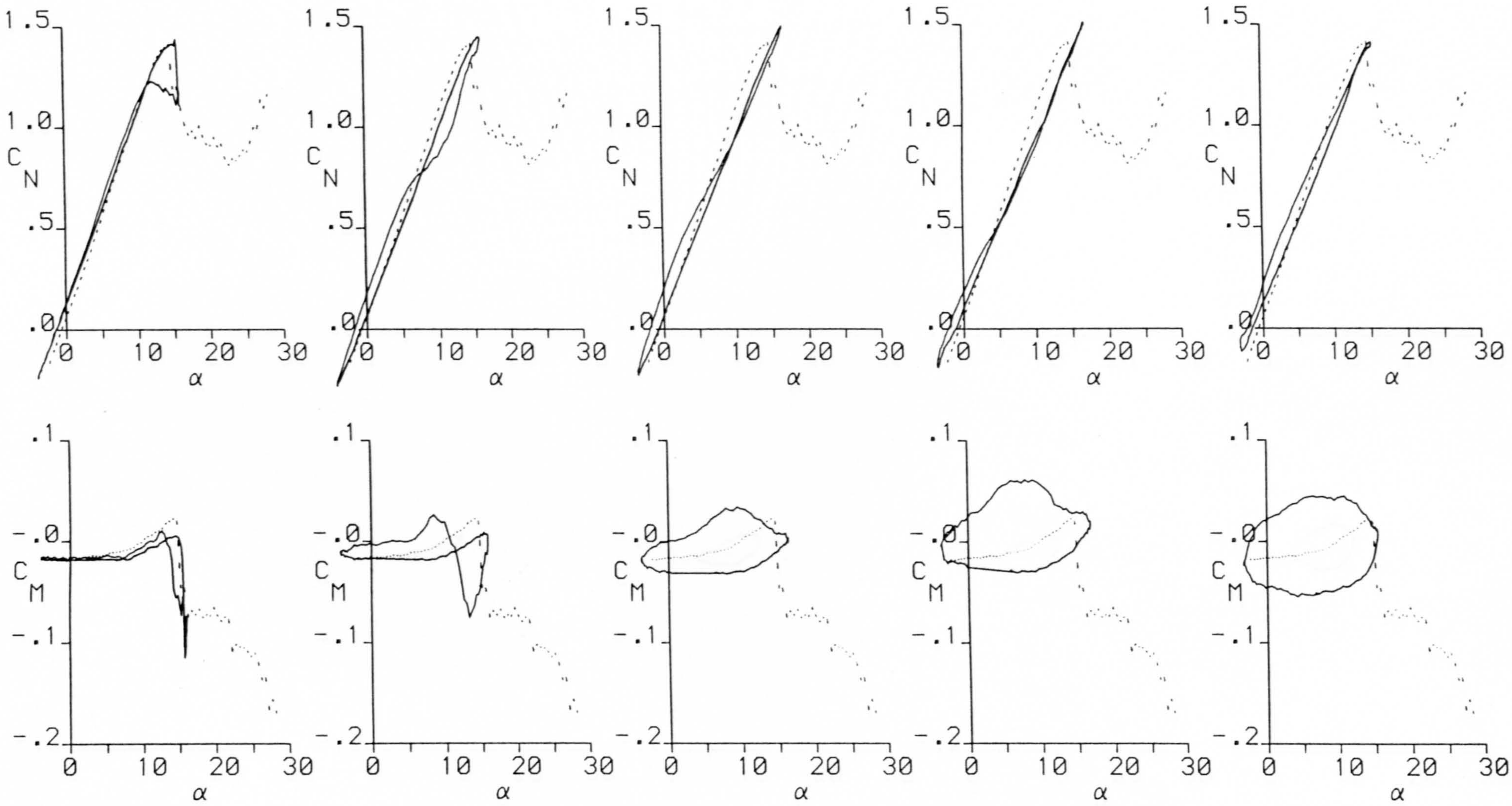

FIG.(7.52) EFFECT OF REDUCED FREQUENCY VARIATION AT α_m = 6 AND α_a =10

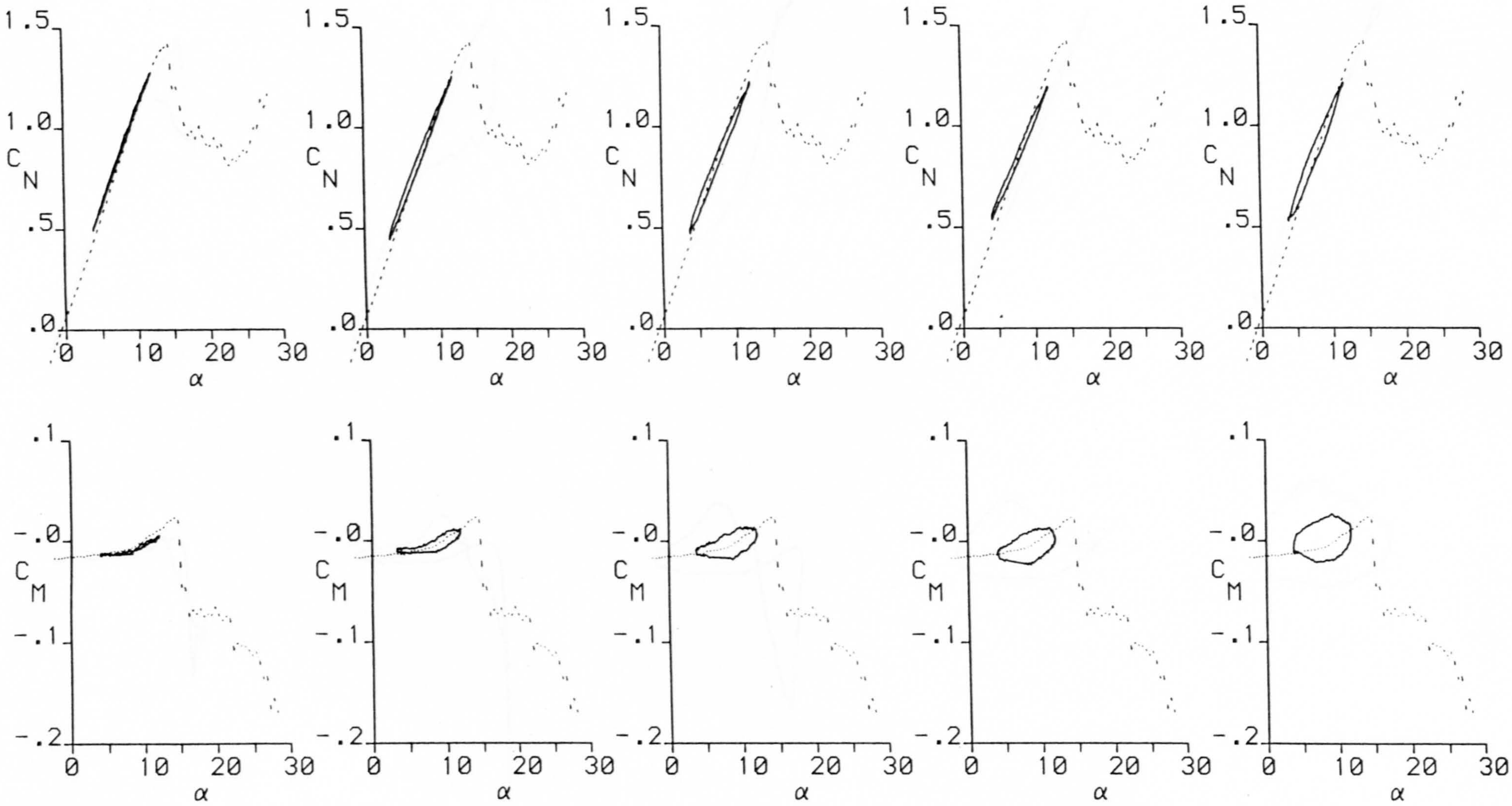

FIG.(7.53) EFFECT OF REDUCED FREQUENCY VARIATION AT α_m = 8 AND α_a = 4

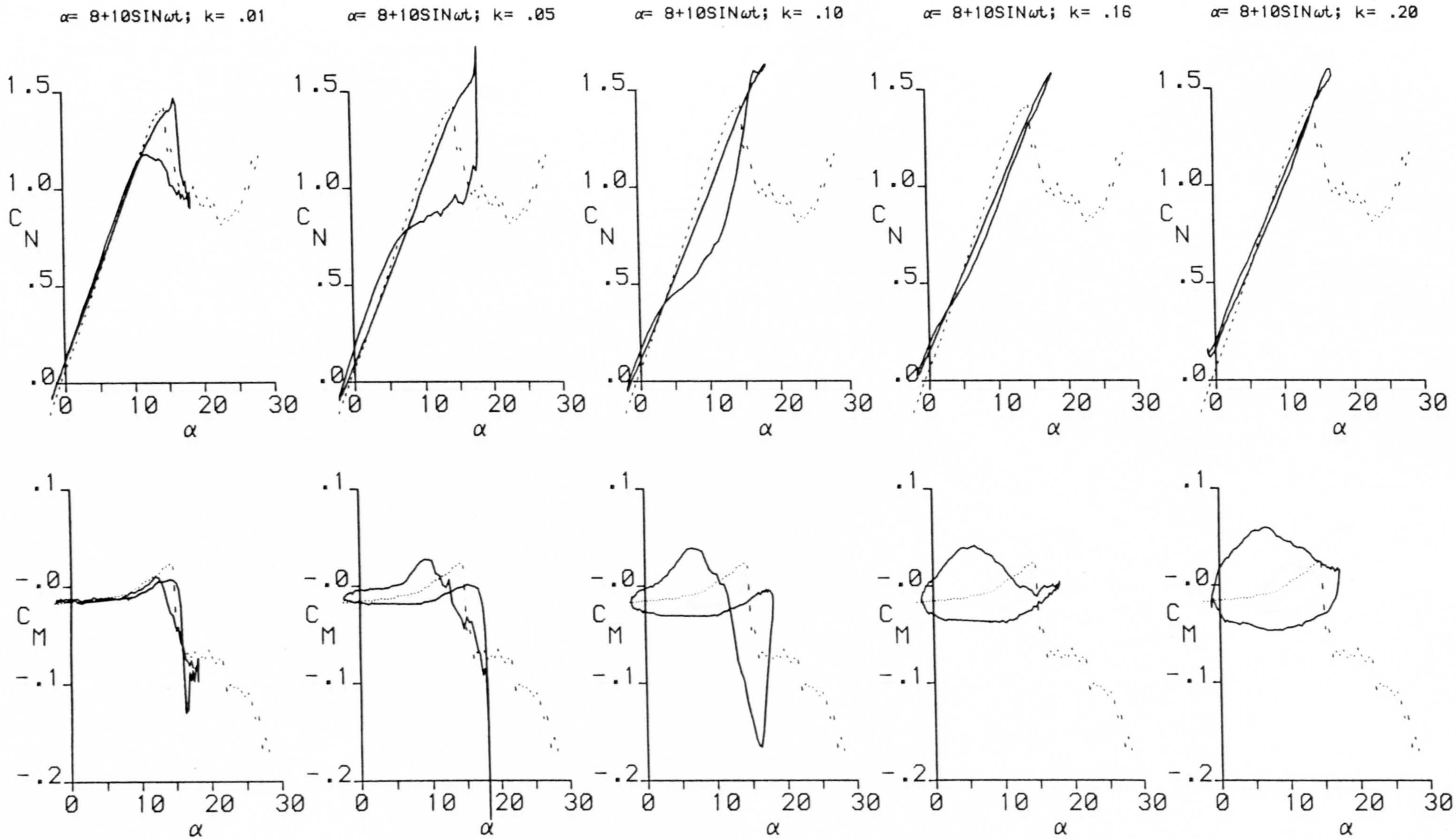

FIG.(7.54) EFFECT OF REDUCED FREQUENCY VARIATION AT α_m = 8 AND α_a =10

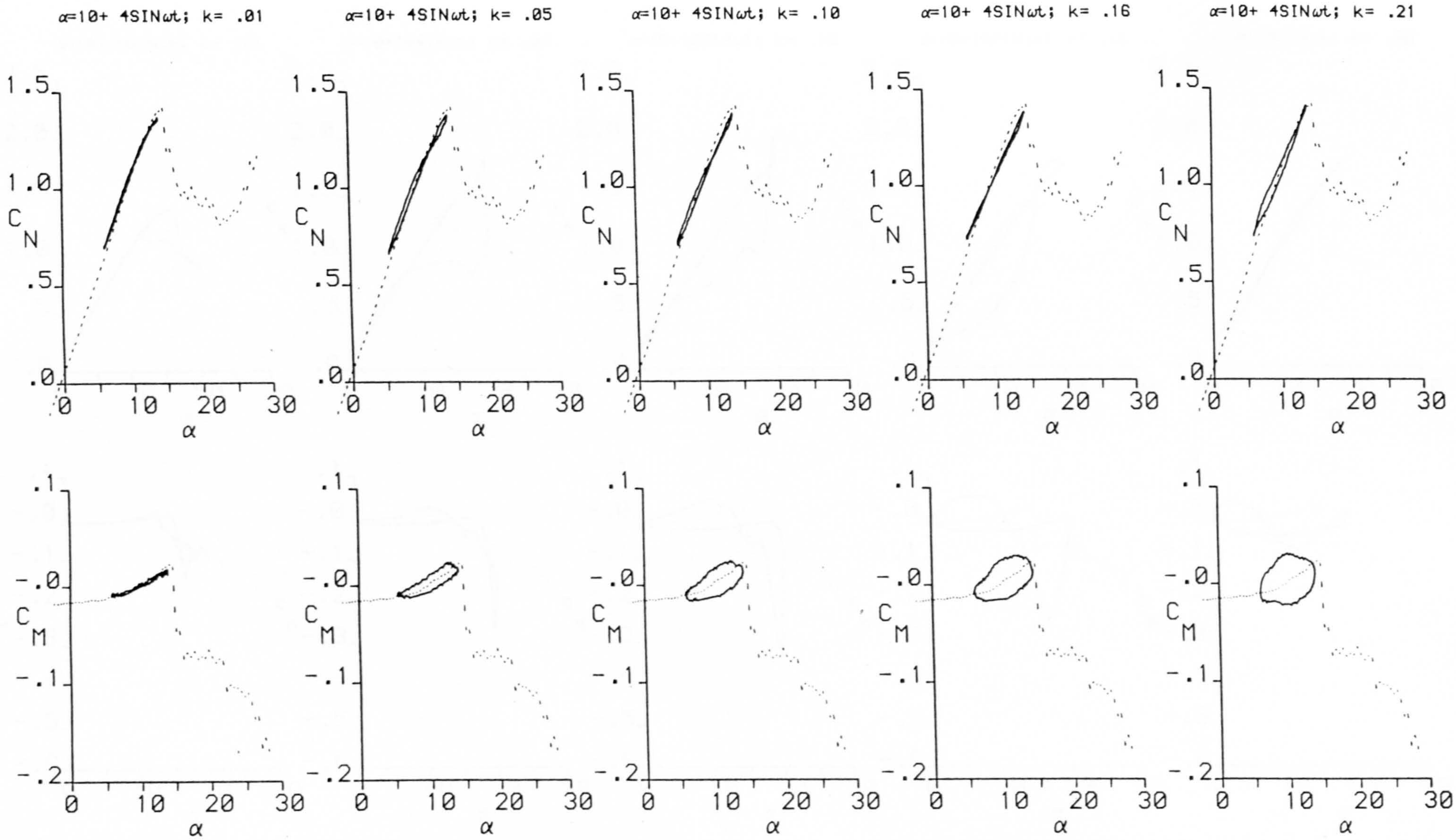

FIG.(7.55) EFFECT OF REDUCED FREQUENCY VARIATION AT α_m = 10 AND α_a = 4

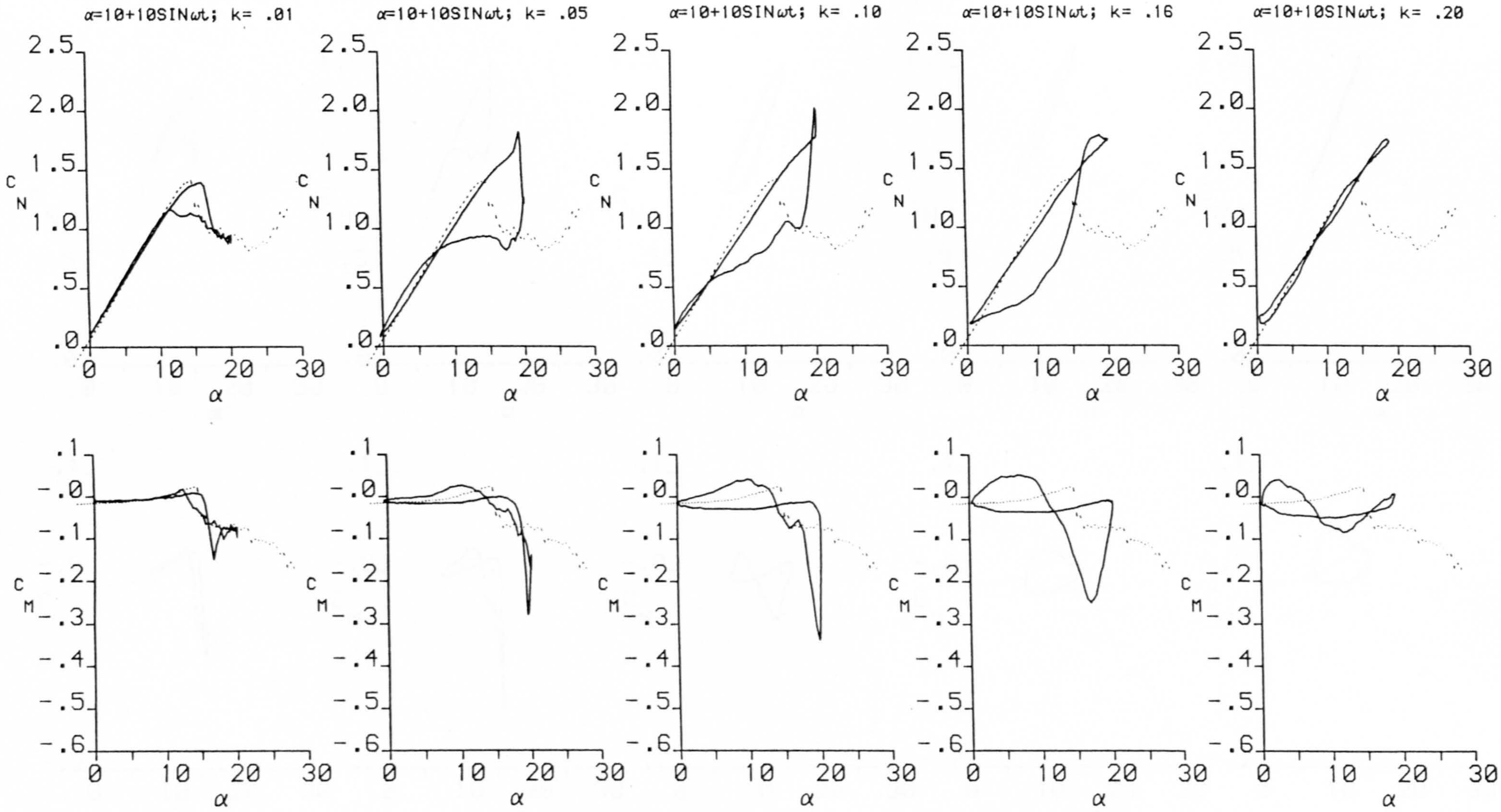

FIG.(7.56) EFFECT OF REDUCED FREQUENCY VARIATION AT α_m = 10 AND α_a =10

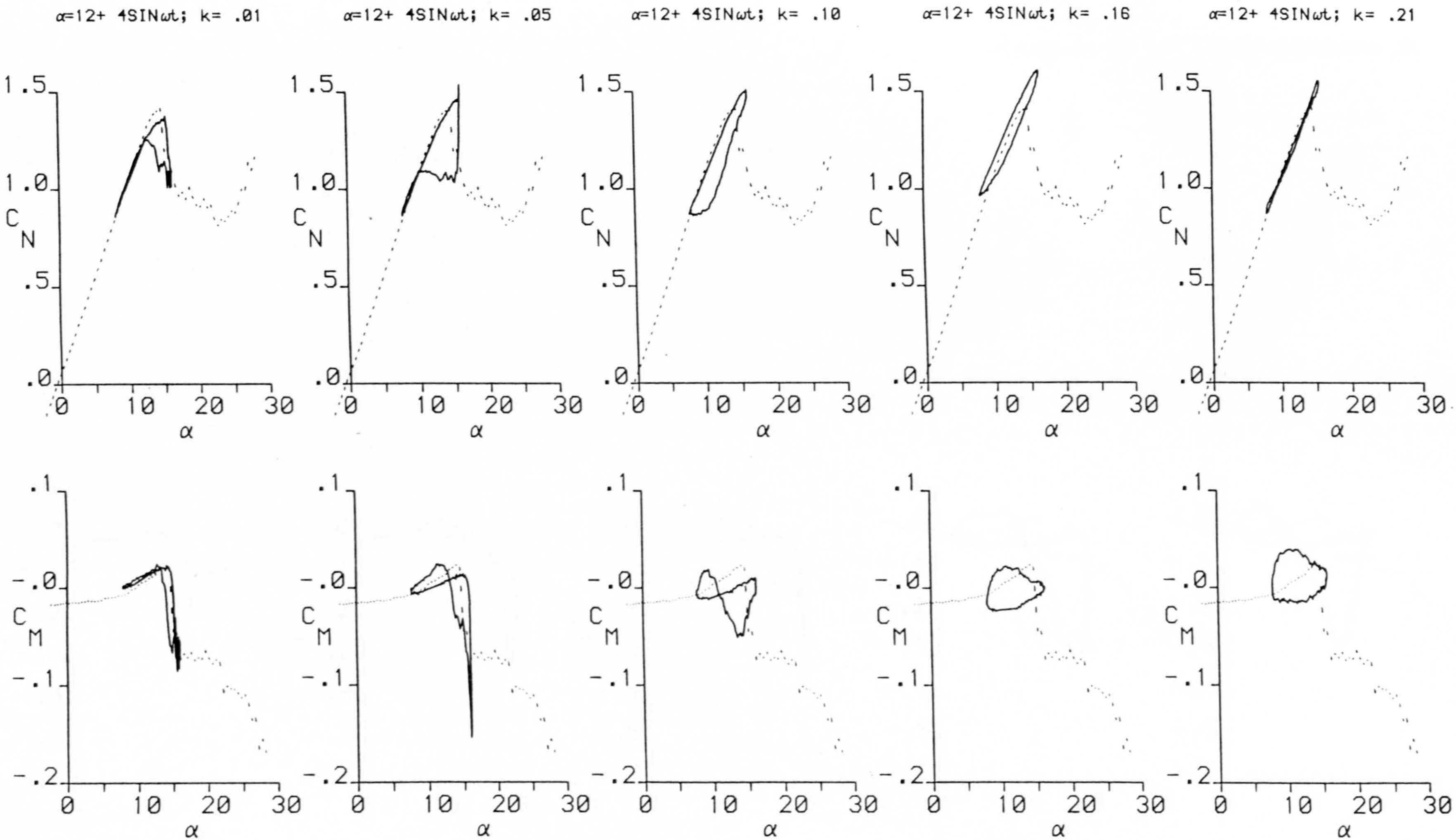

FIG.(7.57) EFFECT OF REDUCED FREQUENCY VARIATION AT $\alpha_m = 12$ AND $\alpha_a = 4$

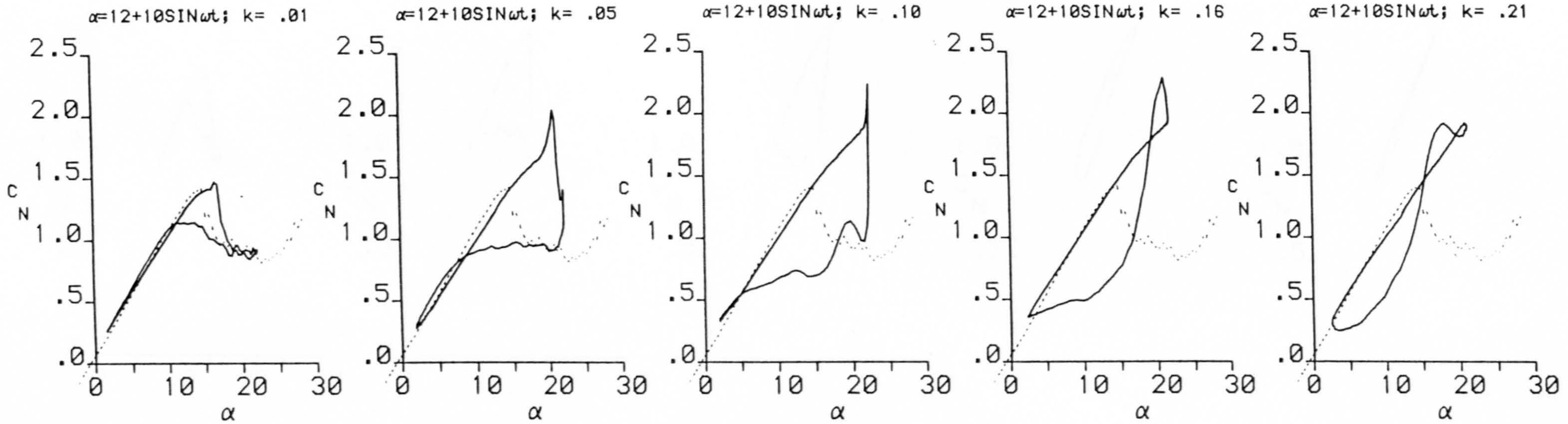

FIG.(7.58) EFFECT OF REDUCED FREQUENCY VARIATION AT α_m = 12 AND α_a =10

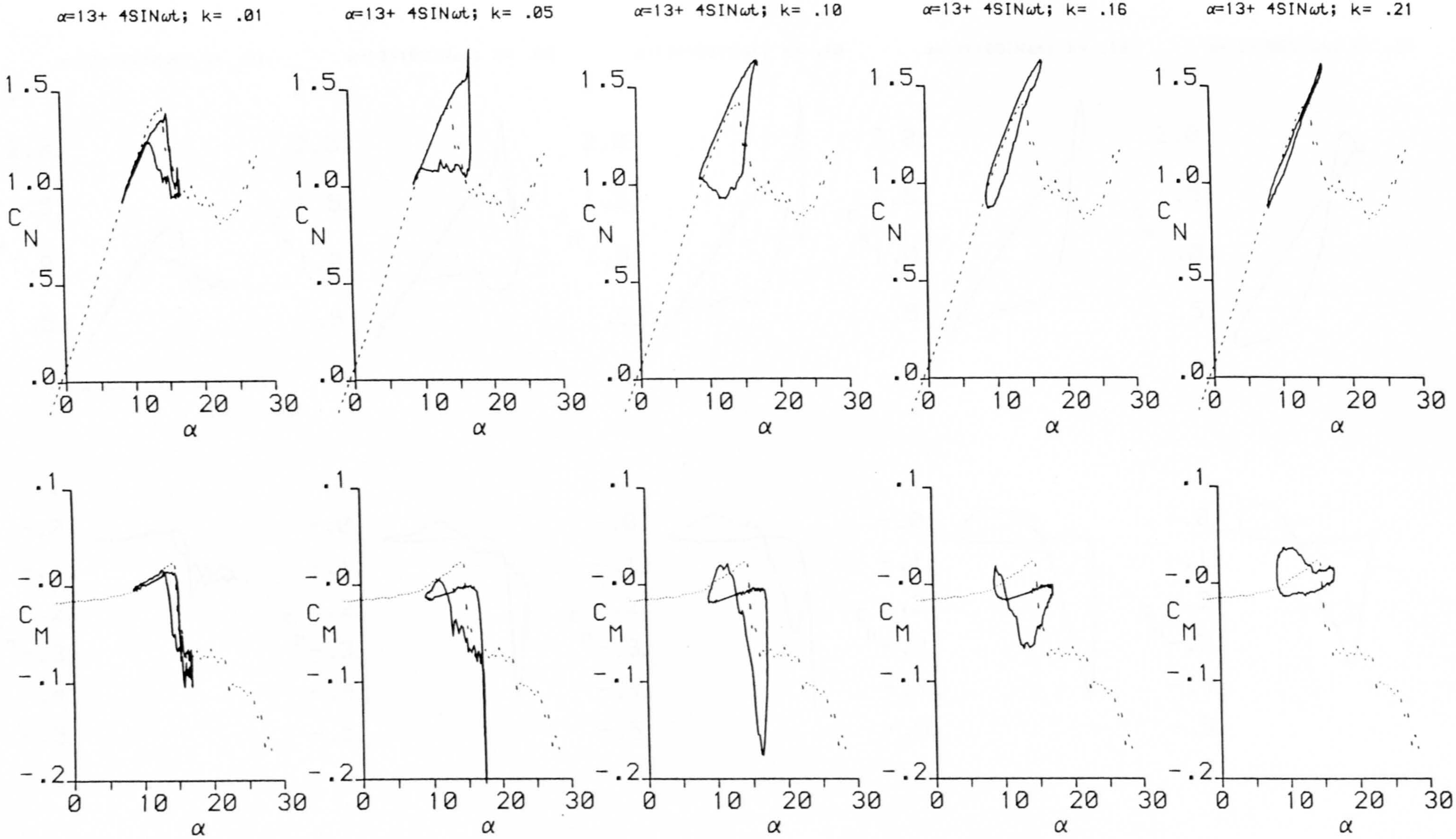

FIG.(7.59) EFFECT OF REDUCED FREQUENCY VARIATION AT α_m = 13 AND α_a = 4

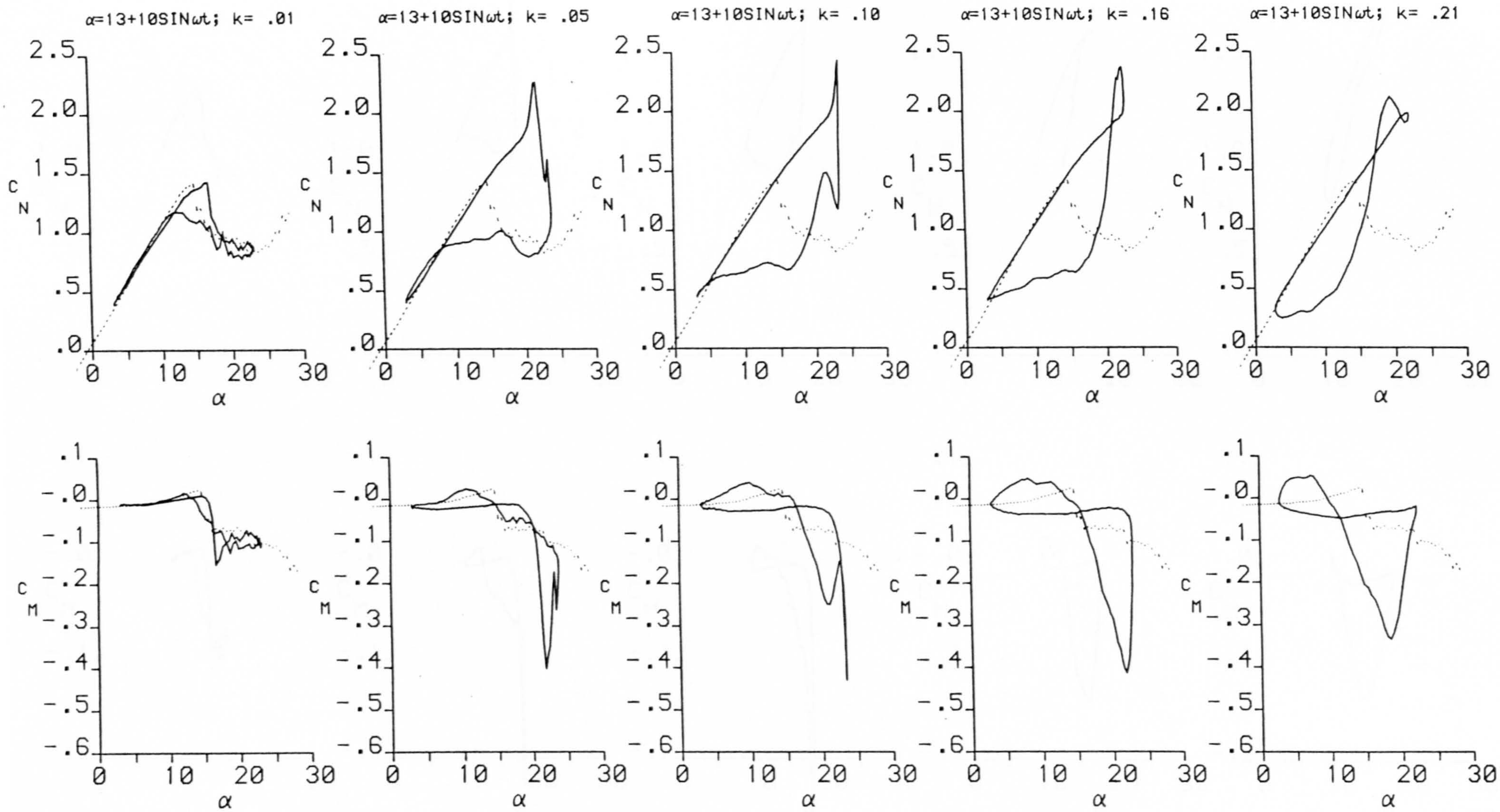

FIG.(7.60) EFFECT OF REDUCED FREQUENCY VARIATION AT α_m = 13 AND α_a =10

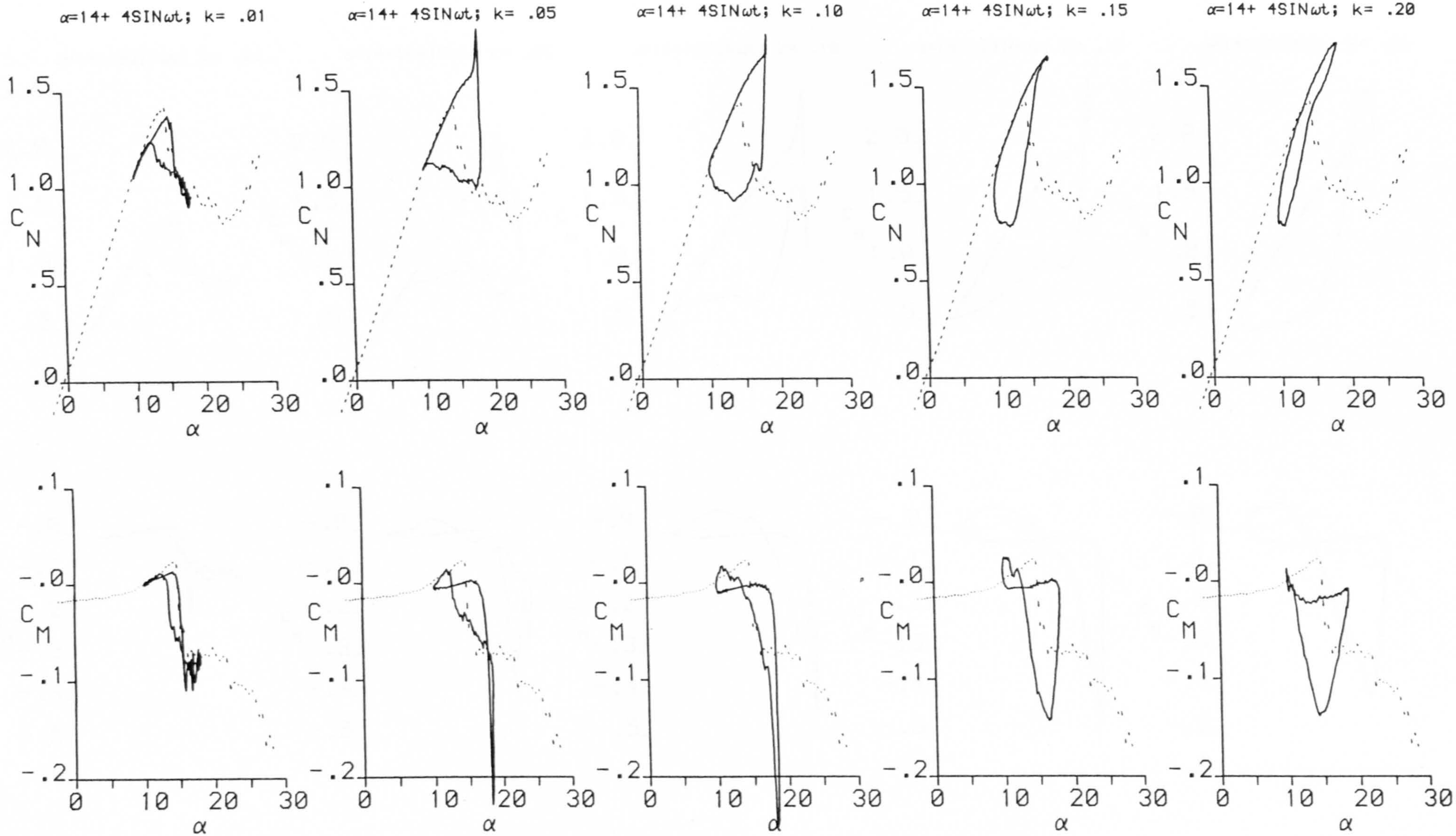

FIG.(7.61) EFFECT OF REDUCED FREQUENCY VARIATION AT α_m = 14 AND α_a = 4

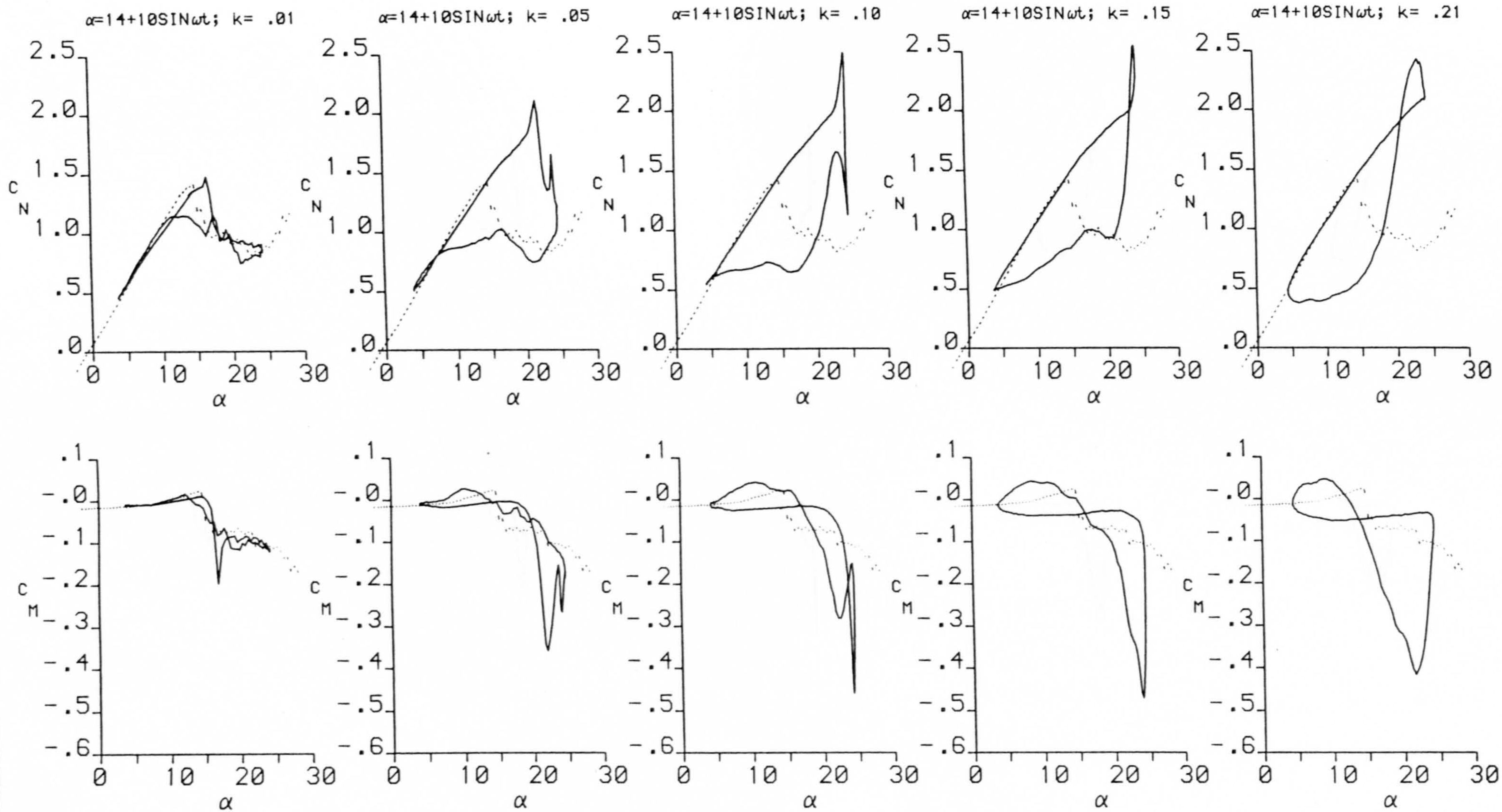

FIG.(7.62) EFFECT OF REDUCED FREQUENCY VARIATION AT α_m = 14 AND α_a =10

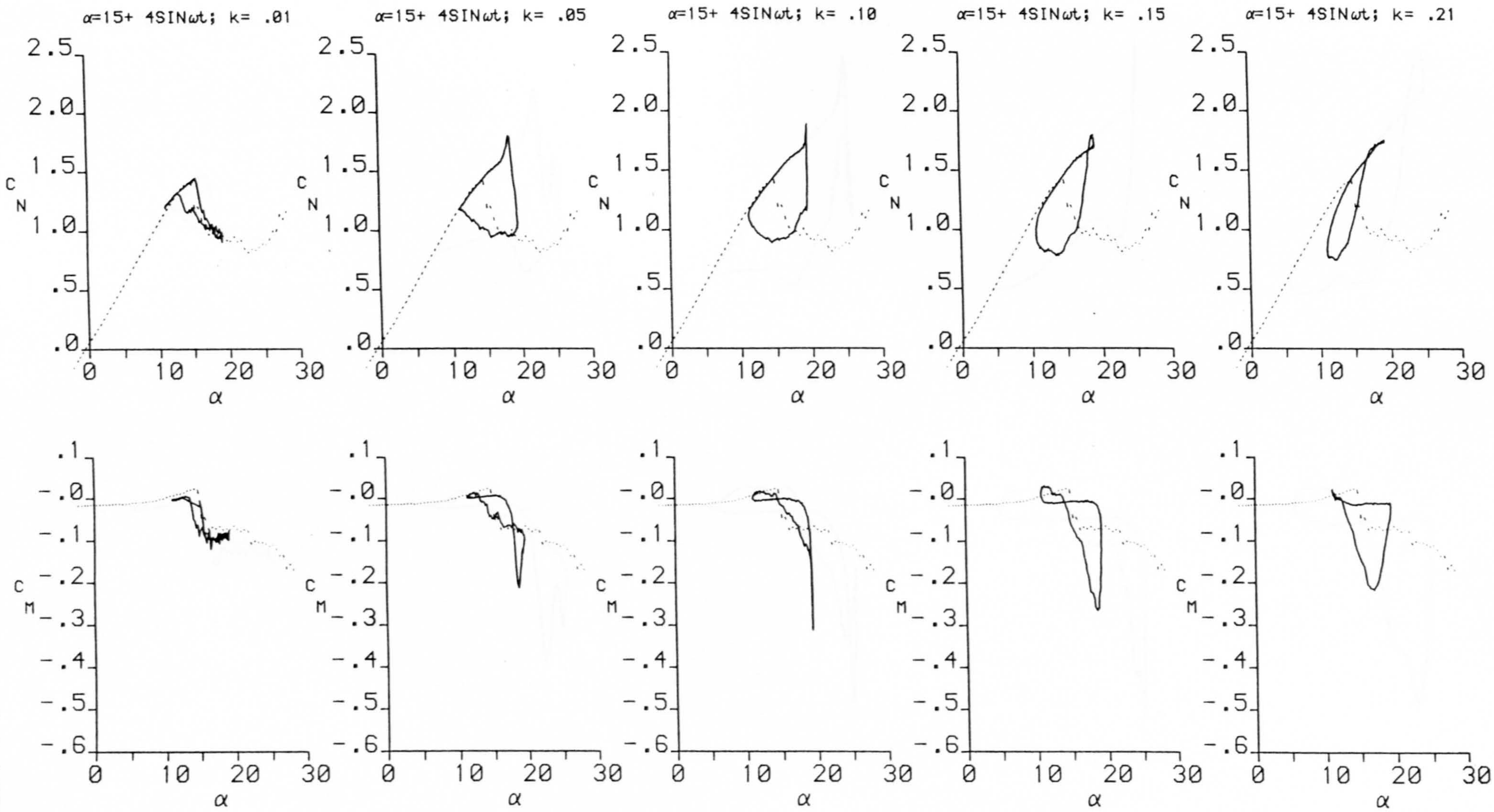

FIG.(7.63) EFFECT OF REDUCED FREQUENCY VARIATION AT α_m = 15 AND α_a = 4

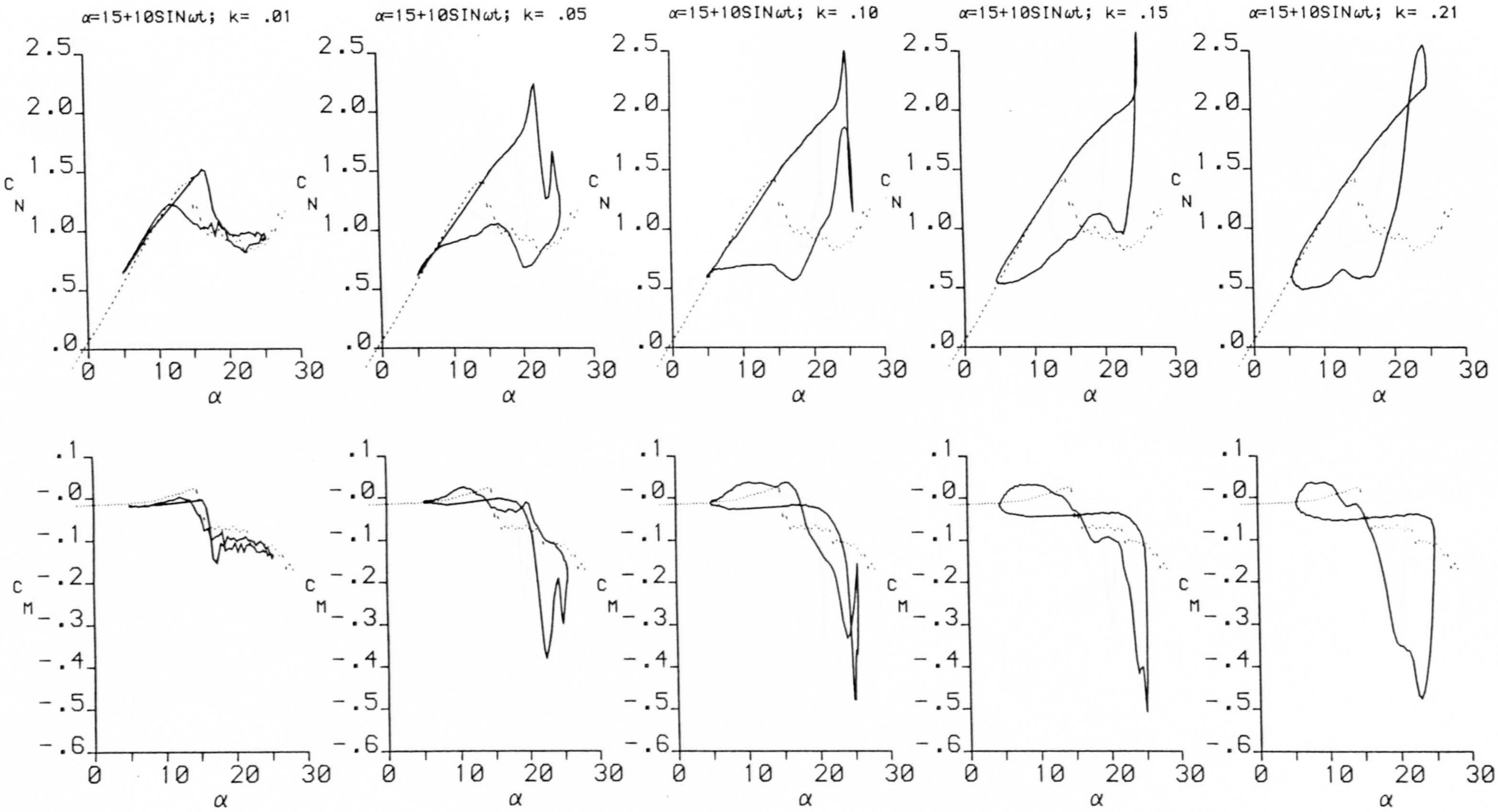

FIG.(7.64) EFFECT OF REDUCED FREQUENCY VARIATION AT α_m = 15 AND α_a =10

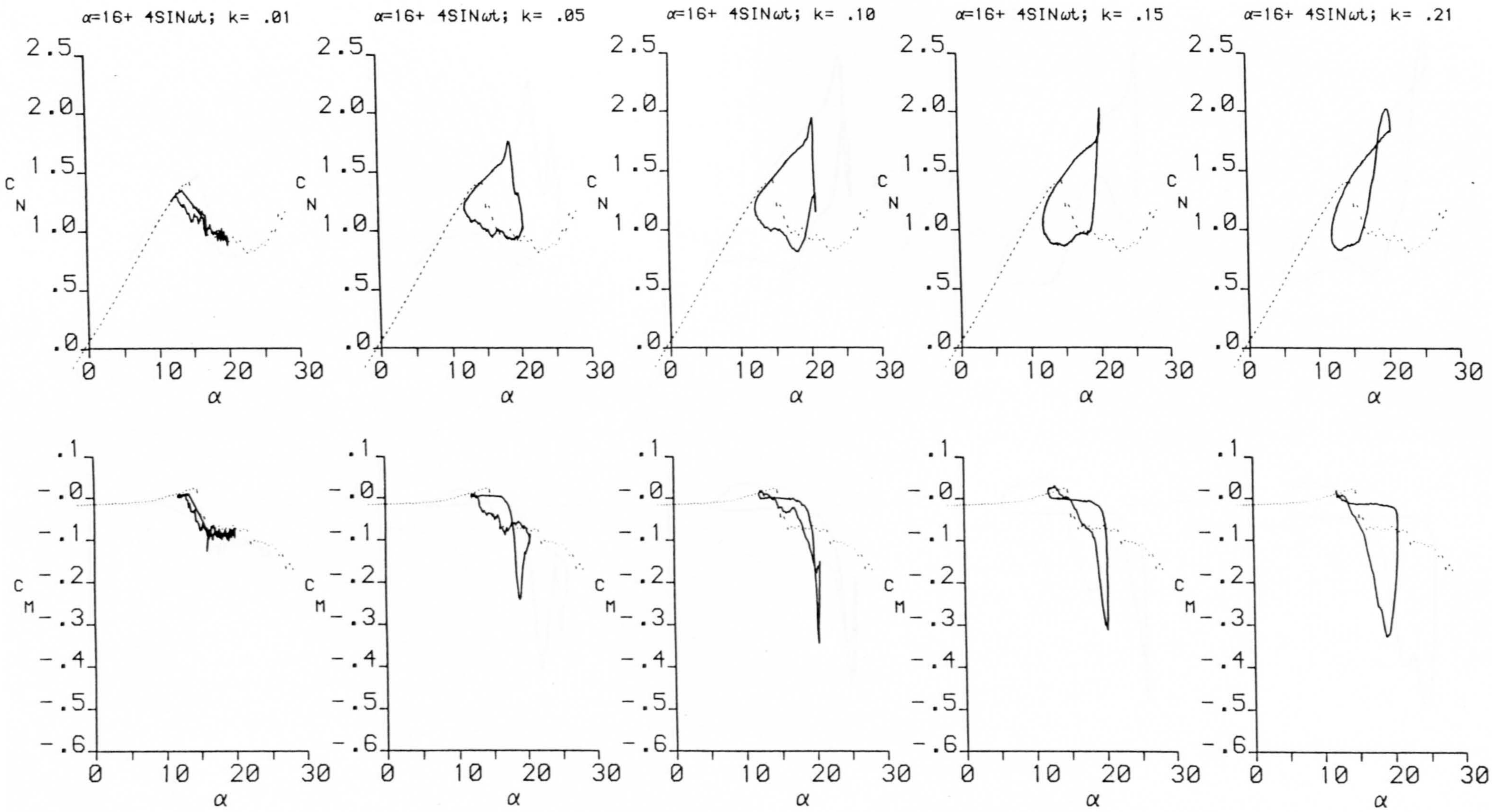

FIG.(7.65) EFFECT OF REDUCED FREQUENCY VARIATION AT α_m = 16 AND α_a = 4

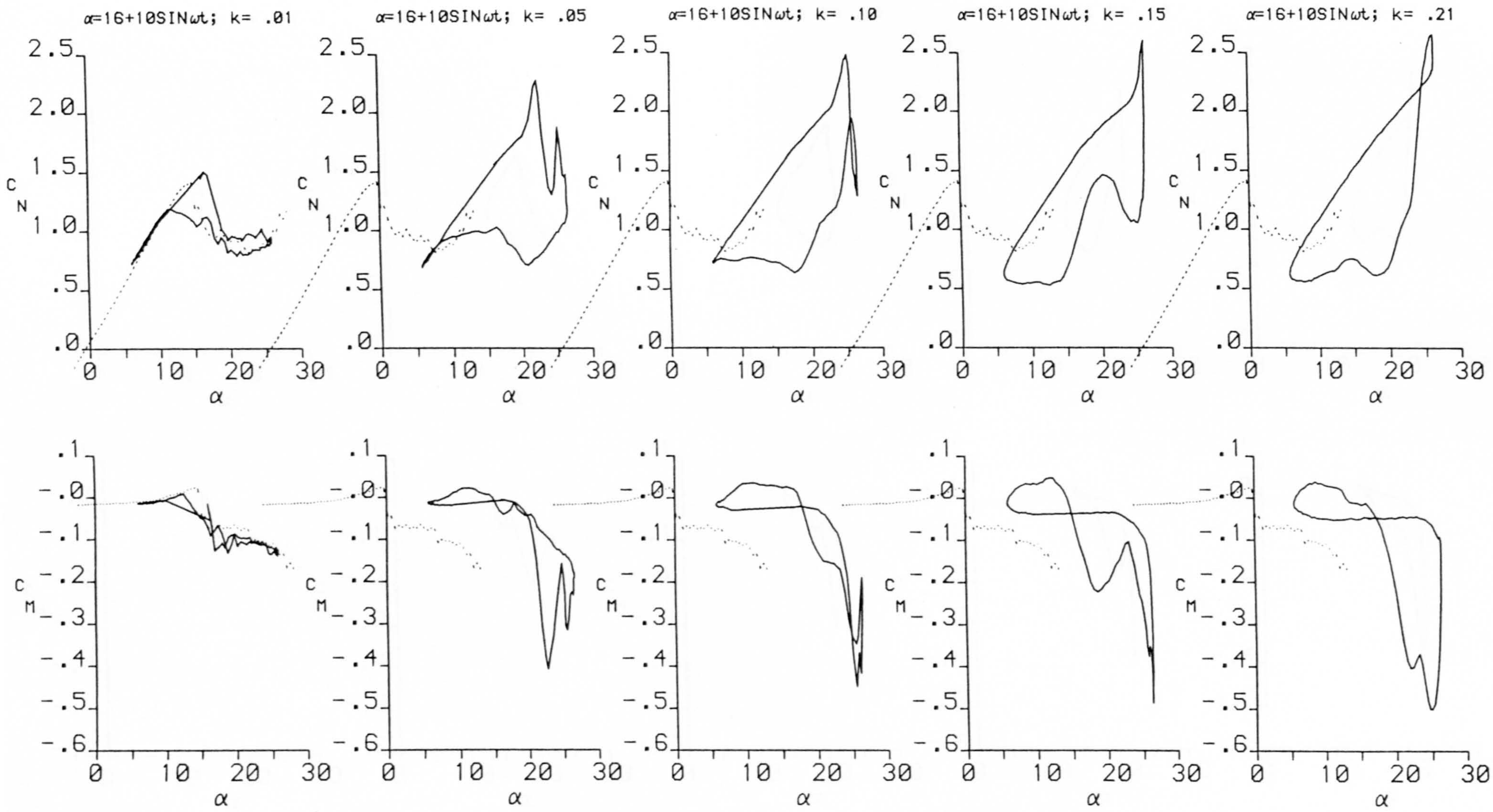

FIG.(7.66) EFFECT OF REDUCED FREQUENCY VARIATION AT α_m = 16 AND α_a =10

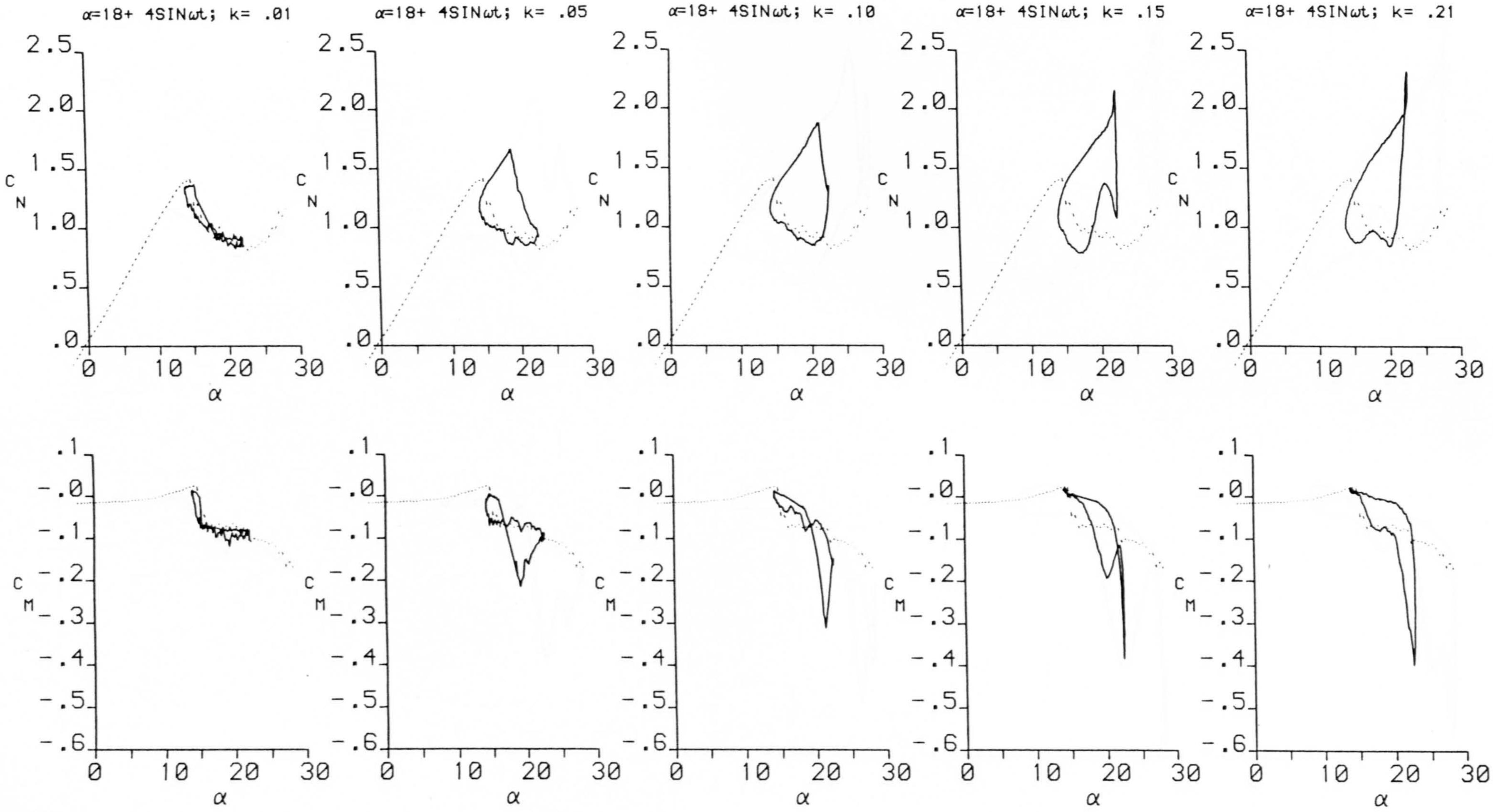

FIG.(7.67) EFFECT OF REDUCED FREQUENCY VARIATION AT α_m = 18 AND α = 4

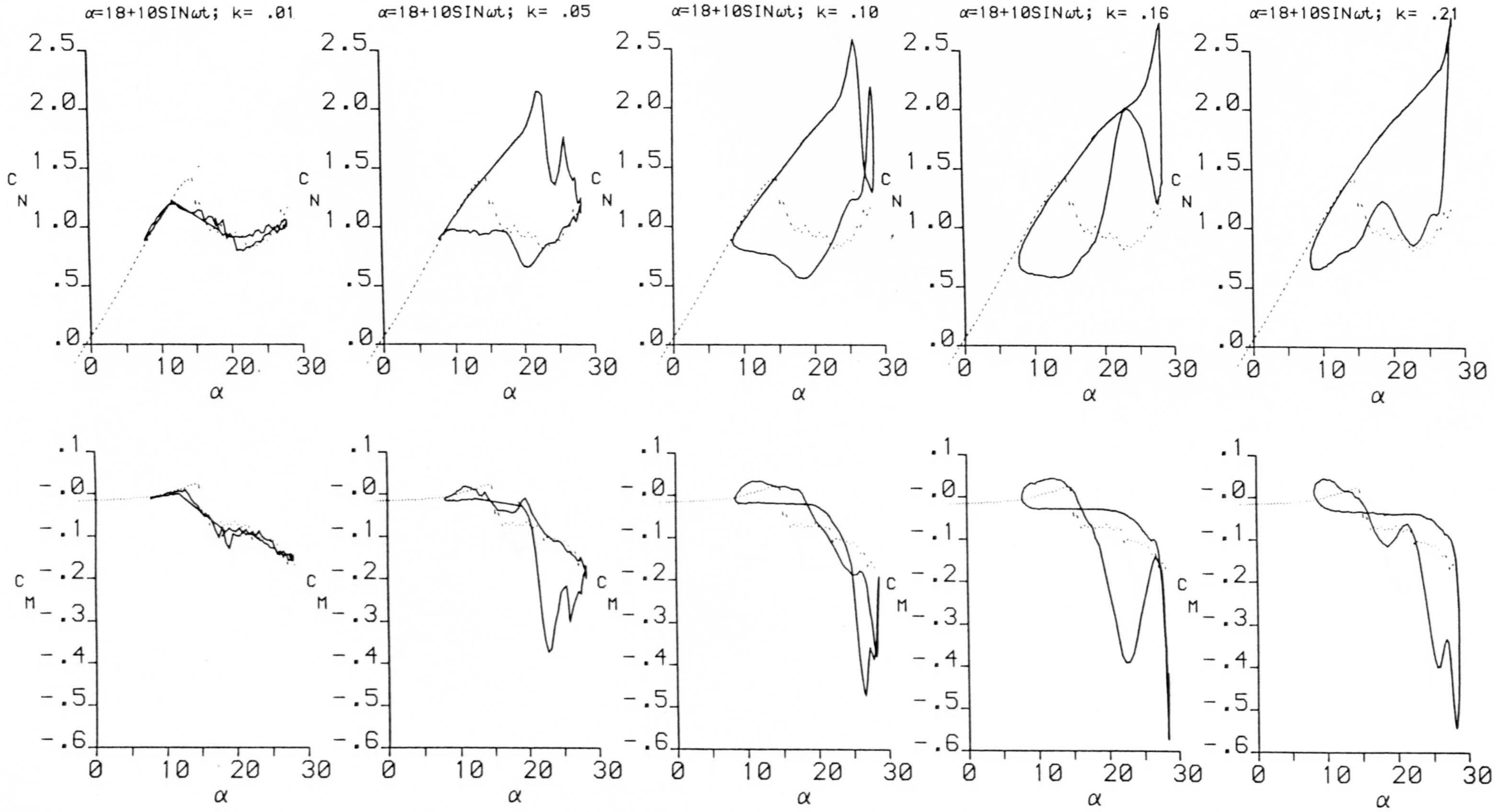

FIG.(7.68) EFFECT OF REDUCED FREQUENCY VARIATION AT α_m = 18 AND α_a =10

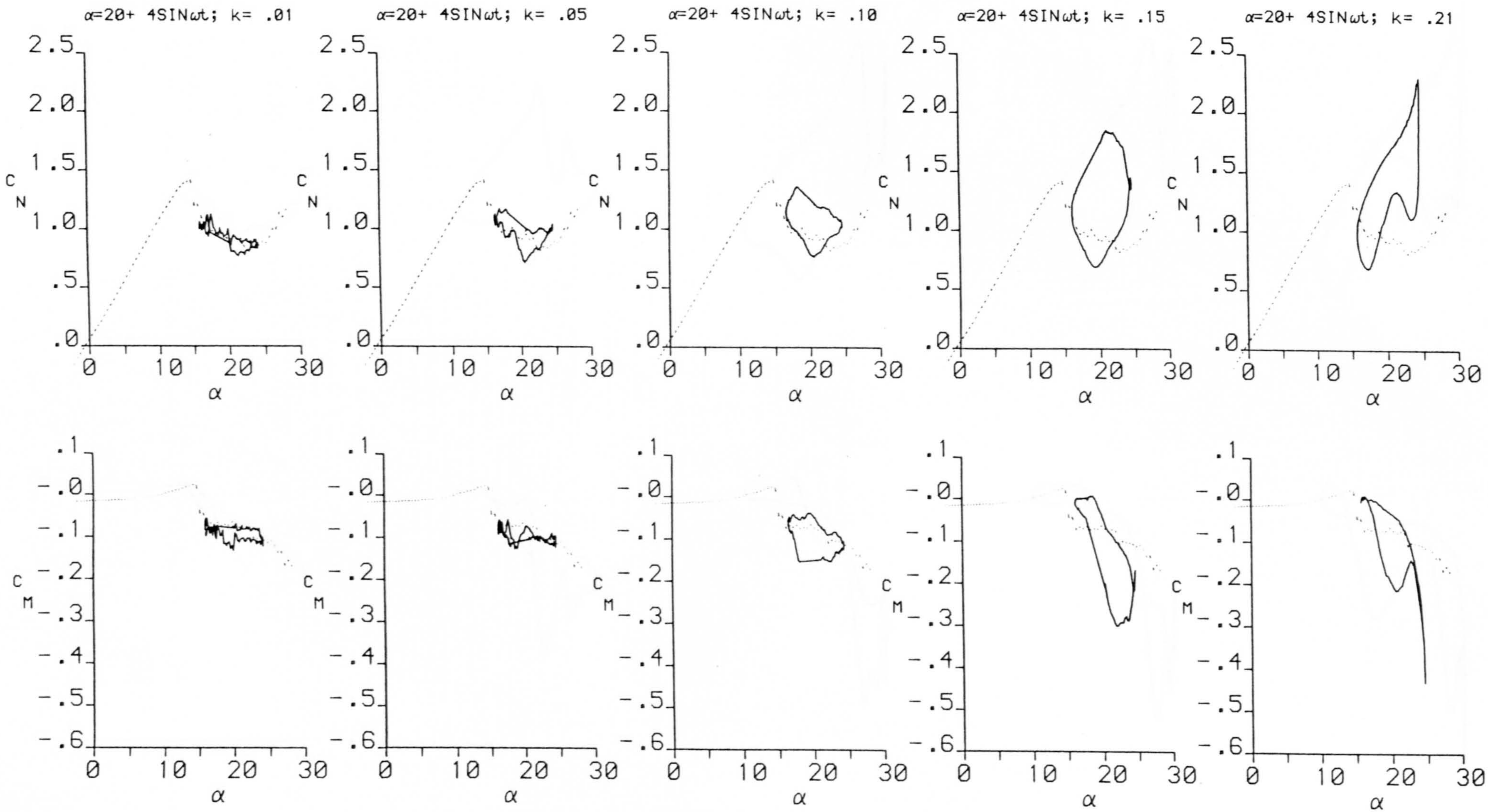

FIG.(7.69) EFFECT OF REDUCED FREQUENCY VARIATION AT $\alpha_m = 20$ AND $\alpha_a = 4$

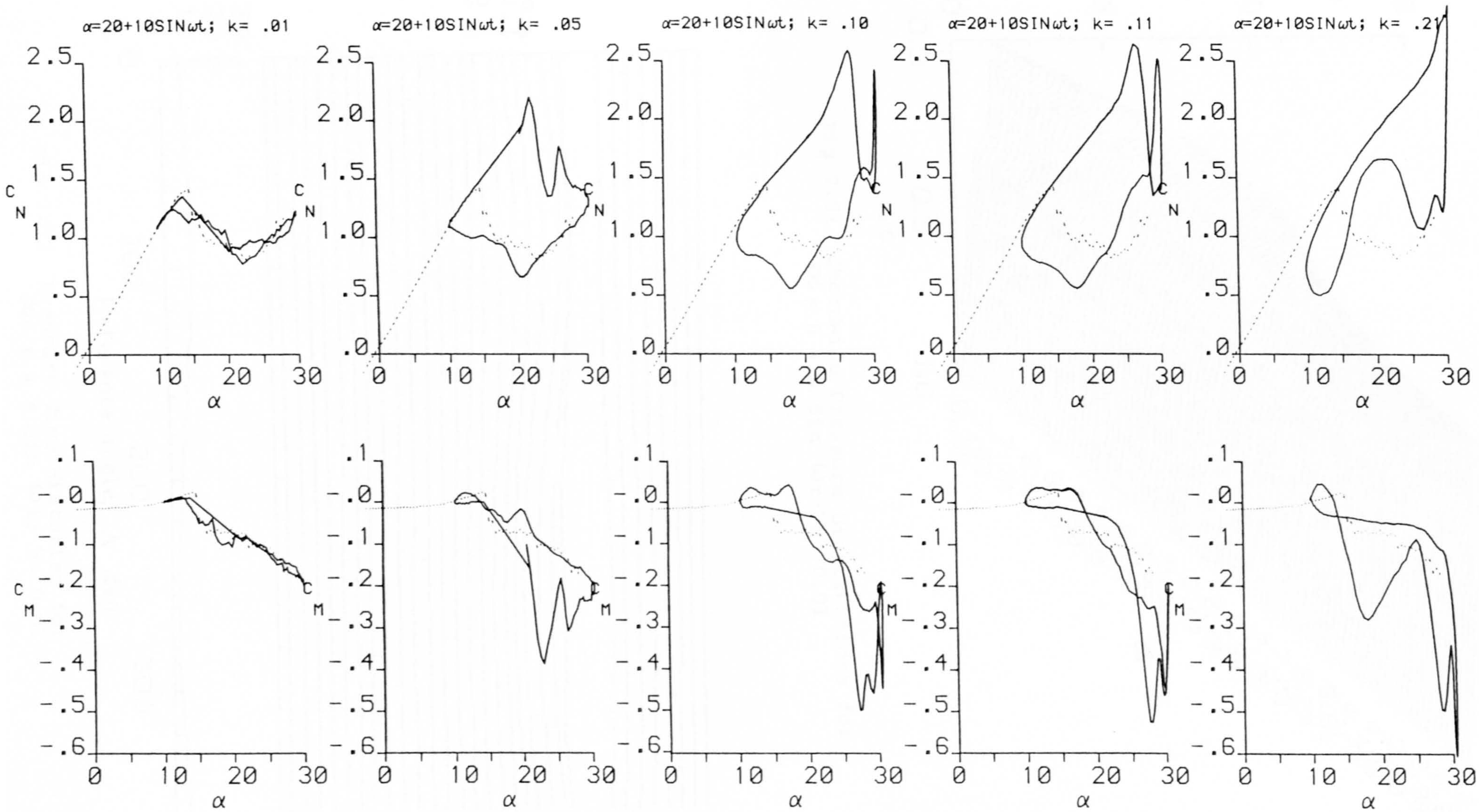

FIG.(7.70) EFFECT OF REDUCED FREQUENCY VARIATION AT α_m = 20 AND α_a =10

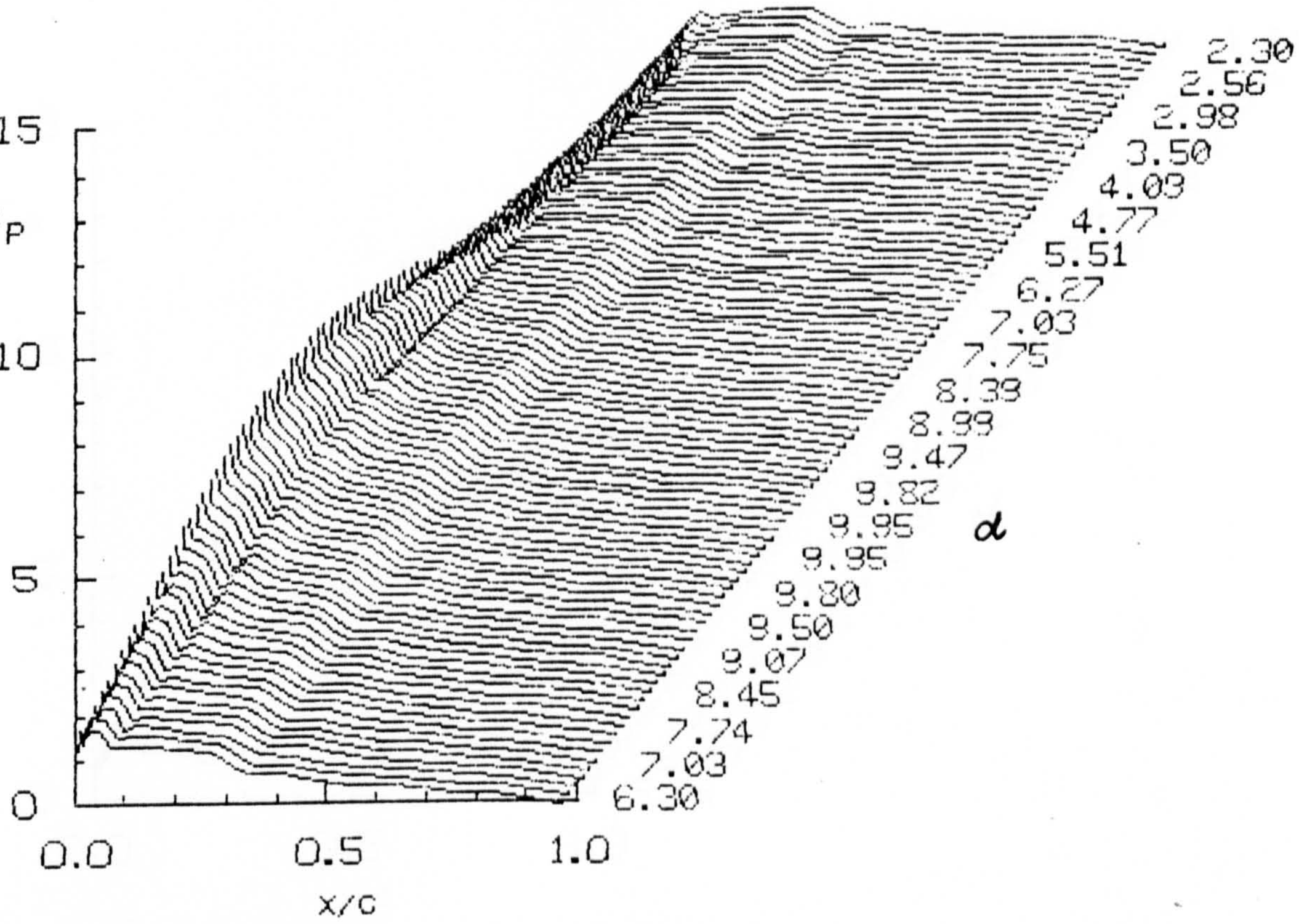

Fig 7.71 Chordwise Pressure Distributions for $\alpha = 6 + 4 \sin \omega t$; k= 0.01

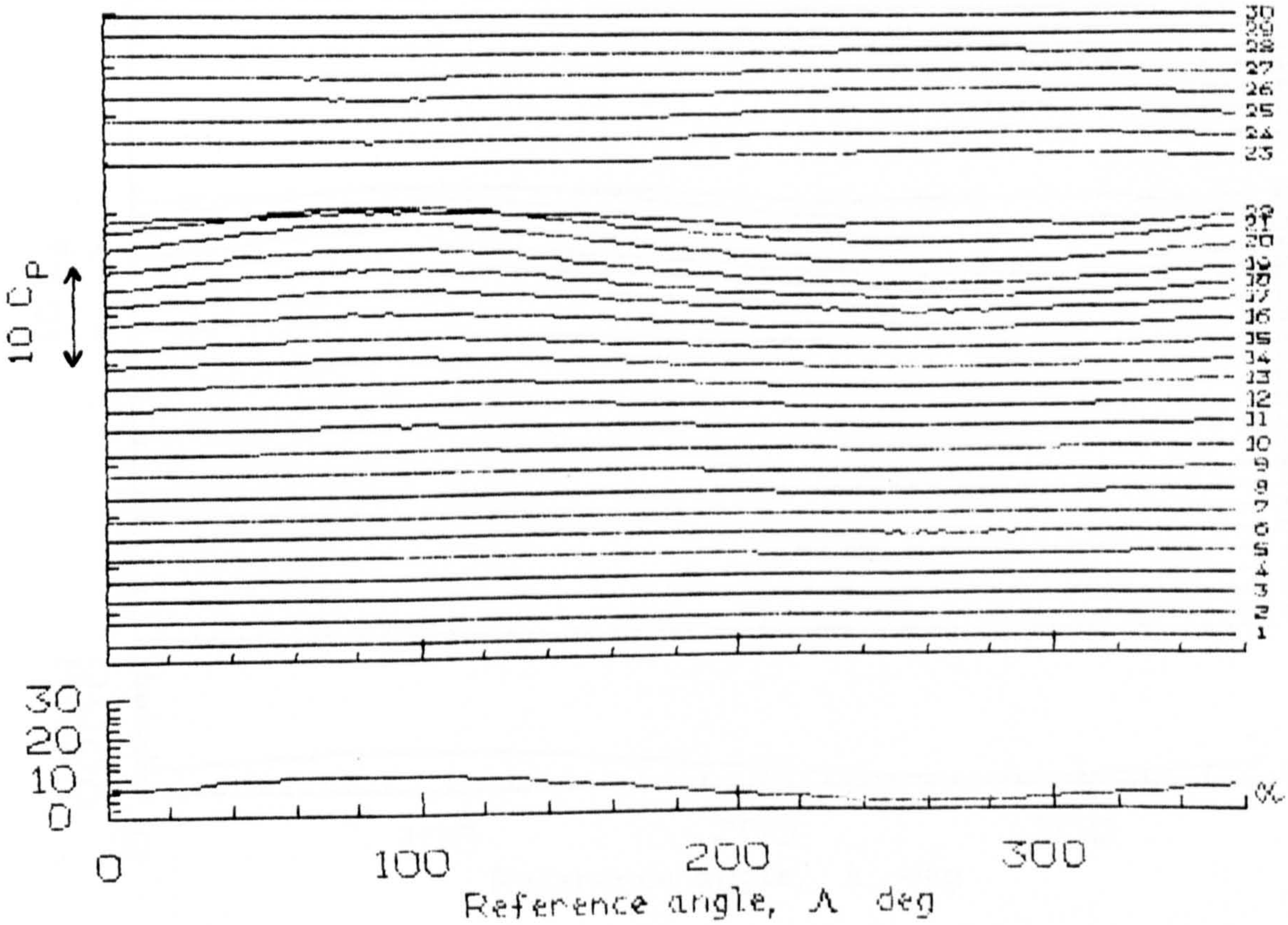

Fig 7.72 Pressure Time Histories for $\alpha = 6 + 4 \sin \omega t$; k= 0.01

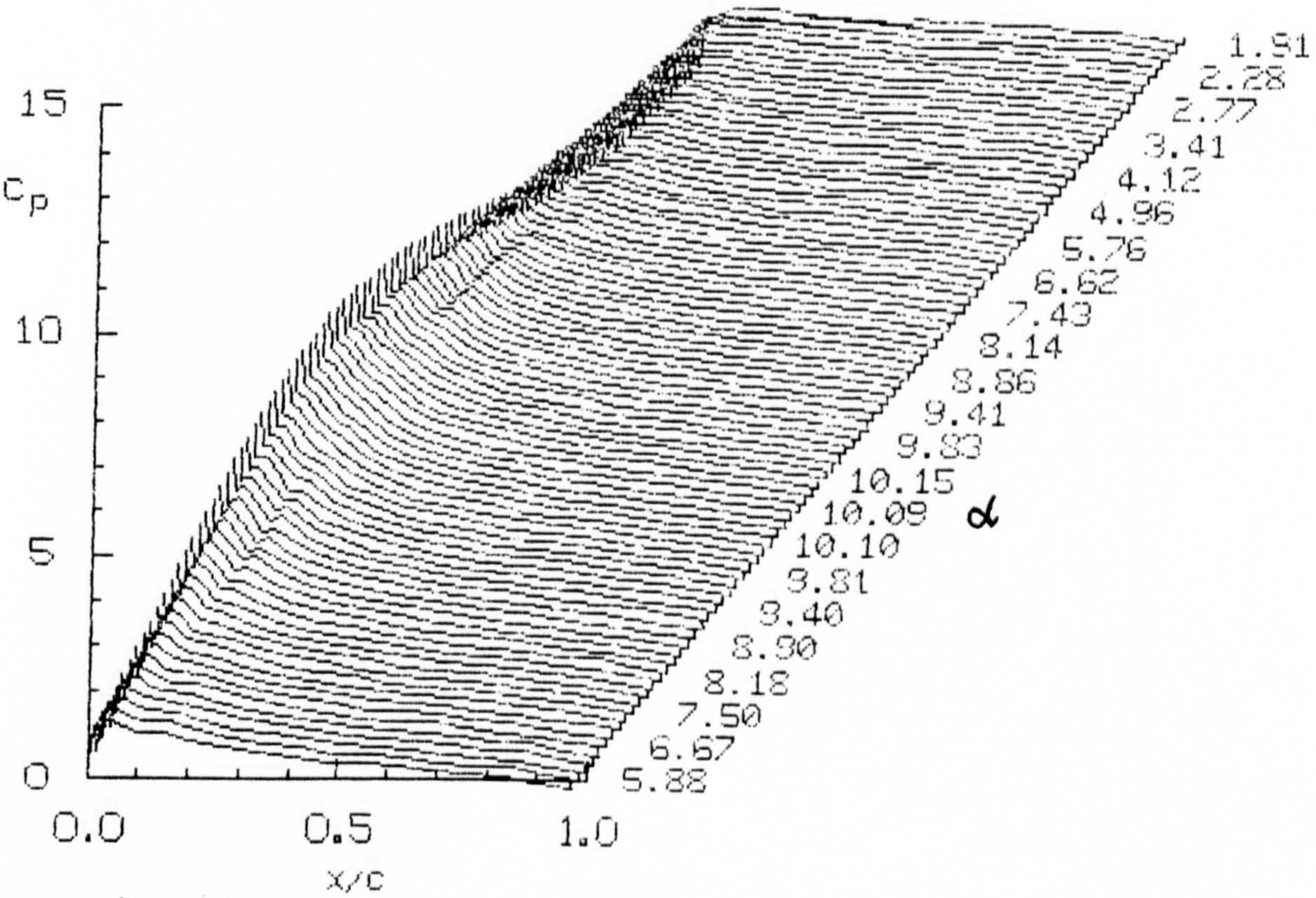

Fig 7.73 Chordwise Pressure Distributions for $\alpha = 6 + 4 \sin \omega t$; k= 0.05

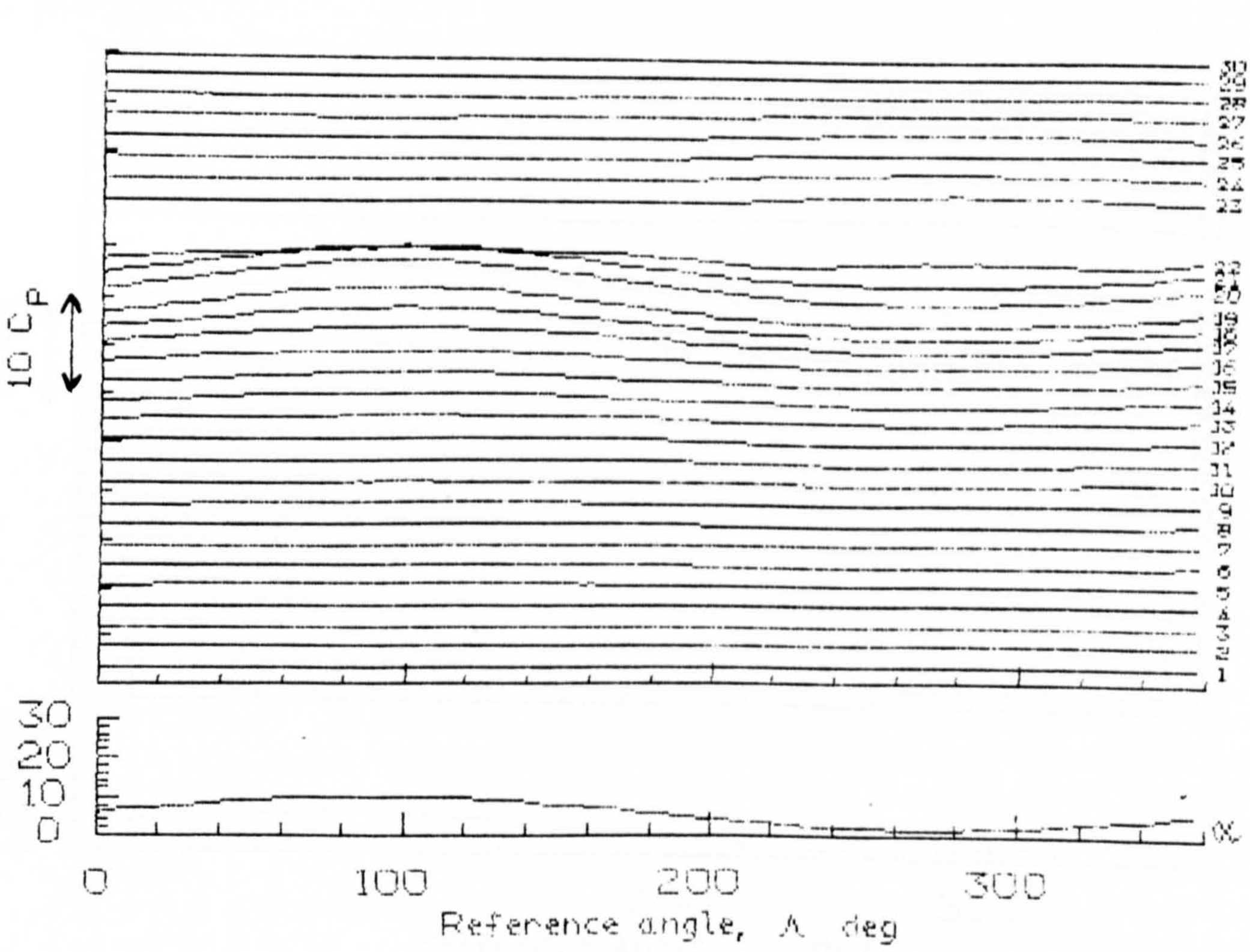

Fig 7.74 Pressure Time Histories for $\alpha = 6 + 4 \sin \omega t$; k= 0.05

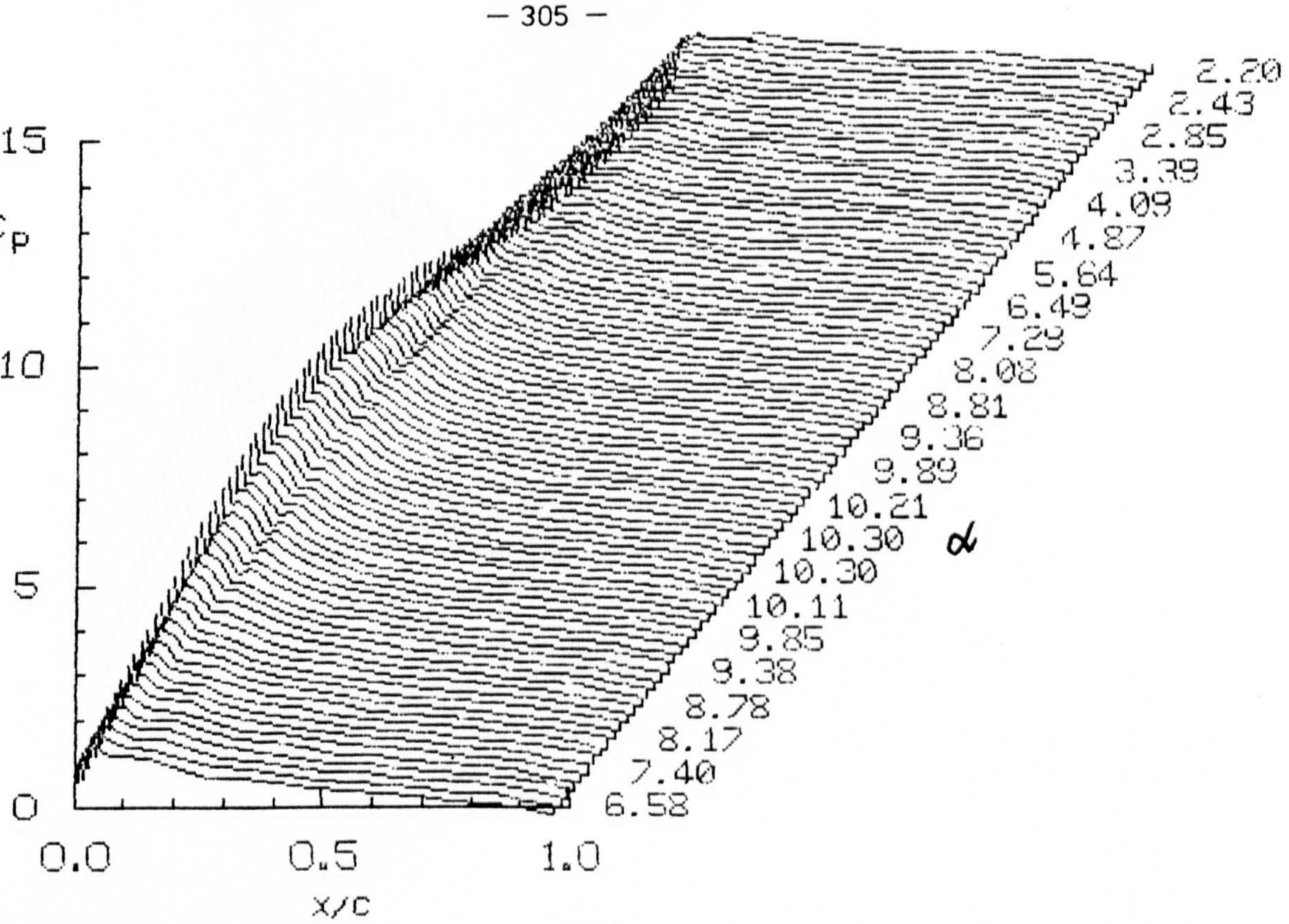

Fig 7.75 Chordwise Pressure Distributions for $\alpha = 6 + 4 \sin \omega t$; k= 0.10

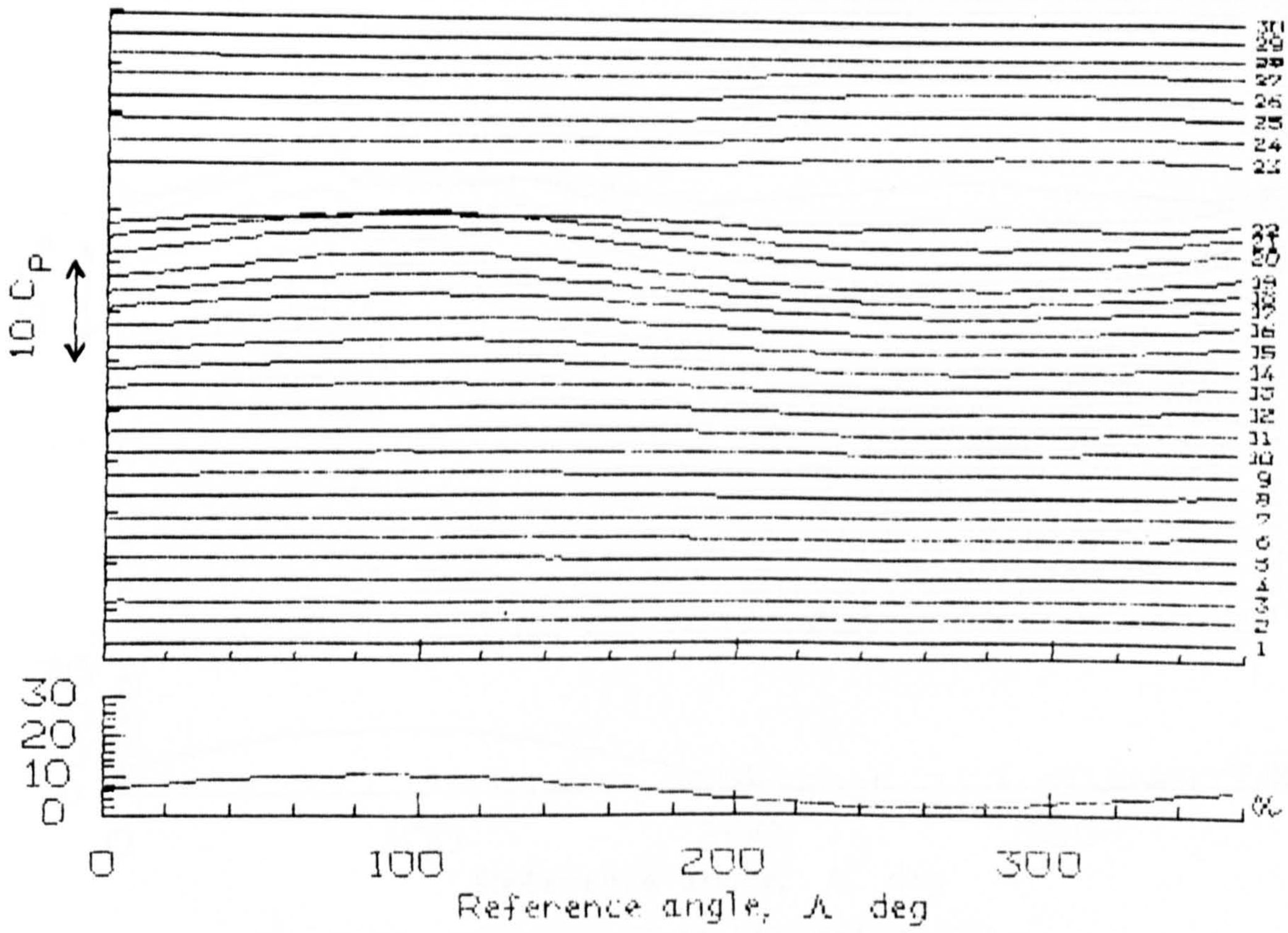

Fig 7.76 Pressure Time Histories for $\alpha = 6 + 4 \sin \omega t$; k= 0.10

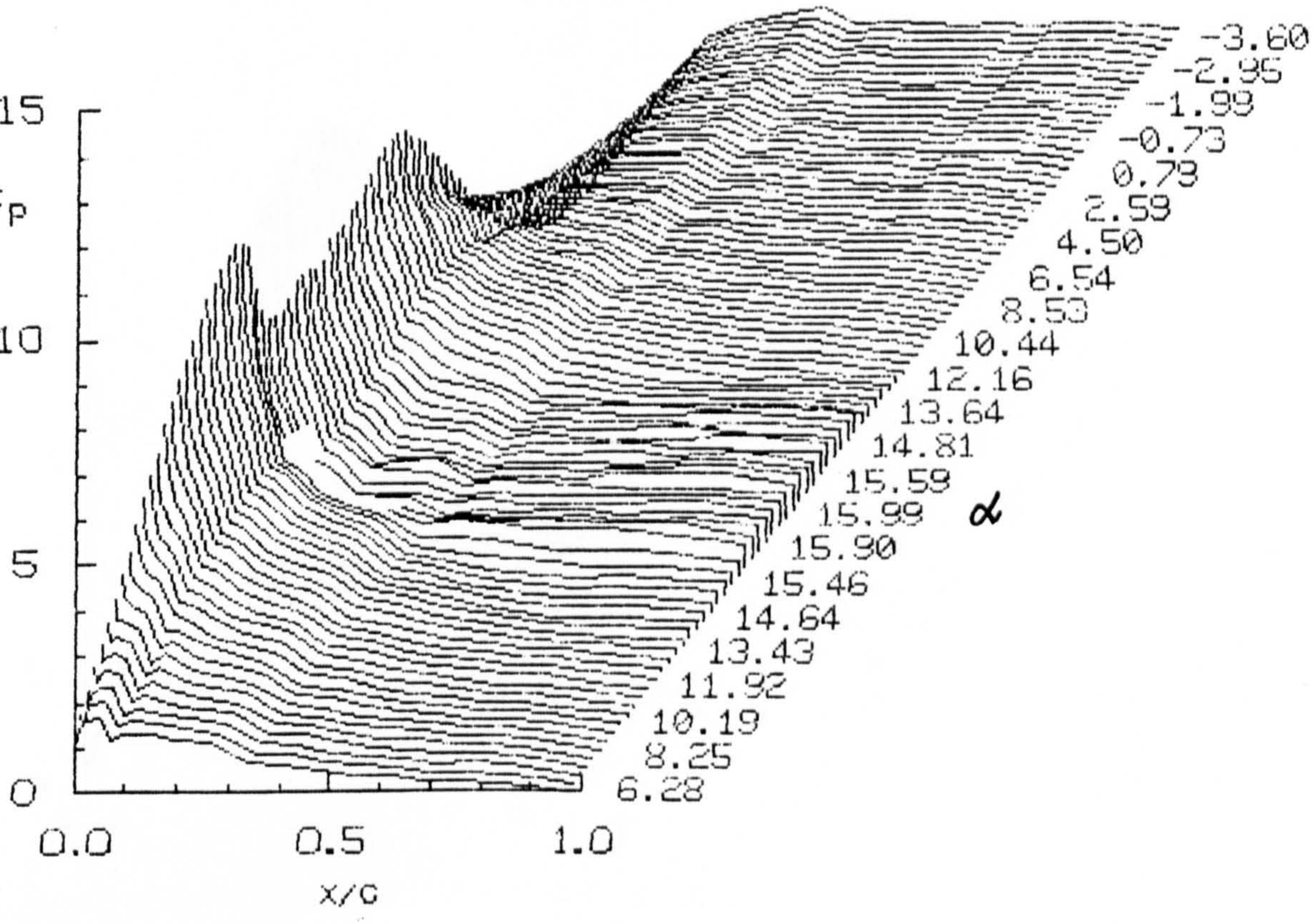

Fig 7.77 Chordwise Pressure Distributions for $\alpha = 6 + 10 \sin \omega t$; k= 0.01

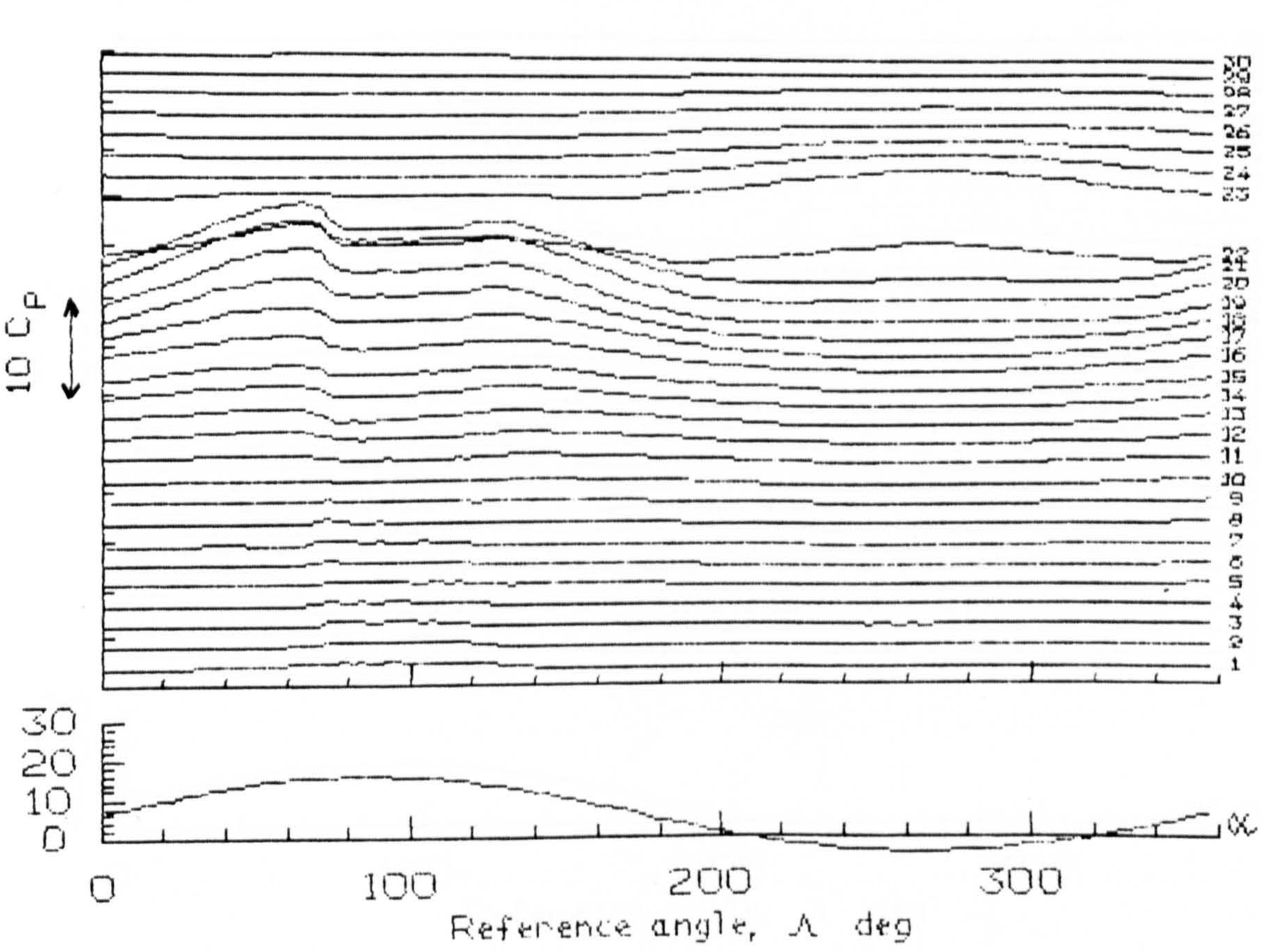

Fig 7.78 Pressure Time Histories for $\alpha = 6 + 10 \sin \omega t$; k= 0=01

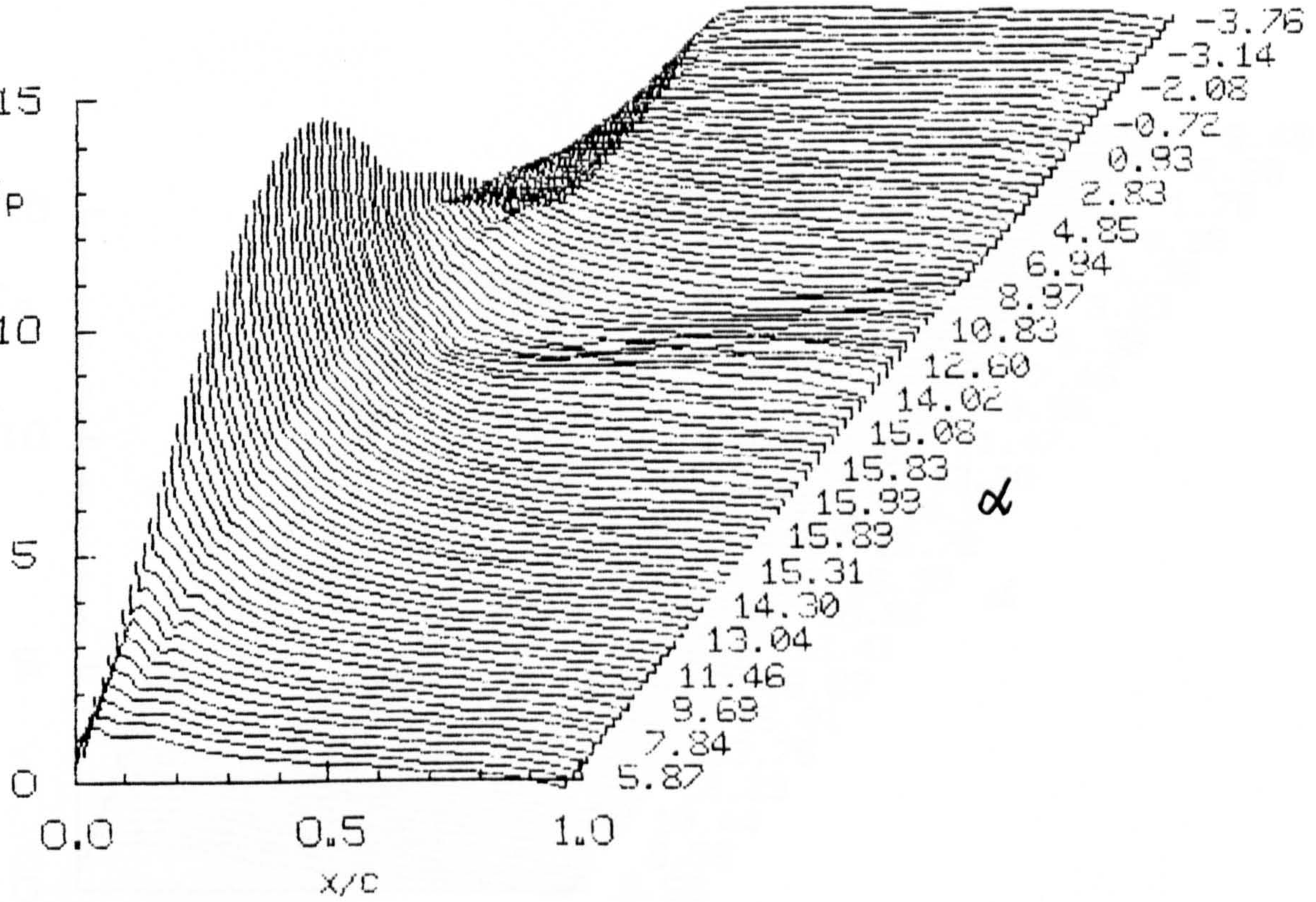

Fig 7.79 Chordwise Pressure Distributions for $\alpha = 6 + 10 \sin \omega t$; k= 0.05

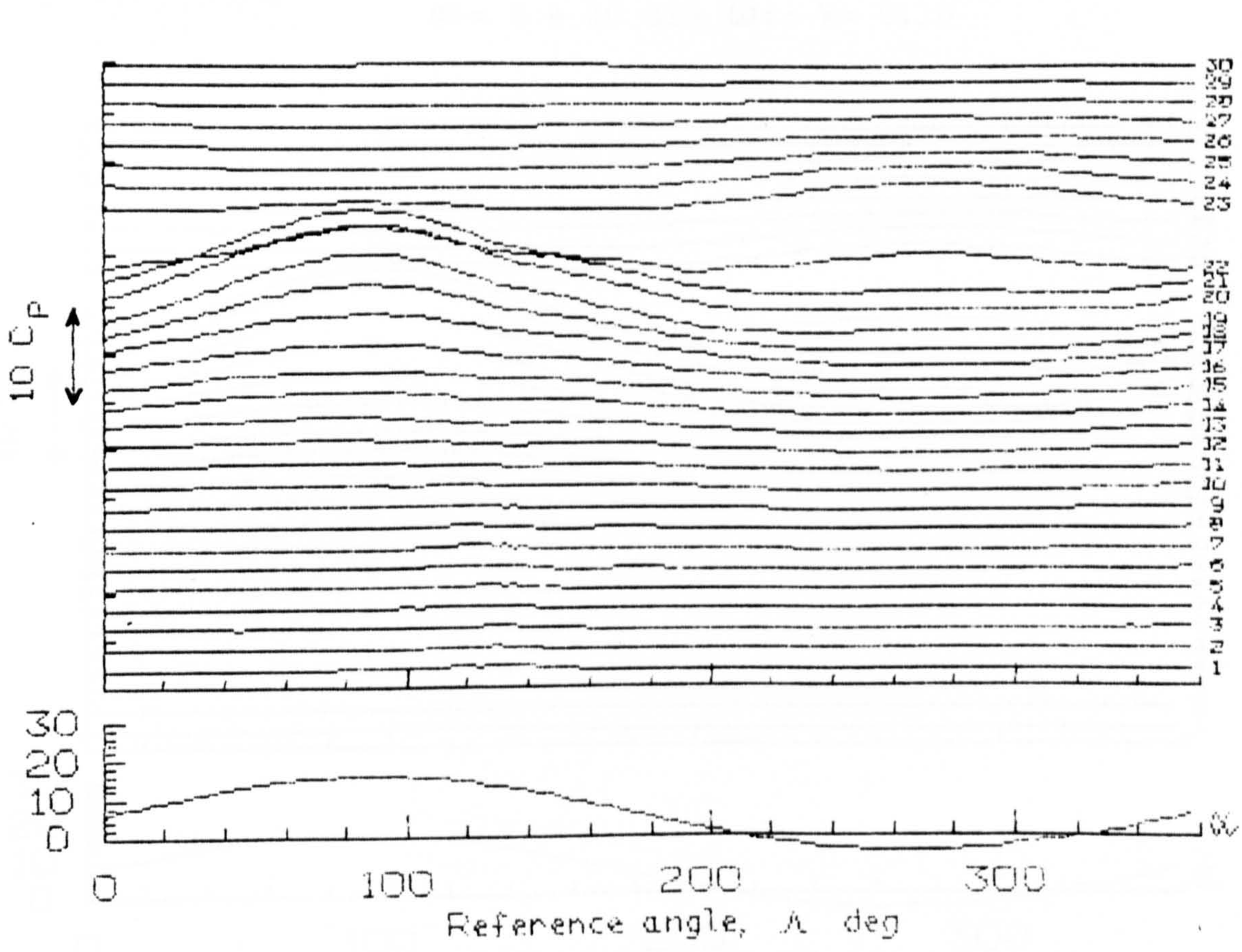

Fig 7.80 Pressure Time Histories for $\alpha = 6 + 10 \sin \omega t$; k= 0.05

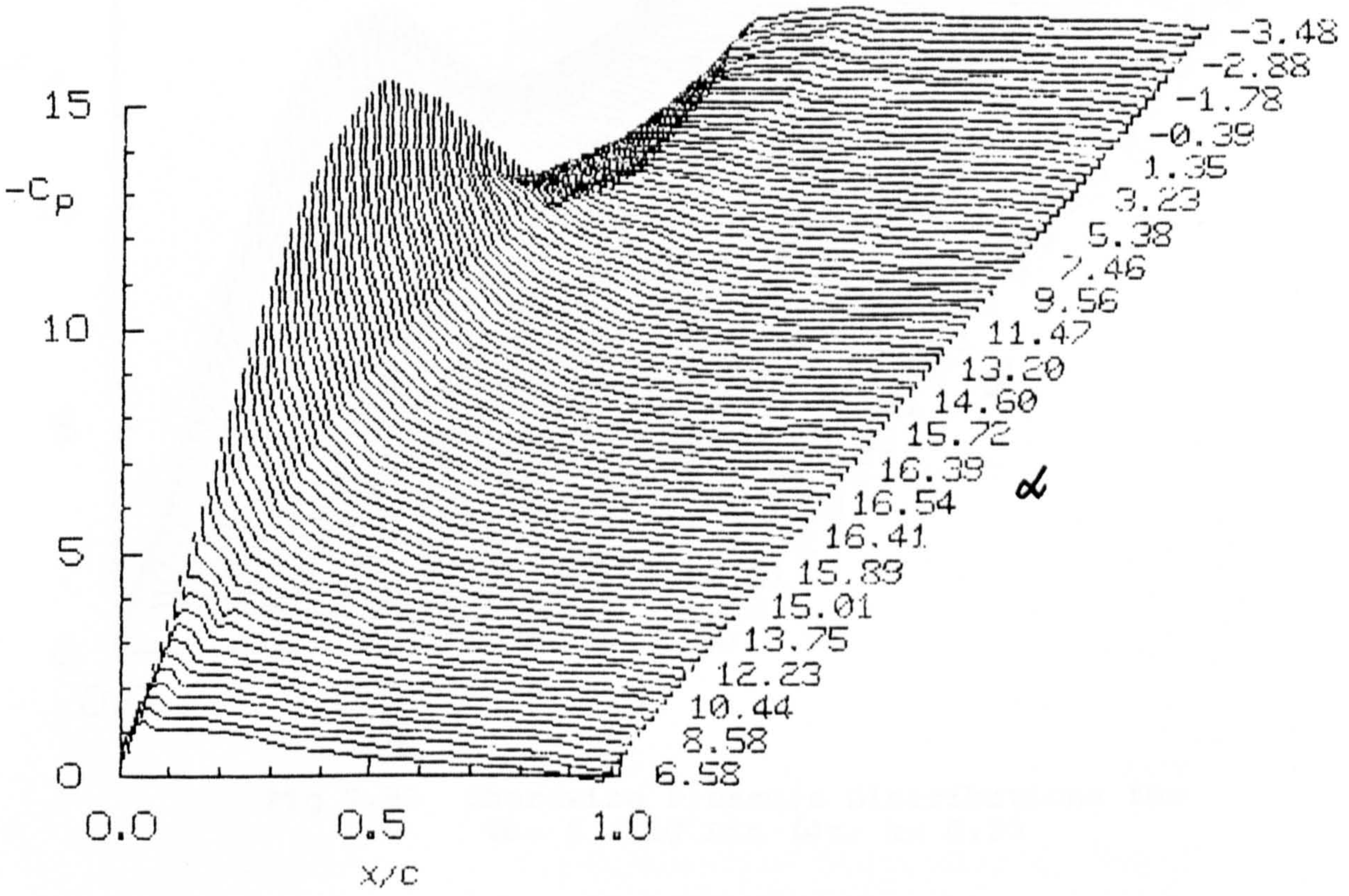

Fig 7.81 Chordwise Pressure Distributions for $\alpha = 6 + 10 \sin \omega t$; k= 0.10

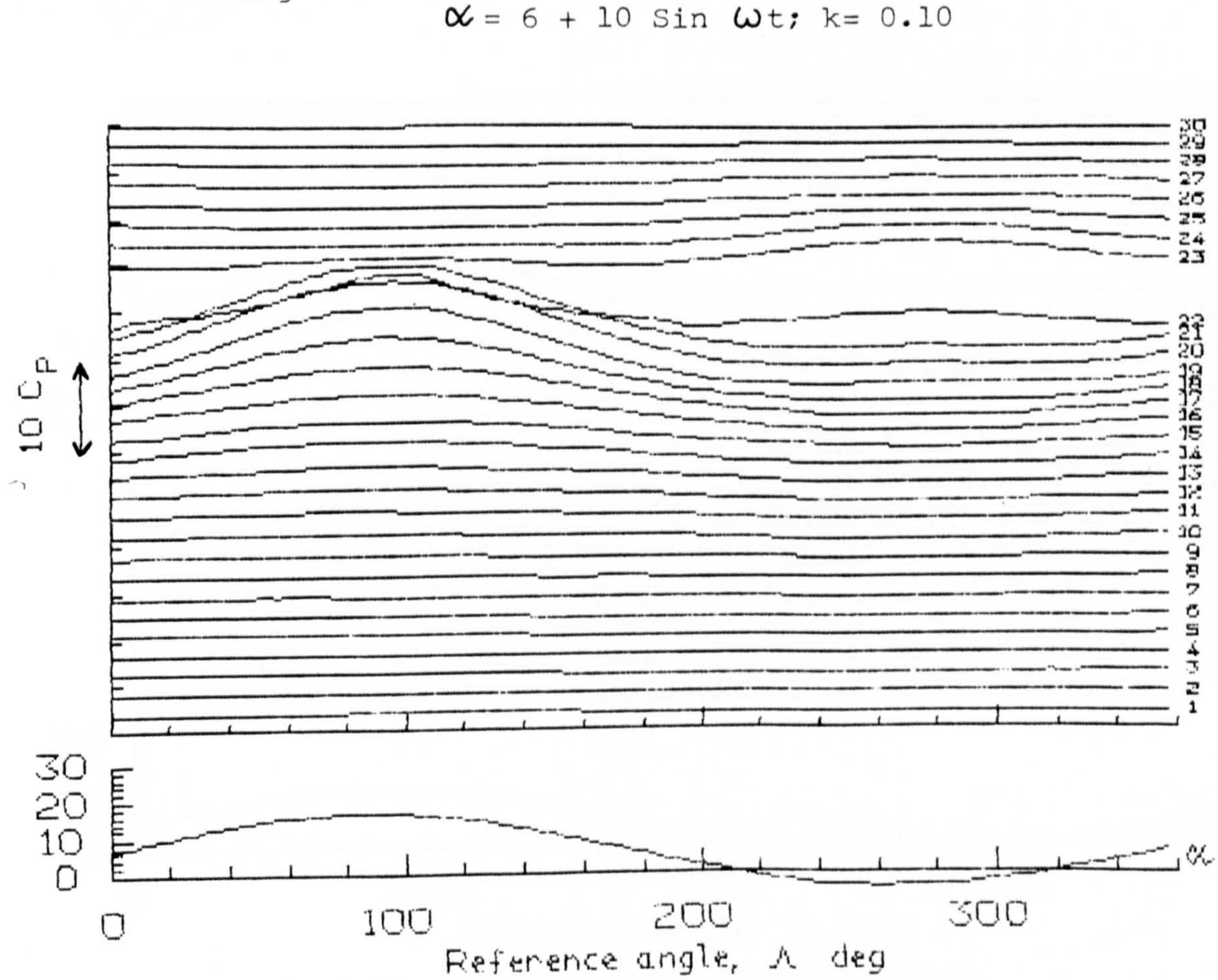

Fig 7.82 Pressure Time Histories for $\alpha = 6 + 10 \sin \omega t$; k= 0.10

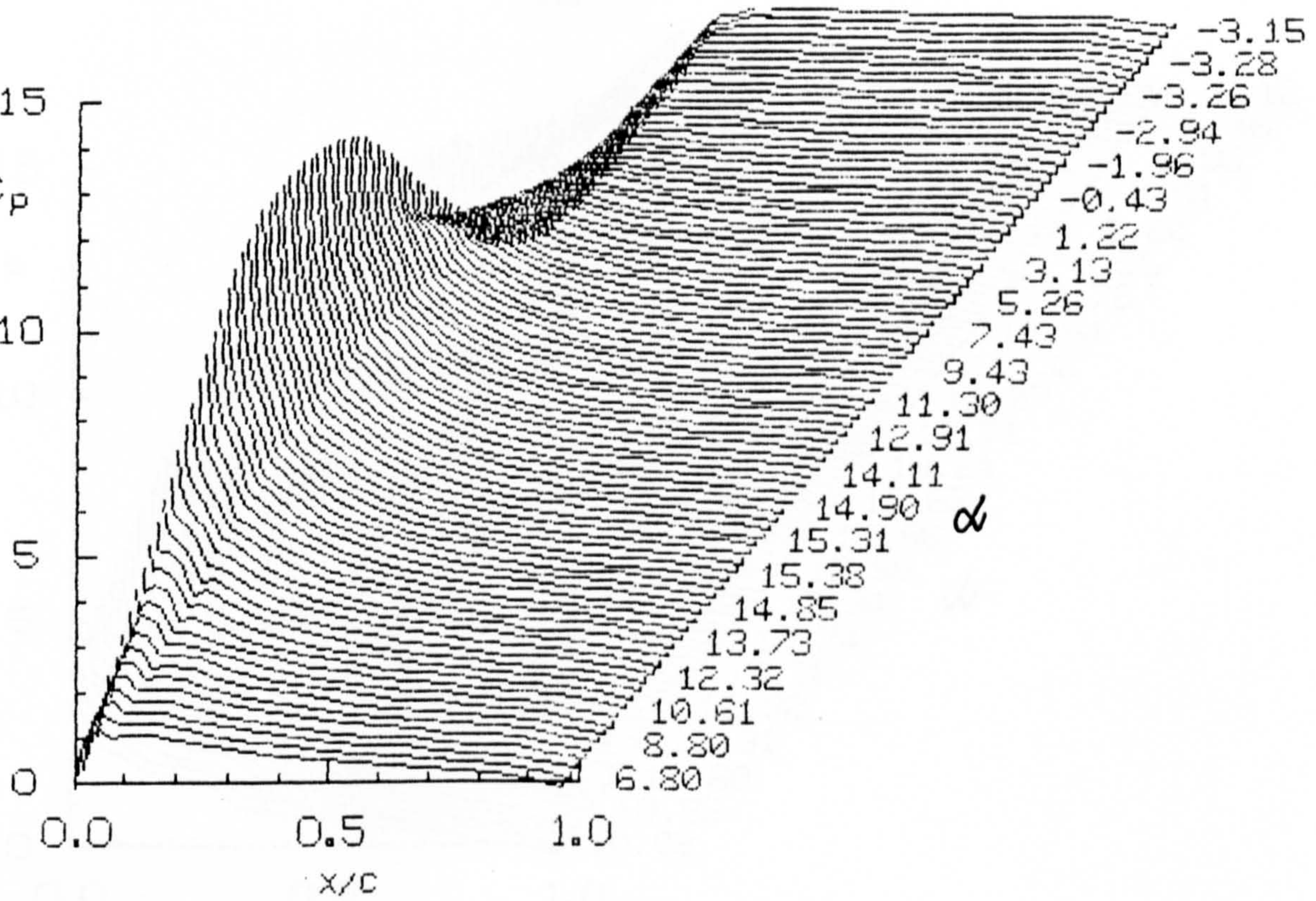

Fig 7.83 Chordwise Pressure Distributions for $\alpha = 6 + 10 \sin \omega t$; k= 0.20

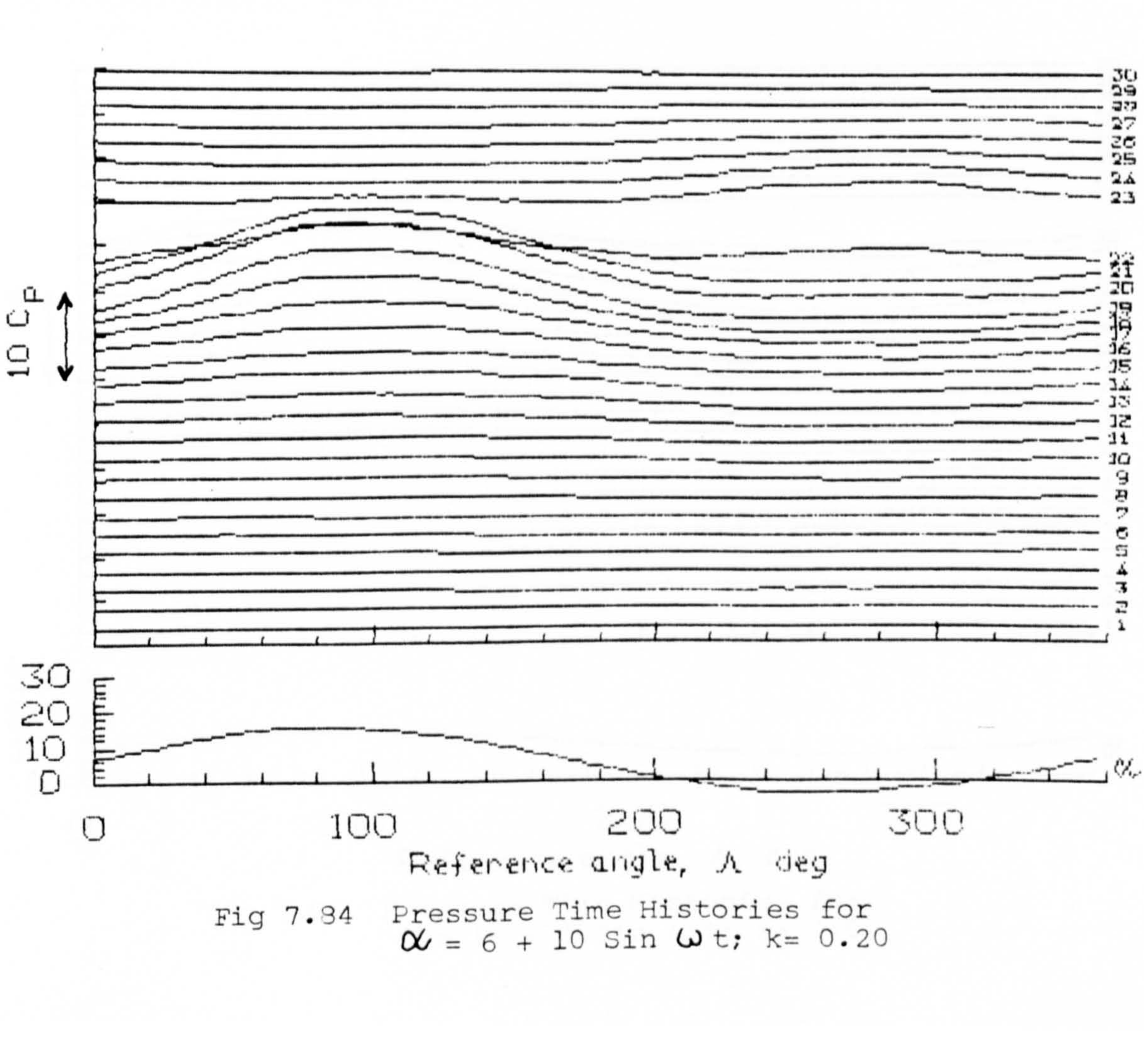

Fig 7.84 Pressure Time Histories for $\alpha = 6 + 10 \sin \omega t$; k= 0.20

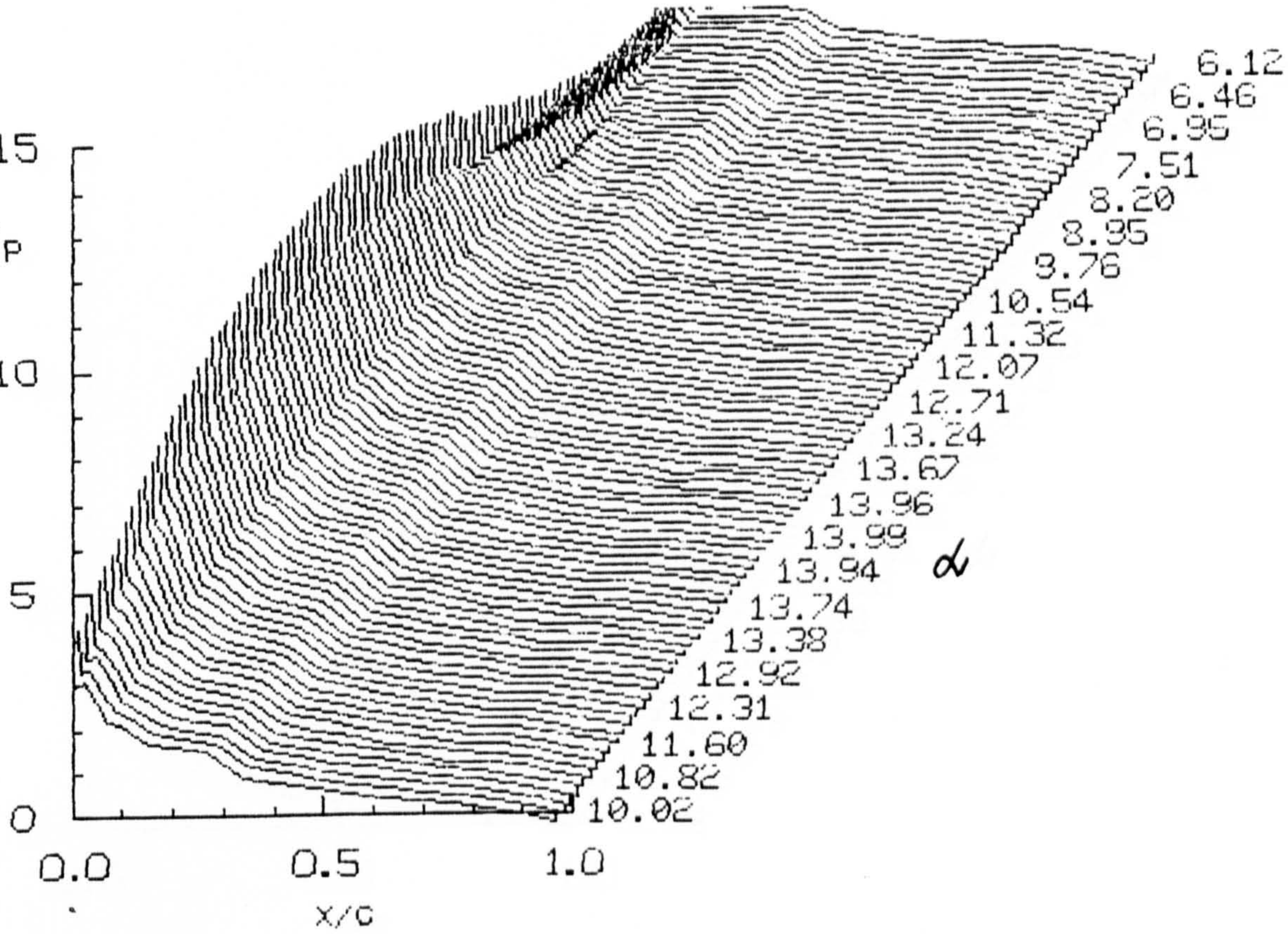

Fig 7.85 Chordwise Pressure Distributions for $\alpha = 10 + 4 \sin \omega t$; k= 0.01

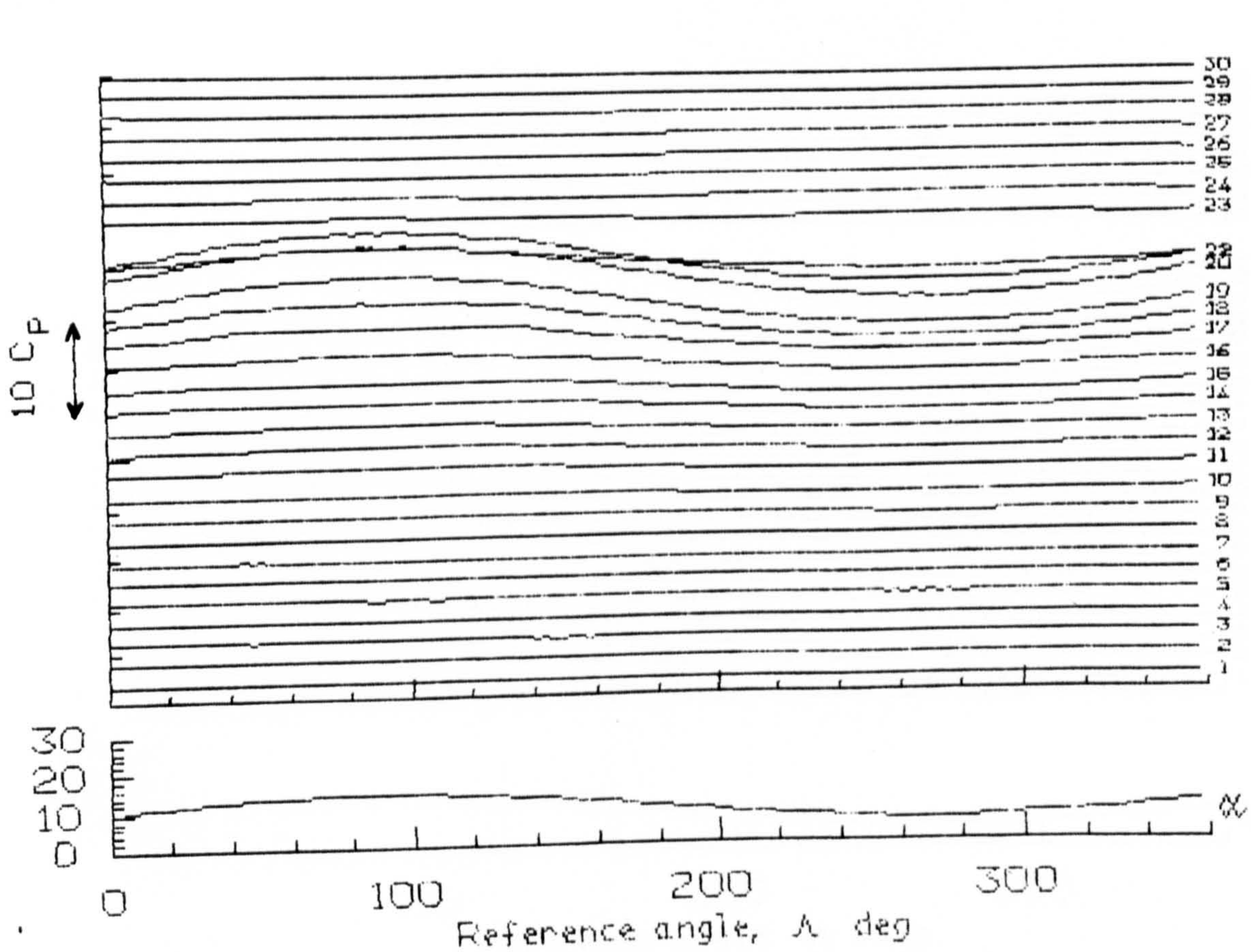

Fig 7.86 Pressure Time Histories for $\alpha = 10 + 4 \sin \omega t$; k= 0.01

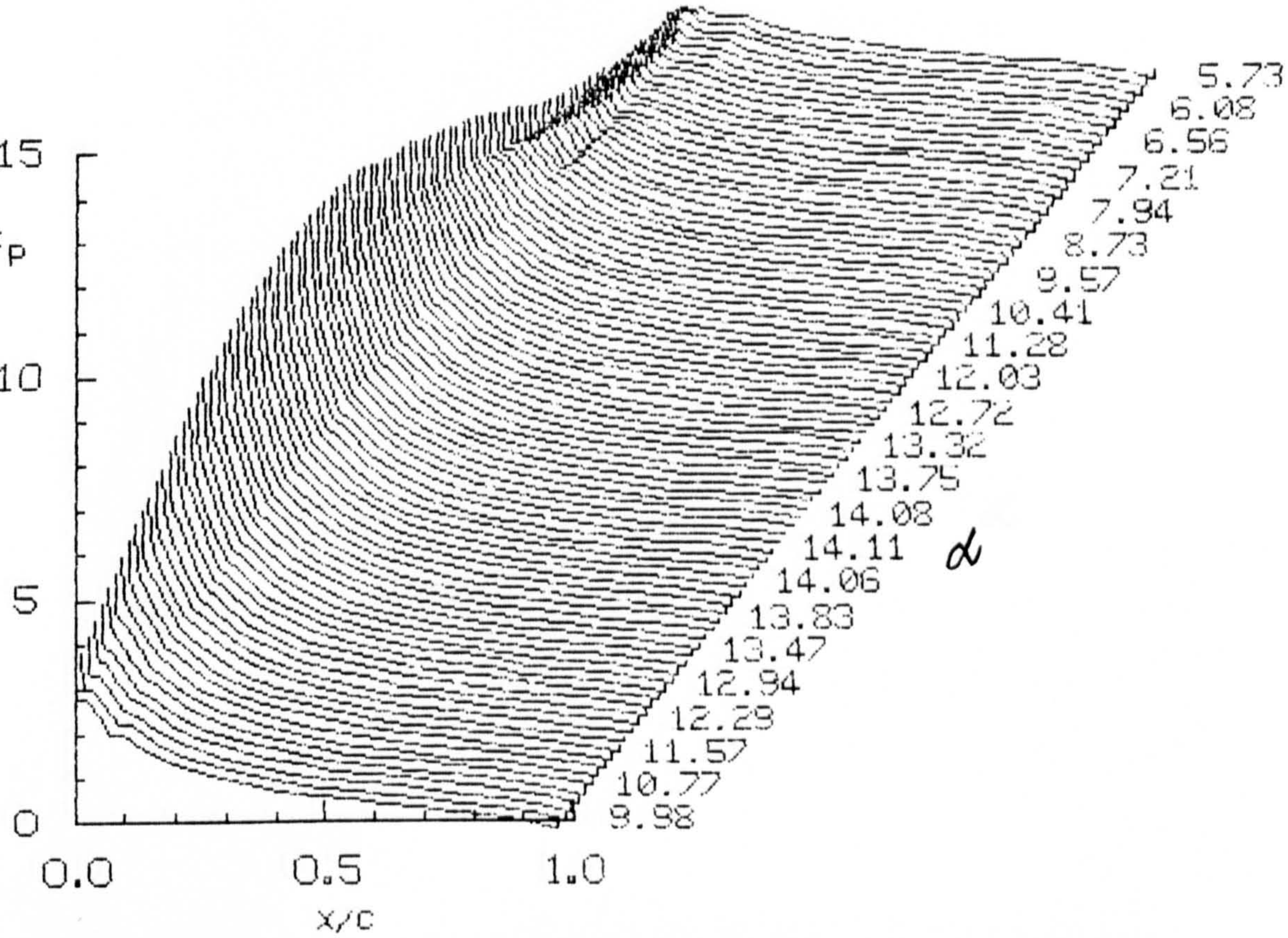

Fig 7.87 Chordwise Pressure Distributions for $\alpha = 10 + 4 \sin \omega t$; k= 0.05

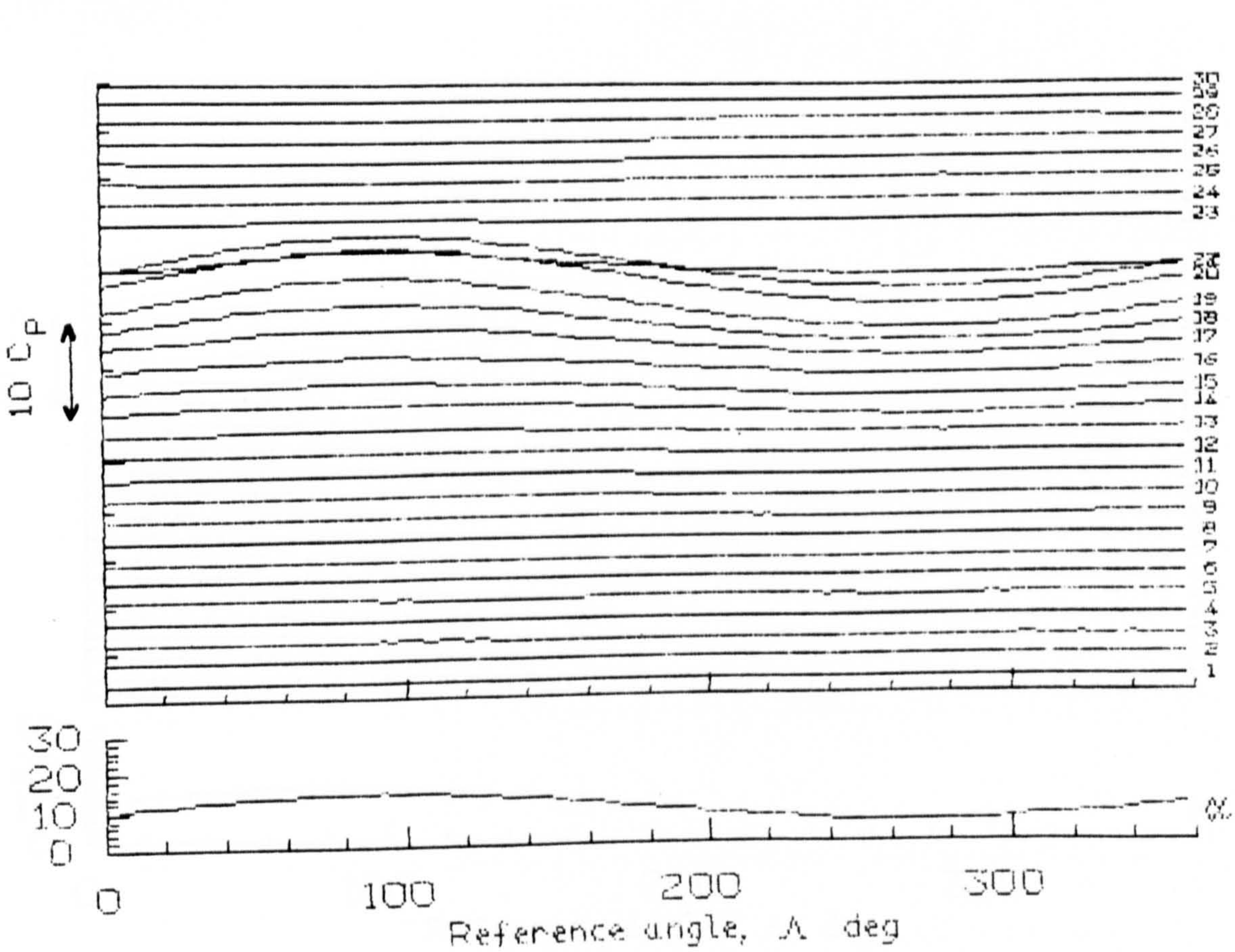

Fig 7.88 Pressure Time Histories for $\alpha = 10 + 4 \sin \omega t$; k= 0.05

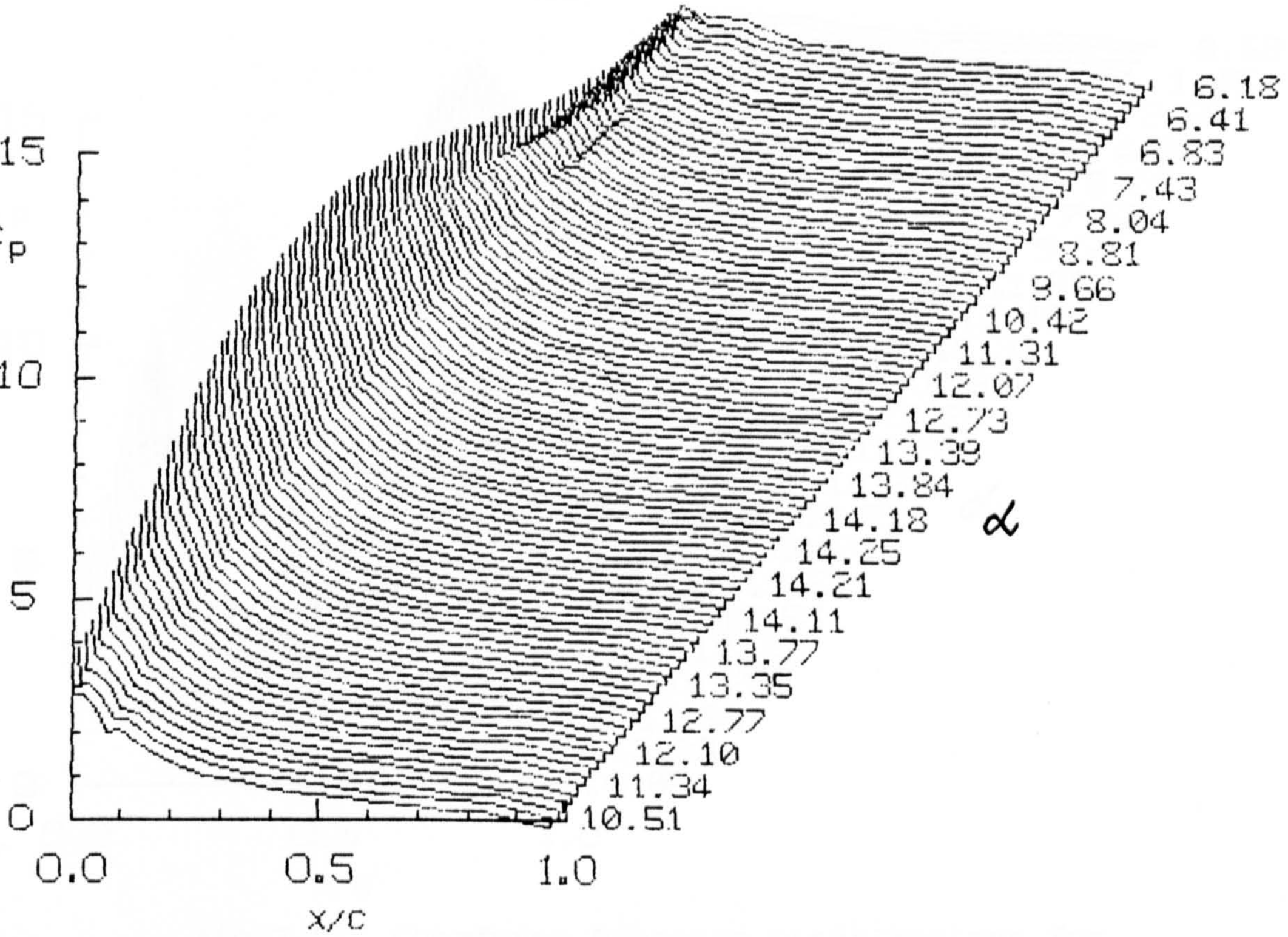

Fig 7.89 Chordwise Pressure Distributions for $\alpha = 10 + 4 \sin \omega t$; k= 0.10

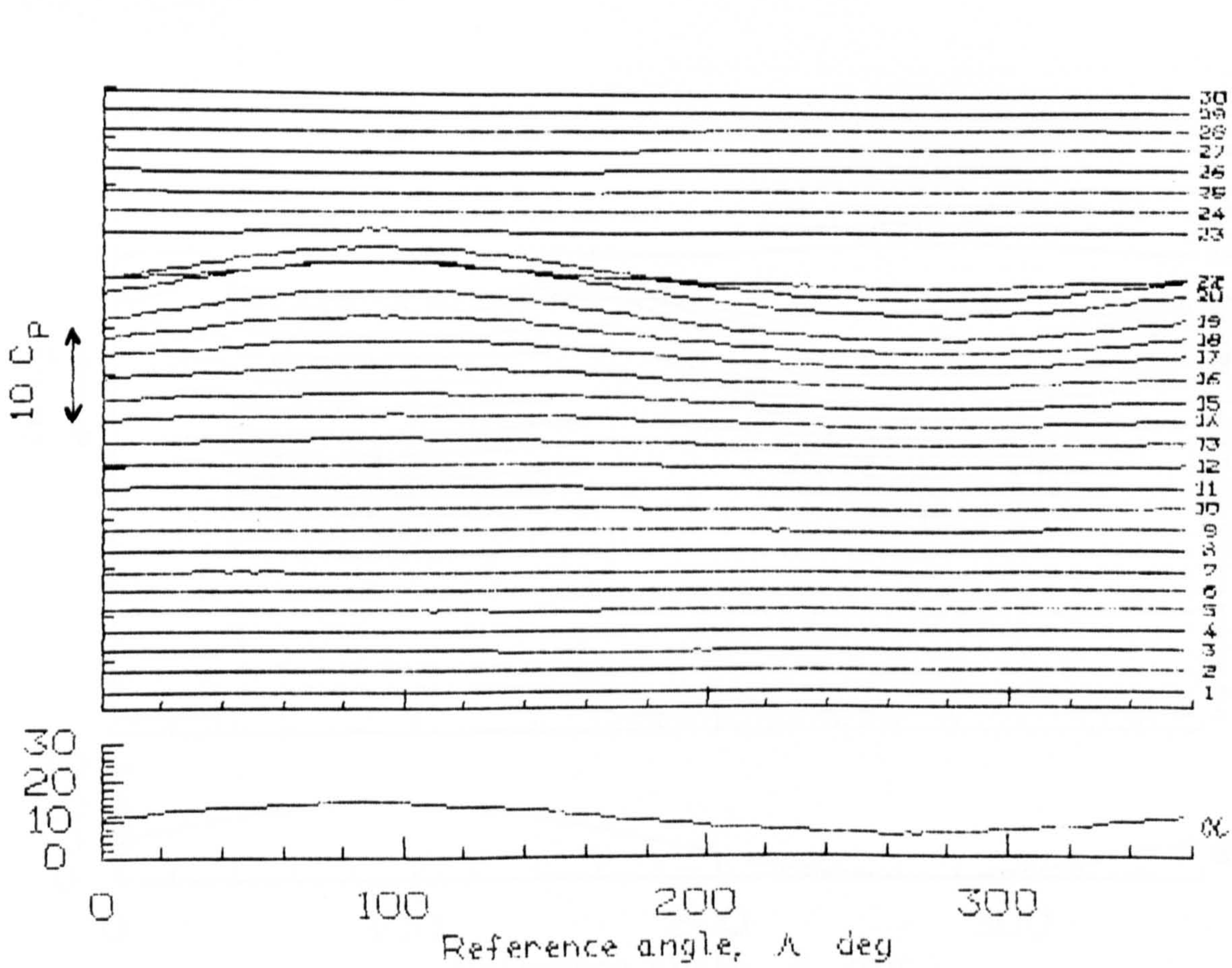

Fig 7.90 Pressure Time Histories for $\alpha = 10 + 4 \sin \omega t$; k= 0.10

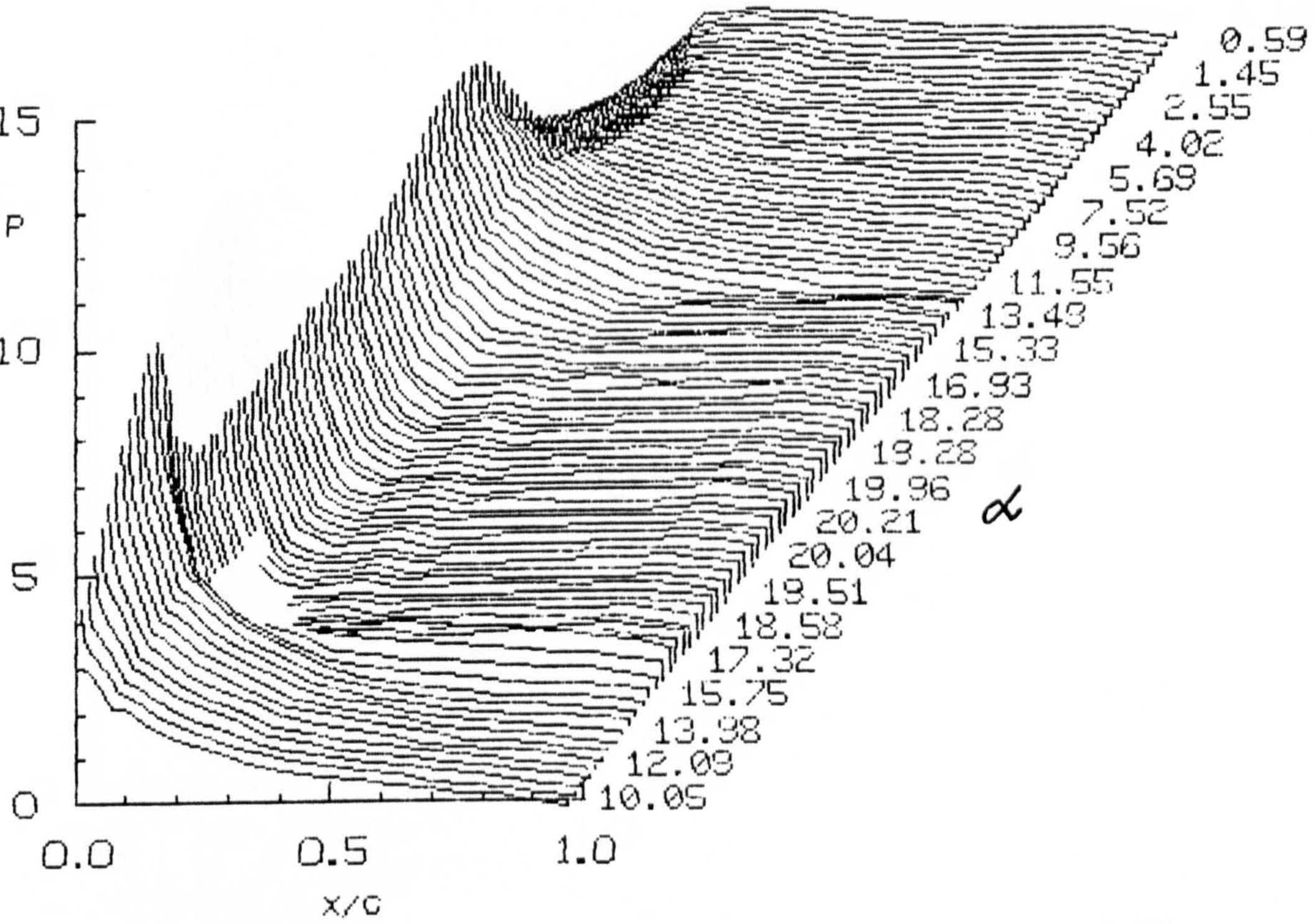

Fig 7.91 Chordwise Pressure Distributions for $\alpha = 10 + 10 \sin \omega t$; k= 0.01

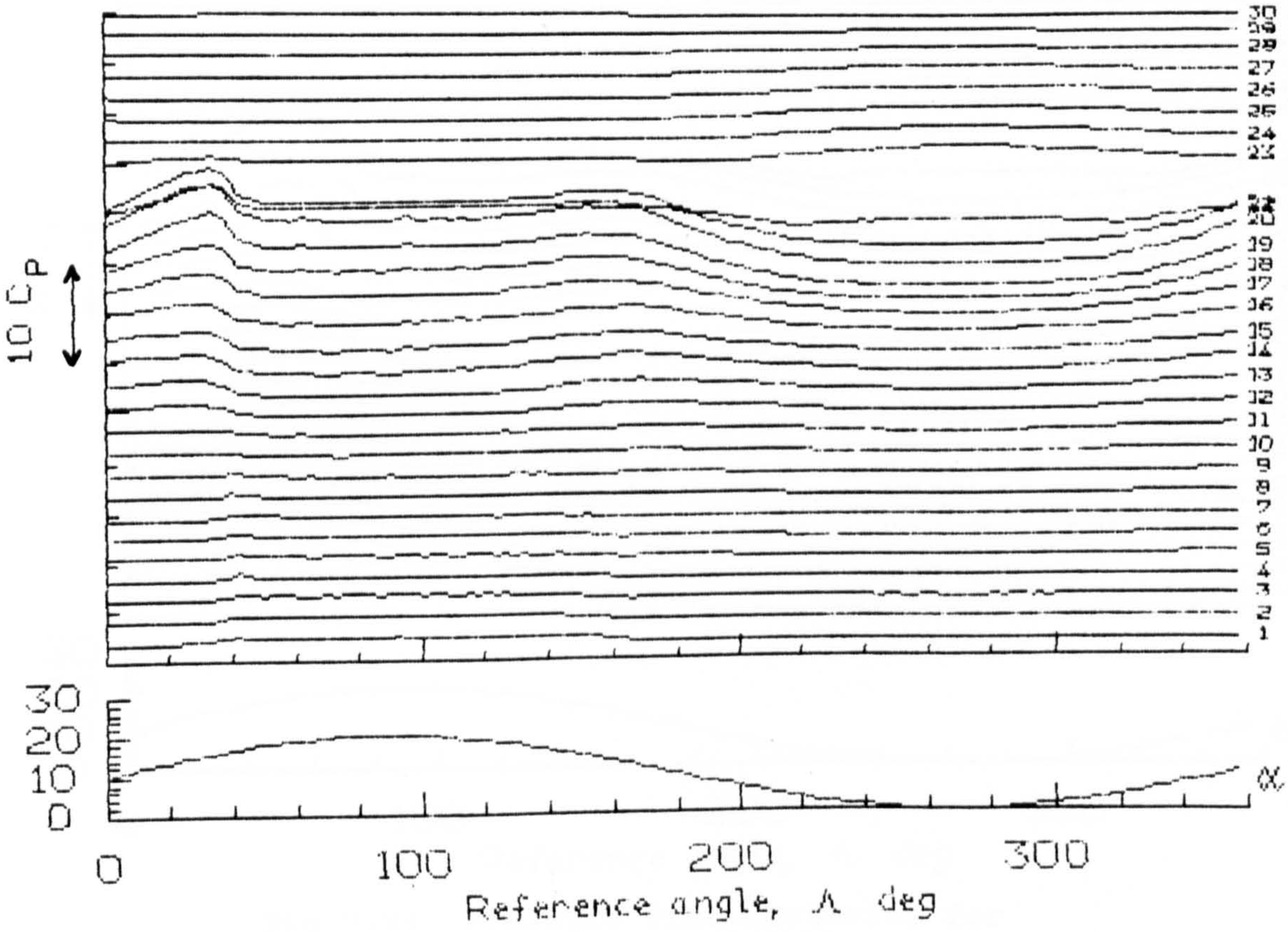

Fig 7.92 Pressure Time Histories for $\alpha = 10 + 10 \sin \omega t$; k= 0.01

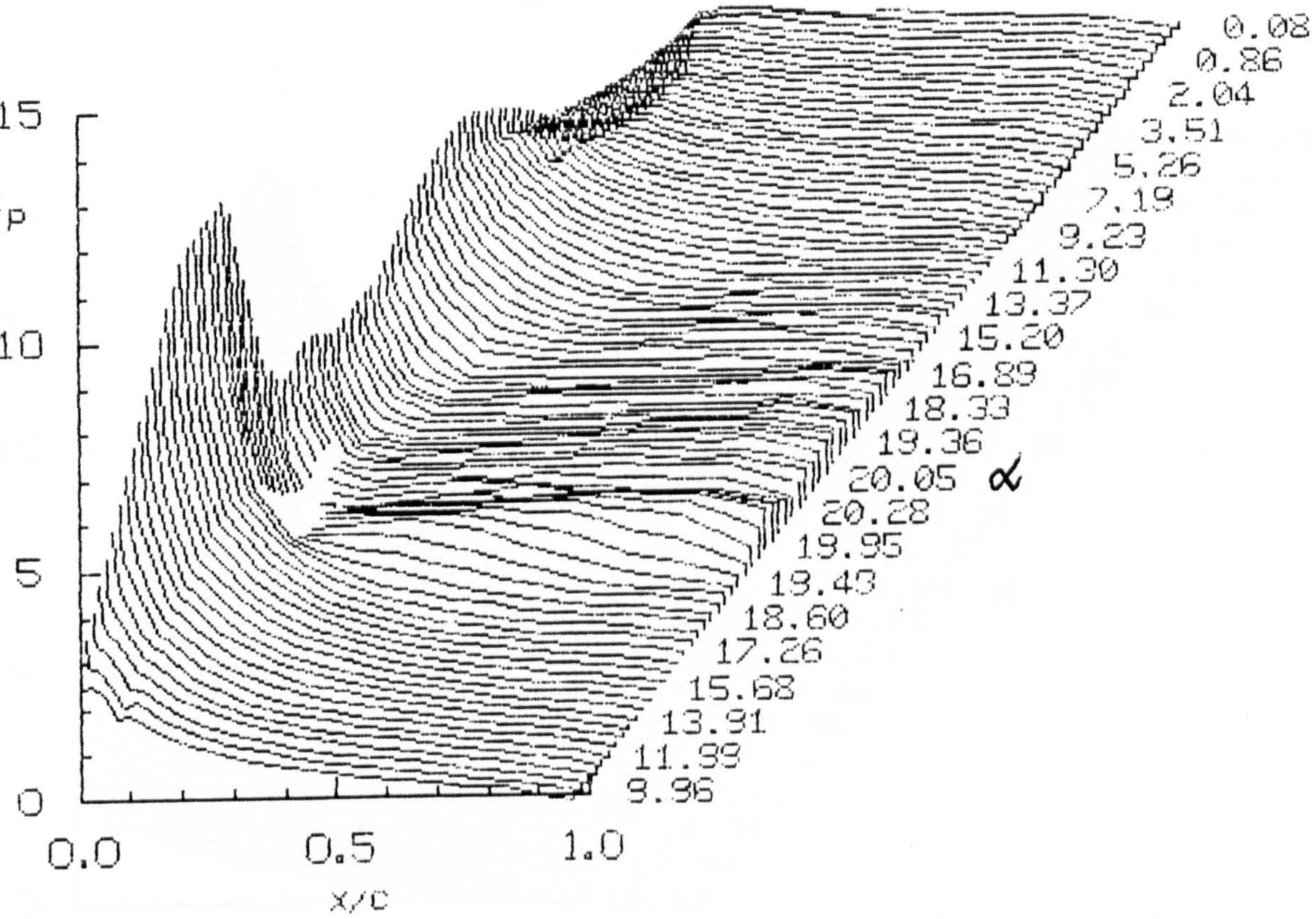

Fig 7.93 Chordwise Pressure Distributions for $\alpha = 10 + 10 \sin \omega t$; k= 0.05

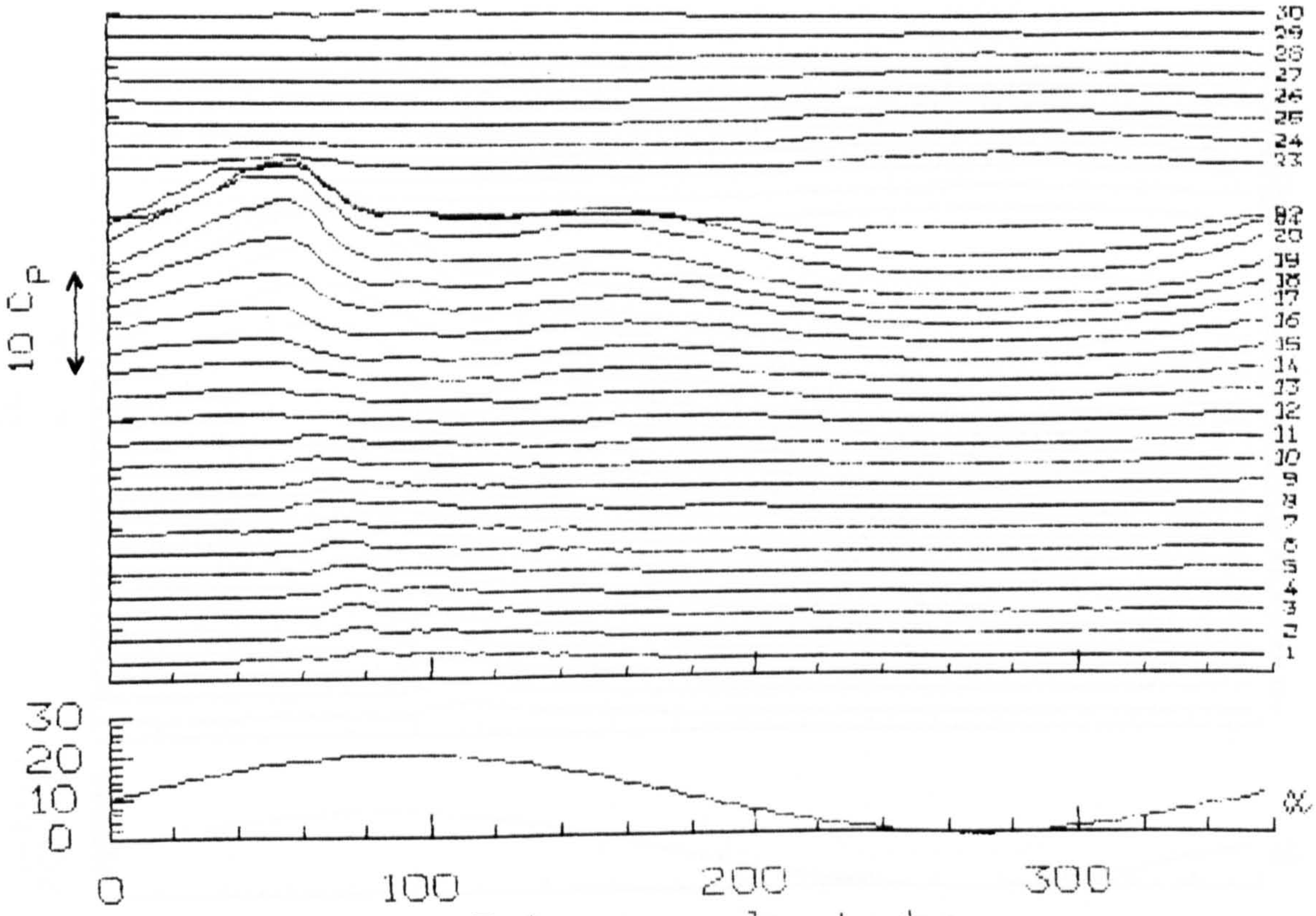

Fig 7.94 Pressure Time Histories for $\alpha = 10 + 10 \sin \omega t$; k= 0.05

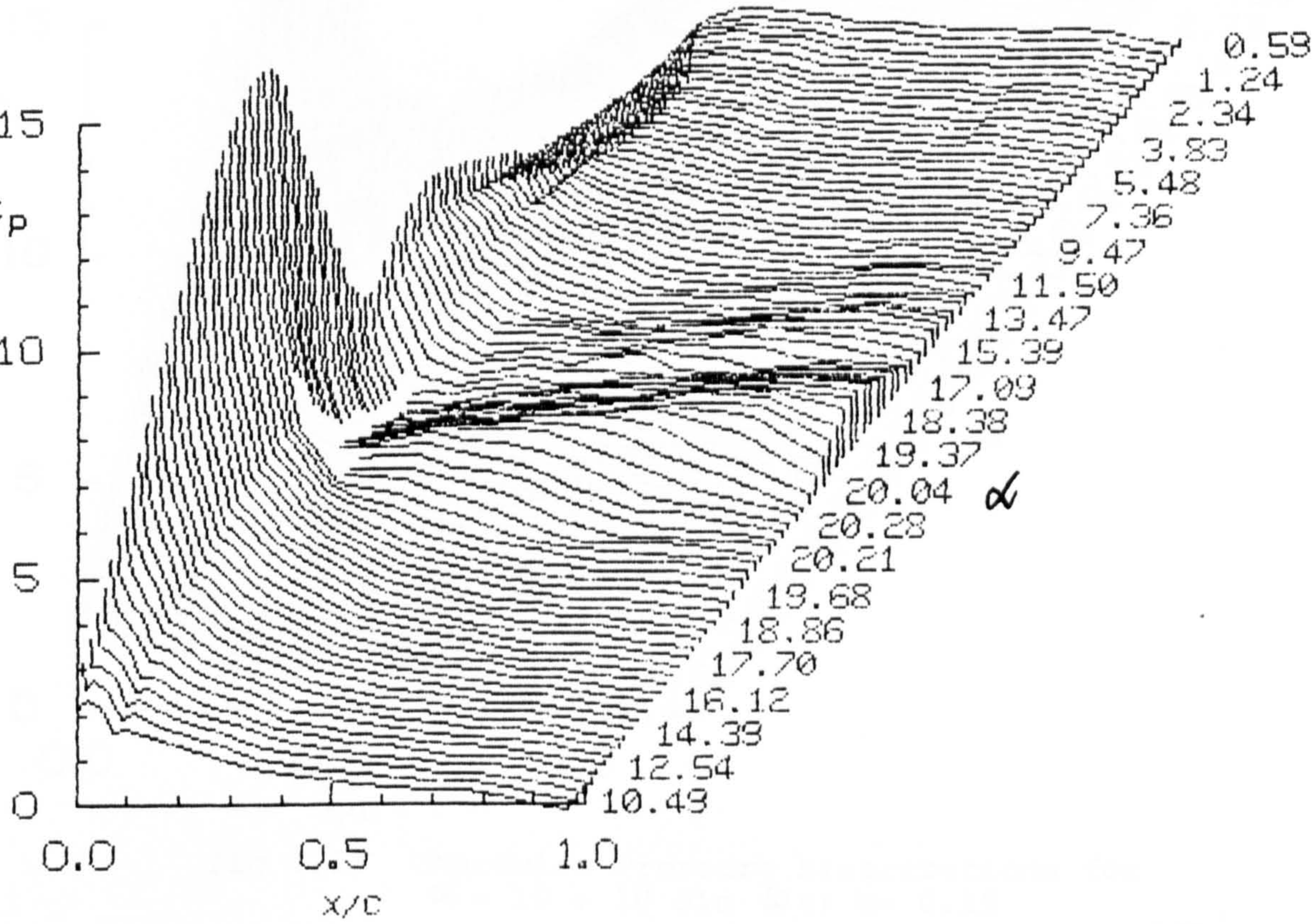

Fig 7.95 Chordwise Pressure Distributions for $\alpha = 10 + 10 \sin \omega t$; k= 0.10

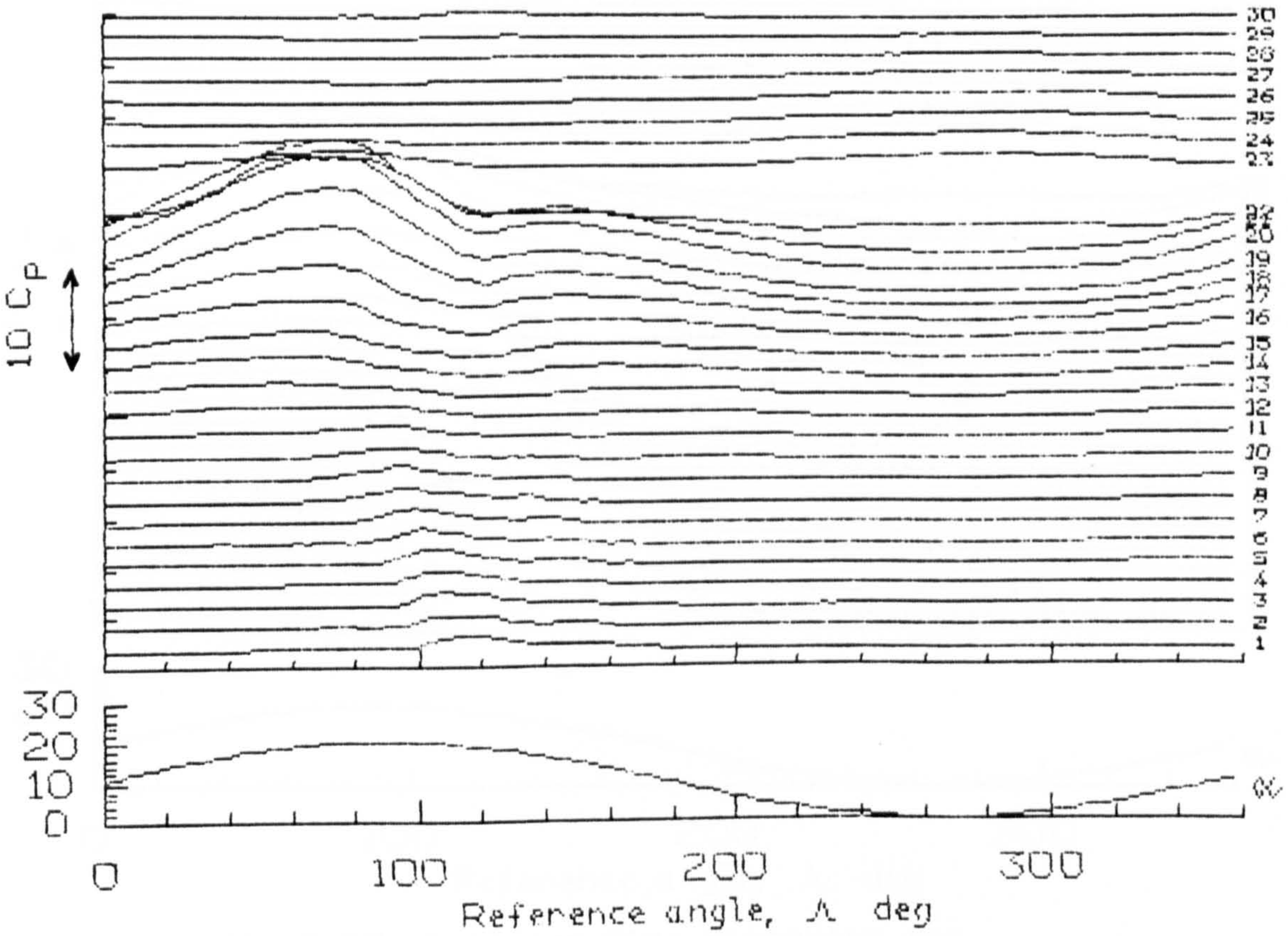

Fig 7.96 Pressure Time Histories for $\alpha = 10 + 10 \sin \omega t$; k= 0.10

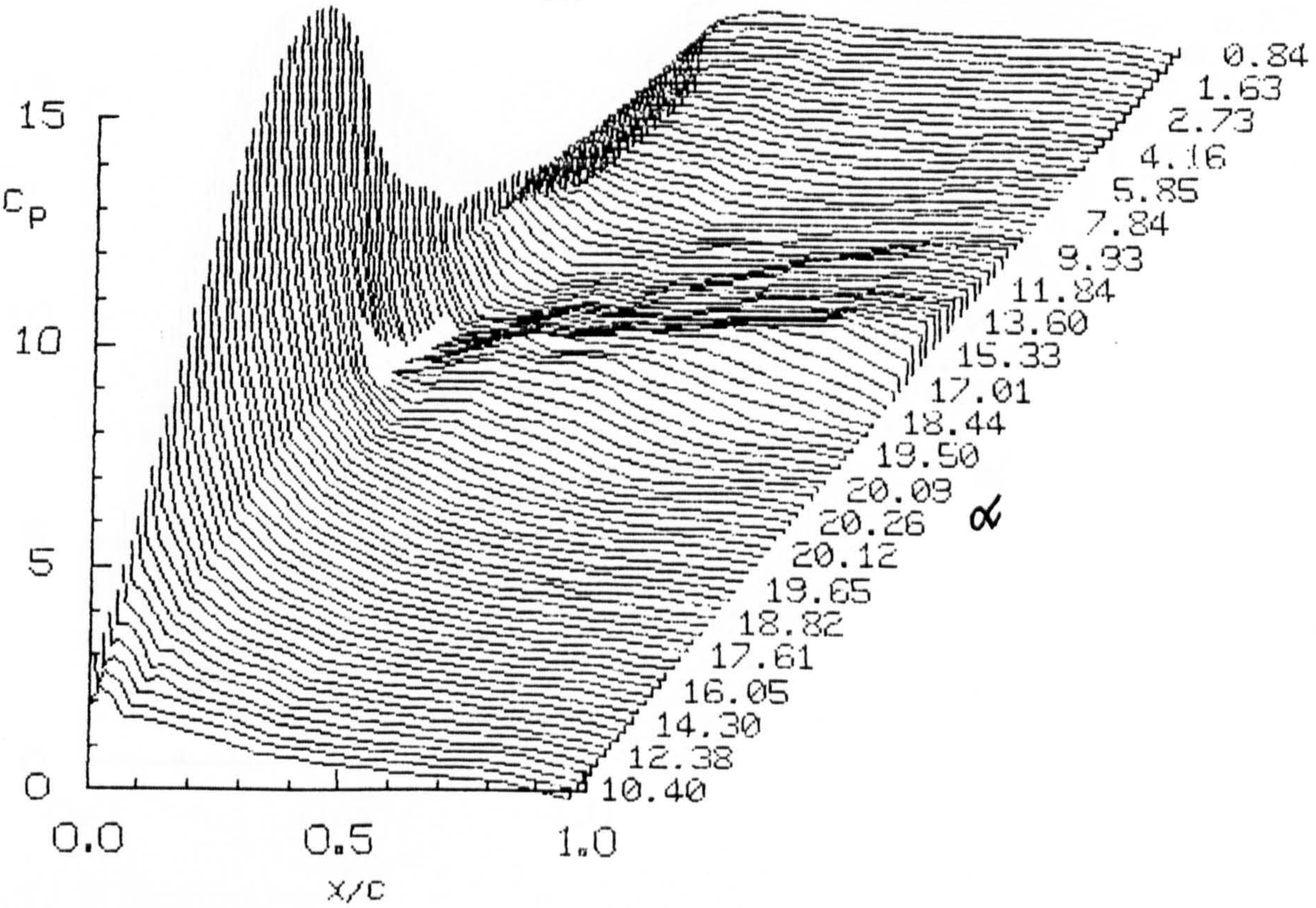

Fig 7.97 Chordwise Pressure Distributions for $\alpha = 10 + 10 \sin \omega t$; k= 0.15

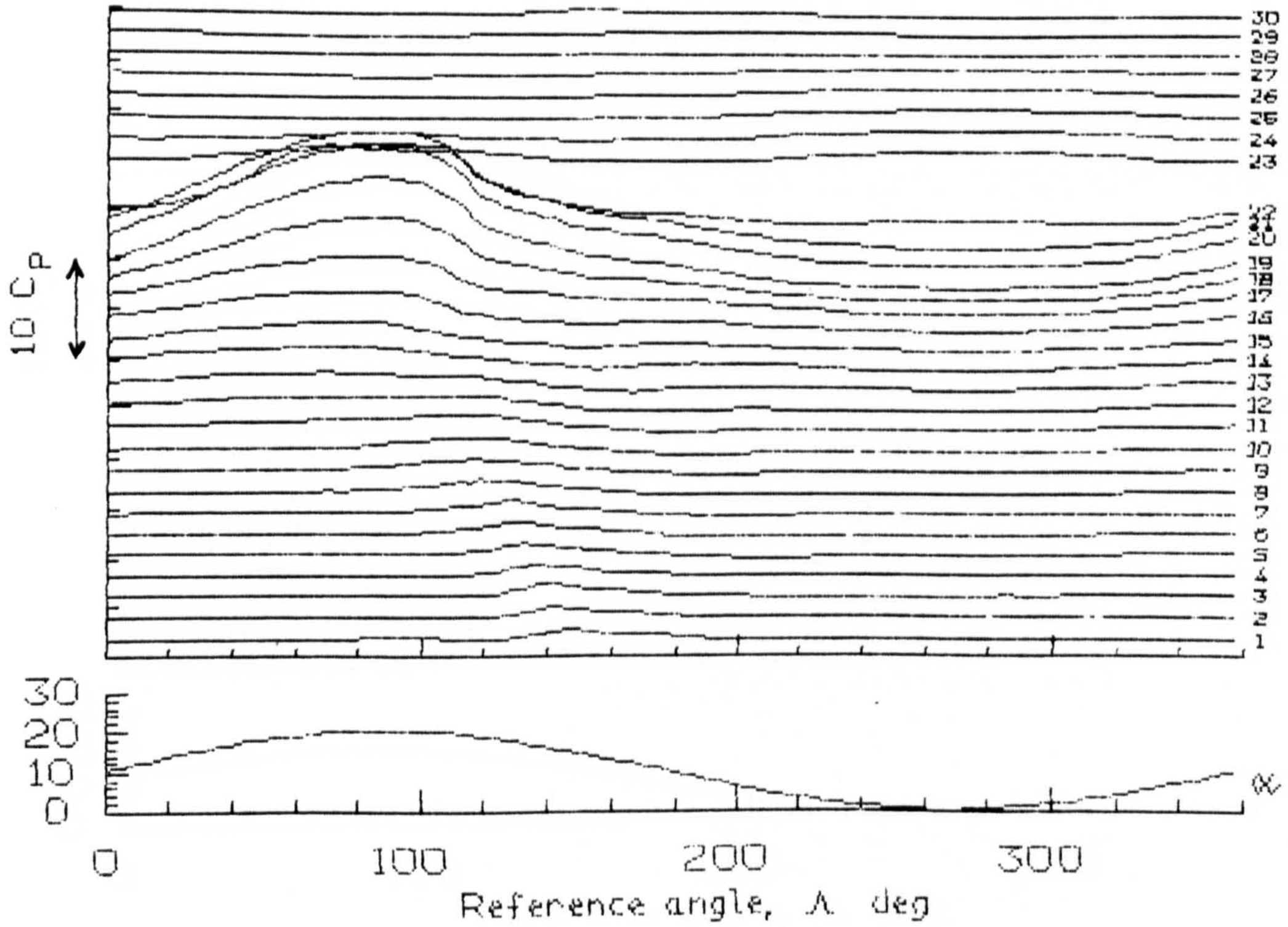

Fig 7.98 Pressure Time Histories for $\alpha = 10 + 10 \sin \omega t$; k= 0.15

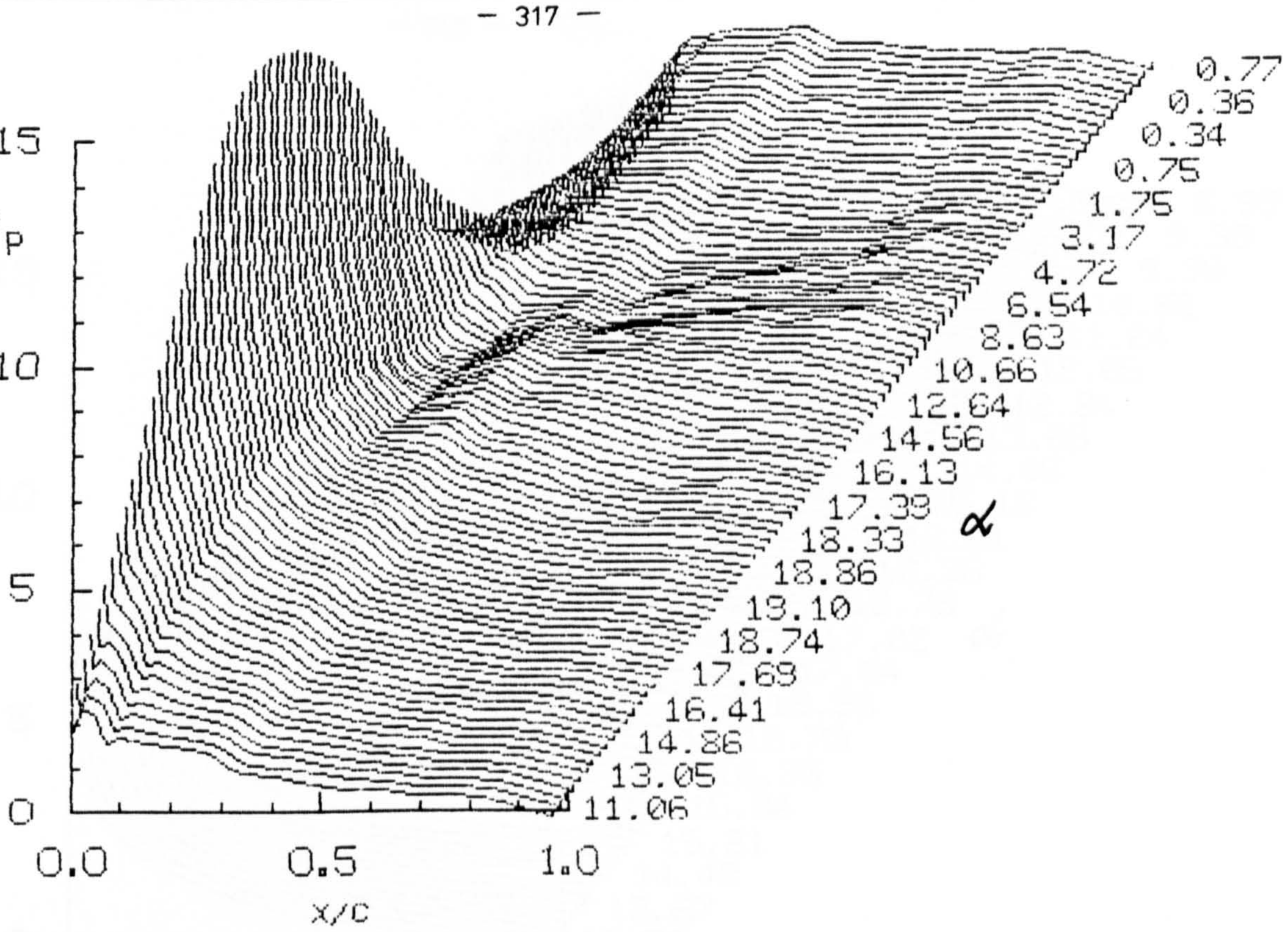

Fig 7.99 Chordwise Pressure Distributions for $\alpha = 10 + 10 \sin \omega t$; k= 0.20

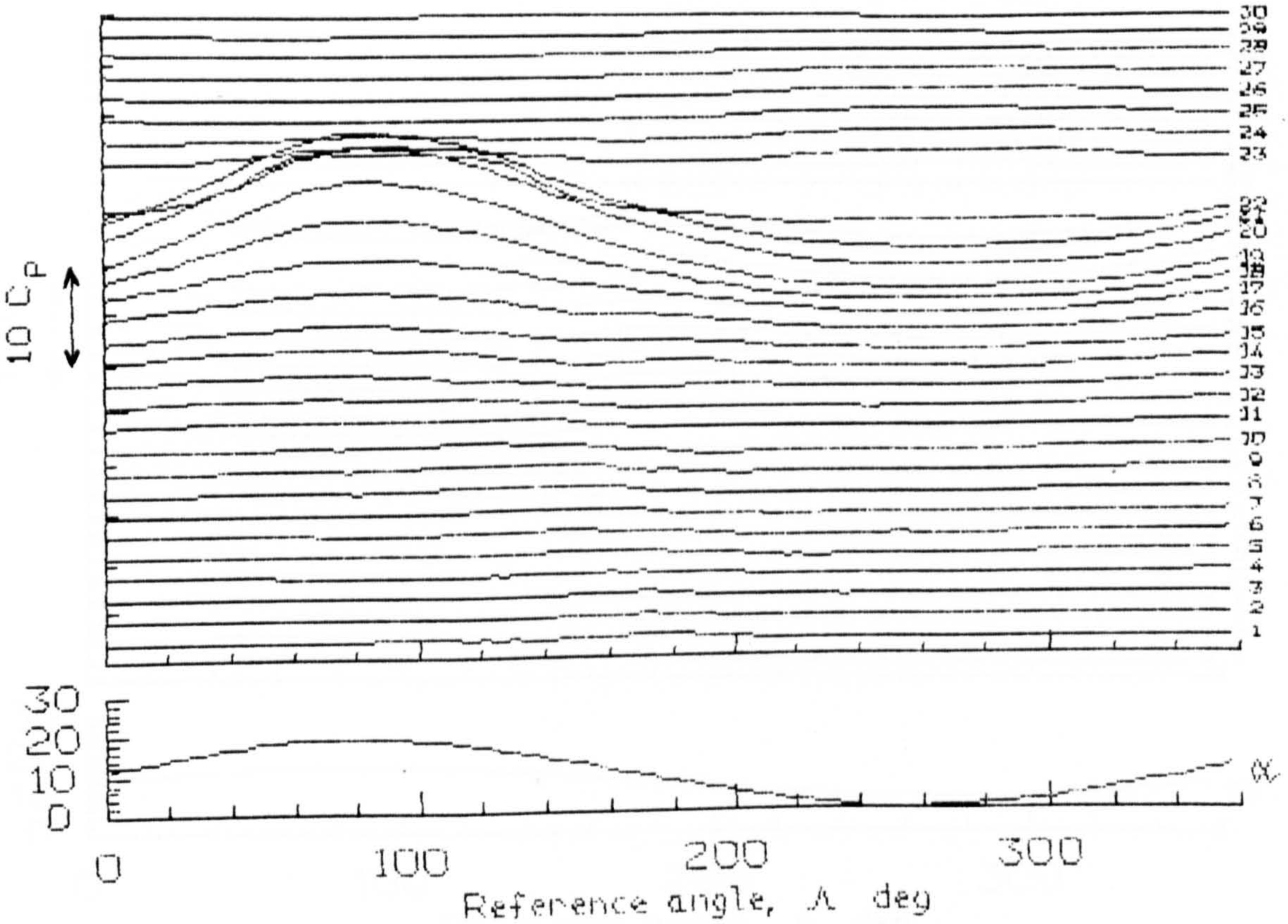

Fig 7.100 Pressure Time Histories for $\alpha = 10 + 10 \sin \omega t$; k= 0.20

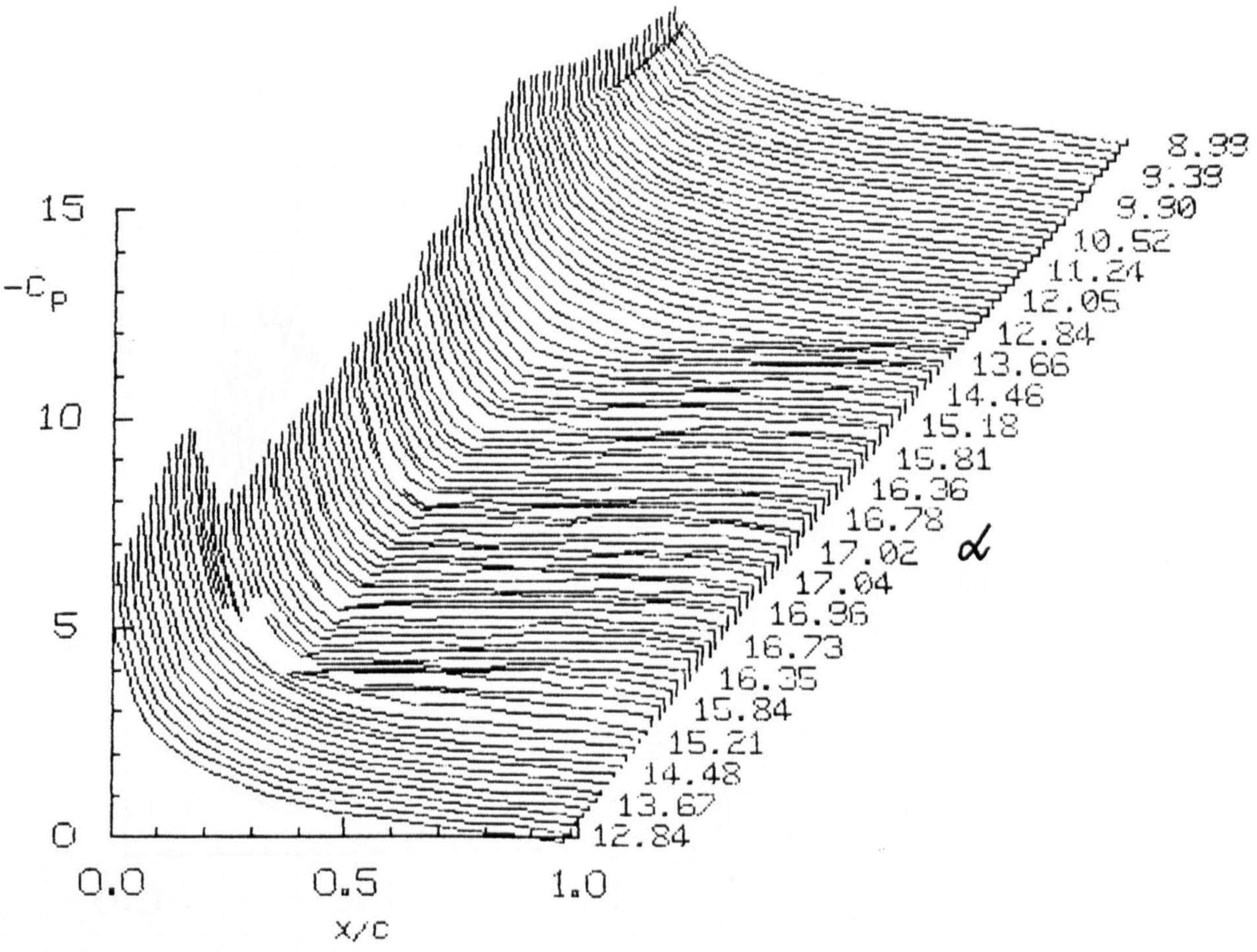

Fig 7.101 Chordwise Pressure Distributions for $\alpha = 13 + 4 \sin \omega t$; k= 0.01

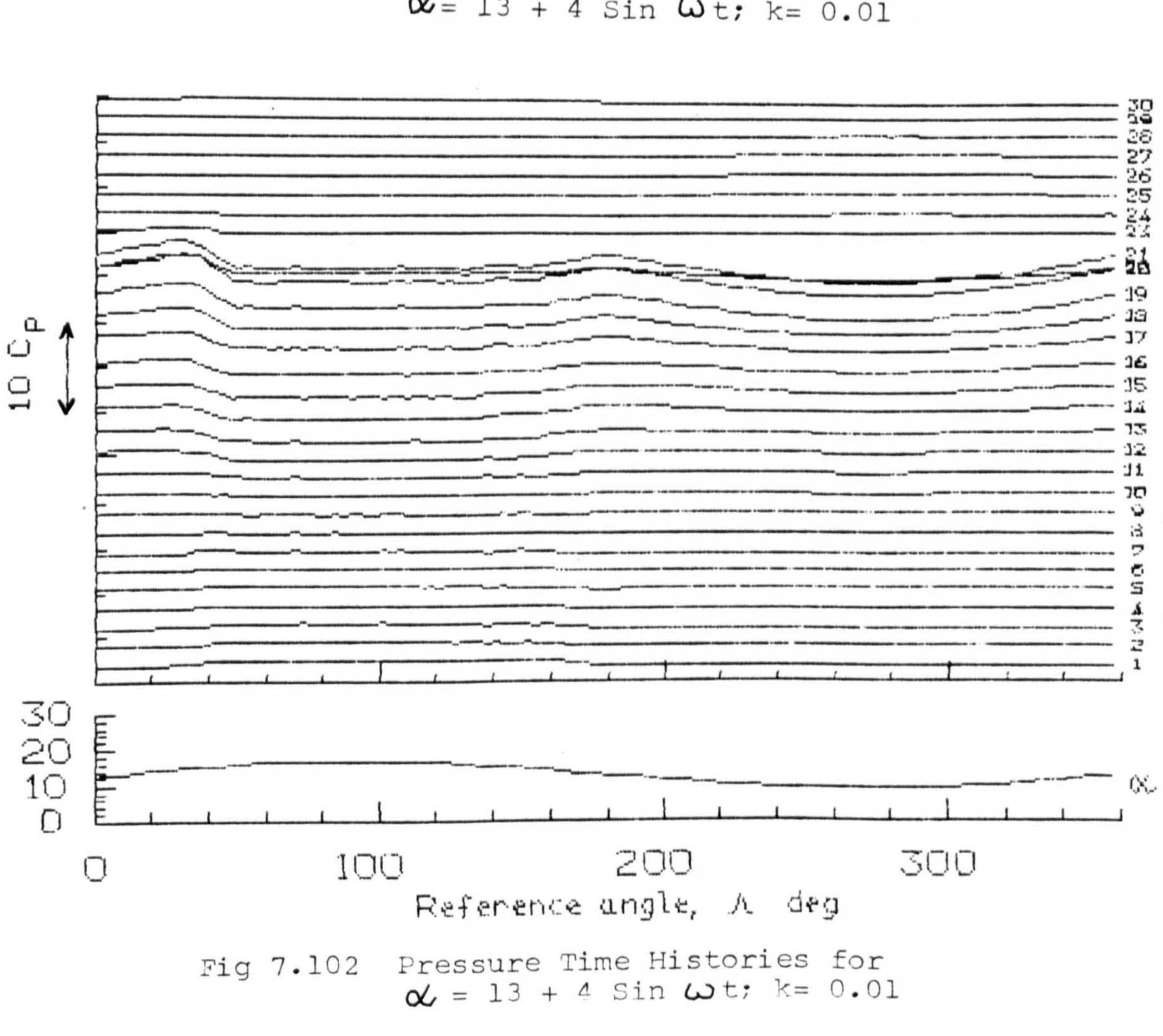

Fig 7.102 Pressure Time Histories for $\alpha = 13 + 4 \sin \omega t$; k= 0.01

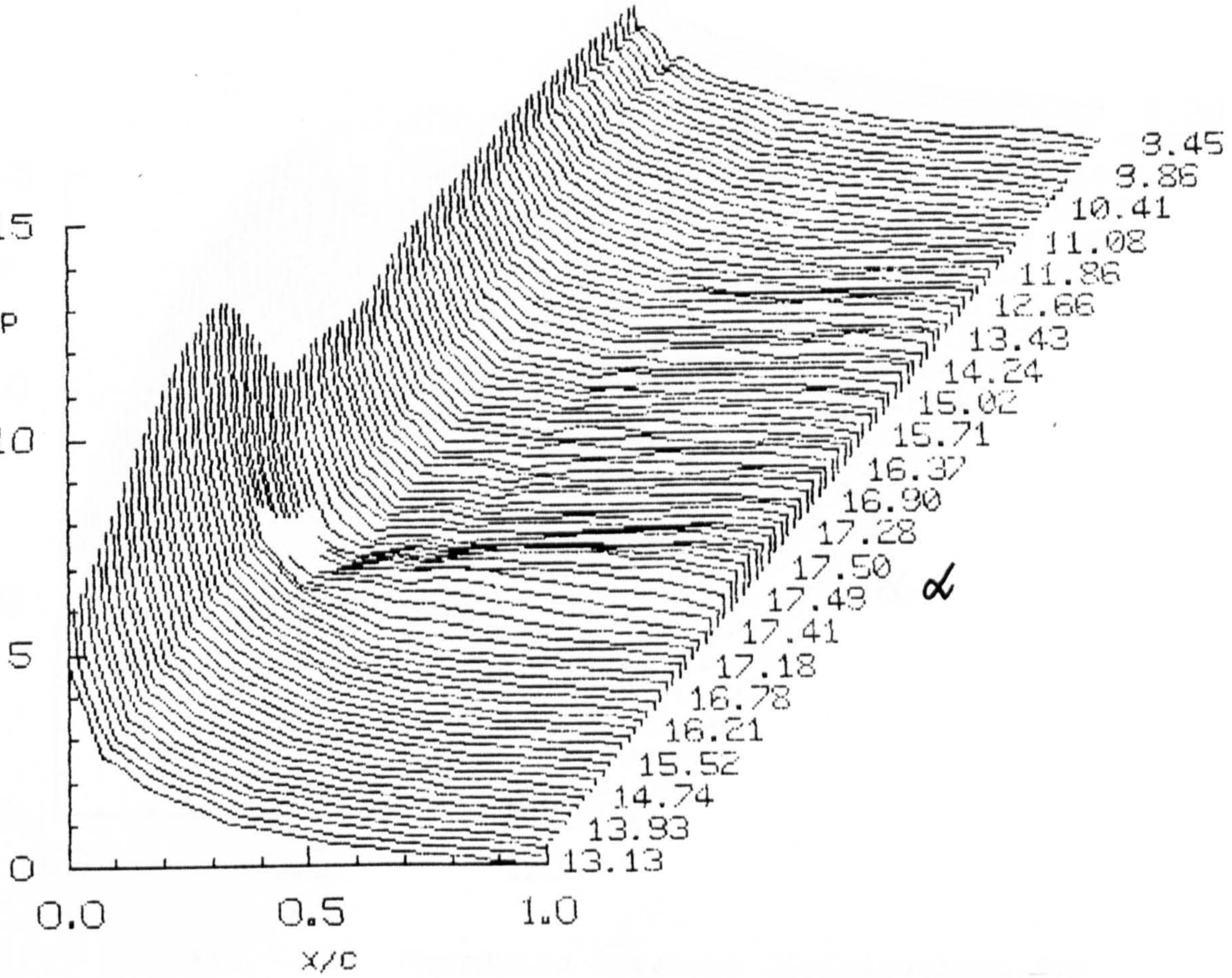

Fig 7.103 Chordwise Pressure Distributions for $\alpha = 13 + 4 \sin \omega t$; k= 0.05

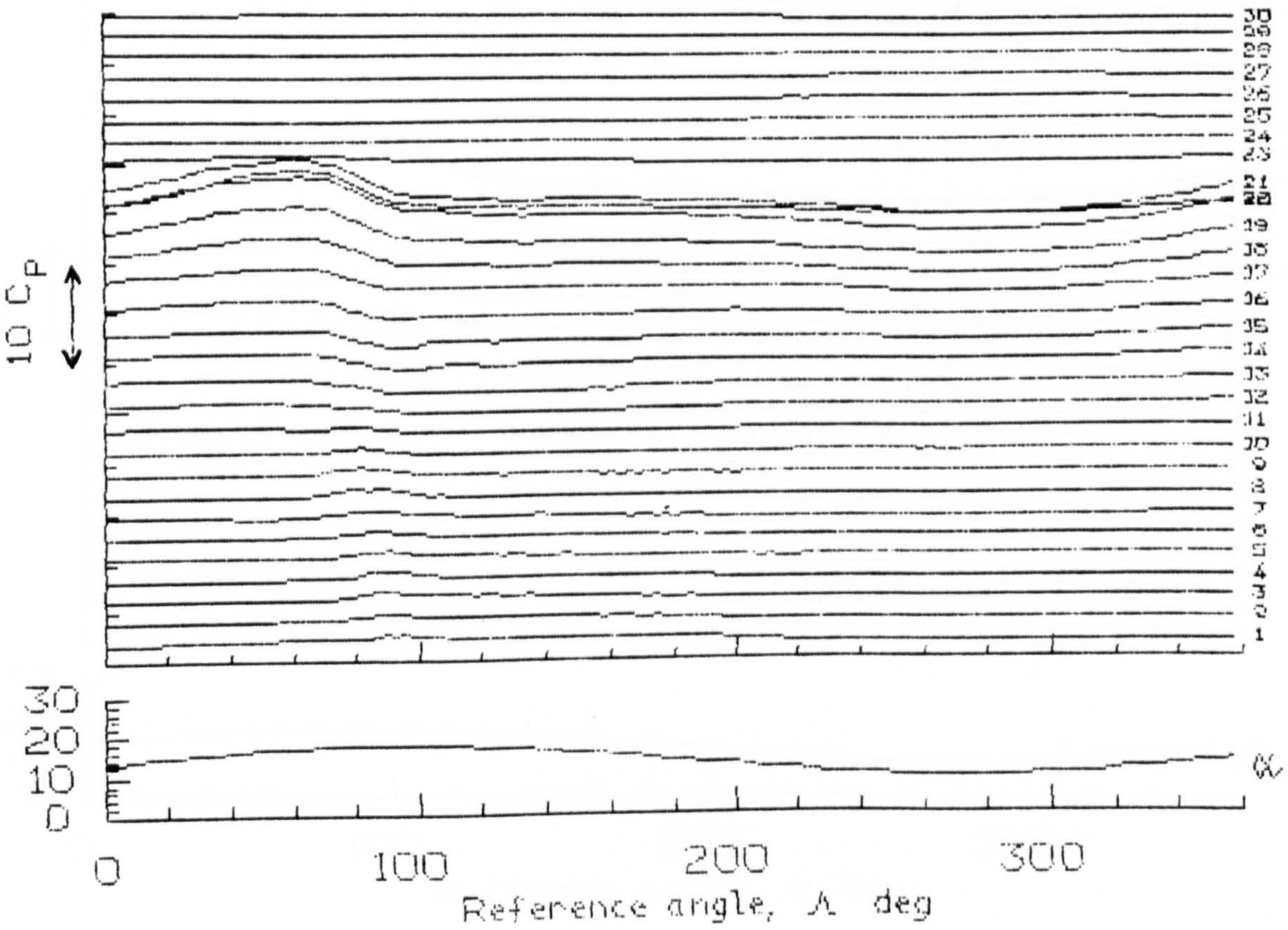

Fig 7.104 Pressure Time Histories for $\alpha = 13 + 4 \sin \omega t$; k= 0.05

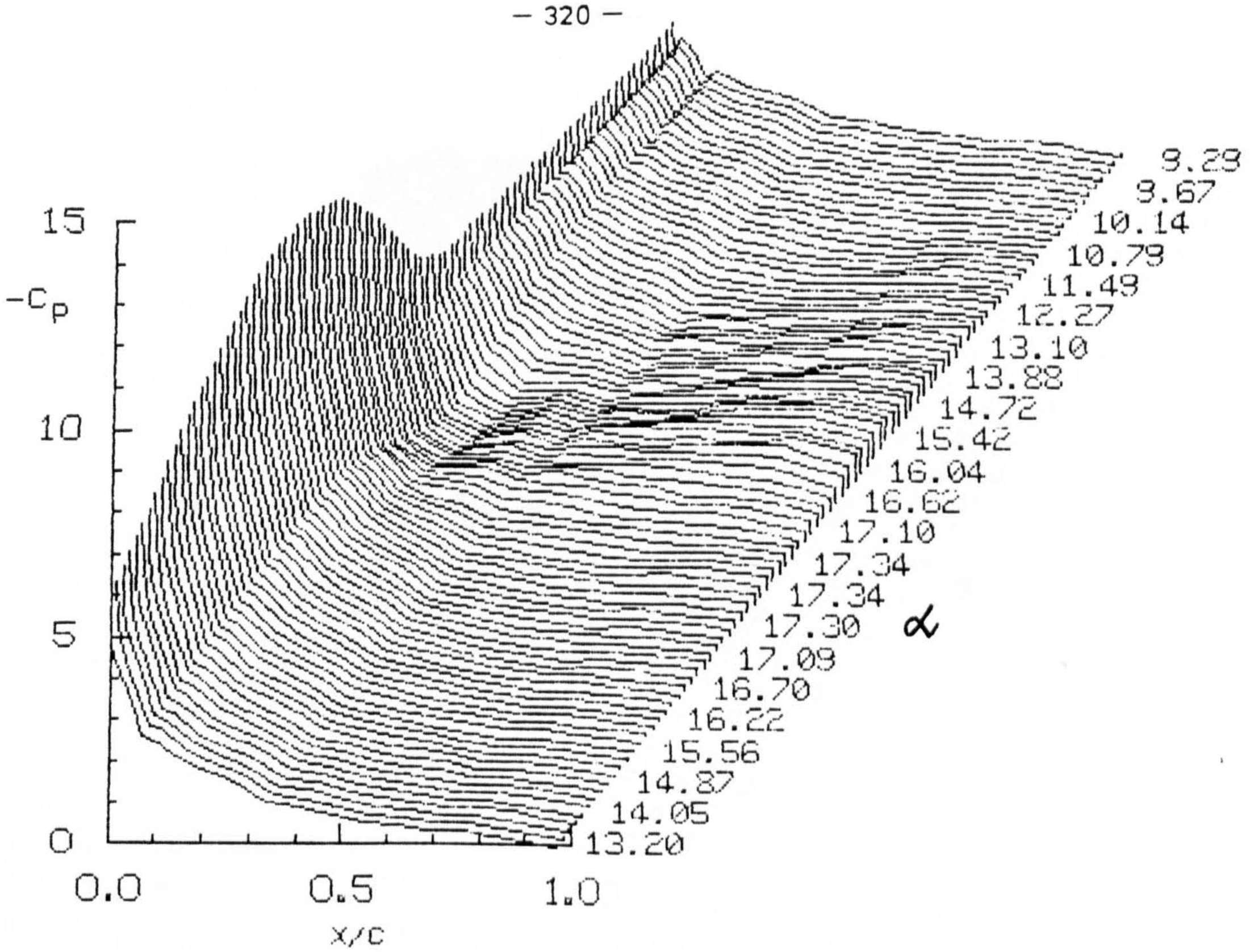

Fig 7.105 Chordwise Pressure Distributions for $\alpha = 13 + 4 \sin \omega t$; k= 0.10

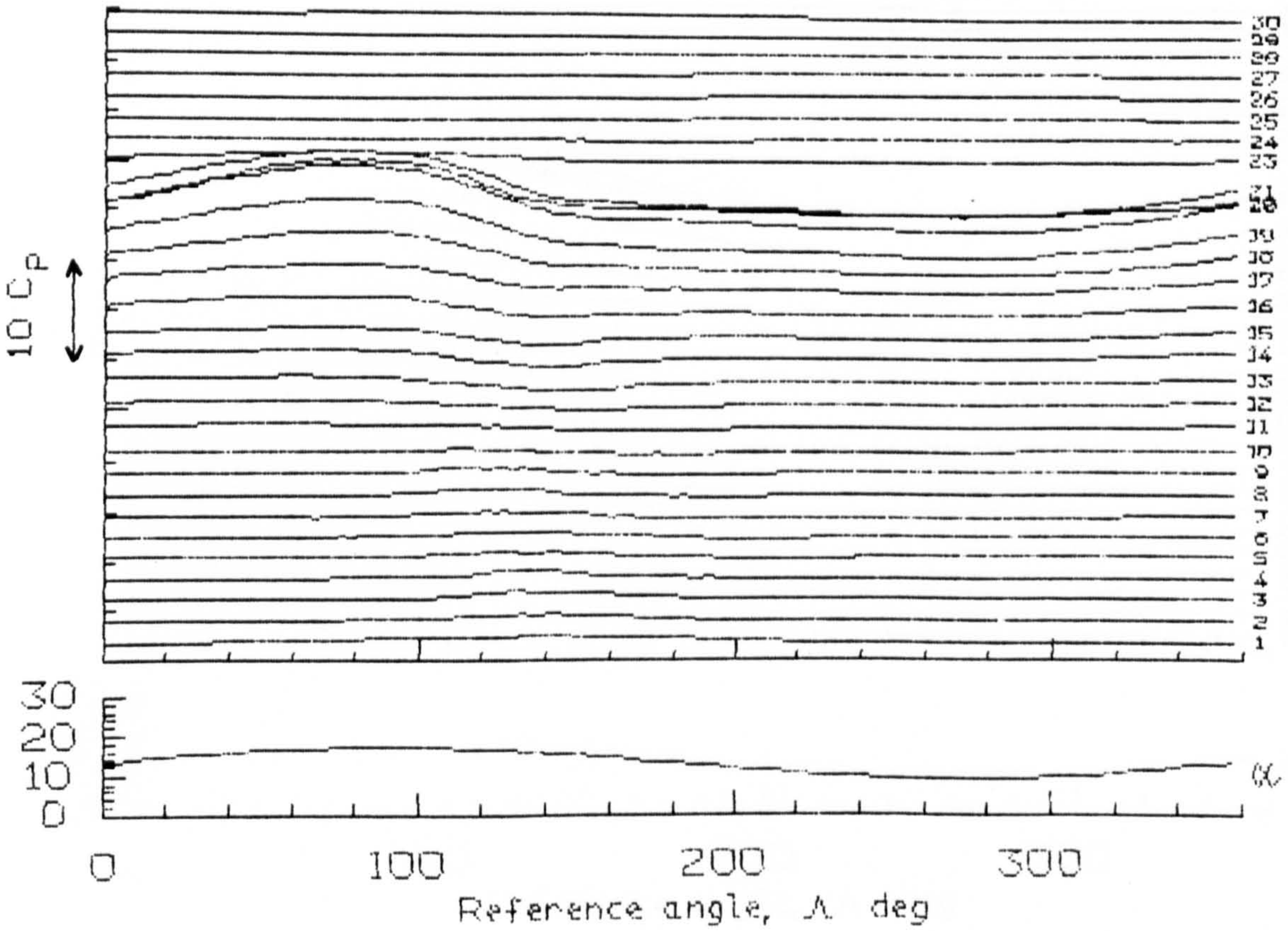

Fig 7.106 Pressure Time Histories for $\alpha = 13 + 4 \sin \omega t$; k= 0.10

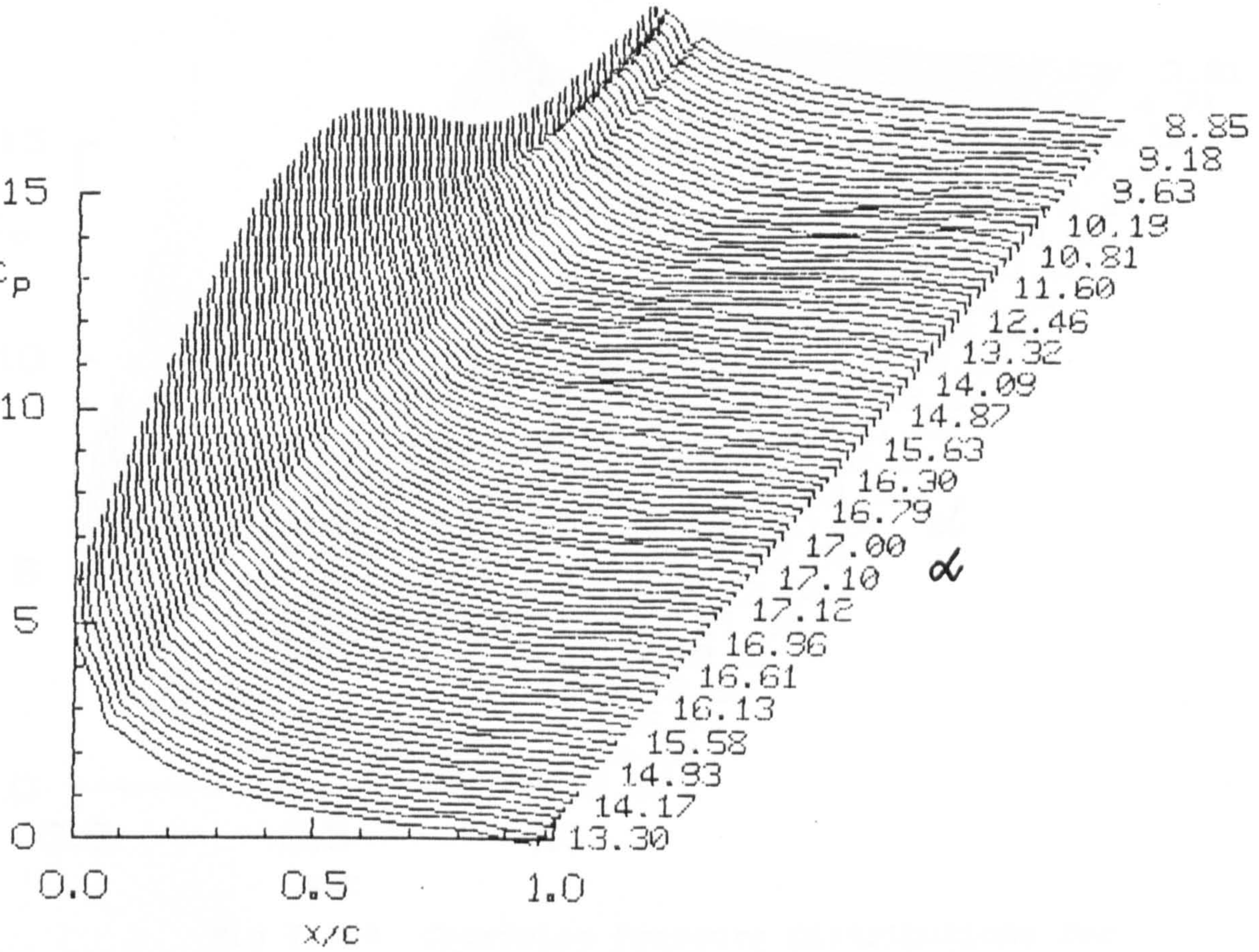

Fig 7.107 Chordwise Pressure Distributions for $\alpha = 13 + 4 \sin \omega t$; k= 0.15

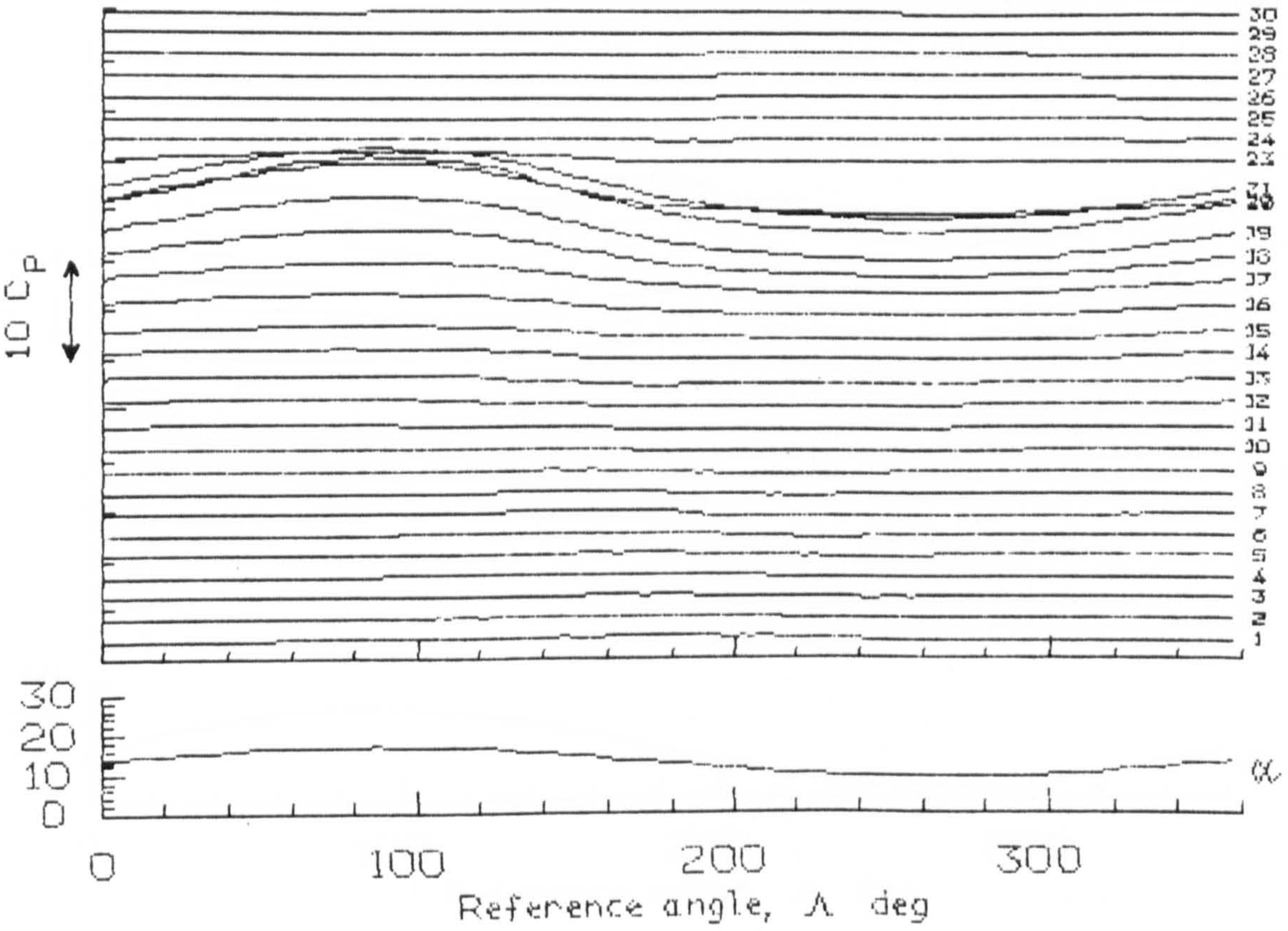

Fig 7.108 Pressure Time Histories for $\alpha = 13 + 4 \sin \omega t$; k= 0.15

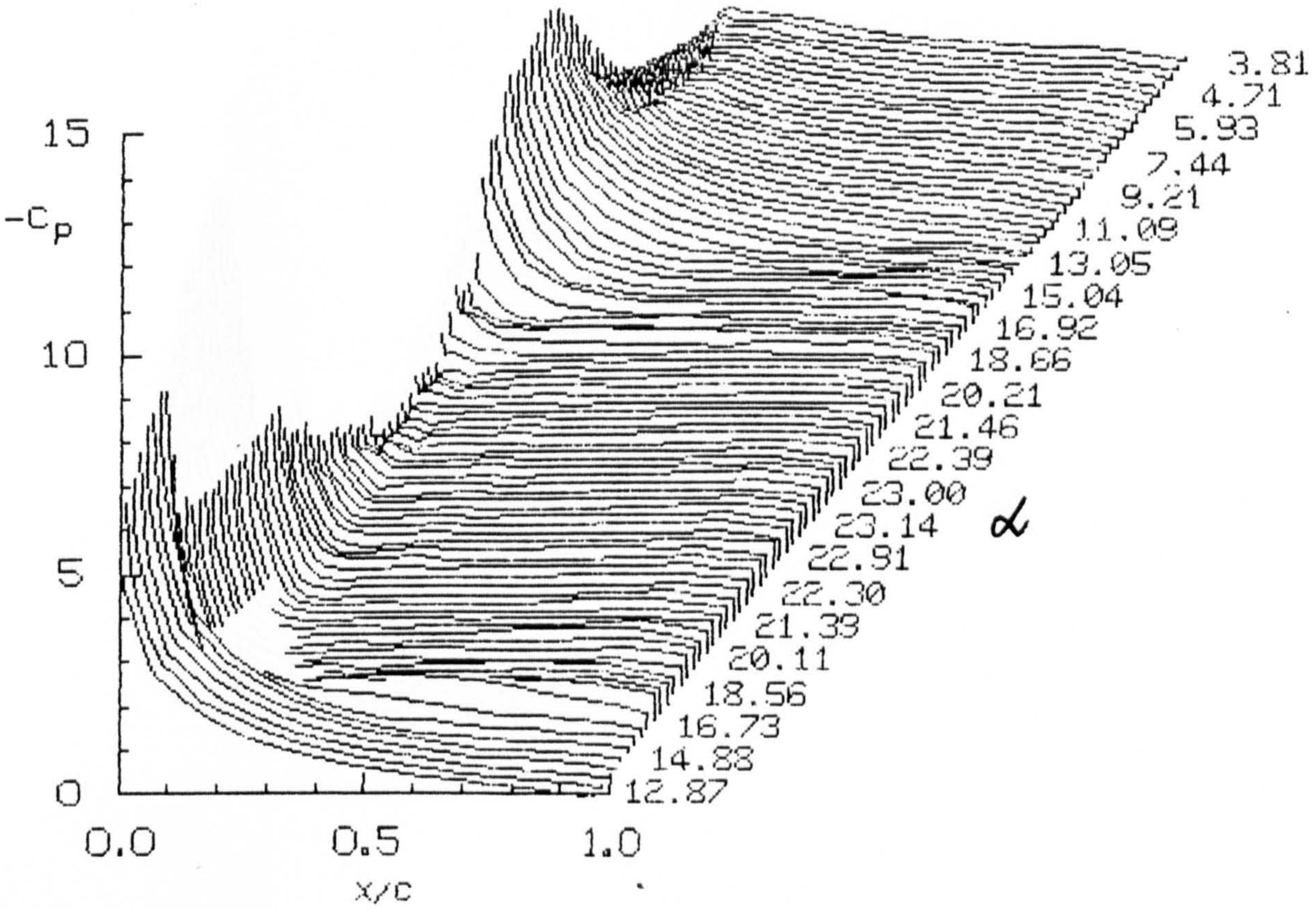

Fig 7.109 Chordwise Pressure Distributions for $\alpha = 13 + 10 \sin \omega t$; k= 0.01

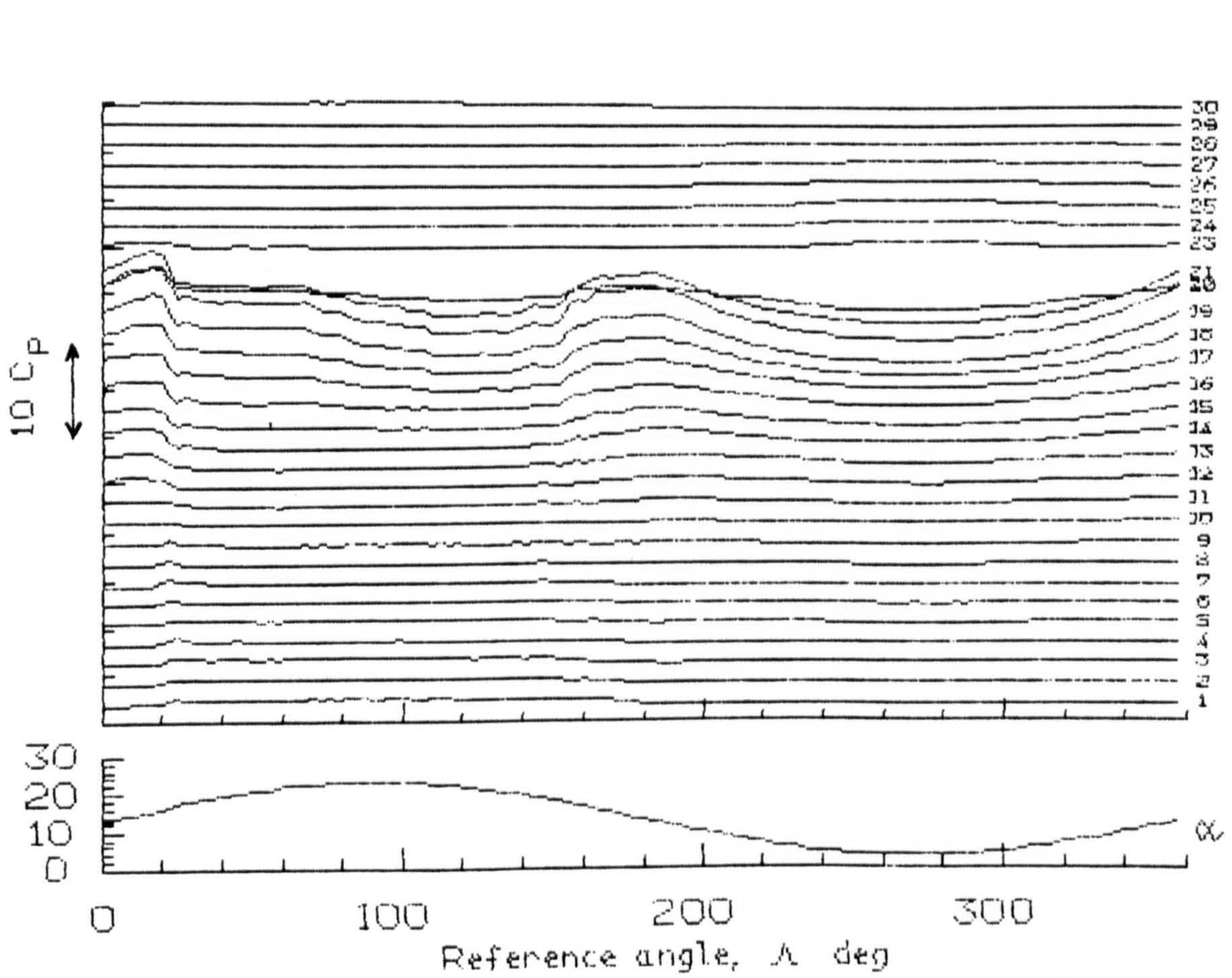

Fig 7.110 Pressure Time Histories for $\alpha = 13 + 10 \sin \omega t$; k= 0.01

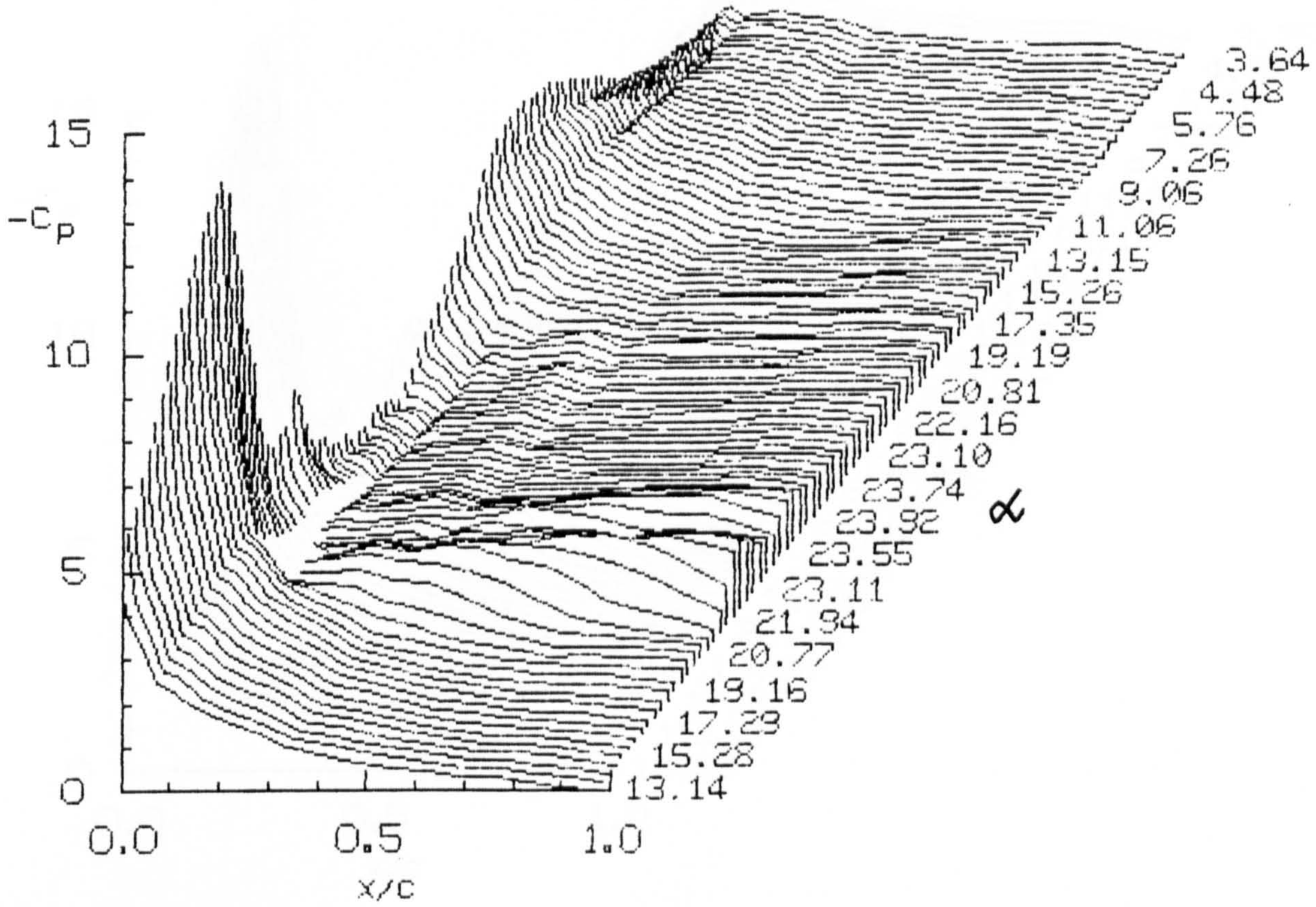

Fig 7.111 Chordwise Pressure Distributions for $\alpha = 13 + 10 \sin \omega t$; k= 0.05

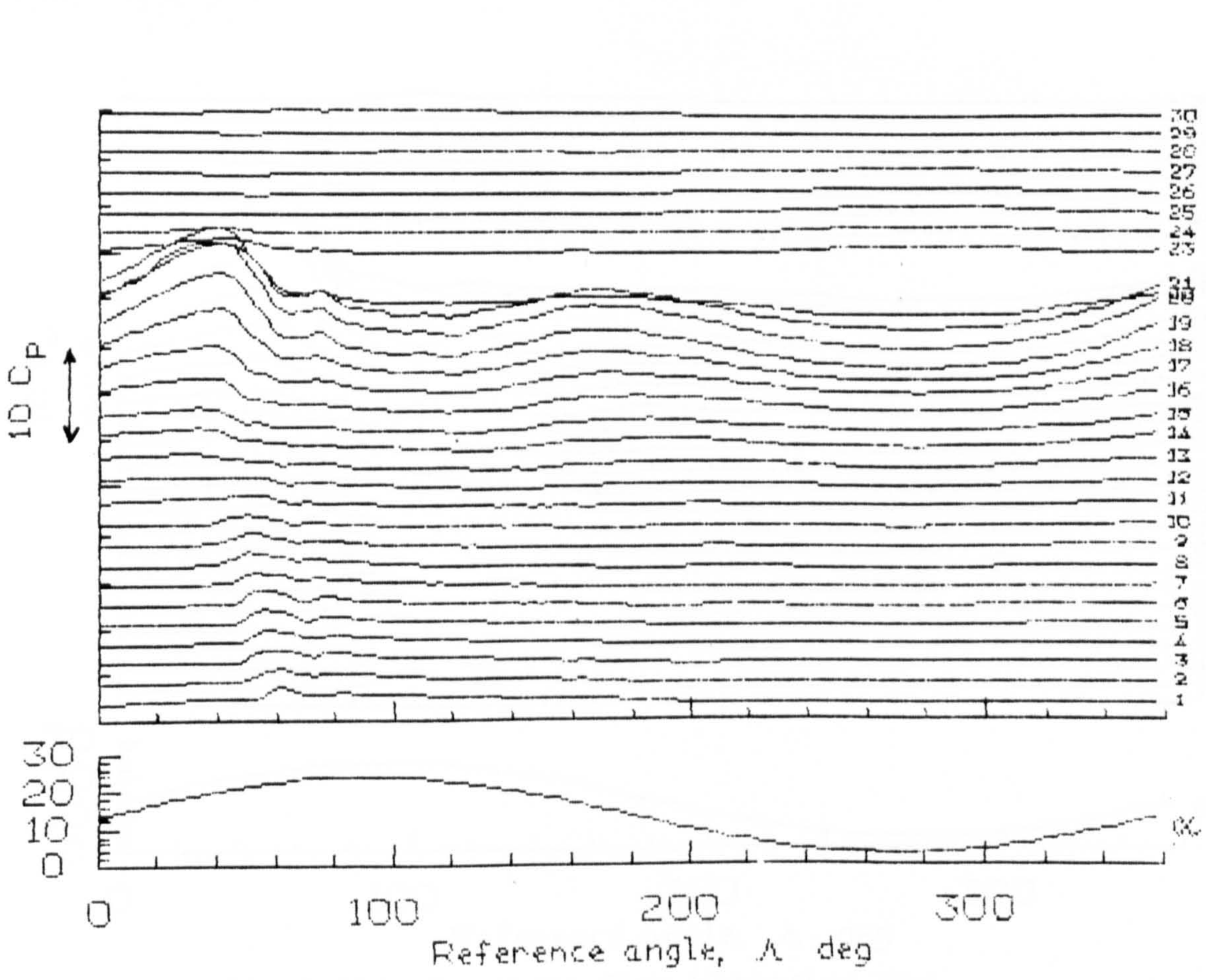

Fig 7.112 Pressure Time Histories for $\alpha = 13 + 10 \sin \omega t$; k= 0.05

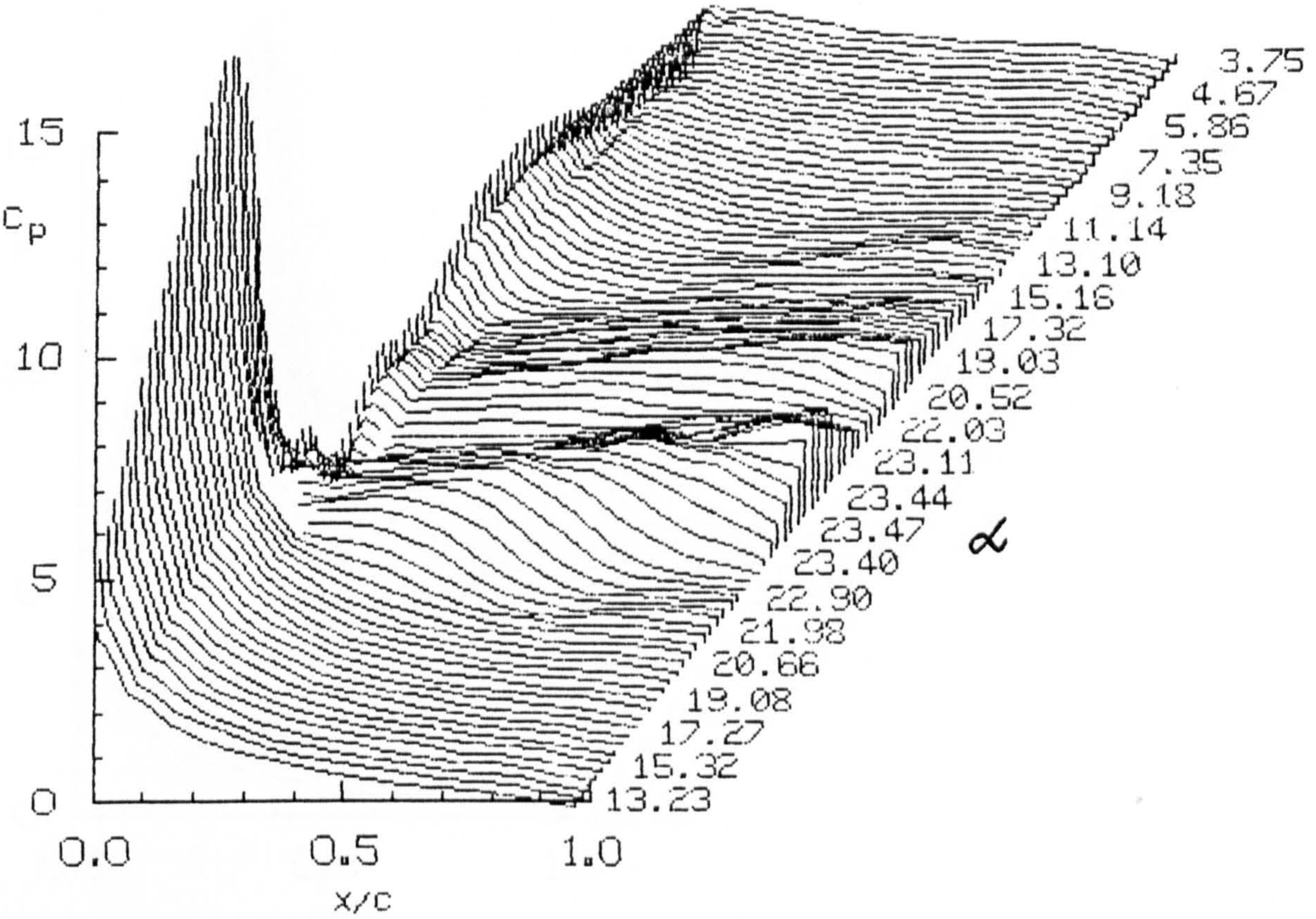

Fig 7.113 Chordwise Pressure Distributions for $\alpha = 13 + 10 \sin \omega t$; k= 0.10

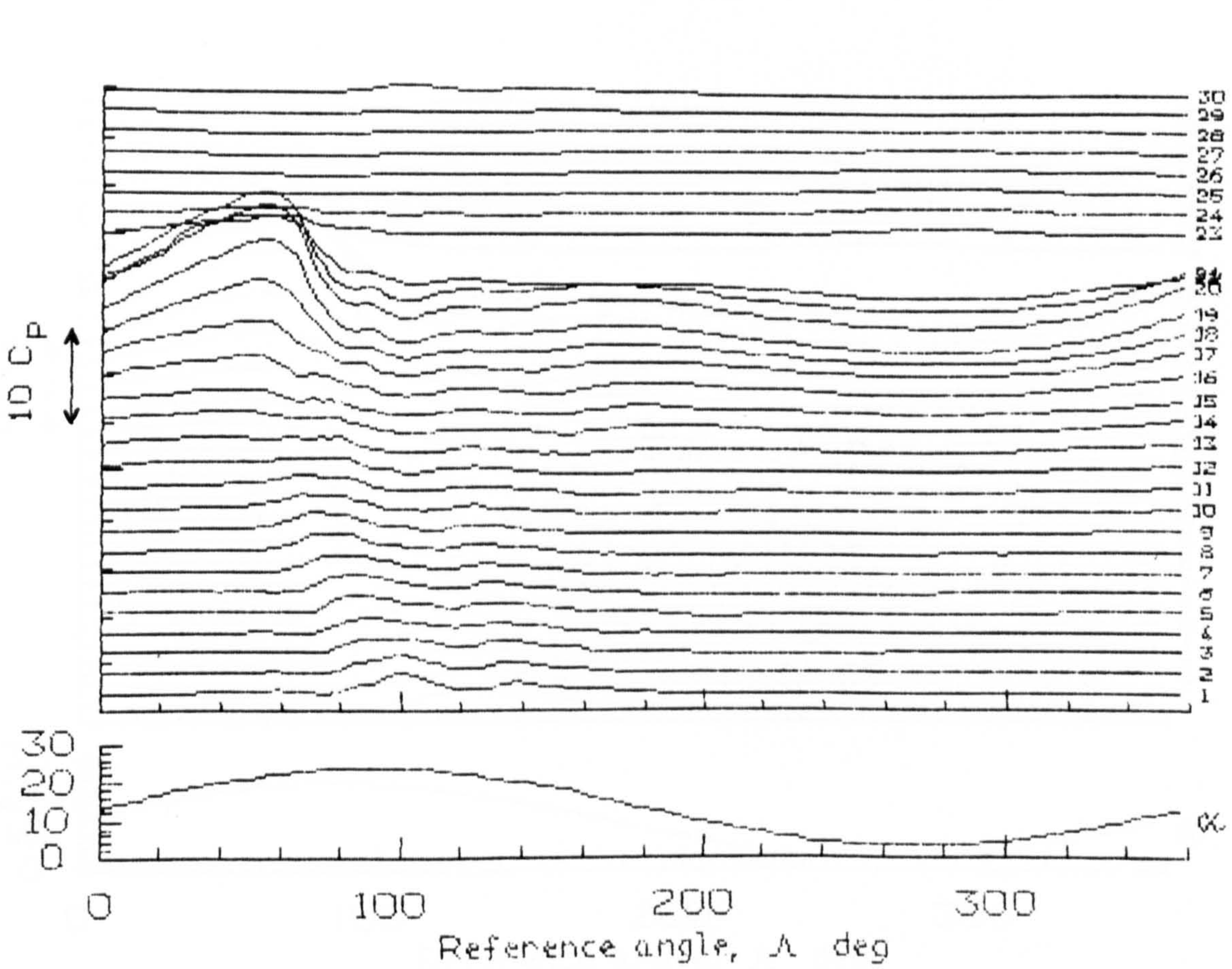

Fig 7.114 Pressure Time Histories for $\alpha = 13 + 10 \sin \omega t$; k= 0.10

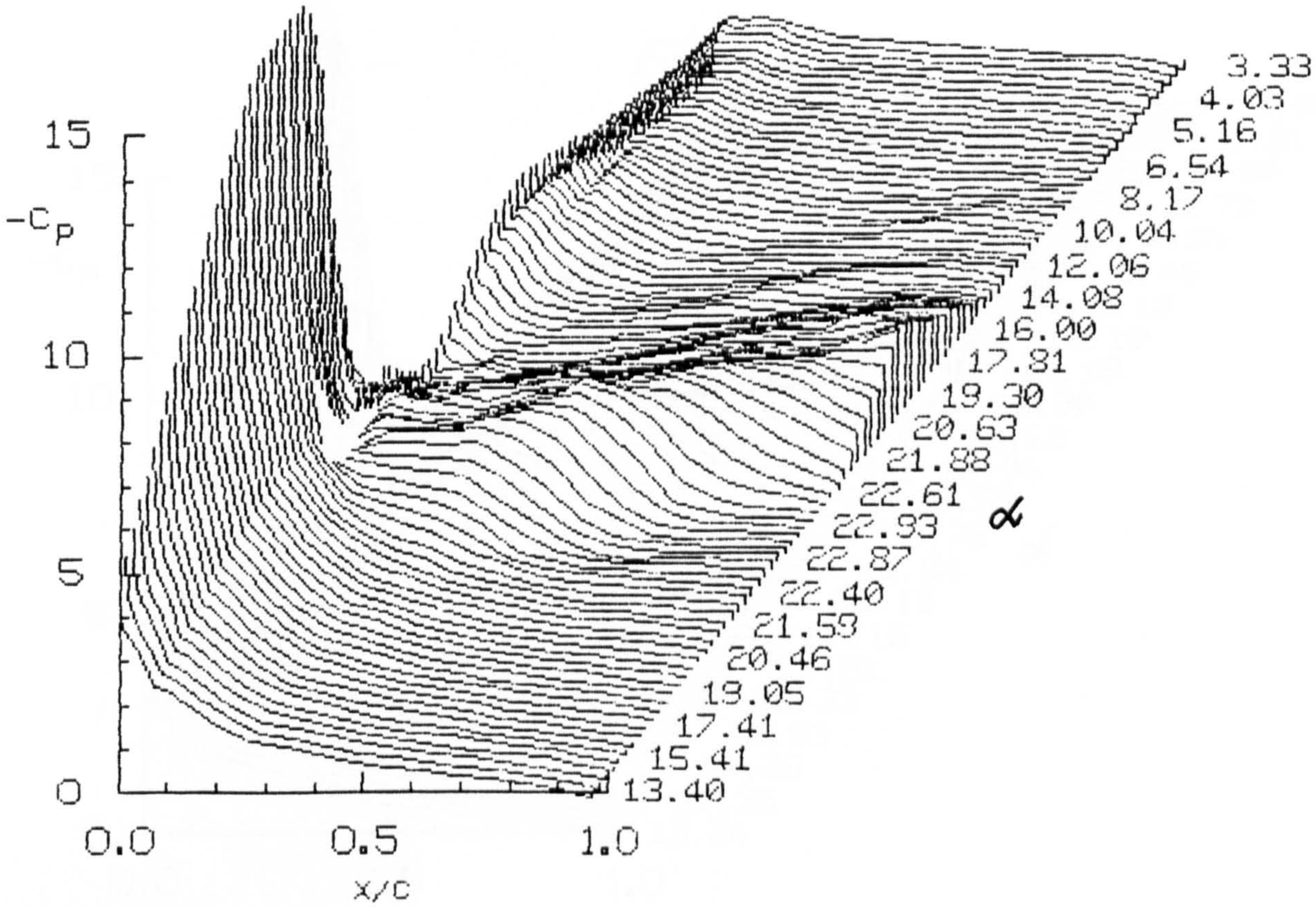

Fig 7.115 Chordwise Pressure Distributions for $\alpha = 13 + 10 \sin \omega t$; k= 0.15

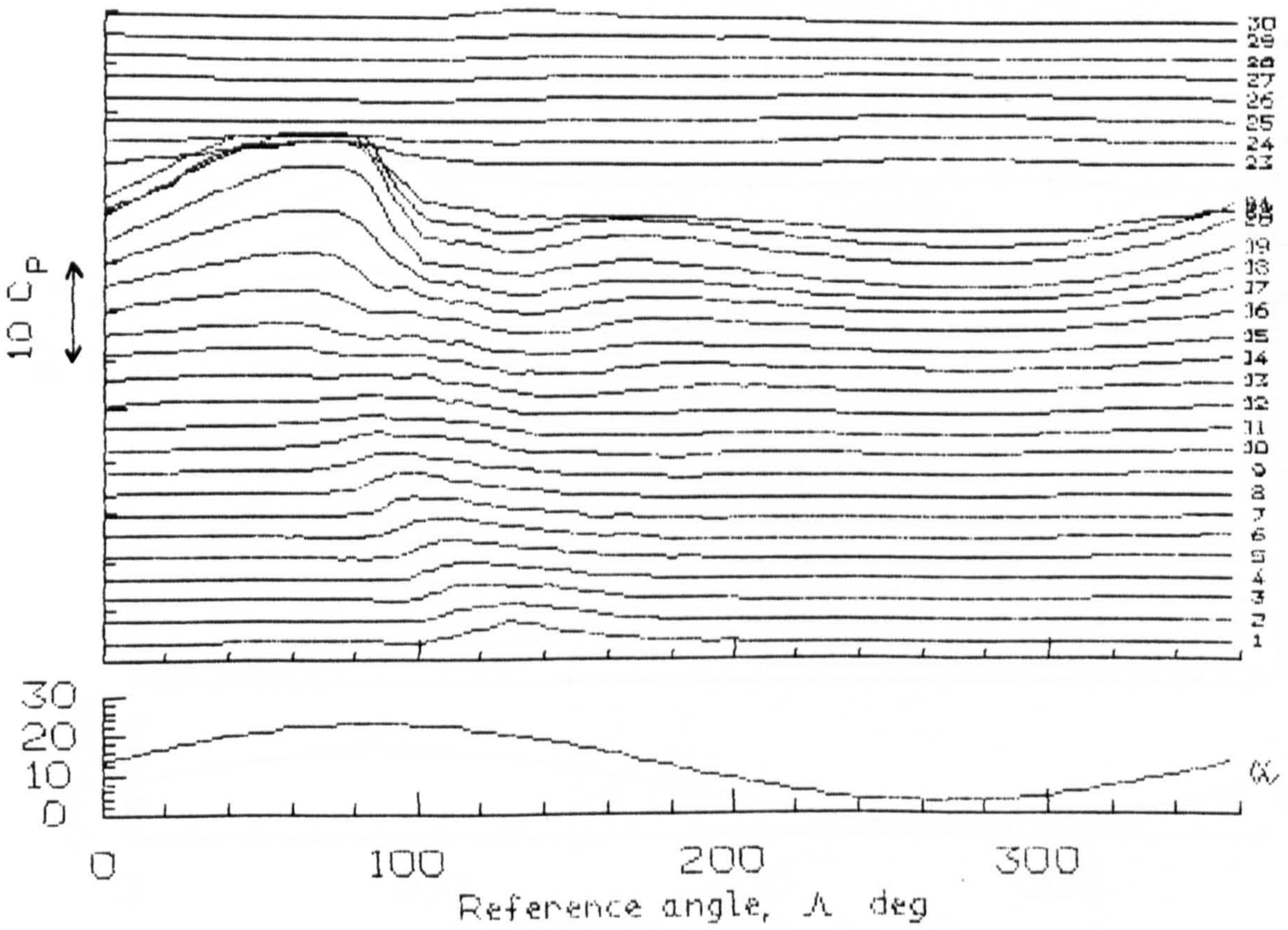

Fig 7.116 Pressure Time Histories for $\alpha = 13 + 10 \sin \omega t$; k= 0.15

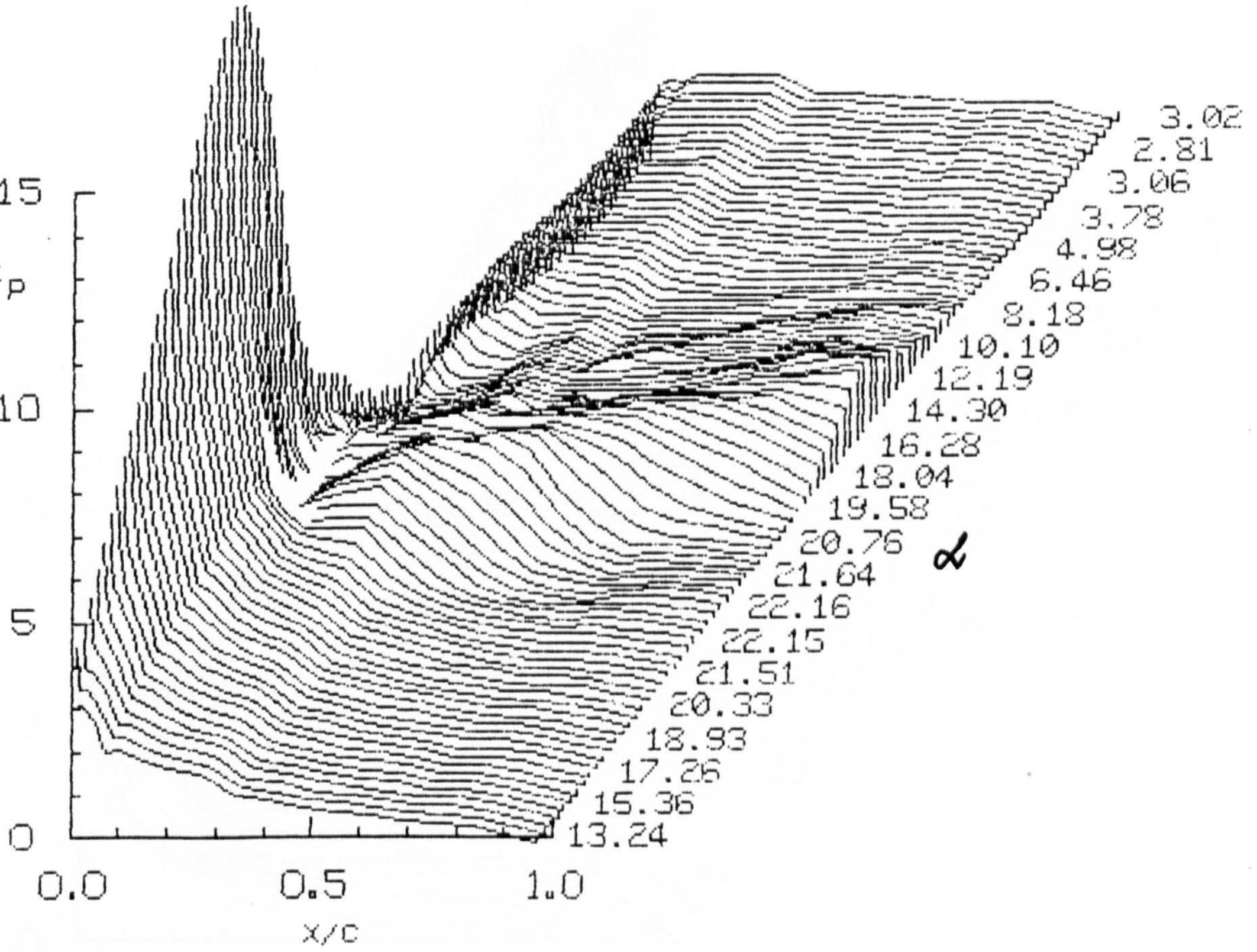

Fig 7.117 Chordwise Pressure Distributions for $\alpha = 13 + 10 \sin \omega t$; k= 0.20

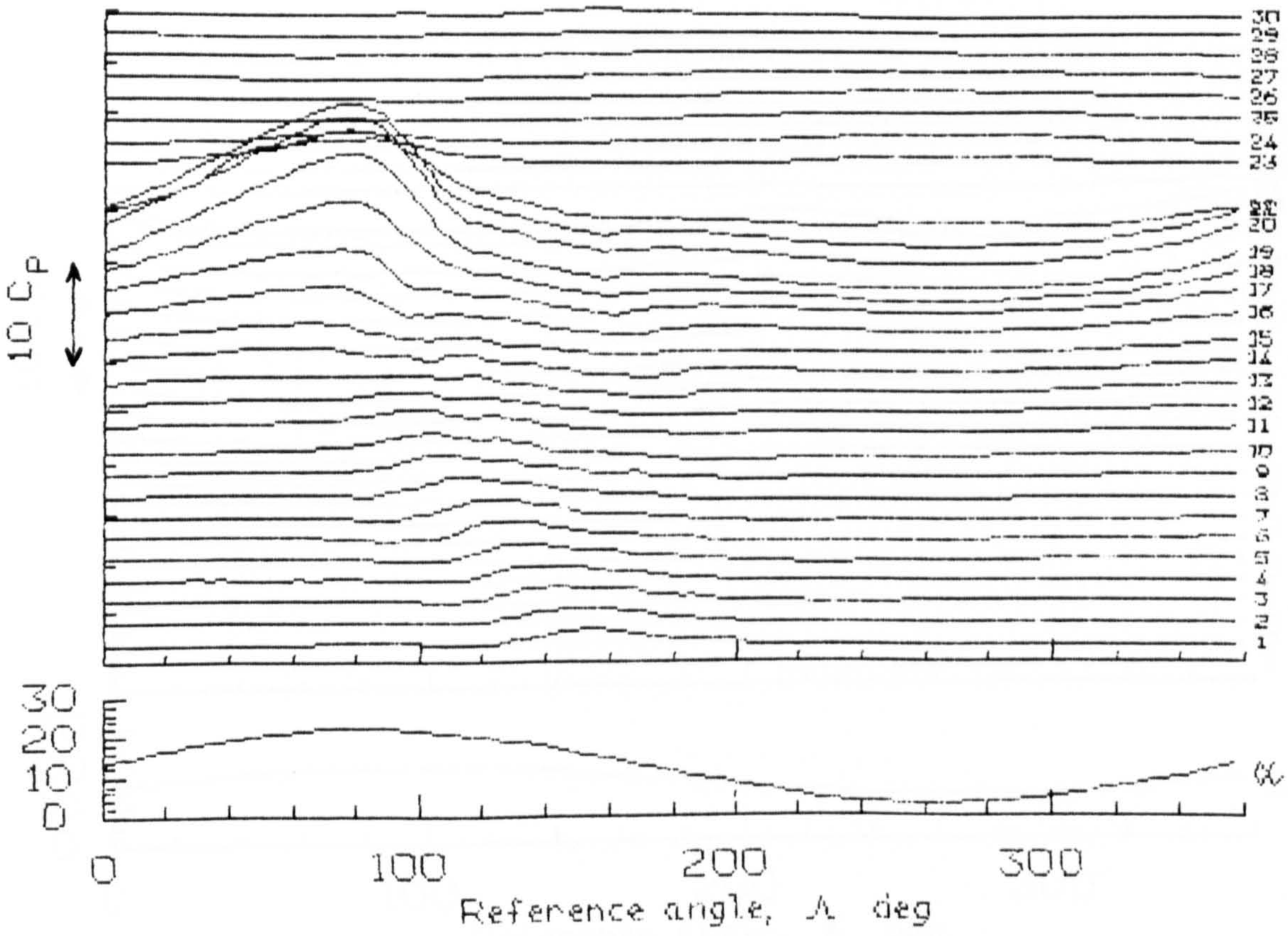

Fig 7.118 Pressure Time Histories for $\alpha = 13 + 10 \sin \omega t$; k= 0.20

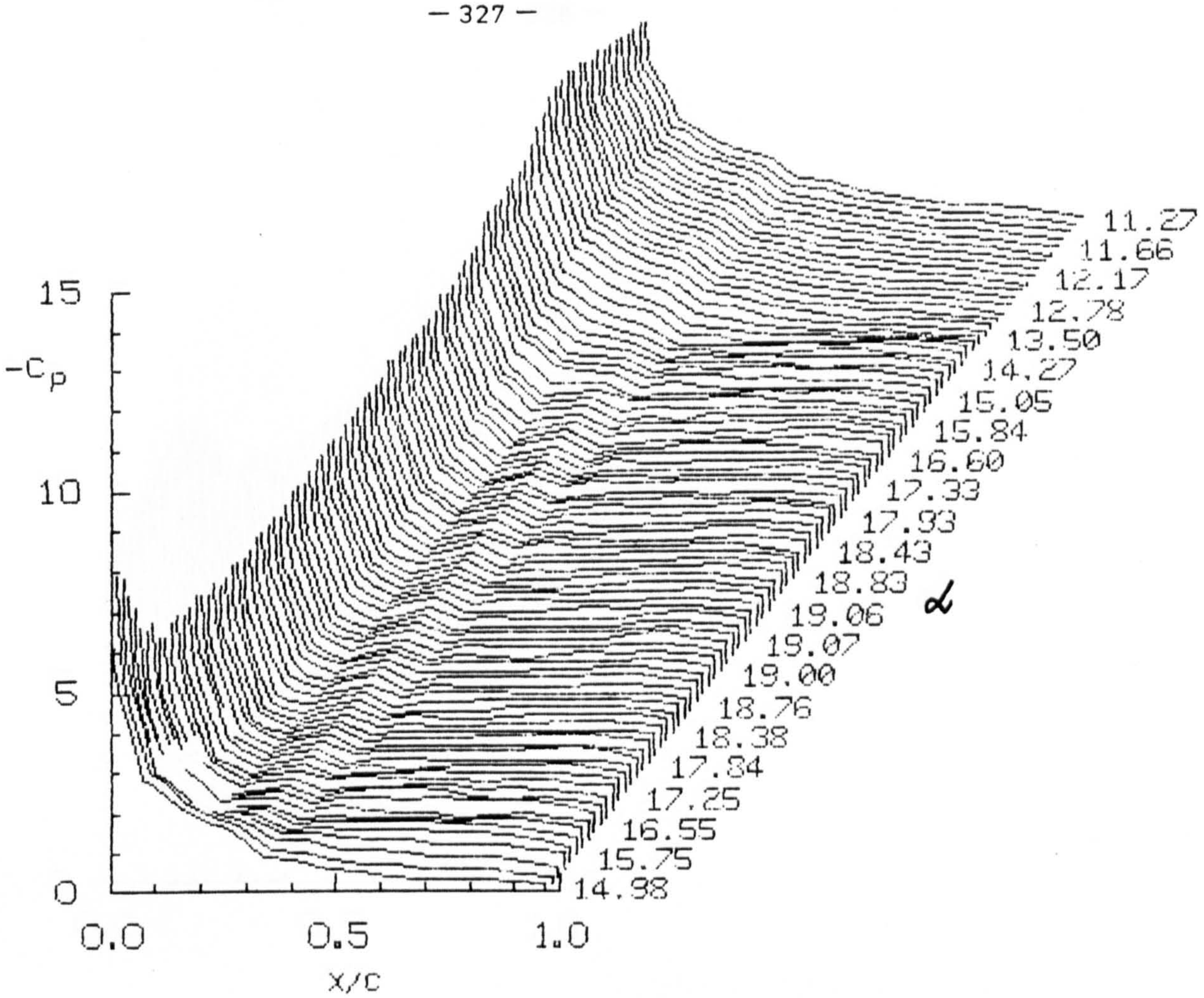

Fig 7.119 Chordwise Pressure Distributions for $\alpha = 15 + 4 \sin \omega t$; k= 0.01

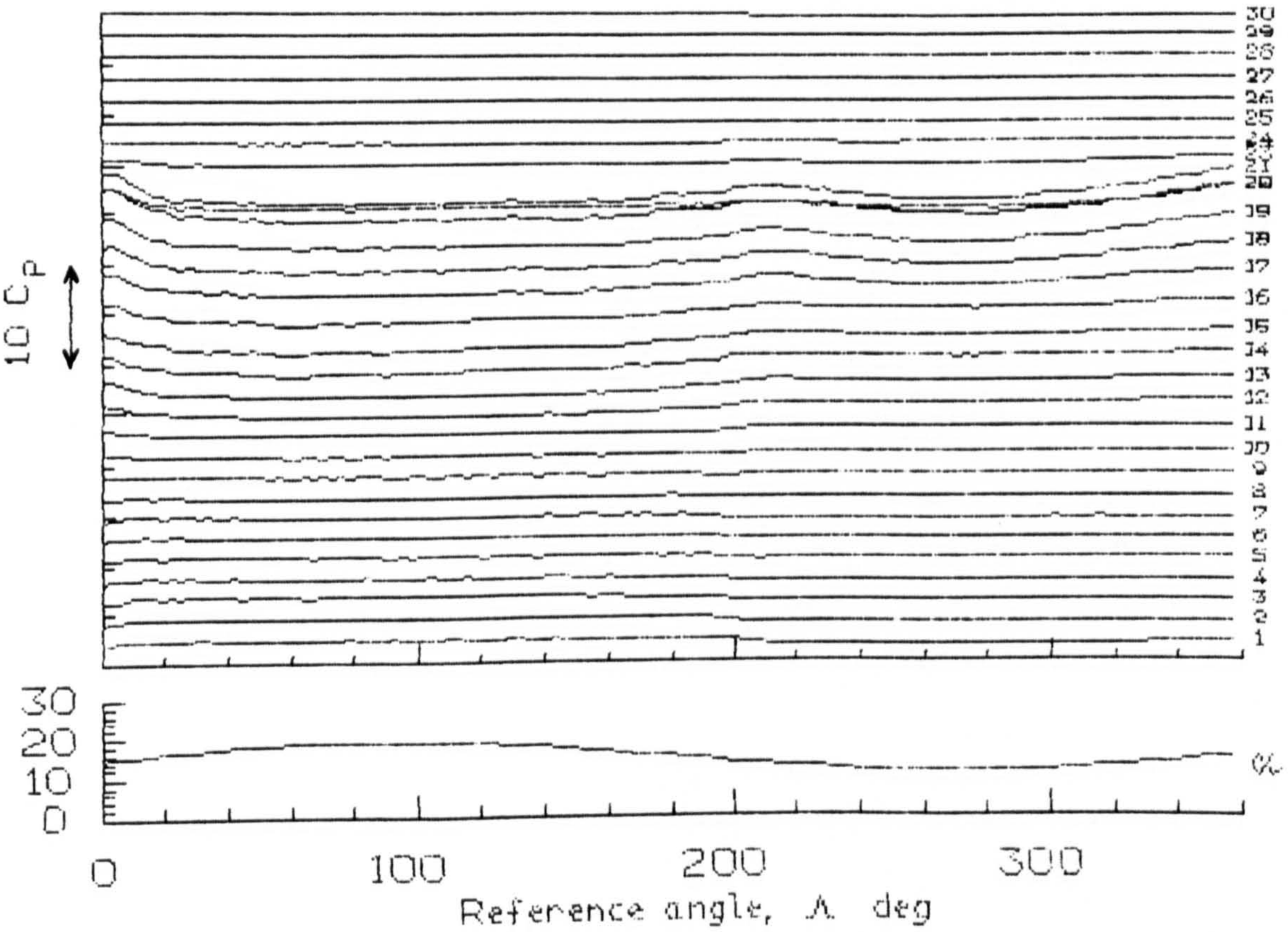

Fig 7.120 Pressure Time Histories for $\alpha = 15 + 4 \sin \omega t$; k= 0.01

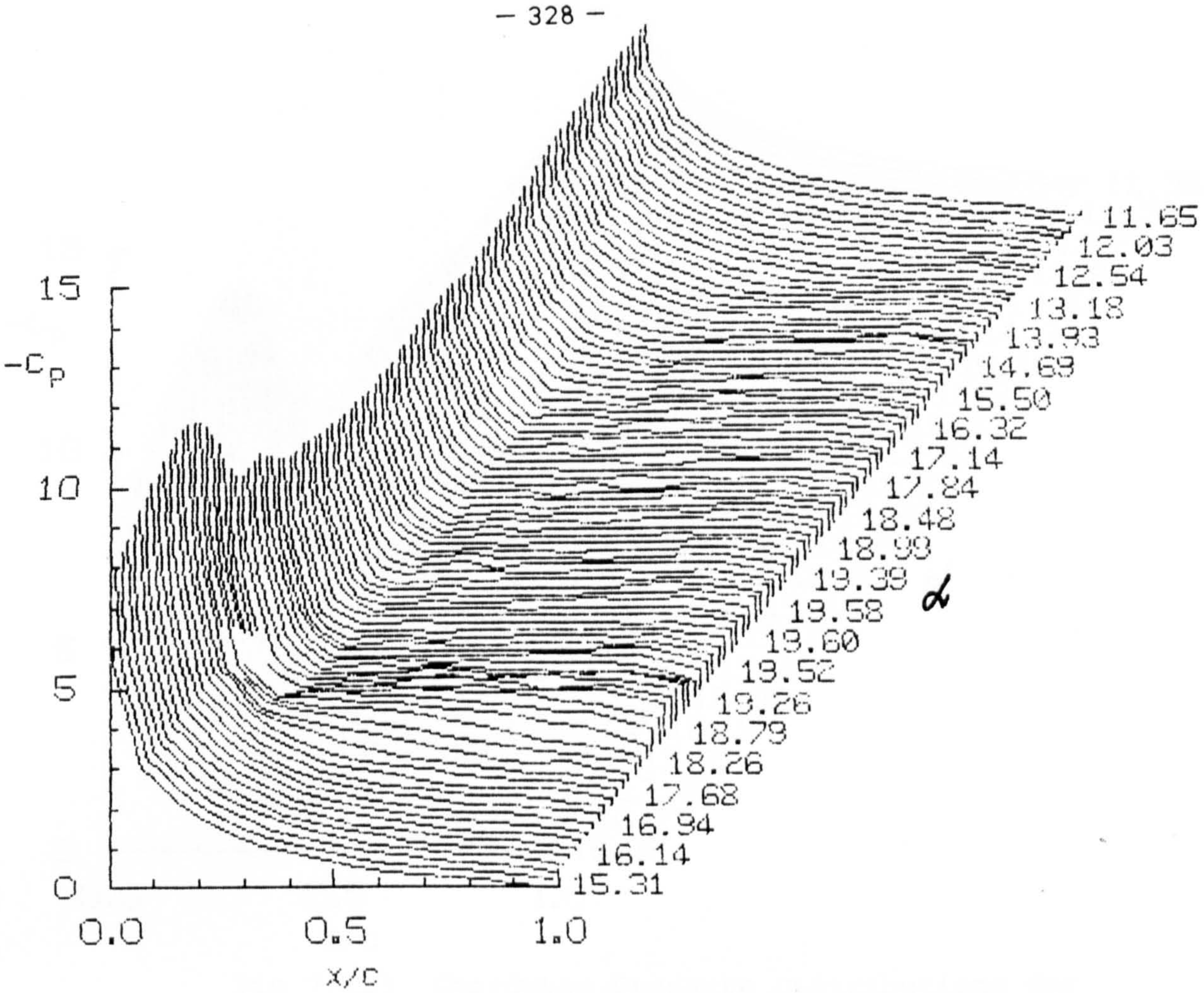

Fig 7.121 Chordwise Pressure Distributions for $\alpha = 15 + 4 \sin \omega t$; k= 0.05

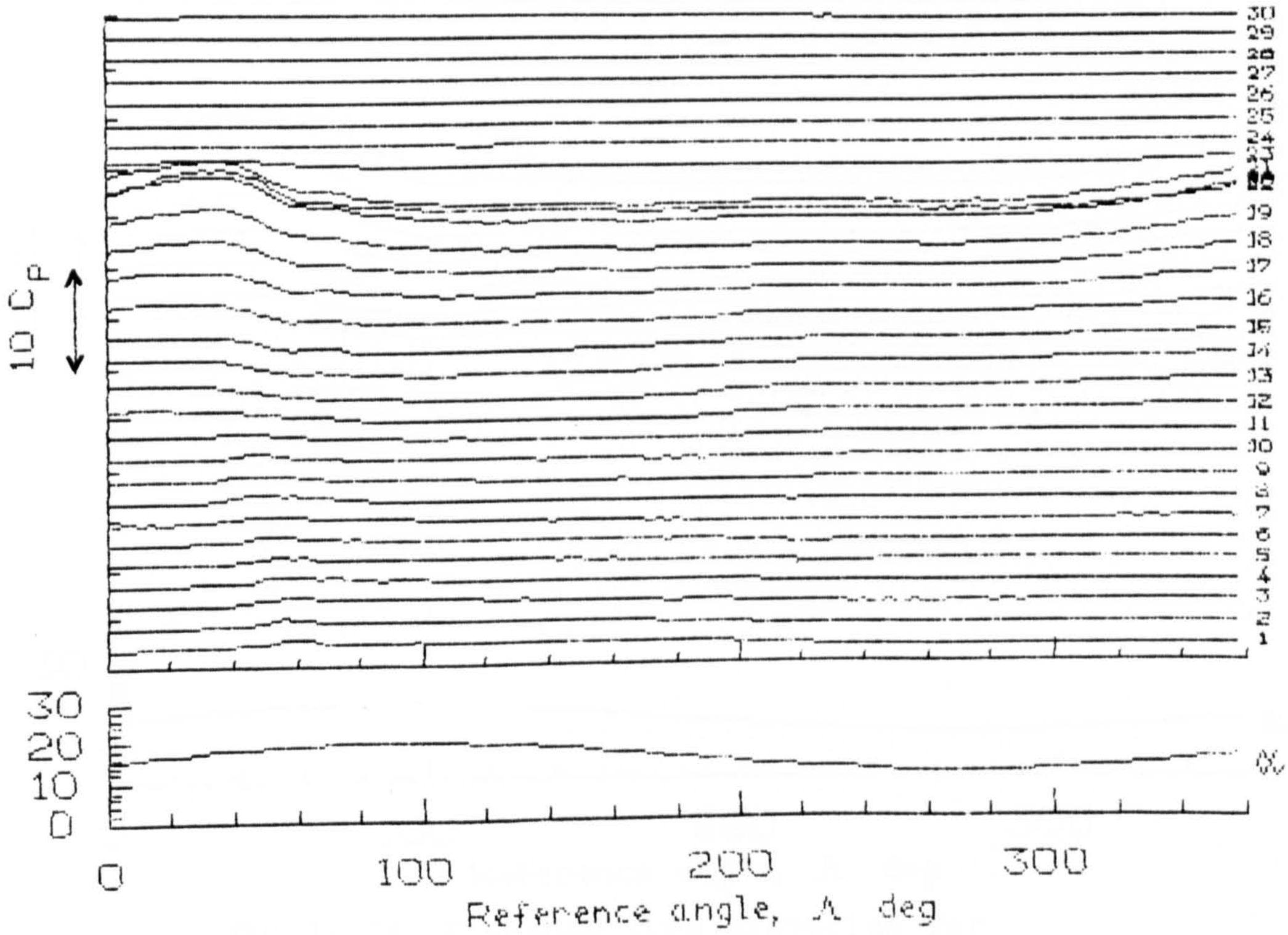

Fig 7.122 Pressure Time Histories for $\alpha = 15 + 4 \sin \omega t$; k= 0.05

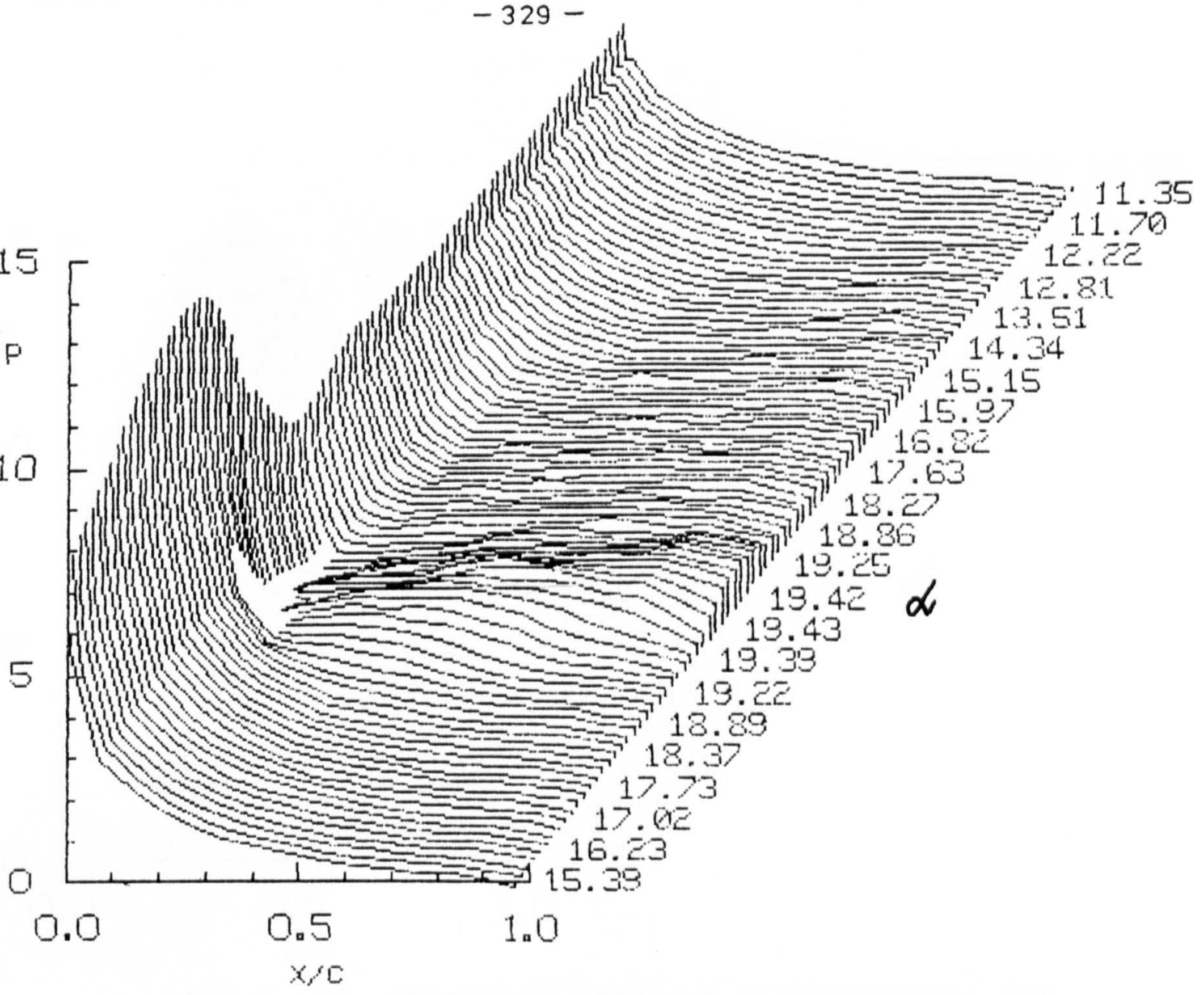

Fig 7.123 Chordwise Pressure Distributions for $\alpha = 15 + 4 \sin \omega t$; k= 0.10

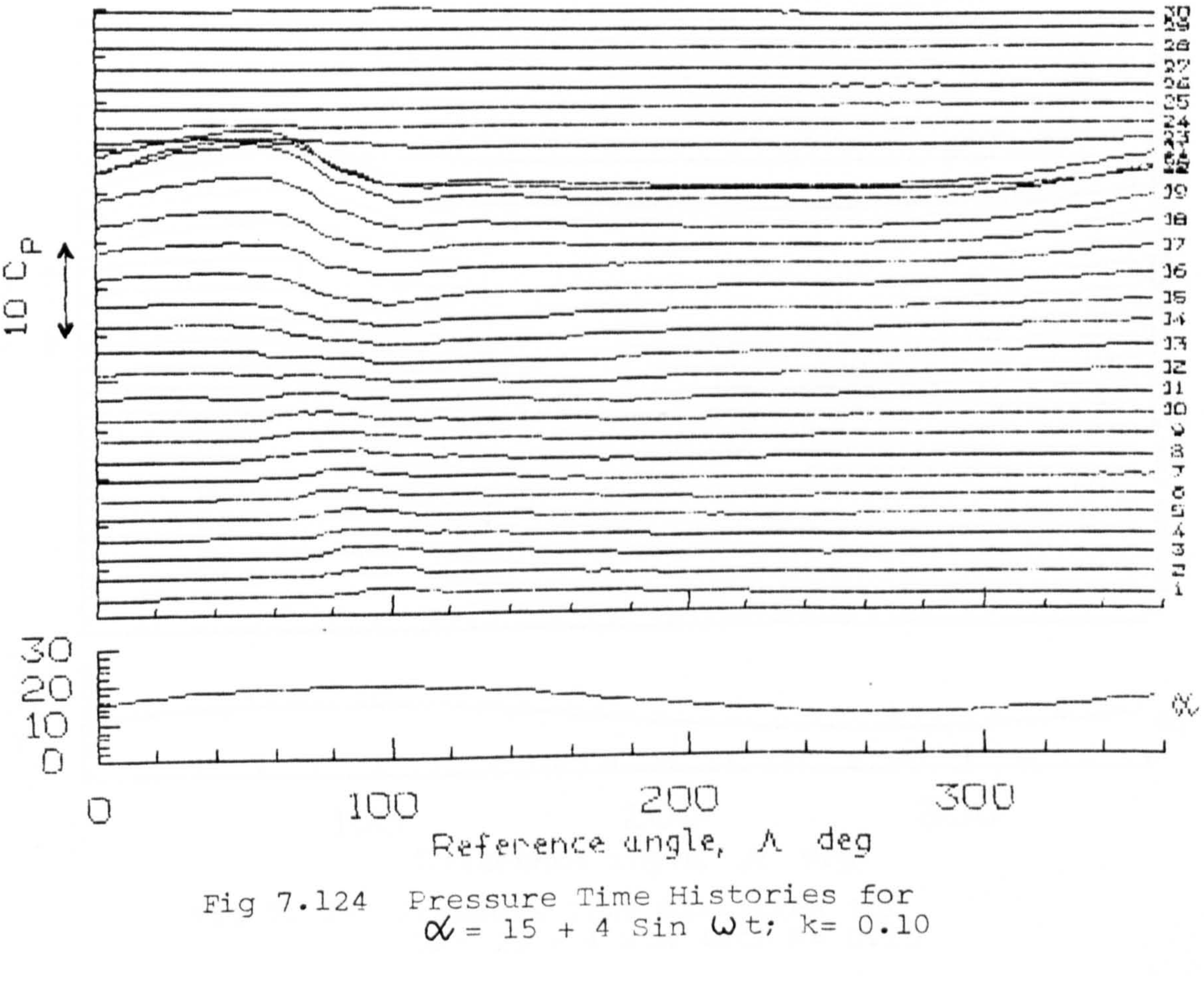

Fig 7.124 Pressure Time Histories for $\alpha = 15 + 4 \sin \omega t$; k= 0.10

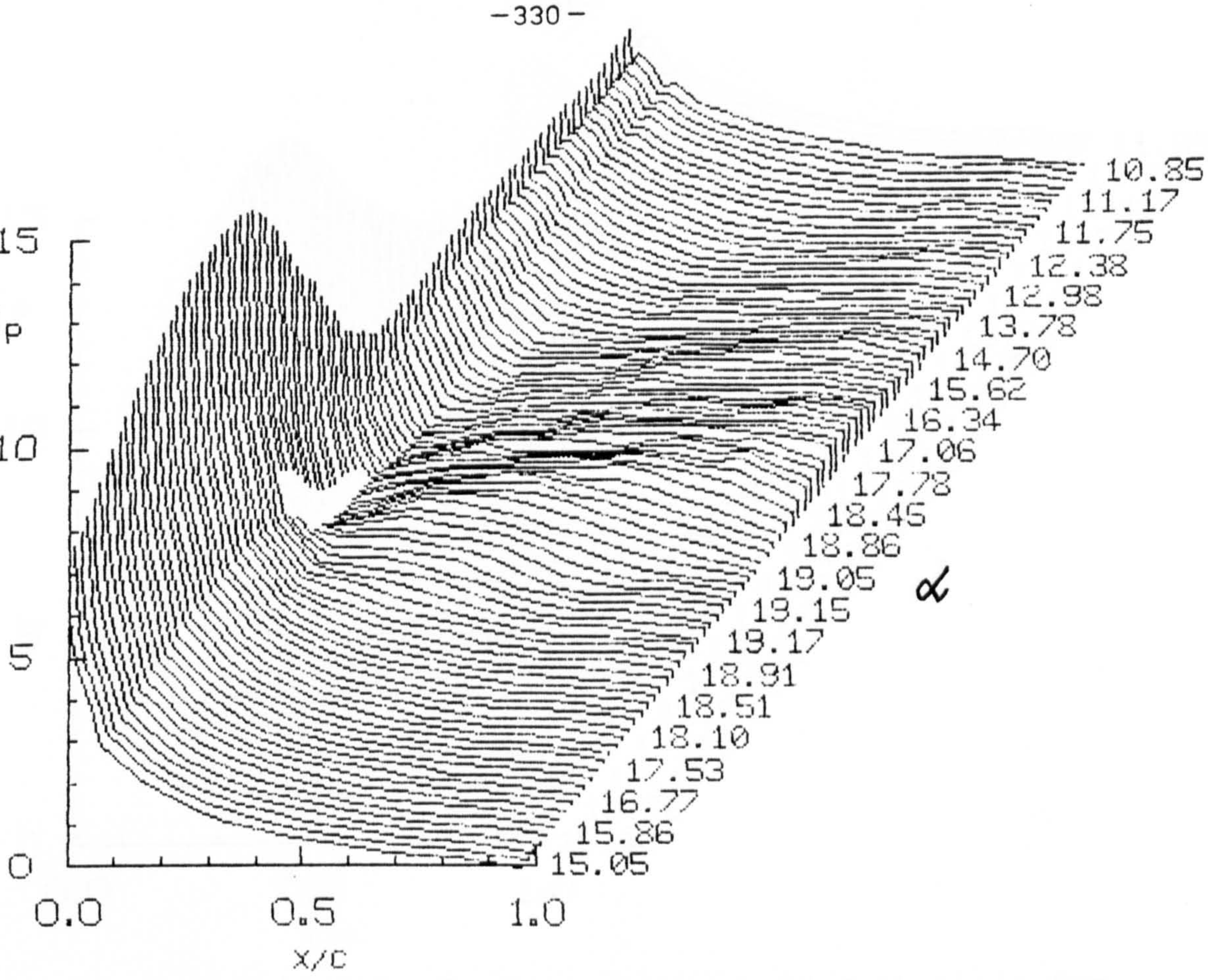

Fig 7.125 Chordwise Pressure Distributions for $\alpha = 15 + 4 \sin \omega t$; k= 0.15

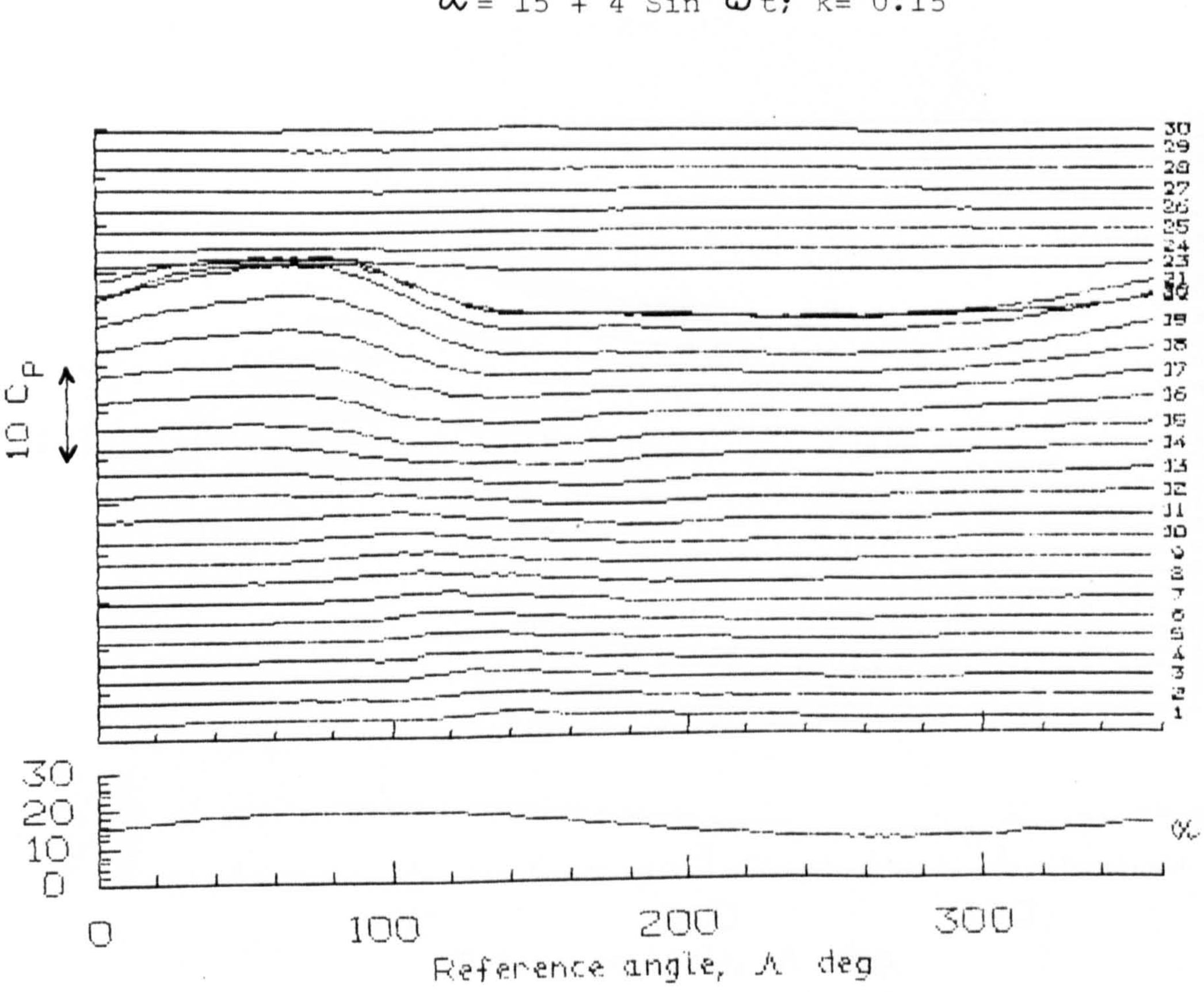

Fig 7.126 Pressure Time Histories for $\alpha = 15 + 4 \sin \omega t$; k= 0.15

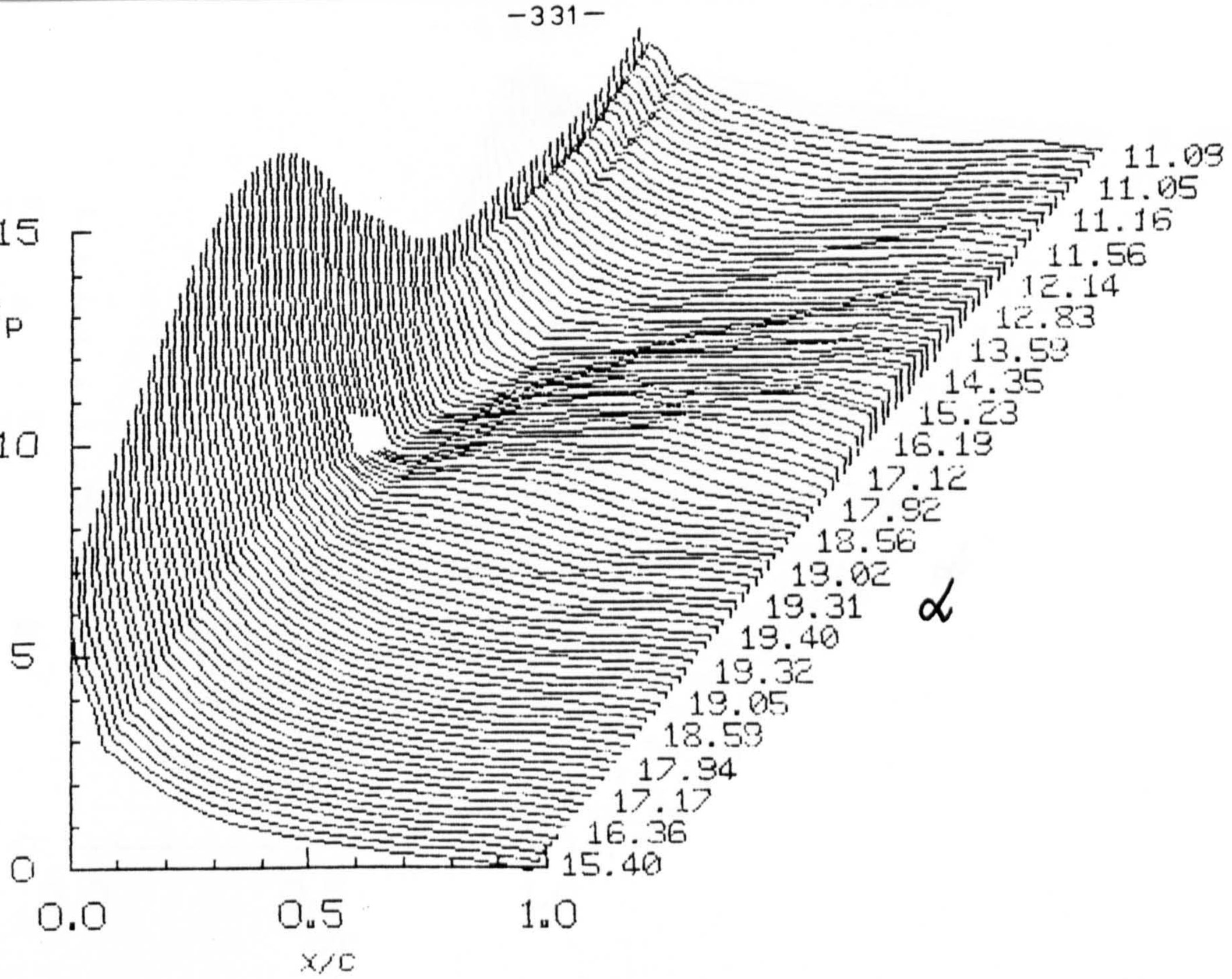

Fig 7.127 Chordwise Pressure Distributions for $\alpha = 15 + 4 \sin \omega t$; k= 0.20

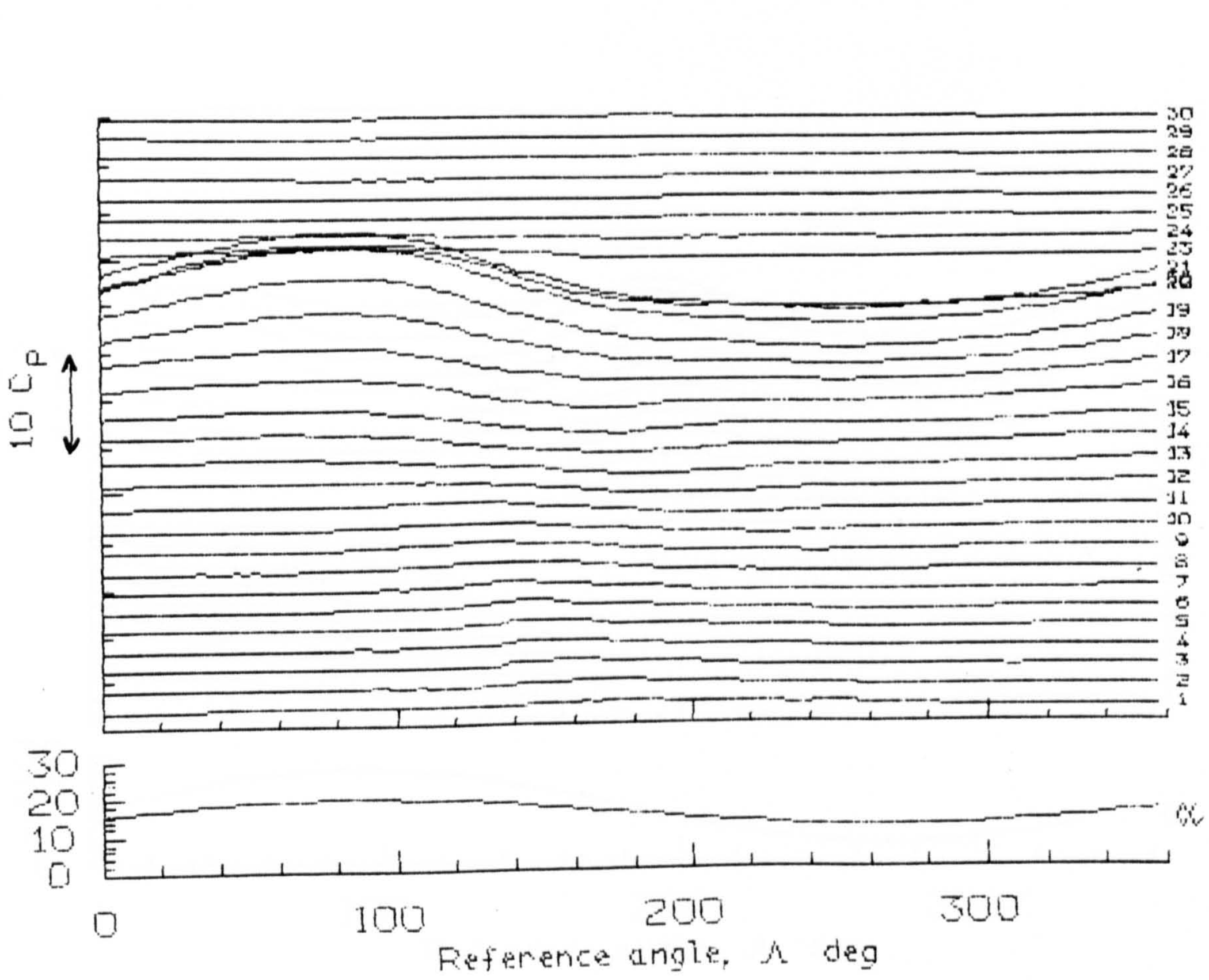

Fig 7.128 Pressure Time Histories for $\alpha = 15 + 4 \sin \omega t$; k= 0.20

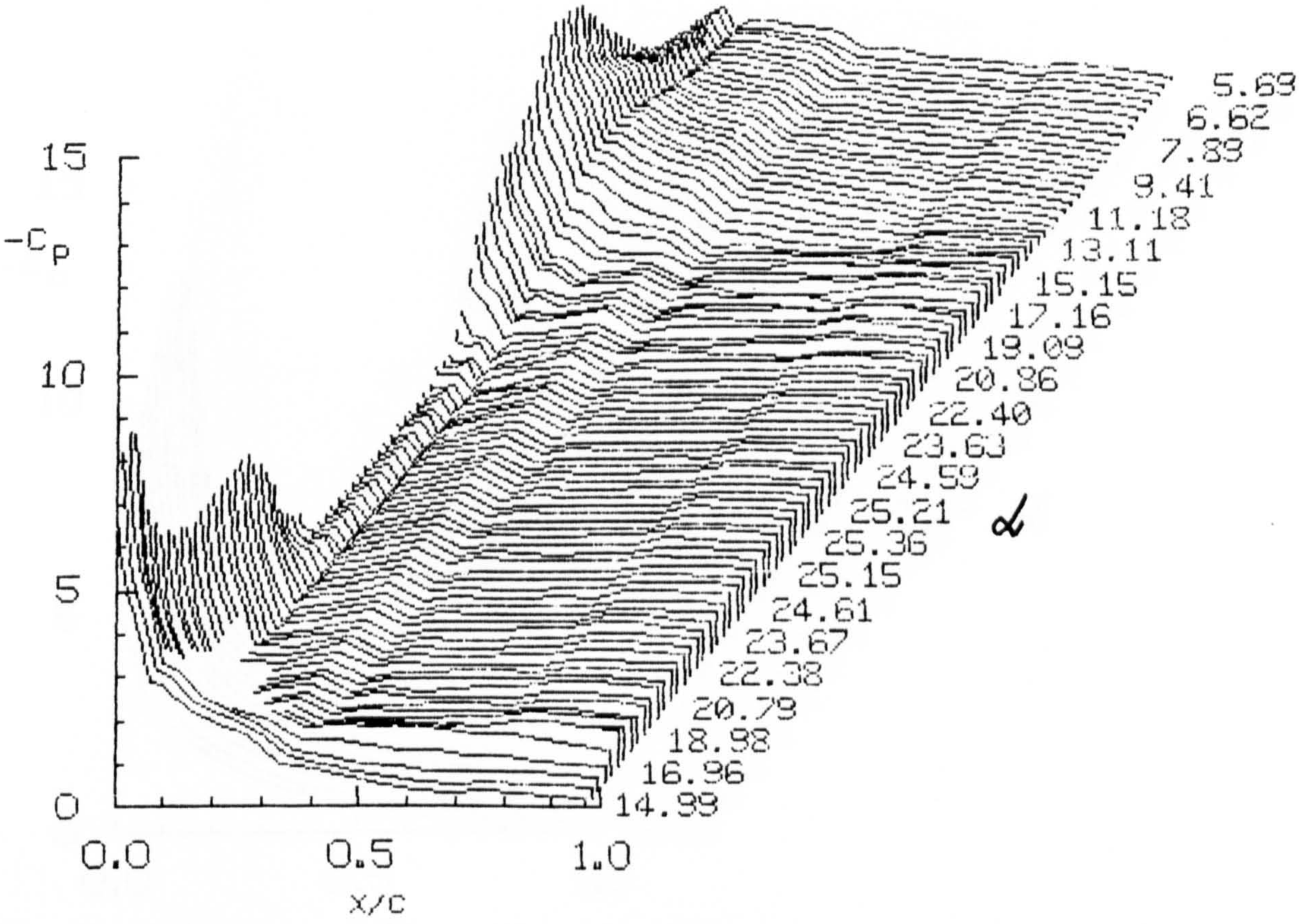

Fig 7.129 Chordwise Pressure Distributions for $\alpha = 15 + 10 \sin \omega t$; k= 0.01

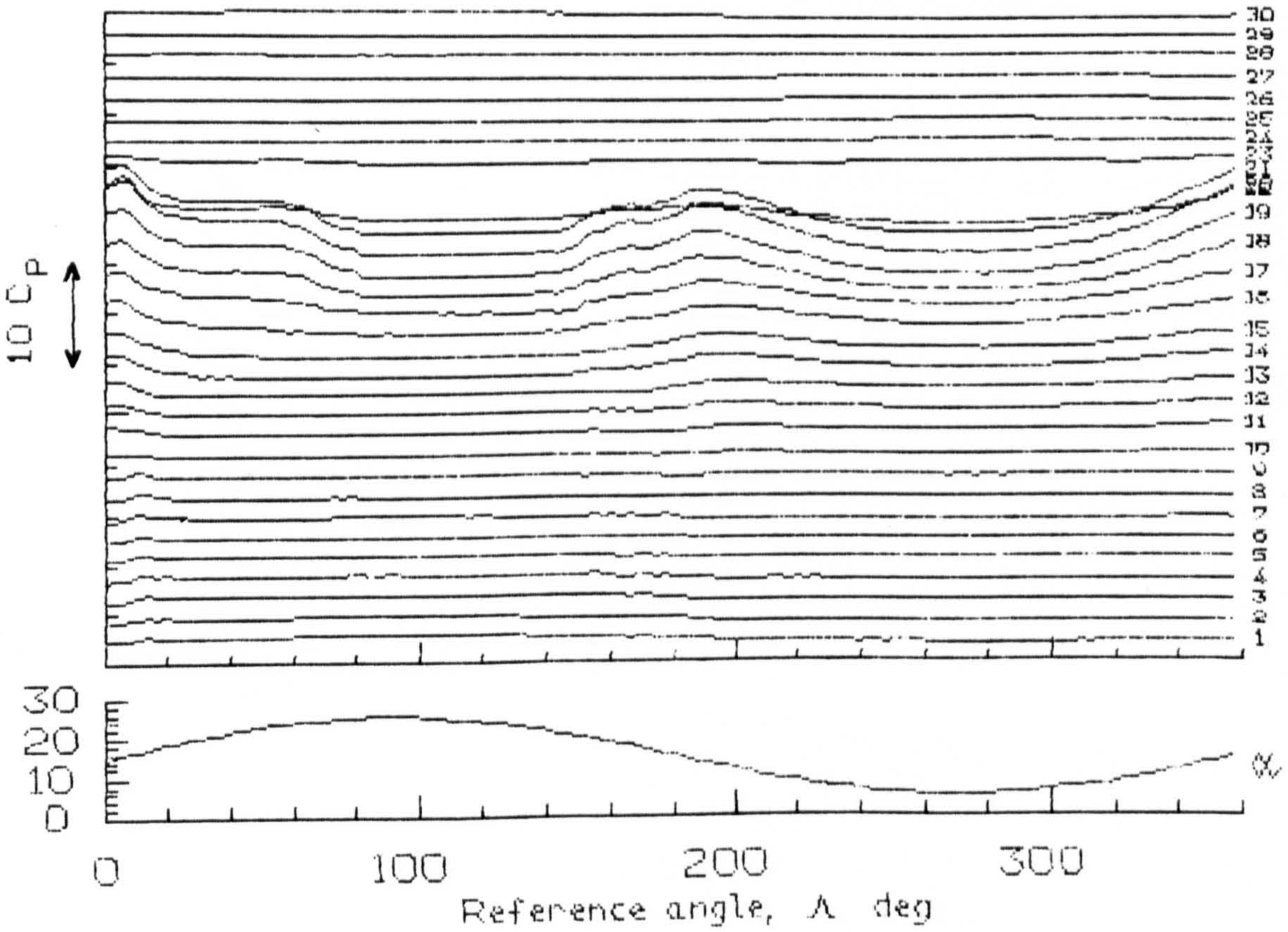

Fig 7.130 Pressure Time Histories for $\alpha = 15 + 10 \sin \omega t$; k= 0.01

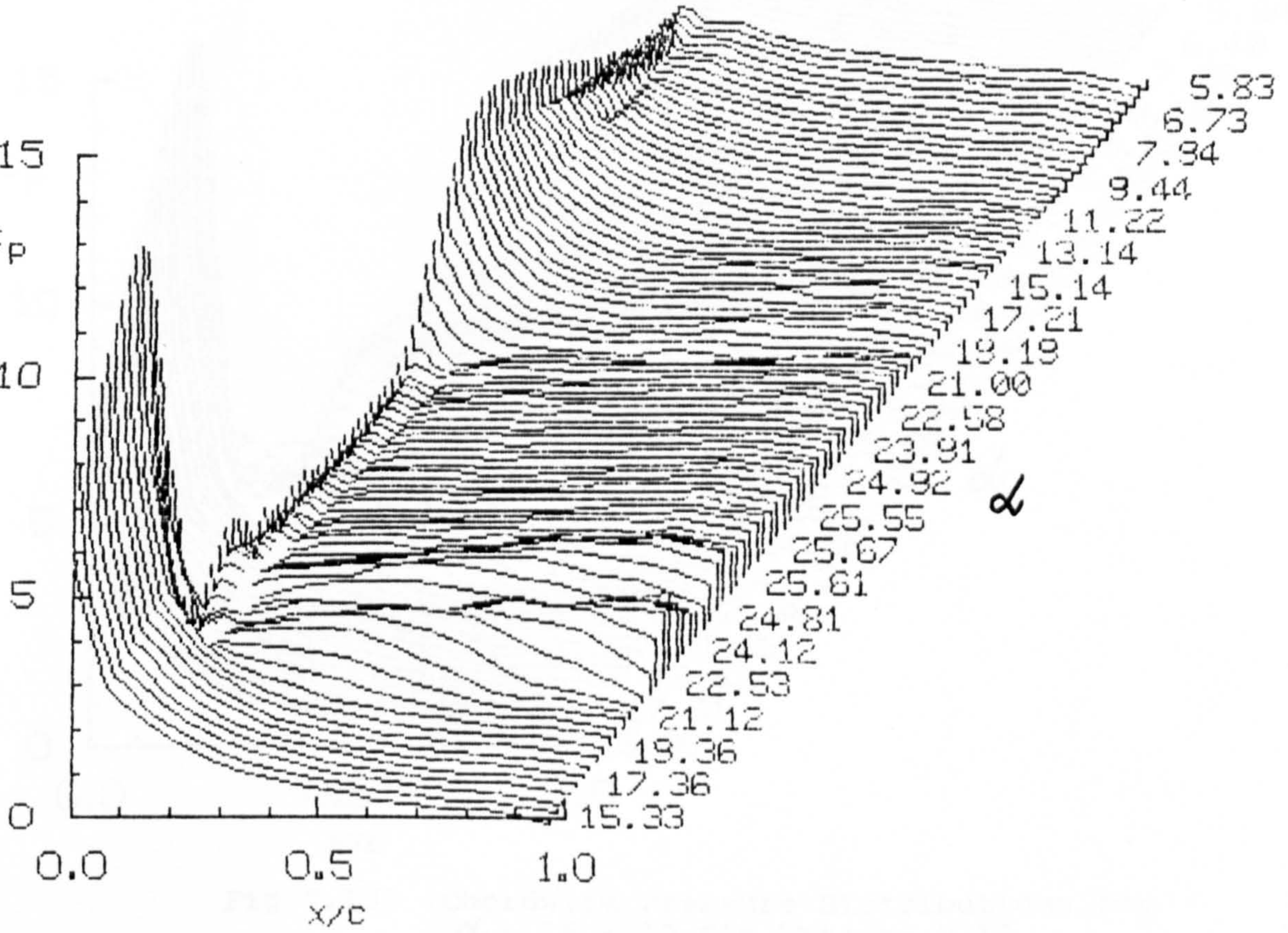

Fig 7.131 Chordwise Pressure Distributions for $\alpha = 15 + 10 \sin \omega t$; k= 0.05

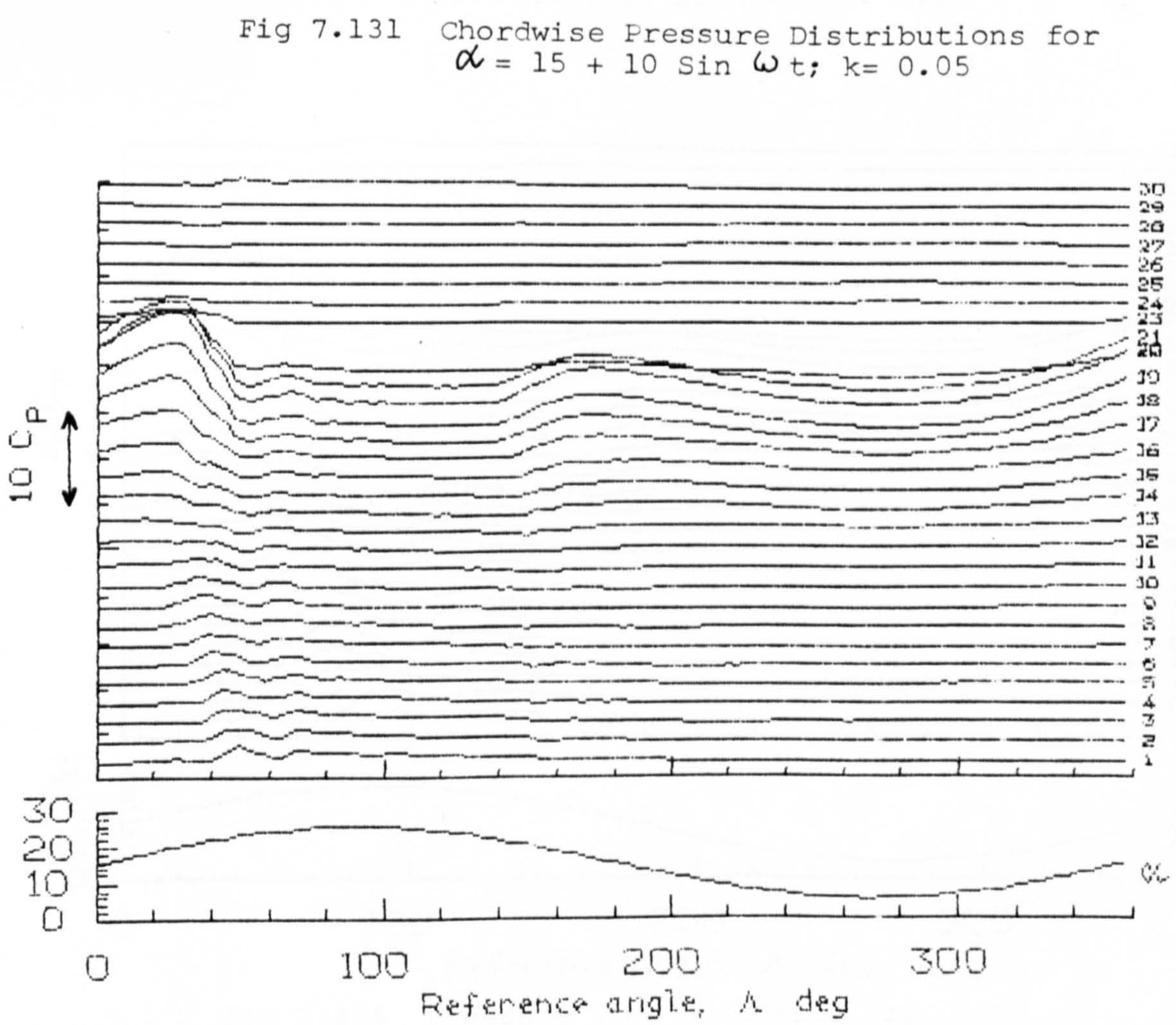

Fig 7.132 Pressure Time Histories for $\alpha = 15 + 10 \sin \omega t$; k= 0.05

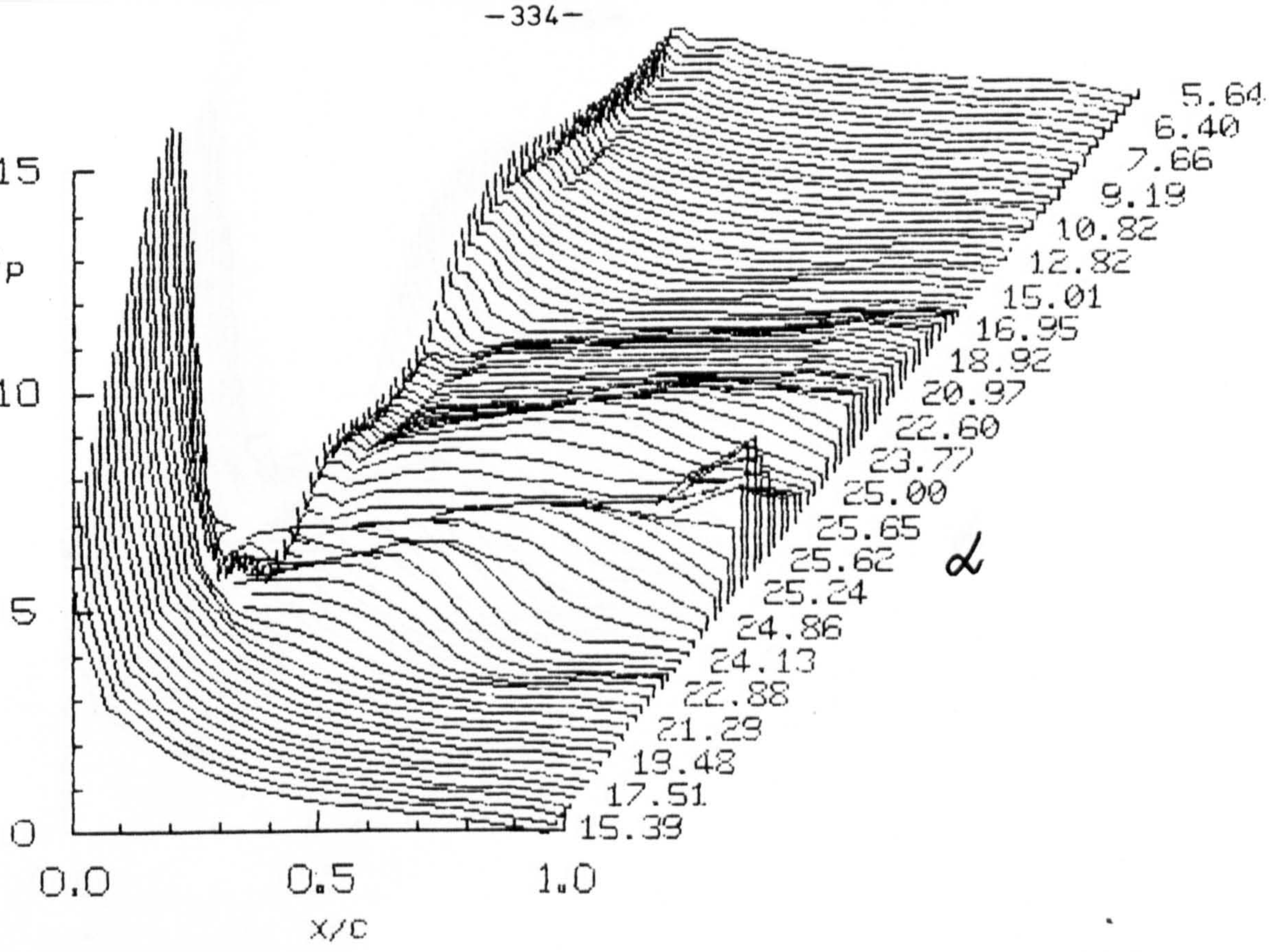

Fig 7.133 Chordwise Pressure Distributions for $\alpha = 15 + 10 \sin \omega t$; k= 0.10

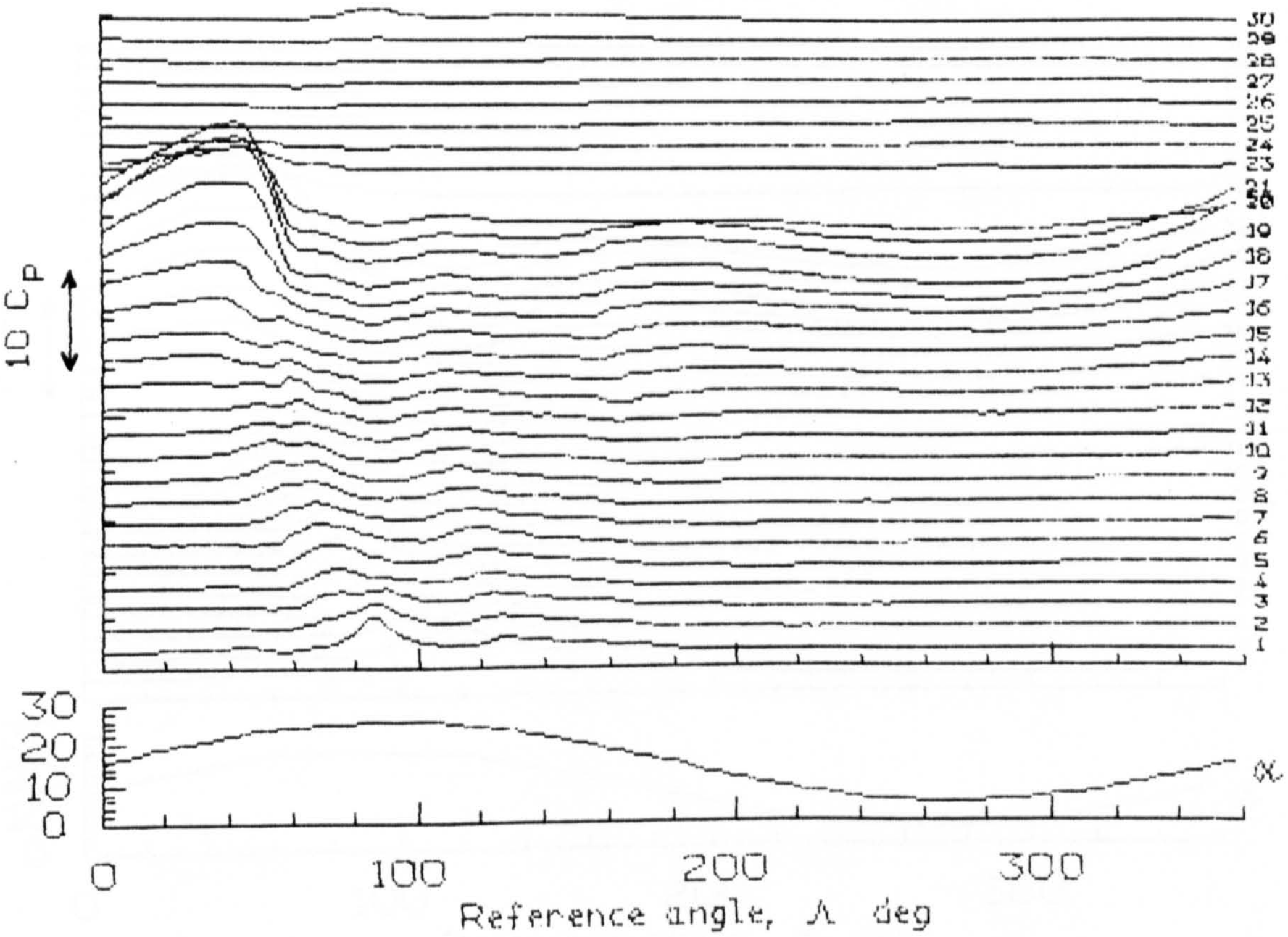

Fig 7.134 Pressure Time Histories for $\alpha = 15 + 10 \sin \omega t$; k= 0.10

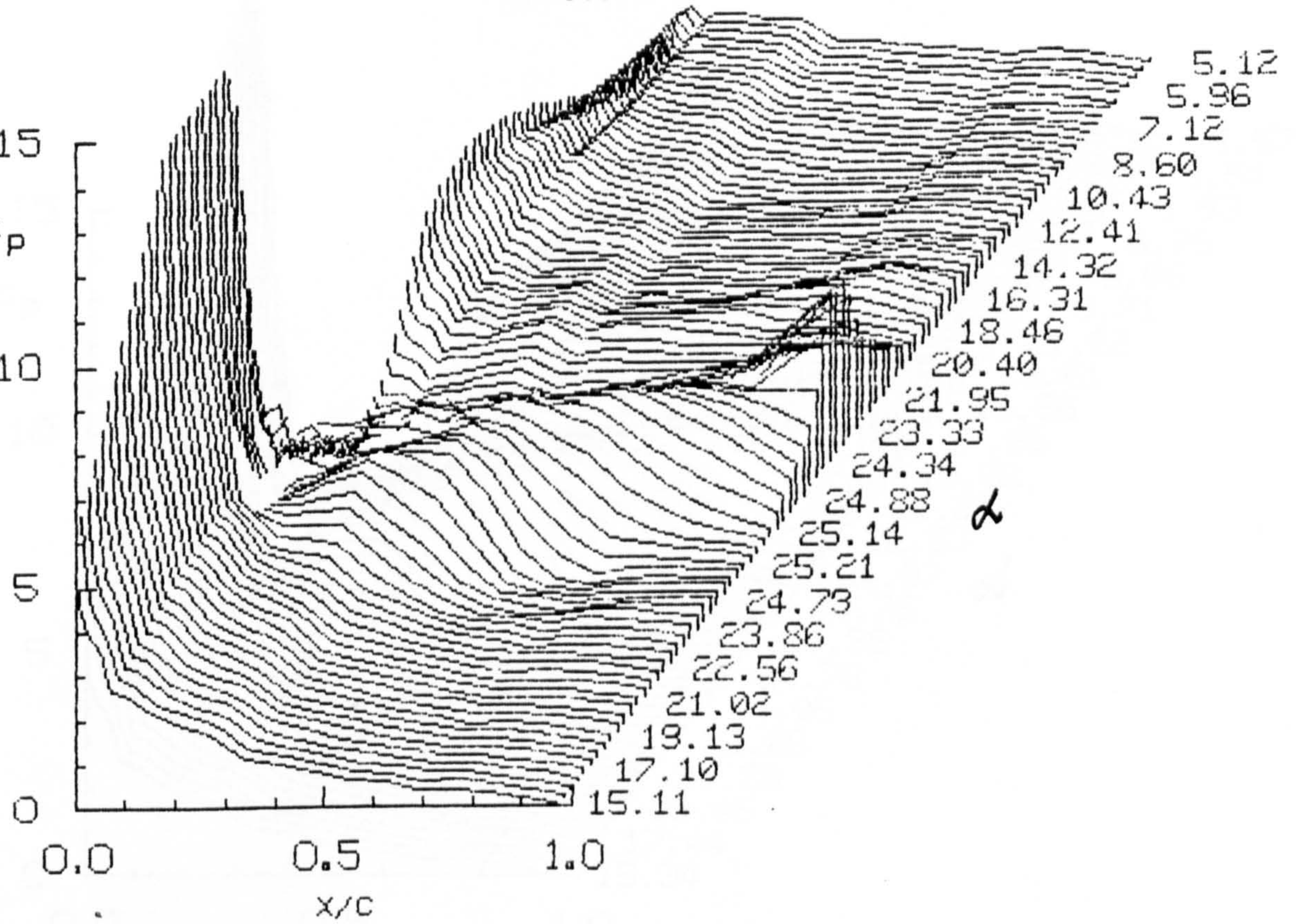

Fig 7.135 Chordwise Pressure Distributions for $\alpha = 15 + 10 \sin \omega t$; k= 15

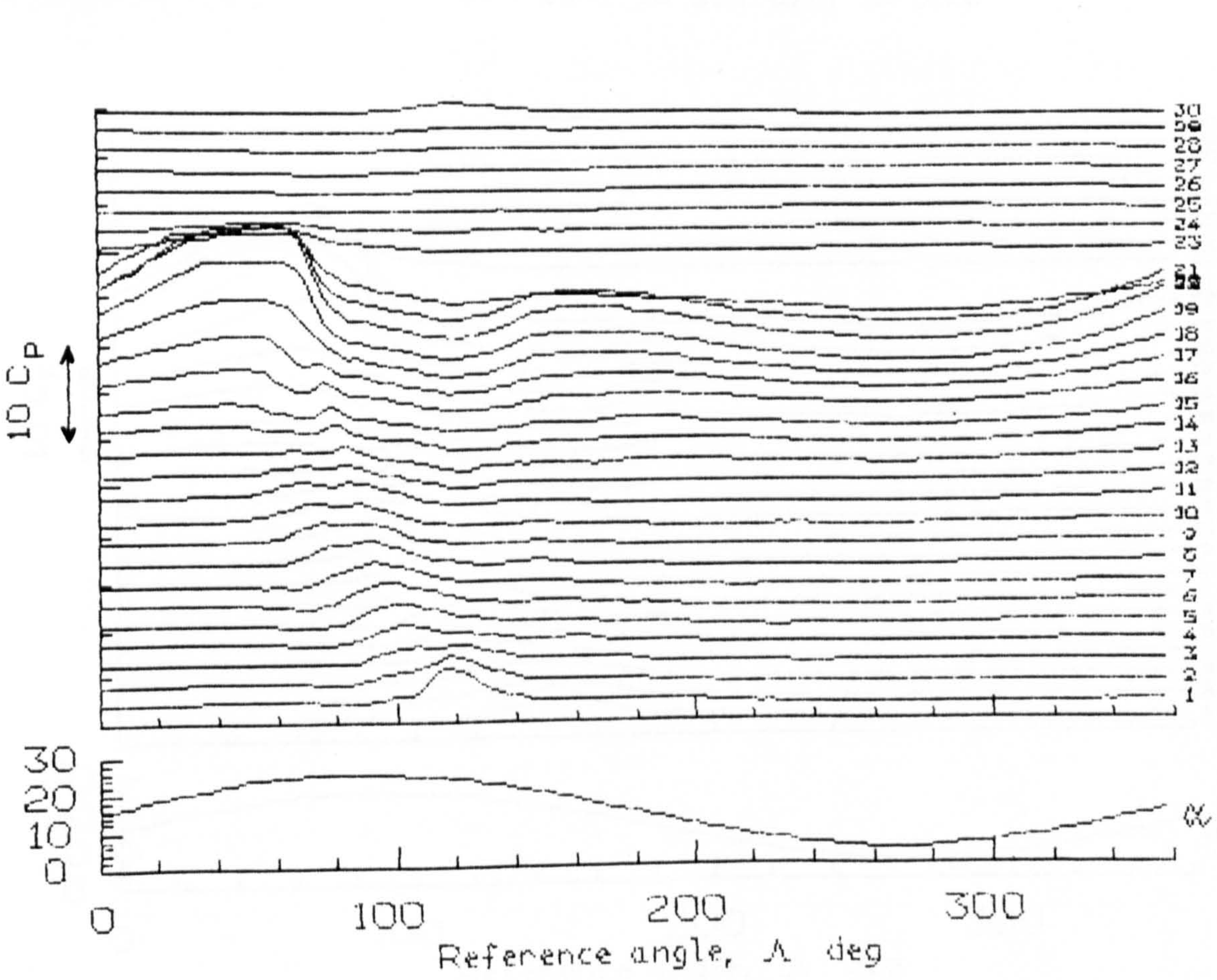

Fig 7.136 Pressure Time Histories for $\alpha = 15 + 10 \sin \omega t$; k= 0.15

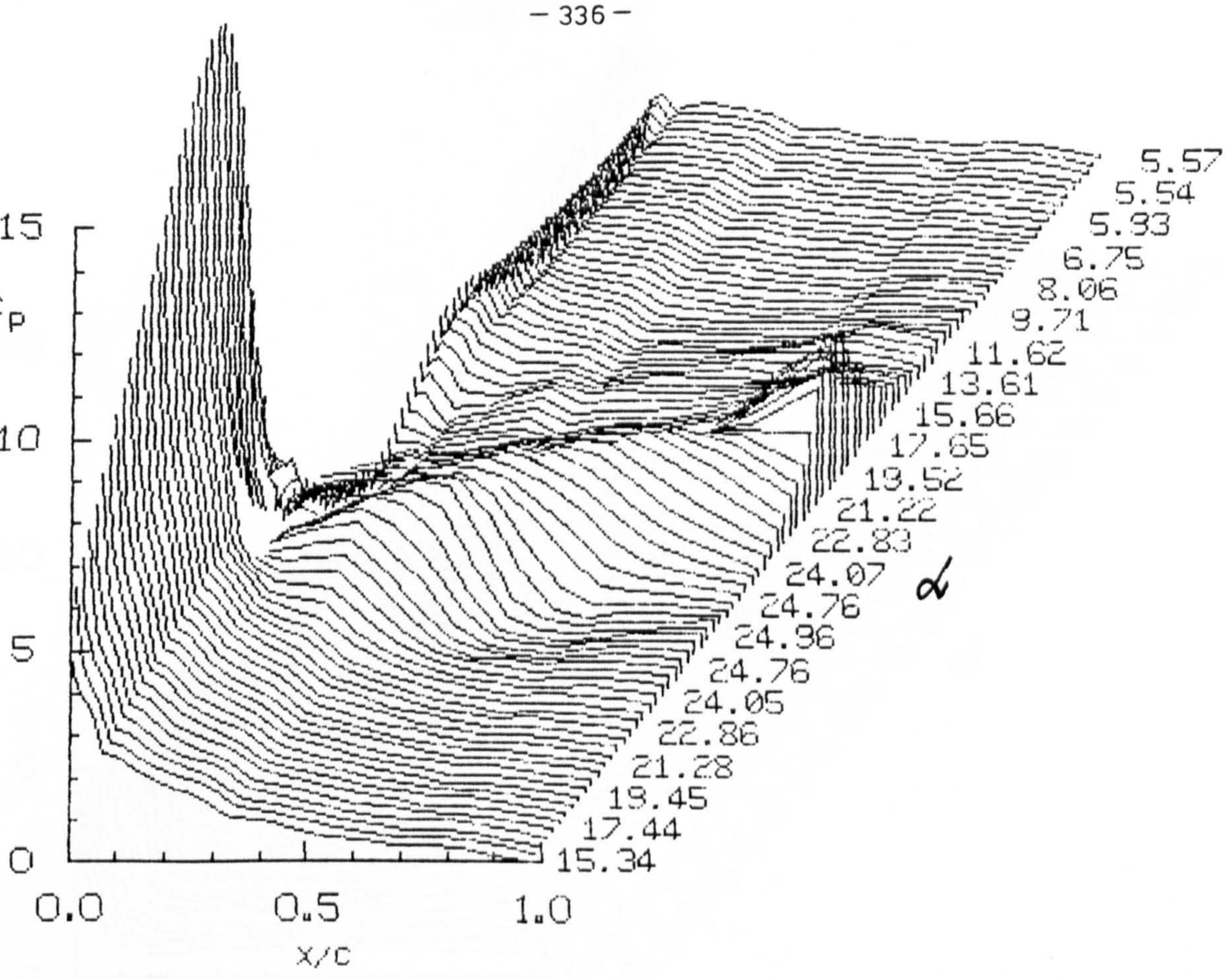

Fig 7.137 Chordwise Pressure Distributions for $\alpha = 15 + 10 \sin \omega t$; k= 0.20

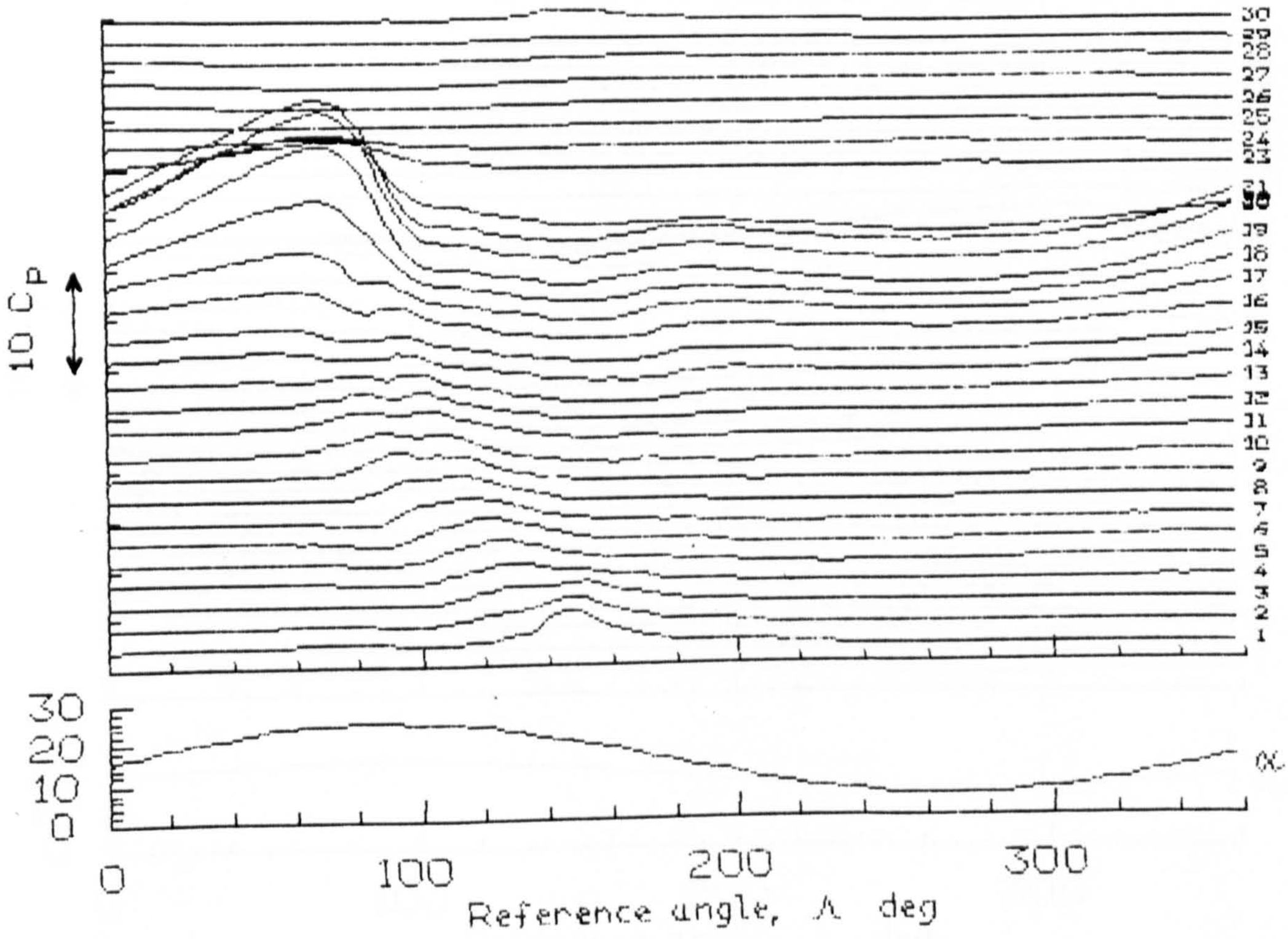

Fig 7.138 Pressure Time Histories for $\alpha = 15 + 10 \sin \omega t$; k= 0.20

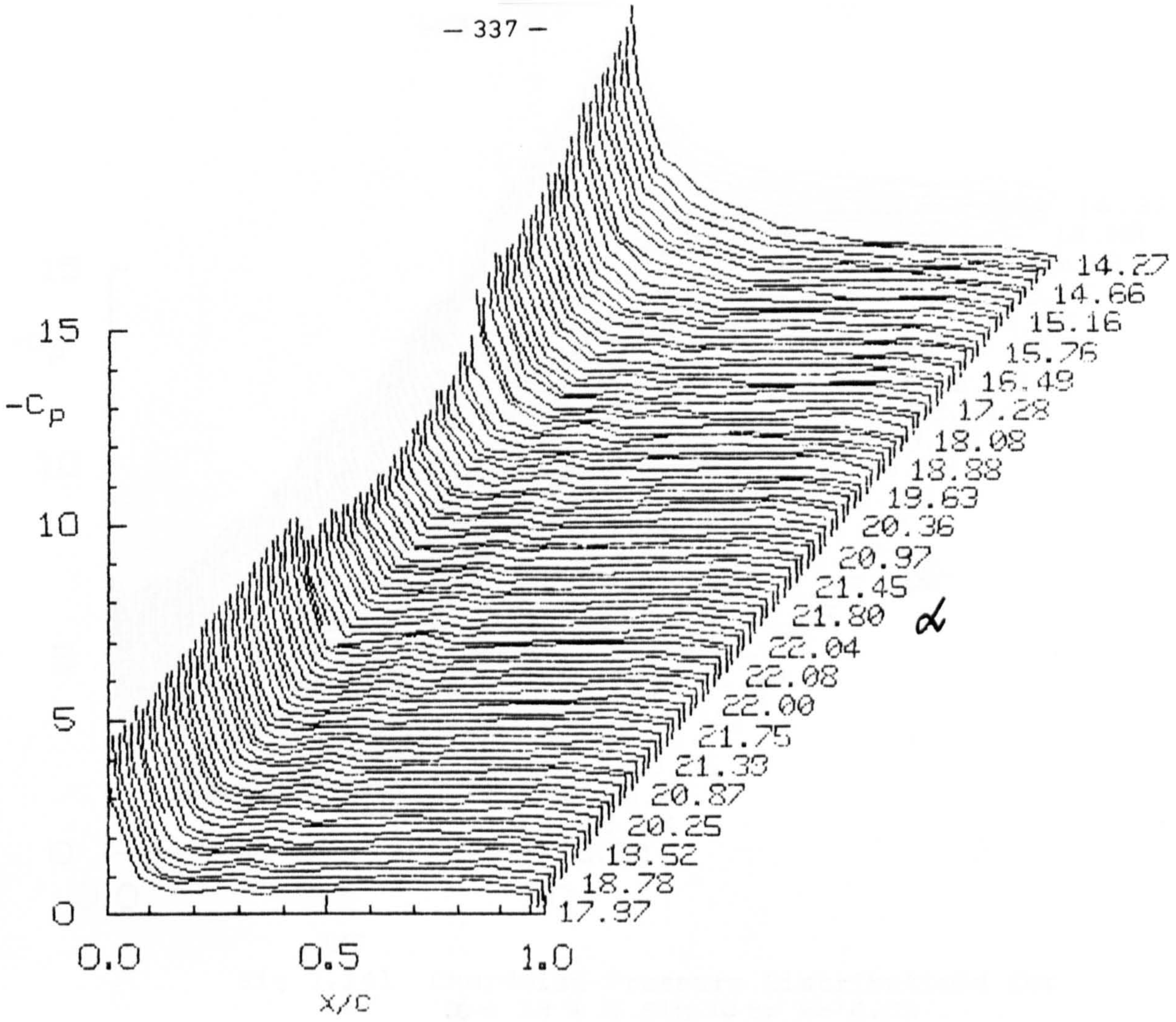

Fig 7.139 Chordwise Pressure Distributions for $\alpha = 18 + 4 \sin \omega t$; k= 0.01

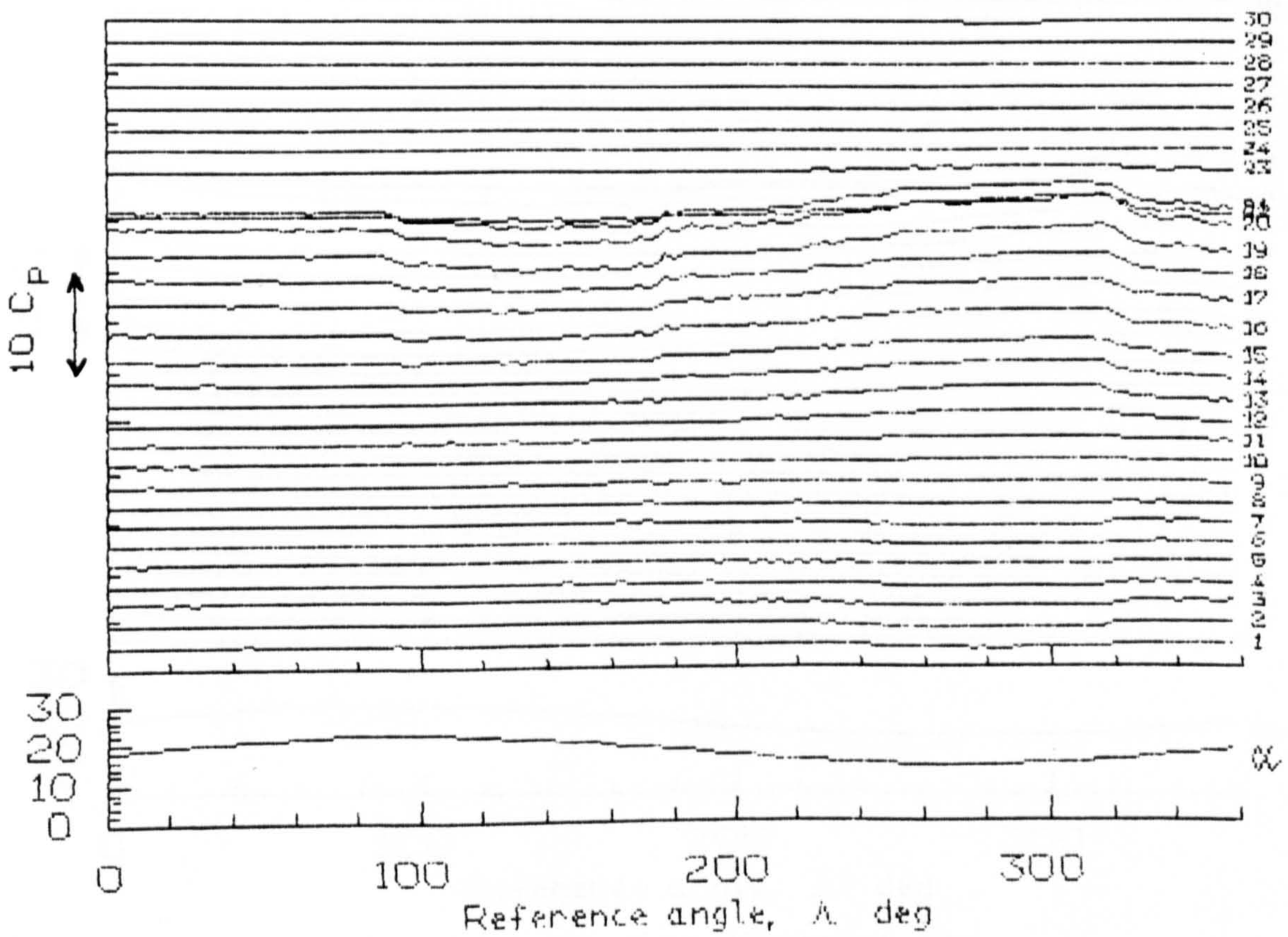

Fig 7.140 Pressure Time Histories for $\alpha = 18 + 4 \sin \omega t$; k= 0.01

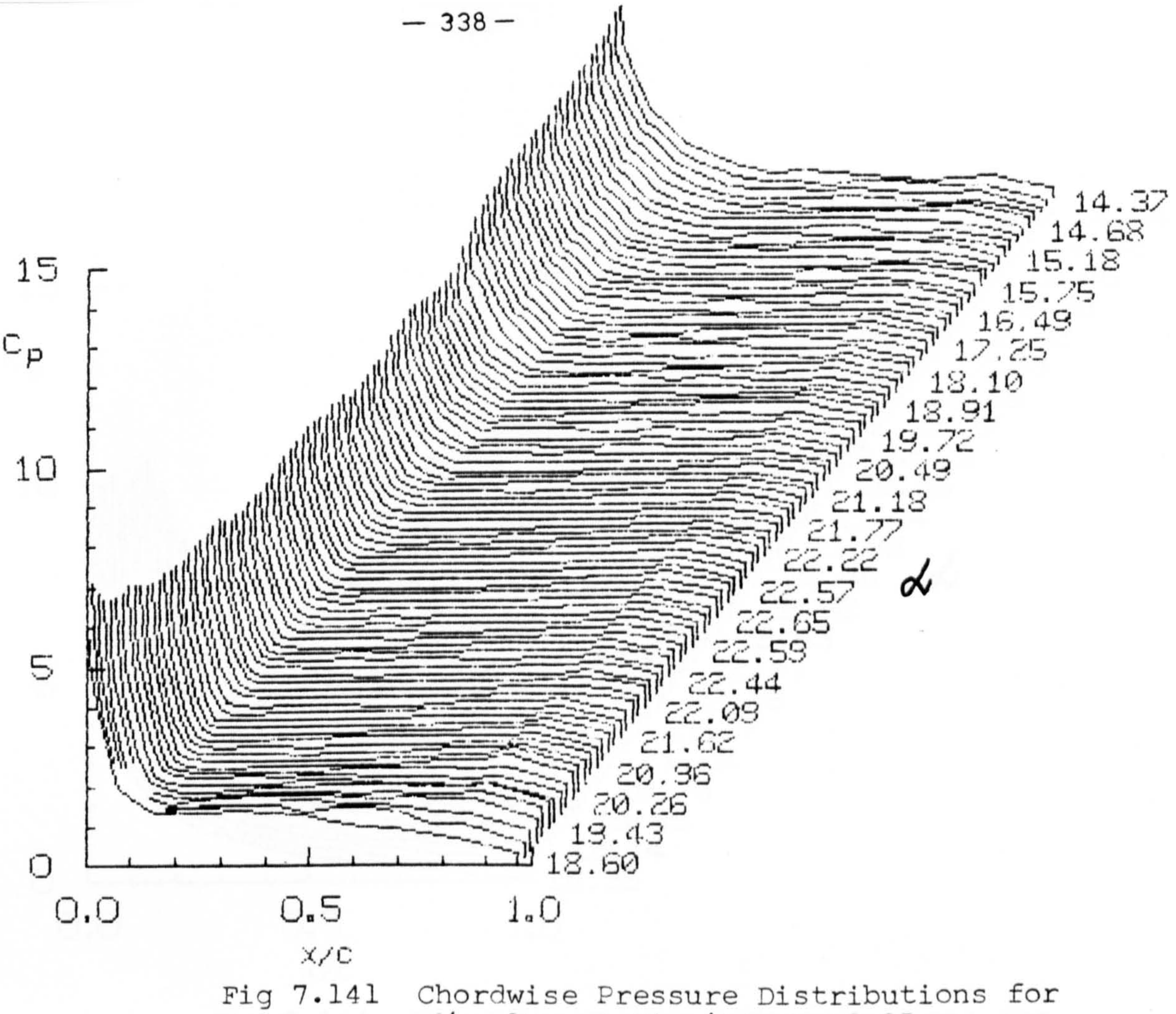

Fig 7.141 Chordwise Pressure Distributions for $\alpha = 18 + 4 \sin \omega t$; k= 0.05

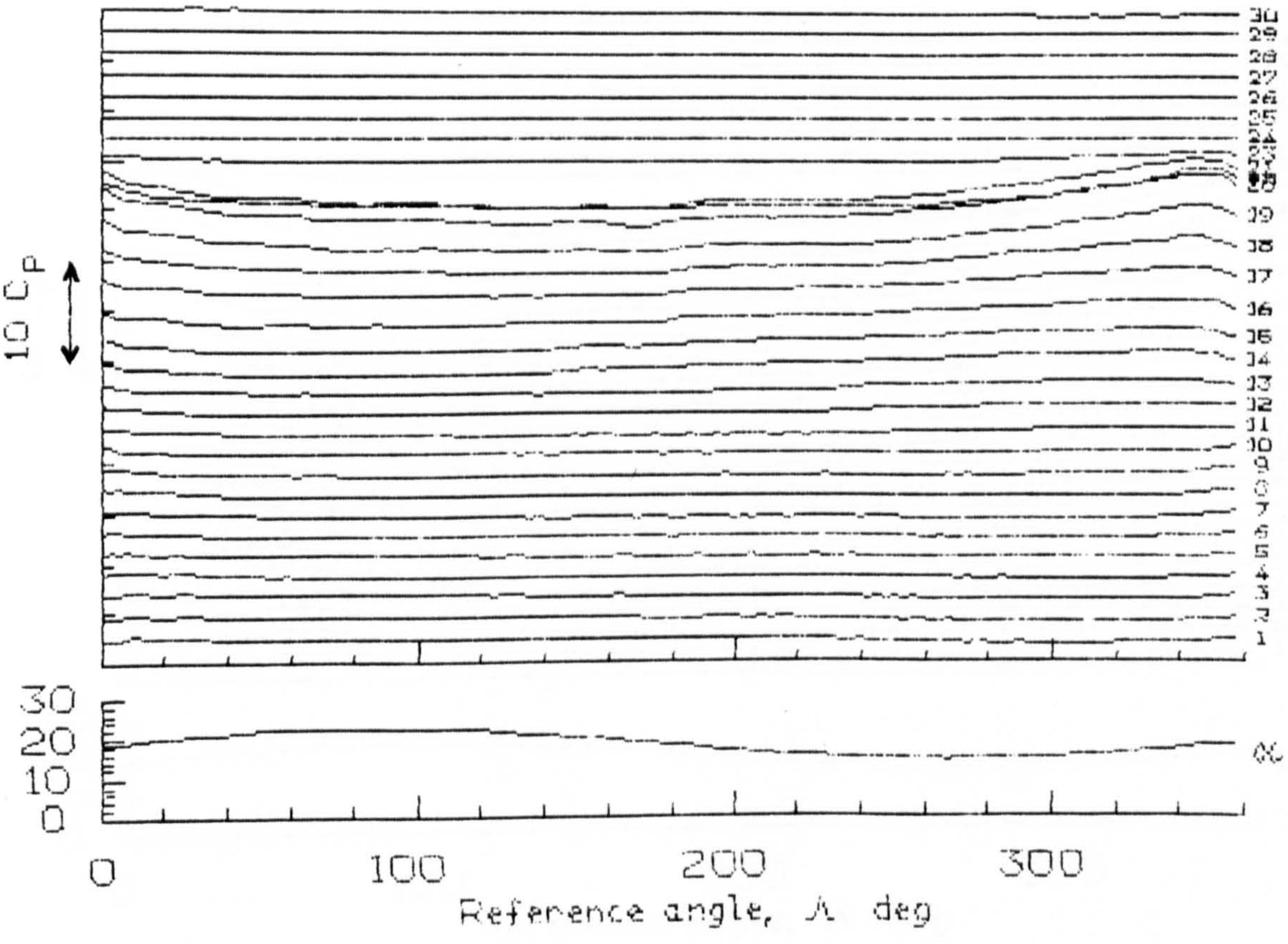

Fig 7.142 Pressure Time Histories for $\alpha = 18 + 4 \sin \omega t$; k= 0.05

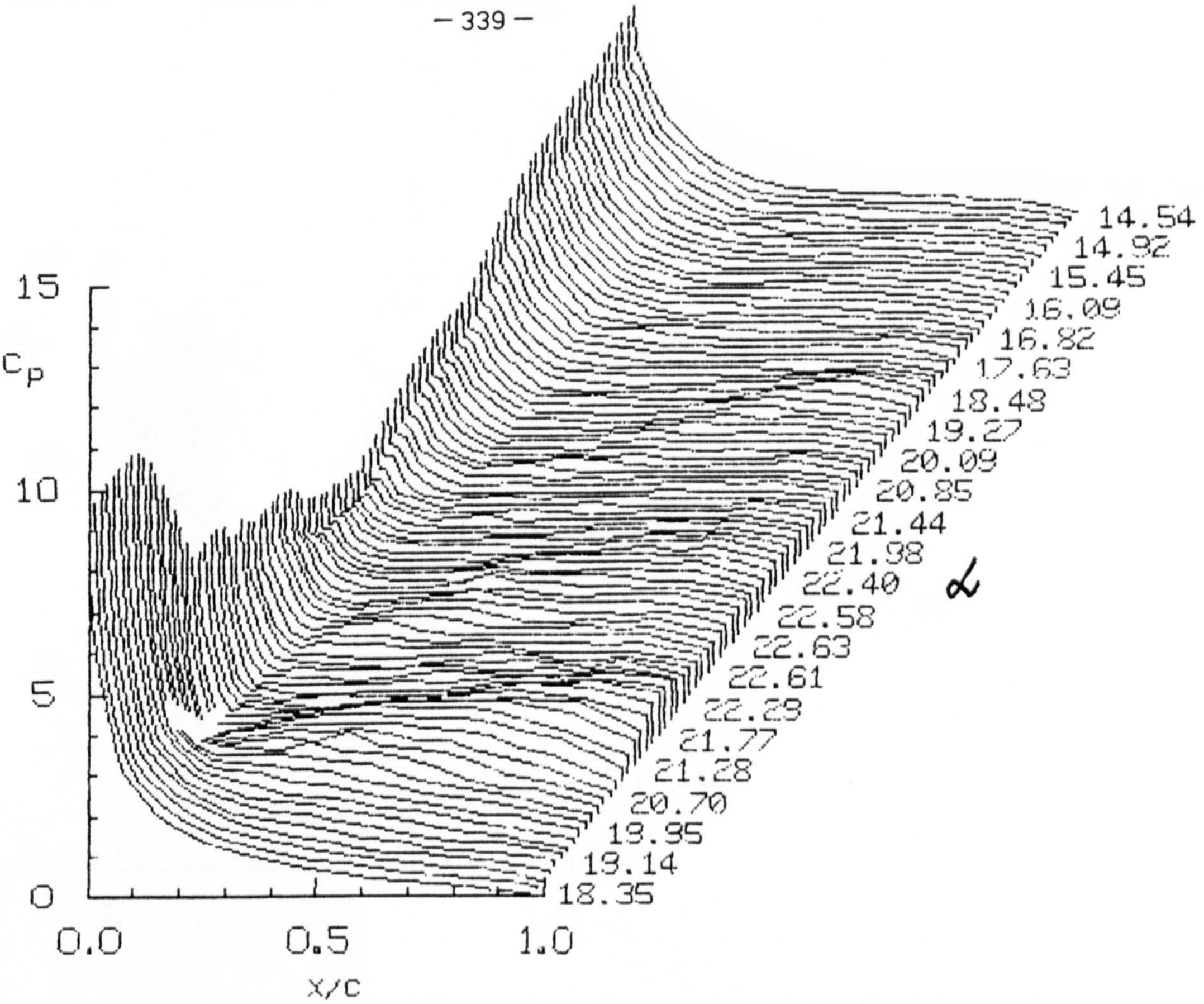

Fig 7.143 Chordwise Pressure Distributions for
$\alpha = 18 + 4 \sin \omega t$; k= 0.10

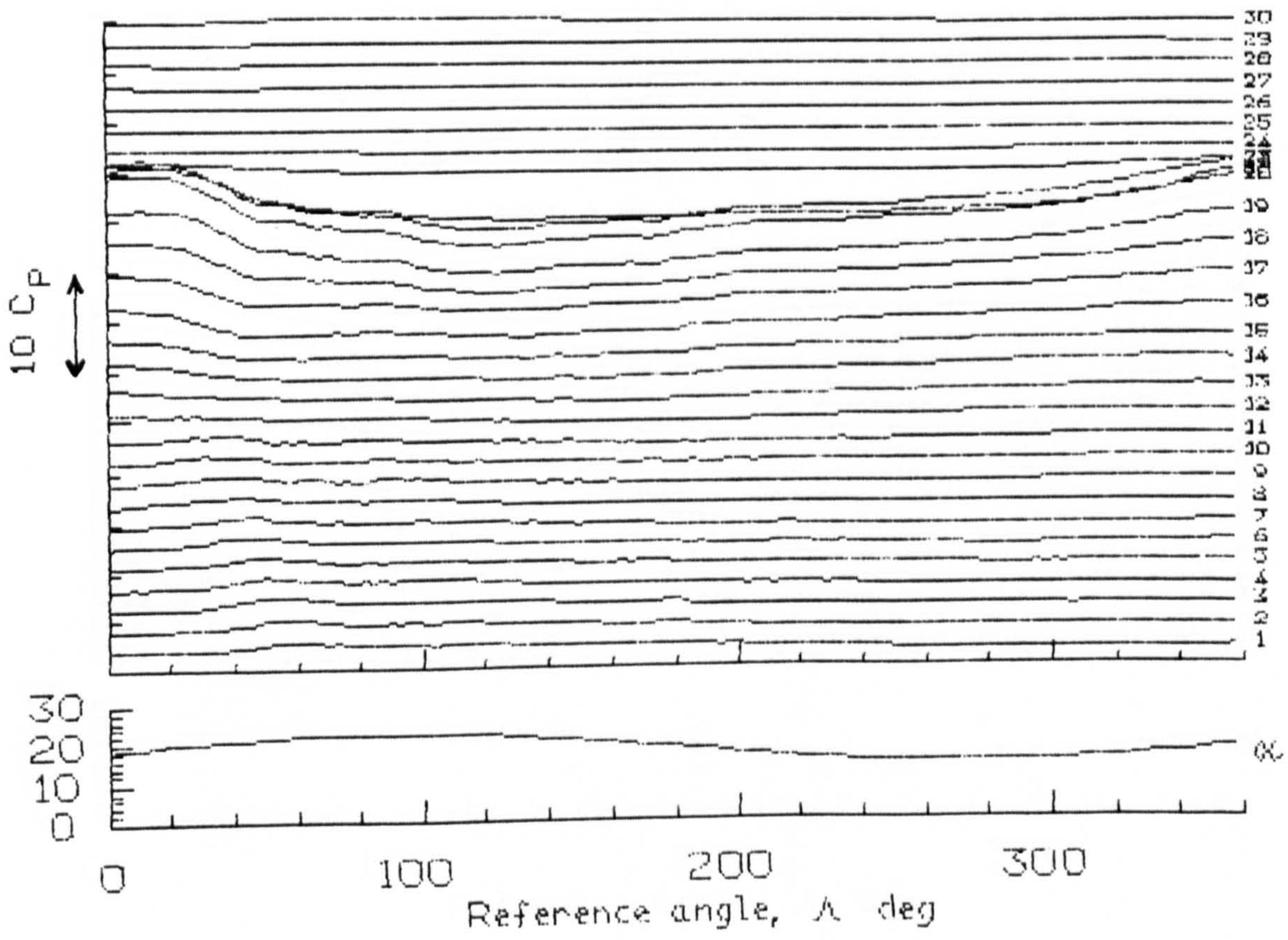

Fig 7.144 Pressure Time Histories for
$\alpha = 18 + 4 \sin \omega t$; k= 0.10

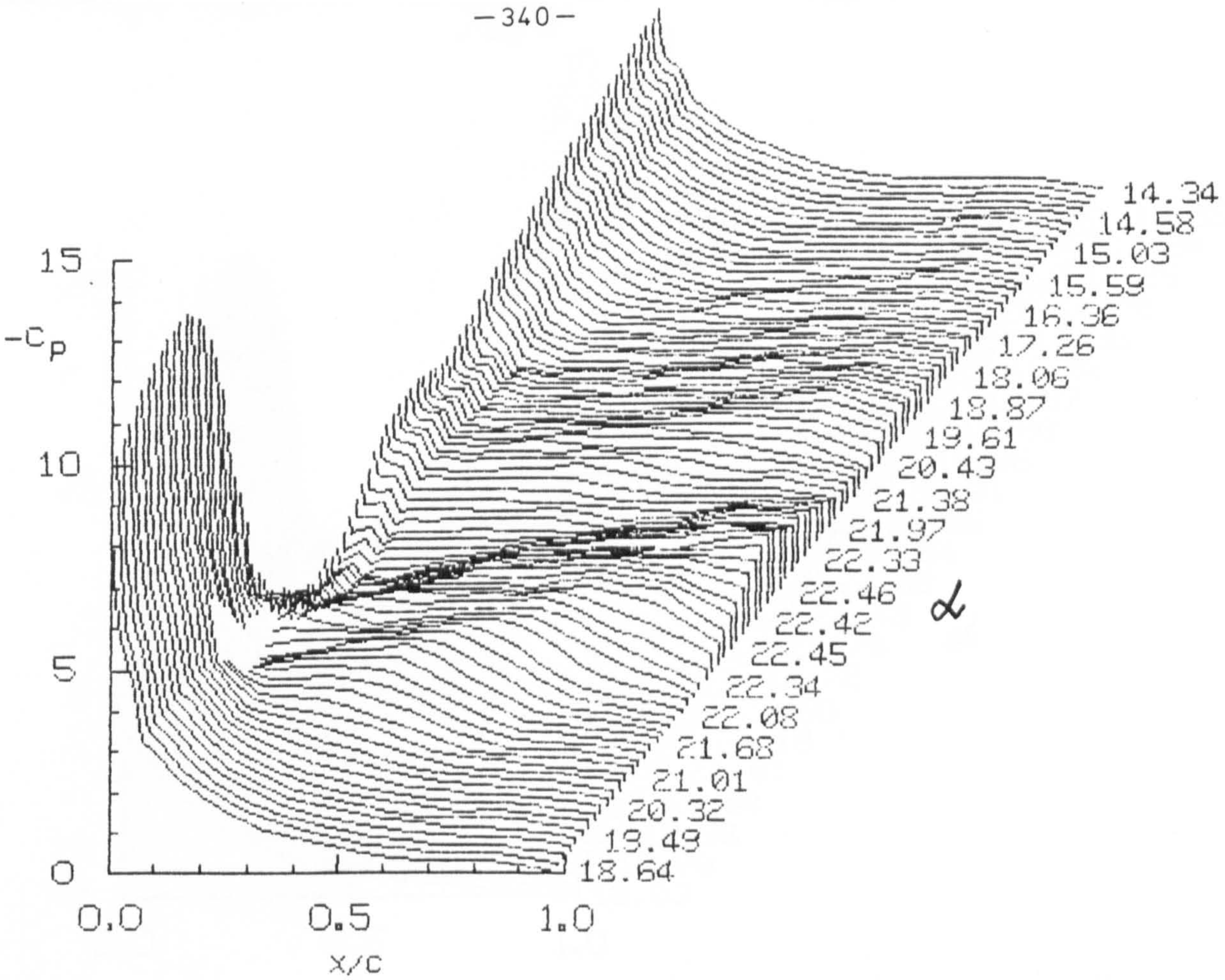

Fig 7.145 Chordwise Pressure Distributions for
$\alpha = 18 + 4 \sin \omega t$; k= 0.15

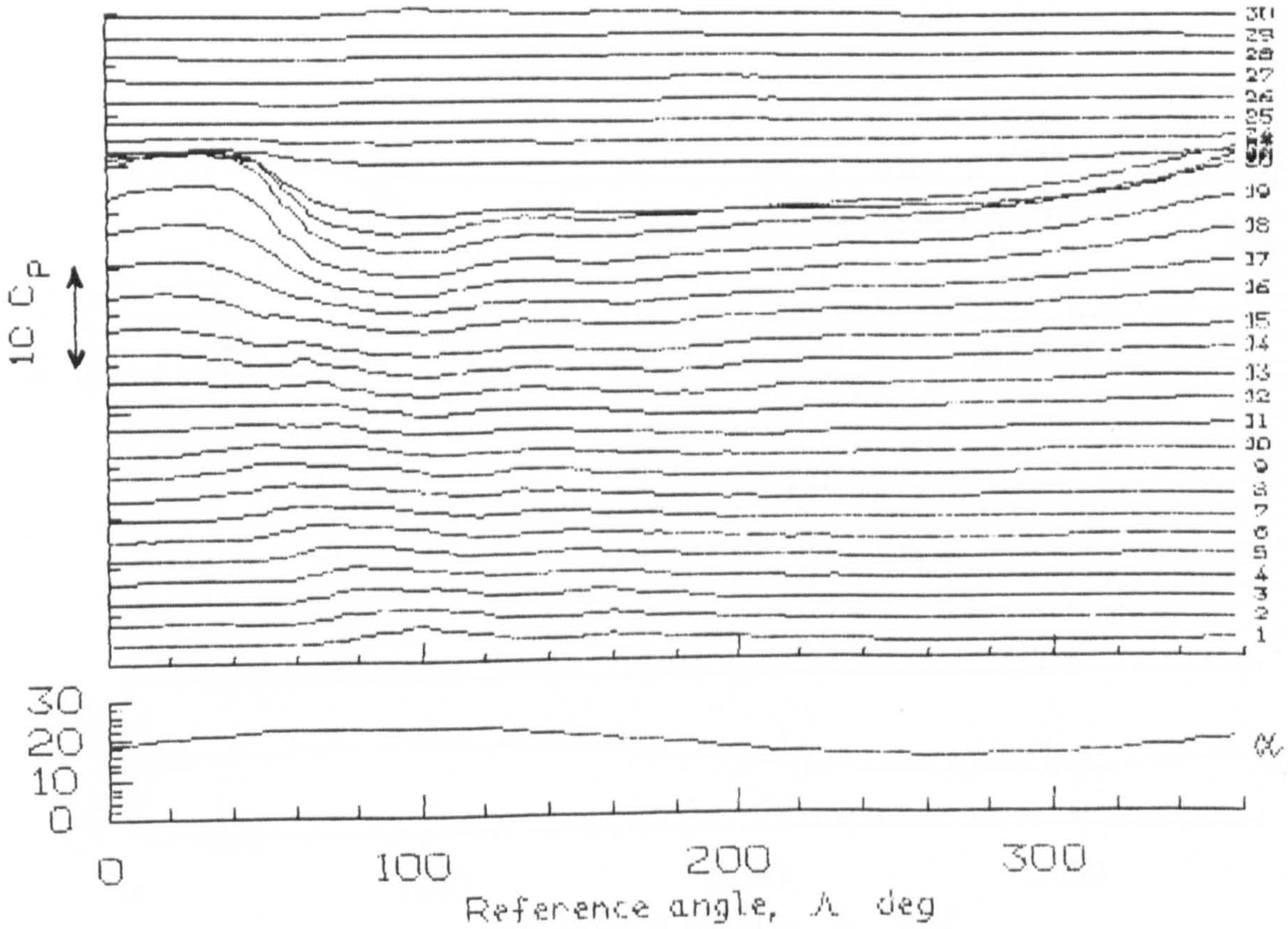

Fig 7.146 Pressure Time Histories for
$\alpha = 18 + 4 \sin \omega t$; k= 0.15

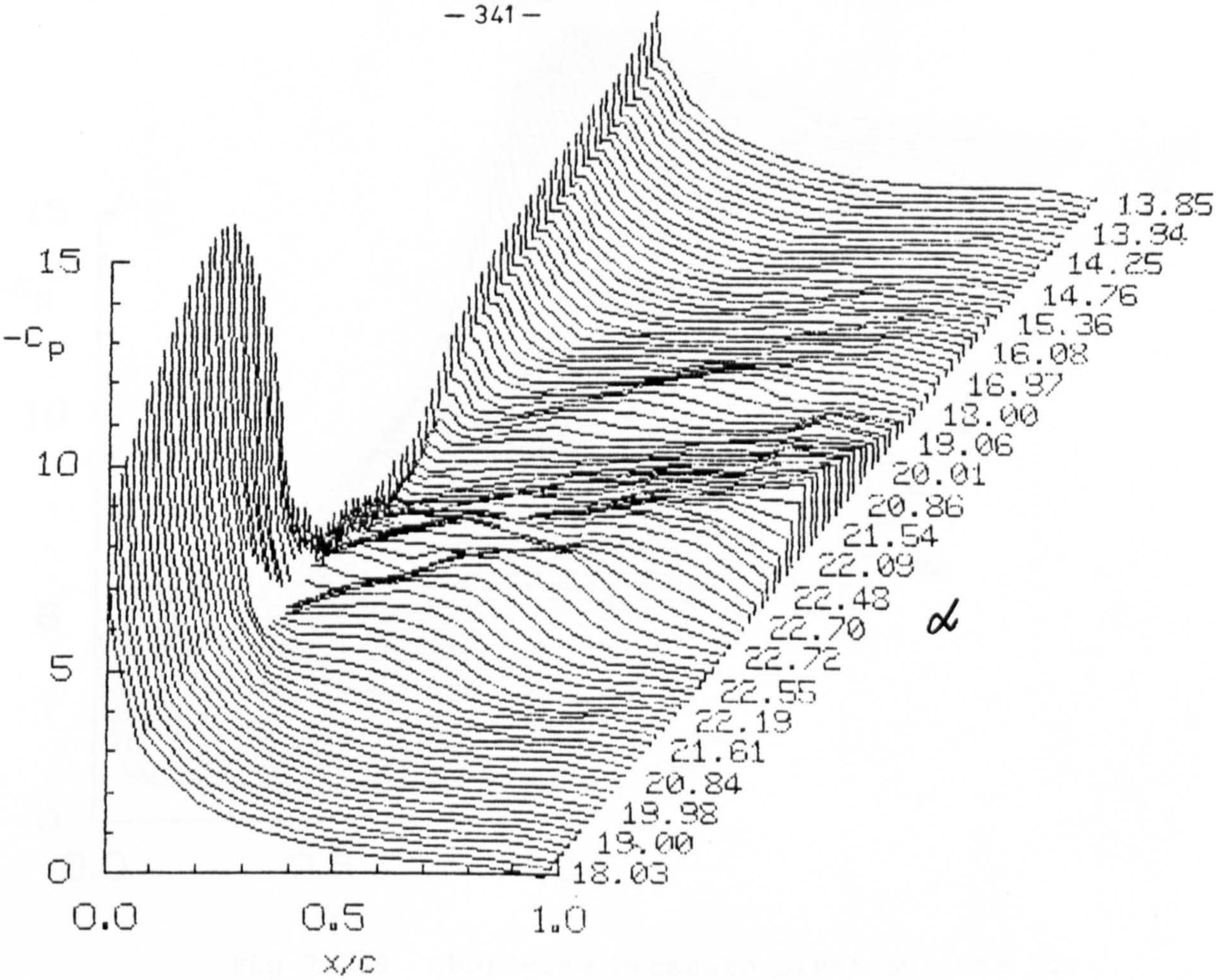

Fig 7.147 Chordwise Pressure Distributions for $\alpha = 18 + 4 \sin \omega t$; k= 0.20

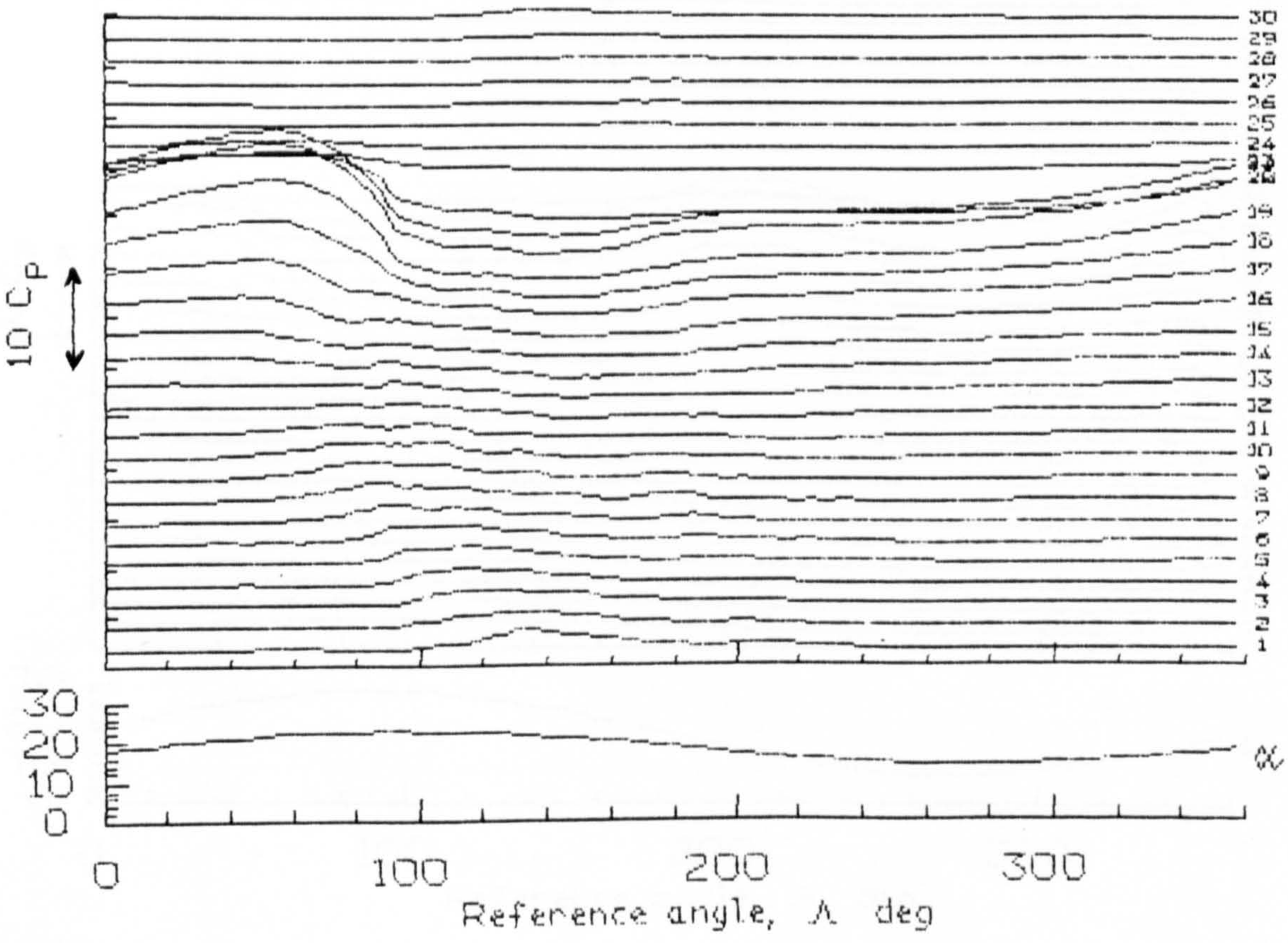

Fig 7.148 Pressure Time Histories for $\alpha = 18 + 4 \sin \omega t$; k= 0.20

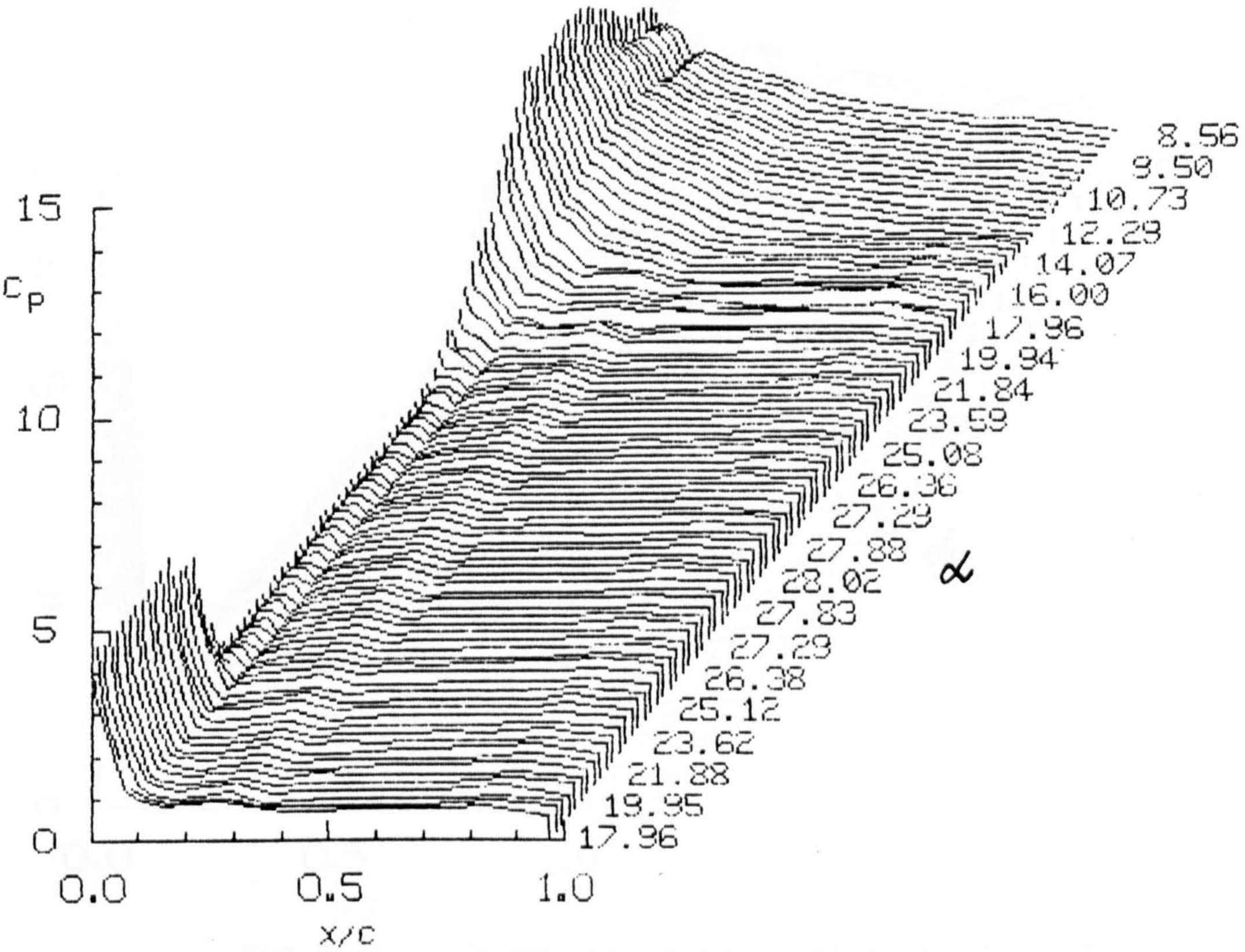

Fig 7.149 Chordwise Pressure Distributions for
$\alpha = 18 + 10 \sin \omega t$; k= 0.01

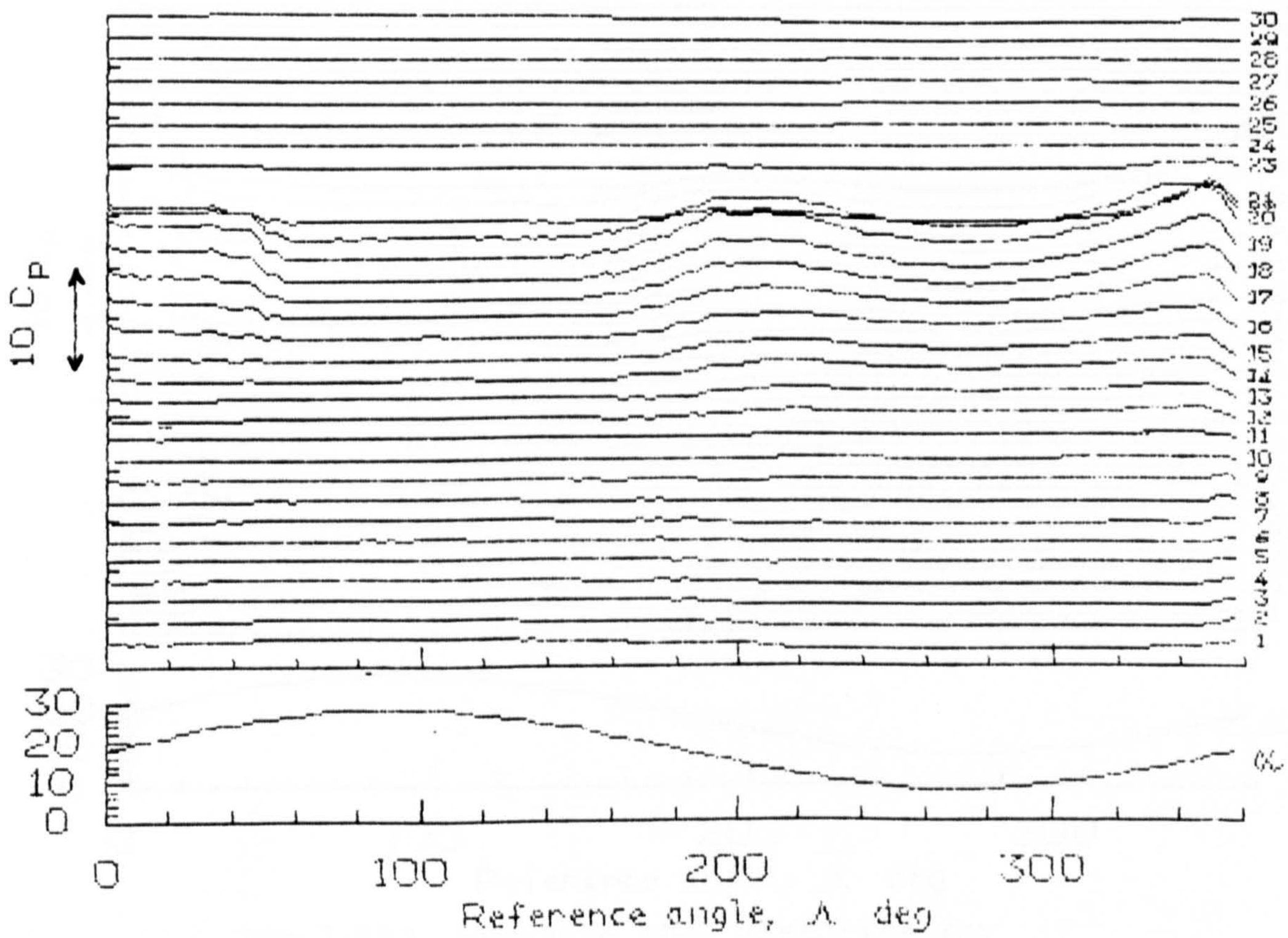

Fig 7.150 Pressure Time Histories for
$\alpha = 18 + 10 \sin \omega t$; k= 0.01

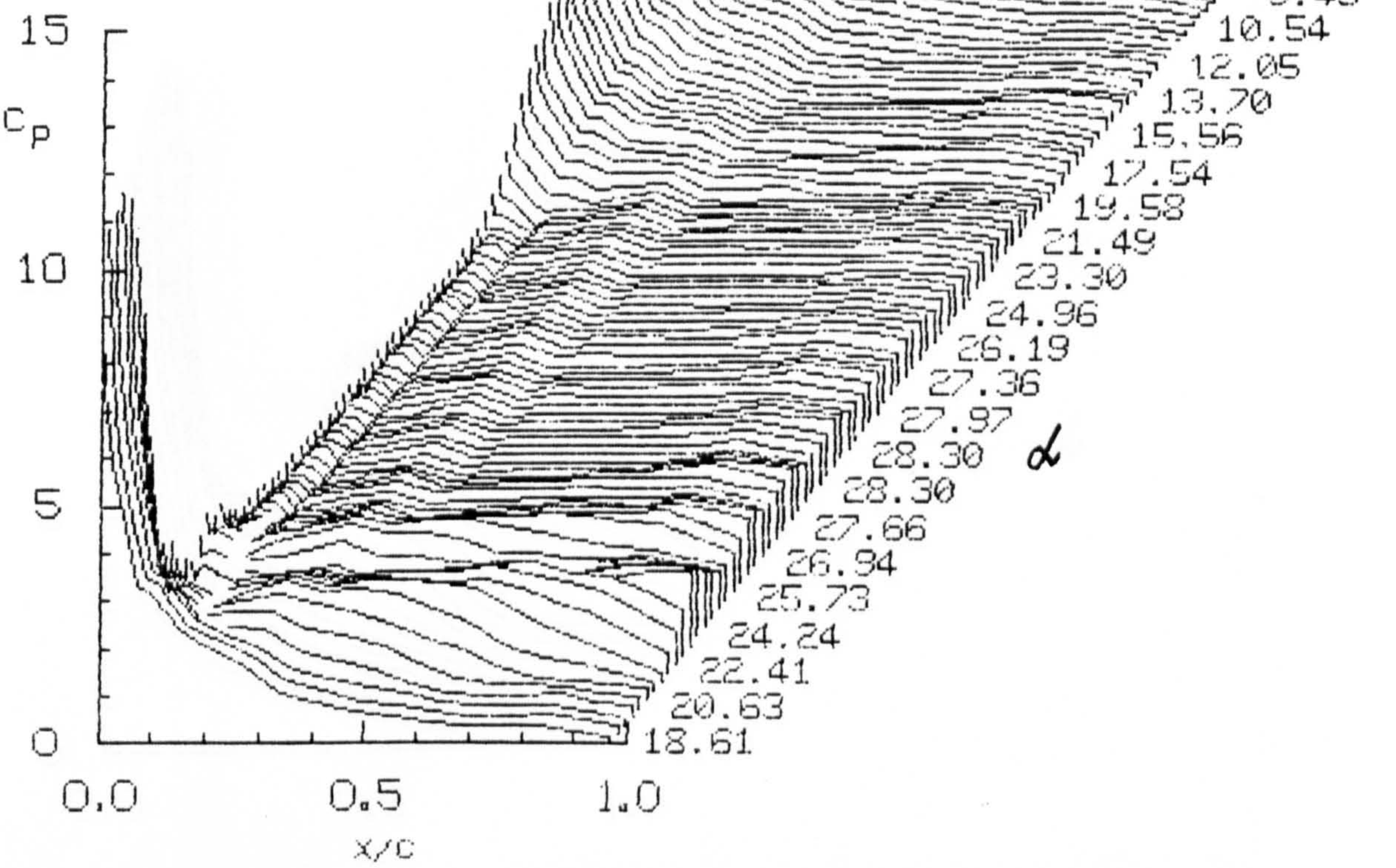

Fig 7.151 Chordwise Pressure Distributions for $\alpha = 18 + 10 \sin \omega t$; k= 0.05

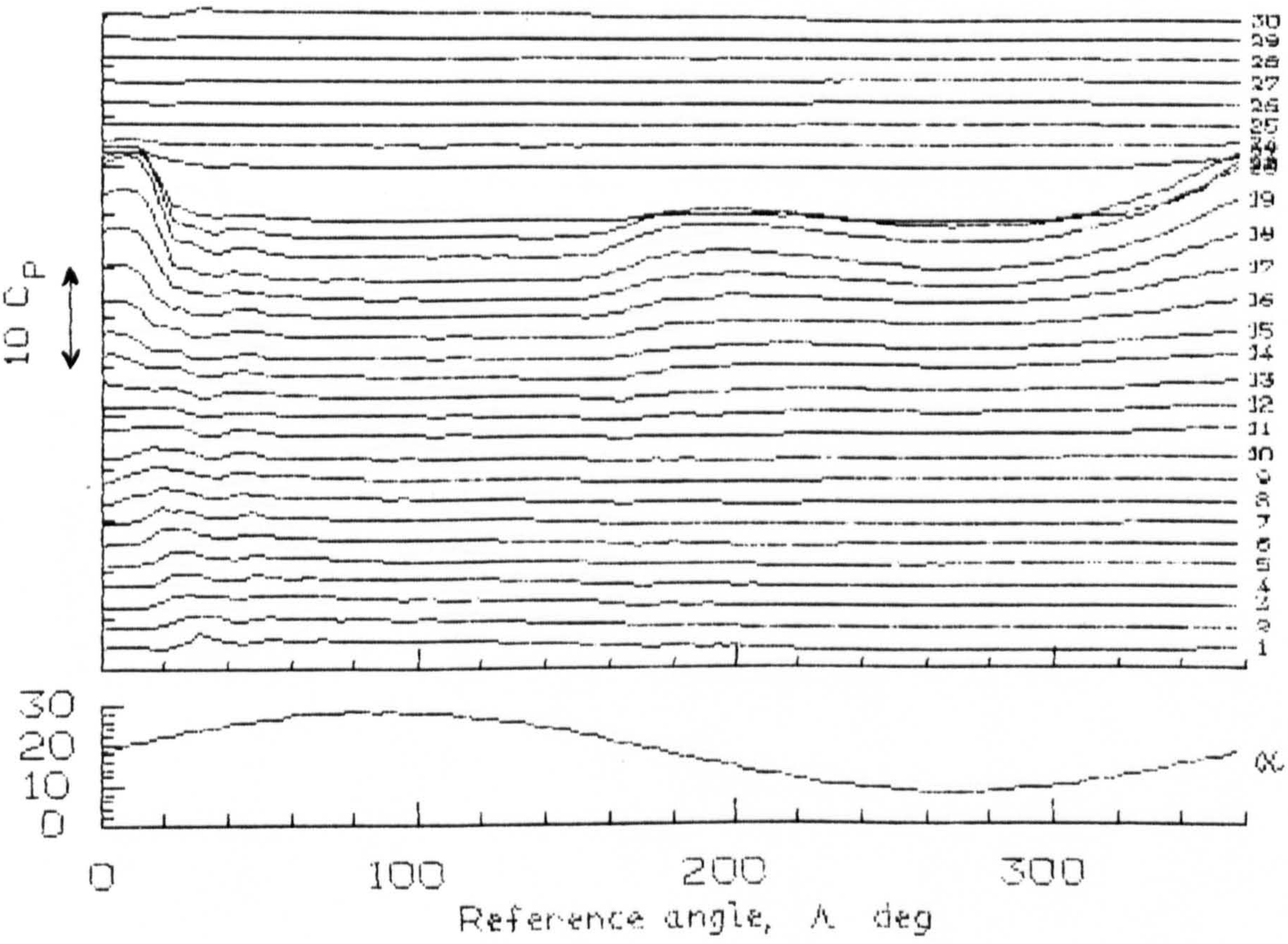

Fig 7.152 Pressure Time Histories for $\alpha = 13 + 10 \sin \omega t$; k= 0.05

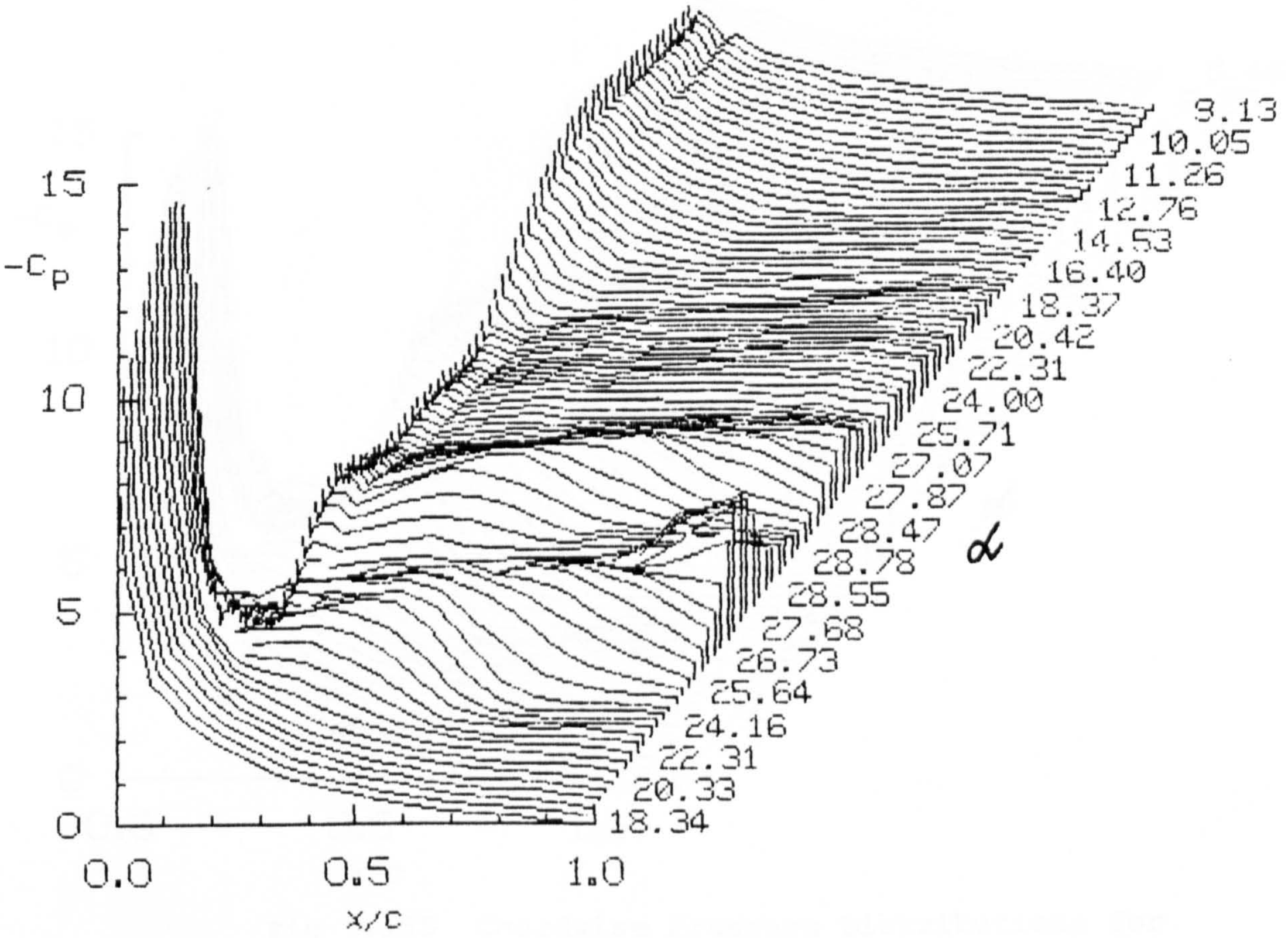

Fig 7.153 Chordwise Pressure Distributions for $\alpha = 18 + 10 \sin \omega t$; k= 0.10

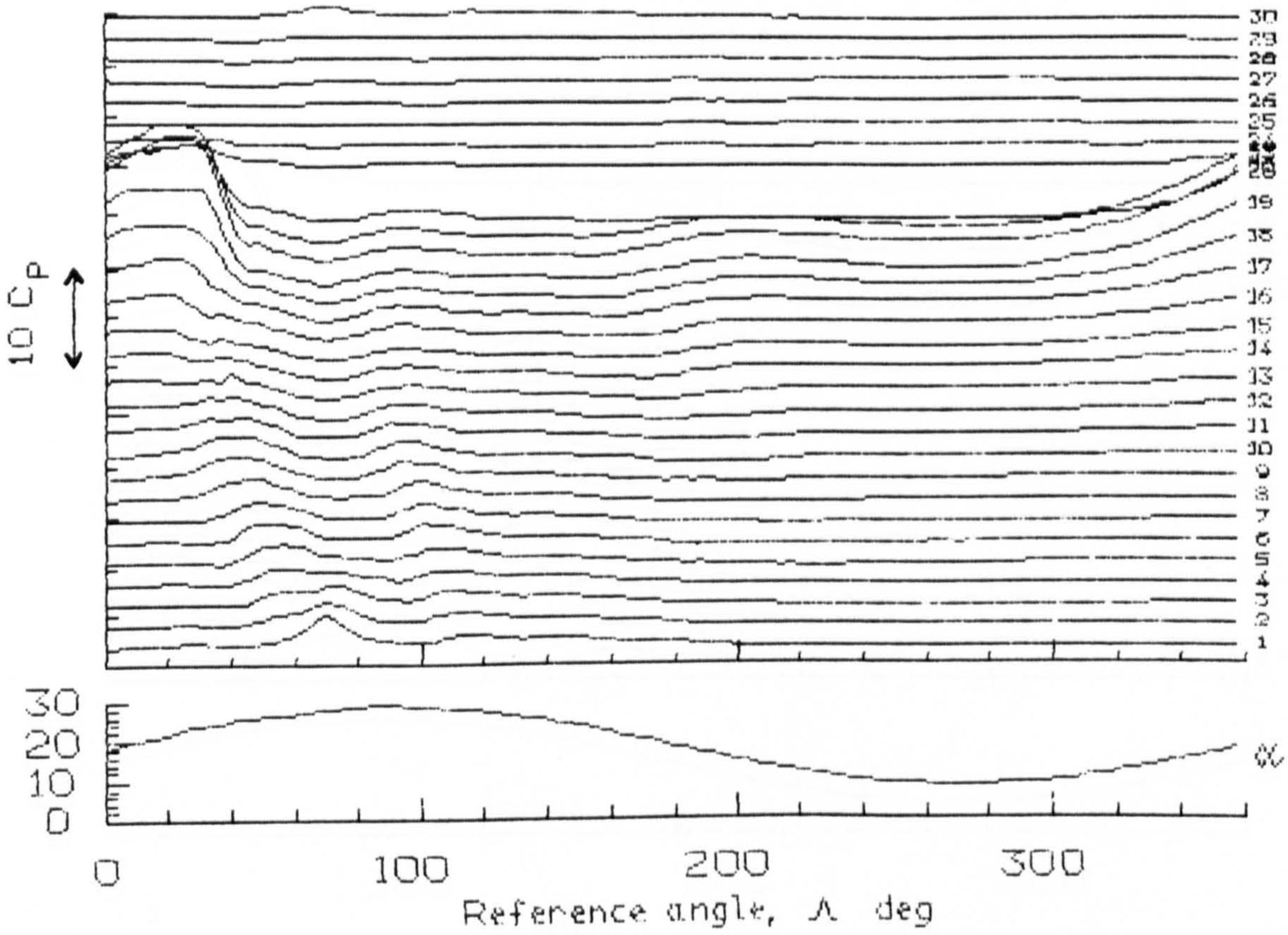

Fig 7.154 Pressure Time Histories for $\alpha = 18 + 10 \sin \omega t$; k= 0.10

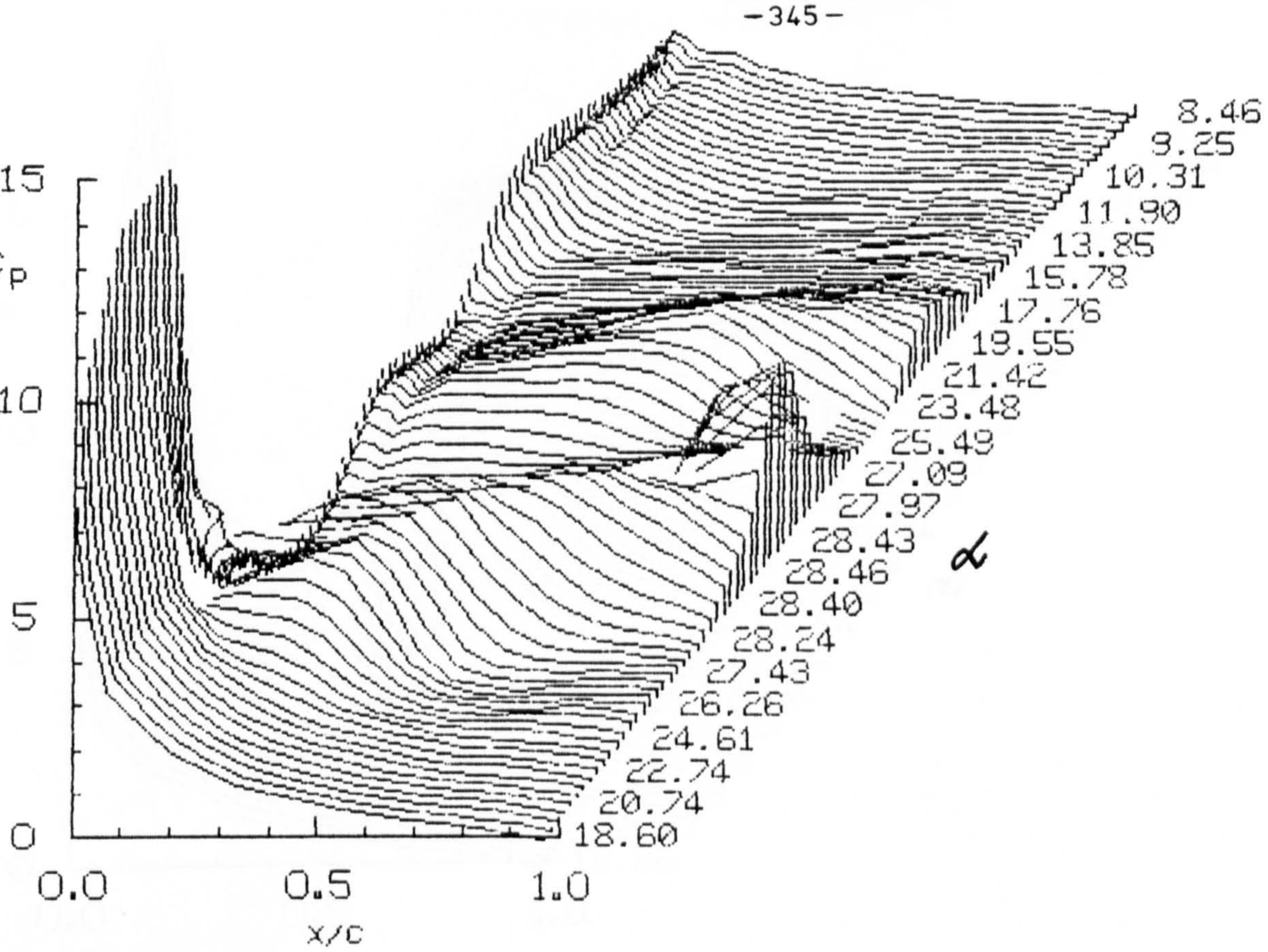

Fig 7.155 Chordwise Pressure Distributions for $\alpha = 18 + 10 \sin \omega t$; k= 0.15

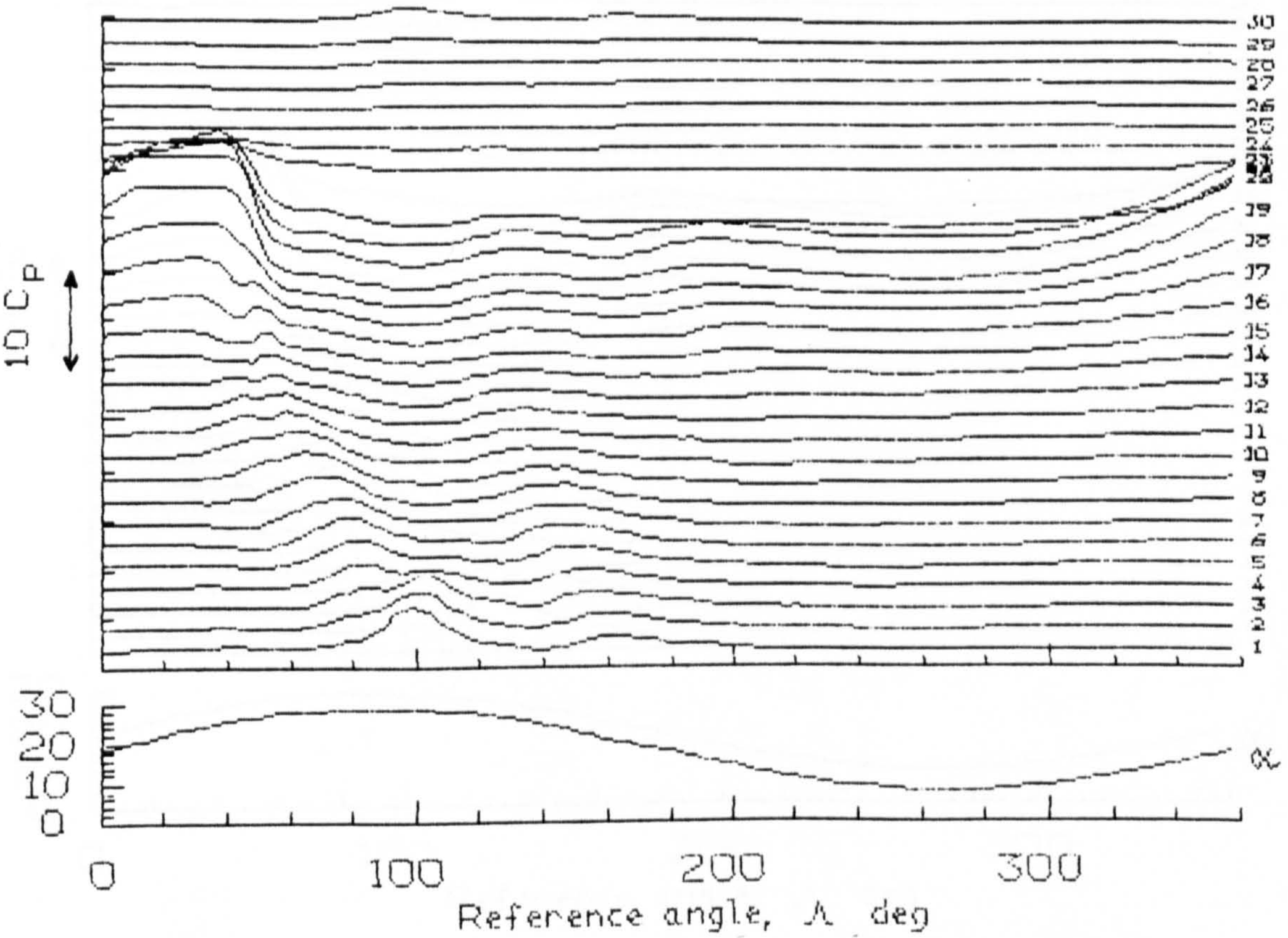

Fig 7.156 Pressure Time Histories for $\alpha = 18 + 10 \sin \omega t$; k= 0.15

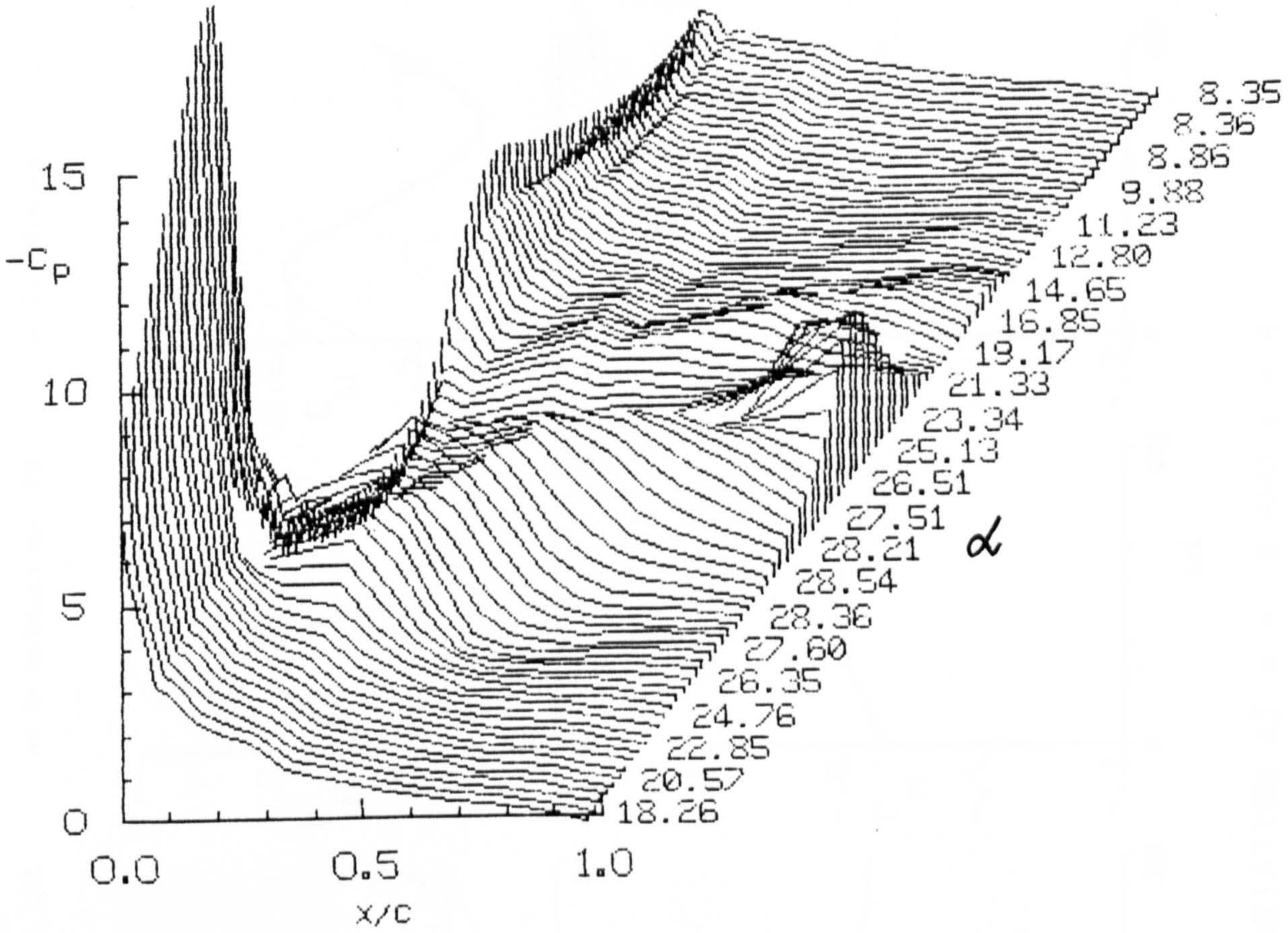

Fig 7.157 Chordwise Pressure Distributions for $\alpha = 18 + 10 \sin \omega t$; k= 0.20

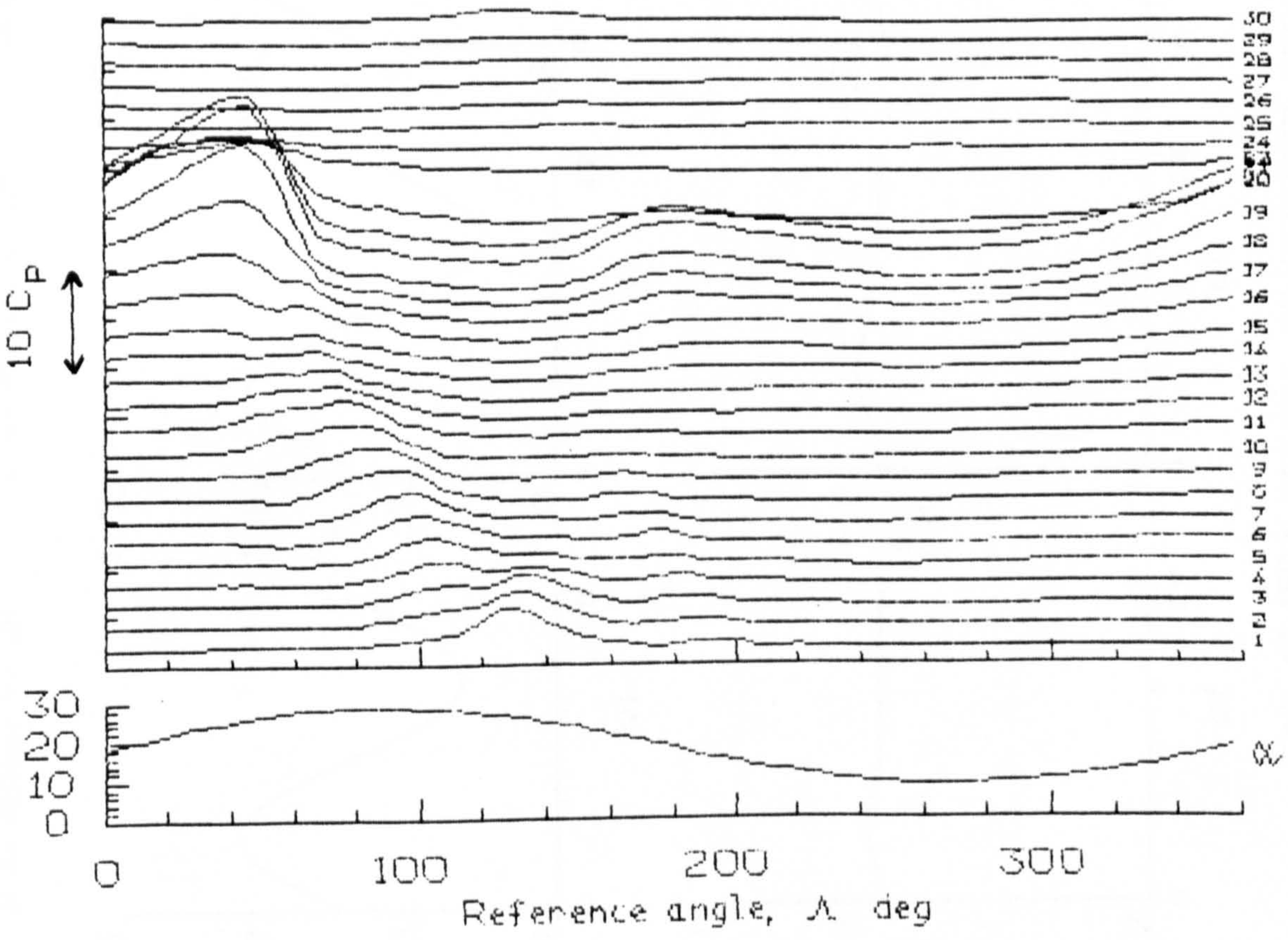

Fig 7.158 Pressure Time Histories for $\alpha = 18 + 10 \sin \omega t$; k= 0.20

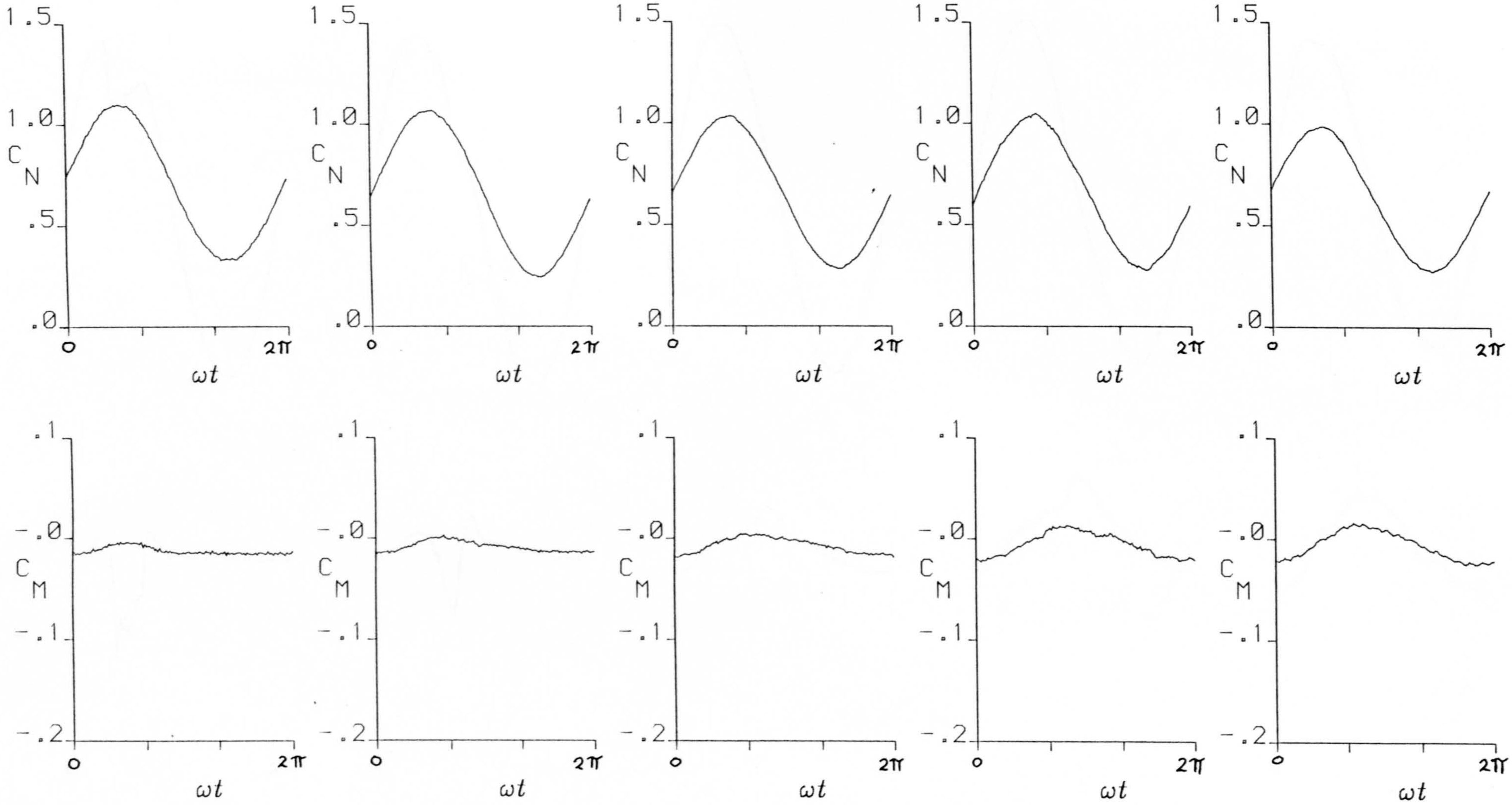

FIG.(7.159) EFFECT OF REDUCED FREQUENCY VARIATION AT α_m = 6 AND α_a = 4

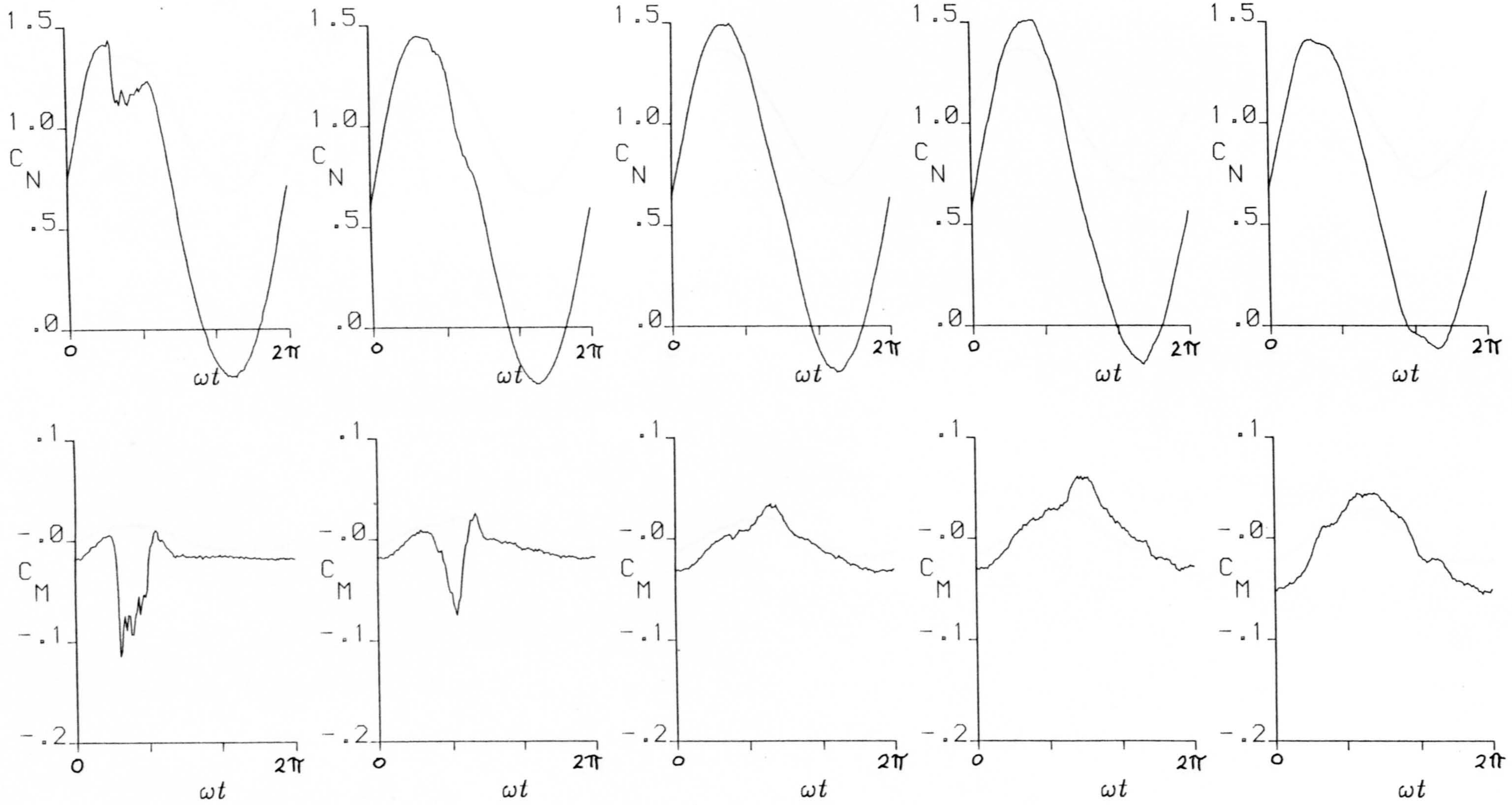

FIG.(7.160) EFFECT OF REDUCED FREQUENCY VARIATION AT α_m = 6 AND α_a =10

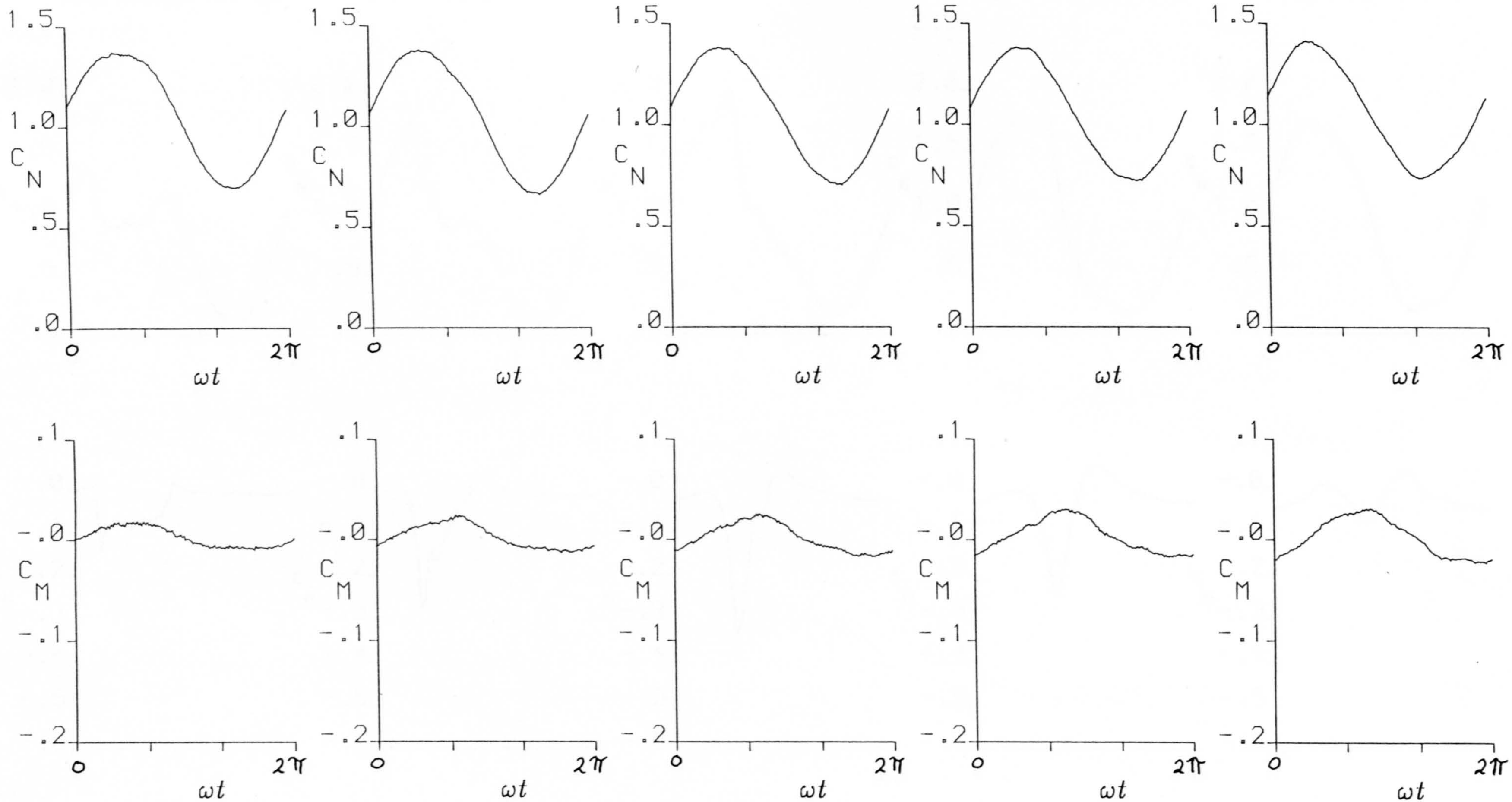

FIG.(7.161) EFFECT OF REDUCED FREQUENCY VARIATION AT α_m = 10 AND α_a = 4

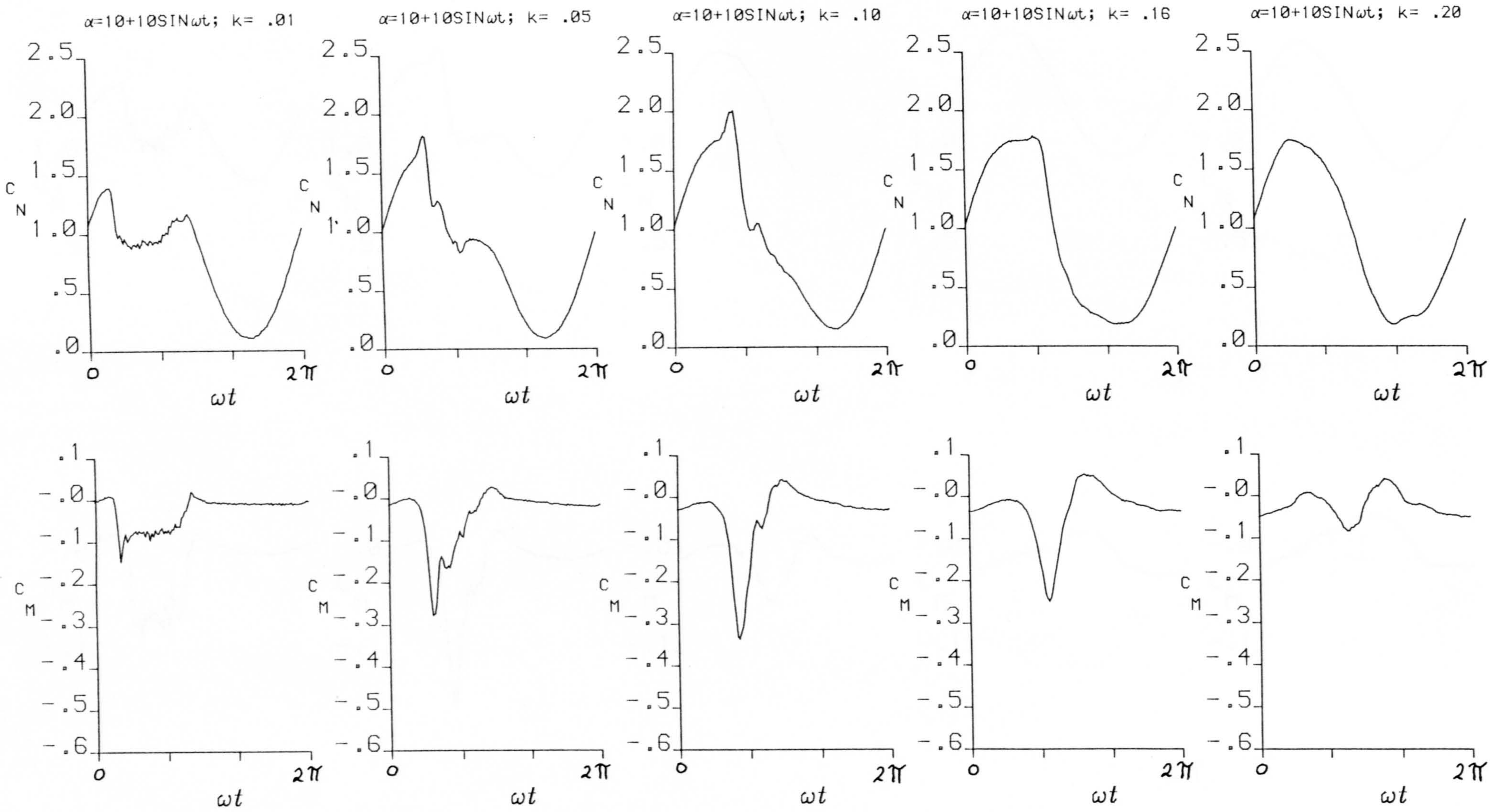

FIG.(7.162) EFFECT OF REDUCED FREQUENCY VARIATION AT α_m = 10 AND α_a =10

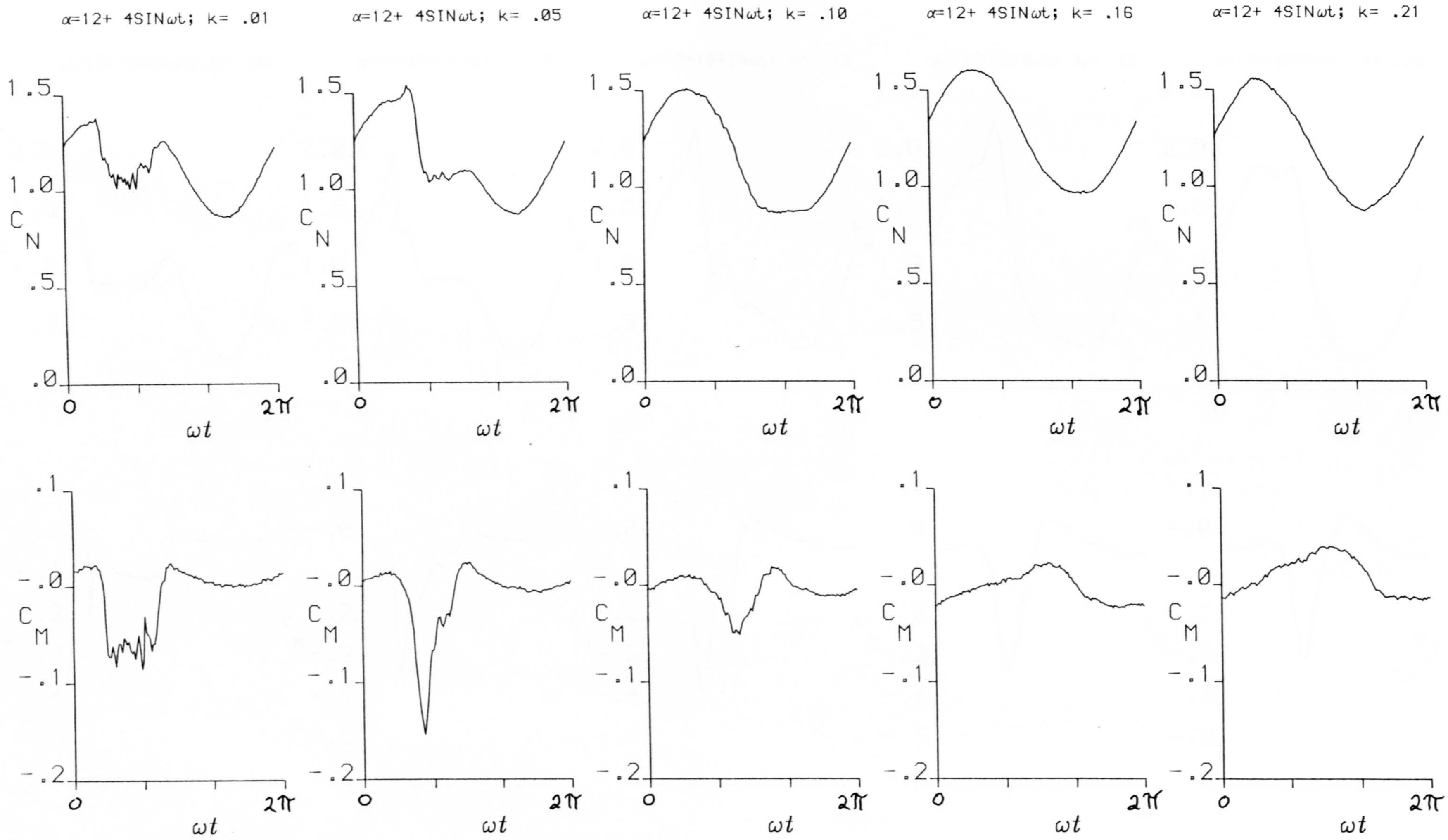

FIG.(7.163) EFFECT OF REDUCED FREQUENCY VARIATION AT α_m = 12 AND α_a = 4

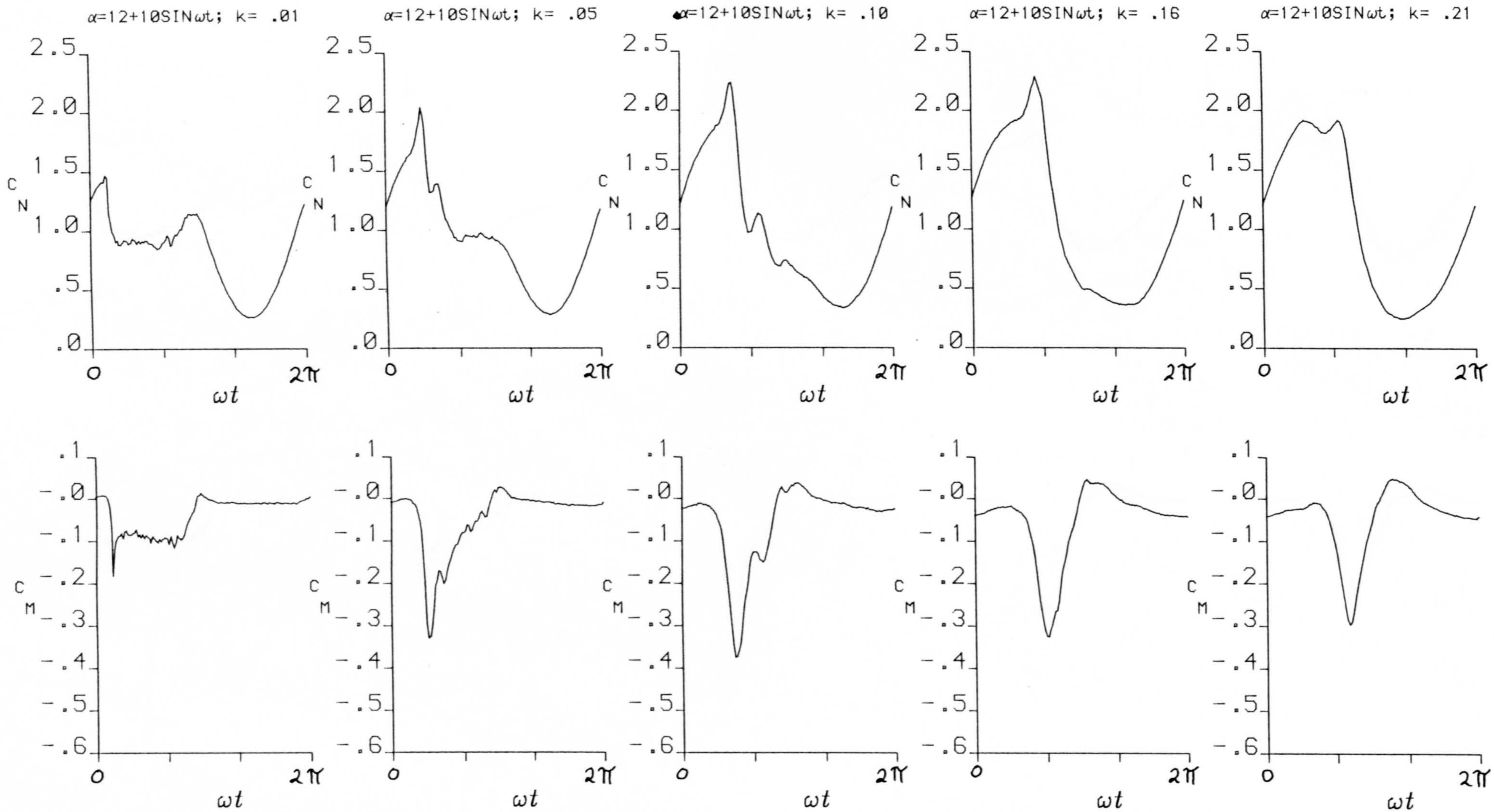

FIG.(7.164) EFFECT OF REDUCED FREQUENCY VARIATION AT α_m = 12 AND α_a =10

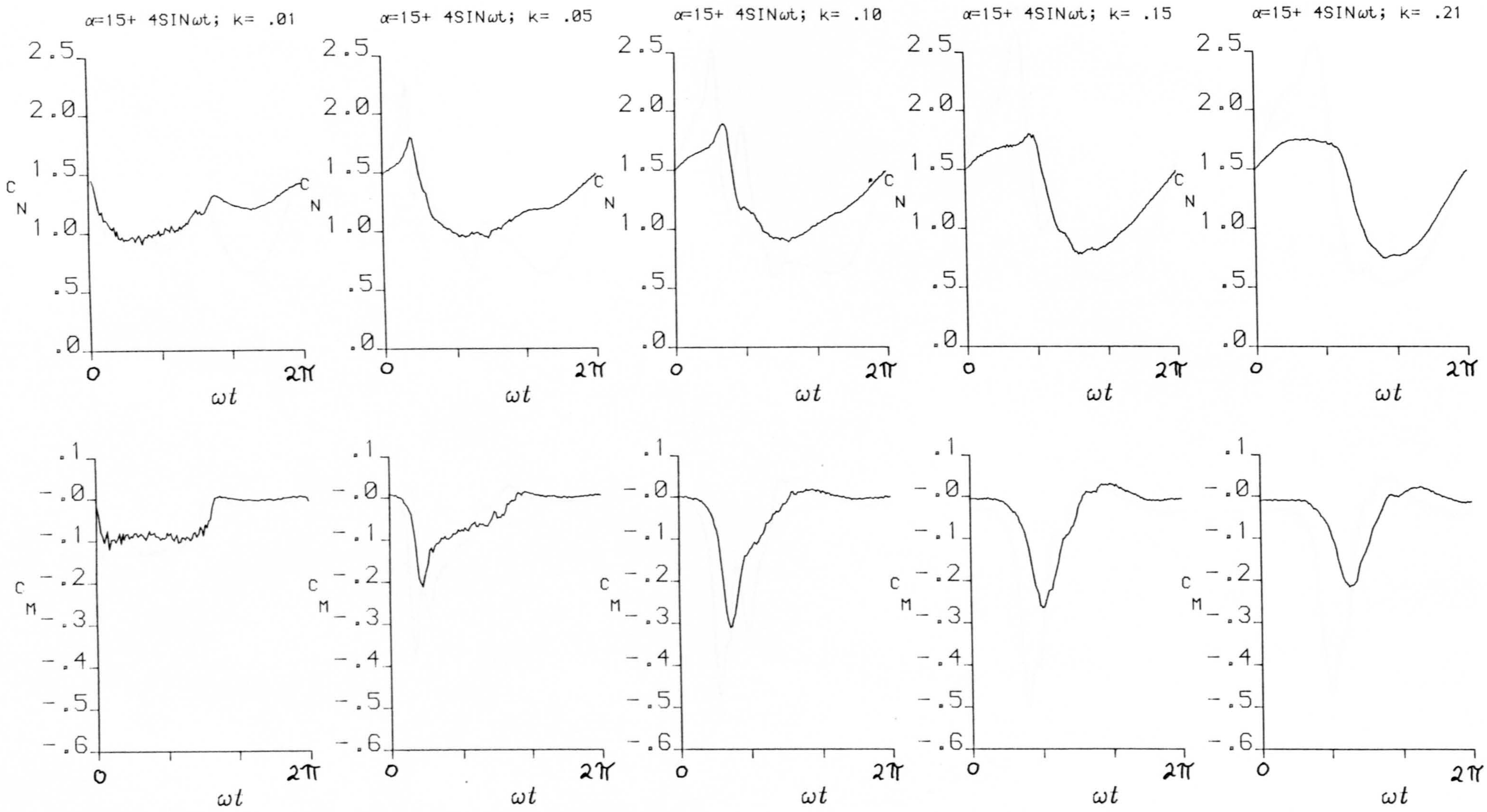

FIG.(7.165) EFFECT OF REDUCED FREQUENCY VARIATION AT α_m = 15 AND α_a = 4

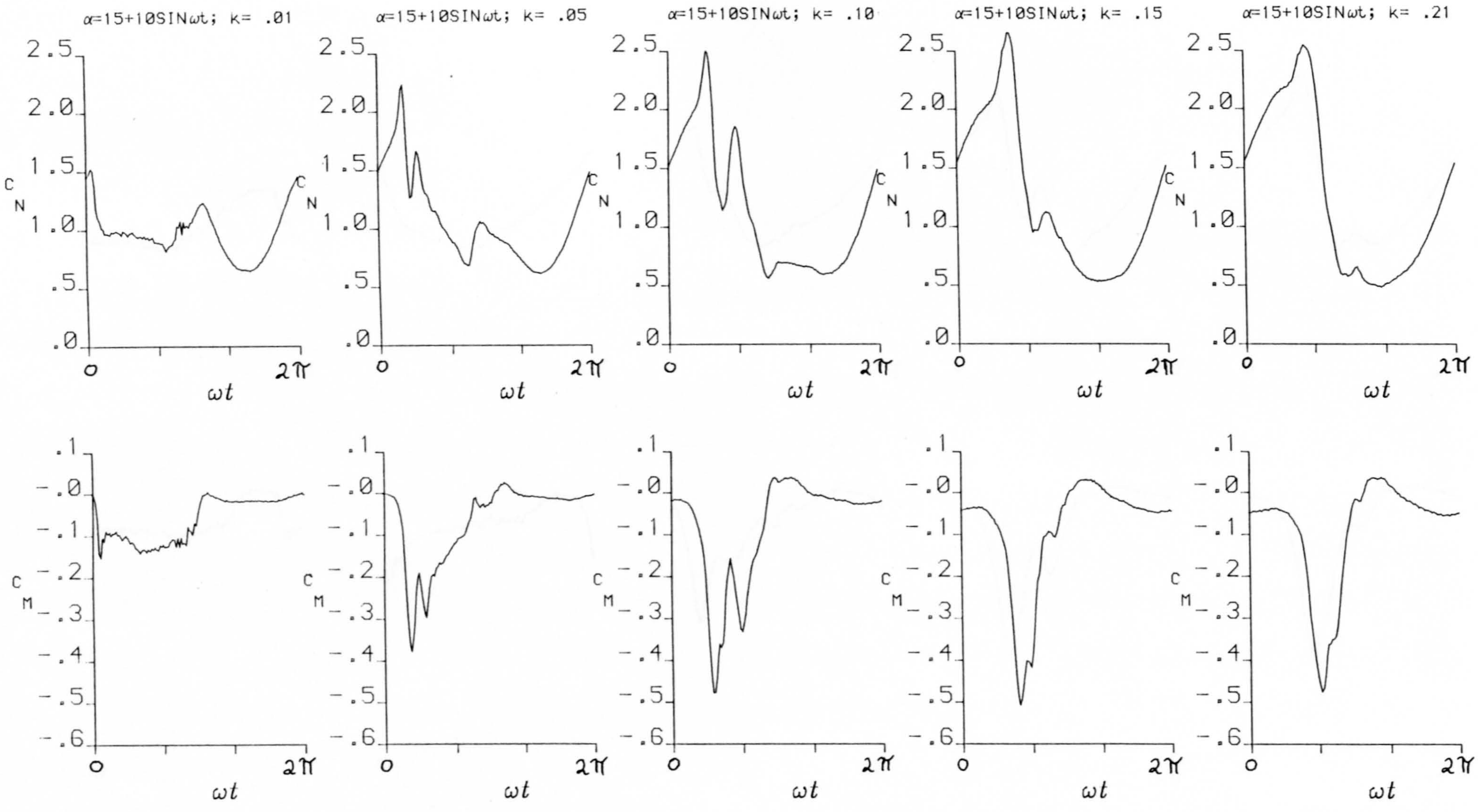

FIG.(7.166) EFFECT OF REDUCED FREQUENCY VARIATION AT α_m = 15 AND α_a =10

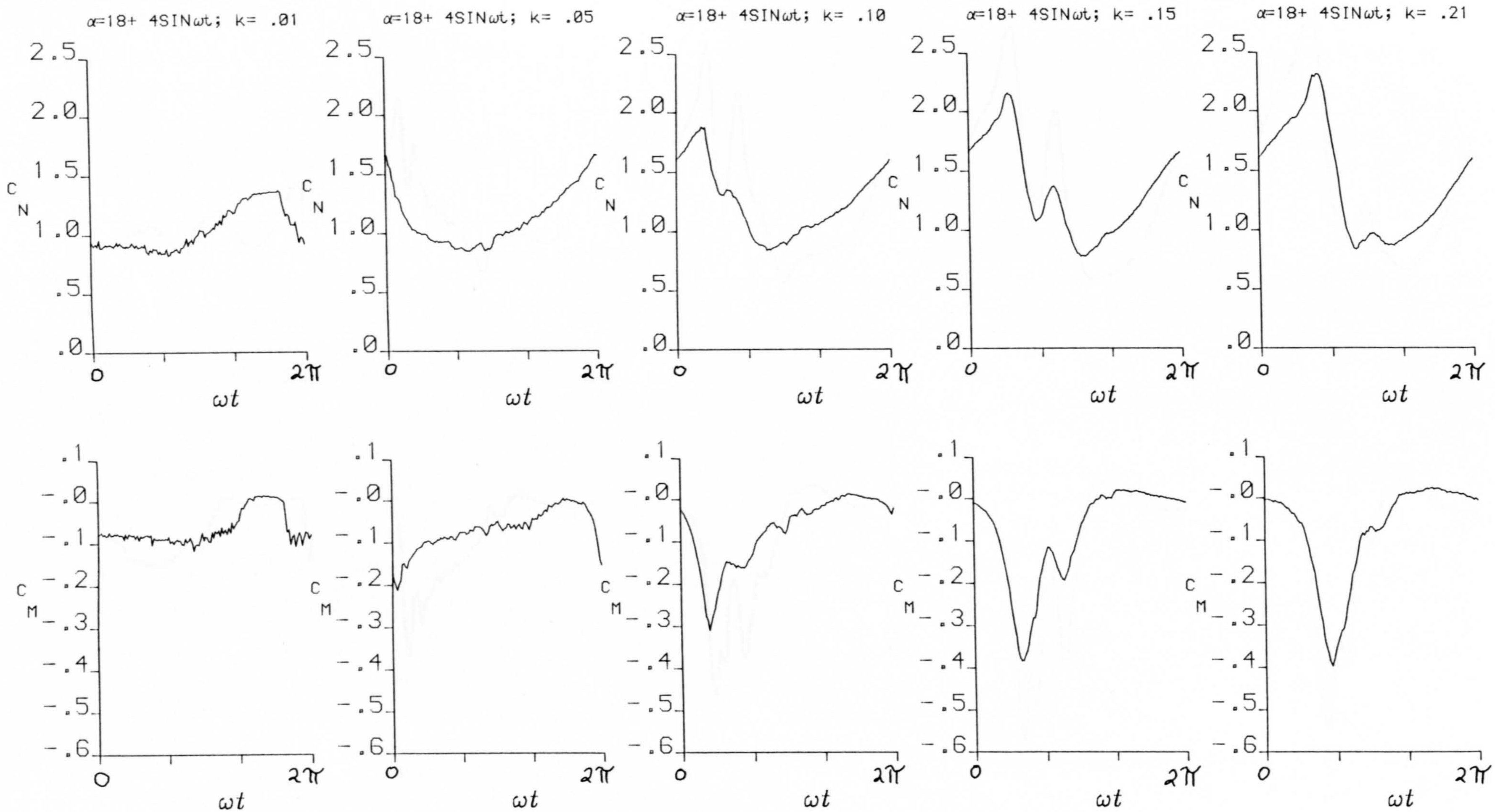

FIG.(7.167) EFFECT OF REDUCED FREQUENCY VARIATION AT α_m = 18 AND α_a = 4

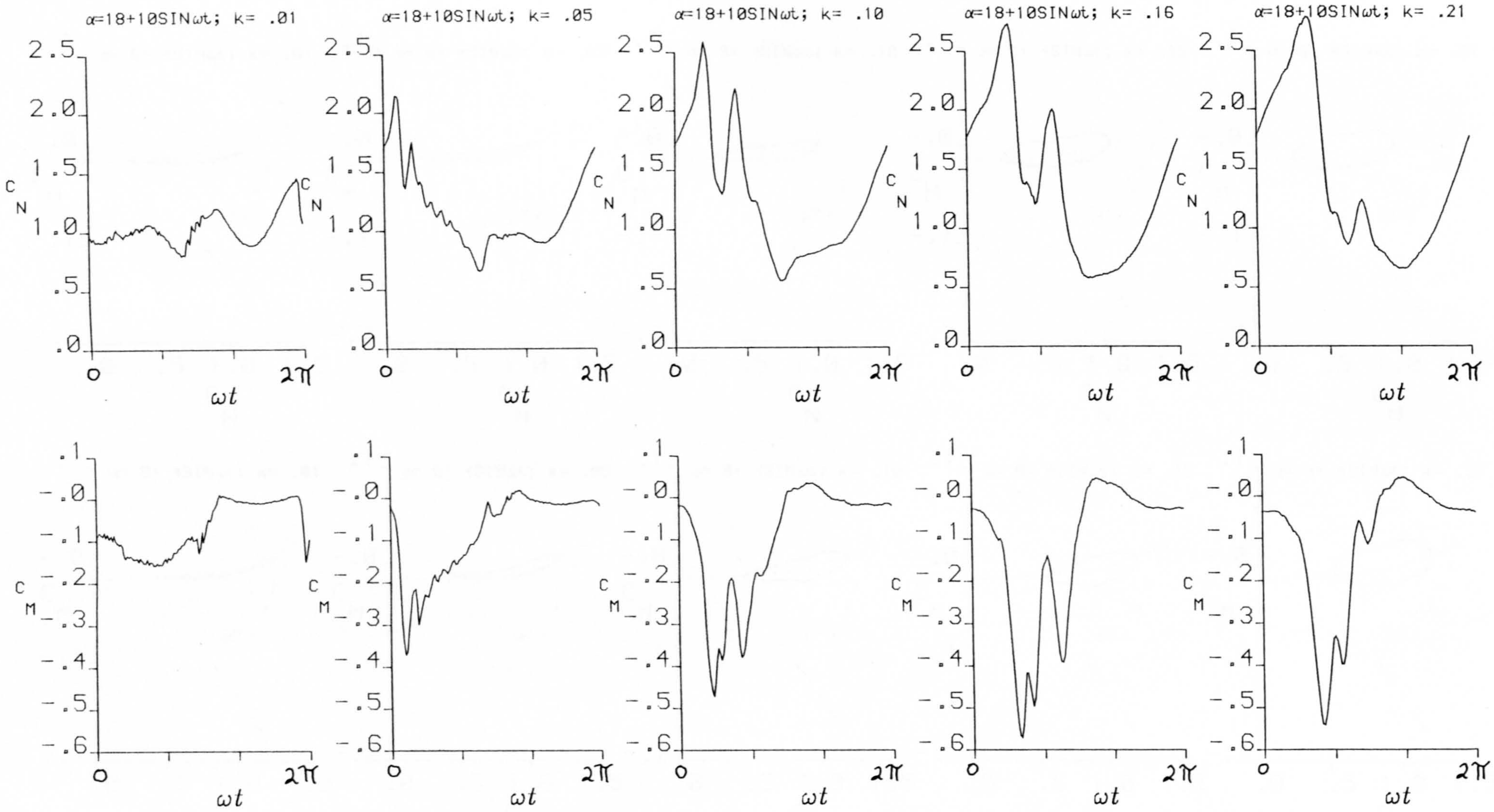

FIG.(7.168) EFFECT OF REDUCED FREQUENCY VARIATION AT α_m = 18 AND α_a =10

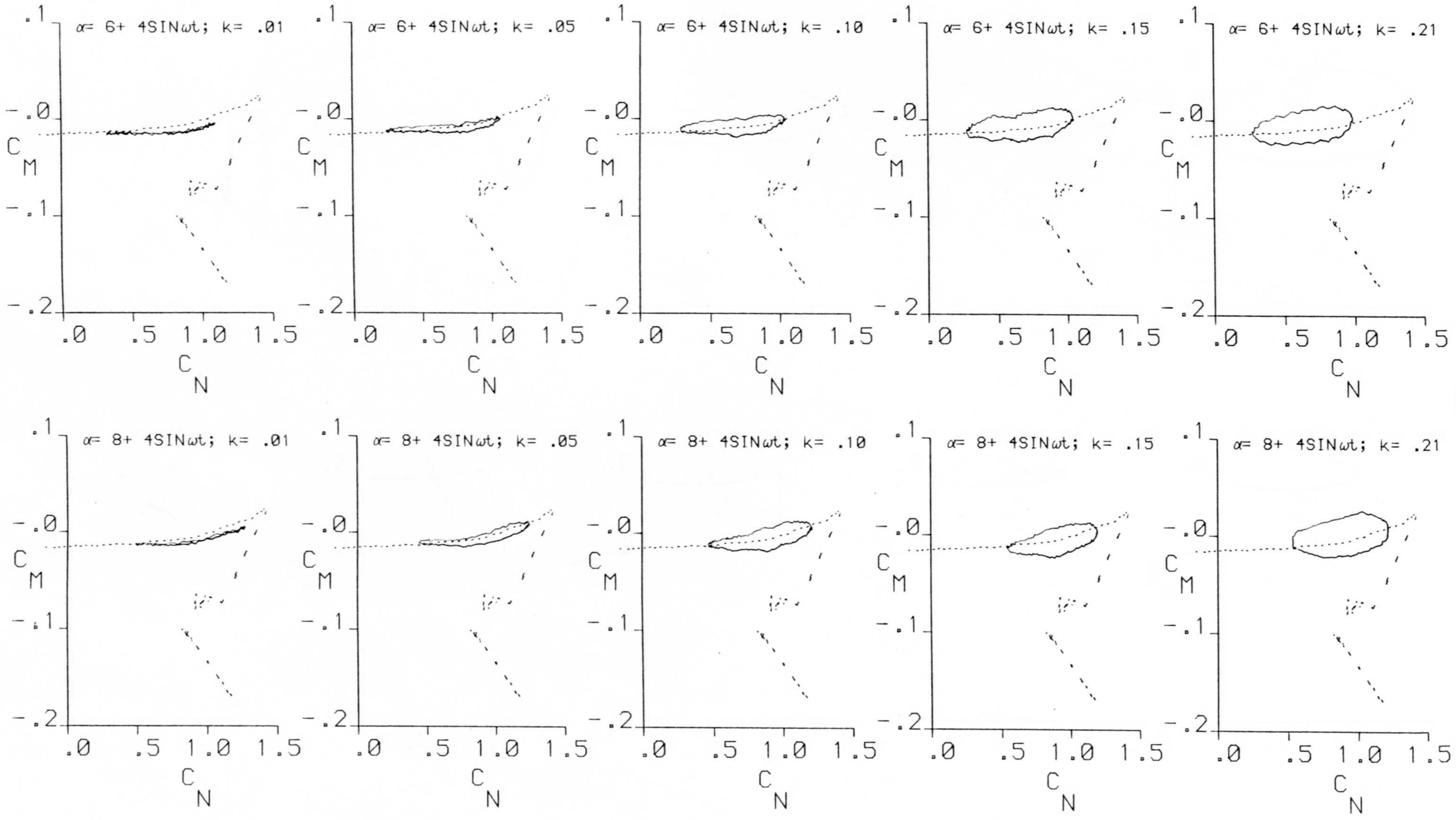

FIG.(**7.169**) EFFECT OF REDUCED FREQUENCY VARIATION AT $\alpha = 6^{\circ}$ & 8° ; $\alpha = 4^{\circ}$

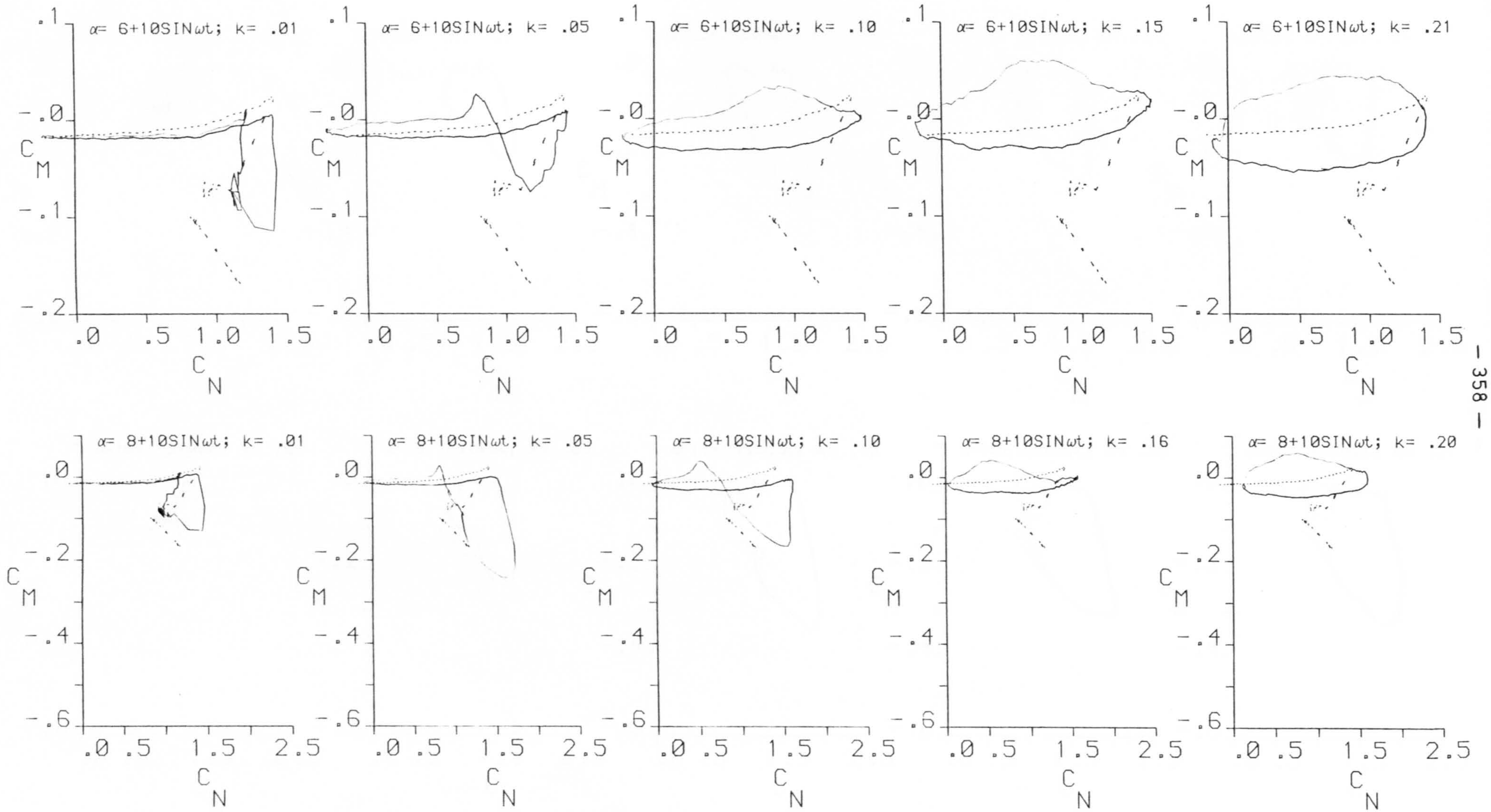

FIG.(7.170) EFFECT OF REDUCED FREQUENCY VARIATION AT α_m = 6° & 8° ; α_a = 10°

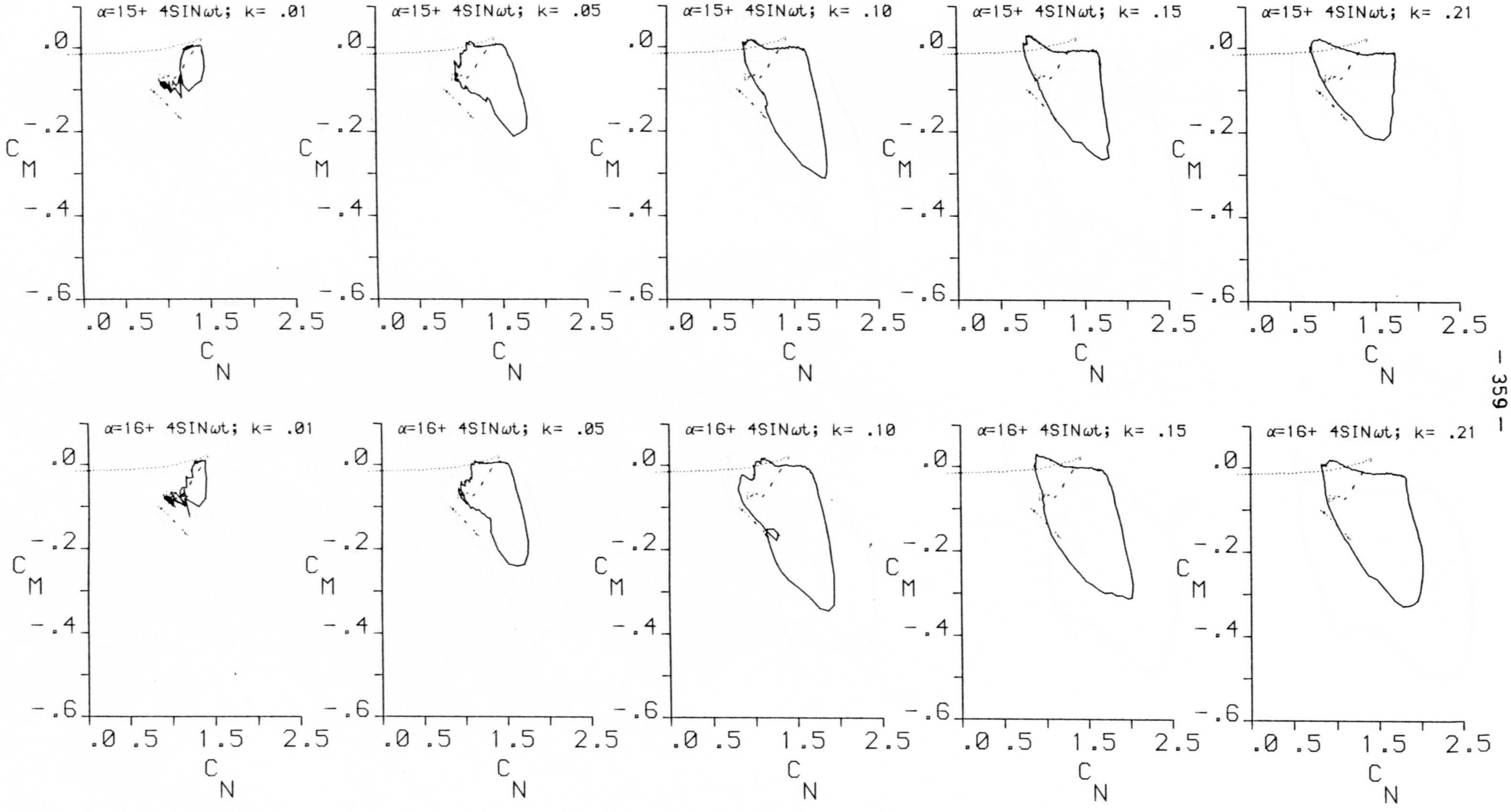

FIG.(7.171) EFFECT OF REDUCED FREQUENCY VARIATION AT $\alpha_m = 15^\circ$ & 16° ; $\alpha_n = 4^\circ$

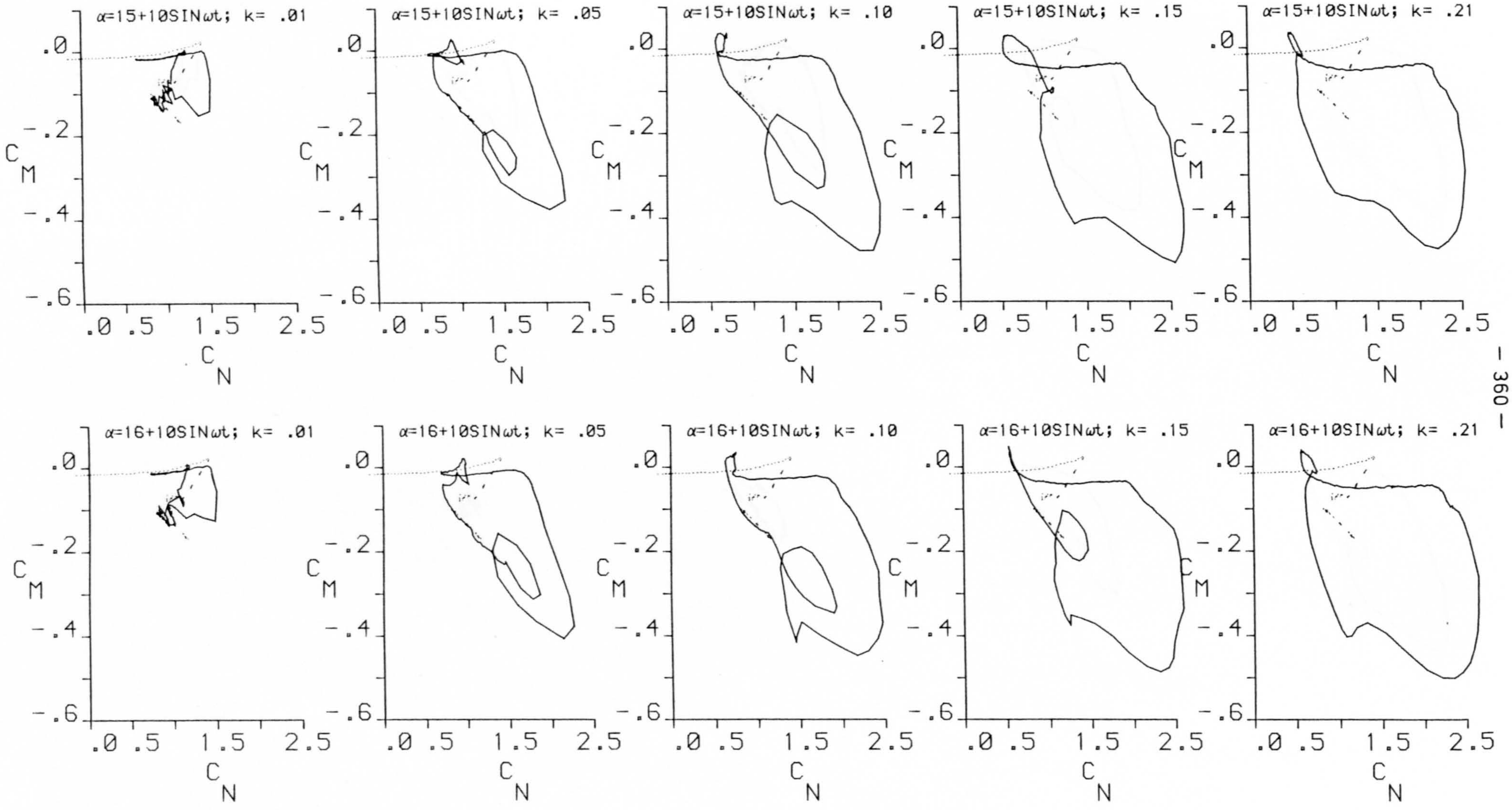

FIG.(7.172) EFFECT OF REDUCED FREQUENCY VARIATION AT $\alpha_m = 15^\circ$ & 16° ; $\alpha_a = 10^\circ$

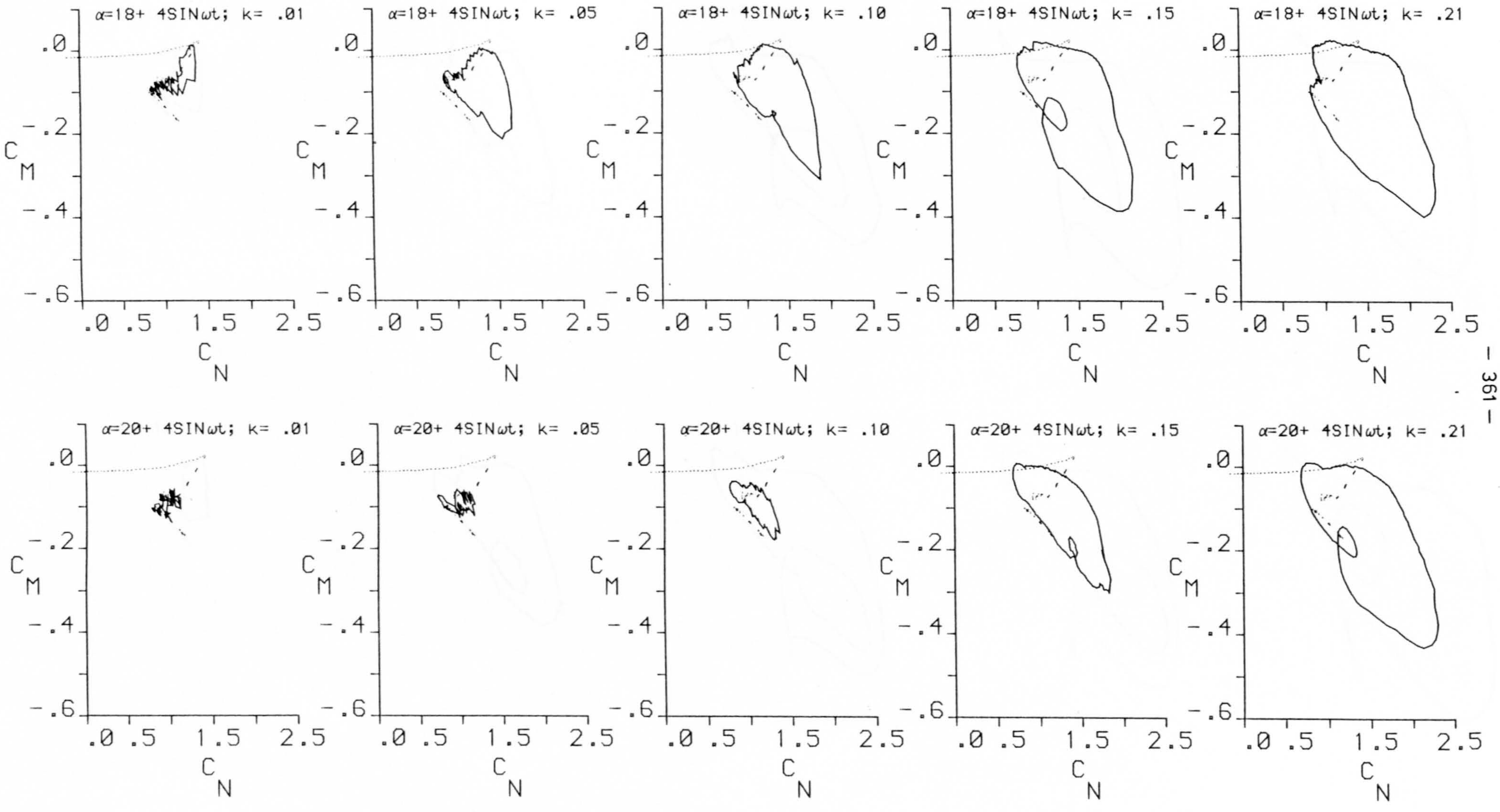

FIG.(7.173) EFFECT OF REDUCED FREQUENCY VARIATION AT $\alpha_m = 18^\circ$ & 20° ; $\alpha_a = 4^\circ$

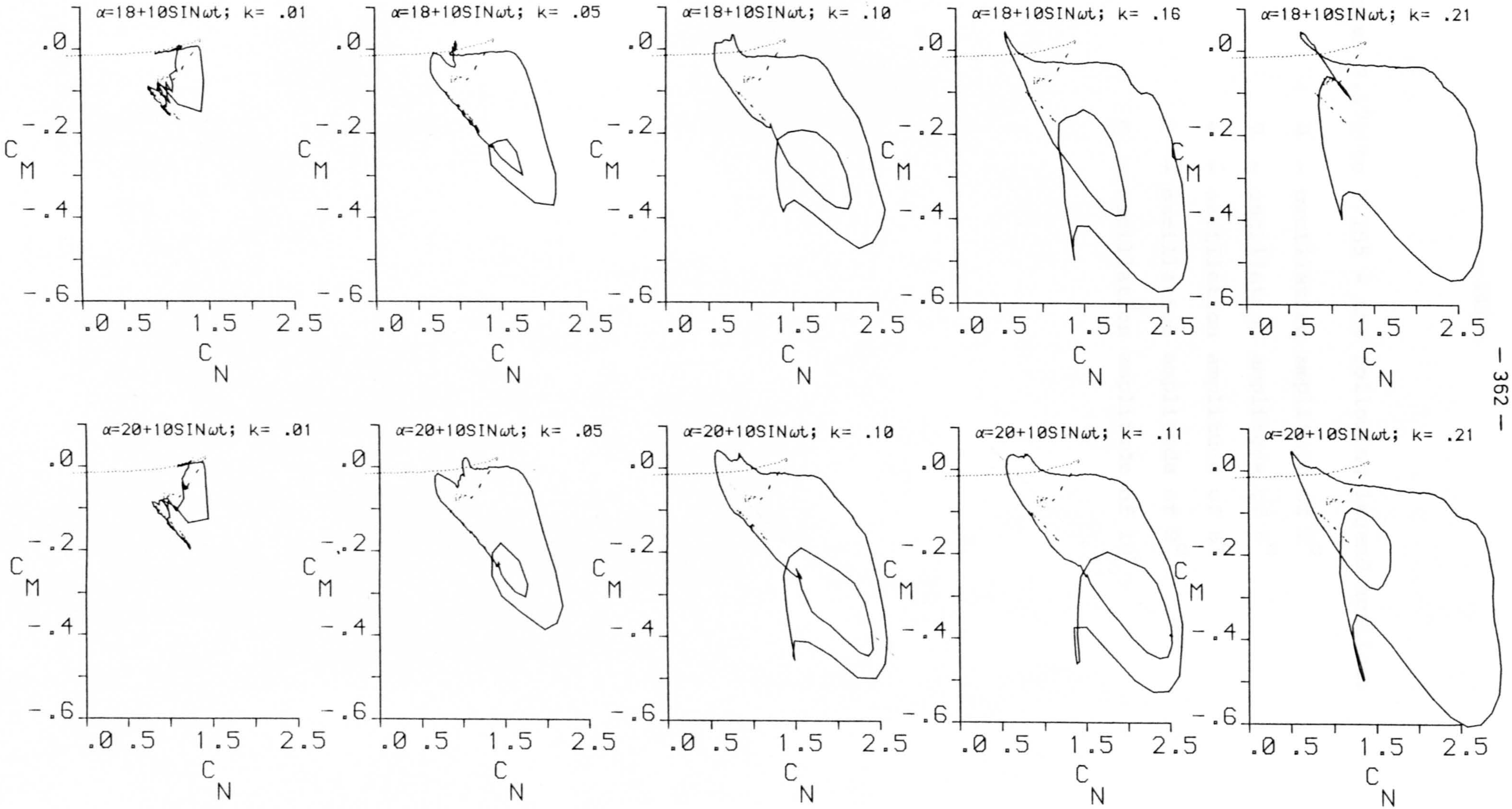

FIG.(7.174) EFFECT OF REDUCED FREQUENCY VARIATION AT $\alpha_m = 18^\circ$ & 20° ; $\alpha_a = 10^\circ$

Figures 7.171 to 7.185 - the following legend applies:

Δ - oscillation amplitude of 2^{o}

∇ - oscillation amplitude of 4^{o}

$+$ - oscillation amplitude of 6^{o}

X - oscillation amplitude of 8^{o}

$\square$ - oscillation amplitude of 10^{o}

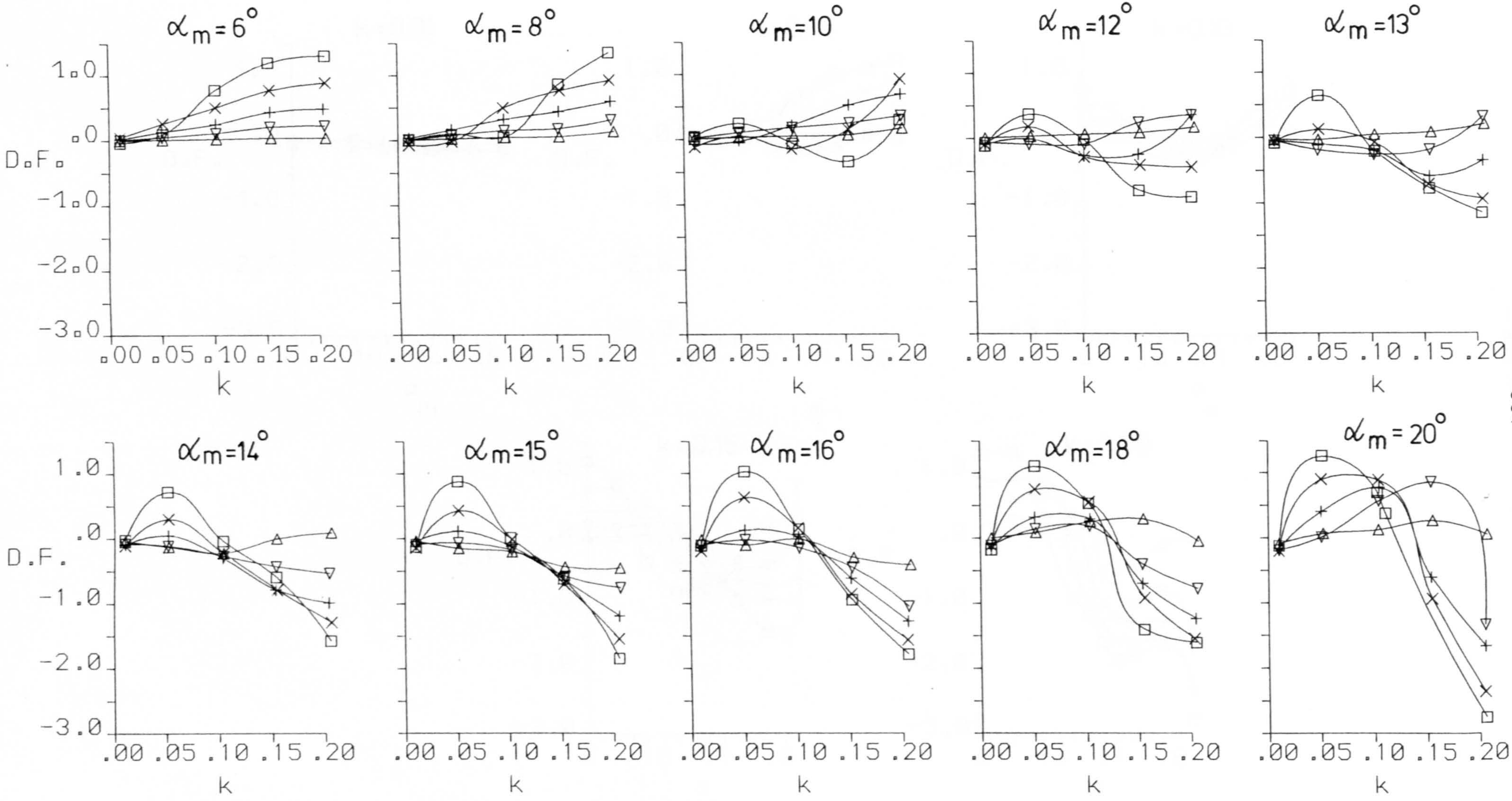

Fig 7.175 Effect of reduced frequency on aerofoil damping for various mean angles and amplitudes.

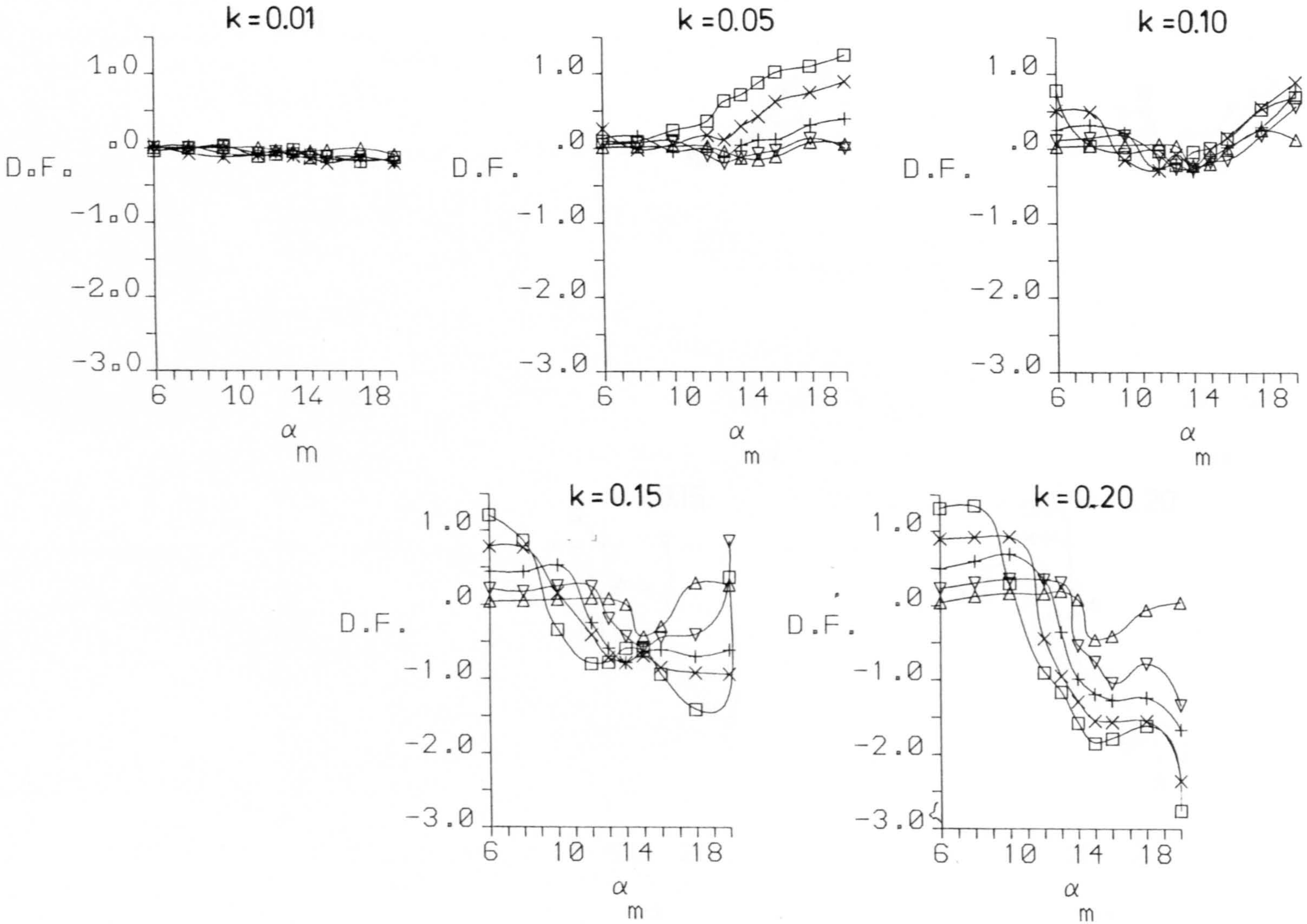

Fig 7.176 Mean angle of attack versus aerofoil damping for various amplitudes and reduced frequencies.

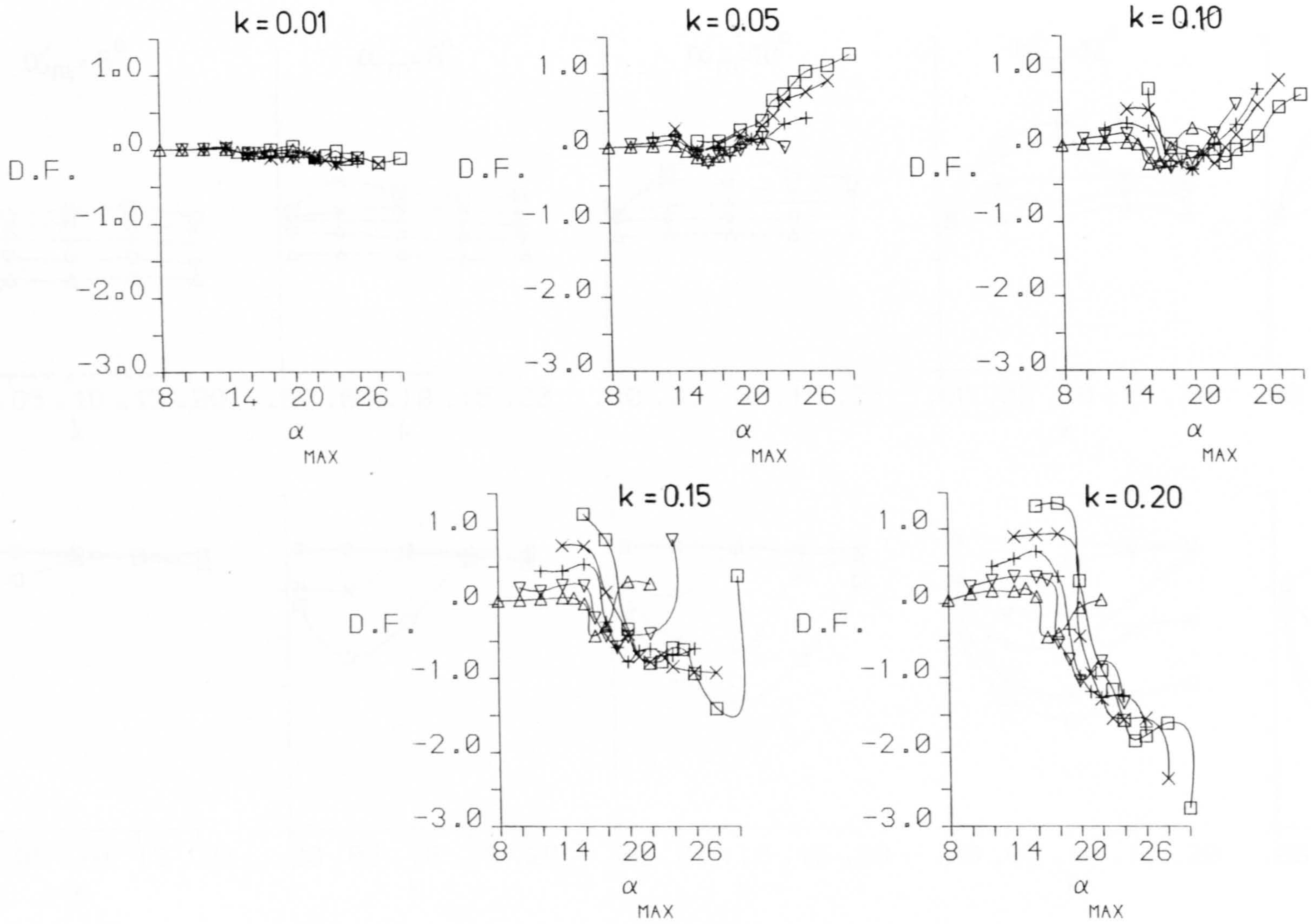

Fig 7.177 Maximum angle of attack versus aerofoil damping for various amplitudes and reduced frequencies.

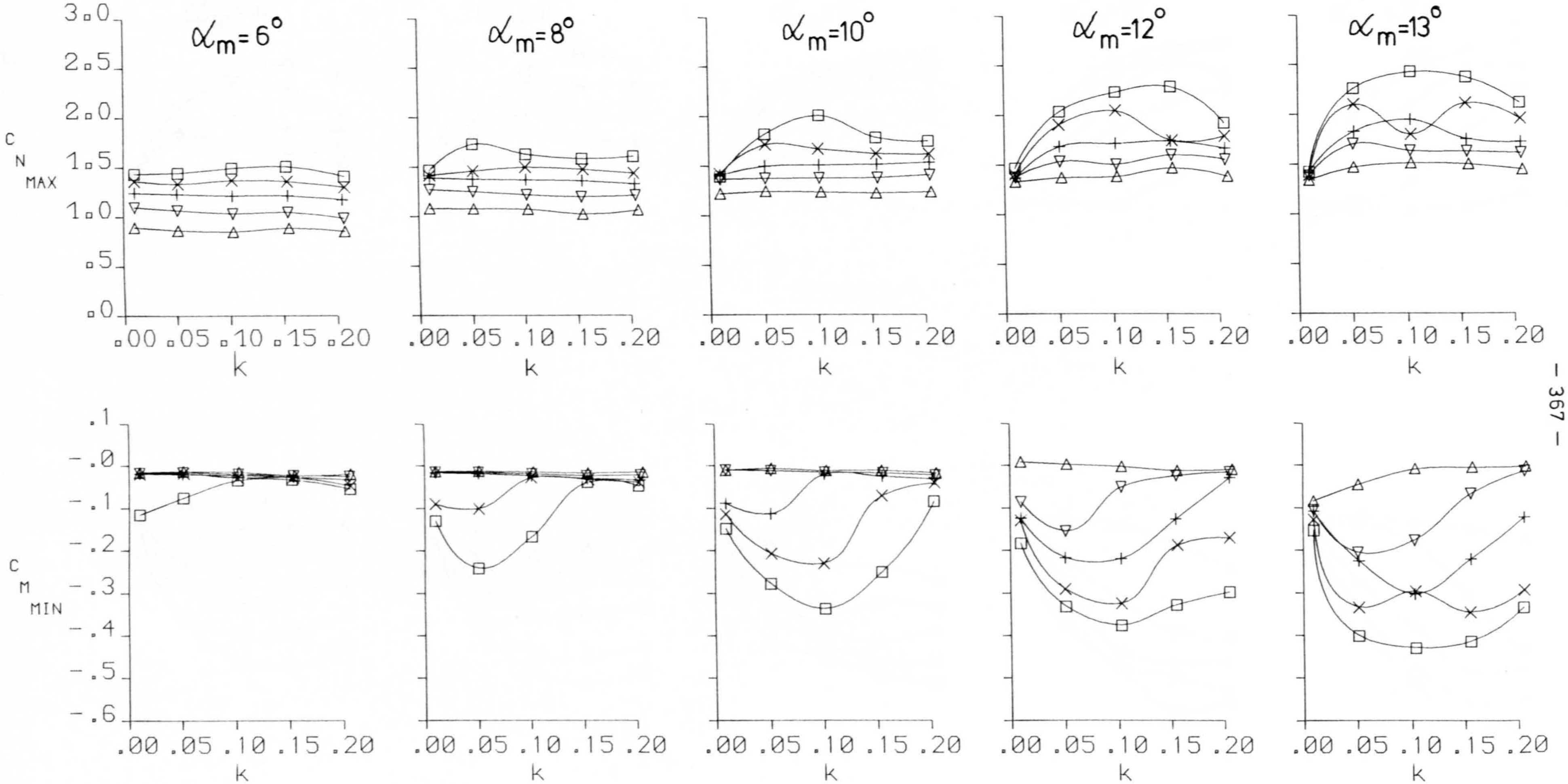

Fig 7.178 Effect of reduced frequency on maximum normal force and minimum pitching moment for various mean angles and amplitudes.

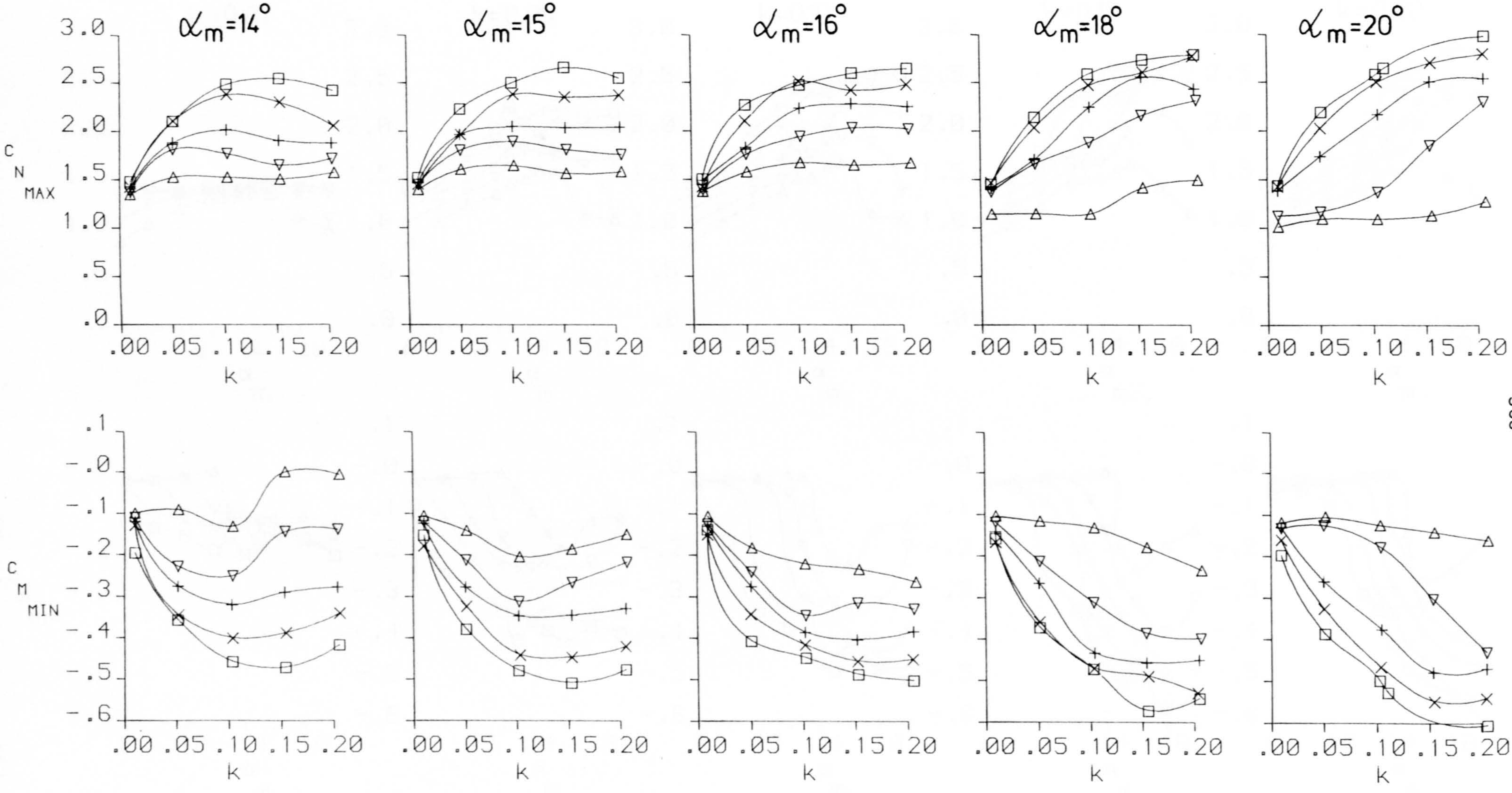

Fig 7.173 - Continued.

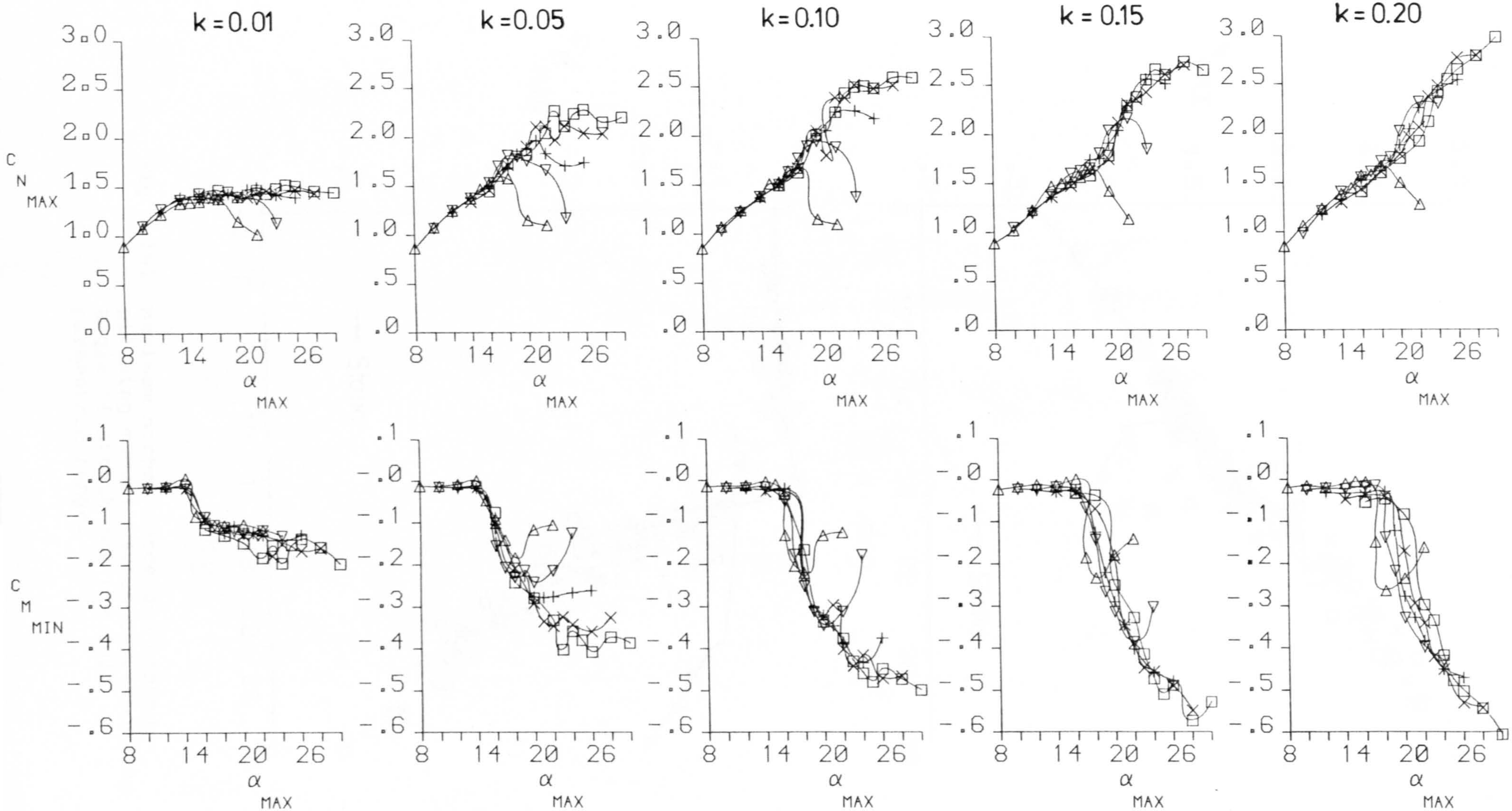

Fig 7.180 Maximum angle of attack versus maximum normal force and minimum pitching moment for various amplitudes and reduced frequencies.

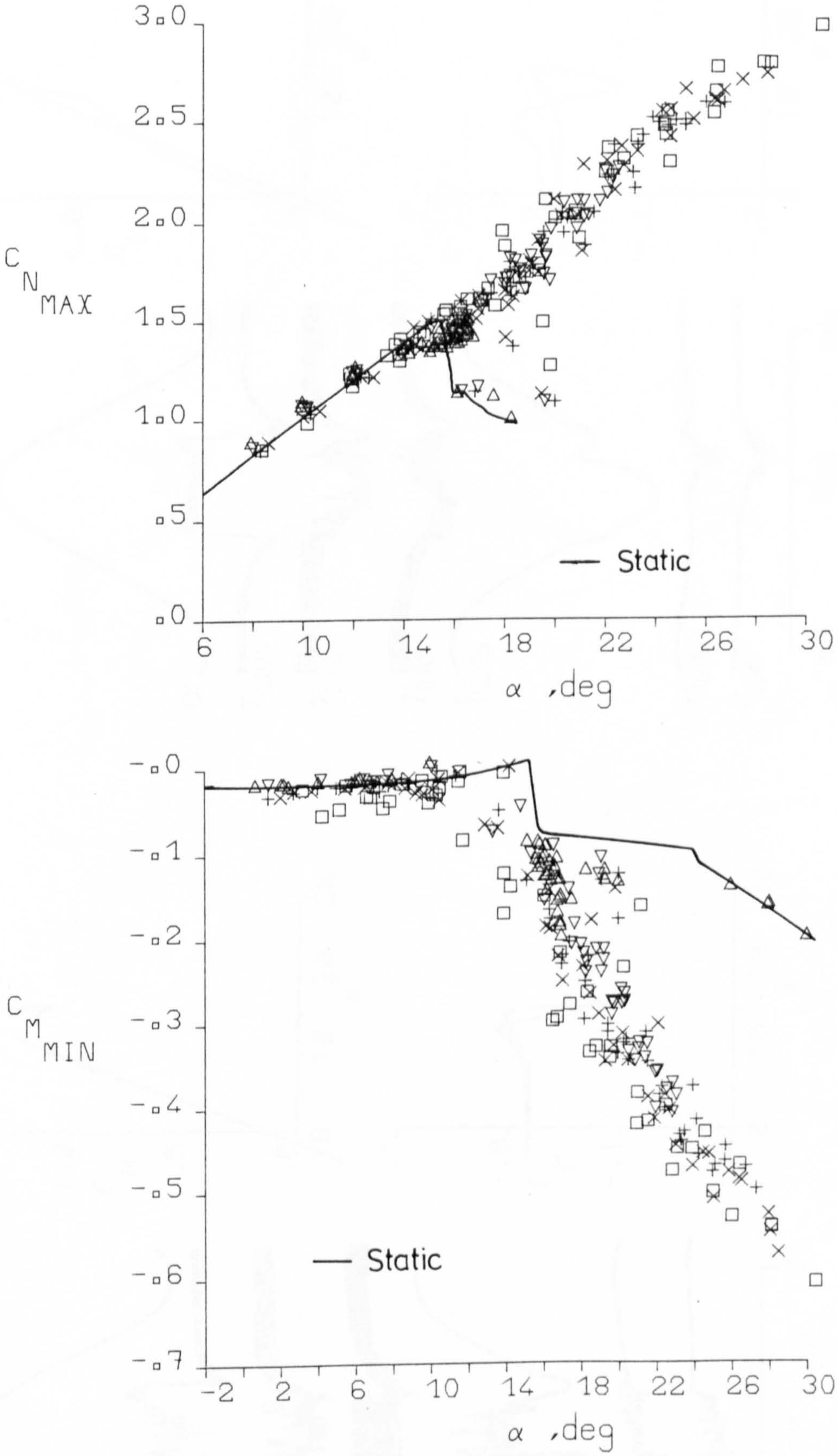

Fig 7.181 Maximum normal force and minimum pitching moment versus corresponding angle of attack for the full parametric range.

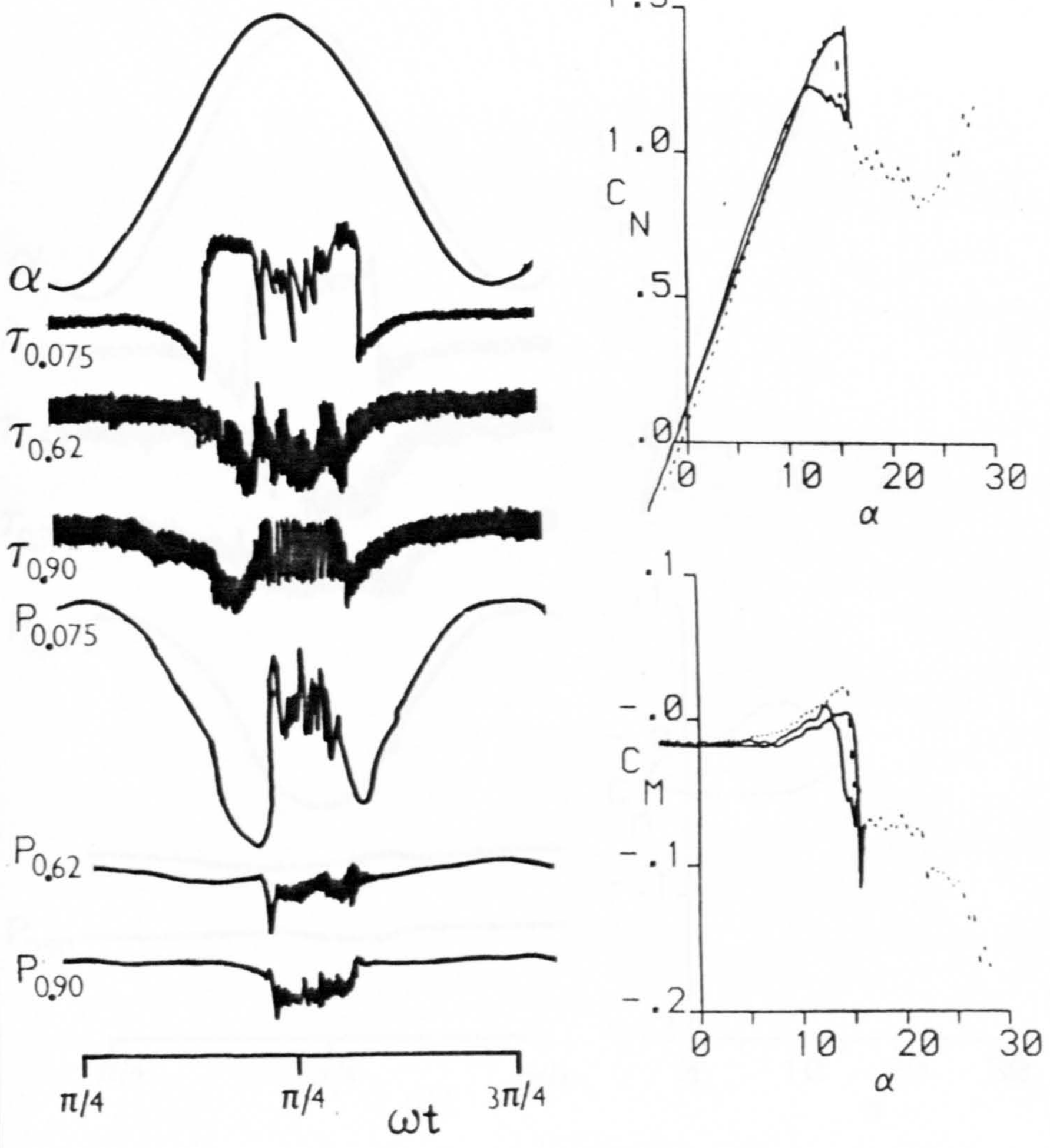

Fig 7.182 Hot-film and pressure transducer responses for $\alpha = 6 + 10 \sin \omega t$; k= 0.01

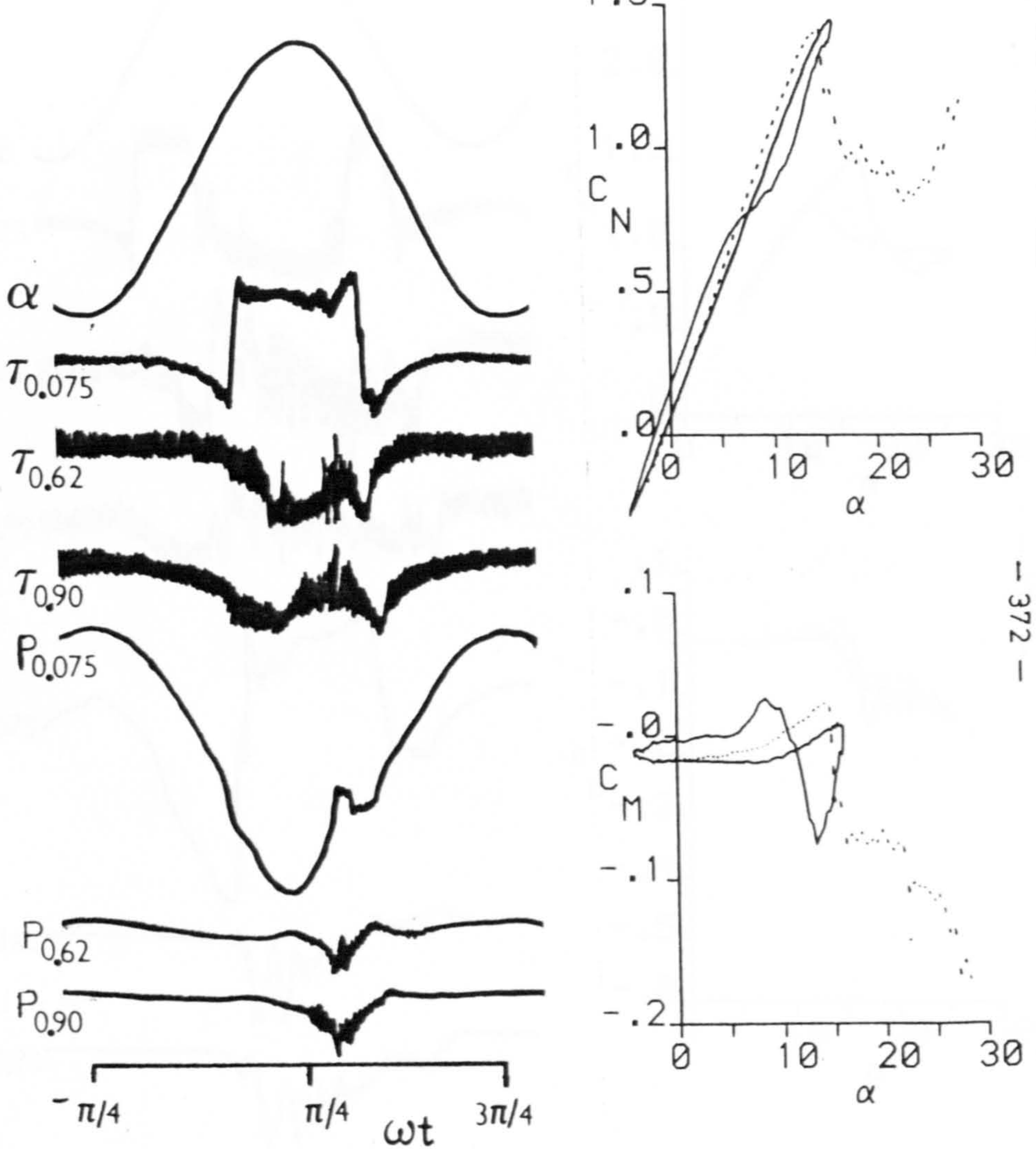

Fig 7.183 Hot-film and pressure transducer responses for $\alpha = 6 + 10 \sin \omega t$; k= 0.05

TEXT CUT OFF IN ORIGINAL

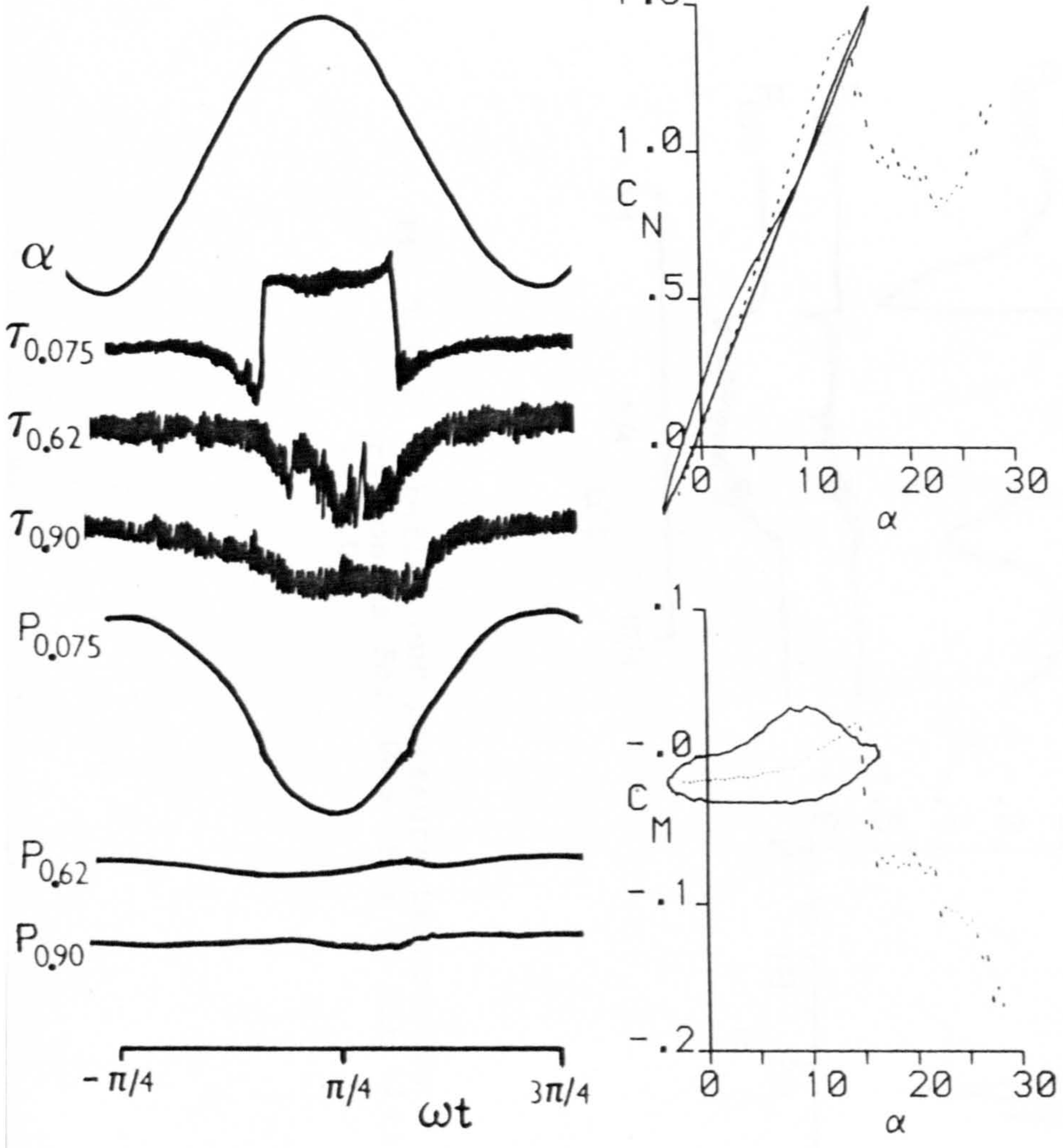

Fig 7.184 Hot-film and pressure transducer responses for $\alpha = 6 + 10 \sin \omega t$; k= 0.10

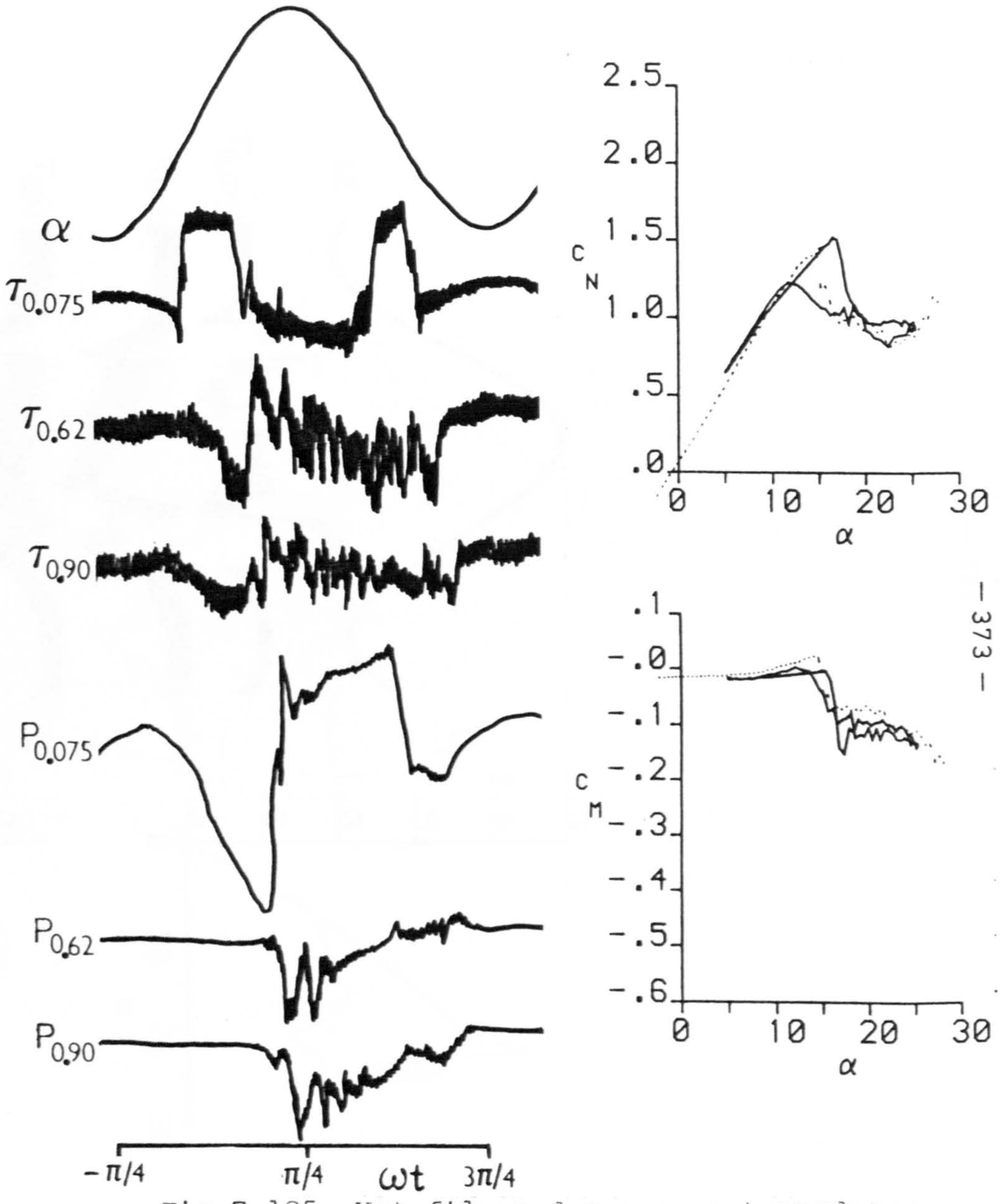

Fig 7.185 Hot-film and pressure transducer responses for $\alpha = 15 + 10 \sin \omega t$; k= 0.01

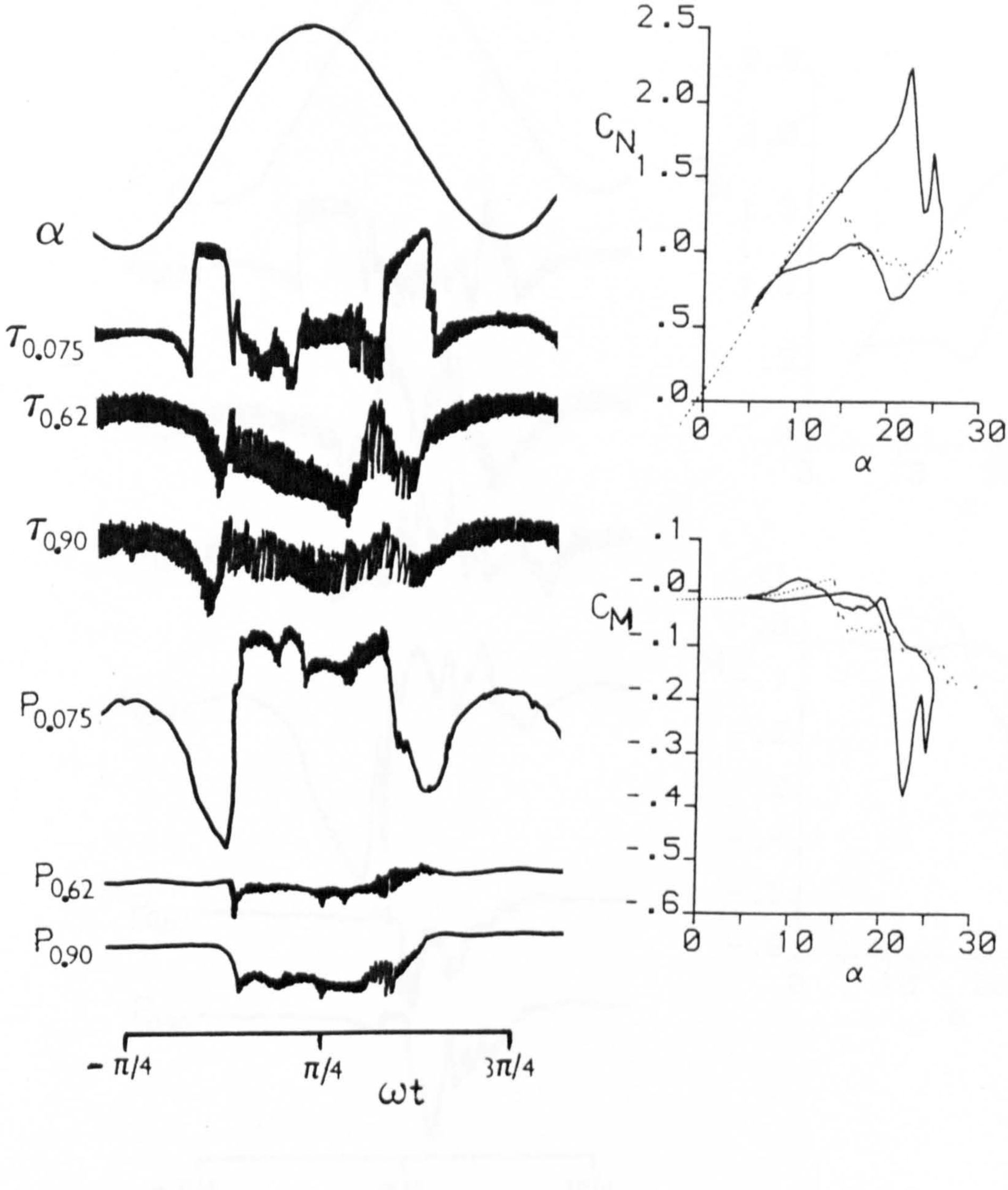

Fig 7.186 Hot-film and pressure transducer responses for $\alpha = 15 + 10 \sin \omega t$; k= 0.05

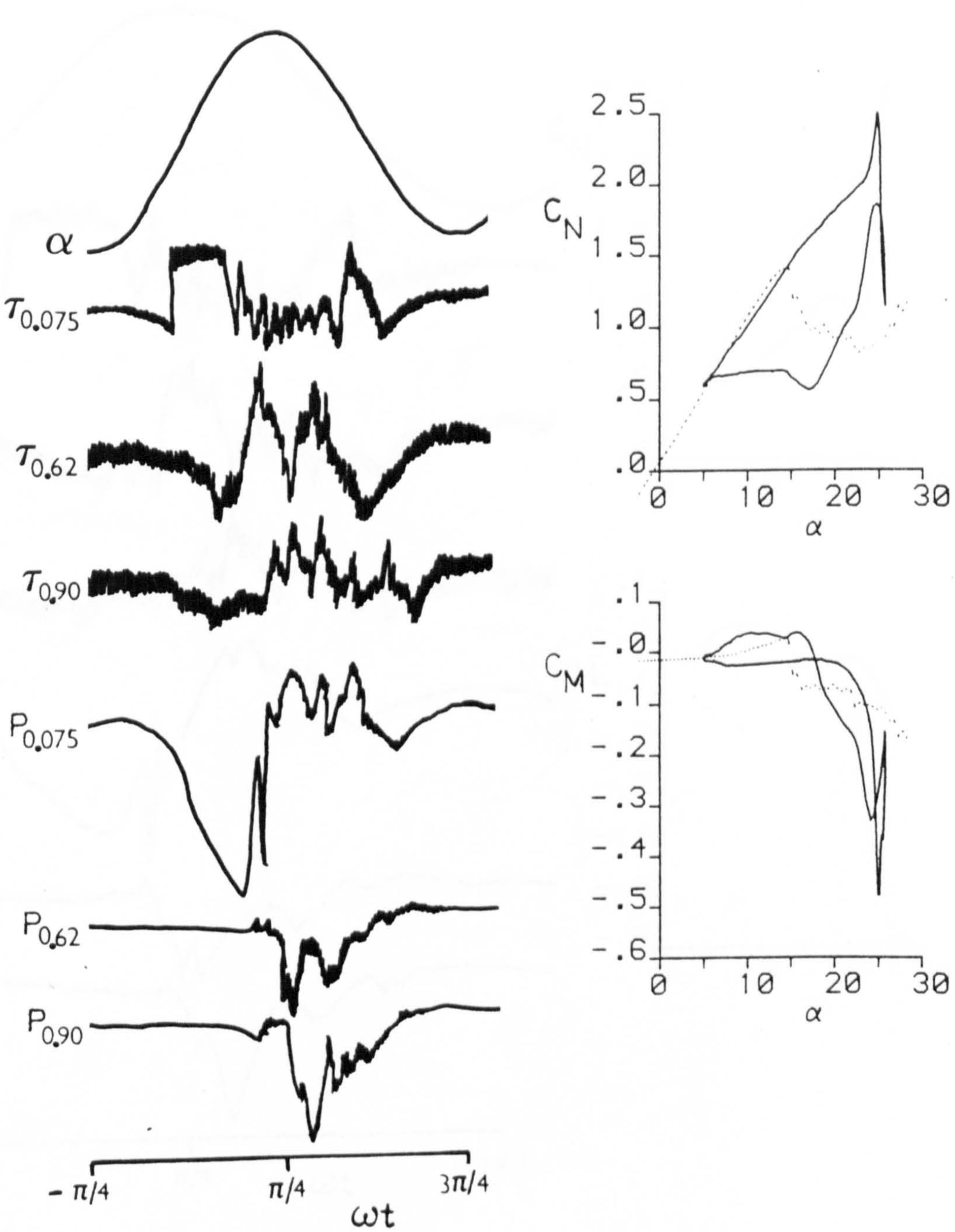

Fig 7.187 Hot-film and pressure transducer responses for $\alpha = 15 + 10 \sin \omega t$; k= 0.10

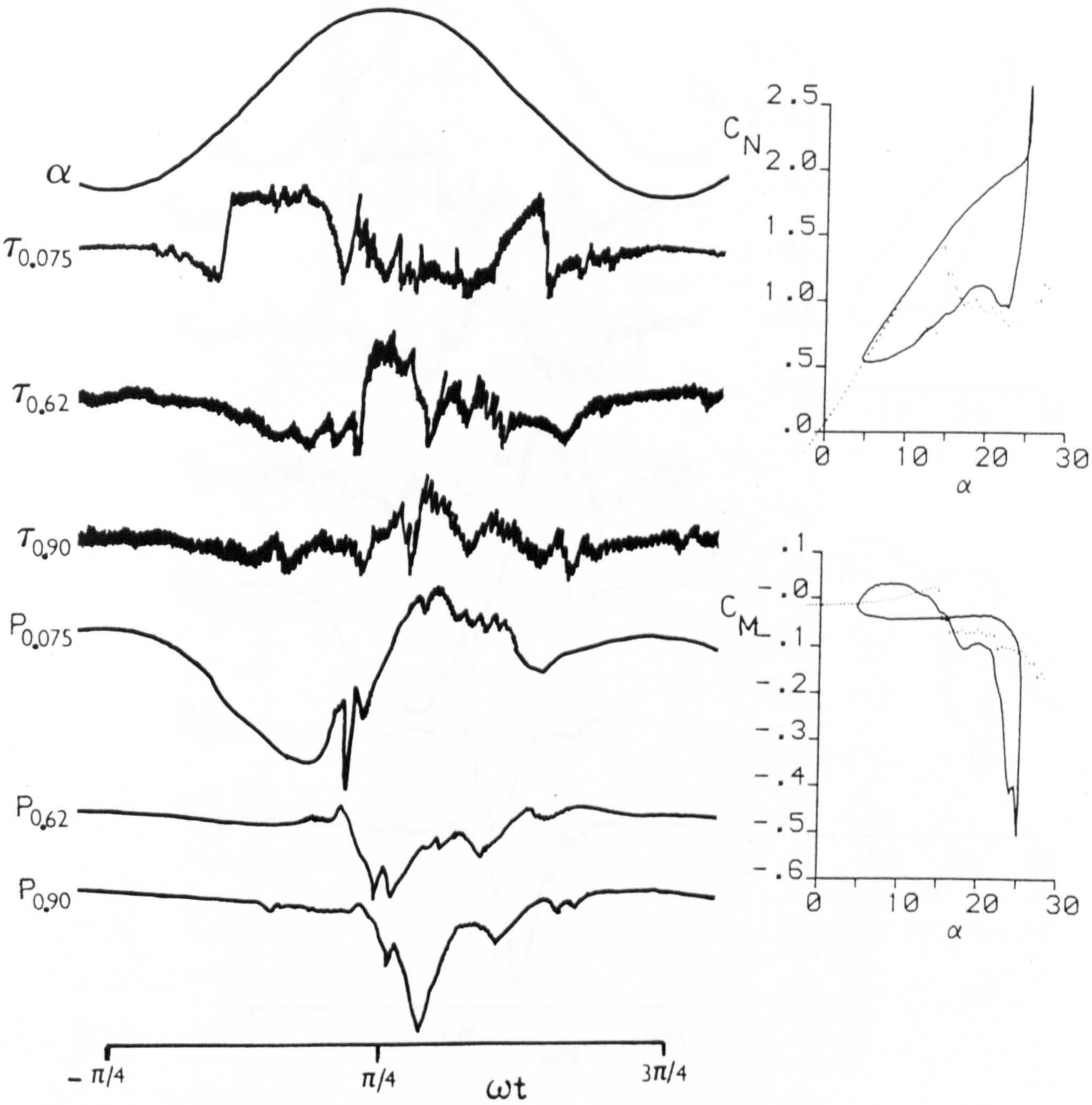

Fig 7.188 Hot-film and pressure transducer responses for $\alpha = 15 + 10 \sin \omega t$; k= 0.15

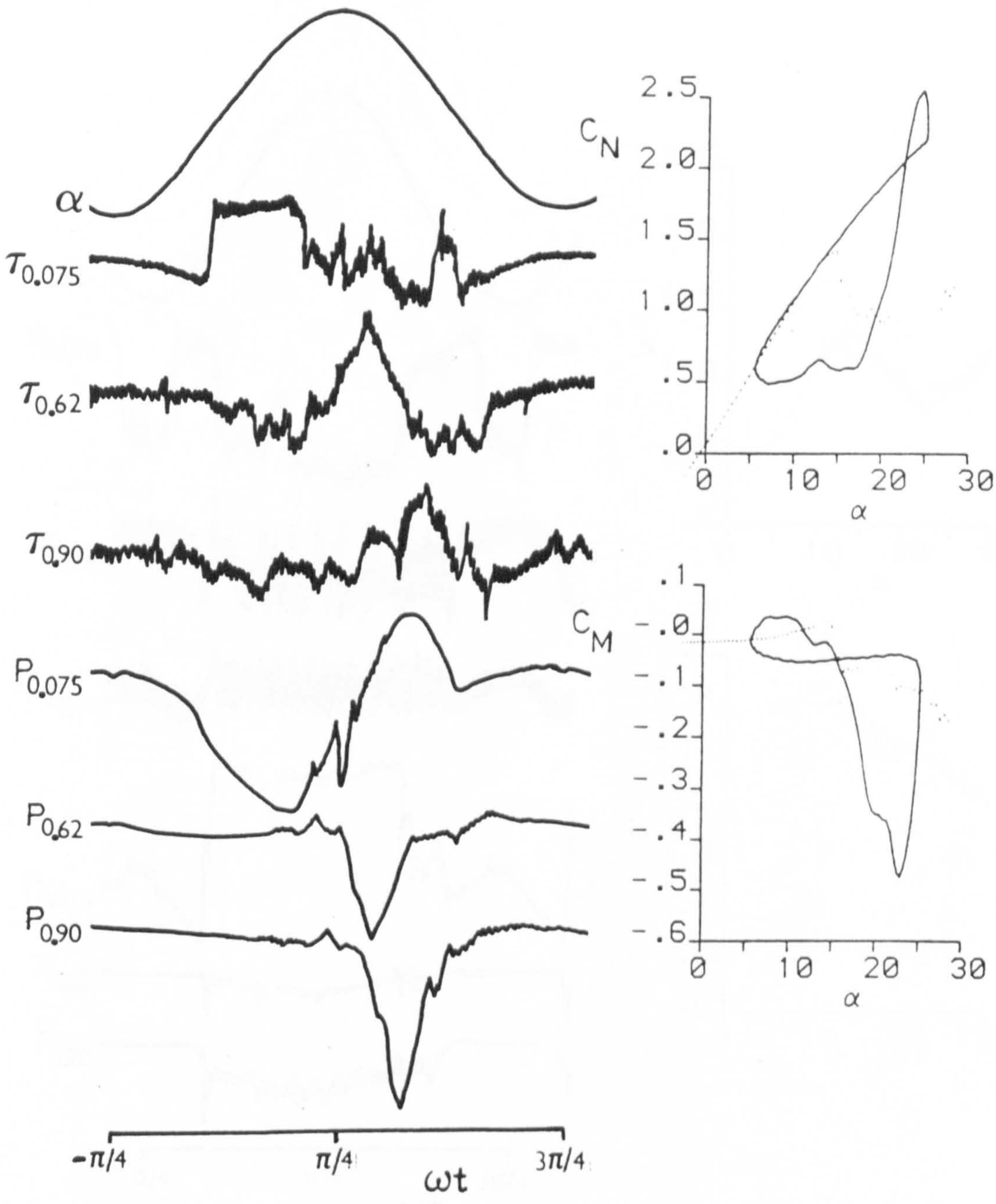

Fig 7.189 Hot-film and pressure transducer responses for $\alpha = 15 + 10 \sin \omega t$; k= 0.20

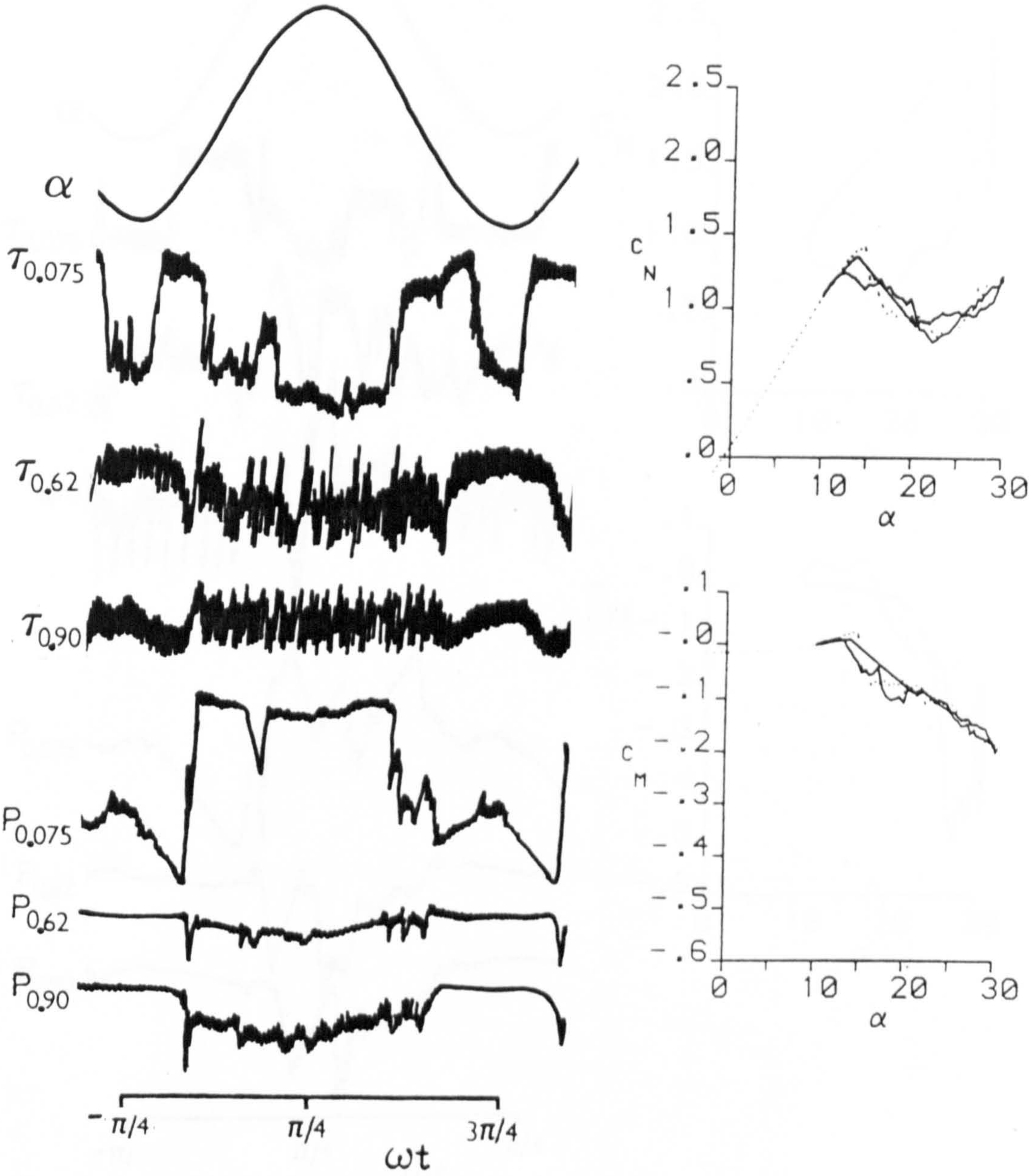

Fig 7.190 Hot-film and pressure transducer responses for $\alpha = 20 + 10 \sin \omega t$; k= 0.01

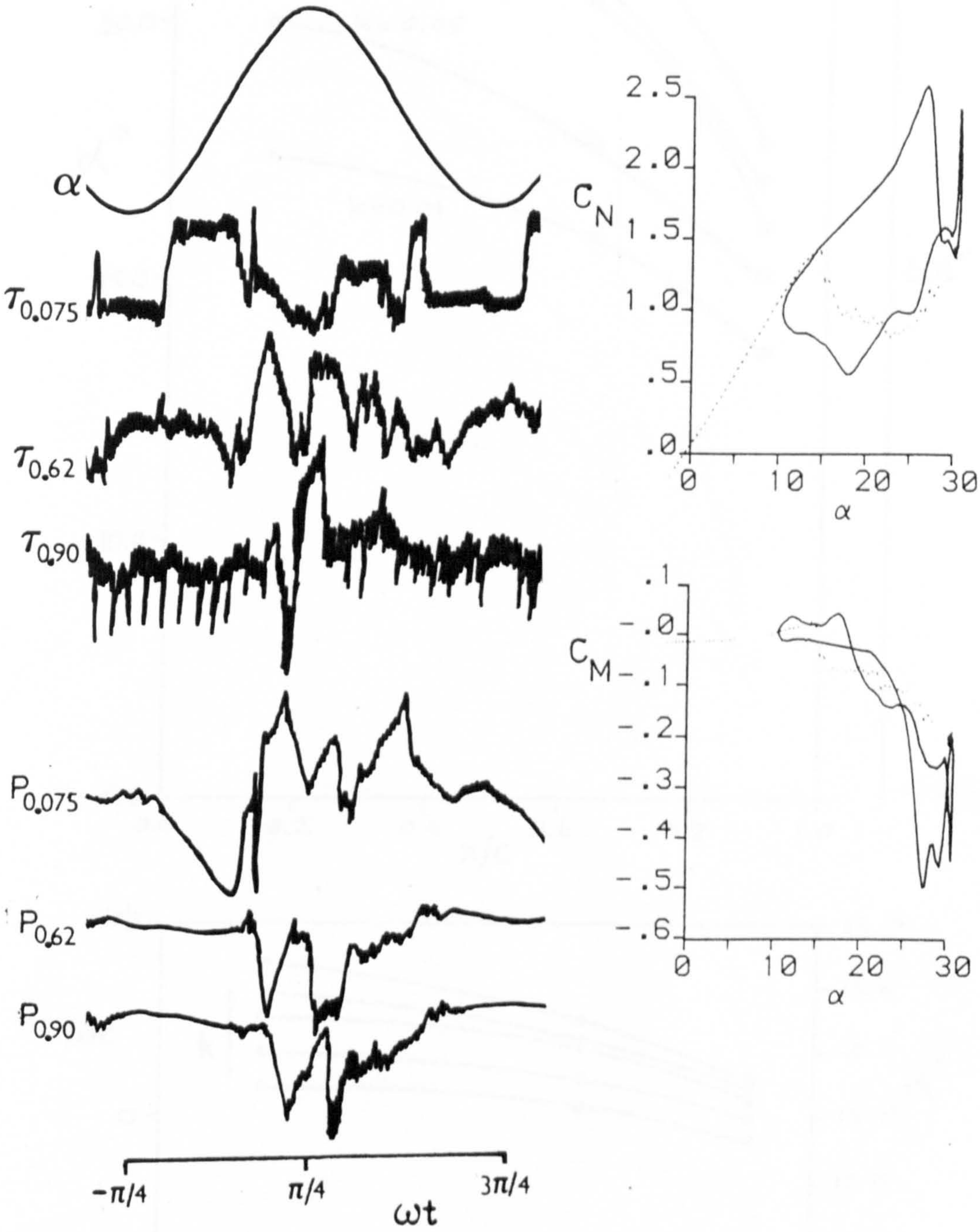

Fig 7.191 Hot-film and pressure transducer responses for $\alpha = 20 + 10 \sin \omega t$; k= 0.10

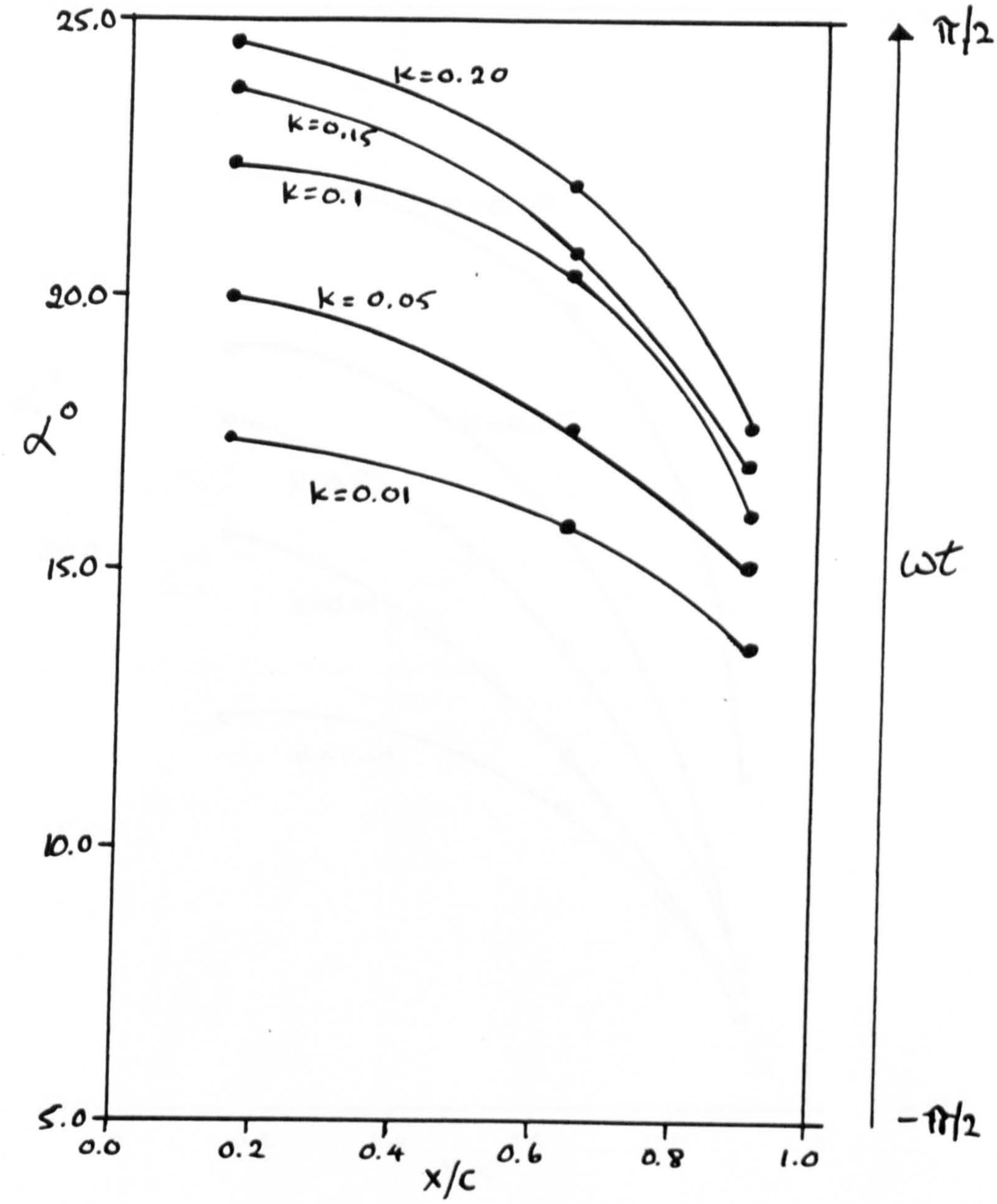

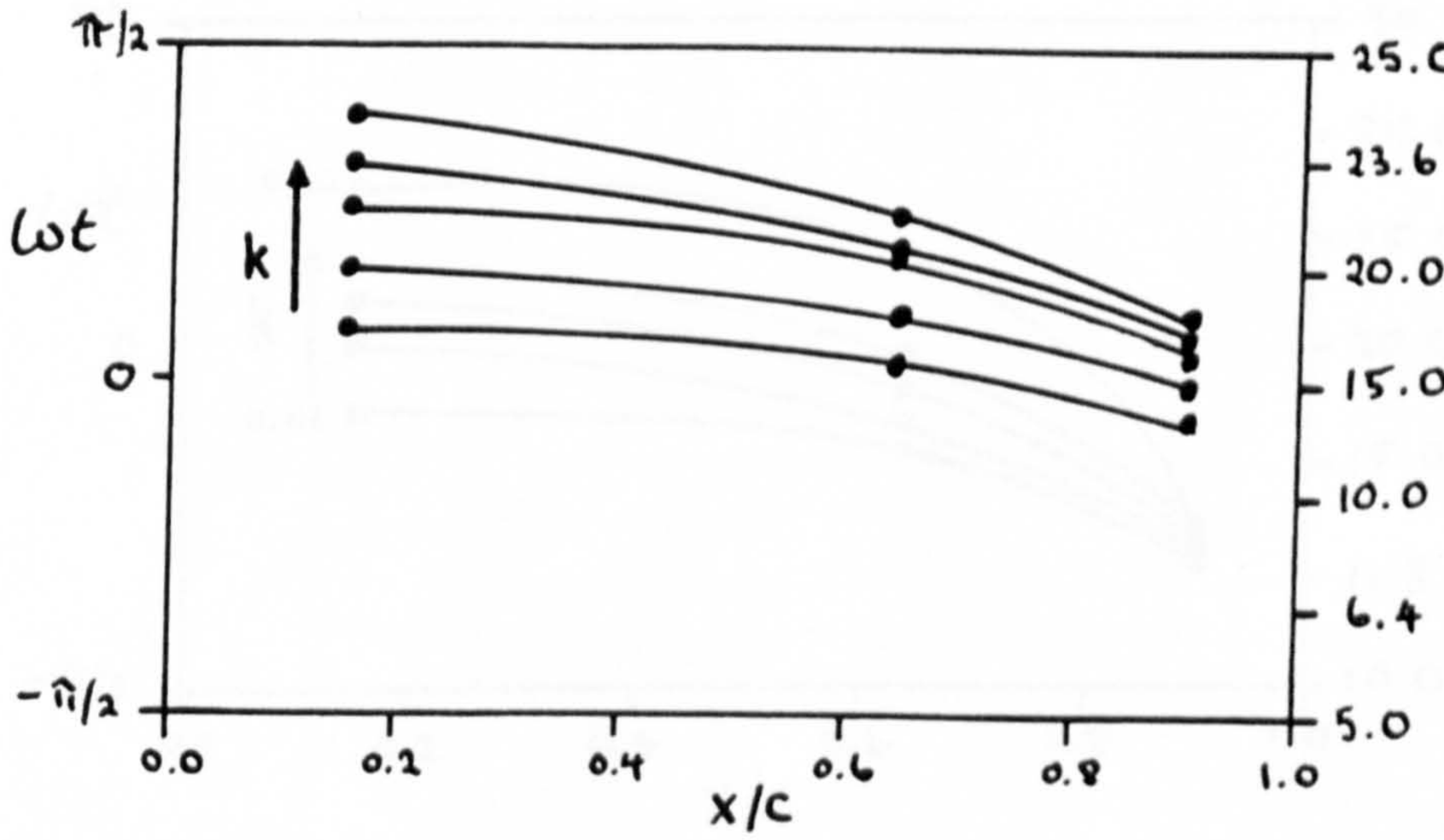

Fig 7.192 Positions of flow reversal for various reduced frequencies at a mean angle of 15° and amplitude of 10°.

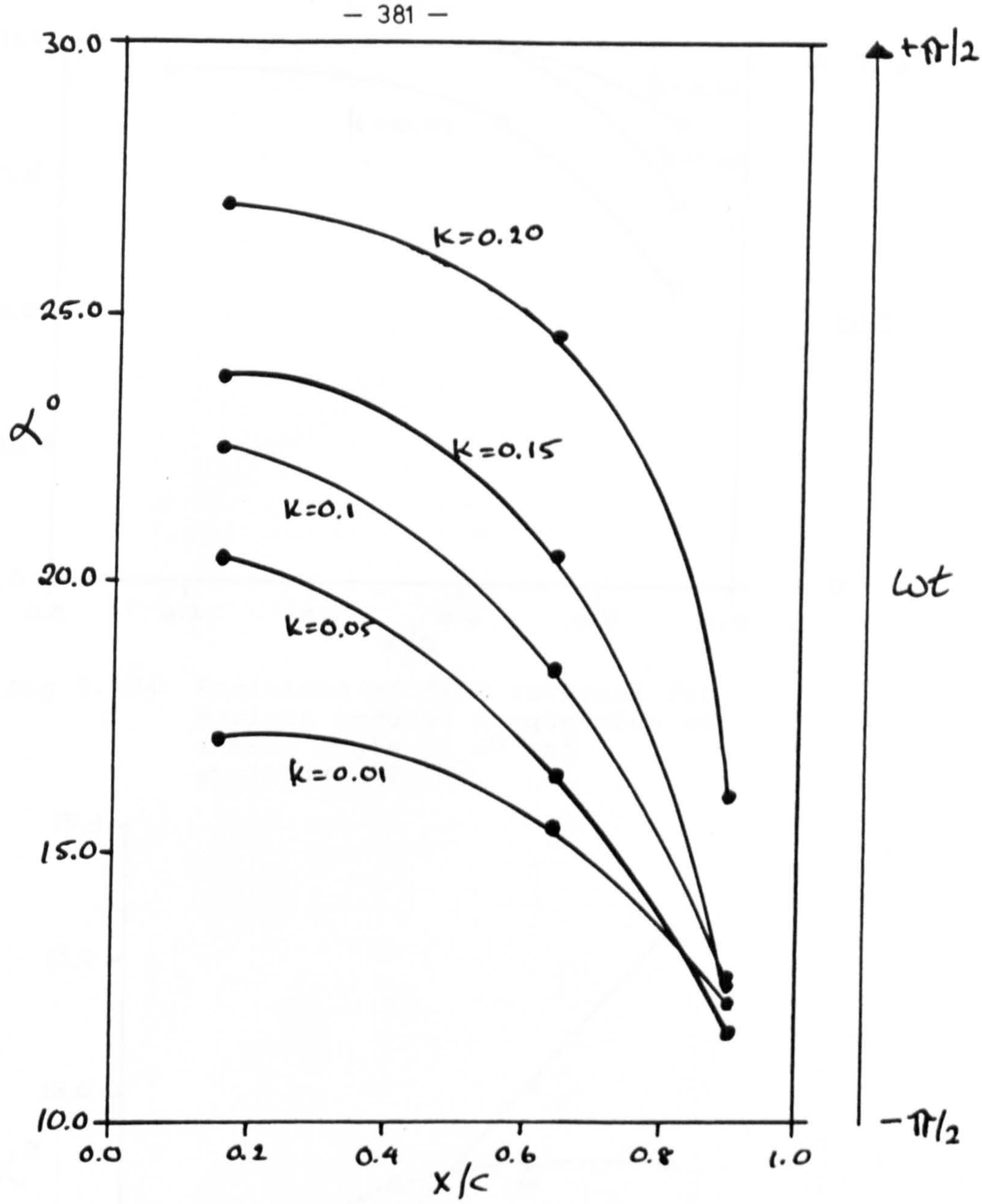

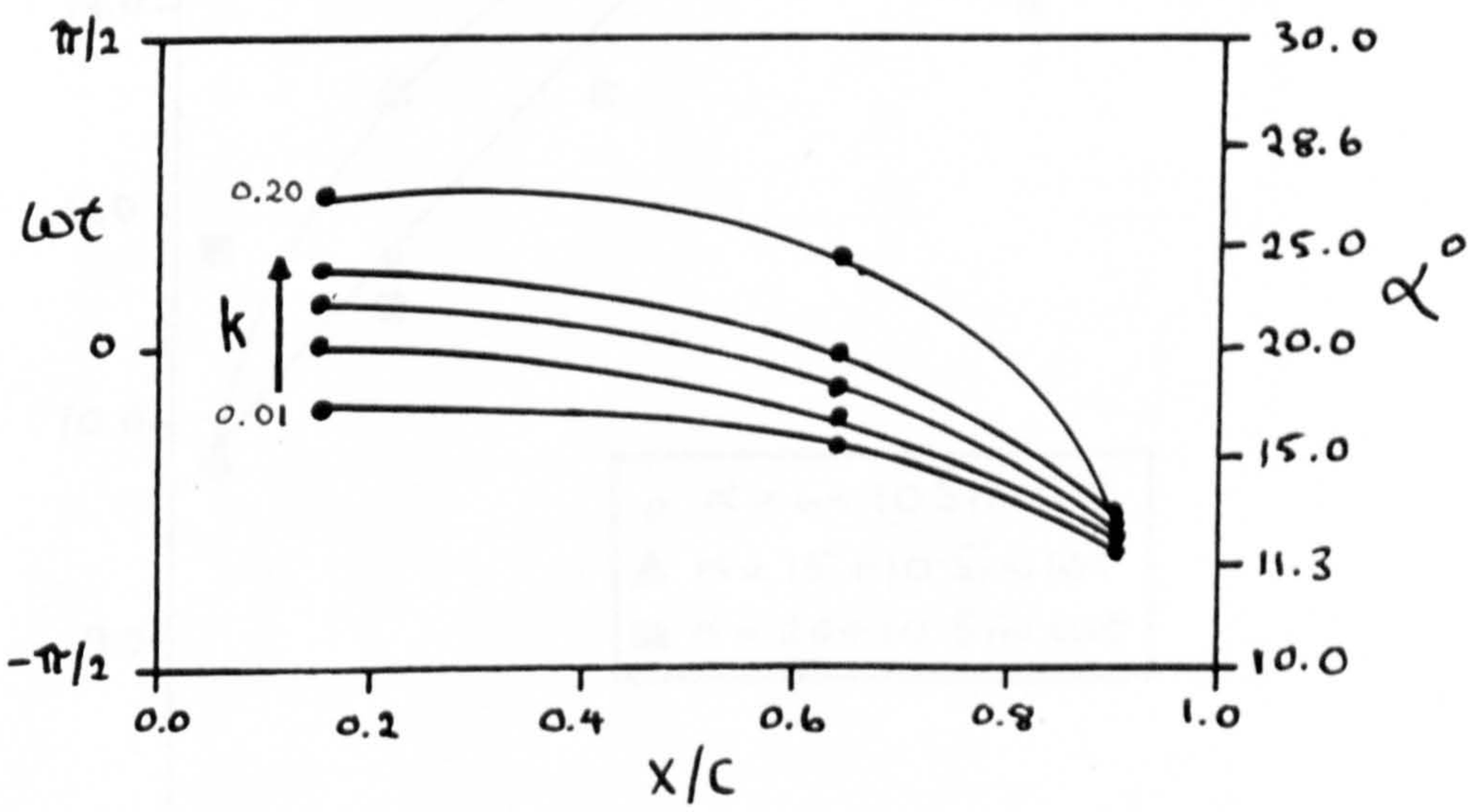

Fig 7.193 Positions of flow reversal for various reduced frequencies at a mean angle of 20° and amplitude of 10°.

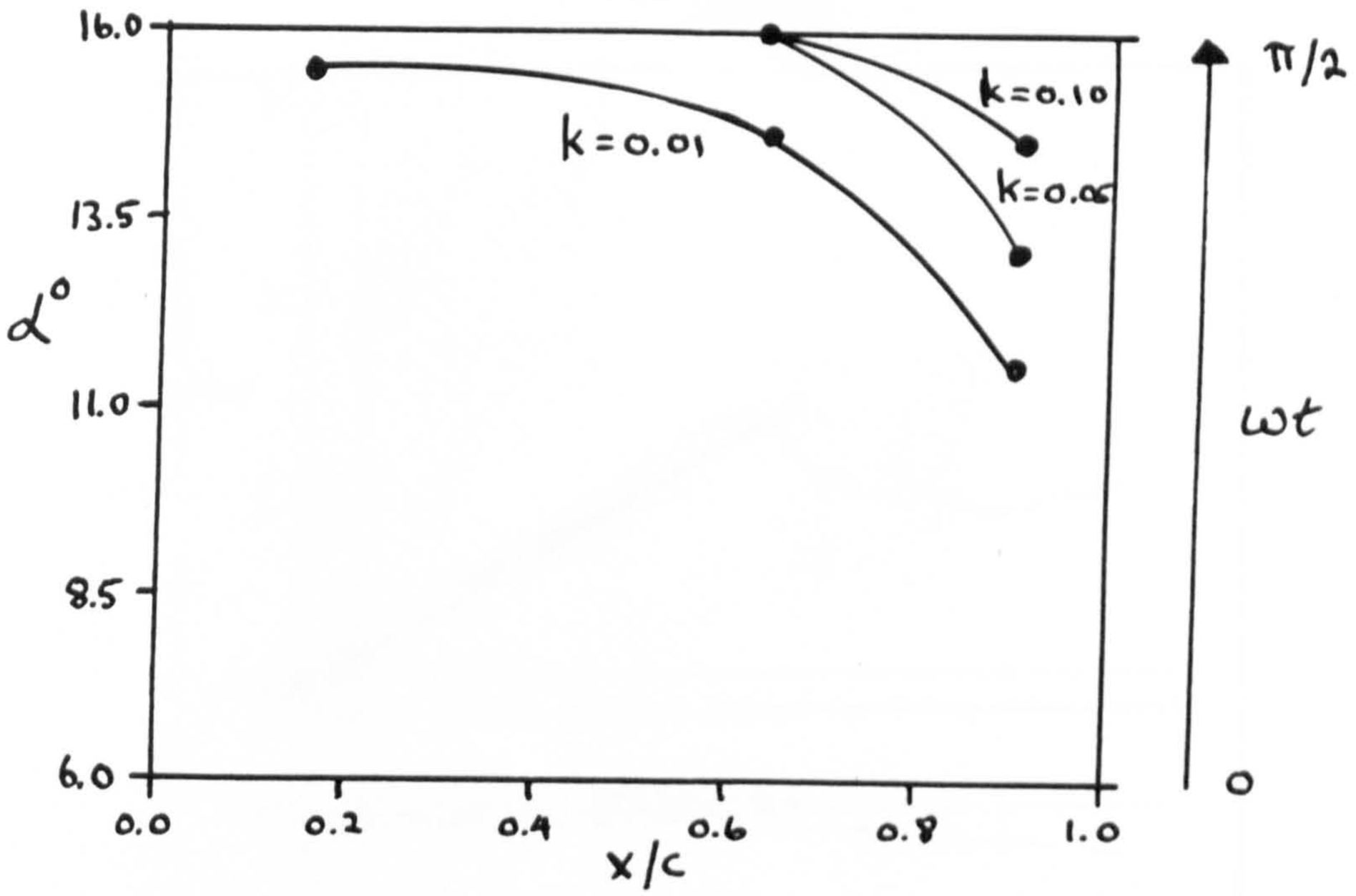

Fig 7.194 Positions of flow reversal for various reduced frequencies at a mean angle of 6° and amplitude of 10°.

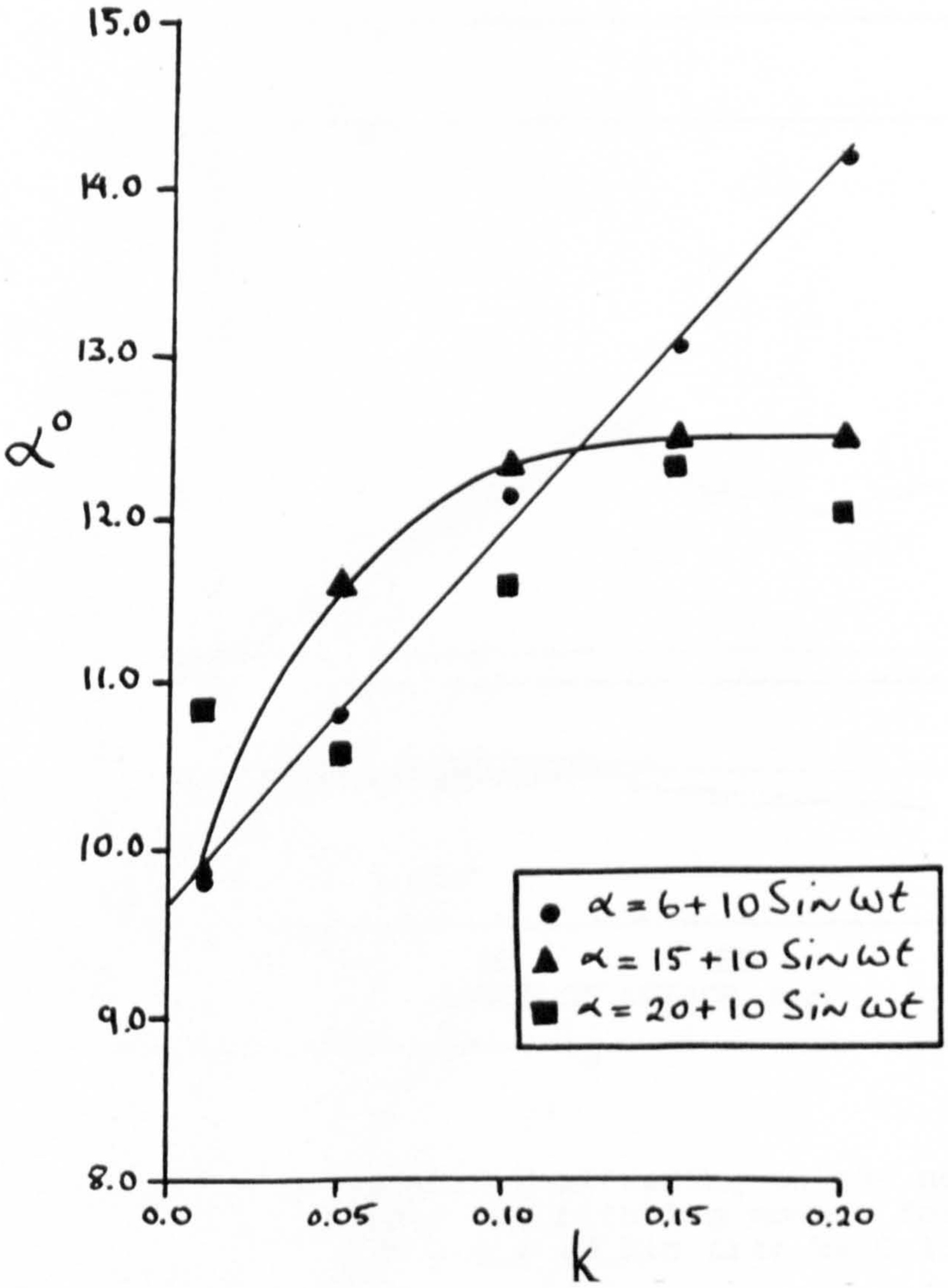

Fig 7.195 Angle of attack for transition at 7.5% chord versus reduced frequency, for mean angles of 6°, 15° and 20° at an amplitude of 10°.

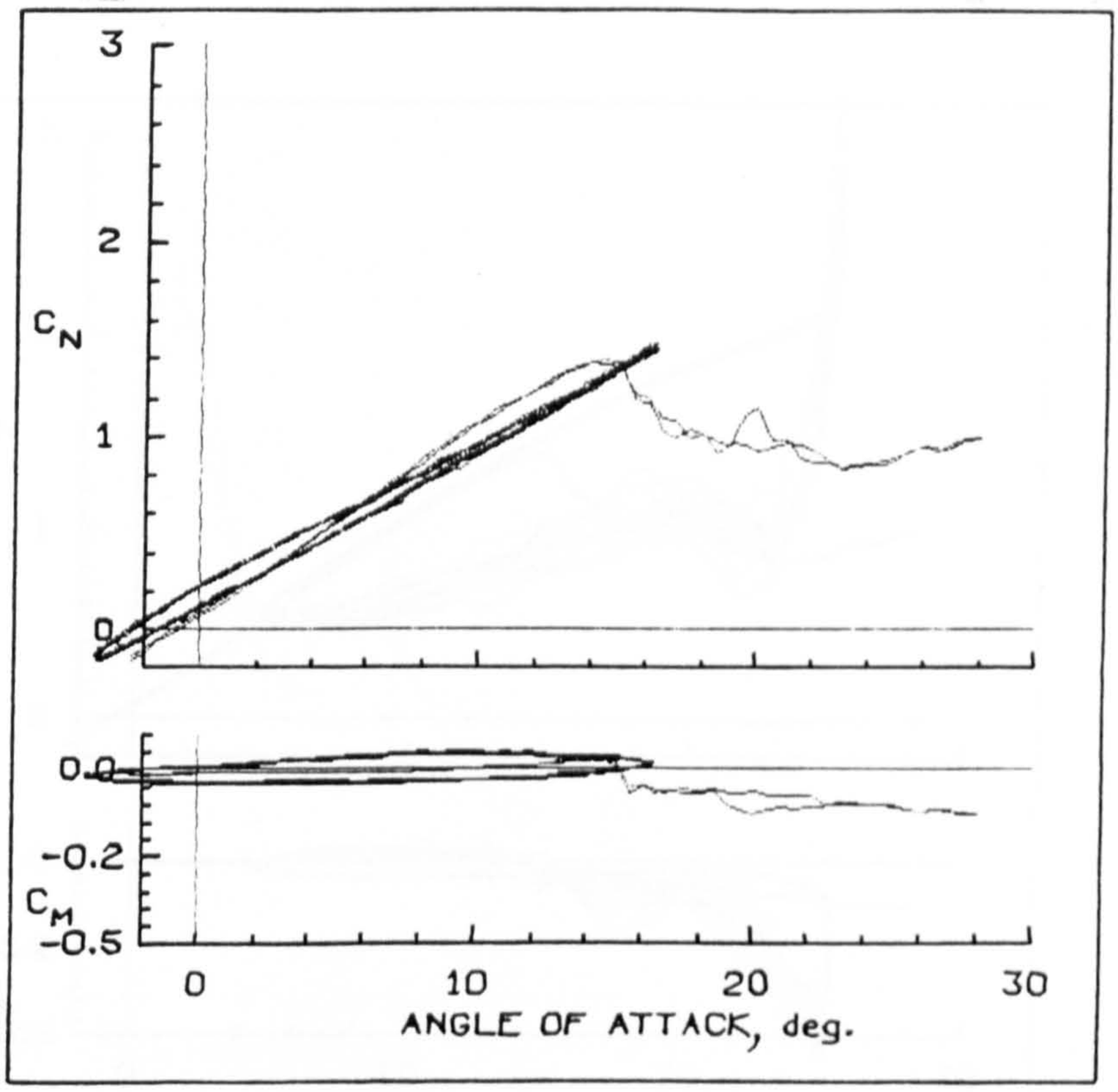

Fig 7.196 Effect of averaging on the normal force and pitching moment for $\alpha = 6 + 10 \sin \omega t$; k= 0.15

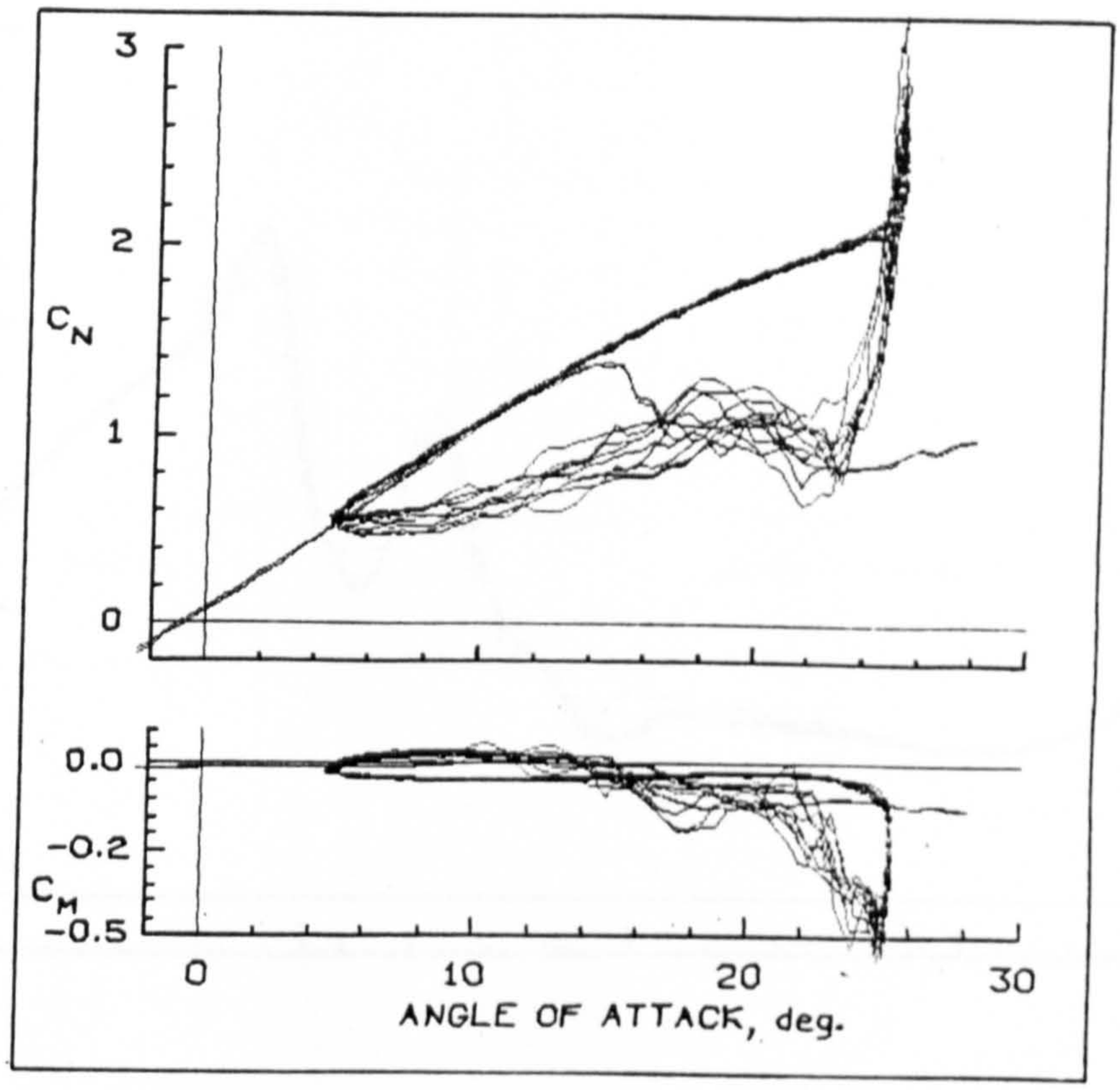

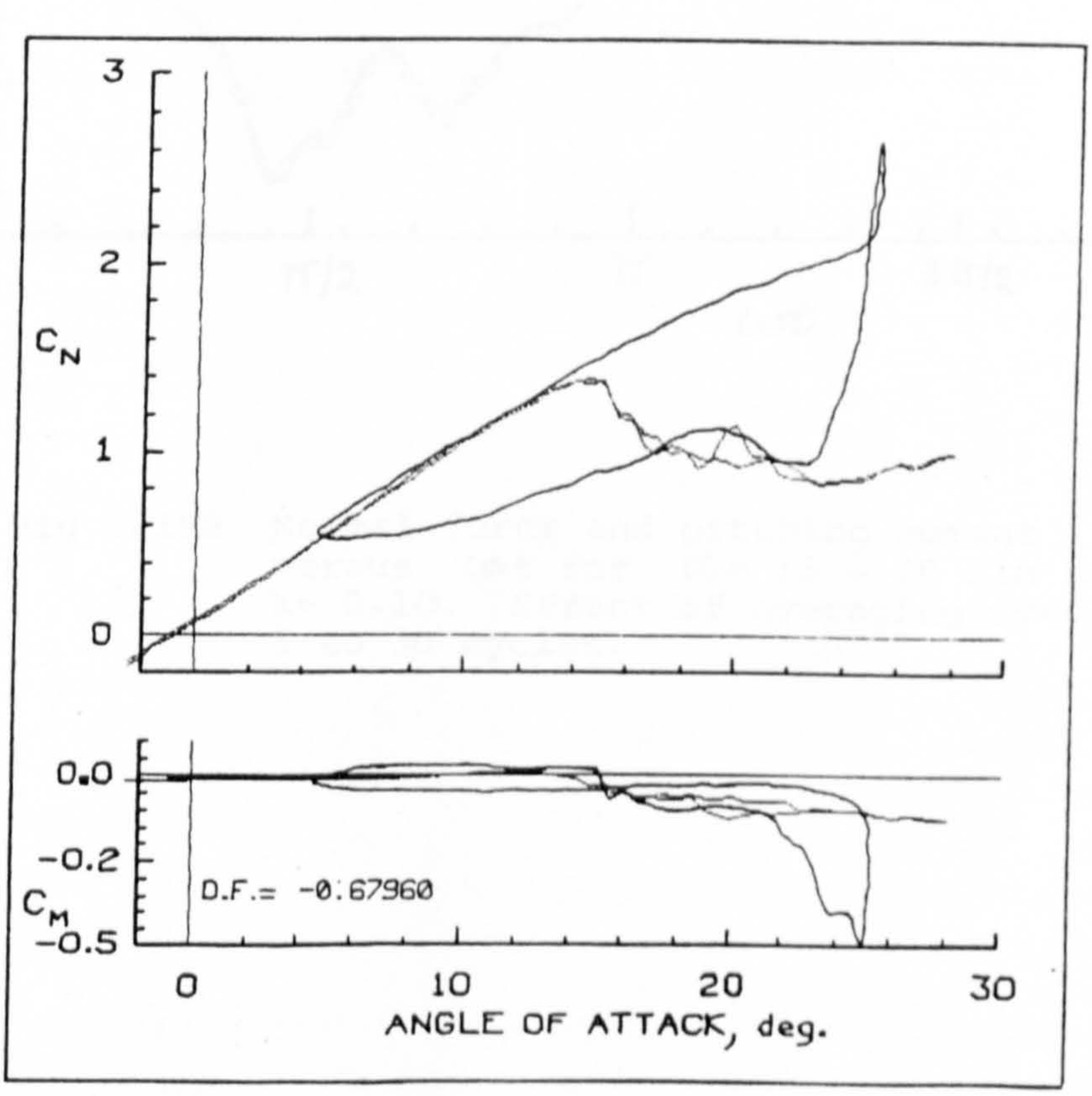

Fig 7.197 Effect of averaging on the normal force and pitching moment for $\alpha = 15 + 10 \sin \omega t$; k= 0.15

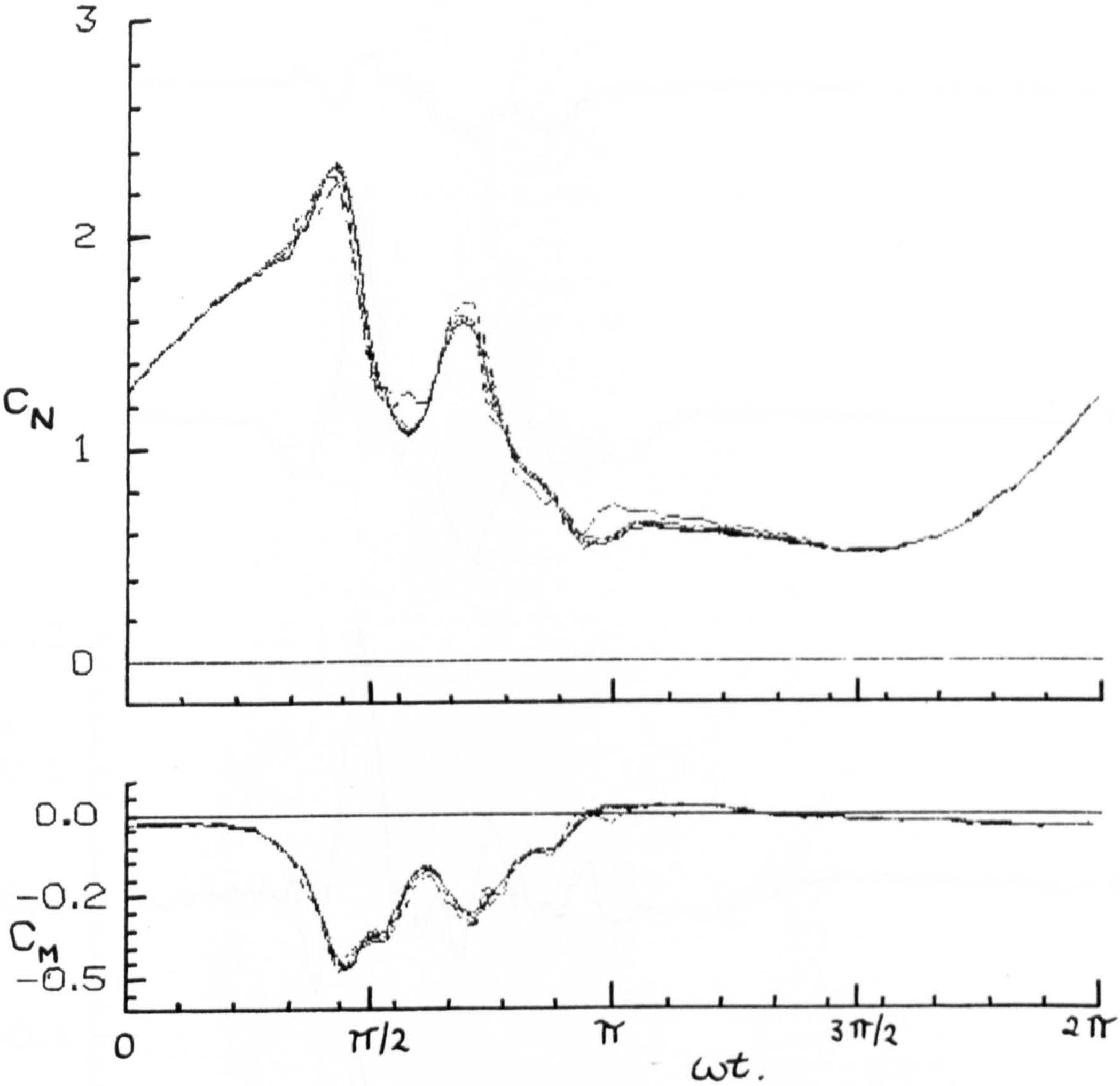

Fig 7.198 Normal force and pitching moment versus ωt for $\alpha = 15 + 10 \sin \omega t$; k= 0.10. Effect of averaging over 1 to 30 cycles.

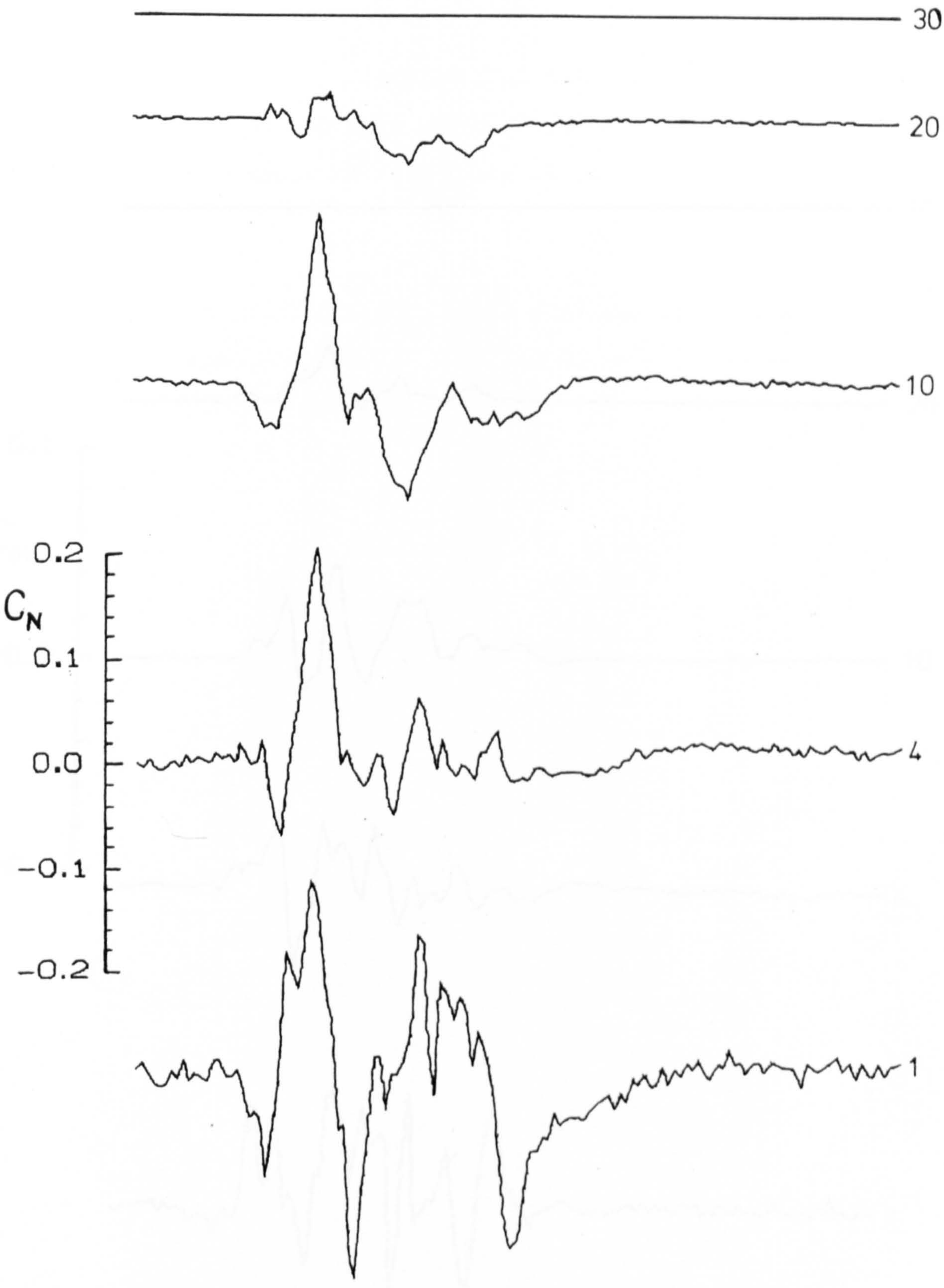

Fig 7.199 Normal force arithmetic differences between averaging over 30,20,10,4 and 1 cycles ($\alpha = 15 + 10 \sin \omega t$; k= 0.10).

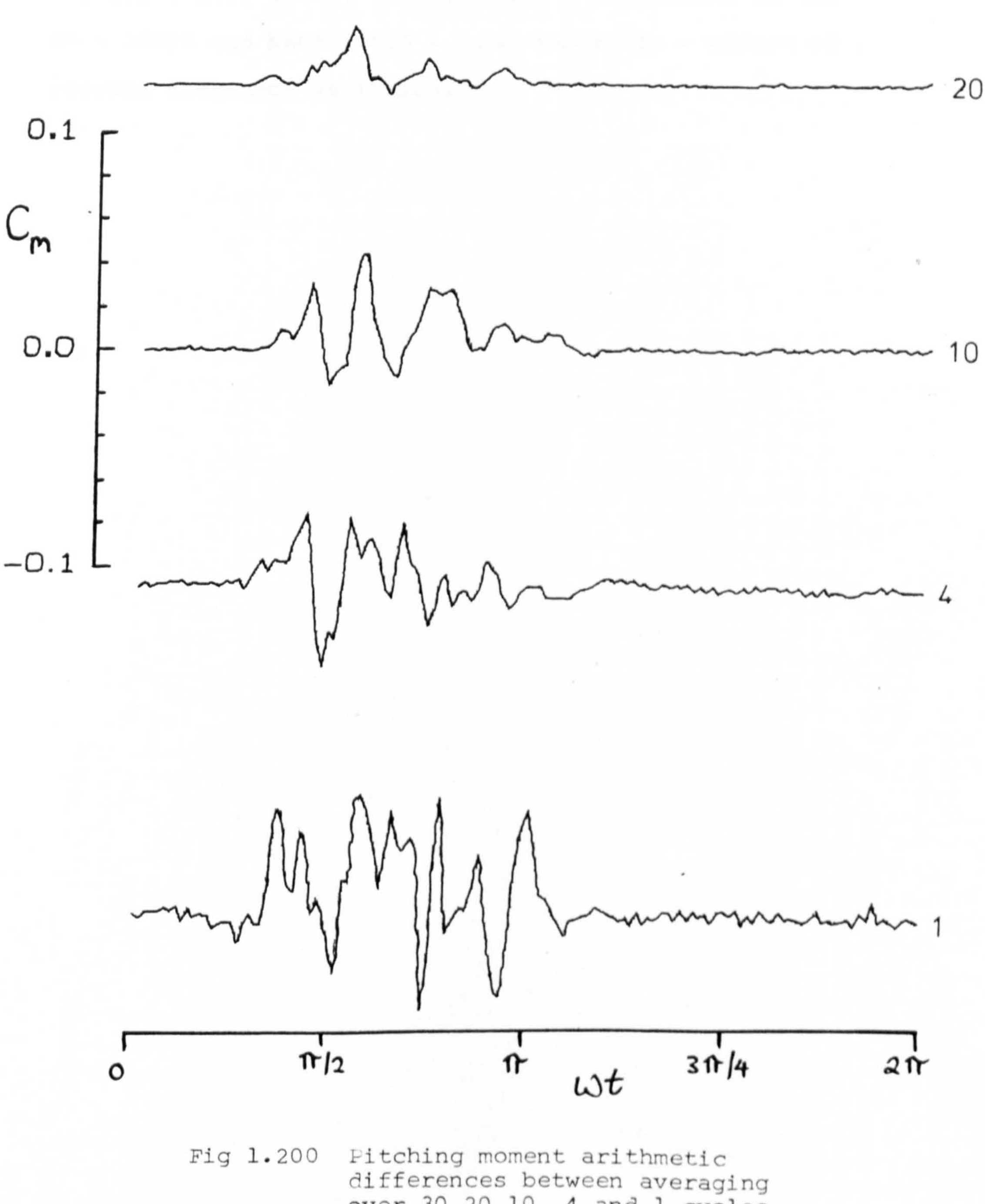

Fig 1.200 Pitching moment arithmetic differences between averaging over 30,20,10, 4 and 1 cycles (α = 15 + 10 Sin ωt; k= 0.10)

Figures 7.201, 7.202, 7.203, 7.204, 7.205 ÷ Comparison of the NACA 23012 and NACA 23010 - 1.58 aerofoils - effect of mean angle of attack variation.

Figures 7.206, 7.207, 7.208, 7.209 ÷ Comparison of the NACA 23012 and NACA 23010 - 1.58 aerofoils - effect of reduced frequency variation.

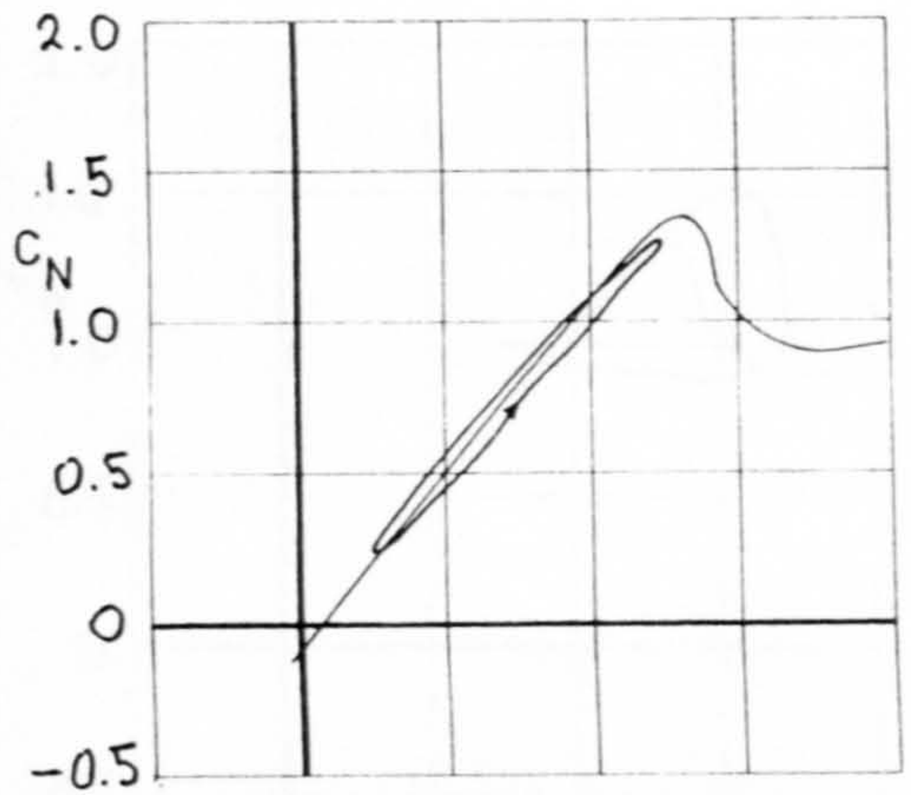

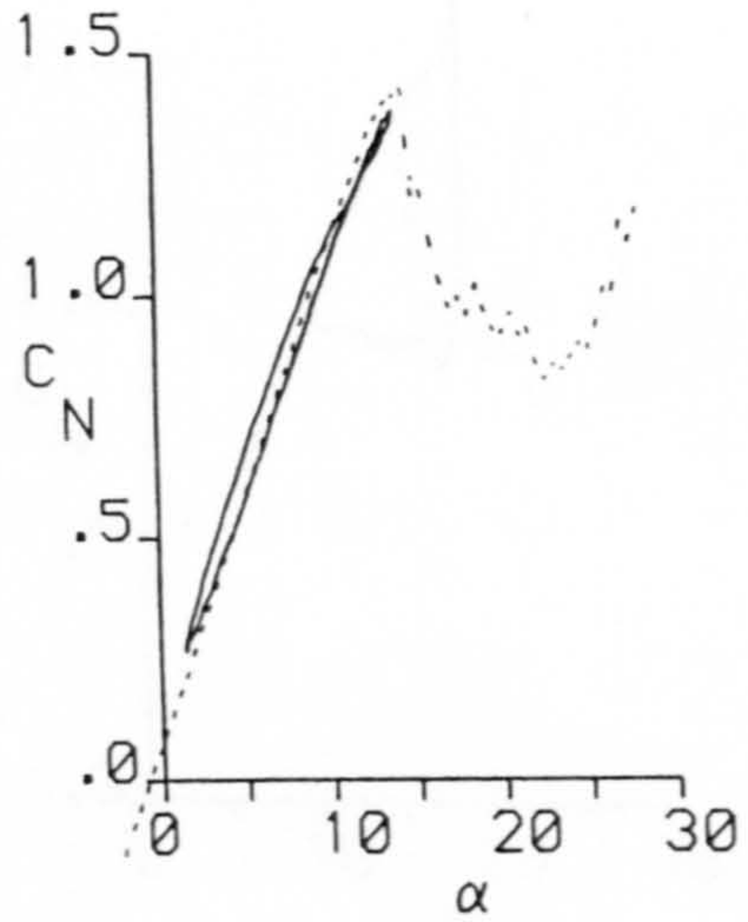

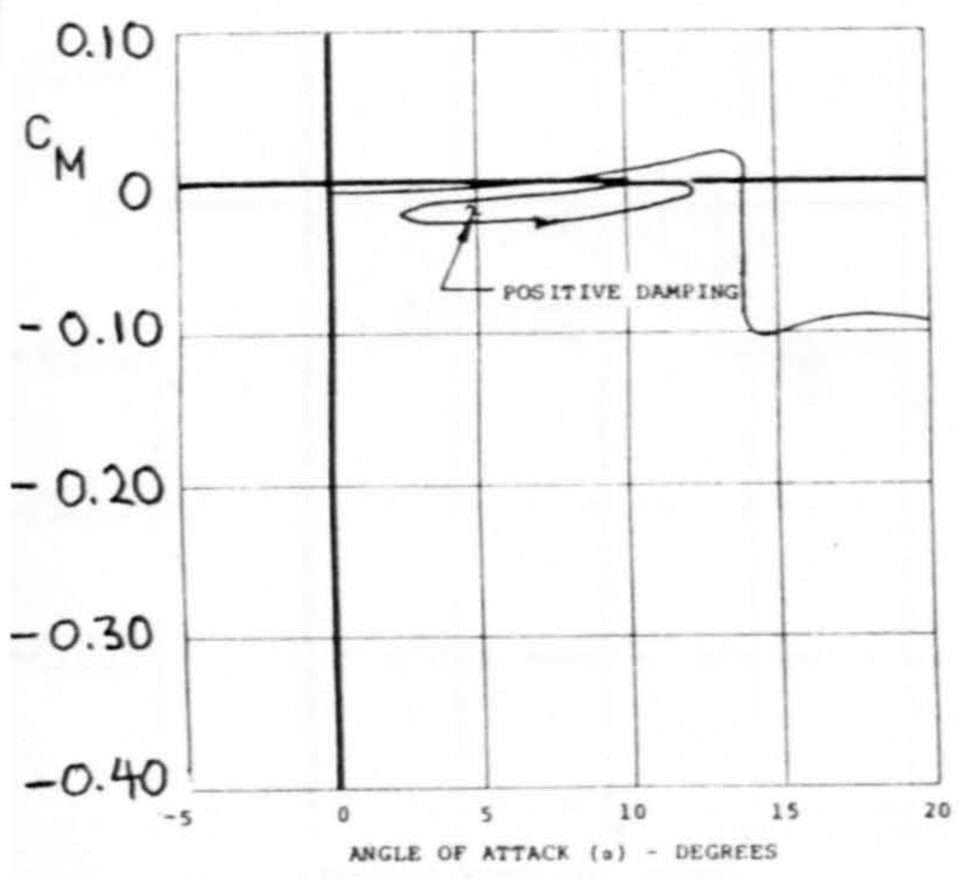

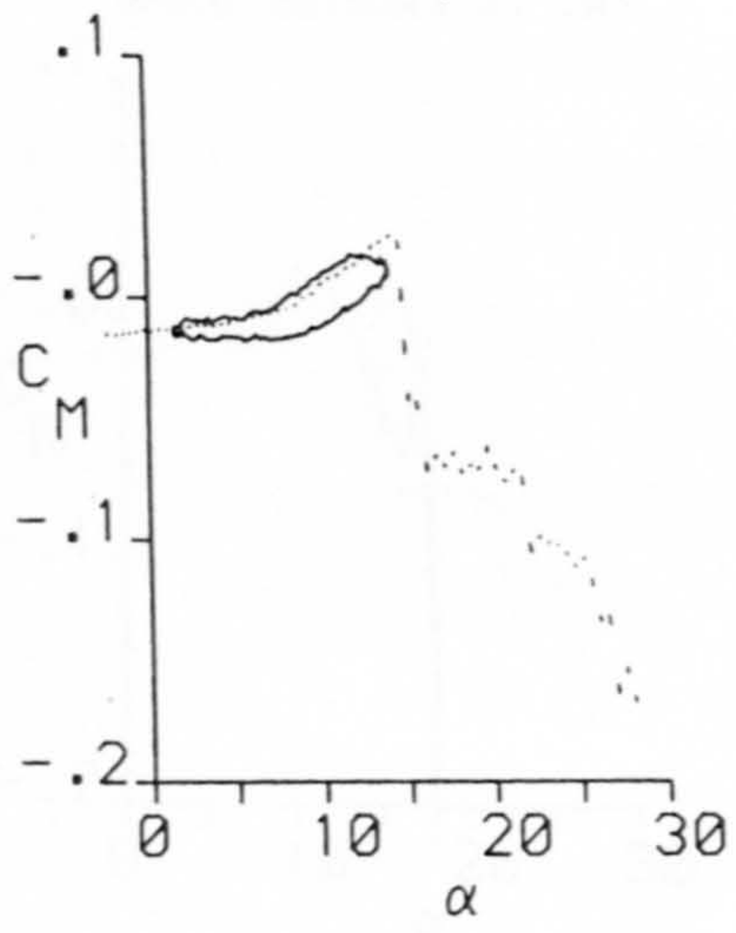

Figure 7.201

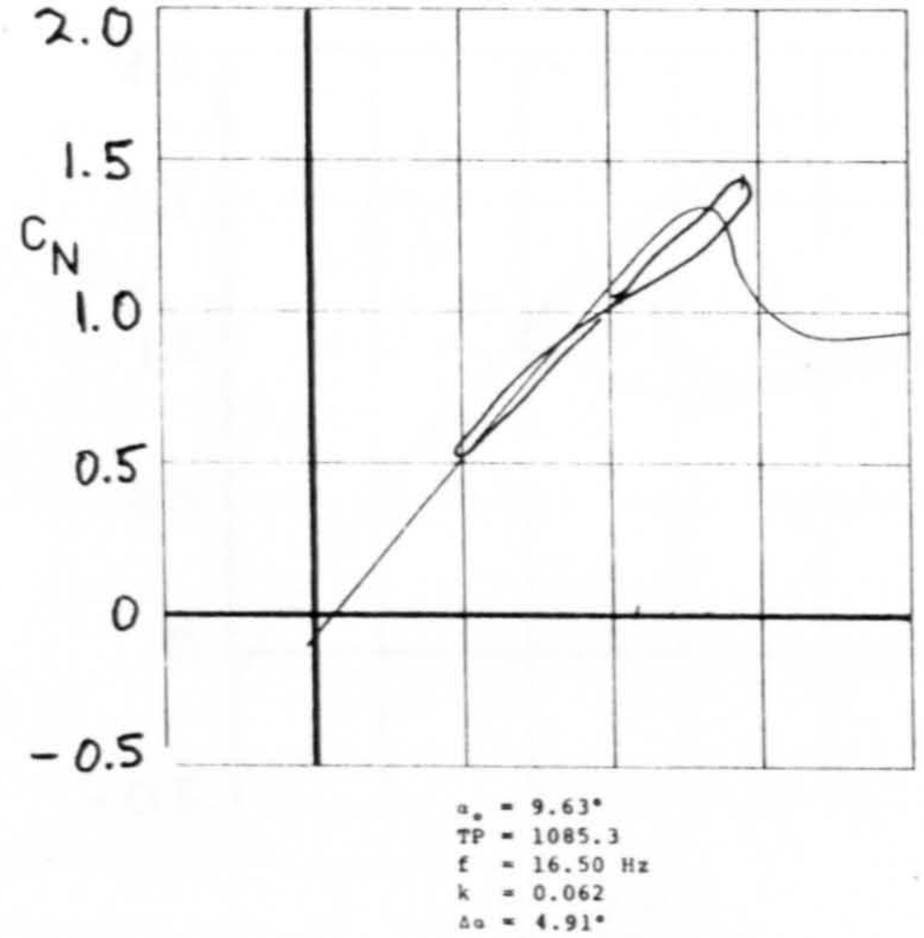

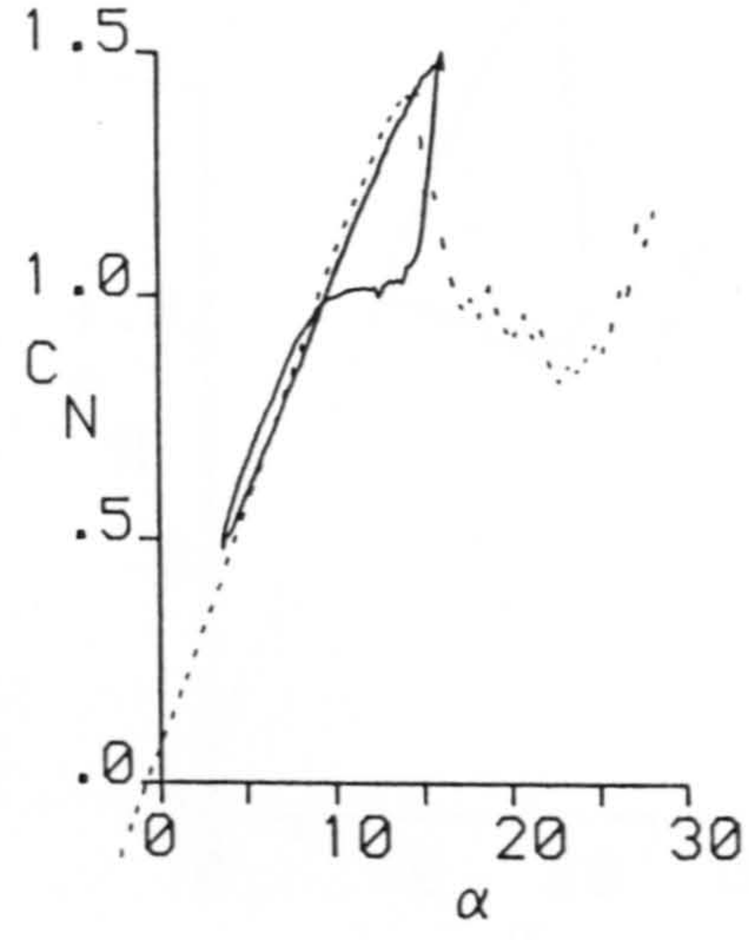

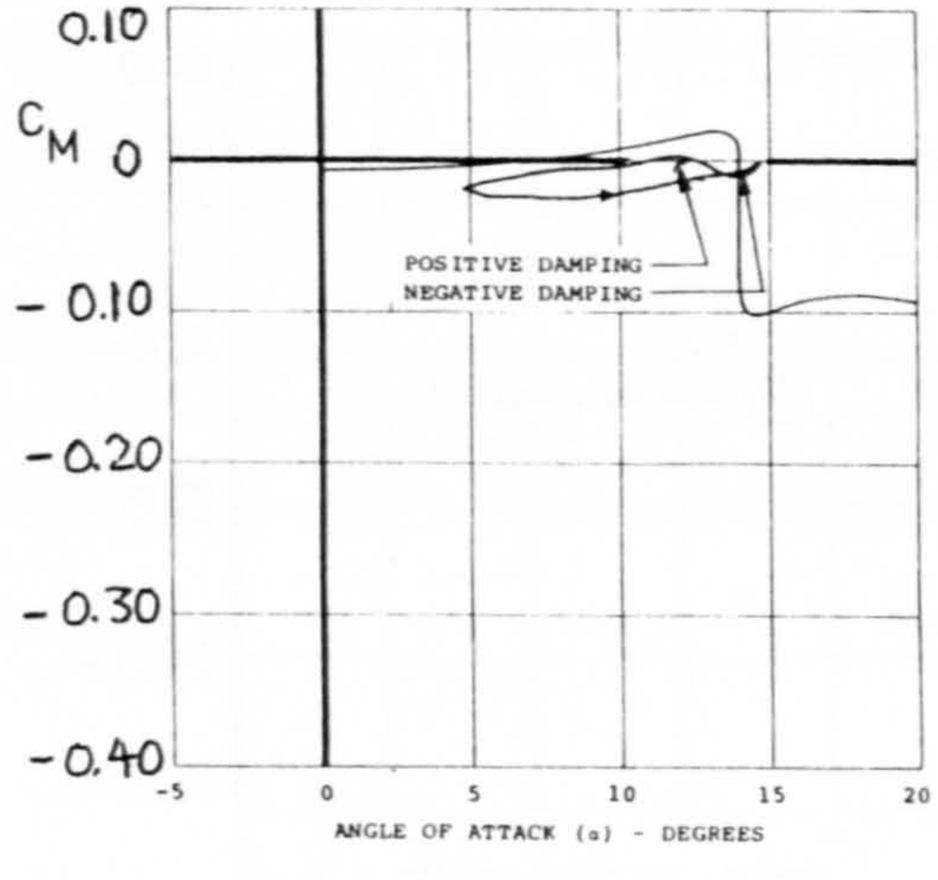

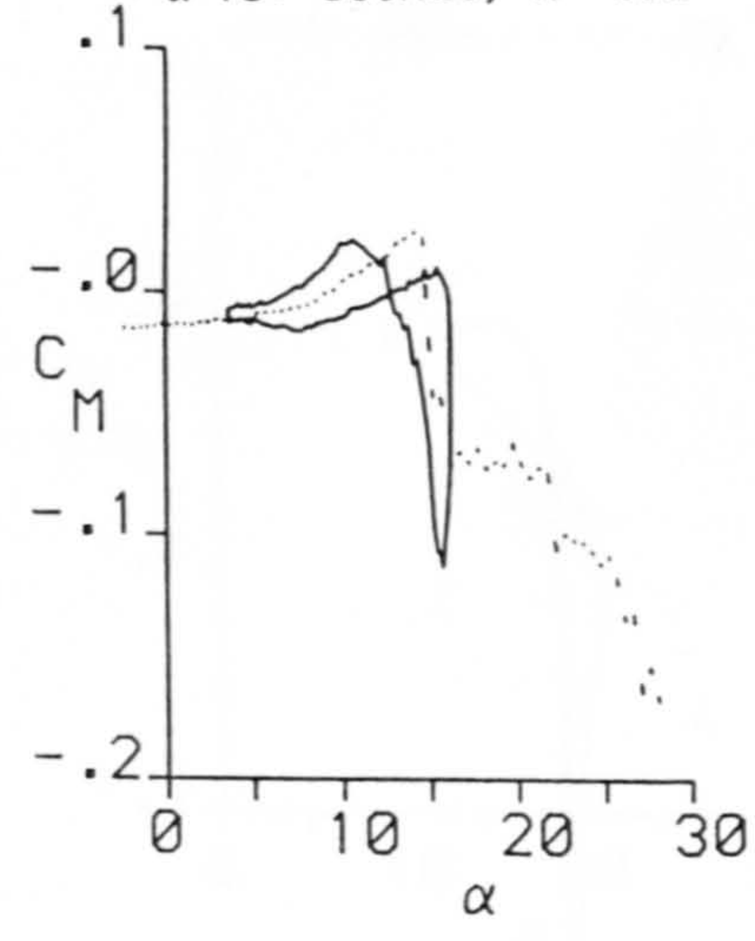

Figure 7.202

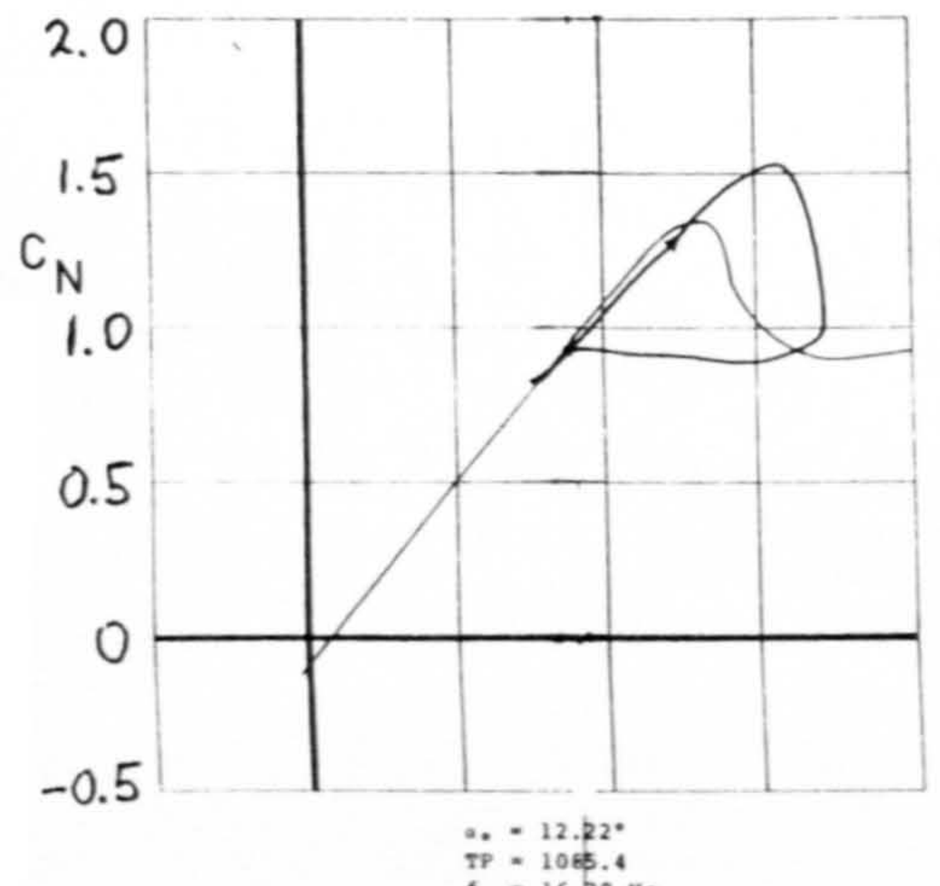

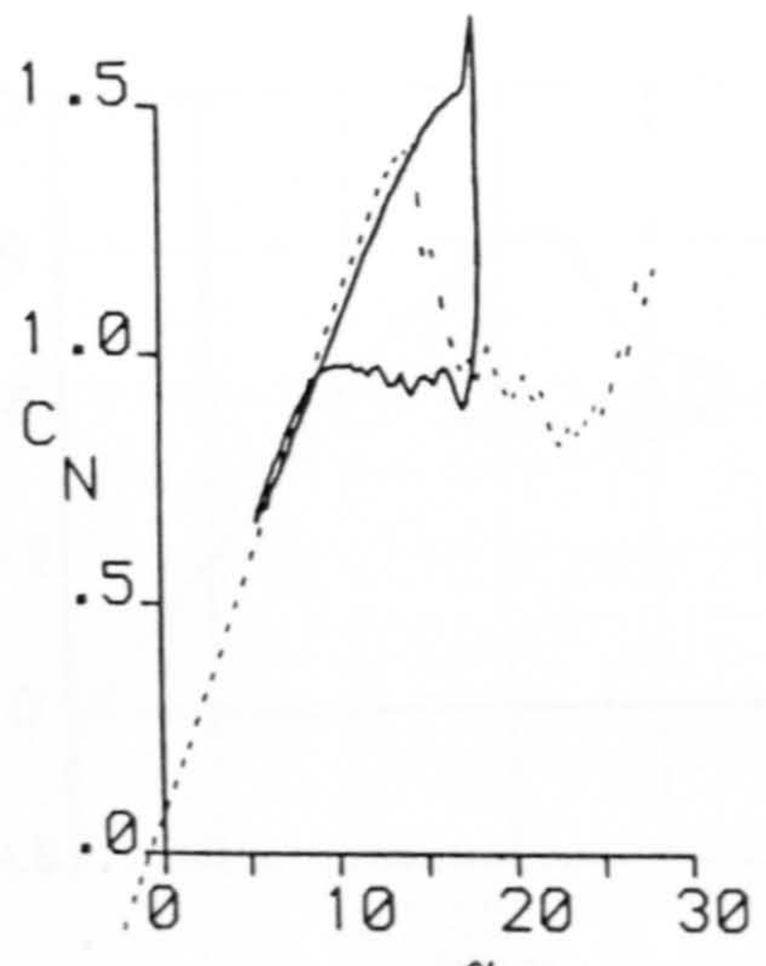

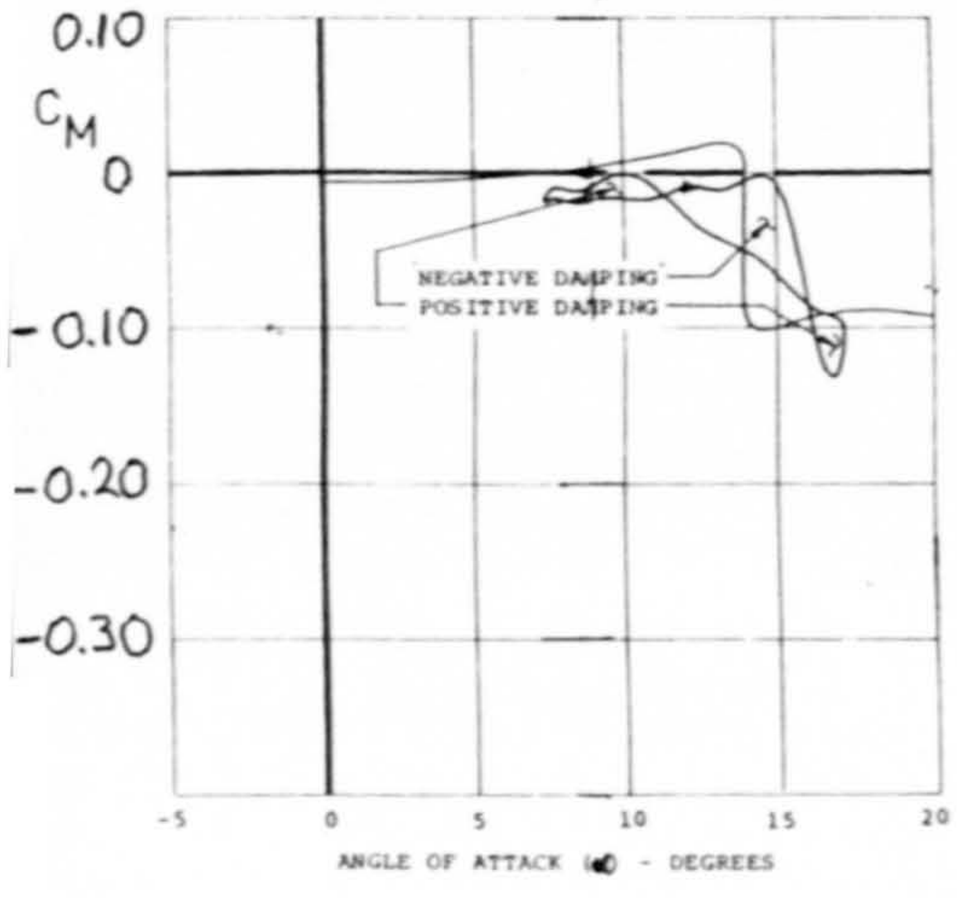

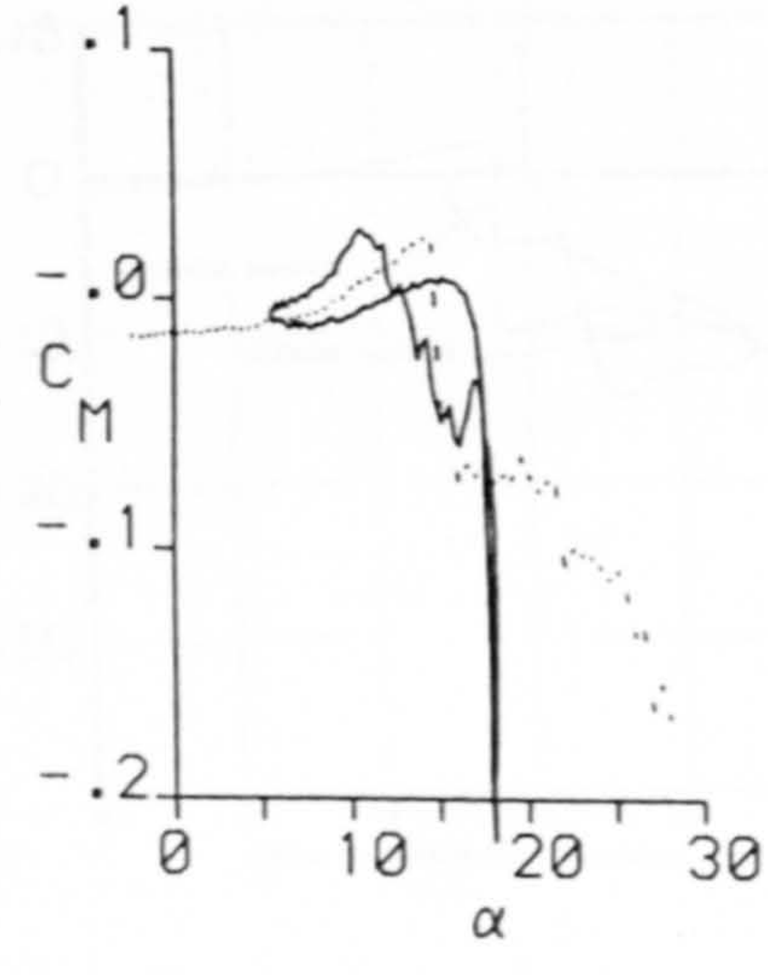

Figure 7.203

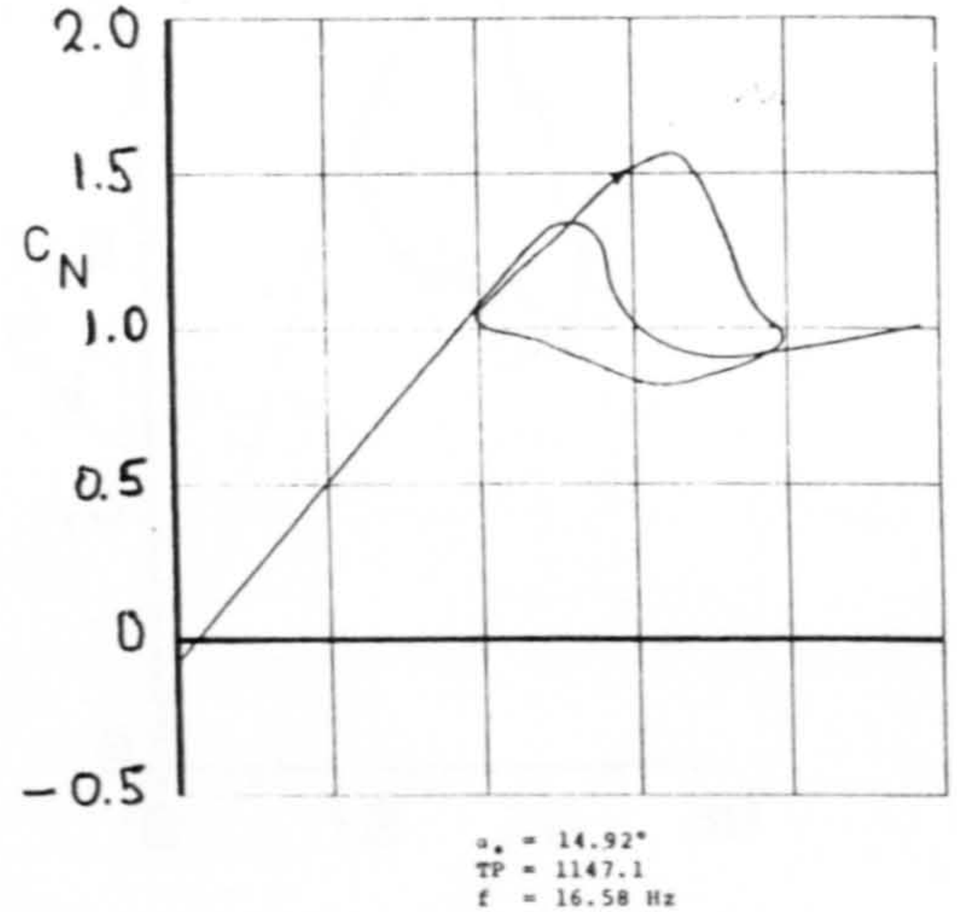

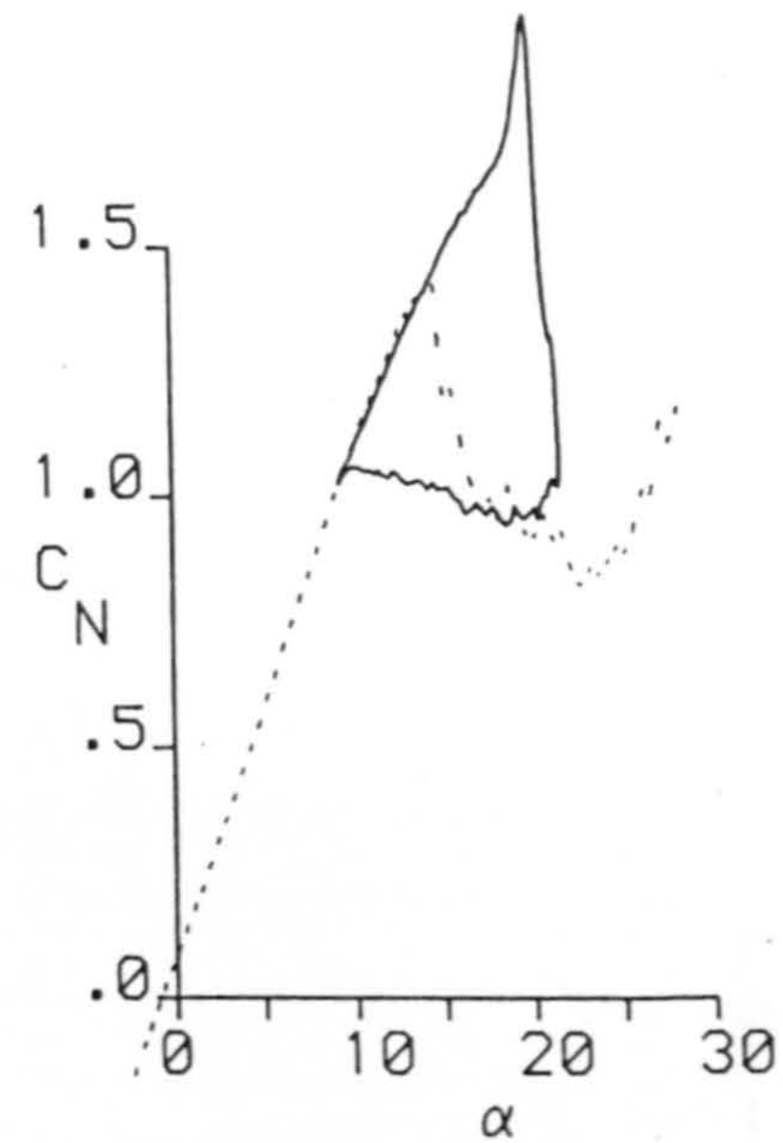

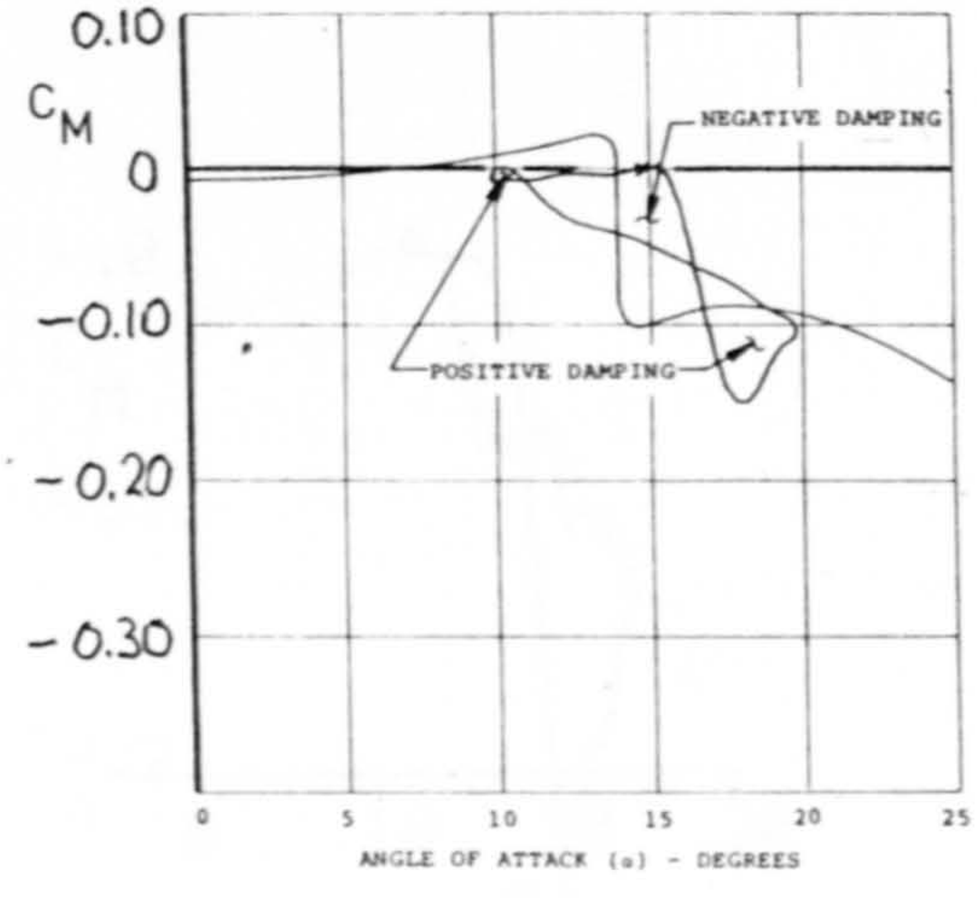

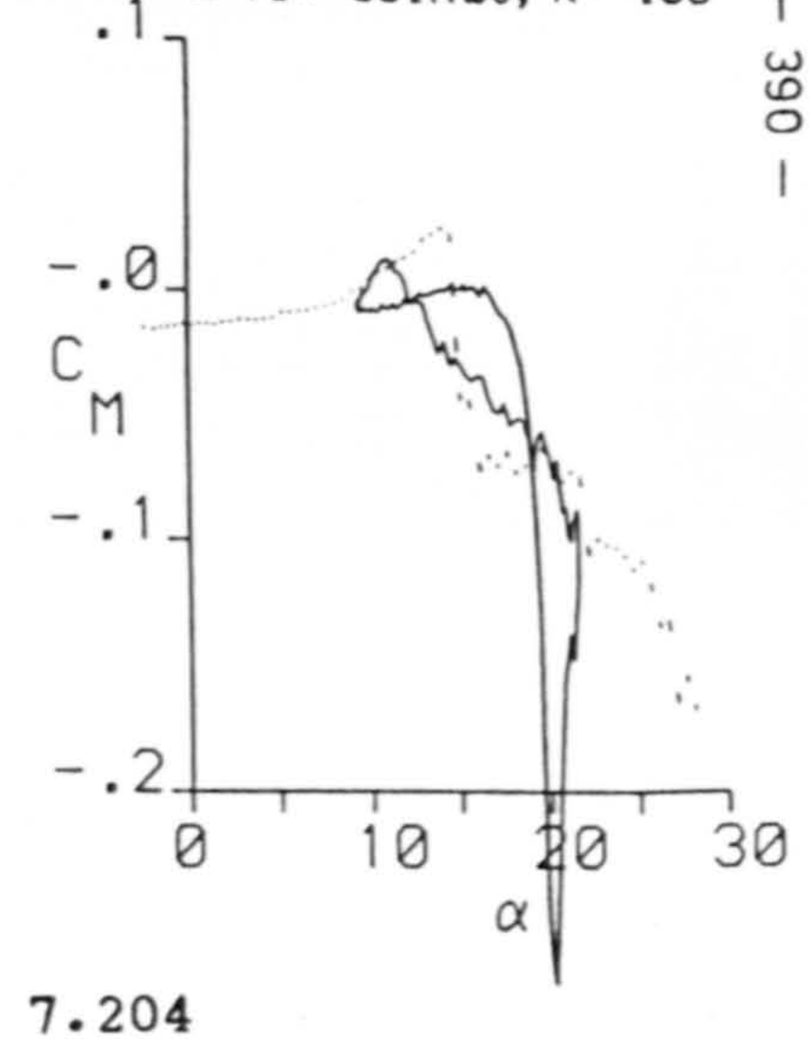

Figure 7.204

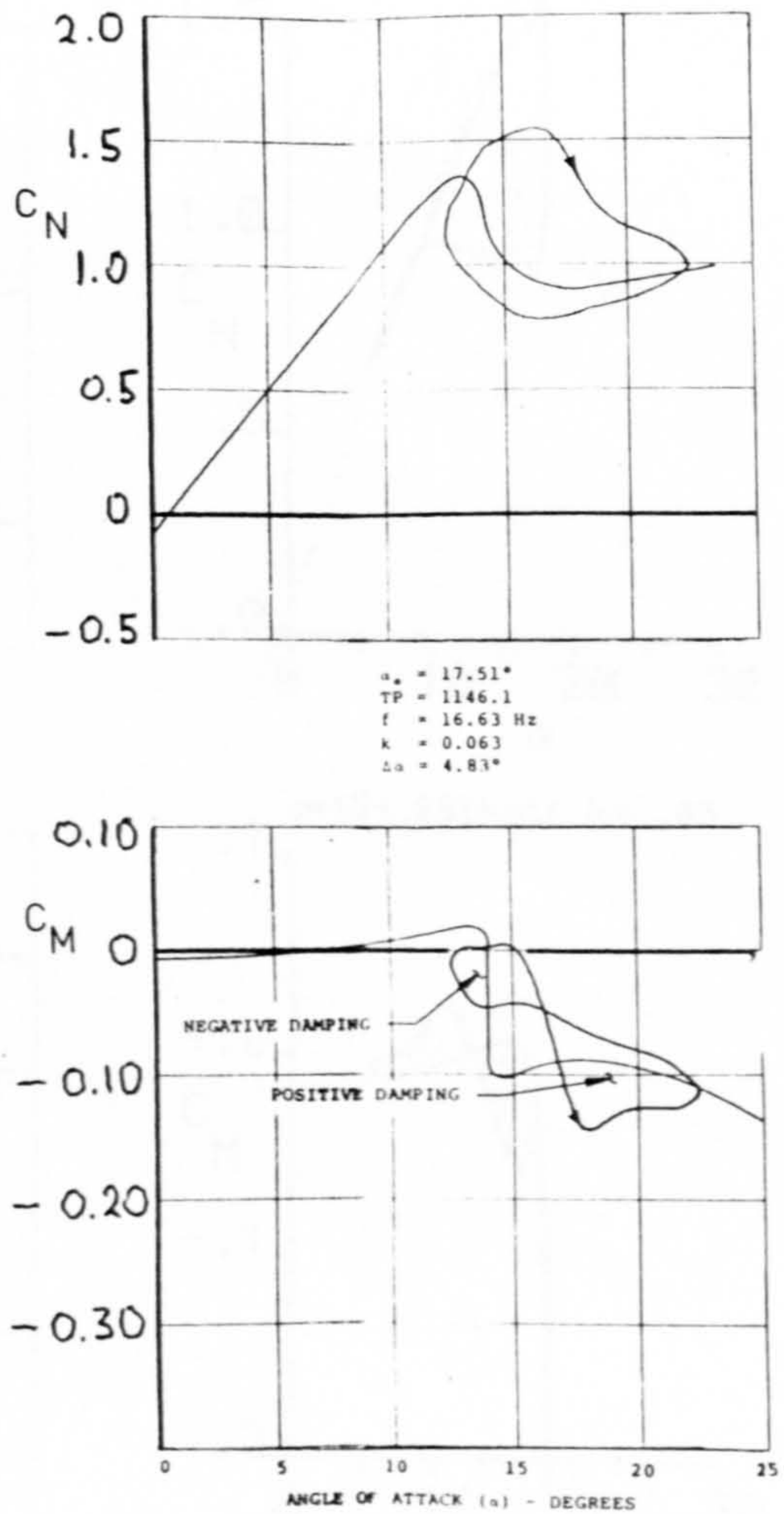
2.0
1.5
C_N
1.0
0.5
0
−0.5
$\alpha_* = 17.51°$
TP = 1146.1
f = 16.63 Hz
k = 0.063
$\Delta\alpha = 4.83°$
0.10
C_M 0
− 0.10
− 0.20
− 0.30
NEGATIVE DAMPING
POSITIVE DAMPING
0
5
10
15
20
25
ANGLE OF ATTACK (α) - DEGREES

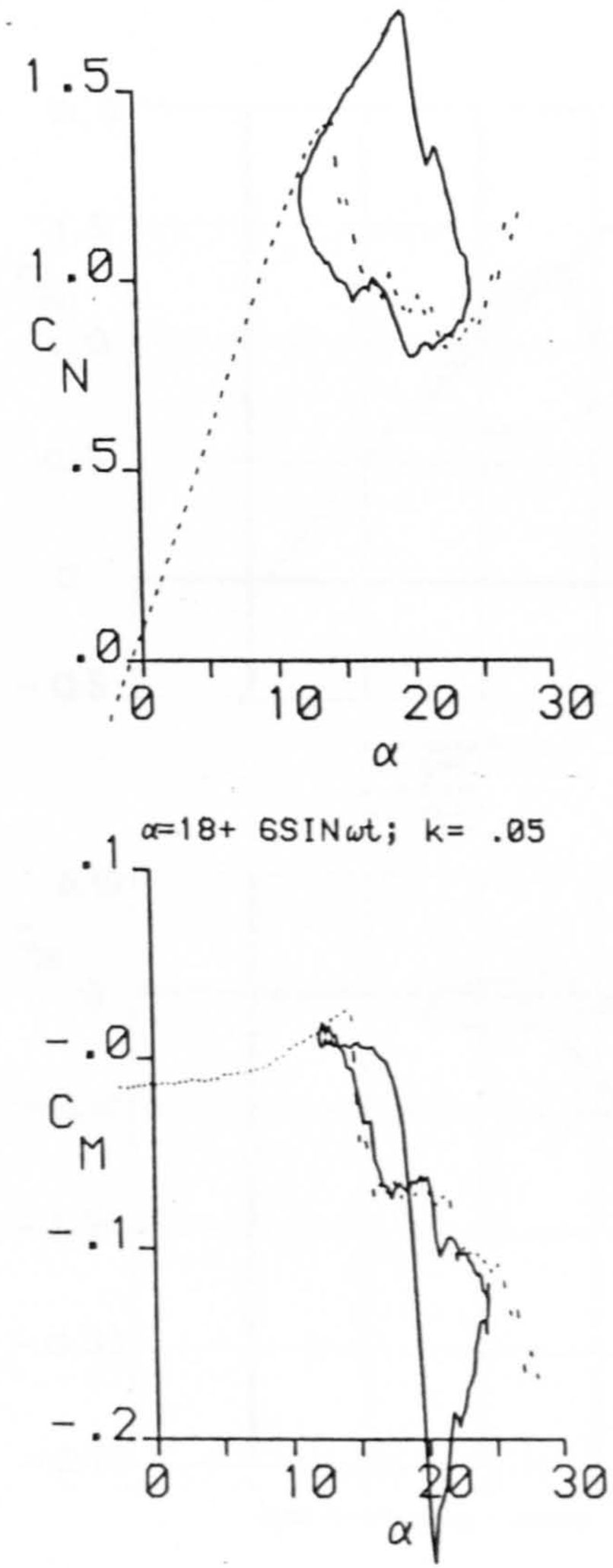
1.5
1.0
C_N
.5
.0
0
10
20
30
α
α=18+ 6SINωt; k= .05
.1
−.0
C_M
−.1
−.2
0
10
20
30
α

Figure 7.205

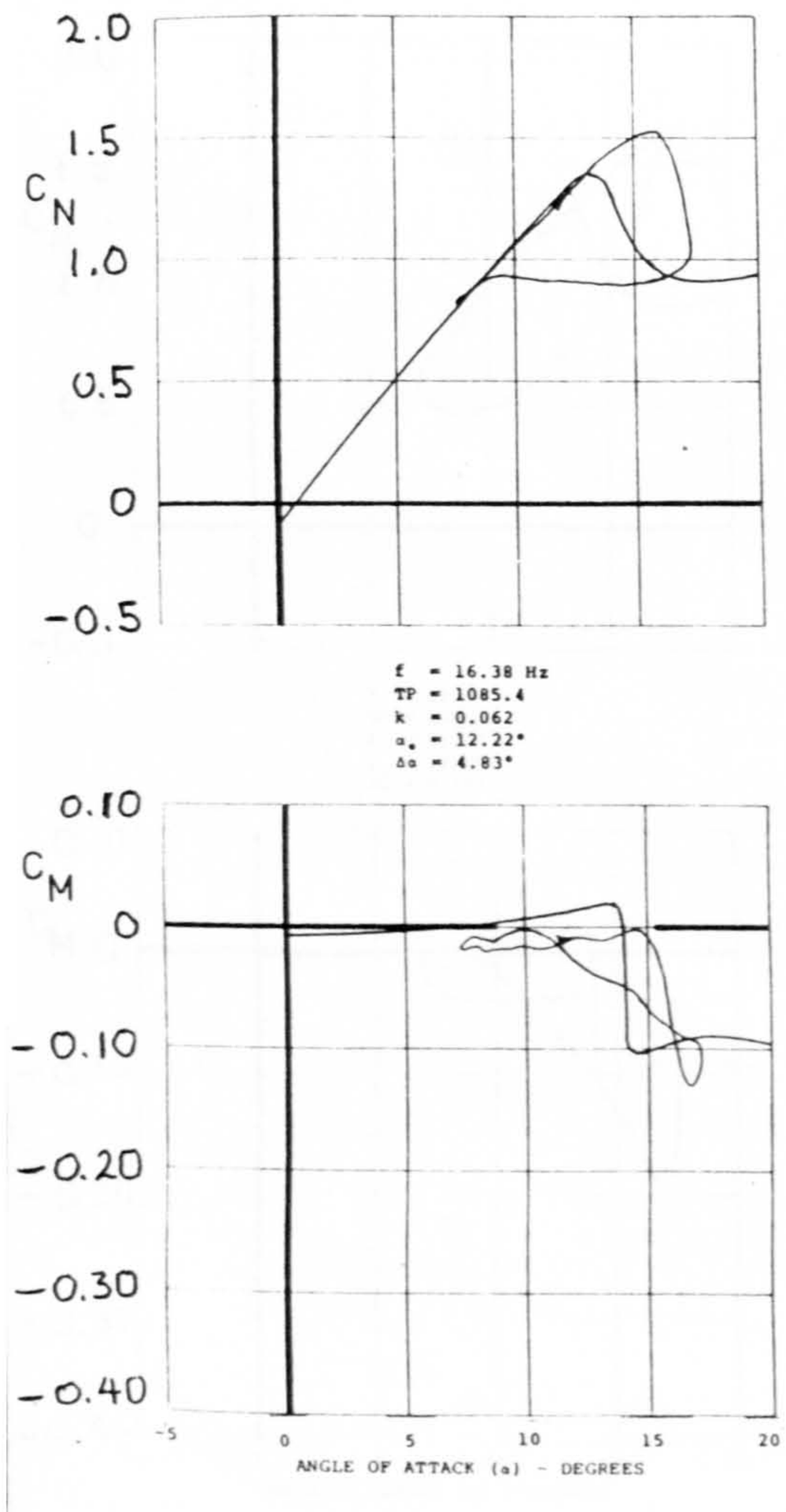

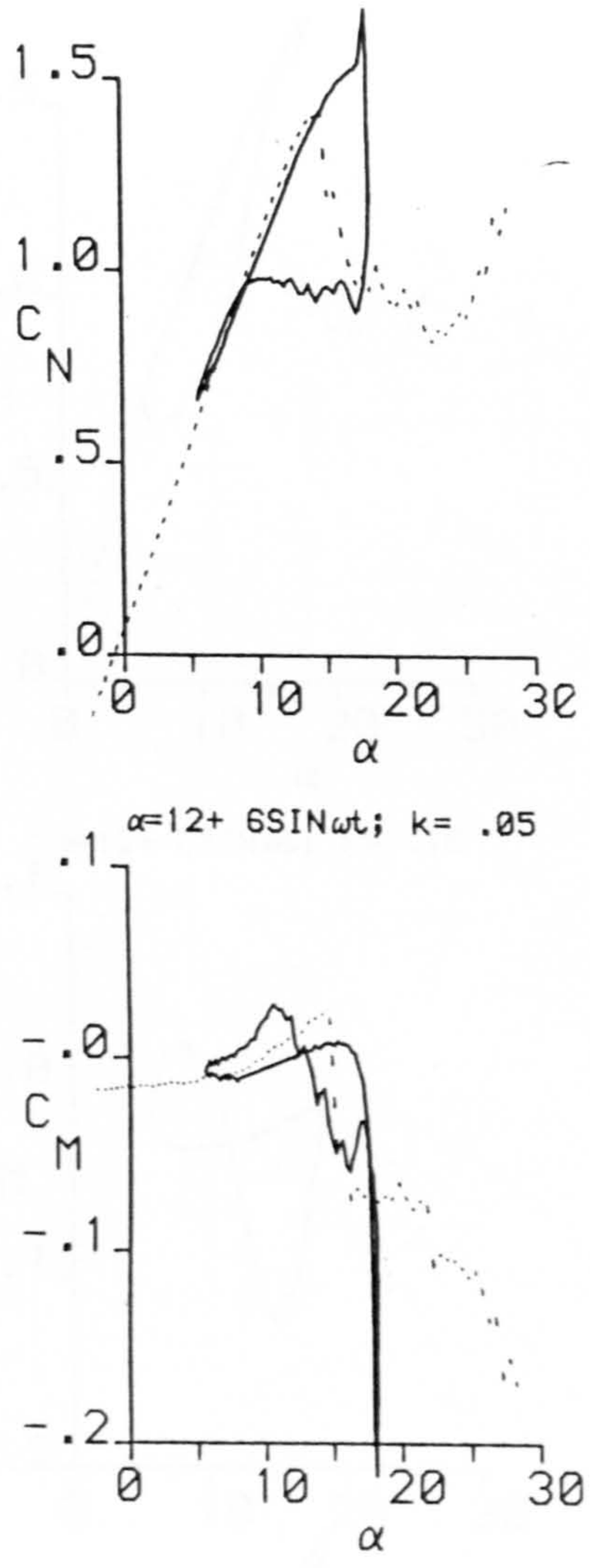

Figure 7.206

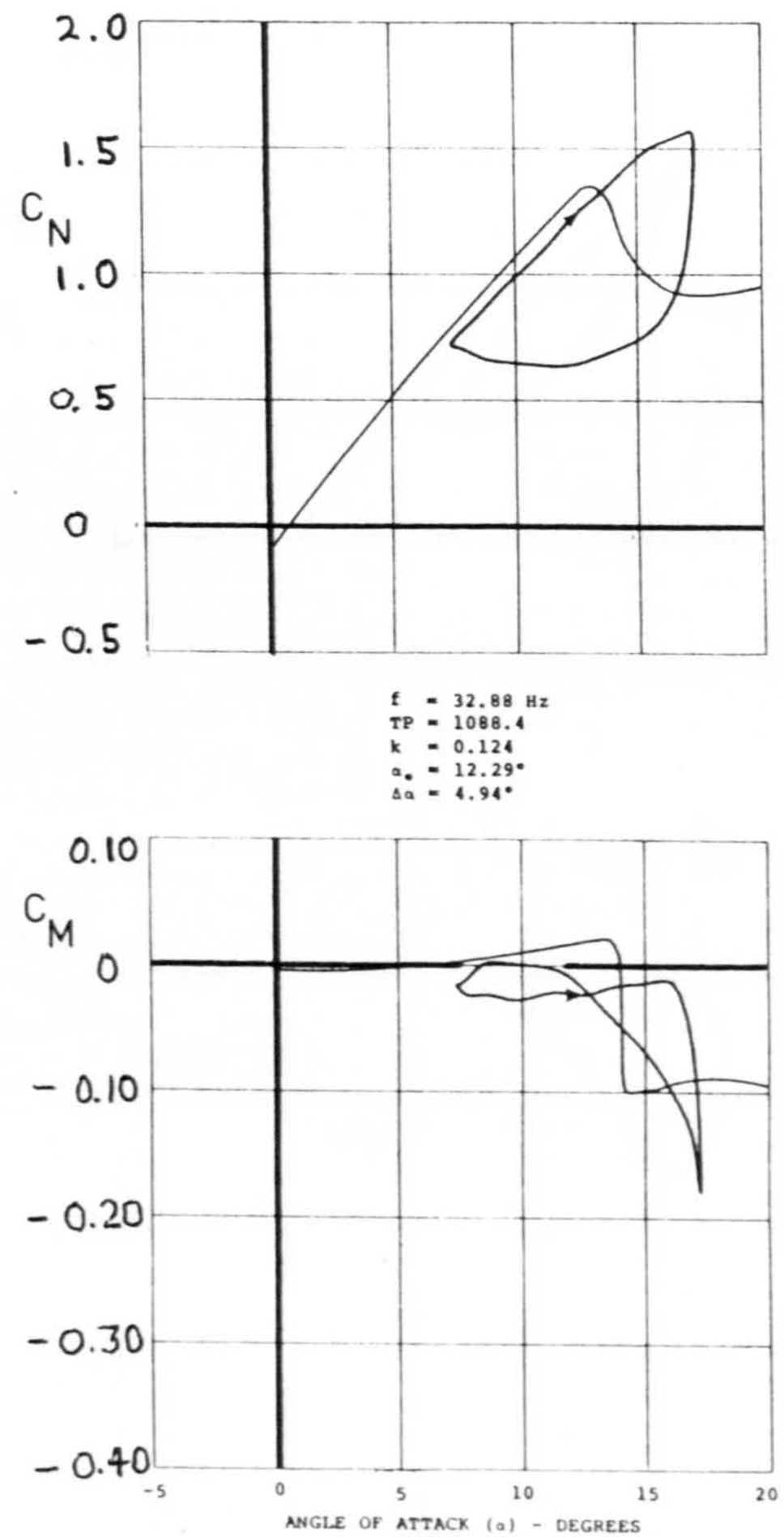

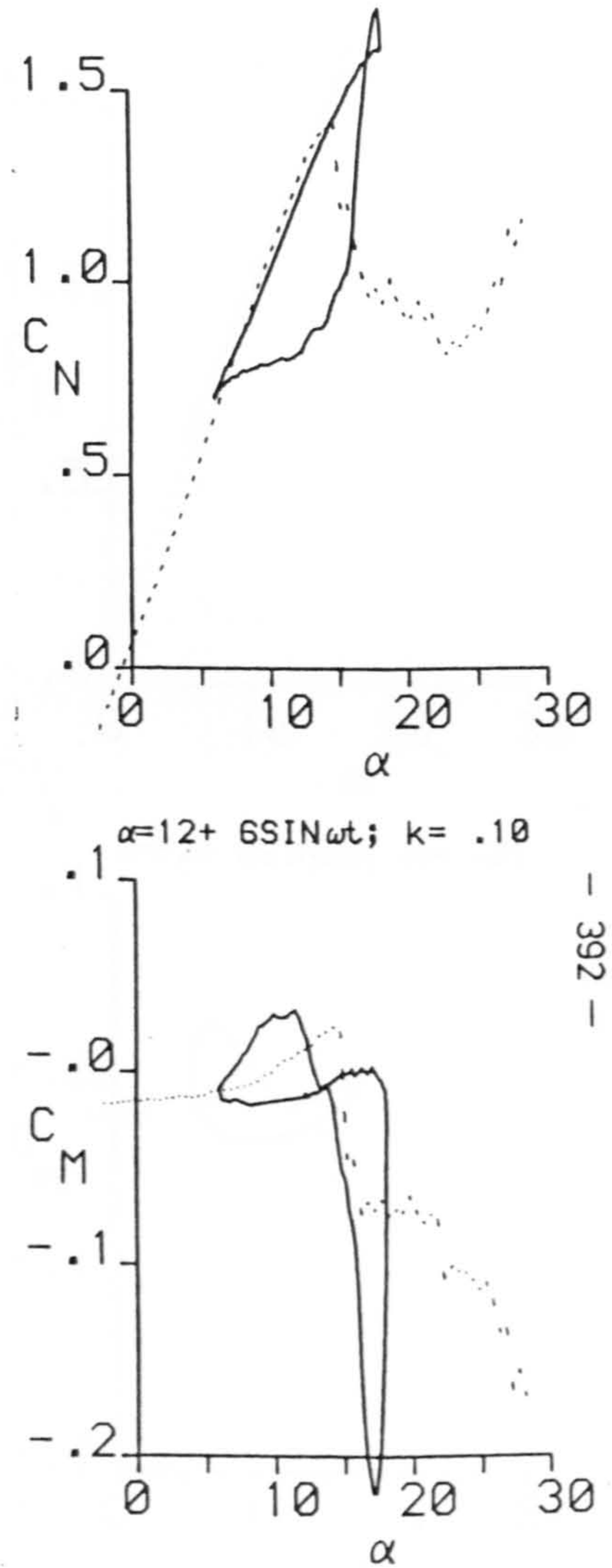

Figure 7.207

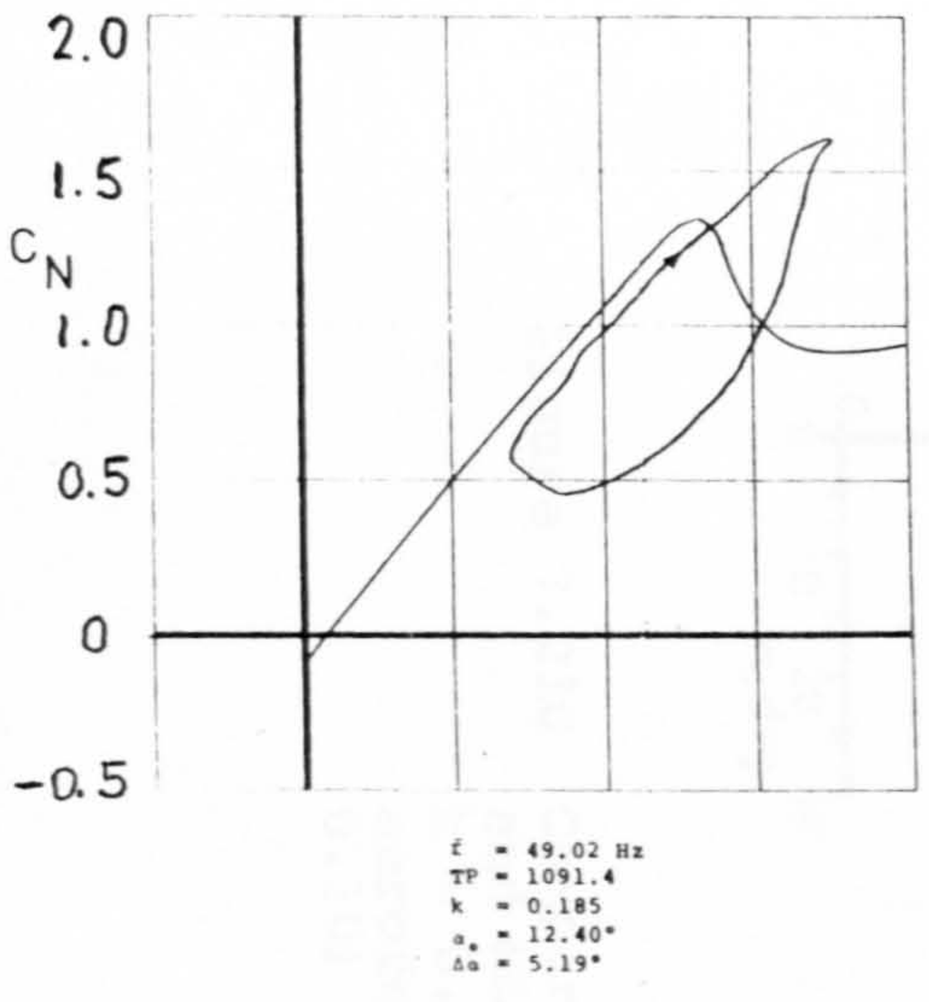

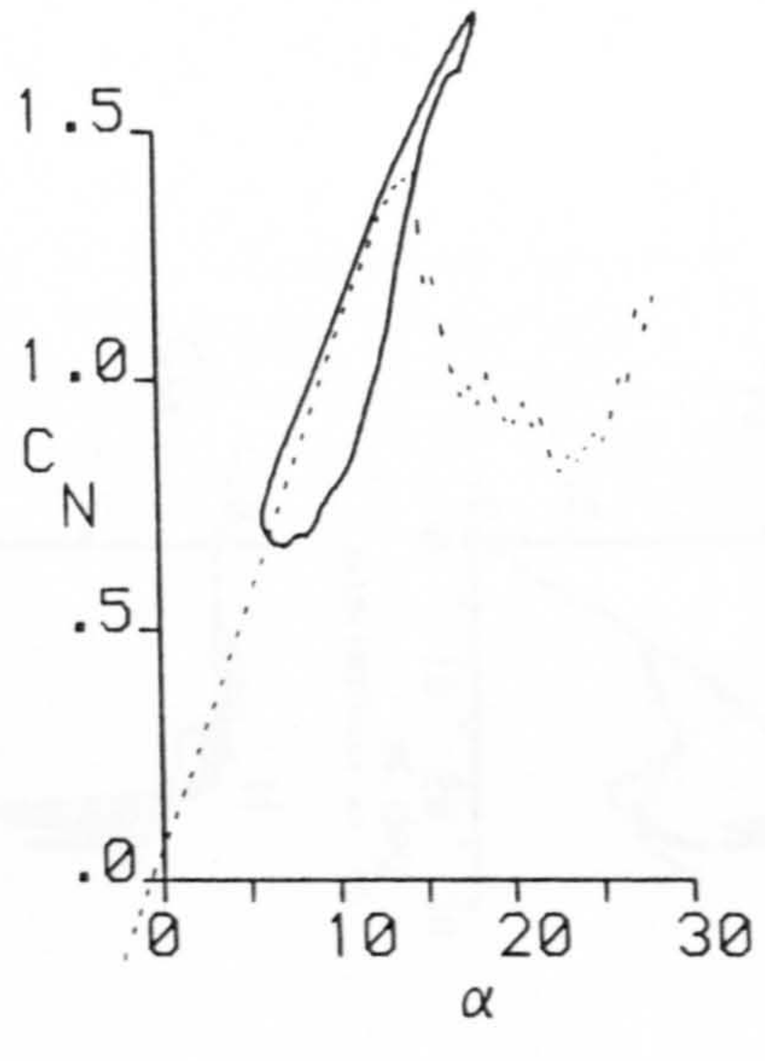

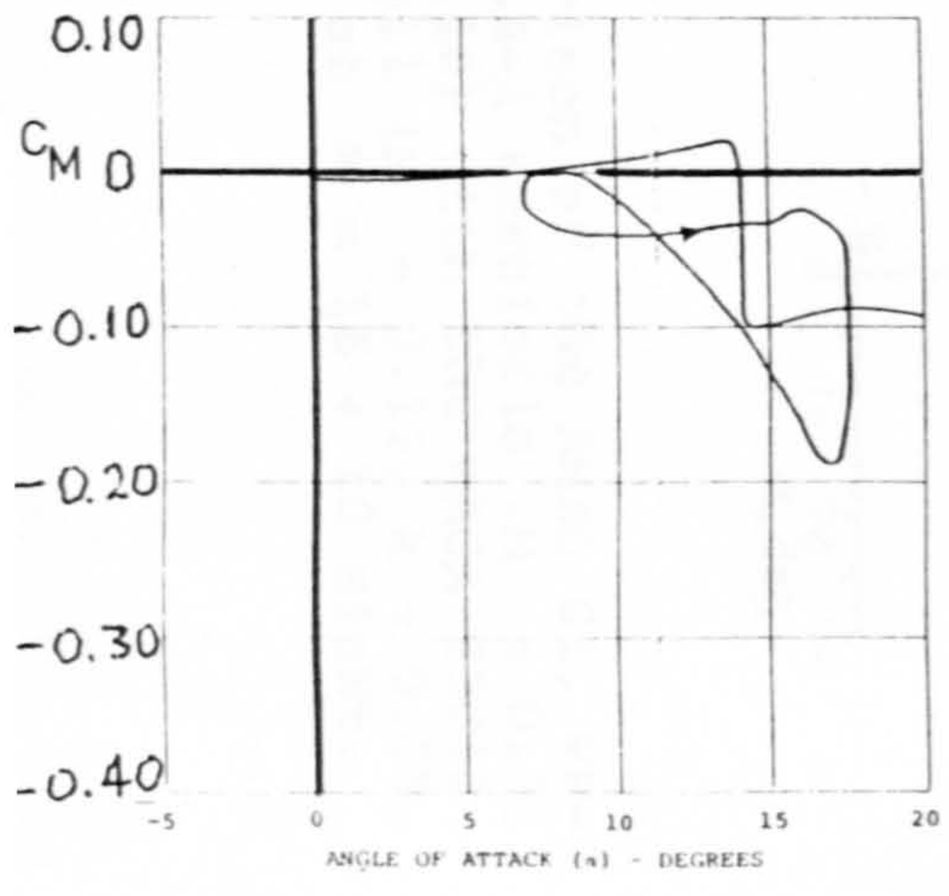

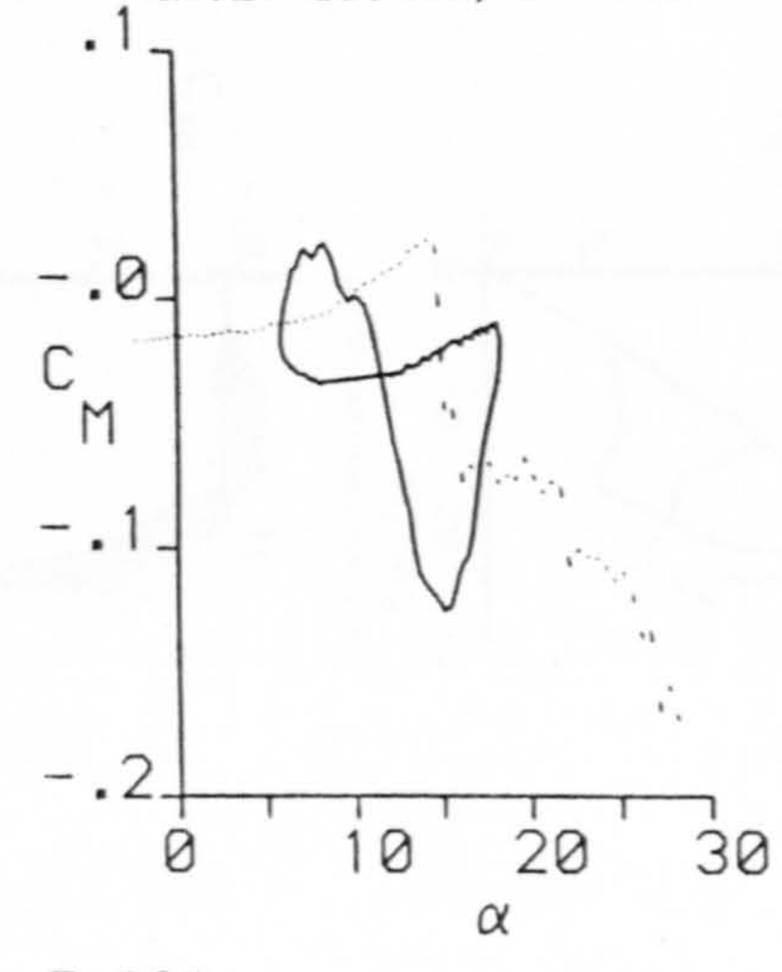

Figure 7.208

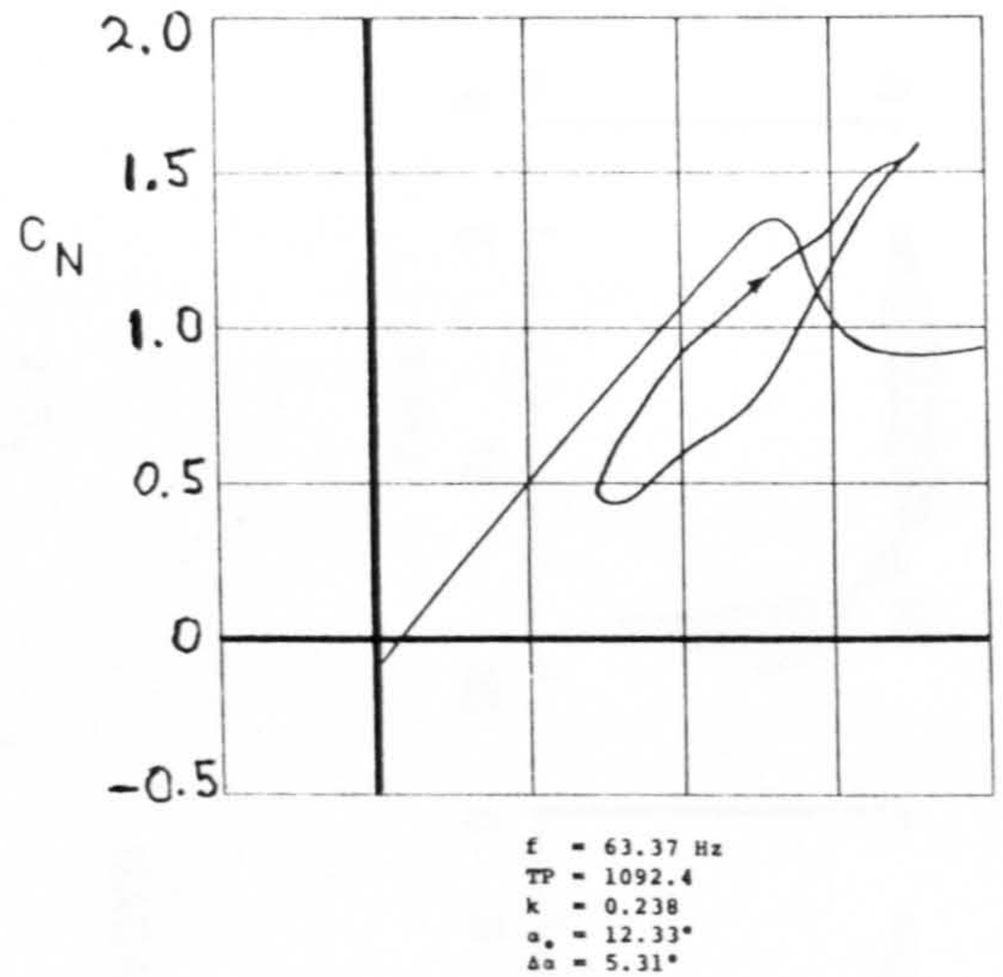

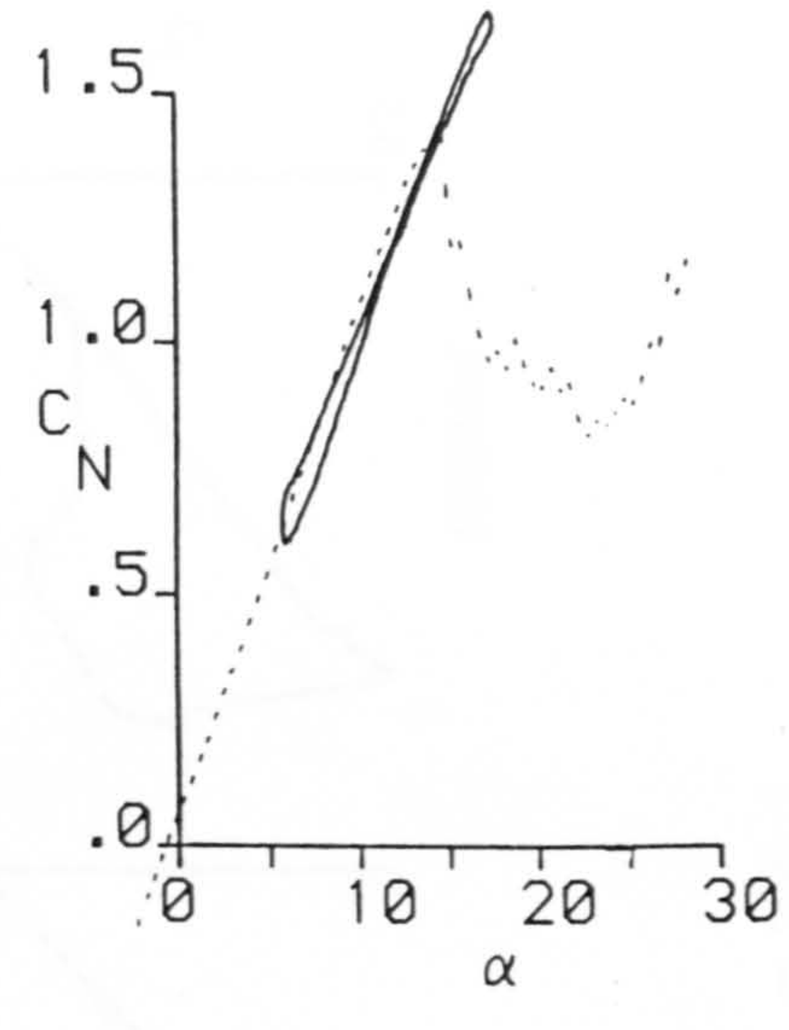

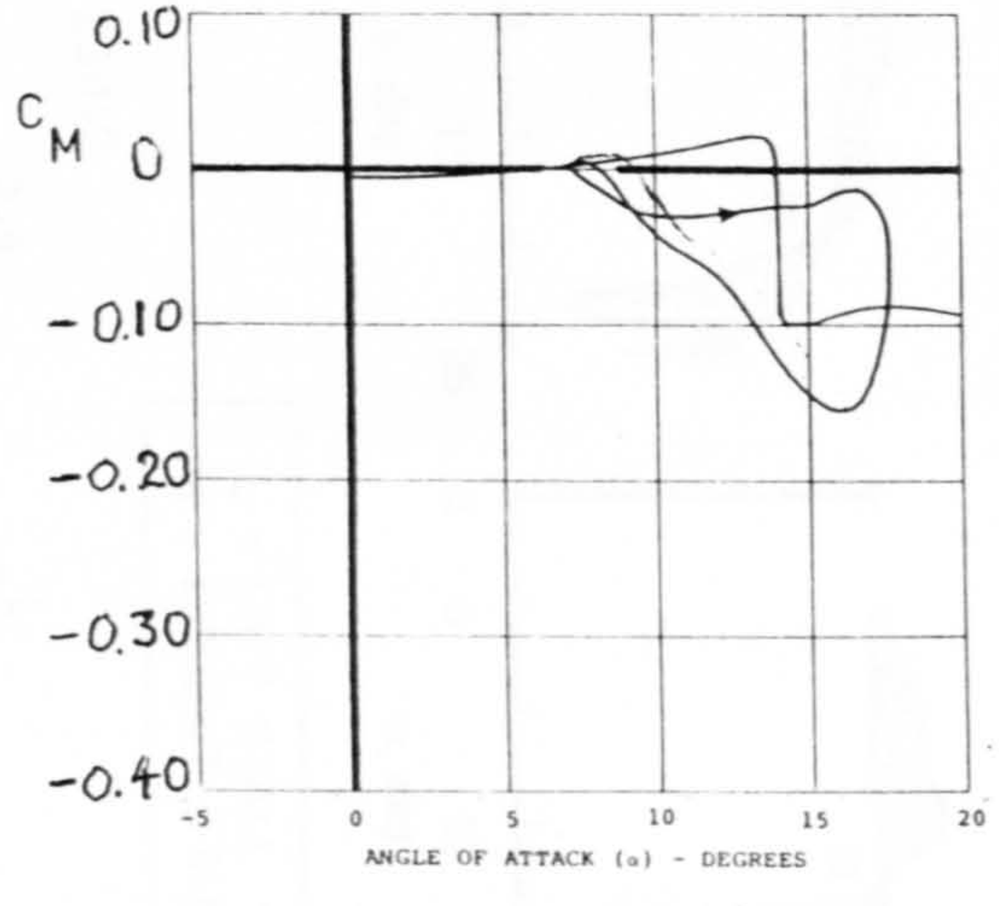

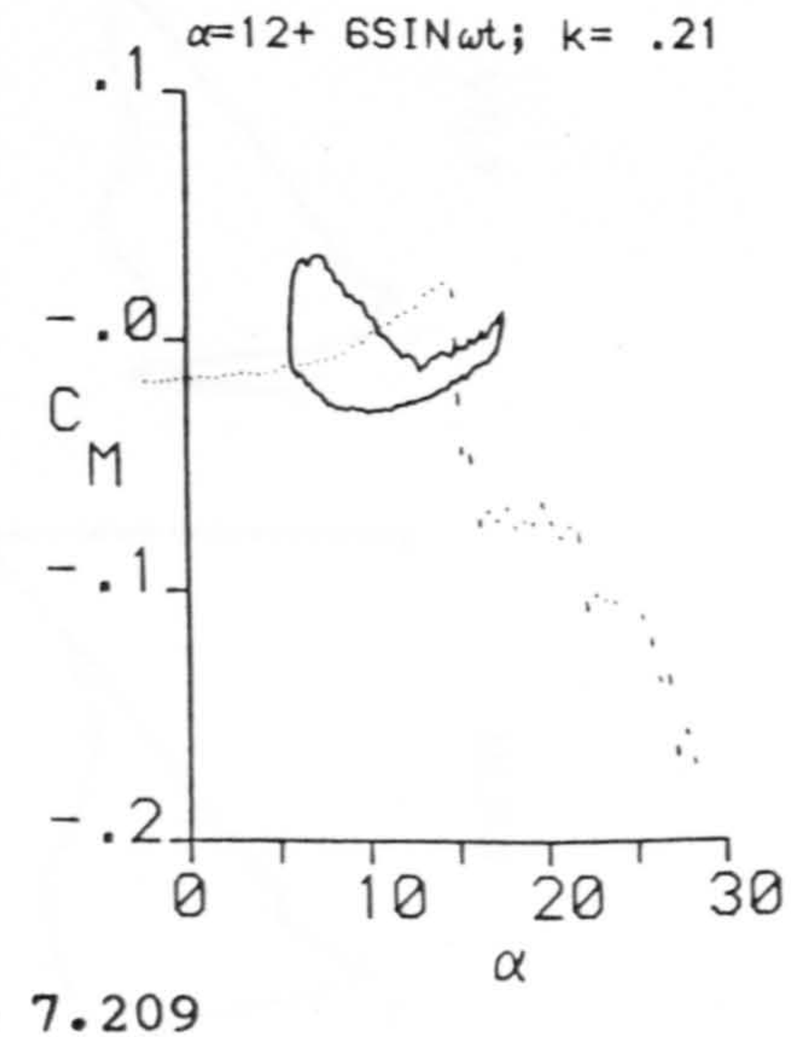

Figure 7.209

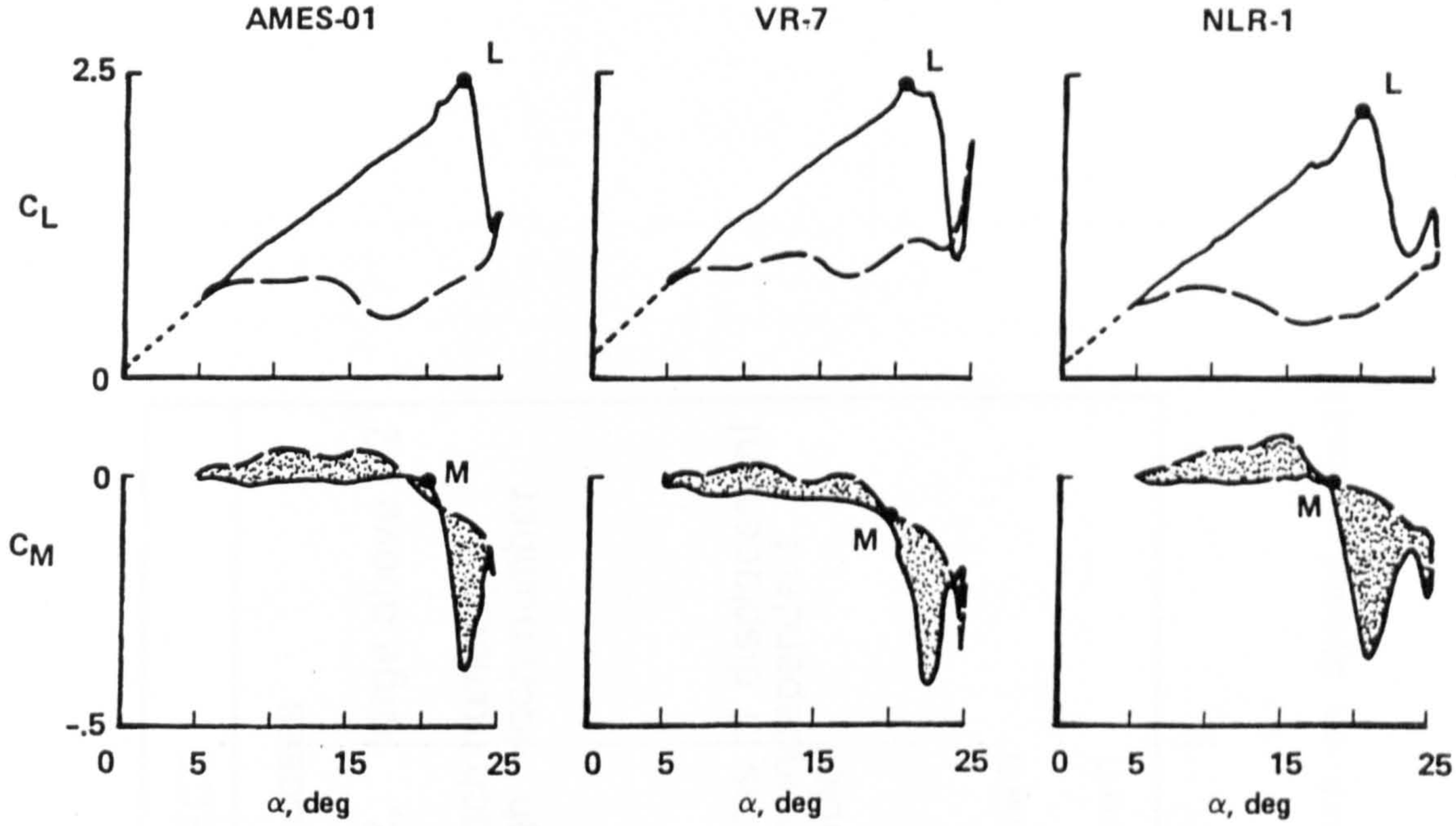

NACA 23012

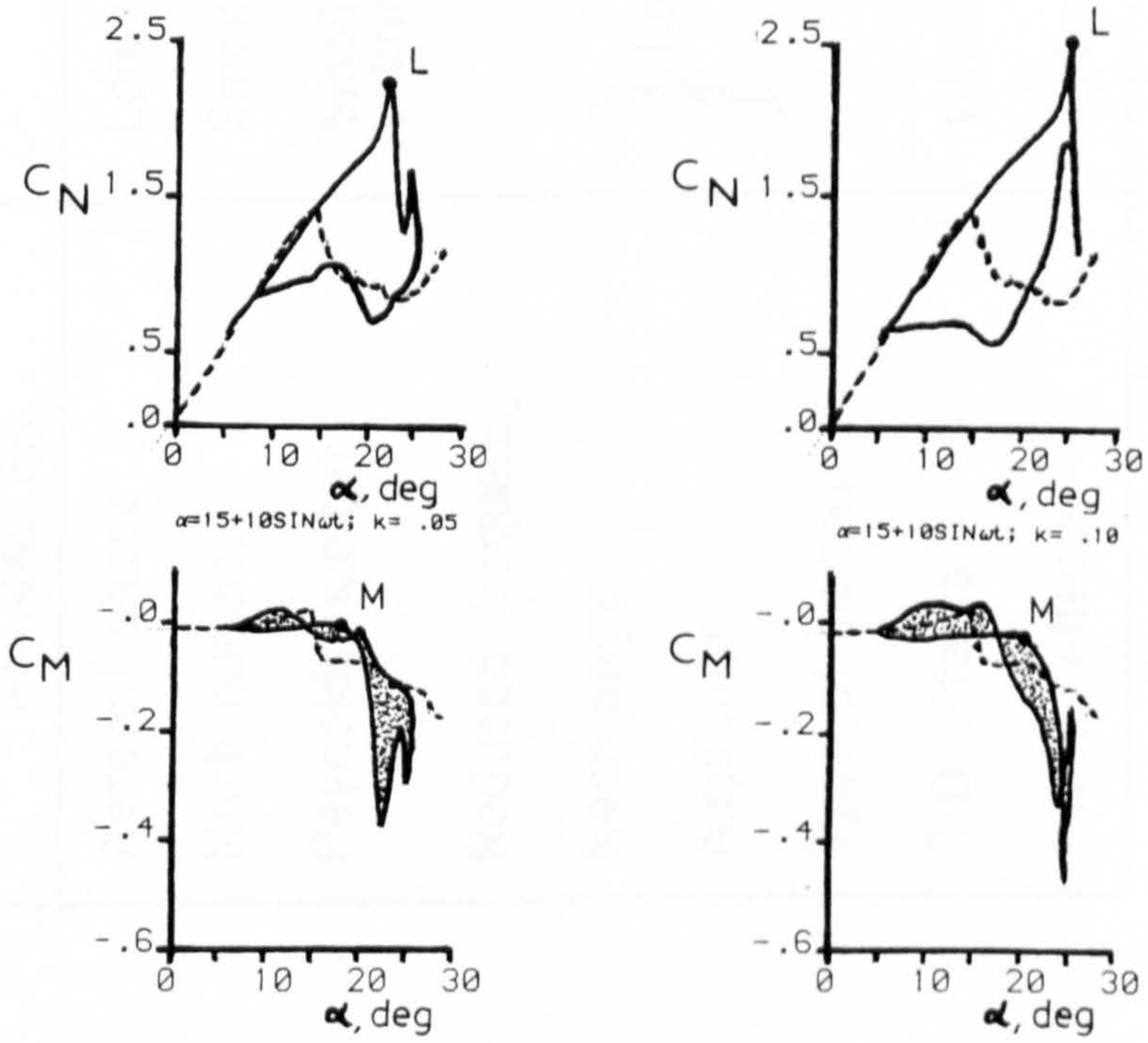

Figure 7.210 Comparison of the AMES-01, VR-7 and NLR-1 aerofoils ($M = 0.3$, $k = 0.10$) with the NACA 23012 aerofoil ($M = 0.12$, $k = 0.05$, 0.10) at $\alpha = 15 + 10\ \mathrm{Sin}\omega t$.

PARAMETER	EFFECT
Aerofoil shape	Large in some cases
Mach number	Small below 0.2, large above 0.2
Reynolds number	Small at low Mach number, unknown at high Mach number
Reduced frequency	} Large (in terms of displacement as an independent variable)
Mean angle	
Amplitude	
Type of motion	
3-D effects	Virtually unknown
Tunnel effects	Virtually unknown

Table 1.1 Importance of various parameters on dynamic stall.

NOMINAL VALUES			VALUES FROM F.F.T. [1]			
α_m°	α_a°	F (Hz)	α_m°	α_a°	α_2°	ϕ_2°
6.0	2.0	0.233	5.29	2.02	0.00	0.00
6.0	6.0	0.233	5.89	6.16	0.06	-265.2
6.0	10.0	0.233	5.66	10.02	0.13	-265.8
13.0	2.0	0.233	12.99	2.052	0.00	0.00
13.0	6.0	0.233	12.93	6.14	0.00	0.00
13.0	10.0	0.233	12.99	9.98	0.00	0.00
20.0	2.0	0.233	19.97	2.05	0.00	0.00
20.0	6.0	0.233	19.97	6.14	0.00	0.00
20.0	10.0	0.233	19.97	9.98	0.00	0.00
6.0	2.0	3.498	6.43	226	0.00	0.00
6.0	6.0	3.498	6.34	6.41	0.03	-184.0
6.0	10.0	3.498	6.46	10.31	0.14	-209.1
13.0	2.0	3.498	12.99	2.06	0.00	0.00
13.0	6.0	3.498	12.80	6.08	0.00	0.00
13.0	10.0	3.498	12.80	9.97	0.00	0.00
20.0	2.0	3.498	20.22	2.03	0.00	0.00
20.0	6.0	3.498	20.22	6.14	0.00	0.00
20.0	10.0	3.498	19.97	10.04	0.00	0.00

$$\alpha = \alpha_m + \alpha_a \sin \omega t + \alpha_2 \sin(\omega t + \phi_2)$$

Table 3.1 Fourier analysis of sinusoidal angle-of-attack variation.

	DEC SOFTWARE		CUSTOMISED SOFTWARE	
	32 CHANNEL RATE	SINGLE CHANNEL RATE	32 CHANNEL RATE	SINGLE CHANNEL RATE
LSI 11/03 PROCESSOR	200Hz	8,500Hz	410Hz	13,700Hz
LSI 11/23 PLUS FLOATING POINT CHIP	NO DATA	NO DATA	510Hz	16,500Hz
LSI 11/23 PLUS FPF-11 FLOATING POINT HARDWARE	310Hz	11,500Hz	550Hz	17,650Hz
LSI 11/23 PLUS FPF-11 WITH LINE CLOCK DISABLED	NO DATA	NO DATA	605Hz	19,450Hz
LSI 11/23 PLUS FPF-11. LINE CLOCK DISABLED STARTING NEXT CONVERSION BEFORE MOVING PREVIOUS CONVERSION TO MEMORY	NO DATA	NO DATA	625Hz	20,500Hz

Table 4.1 Comparison of maximum A/D sampling rates with various hardware/software configurations.

LOCATION	CONTENTS	LOCATION	CONTENTS
1	Run number	27	No. of processed blocks
2	Day of test	28	Cp's = 0, Volts = 1
3	Month of test	29	Spare
4	Year of test	30	Spare
5	Temperature (^{o}C)	31	Spare
6	Pressure (MM Hg)	32	Spare
7	Motion Type (0,1,2)	33	Transducer Calibration Values
8	Mean Angle		
9	Amplitude		
10	Oscillation Frequency		
11	No. of Sweeps/Cycle		
12	No. of Data Values/Cycle	64	
13	No. of Cycles	65	Channel Gain Values
14	Total No. of Samples		
15	No. of Blocks on Disk		
16	Clock: IRATE		
17	Clock: IPRSET		
18	Sampling Frequency (Hz)	96	
19	Dynamic Pressure	97	Channel Offset Values
20	Reynolds Number		
21	Mach Number		
22	Reduced Frequency		
23	Velocity (MS^{-1})		
24	No. Blocks/Cycle	128	
25	No. of Data Points in unfilled silo		
26	Averaged = 1 Unaveraged = 0		

Table 4.2 Contents of the run information buffer (first 256 word block in file).

0	1	2	3	4	5	6	7	8	9	10	11	12	13	14	15
16	17	18	19	20	21	22	23	24	25	26	27	28	29	30	31
0	1	2	3	4	5	6	7	8	9	10	11	12	13	14	15
16	17	18.	19	20	21	22	23	24	25	26	27	28	29	30	31
0	1	2	3	4	5	6	7	8	9	10	11	12	13	14	15
16	17	18	19	20	21	22	23	24	25	26	27	28	29	30	31
0	1	2	3	4	5	6	7	8	9	10	11	12	13	14	15
16	17	18	19	20	21	22	23	24	25	26	27	28	29	30	31

1

2

3

4

0	1	2	3	4	5	6	7	8	9	10	11	12	13	14	15
16	17	18	19	20	21	22	23	24	25	26	27	28	29	30	31

N

□ 1 WORD = 2 BYTES

1 BLOCK = 256 WORDS

Table 4.3 Sequence of channel A/D conversions in a raw data file.

0	1	2	3	4	5	6	7
8	9	10	11	12	13	14	15
16	17	18	19	20	21	22	23
24	25	26	27	28	29	30	31

} 1

0	1	2	3	4	5	6	7
8	9	10	11	12	13	14	15
16	17	18	19	20	21	22	23
24	25	26	27	28	29	30	31

} 2

0	1	2	3	4	5	6	7
8	9	10	11	12	13	14	15
16	17	18	19	20	21	22	23
24	25	26	27	28	29	30	31

} N

2 WORDS = 4 BYTES

1 BLOCK = 256 WORDS

Table 4.4 Sequence of channel A/D conversions in a processed data file.

MEAN ANGLES α_m	6	8	10	12	13	14	15	16	18	20
AMPLITUDES α_a	2		4		6		8		10	
REDUCED FREQUENCIES	0.01		0.05		0.10		0.15		0.20	
REYNOLDS NUMBERS	1.0×10^6					1.5×10^6				

N.B. BOXES MARKED WITH A ◥ DENOTE HOT FILM DATA RECORDED.

Table 5.1 Discrete values of mean angle, amplitude, reduced frequency and Reynolds number for oscillatory aerofoil tests.